JAERI-Review
99-007

研究炉利用における研究成果集（平成9年度）

1999年3月

（編）豊田政幸・小山芳己

日本原子力研究所
Japan Atomic Energy Research Institute

本レポートは，日本原子力研究所が不定期に公刊している研究報告書です。
入手の問合わせは，日本原子力研究所研究情報部研究情報課（〒319-1195 茨城県那珂郡東海村）あて，お申し越しください。なお，このほかに財団法人原子力弘済会資料センター（〒319-1195 茨城県那珂郡東海村日本原子力研究所内）で複写による実費領布をおこなっております。

This report is issued irregularly.
Inquiries about availability of the reports should be addressed to Research Information Division, Department of Intellectual Resources, Japan Atomic Energy Research Institute, Tokai-mura, Naka-gun, Ibarakiken 319-1195, Japan.

編集兼発行　日本原子力研究所

研究炉利用における研究成果集（平成９年度）

日本原子力研究所東海研究所研究炉部
（編）豊田　政幸・小山　芳己

（1999年２月３日受理）

平成９年度における研究炉での実験利用、照射利用を行った利用者（原研外を含む）からの成果の提出を受け、これを取りまとめたものである。

東海研究所：〒319-1195　茨城県那珂郡東海村白方白根2-4

Activity Report on the Utilization of Research Reactors (Japanese Fiscal Year, 1997)

(Eds.) Masayuki TOYODA and Yoshimi KOYAMA

Department of Research Reactor
Tokai Research Establishment
Japan Atomic Energy Research Institute
Tokai-mura, Naka-gun, Ibaraki-ken

(Received February 3, 1999)

This is the first issue of the activity report on the utilization of research reactors in the fields of neutron beam experiments, neutron activation analysis, radioisotope production, etc., performed during Japanese Fiscal Year 1997 (April 1, 1997-March 31, 1998).

All reports in this volume were described by users from JAERI and also users from the other organizations, i.e., universities, national research institutes and private companies, who have utilized our research reactor utilization facilities for the purpose of the above studies.

Keywords : Research Reactor, Neutron Scattering, Neutron Radiography, Prompt Gamma-ray Analysis, Neutron Activition Analysis, Neutron Beam, Irradiation

目　　次

Contents

はじめに

平成９年度における研究炉の共同利用運転は、ＪＲＲ－２が平成８年１２月１９日をもって運転を終結したこと、ＪＲＲ－４が燃料濃縮度低減化計画に伴う改造工事を行ったことにより、ＪＲＲ－３Ｍの７サイクルであった。これに伴いさまざまな利用が行われた。本報告書は、これらの当該利用の成果を利用者（原研外利用者を含む）に提出して頂き取りまとめたものである。

提出して頂いた成果の件数は、中性子散乱１９６件、中性子ラジオグラフィ８件、即発γ線分析１０件、放射化分析１８件、原子炉材料２件、ＲＩの製造３件、その他９件で合計２４６件であった。事情により、利用成果を提出して頂けなかった利用者については、その利用内容の一覧を付録に掲載した。なお、本報告書では、中性子散乱、放射化分析等の分野において、下記の報告書の原稿を転載させて頂いた。

最後に、原稿を提出して頂いた利用者の皆様および編集作業に協力して頂いた本田由里恵さんに感謝するとともに、今後とも研究炉が有効に利用されることを期待します。

研究炉利用課長
桜井　文雄

---

1) レポート番号：Vol.5（第５巻）
標　　題　：ACTIVITY REPORT ON NEUTRON SCATTERING RESEARCH
issued by ISSP-NSL,Univ.of Tokyo
（東大物性研発行）
編　　者　：M.Nagao and Y.Fujii（長尾道弘、藤井保彦）
発 行 年　：１９９８年

2) レポート番号：UTRCN-G-27
標　　題　：原研施設利用共同研究成果報告書（平成９年度）
編　　者　：東京大学原子力研究総合センター
発 行 年　：１９９８年

This is a blank page.

研究成果一覧

中性子散乱
1）磁 性

研究テーマ 「表　題」	所属 担当者	利用原子炉 及び装置名	頁
強相関電子系の中性子散乱による研究 「$CuGe_{1-x}Si_xO_3$の磁気相図」	Department of Physics, Aoyama-Gakuin University J.Akimitsu,O.Fujita Neutron Scattering Laboratory,Institute for Solid State Physics,The University of Tokyo M.Nishi,K.Kakurai,Y.Fujii Neutron Scattering Group,Advanced Science Research Center,JAERI S.Katano	JRR-3M 2G (TAS-1)	81
強相関電子系の中性子散乱による研究 「梯子格子物質；$Sr_{2.5}Ca_{11.5}Cu_{24}O_{41}$における反強磁性磁気秩序」	Department of Physics,Aoyama-Gakuin University J.Akimitsu,T.Nagata,H.Fujino Neutron Scattering Laboratory,Institute for Solid State Physics,The University of Tokyo M.Nishi,K.Kakurai Neutron Scattering Group,Advanced Science Research Center,JAERI S.Katano	JRR-3M 2G (TAS-1)	83
強相関電子系の中性子散乱による研究 「少数キャリアー物質CePの外場の下における中性子散乱による研究」	Advanced Science Research Center,JAERI T.Osakabe.Y.Haga Department of Physics,Tokyo Metropolitan University M.Kohgi,K.Iwasa Department of Physics,Tohoku University T.Suzuki	JRR-3M 2G (TAS-1)	85
強相関電子系の中性子散乱による研究 「$KCr_3(OD)_6(SO_4)_2$ (Cr-jarosite)の磁気構造」	JAERI T.Inami Faculty of Integrated Human Studies,Kyoto University Y.Oka	JRR-3M T2-4 (TAS-2)	87
強相関電子系の中性子散乱による研究 「$RbFe(MoO_4)_2$と$CsFe(SO_4)_2$の磁気構造」	JAERI T.Inami	JRR-3M T2-4 (TAS-2)	88

中性子散乱
1）磁 性

強相関電子系の中性子散乱による研究 「Jarosite($KFe_3(OH)_6(SO_4)_2$)の磁気構造」	JAERI T.Inami Institute for Chemical Research,Kyoto University M.Takano Faculty of Integrated Human Studies,Kyoto University Y.Oka	JRR-3M 1G (HRPD)	89
強相関電子系の中性子散乱による研究 「Ca_3BMnO_6(B=Zn,Ni)の磁気構造」	JAERI T.Inami Institute for Chemical Research,Kyoto University S.Kawasaki,M.Takano	JRR-3M 1G (HRPD)	90
強相関電子系の中性子散乱による研究 「層状混合原子価系$LuFe_2O_4$の強磁場下の中性子散乱」	Advanced Research Institute for Science and Engineering,Waseda University K.Kitsuta,N.Ikeda,Y.Yamada JAERI T.Inami,K.Katano	JRR-3M 2G (TAS-1)	91
電子デバイス材料の構造と物性に関する研究 「窒素侵入型化合物$Y_2Fe_{17}N_{3.1}$の中性子回折」	Faculty of Integrated Arts and Sciences, Hiroshima University K.Koyama,H.Fujii,M.Akayama Department of Applied Physics,Tohoku University T.Kajitani Advanced Science Research Center,JAERI Y.Morii	JRR-3M 1G (HRPD)	92
電子デバイス材料の構造と物性に関する研究 「希土類－鉄金属間化合物Ce_2Fe_{17}の中性子回折実験」	Faculty of Integrated Arts and Science, Hiroshima University H.Fukuda,H.Fujii,T.Ekino Van der Waals-Zeeman Institute,University of Amsterdam Y.Janssen Advanced Science Research Center,JAERI Y.Morii	JRR-3M 1G (HRPD) C2-1 (LTAS)	94
Mn_7Sn_4の磁気転移の中性子回折による研究 「Mn_7Sn_4の磁気転移の中性子回折による研究」	Faculty of Science and Technology,Keio University S.Anzai,T.Kobayashi Institute of Materials Research,Tohoku University Y.Yamaguchi,M.Ohashi,K.Ohoyama Institute for Solid State Physics,University of Tokyo K.Motojima	JRR-3M T1-3 (HERMES) (KPD)	96

中性子散乱
1）磁 性

R-Mn-X 系化合物の磁気構造 「中性子回折によるDyMnSi磁気相転移の研究」	Department of Physics,Tohoku University H.Kobayashi,T.Kamimura Institute for Materials Research,Tohoku University M.Ohashi,H.Onodera,Y.Yamaguchi	JRR-3M T1-3 (HERMES) (KPD)	98
単結晶$(Fe_{0.98}Ru_{0.02})_2P$の中性子回折 「単結晶Ce_2Fe_{17}の中性子回折」	Department of Physics,Faculty of Science Saitama University Y.Uwatoko,E.Matsuoka,T.Ohki,H.Kosaka Science University of Tokyo K.Motoya	JRR-3M T1-1 (HQR)	99
ErNiSnの磁気構造 「ErNiSnの中性子回折」	Faculty of Education,Tottori University Y.Andoh Japan Advanced Institute of Science and Technology M.Kurisu,G.Nakamoto,T.Nobata, S.Nakamura,R.Hara Research Reactor Institute,Kyoto University S.Kawano	JRR-3M T1-1 (HQR)	100
$La_xSr_{1-x}MnO_{2.5+0.5x}$の磁気構造 「$SrMnO_{2.5}$の中性子回折」	Faculty of Science and Technology,Ryukoku University K.Inoue Toyohashi University of Technology T.Mori,N.Kamegashira Institute for Materials Research Tohoku University Y.Yamaguchi,K.Ohoyama,M.Ohashi	JRR-3M T1-3 (HERMES) (KPD)	101
希土類化合物Nd_7Ni_3単結晶の磁気構造 「希土類化合物Nd_7Ni_3の中性子回折」	Research Reactor Institute,Kyoto University S.Kawano,X.Xu Faculty of School of Education,Hiroshima University T.Tsutaoka,T.Kasagi Faculty of Education,Tottori University Y.Andoh Japan Advanced Institute of Science and Technology M.Kurisu	JRR-3M T1-1 (HQR)	102
希土類金属間化合物DyCuSiの変調磁気構造と格子変調 「DyCuSiの中性子回折」	Institute for Materials Research,Tohoku University K.Ishimoto,S.Takahashi,H.Miki,H.Onodera, H.Yamauchi,Y.Yamaguchi Faculty of Engineering,Yamagata University M.Ohashi	JRR-3M T1-3 (HERMES) (KPD)	103

中性子散乱
1）磁 性

重希土類ヘキサボライド(REB_6;RE=Tb,Dy,Ho)の磁気構造の研究 「DyB_6の粉末中性子回折」	Institute for Materials Research,Tohoku University K.Takahashi,H.Nojiri,K.Ohoyama, M.Ohashi,Y.Yamaguchi,M.Motokawa Department of Physics,Tohoku University S.Kunii	JRR-3M T1-3 (HERMES) (KPD)	104
HoNiSn単結晶の中性子回折 「HoNiSnの中性子回折」	Japan Advanced Institute of Science and Technology M.Kurisu,G.Nakamoto,T.Nobata, S.Nakamura Faculty of Engineering,Kyushu Kyoritsu University Y.Makihara Faculty of Education,Tottori University Y.Andoh Research Reactor Institute,Kyoto University S.Kawano	JRR-3M T1-1 (HQR)	105
MnAl磁石の中性子回折による研究 「MnAl高温相のshort range order」	Faculty of Engineering,Ehime University S.Tomiyoshi,H.Odahara Institute for Materials Research,Tohoku University M.Ohashi,Y.Yamaguchi	JRR-3M T1-2 (KSD)	106
$CePt_2Sn_2$と$NdGa_2$は「量子スピン液体」状態か？ 「近藤反強磁性体$CePt_2Sn_2$の中性子回折」	Department of Physics,Tokyo Metropolitan University H.Kadowaki,T.Sasaki Department of Physics,Columbia University K.M.Kojima,Y.J.Uemura,G.M.Luke, Y.Fudamoto Advanced Science Research Center,JAERI T.Osakabe,Y.Koike,N.Metoki,S.Katano Institute for Material Research,Tohoku University K.Ohoyama,M.Ohashi Faculty of Science,Hiroshima University Y.Echizen,T.Takabatake	JRR-3M T1-3 (HERMES) (KPD)	107
非晶質ホイスラー合金の磁性 「非晶質ホイスラー合金$Cu_2MnAl_{1-x}Zr_x$の中性子回折」	Faculty of Science,Ehime University T.Kamimori,Y.shiraga,K.Konishi,H.Tagne, M.Goto Faculty of Engineering,Ehime University S.Tomiyoshi Institute for Material Research,Tohoku University K.Ohoyama,M.Ohashi,Y.Yamaguchi	JRR-3M T1-3 (HERMES) (KPD)	109

中性子散乱
1）磁 性

ランタノイド複合酸化物の磁気構造 「粉末中性子回折による$SrTbO_3$,$BaTbO_3$の結晶構造と磁気構造」	Division of Chemistry,Graduate School of Science,Hokkaido University K.Tezuka,M.Itoh,M.Haga,Y.Hinatsu JAERI Y.Shimojo,Y.Morii	JRR-3M 1G (HRPD)	110
ランタノイド複合酸化物の磁気構造 「ペロブスカイト$La_{0.85}Sr_{0.15}CrO_3$の中性子回折」	Division of Chemistry,Graduate School of Science,Hokkaido University K.Tezuka,Y.Hinatsu JAERI A.Nakamura,T.Inami,Y.Shimojo,Y.Morii	JRR-3M 1G (HRPD)	111
量子凝縮相の研究 「$U_3Pd_{20}Si_6$の結晶及び磁気構造」	Physics Department,Graduate School of Science,Tohoku University N.Tateiwa,T.Komatsubara Advanced Science Research Center,JAERI N.Metoki,Y.Koike Center for Very Low Temperature Science, Tohoku University N.Kimura	JRR-3M 1G (HRPD) 2G (TAS-1) C2-1 (LTAS)	112
量子凝縮相の研究 「$Nd_3Pd_{20}Ge_6$における磁気転移の研究」	Physics Department,Graduate School of Science,Tohoku University N.Tateiwa,M.Nakayama,T.Komatsubara Advanced Science Research Center,JAERI N.Metoki,Y.Koike Center for Very Low Temperature Science, Tohoku University N.Kimura	JRR-3M C2-1 (LTAS)	114
$ErRu_2Si_2$の磁場制御された二重変調磁気構造の研究 「$ErRu_2Si_2$の磁気構造とメタ磁性の研究」	Department of Earth and Space Science, Osaka University M.Sato,N.Chigusa,Y.Yamamoto, T.Takeuchi,S.Kawarazaki,Y.Miyako	JRR-3M 4G (GPTAS) 5G (PONTA)	115
メタ磁性$Y_2Cu_2O_5$の磁場中磁気構造 「メタ磁性$Y_2Cu_2O_5$の磁場中磁気構造」	Institute for Material Research,Tohoku University M.Motokawa,Y.Matsuoka Institute for Solid State Physics,University of Tokyo K.Kakurai	JRR-3M 5G (PONTA)	116

中性子散乱
1）磁 性

$(La,Sr)_{n+1}Mn_nO_{3n+1}$のスピン・電荷ダイナミクス 「二重層状Mn酸化物$La_{2-2x}Sr_{1+2x}Mn_2O_7$の磁気構造」	Neutron Scattering Laboratory,Institute for Solid State Physics,University of Tokyo M.Kubota,H.Yoshizawa CREST,Department of Physics,Tohoku University H.Fujioka,K.Hirota,Y.Endoh CIRSE and Department of Applied Physics, Nagoya University Y.Moritomo	JRR-3M 6G (TOPAN)	117
重い電子系化合物Ce_2X (X=Sb,Bi)の磁気構造解析 「重い電子系化合物Ce_2X (X=Sb,Bi)の磁気構造」	Institute for Materials Research,Tohoku University K.Ohoyama,H.Hayashi,M.Ohashi, H.Onodera,Y.Yamaguchi Department of Physics,Tokyo Metropolitan University M.Kohgi Department of Physics,Tohoku University T.Suzuki	JRR-3M T1-3 (HERMES) (KPD)	118
正方晶DyB_2C_2における四重極相互作用と磁性 「DyB_2C_2の磁気構造」	Institute for Materials Research,Tohoku University H.Yamauchi,H.Onodera,M.Ohashi, K.Ohoyama,T.Onimaru,M.Kosaka, Y.Yamaguchi	JRR-3M T1-3 (HERMES) (KPD)	119
Pd及びPt合金のフェルミ面効果の研究 「Pd及びPt合金の非整合磁気構造」	Department of Applied Physics,School of Science and Engineering,Waseda University R.Abe,N.Hiruma,K.Hirano,K.Fushimi, A.Murakami,T.Sunaga,T.Ichikawa, Y.Tsunoda	JRR-3M T1-1 (HQR)	121
CePの磁気ポーラロン状態の編曲中性子による研究 「CePの磁気ポーラロン状態の磁気構造因子」	Department of Physics,Tokyo Metropolitan University K.Iwasa,M.Kohgi Advanced Science Research Center,JAERI Y.Haga Department of Physics,Tohoku University T.Suzuki Institute for Solid State Physics,University of Tokyo K.Kakurai,M.Nishi,K.Nakajima Laboratoire Léon Brillouin,CEA-CNRS P.Link,A.Gukasov,J.-M.Mignot	JRR-3M 5G (PONTA)	122

中性子散乱
1）磁 性

金属相酸化バナジウムの磁気構造と励起 「金属相$(V_{1-x}Ti_x)_2O_3$の磁気構造と励起」	Department of Physics,Faculty of Science and Technology,Science University of Tokyo K.Motoya,T.Kawasaki Institute for Solid State Physics,University of Tokyo S.Shin	JRR-3M T1-1 (HQR) 4G (GPTAS)	124
La_2CoO_4のスピンダイナミクスとそのホールドープの効果の研究 「La_2CoO_4のスピン波励起」	Neutron Scattering Laboratory,Institute for Solid State Physics,University of Tokyo K.Nakajima	JRR-3M 5G (PONTA)	126
金属反強磁性体 $Nd_{0.45}Sr_{0.55}MnO_3$における異方的スピン波 「$Pr_{1-x}Ca_xMnO_3$系の電荷秩序および金属・絶縁体転移とスピンダイナミクス」	Neutron Scattering Laboratory,Institute for Solid State Physics,University of Tokyo H.Yoshizawa The Institute of Physical and Chemical Research (RIKEN) H.Kawano Solid State Division,Oak Ridge National Laboratory A.Fernandez-Baca Joint Research Center for Atom Technology H.Kuwahara Department of Applied Physics,University of Tokyo Y.Tokura	JRR-3M C1-1 (HER)	127
2次元ハイゼンベルグフラクトン 「2次元パーコレーションハイゼンベルグ反強磁性体のスピン動特性」	Neutron Science Laboratory,High Energy Accelerator Research Organization S.Itoh,H.Ikeda Neutron Scattering Laboratory,Institute for Solid State Physics,The University of Tokyo H.Yoshizawa	JRR-3M 4G (GPTAS)	129
スピン・パイエルス化合物 NaV_2O_5の磁気励起 「NaV_2O_5のスピン・ダイナミクスー中性子非弾性散乱」	Neutron Scattering Laboratory,Institute for Solid State Physics,The University of Tokyo T.Yoshihama,M.Nishi,K.Nakajima,Y.Fujii CREST,Japan Science and Technology Corporation K.Kakurai Material Design and Characterization Laboratory,Institute for Solid State Physics, The University of Tokyo M.Isobe,C.Kagami,Y.Ueda	JRR-3M 5G (PONTA)	130

中性子散乱
1）磁 性

反強磁性絶縁体 $Pr_{1-x}Ca_xMnO_3$系の異常強磁性スピン揺らぎ 「$Pr_{1-x}Ca_xMnO_3$系の電荷秩序および金属・絶縁体転移とスピンダイナミクス」	Neutron Scattering Laboratory,Institute for Solid State Physics,University of Tokyo R.Kajimoto,T.Kakeshita,Y.Oohara, H.Yoshizawa Joint Research Center for Atom Technology Y.Tomioka Department of Applied Physics,University of Tokyo Y.Tokura	JRR-3M 4G (GPTAS) C1-1 (HER)	132
近藤格子上の磁気秩序の研究 「$Ce(Ru_{1-1}Rhx)_2Si_2$のスピン揺らぎの観測」	Department of Earth and Space Science, Osaka University M.Sato,N.Chigusa,S.Kawarazaki,Y.Miyako Department of Physics,Tokyo Metropolitan University H.Kadowaki	JRR-3M 4G (GPTAS) C1-1 (HER)	134
スピングラス $Mn_{0.55}Mg_{0.45}TiO_3$の磁場中における振舞い 「スピングラス $Mn_{0.55}Mg_{0.45}TiO_3$の磁場中における振舞い」	Graduate School of Humanities and Sciences, Ochanomizu University A.Ito The Institute of Physical and Chemical Research (RIKEN) A.Fukaya Neutron Scattering Laboratory,Institute for Solid State Physics,University of Tokyo K.Kakurai,K.Nakajima	JRR-3M 5G (PONTA)	135
準結晶における磁性の研究 「Zn-Mg-Ho系準結晶における異方的な磁気励起」	National Research Institute for Metals T.J.Sato,A.P.Tsai CREST,Japan Science and Technology Corporation H.Takakura Institute for Materials Research,Tohoku University K.Shibata	JRR-3M 4G (GPTAS)	137
二重スピン鎖系$TlCuCl_3$のエネルギーギャップと磁気励起 「二重スピン鎖系$TlCuCl_3$の磁気励起」	Department of Physics,Tokyo Institute of Technology T.Kato,K.Takatsu,H.Tanaka Department of Physics,Sophia University W.Shiramura Neutron Scattering Laboratory,Institute for Solid State Physics,The University of Tokyo K.Nakajima,K.Kakurai	JRR-3M 5G (PONTA)	139

中性子散乱
1）磁 性

$BaCo_{1-x}Ni_xS_2$の圧力下における中性子散乱 「２次元モット系$BaCo_{1-x}Ni_xS_2$の磁気励起」	Department of Physics,Division of Material Science,Nagoya University H.Sasaki,H.Harashima,K.Kodama,M.Sato CREST,Japan Science and Technology Corporation K.Kakurai Department of Appied Physics,Tohoku University S.Shamoto Neutron Scattering Laboratory,Institute for Solid State Physics,The University of Tokyo M.Nishi	JRR-3M 5G (PONTA)	140
半導体的近藤物質CeRhSbのスピン相関 「近藤半導体CeRhSbでの磁気励起」	Institute for Materials Research,Tohoku University K.Ohoyama Department of Physics,Tokyo Metropolitan University M.Kohgi Department of Quantum Matter,Graduate School of Advanced Science of Matter,Hiroshima University T.Yoshino,T.Takabatake	JRR-3M 6G (TOPAN)	142
$(La_{1-x-y}Y_y)Sr_xMnO_3$の巨大磁気抵抗とスピンダイナミクス 「バンド幅を制御したMnペロブスカイト$(La_{1-x-y}Y_y)Sr_xMnO_3$の磁気励起」	CREST,Department of Physics,Tohoku University K.Hirota,A.Nishizawa,Y.Endoh	JRR-3M 6G (TOPAN)	143
Yb_4As_3のチャージオーダーと重い電子異常 「Yb_4As_3のチャージオーダー状態における磁気励起」	Tokyo Metropolitan University M.Kohgi,K.Iwasa,H.Kadowaki Niigata University A.Ochiai Tohoku University H.Aoki,T.Suzuki	JRR-3M C1-1 (HER)	145
AV_2O_5(A=Mg,Li,Cs)における量子スピンゆらぎの研究 「LiV_2O_5の中性子非弾性散乱による研究」	Neutron Scattering Laboratory,Institute for Solid State Physics,University of Tokyo Y.Takeo,T.Yoshihama,M.Nishi,K.Nakajima CREST,Japan Science and Technology Corporation K.Kakurai Material Design and Characterization Laboratory,Institute for Solid State Physics,University of Tokyo M.Isobe,Y.Ueda	JRR-3M 5G (PONTA)	147

中性子散乱
1）磁 性

AV_2O_5(A=Mg,Li,Cs)における量子スピンゆらぎの研究 「SrV_3O_7の中性子磁気散乱による研究」	Neutron Scattering Laboratory,Institute for Solid State Physics,University of Tokyo Y.Takeo,T.Yoshihama,M.Nishi, K.Nakajima Material Design and Characterization Laboratory,Institute for Solid State Physics,University of Tokyo M.Isobe,Y.Ueda Department of Physics,Division of Material Science,Nagoya University K.Kodama,H.Harashina,M.Sato CREST,Japan Science and Technology Corporation K.Kakurai	JRR-3M 5G (PONTA)	148
$LiMn_2O_4$の構造と磁気的性質 「$LiMn_2O_4$の中性子散乱」	Department of Applied Physics,School of Science and Engineering,Waseda University Y.Kasuya,Y.Tsunoda Advanced Research Center for Scinece and Engineering,Waseda University I.Tomeno	JRR-3M T1-1 (HQR)	149
非フェルミ流体状態におけるCe_7Ni_3の磁気励起 「Ce_7Ni_3の中性子散乱」	Faculty of Science and Technology,Science University of Tokyo K.Motoya,T.Kawasaki Faculty of Science,Tokyo Metropolitan University H.Kadowaki Faculty of Science,Hiroshima University K.Umeo,T.Takabatake Institute for Solid State Physics,The University of Tokyo H.Okumura,K.Kakurai JAERI T.Osakabe	JRR-3M 5G (PONTA) T1-1 (HQR) C1-1 (HER)	150
$ZnFe_2O_4$単結晶の中性子磁気散乱 「$ZnFe_2O_4$単結晶の中性子磁気散乱」	Department of Applied Physics,School of Science and Engineering,Waseda University K.Kamazawa,K.Odaka,Y.Tsunoda,K.Kohn	JRR-3M T1-1 (HQR)	152
パイライト及びスピネル構造を持つ3d遷移金属化合物の磁性と伝導 「$NiS_{2-x}Se_x$の金属絶縁体転移と反強磁性」	Department of Physics,Tohoku University M.Matsuura,H.Hiraka,Y.Endoh Institute for Chemical Research,Kyoto University K.Yamada	JRR-3M 6G (TOPAN)	153

中性子散乱
1）磁 性

圧力下における2次元強磁性体Cs_2CuF_4および$(CH_3NH_3)_2CuCl_4$の構造および磁気相転移 「2次元反強磁性体$(C_2H_5NH_3)_2CuCl_4$の圧力誘起弱強磁性」	Department of Physics,Faculty of Science, Chiba University H.Manaka,I.Yamada Institute for Solid State Physics,University of Tokyo M.Nishi	JRR-3M T1-1 (HQR)	154
TOPAN（東北大学中性子分光器）IMT 「$La_{1.95}Sr_{0.05}CuO_4$における準3次元反強磁性秩序」	Department of Physics,Tohoku University S.Wakimoto,S.Ueki,K.Yamada,Y.Endoh	JRR-3M 6G (TOPAN)	155
三角格子反強磁性体 「三角格子反強磁性体$CuFeO_2$の部分秩序相」	Department of Physics,Faculty of Science, University of Tokyo S.Mitsuda,T.Uno,M.Mase,N.Kasahara	JRR-3M T1-1 (HQR) 4G (GPTAS)	156
$U(Ru_{1-x}Rh_x)_2Si_2$における弱い反強磁性スピン揺動を伴う相転移に関する研究 「URu_2Si_2における微弱反強磁性モーメントの不純物効果」	Graduate School of Science,Hokkaido University H.Amitsuka,A.Okumura,K.Ikeda, K.Kuwahara Advanced Science Research Center,JAERI T.Honma	JRR-3M T1-1 (HQR)	158
$La_2NiO_{4+\delta}$におけるホールストリップとその磁性への効果の研究 「$La_2NiO_{4.125}$における二次元磁気相関におよぼす酸素の秩序化の効果」	Neutron Scattering Laboratory,Institute for Solid State Physics,University of Tokyo K.Nakajima Institute of Inorganic Synthesis,Yamanashi University S.Hosoya Department of Physics,Tohoku University Y.Endoh	JRR-3M 5G (PONTA)	159
縮退度の高い非ランダム磁性体におけるスローダイナミックス 「擬一次元磁性体$CoNb_2O_6$における二次元面間磁気相関緩和」	Department of Physics,Faculty of Science, University of Tokyo S.Kobayashi,S.Mitsuda Institute for Solid State Physics,University of Tokyo H.Yoshizawa,M.Ishikawa Department of Materials Science and Engineering Ehime University K.Miyatani School of Science and Engineering,Waseda University K.Kohn	JRR-3M 4G (GPTAS)	160

中性子散乱
1）磁 性

重い電子系混合物におけるメタ磁性と反強磁性相関の関係 「$CeNi_2Ge_2$における反強磁性相関」	Department of Physics,Tokyo Metropolitan University H.Kadowaki Faculty of Engineering,Toyama Prefectural University T.Fukuhara,K.Maezawa	JRR-3M 4G (GPTAS)	161
$CsVCl_3$のスピン相関関数 「$CsVCl_3$における磁気相関」	Neutron Science Laboratory,High Energy Accelerator Research Organization S.Itoh Neutron Scattering Laboratory,The University of Tokyo K.Kakurai,K.Nakajima Department of Physics,Tohoku University Y.Endoh Department of Physics,Tokyo Institute of Technology H.Tanaka	JRR-3M 5G (PONTA)	162
CaV_4O_9、CaV_3O_7の磁気散乱（スピンギャップ研究） 「1次元量子スピン系$CuNb_2O_6$のスピンギャップ研究」	Department of Physics,Division of Material Science,Nagoya University K.Kodama,H.Harashina,H.Sasaki,M.Kato, M.Sato Neutron Scattering Laboratory,Institute for Solid State Physics,The University of Tokyo M.Nishi CREST,Japan Science and Technology Corporation K.Kakurai	JRR-3M 5G (PONTA)	163
CeNiSnの低エネルギースピンギャップの検証 「近藤半導体CeNiSnのスピンギャップ」	Department of Physics,Tokyo Metropolitan University H.Kadowaki Faculty of Science,Hiroshima University T.Takabatake	JRR-3M C1-1 (HER)	165
低濃度キャリアー近藤系$Ce_{0.9}La_{0.1}P$の磁気構造に対するLa置換効果 「低濃度キャリアー系$Ce_{0.9}La_{0.1}P$の結晶場の圧力効果」	Neutron Scattering Laboratory,Institute for Solid State Physics,The University of Tokyo M.Kubota,Y.Oohara,H.Yoshizawa Institute for Solid State Physics,The University of Tokyo N.Mori College of Humanities and Sciences,Nihon University H.Takahashi Department of Physics,Tohoku University A.Uesawa,T.Suzuki	JRR-3M 4G (GPTAS)	166

中性子散乱
1）磁 性

$CeRh_2Si_2$の圧力誘起超伝導と磁気揺らぎの研究 「$CeRh_2Si_2$の反強磁性の圧力効果」	Department of Earth and Spece Science, Osaka University M.Sato,N.Chigusa,S.Kawarazaki,Y.Miyako Advanced Science Research Center,JAERI Y.Koike,N.Metoki Institute for Solid State Physics,Tokyo University M.Nishi	JRR-3M 4G (GPTAS) 2G (TAS-1)	168
磁性体における多重磁気モードの研究 「$(Cr_{1-x}Mn_x)_2As$における多重磁気モード」	Institute for Materials Research,Tohoku University Y.Yamaguchi,K.Ohoyama,T.Kanouchi, M.Ohashi,K.Ishimoto	JRR-3M T1-3 (HERMES) (KPD)	169
スピン量子数S=1/2&1スピン交替フェリ磁性鎖の磁性 「スピン量子数S=1/2&1スピン交替フェリ磁性鎖$NiCu(pba)(D_2O)_3 2D_2O$の研究」	The Institute of Physical and Chemical Research (RIKEN) M.Hagiwara Neutron Scattering Laboratory,Institute for Solid State Physics,University of Tokyo K.Kakurai Graduate School of Mathematics,Nagoya University K.Minami CREST,Japan Science and Technology Corporation Y.Narumi,K.Kindo KYOKUGEN,Osaka University K.Tatani	JRR-3M 5G (PONTA)	170
インターカレーション化合物の結晶構造と磁性 「Fe_xTiS_2化合物の結晶構造と磁性」	Faculty of Engineering,Ibaraki University M.Shintomi,Y.Tazuke,H.Takahashi JAERI Y.Morii,K.Hojou	JRR-3M 1G (HRPD)	171
フラストレート磁性体RMn_2の磁気構造と格子歪み 「YMn_2及び関連化合物の磁気構造と格子歪み」	Department of Materials Science and Engineering,Kyoto University M.Shiga,H.Nakamura JAERI N.Metoki	JRR-3M 1G (HRPD)	173
γ-Mn合金の結晶変態と磁気構造 「γ-MnM,(M=Pt,Pd and Rh)合金の斜方晶相における磁気構造」	Shibaura Institute of Technology T.Hori,H.Shiraishi JAERI Y.Tsuchiya,S.Funahashi,Y.Shimojo, K.Hojou	JRR-3M 1G (HRPD) 2G (TAS-2)	174

中性子散乱
2）高分子

高分子の結晶構造とダイナミックス 「重水素化ポリエチレンの中性子構造解析」	Department of Macromolecular Science, Faculty of Science,Osaka University Y.Takahashi	JRR-3M 1G (HRPD)	177
高分子の結晶構造とダイナミックス 「ポリビニルアルコールの中性子構造解析」	Department of Macromolecular Science, Faculty of Science,Osaka University Y.Takahashi	JRR-3M 1G (HRPD) T2-4 (TAS-2)	179
アモルファス高分子における非ガウス性の評価 「平均2乗変位の分布より見たアモルファスポリマーの動的不均一性」	Institute for Chemical Research,Kyoto University I.Tsukushi,T.Kanaya,K.Kaji	JRR-3M 4G (GPTAS)	181
アモルファス高分子における非ガウス性の評価 「アモルファスポリイミドの速いダイナミックスにおける振動ソフトニングの役割」	Institute for Chemical Research,Kyoto University J.Hansen,T.Kanaya,K.Nishida,K.Kaji	JRR-3M C1-1 (HER)	183
オリゴペプチドの溶液中における会合構造の超二次構造 「オリゴペプチド会合体の溶液中における超二次構造（中性子小角散乱）」	Department of Applied Chemistry,Nagoya Institute of Technology H.Okabayashi,M.Takai,M.Ishida BSF,National Laboratory for High Energy Physics M.Furusaka Department of Physics,Faculty of Social and Information Studies,Gunma University M.Hirai	JRR-3M C1-2 (SANS-U)	184
オリゴペプチドの溶液中における会合構造の超二次構造 「オリゴペプチド会合体の溶液中における超二次構造(中性子スピンエコー法)」	Department of Applied Chemistry,Nagoya Institute of Technology H.Okabayashi,M.Takai,M.Ishida Faculty of Integrated Arts and Sciences, Hiroshima University H.Seto,T.Takeda	JRR-3M C2-2-2 (NSE)	185
状態記憶効果を示す高分子ゲルの構造解析 「小角中性子散乱による4-Acrylamido-salicylic acid gelの多重相の研究」	Department of Materials Science and Engineering,Chiba University M.Annaka,T.Nakahira Department of Polymer Science and Engineering,Kyoto Institute of Technology F.Ikkai,M.Shibayama	JRR-3M C1-2 (SANS-U)	186

中性子散乱
2）高分子

化学架橋ゲルのゲル化過程「時系列小角中性子散乱によるポリN-イソプロピルアクリルアミドのゲル化過程」	Department of Polymer Science and Engineering,Kyoto Institute of Technology M.Shibayama,T.Norisuye,S.Nomura	JRR-3M C1-2 (SANS-U)	188
高圧によるマイクロエマルジョンの構造相転移、及び双連結構造形成のkinetics「三元系マイクロエマルジョンにおける圧力誘起構造相転移の中性子小角散乱による研究」	Neutron Scattering Laboratory Institute for Solid State Physics,The University of Tokyo M.Nagao Faculty of Integrated Arts and Sciences, Hiroshima University H.Seto,D.Okuhara	JRR-3M C1-2 (SANS-U)	189
中性子小角散乱法による高分子多成分系の相溶性及び相転移に関する研究「高分子混合系とマイクロエマルジョン系の共連続構造のキャラクタリゼーション」	Hashimoto Polymer Phasing Project,ERATO, Japan Science and Technology Corporation H.Jinnai,Y.Nishikawa,K.Kimishima Department of Polymer Chemistry,Kyoto University T.Hashimoto JAERI S.Koizumi	JRR-3M C3-2 (SANS-J)	191
中性子小角散乱法による高分子多成分系の相溶性及び相転移に関する研究「N-イソプロピルアクリルアミドゲルの超小角散乱」	Hashimoto Polymer Phasing Project,ERATO, Japan Science and Technology Corporation T.Okamoto,Y.Hirokawa JAERI K.Aizawa Graduate School of Engineering,Kyoto University T.Hashimoto	JRR-3M 3G (PNO)	193
中性子小角散乱法による高分子構造の研究「中性子小角散乱によるセグメント化ポリウレタンのミクロ相分離構造の研究」	National Atomic Energy Agency,Indonesia Sudaryanto JAERI S.Koizumi	JRR-3M C3-2 (SANS-J)	194
強相関電子系の中性子散乱による研究「中性子偏極解析によるガラス形成物質の弾性非干渉性構造因子の観察 Ⅰ」	Advanced Science Research Center,JAERI S.Koizumi,T.Inami	JRR-3M 2G (TAS-1) T2-4 (TAS-2)	196

中性子散乱
2）高分子

強相関電子系の中性子散乱による研究 「中性子偏極解析によるガラス形成物質の弾性非干渉性構造因子の観察 II」	Advanced Science Research Center,JAERI S.Koizumi,T.Inami	JRR-3M 2G (TAS-1) T2-4 (TAS-2)	198
高分子多成分系のパターン形成に関する研究 「光散乱・中性子散乱による高分子準希薄溶液の構造形成に関する研究」	Department of Polymer Chemistry,Graduate School of Engineering,Kyoto University S.Saito,K.Matsuzaka,S.Suehiro, T.Hashimoto JAERI S.Koizumi	JRR-3M C3-2 (SANS-J)	201
高分子多成分系のパターン形成に関する研究 「強偏斥高分子混合系の界面散乱」	Kyoto University H.Takeno,T.Hashimoto BASF Martin Weber JAERI S.Koizumi	JRR-3M C3-2 (SANS-J)	202
高分子多成分系の静的階層構造の研究 「牛血清アルブミンゲルのPNO研究」	Graduate School of Engineering,Yamagata University Y.Izumi,K.Soma Advanced Science Research Center,JAERI K.Aizawa,S.Koizumi,H.Tomimitsu	JRR-3M 3G (PNO)	203
二様分子量分布を持つポリスチレン鎖のバルク中の拡がり 「低分子量同族体で希釈されたポリスチレンのバルク中の拡がり」	Neutron Scattering Laboratory Institute for Solid State Physics,The University of Tokyo Y.Matsushita,J.Suzuki Department of Applied Chemistry,School of Engineering,Nagoya University N.Takabayashi,I.Noda Neutron Science Laboratory,IMSS,High Energy Accelerator Research Organization N.Torikai	JRR-3M C1-2 (SANS-U)	204
バルク状態並びに溶液中の２元ブロック共重合体の秩序無秩序転移 「対称なスチレン-２ビニルピリジンのバルク並びに溶液中の秩序無秩序転移」	Department of Applied Chemistry,Faculty of Engineering,Nagoya University Y.Takahashi,S.Kitade,N.Noda,N.Ochiai, I.Noda Institute for Solid State Physics,University of Tokyo Y.Matsushita,M.Imai	JRR-3M C1-2 (SANS-U)	205

中性子散乱
2）高分子

逆ミセル系の構造形成と構造ダイナミックス 「中性子スピンエコー法によるW/O AOTマイクロエマルジョンのダイナミックス研究」	Department of Physics,Gunma University M.Hirai,H.Iwase,S.Arai,S.Yabuki, T.Takizawa Meiwa Women's Junior College R.K.Hirai Faculty of Integrated Arts and Science, Hiroshima University T.Takeda,H.Seto Institute for Solid State Physics,University of Tokyo M.Nagao	JRR-3M C2-2-2 (NSE)	206
ジアルキルホスフェイト分子の非対称と二分子膜形成との相関 「ジアルキルホスフェイト分子の非対称と二分子膜形成との相関（中性子スピンエコー法）」	Department of Applied Chemistry,Nagoya Institute of Technology H.Okabayashi,N.Hattori,S.Sasuga,M.Takai, N.Ichiyanagi Faculty of Integrated Arts and Science, Hiroshima University H.Seto,T.Takeda	JRR-3M C2-2-2 (NSE)	207
高分子ミセルのコロナ部分の分子鎖ダイナミックス 「中性子スピンエコー法による高分子ミセルの呼吸モード」	Institute for Chemical Research,Kyoto University T.Kanaya,H.Watanabe,K.Kaji Institute for Solid State Physics,University of Tokyo Y.Matsushita,M.Nagao,Y.Fujii Faculty of Integrated Arts and Science, Hiroshima University T.Takeda,H.Seto	JRR-3M C2-2-2 (NSE)	208
中性子反射率測定に基づくポリマーブレンド超薄膜中の分子鎖凝集構造評価 「中性子反射率測定に基づく2様分子量分布を有するポリスチレンブレンド超薄膜中の分子鎖凝集構造評価」	Department of Materials Physics and Chemistry Graduate School of Engineering Kyushu University T.Kajiyama,K.Tanaka,A.Takahara Research Reactor Institute,Kyoto University S.Tasaki,T.Ebisawa Neutron Scattering Laboratory,Institute for Solid State Physics,The University of Tokyo Y.Matsushita	JRR-3M C3-1-2 (MINE)	209

中性子散乱
2）高分子

中性子反射率測定に基づく分子鎖末端構造を制御したブロック共重合体薄膜構造評価 「中性子反射率測定に基づくポリ(スチレン-b-メチルメタクリレート)ブロック共重合体薄膜の凝集構造評価」	Department of Materials Physics and Chemistry Graduate School of Engineering Kyushu University A.Takahara,K.Nakamura,K.Tanaka, T.Kajiyama Research Reactor Institute,Kyoto University S.Tasaki,T.Ebisawa Neutron Scattering Laboratory,Institute for Solid State Physics,The University of Tokyo Y.Matsushita	JRR-3M C3-1-2 (MINE)	211
中性子反射率法による固－液界面における両親媒性高分子の形態とその集合状態の解析 「中性子反射率法による固－液界面における両親媒性高分子の形態とその集合状態の解析」	Department of Polymer Chemistry,Kyoto University H.Endo,K.Kago,K.Matsumoto,H.Matsuoka, H.Yamaoka	JRR-3M C3-1-2 (MINE)	212
ループ状の相図を有するブロック共重合体の相転移に関する研究 「ループ状の相図を有するブロック共重合体の相転移」	Department of Polymer Chemistry,Graduate School of Engineering,Kyoto University T.Hashimoto,H.Hasegawa,M.Takenaka, M.Sawamoto Neutron Scattering Laboratory,The Institute for Solid State Physics,The University of Tokyo M.Nagao,M.Imai	JRR-3M C1-2 (SANS-U)	213
ブロック共重合体の秩序－無秩序転移に関する研究 「圧力ジャンプにより誘起された高分子ブロック共重合体の秩序化過程のダイナミックス」	Department of Polymer Chemistry,Graduate School of Engineering,Kyoto University T.Hashimoto,N.Sakamoto,H.Takenaka, H.Hasegawa Neutron Scattering Laboratory,The Institute for Solid State Physics,The University of Tokyo M.Nagao,M.Imai	JRR-3M C1-2 (SANS-U)	214
高分子ブロック共重合体の相溶性に及ぼす圧力効果の研究 「高分子ブロック共重合体の相溶性に及ぼす圧力効果」	Department of Polymer Chemistry,Graduate School of Engineering,Kyoto University H.Hasegawa,N.Sakamoto,H.Takeno, T.Hashimoto Neutron Scattering Laboratory,The Institute for Solid State Physics,The University of Tokyo M.Nagao,M.Imai	JRR-3M C1-2 (SANS-U)	215

中性子散乱
2）高分子

重水素化ポリブタジエン／ポリブタジエンブレンドの相溶性に及ぼす圧力効果のミクロ構造依存性 「高分子の相溶性およびその圧力依存性におけるミクロ構造の効果」	Department of Polymer Chemistry,Graduate School of Engineering,Kyoto University H.Hasegawa,N.Sakamoto,H.Takeno, T.Hashimoto Neutron Scattering Laboratory,The Institute for Solid State Physics,The University of Tokyo M.Nagao,M.Imai	JRR-3M C1-2 (SANS-U)	216
多糖／水系の高次構造形成と機能発現 「生体・高分子のゾルーゲル転移の普遍性」	Graduate School of Engineering,Yamagata University Y.Izumi,K.Soma,J.Suzuki Institute for Solid State Physics,University of Tokyo M.Hashimoto,T.Takahashi	JRR-3M C1-3 (ULS)	217
電解質多糖類カラギーナンのゾルーゲル転移 「κカラギーナンのゲル→ゾル転移における構造変化の観測」	Department of Physics,Kyushu University M.Sugiyama Department of Applied Physics,Fukuoka University N.Hiramatsu,A.Nakamura Institute of Environmental Systems,Kyushu University K.Hara	JRR-3M C1-2 (SANS-U)	218
界面活性剤／水系における立方相ネットワーク構造のゆらぎと成長 「流動場下における界面活性剤／水系のモルフォロジー転移」	Department of Physics,Ochanomizu University M.Imai,K.Nakaya Faculty of Science,Tokyo Metropolitan University T.Kato Faculty of Engineering,Nagoya University Y.Takahashi Institute for Chemical Research,Kyoto University T.Kanaya	JRR-3M C1-2 (SANS-U)	219
弱電荷高分子ゲルの超構造解析 「変形下における弱電荷ゲルの構造解析」	Department of Polymer Science and Engineering,Kyoto Institute of Technology M.Shibayama,K.Kawakubo,F.Ikkai Neutron Scattering Laboratory,The Institute for Solid State Physics,The University of Tokyo M.Imai	JRR-3M C1-2 (SANS-U)	221

中性子散乱
2）高分子

多糖類高分子ゲルの構造 「微細結晶セルロースの内部構造の観測」	Department of Physics,Kyusyu University M.Sugiyama Institute of Environmental Systems,Kyusyu University K.Hara Department of Applied Physics,Fukuoka University N.Hiramatsu Chemical Technology Department IV,Asahi Chemical Industry Co.,Ltd H.Iijima	JRR-3M C3-2 (SANS-J)	222
リエントラント液晶の構造 「リエントラント液晶の構造」	Institute for Molecular Science O.Oishi,S.Miyajima Neutron Scattering Laboratory,The Institute for Solid State Physics,The University of Tokyo M.Nagao,M.Imai	JRR-3M C1-2 (SANS-U)	223
超小角中性子散乱法によるコロイド分散液中における合金様結晶構造と相転移の解析 「超小角中性子散乱法による分散液中のコロイド結晶の合金様結晶構造と相転移の解析」	Department of Polymer Chemistry,Kyoto University H.Matsuoka,T.Ikeda,H.Yamaoka Institute of Solid State Physics,University of Tokyo M.Hashimoto,T.Takahashi	JRR-3M C1-3 (ULS)	224

中性子散乱
3）構造・励磁

コバロキシム錯体結晶の光異性化 「コバロキシム錯体におけるキラルな1-シアノエチル基の光反転反応のメカニズム」	Department of Chemistry,Tokyo Institute of Technology T.Ohhara,Y.Ohashi Advanced Science Research Center,JAERI I.Tanaka,S.Kumazawa,N.Niimura	JRR-3M 1G-A (BIX-1)	229
コバロキシム錯体結晶の光異性化 「コバロキシム錯体における3-シアノエチル基3-1光異性化反応のメカニズム」	Department of Chemistry,Tokyo Institute of Technology T.Ohhara,J.Harada,Y.Ohashi Advanced Science Research Center,JAERI I.Tanaka,N.Niimura	JRR-3M 1G-A (BIX-1)	230
コバロキシム錯体結晶の光異性化 「$TaCp_2(H)(SiMe_2H)_2$の構造」	Department of Chemistry,University of Southern California R.Bau Advanced Science Research Center,JAERI I.Tanaka,N.Niimura Department of Chemistry,Tokyo Institute of Technology T.Ohhara,Y.Ohashi Department of Chemistry,University of Pennsylvania Q.Jiang D.H.Berry	JRR-3M 1G-A (BIX-1)	231
プロトン及びイオン伝導機構の結晶学的研究 「プロトン伝導性酸化物の中性子回折」	Graduate School of Engineering,Nagoya University T.Nagasaki,N.Noda,T.Matsui JAERI Y.Ishii,Y.Morii	JRR-3M 1G (HRPD)	232
プロトン及びイオン伝導機構の結晶学的研究 「CuClTeの中性子回折」	Department of Physics,Faculty of Science, Ibaraki University M.Hirota,T.Sakuma Applied Physics Group,Faculty of Engineering,Ibaraki University H.Takahashi Natinoal Institute for Research in Inorganic Marerials Y.Onoda JAERI Y.Ishii	JRR-3M T2-4 (TAS-2)	233

中性子散乱
3）構造・励磁

中性子散乱による$Li_2Ge_7O_{15}$の強誘電相転移に関与するソフトフォノンの研究 「中性子散乱による$Li_2Ge_7O_{15}$の強誘電相転移に関与するソフトフォノンの研究」	Department of Physics,Faculty of Science, Shinshu University M.Wada,Takeda Department of Physics,Faculty of Science, Chiba University Y.Noda Department of Electrical Engineering,College of Science and Engineering,Meisei University T.Yamaguchi Research Reactor Institute,Kyoto University Y.Iwata	JRR-3M 4G (GPTAS)	234
圧力下におけるA_2BX_4型強誘電体の単相－双晶相転移とソフトフォノン 「Rb_2ZnBr_4の相転移における静水圧効果」	Department of Quantum Engineering, Graduate School of Engineering,Nagoya University H.Shigematsu,T.Matsui Neutron Scattering Laboratory,Institute for Solid State Physics,University of Tokyo M.Kubota,M.Nishi Department of Physics,Faculty of Science, Yamaguchi University H.Mashiyama	JRR-3M 4G (GPTAS) C1-1 (HER)	235
A_2BX_4型強誘電体の多形転移と格子振動 「中性子非弾性散乱で調べたK_2ZnBr_4のα-β転移の音響フォノンモードの異常」	Department of Physics,Yamaguchi University H.Mashiyama Research Institute for Electronic Science, Hokkaido University M.Takesada Department of Quantum Engineering,Nagoya University H.Shigematsu	JRR-3M 4G (GPTAS) C1-1 (HER)	236
KDPの臨界散漫散乱の新しい見地からの測定 「ヌルマトリックスにしたKDPの散漫散乱とLOフォノン」	Faculty of Science,Chiba University Y.Noda,K.Sano	JRR-3M 4G (GPTAS)	237
カルコゲン化合物半導体の強誘電相転移 「中性子散乱による$TlGaSe_2$の構造相転移の研究」	Department of Environmental Science,Niigata University S.Kashida,Y.Kobayashi Graduate School of Science and Engineering, Niigata University School of Science and Engineering,Waseda University Y.Tsunoda	JRR-3M T1-1 (HQR) C1-1 (HER)	238

中性子散乱
3）構造・励磁

誘電体の低温での構造相転移の研究 「hex-$BaTiO_3$の低温相の構造」	Faculty of Science,Chiba University Y.Noda,K.Akiyama,T.Shobu Advanced Science Research Center,JAERI Y.Morii Electrotechnical Laboratory H.Yamaguchi	JRR-3M 1G (HRPD)	239
強相関電子系の中性子散乱による研究 「$Pr_{1-x}Ca_xMnO_3$の電荷秩序」	Advanced Research Institute for Science and Engineering,Waseda University H.Hino,N.Ikeda,Y.Yamada JAERI S.Katano,T.Inami	JRR-3M 2G (TAS-1)	240
高圧下での結晶構造・相変態の研究 「$Ti_{50}Ni_{30}Cu_{20}$合金におけるマルテンサイト変態の前駆段階の中性子散乱による研究」	Institute of Materials Science,University of Tsukuba X.Ren,K.Taniwaki,N.Miura,K.Otsuka JAERI Y.Morii Siberian Physical Technical Institute Yu.I.Chumlyakov	JRR-3M T2-4 (TAS-2)	241
中性子散乱によるアルカリ金属挿入層状珪酸塩の研究 「アルカリ金属挿入バーミキュライトの格子動力学」	Toyo University,Faculty of Engineering N.Wada Neutron Scattering Laboratory,The Institute for Solid State Physics, The University of Tokyo K.Nakajima,K.Kakurai	JRR-3M 5G (PONTA)	243
中性子散乱による応力測定の研究 「VAMAS標準試料内部ひずみ分布の測定」	JAERI N.Minakawa,Y.Morii,Y.Tsuchiya Mechanical Engineering Research Laboratory, Hitachi Ltd., M.Hayashi,S.Ohokido Nagoya University K.Tanaka,Y.Akiniwa	JRR-3M T2-1 (RESA)	245
アニオン配座を中心とした多元系金属酸化フッ化物の構造の精密化 「$Nd_2Ln_2O_3F_6$(Ln:Y,Eu,Gd)中でのアニオン配座の電気化学特性への影響」	Department of Materials Science and Engineering,Faculty of Engineering,Fukui University M.Takashima,S.Yonezawa,T.Tanioka, Y.Nakajima	JRR-3M T1-3 (HERMES) (KPD)	247

中性子散乱
3）構造・励磁

スカンジウム含有リチウムリン酸塩の構造とイオン伝導性 「スカンジウム含有リチウムリン酸塩の構造とイオン伝導性」	Department of Chemistry and Chemical Engineering,Faculty of Engineering,Niigata University Zuo-Guang Ye,T.Suzuki,K.Yoshida, K.Uematsu,T.Kodama,K.Toda Institute for Material Research,Tohoku University M.Ohashi,M.Sato	JRR-3M T1-3 (HERMES) (KPD)	248
$(La,Sr)_{n+1}Mn_nO_{3n+1}$のスピン電荷ダイナミクス 「マンガン酸化物における反強磁性金属状態」	CIRSE,Nagoya University Y.Moritomo,T.Akimoto,Y.Maruyama, A.Nakamura Department of Physics,Tohoku University K.Hirota Institute for Materials Research,Tohoku University K.Ohoyama,M.Ohashi	JRR-3M T1-3 (KPD)	249
$(La,Sr)_{n+1}Mn_nO_{3n+1}$のスピン電荷ダイナミクス 「$La_{0.5}Sr_{1.5}MnO_4$の電荷整列転移における格子効果」	CIRSE,Nagoya University Y.Moritomo,A.Nakamura Department of Physics,Tokyo Institute of Technology S.Mori,N.Yamamoto Institute for Material Research,Tohoku University K.Ohoyama,M.Ohashi	JRR-3M T1-3 (KPD)	250
粉末中性子回折装置 HERMES (IMT) 「新しい超伝導体 $Li_{0.16}ZrNCl$とその母相 βZrNClの構造研究」	Department of Applied Physics,Tohoku University S.Shamoto,T.Kato,Y.Ono,T.Kajitani Institute for Materials Research,Tohoku University K.Ohoyama,M.Ohashi,Y.Yamaguchi	JRR-3M T1-3 (HERMES) (KPD)	251
水素結合中の水素原子核のイメージング 「KDPの水素結合における水素原子核のイメージングの中性子粉末回折法による研究」	Department of Physics,School of Science, Kitasato University S.Yamamura,Y.Sugawara Advanced Science Research Center,JAERI S.Kumazawa,Y.Ishii,Y.Morii Department of Applied Physics,School of Engineering,Nagoya University E.Nishibori,M.Sakata Department of Material Science, Interdisciplinary Faculty of Science and Engineering,Shimane University M.Takata	JRR-3M 1G (HRPD)	253

中性子散乱
3）構造・励磁

半磁性半導体$Zn_{1-x}Mn_xTe$の非弾性散乱 「$Zn_{0.568}Mn_{0.432}Te$の冷中性子散乱」	Department of Applied Physics,Graduate School of Engineering,Tohoku University T.Kamiya,Y.Ono Research Institute for Scientific Measurements,Tohoku University T.Sato,Y.Oka,T.Kajitani	JRR-3M C3-1-1 (AGNES)	254
超低温の導入による中性子散乱の研究 「Fe-Cu合金の析出現象の中性子小角散乱による研究」	JAERI K.Aizawa,A.Iwase,T.Tobita,M.Suzuki	JRR-3M 3G (PNO)	255
精密中性子光学実験法によるNi基超合金単結晶の観察 「クリープ損傷を施したNi基超合金CMSX-4の構造評価」	JAERI K.Aizawa,H.Tomimitsu Hitachi Research Laboratory,Hitachi,Ltd., H.Tamaki,A.Yoshinari	JRR-3M 3G (PNO)	256
「ウランおよびランタノイド複合酸化物の合成、構造と磁気的性質」	Division of Chemistry,Graduate School of Science,Hokkaido University Y.Hinatsu	JRR-3M 1G (HRPD)	257

中性子散乱
4）超伝導

強相関電子系の中性子散乱による研究 「梯子格子物質；$(Sr_{2.5}Ca_{11.5})Cu_{24}O_{41}$におけるスピンギャップ」	Department of Physics,Aoyama-Gakuin University J.Akimitsu,T.Nagata Neutron Scattering Group,Advanced Science Research Center,JAERI S.Katano Neutron Scattering Laboratory, Institute for Solid State Physics,The University of Tokyo M.Nishi,K.Kakurai	JRR-3M 2G (TAS-1)	263
強相関電子系の中性子散乱による研究 「中性子小角散乱法を用いた$NdBa_2Cu_3O_{7-d}$のメゾスコピック構造の観察」	Department of Materials Science and Engineering,Kyoto University K.Osamura,S.Miyata Advanced Science Research Center,JAERI J.Suzuki Superconductivity Research Laboratory, International Superconductivity Technology Center K.Kuroda,N.Koshizuka	JRR-3M C3-2 (SANS-J)	265
強相関電子系の中性子散乱による研究 「中性子小角散乱法を用いた非双晶$YBa_2Cu_3O_{7-d}$における磁束格子観察」	Department of Materials Science and Engineering,Kyoto University K.Osamura,S.Miyata Advanced Science Research Center,JAERI J.Suzuki Department of Materials Science,JAERI S.Okayasu	JRR-3M C3-2 (SANS-J)	266
強相関電子系の中性子散乱による研究 「$La_{2-x}Sr_xCuO_4$における中性子小角散乱強度の温度依存性と緩和現象」	Department of Materials Science and Engineering,Kyoto University K.Osamura,S.Miyata Advanced Science Research Center,JAERI J.Suzuki Department of Superconductivity Engineering, University of Tokyo T.Sasagawa,K.Kishio	JRR-3M C3-2 (SANS-J)	267
強相関電子系の中性子散乱による研究 「$(Nd,Ce)_2CuO_{4+d}$の小角散乱実験」	Advanced Science Research Center,JAERI J.Suzuki Department of Materials Science and Engineering,Kyoto University S.Miyata National Research Institute for Metals K.Hirata	JRR-3M C3-2 (SANS-J)	268

中性子散乱
4）超伝導

強相関電子系の中性子散乱による研究 「双晶$YBa_2Cu_3O_7$の小角散乱実験」	Advanced Science Research Center,JAERI J.Suzuki Japan Science and Technology Corporation M.Watahiki Department of Materials Science and Engineering,Kyoto University S.Miyata Superconductivity Research Laboratory, International Superconductivity Technology Center M.Murakami	JRR-3M C3-2 (SANS-J)	269
強相関電子系の中性子散乱による研究 「中性子回折による$LaBa_2(Fe_{1-x}Cu_x)_3Oy$の研究」	Department of Materials Science and Engineering,Muroran Institute of Technology T.Ishigaki,K.Kitaguchi,T.Futase JAERI Y.Tsuchiya	JRR-3M 1G (HRPD)	271
ウラン化合物における超伝導の研究 「URu_2Si_2における微少磁気モーメントの異常な温度依存性」	Advanced Science Research Center,JAERI T.Honma,Y.Haga,E.Yamamoto,N.Metoki, Y.Koike Graduate School of Science,Osaka University H.Ohkuni,Y.Onuki	JRR-3M C2-1 (LTAS)	272
ウラン化合物における超伝導の研究 「重い電子系超伝導体UBe_{13}における磁気秩序の欠如」	JAERI Y.Haga,Y.Koike,N.Metoki,E.Yamamoto, T.Honma Graduate School of Science,Osaka University Y.Onuki	JRR-3M C2-1 (LTAS)	274
量子凝縮相の研究 「重い電子系超伝導体UPd_2Al_3における異方的超伝導ギャップ」	Advanced Science Research Center,JAERI N.Metoki,Y.Koike,Y.Haga,Y.Onuki Graduate School of Science,Department of Physics,Osaka University Y.Onuki	JRR-3M C2-1 (LTAS)	275
YBCO B_{2u}モード(24meV)異常と磁気励起との関係 「B_{2u}フォノン測定による擬ギャップ形成研究」	Department of Physics,Division of Material Science,Nagoya University H.Harashima,H.Sasaki,K.Kodama,M.Sato CREST,Japan Science and Technology Corporation K.Kakurai Department of Applied Physics,Faculty of Engineering,Tohoku University S.Shamoto Neutron Scattering Laboratory,Institute for Solid State Physics,The University of Tokyo M.Nishi	JRR-3M 5G (PONTA)	277

中性子散乱
4）超伝導

IMT、日米協力 「Zn及びNdのドープされたLSCOの中性子散乱研究」	Physics Department, Brookhaven National Laboratory J.M.Tranquada Superconductivity Research Course,The University of Tokyo N.Ichikawa Neutron Scattering Laboratory,Institute for Solid State Physics,University of Tokyo K.Kakurai	JRR-3M 5G (PONTA)	278
$La_{2-x}Sr_xCuO_4$のスピン揺動 「$La_{2-x}Sr_xCuO_4$(x=0.12,0.18)のCuO_6八面体の傾きに関係した構造不安定性」	Department of Physics,Tohoku University H.Kimura,C.-H.Lee,K.Yamada Department of Physics, Brookhaven National Laboratory G.Shirane	JRR-3M 6G (TOPAN)	279
BEDT-TTF化合物の中性子散乱による研究 「BEDT-TTF塩の中性子散乱研究」	Department of Applied Physics,Graduate School of Engineering,Tohoku University T.Kajitani,S.Shamoto,Y.Ono,M.Yamada, S.Takashima	JRR-3M C3-1-1 (AGNES)	281
超低温の導入による中性子散乱の研究 「超低温におけるUPt_3の反強磁性秩序の中性子散乱による研究」	Advanced Science Research Center,JAERI Y.Koike,N.Metoki,E.Yamamoto,Y.Haga Center for Low Temperature Science,Tohoku University N.Kimura Graduate School of Science,Osaka University Y.Onuki Faculty of Engineering,Toyama Prefectural University K.Maezawa	JRR-3M C2-1 (LTAS)	282

中性子散乱
5）非晶質・液体

非弾性中性子散乱法による$[(CH_3)nNH_{4-n}]Cl$のメチルアンモニウム分子回転 「非弾性中性子散乱法による$[(CH_3)_3NH]Cl$結晶におけるトリメチルアンモニウム分子のフラストレイト回転」	Department of Physics,Faculty of Science, Kyushu University N.Achiwa,T.Oya,H.Takakura	JRR-3M C3-1-1 (AGNES)	287
サイズを精密に制御された空間内における水分子集団の動力学 「中性子散乱によるMCM-41細孔内水分子のダイナミクスに関する研究」	Department of Chemistry,Faculty of Science, Okayama University of Science S.Kittaka,S.Takahara Department of Chemistry,Faculty of Science, Okayama University Y.Kuroda,T.Mori,H.Hamano Department of Chemistry,Faculty of Science, Fukuoka University T.Yamaguchi Graduate School of Engineering,Tohoku University T.Kajitani	JRR-3M C3-1-1 (AGNES)	288
低分子ガラスの低エネルギー励起の空間スケール 「3-メチルペンタンガラスのボゾンピークに関する散乱ベクトル依存性」	Department of Chemistry,Graduate School of Science,Osaka University O.Yamamuro,T.Matsuo Institute for Chemical Research,Kyoto University I.Tsukushi,T.Kanaya	JRR-3M C1-1 (HER)	290
分子性ガラスの低エネルギー励起に及ぼす分子間水素結合効果 「単価および多価アルコールガラスのボゾンピーク」	Department of Chemistry,Graduate School of Science,Osaka University O.Yamamuro,K.Harabe,T.Matsuo Department of Chemistry,Naruto University of Education K.Takeda Institute for Chemical Research,Kyoto University I.Tsukushi,T.Kanaya	JRR-3M C3-1-1 (AGNES)	292
ガラスの中範囲秩序と物性 「鉛メタケイ酸塩ガラスの中範囲秩序」	JAERI K.Suzuya,H.Ohno Argonne National Laboratory D.L.Price,M.L.Saboungi	JRR-3M 2G (TAS-1)	294

中性子散乱
5）非晶質・液体

プロトン及びイオン伝導機構の結晶学的研究 「AgI-Ag_2O-V_2O_5系ガラスの短距離および中距離秩序」	Faculty of Engineering,Ibaraki University H.Takahashi,K.Shishitsuka Faculty of Science,Ibaraki University T.Sakuma JAERI Y.Shimojo,Y.Ishii	JRR-3M T2-4 (TAS-2)	295
メカニカルミリング法によって得た分子性アモルファス固体の低エネルギー励起 「メカニカルミリング法によって得たアモルファストリメチル-β-シクロデキストリンの低エネルギー励起」	Institute for Chemical Research,Kyoto University I.Tsukushi,T.Kanaya,K.Kaji	JRR-3M C3-1-1 (AGNES)	296
両親媒子系複雑液体のスローダイナミックス 「中性子スピンエコー法による両親媒子系複雑液体のスローダイナミクス」	Faculty of Integrated Arts and Sciences, Hiroshima University T.Takeda,Y.Kawabata,H.Seto,S.K.Ghosh Faculty of Science,Ochanomizu University S.Komura Institute for Solid State Physics,University of Tokyo M.Nagao	JRR-3M C2-2-2 (NSE)	297
マイクロエマルジョンの構造の違いによる界面活性剤膜の運動状態 「紐状ミセルネットワークの中性子スピンエコー実験II」	Faculty of Integrated Arts and Sciences, Hiroshima University H.Seto,T.Takeda,Y.Kawabata,D.Okuhara Department of Chemistry,Tokyo Metropolitan University T.Kato Institute for Solid State Physics,The University of Tokyo M.Nagao Faculty of Science,Ochanomizu University S.Komura	JRR-3M C2-2-2 (NSE)	298
炭化フッ素系界面活性剤水溶液における2次元方向へのミセル成長 「ペルフルオロオクタン酸セシウム水溶液における2次元方向へのミセル成長」	Department of Chemistry,Tokyo Metropolitan University T.Kato,H.Iijima Department of Industrial Chemistry,Tokyo Metropolitan University H.Yoshida The Institute for Solid State Physics, University of Tokyo M.Imai	JRR-3M C1-2 (SANS-U)	299

中性子散乱
5）非晶質・液体

液体カルコゲンの中性子小角散乱 「液体セレンの中性子小角散乱測定」	Faculty of Integrated Arts and Sciences, Hiroshima University M.Inui Faculty of Science,Niigata University K.Maruyama,S.Tamaki Faculty of Science,Kyushu University Y.Kawakita,S.Takeda The Institute for Solid State Physics, University of Tokyo M.Imai	JRR-3M C1-2 (SANS-U)	300
溶融IIIb-Te混合系 「液体In-Te混合系の局所構造」	Department of Physics,Faculty of Science, Kyushu University S.Takeda,Y.Kawakita,S.Yoshioka, H.Nakashima,I.Hiraishi	JRR-3M 4G (GPTAS)	301
ランタノイド（III）有機化合物錯体の構造と溶媒和 「中性子回折法による塩化物イオン水溶液におけるランタンの水和構造」	JAERI T.Yaita,S.Suzuki,H.Narita,S.Tachimori, Y.Ishii	JRR-3M 2G (TAS-1)	302

中性子散乱
6）装　置

研究炉利用高度化の技術開発 「中性子散乱実験用多重極限条件発生装置の性能試験」	Department of Research Reactor,JAERI A.Moriai,S.Ichimura,A.Ohtomo Research Reactor Institute,Kyoto University S.Kawano Faculty of Engineering Sciece,Osaka University A.Onodera	JRR-3M T2-4 (TAS-2)	305
中性子スピンエコー分光器(IMT) 「改3号炉C2-2中性子スピンエコー分光器の改良」	Faculty of Integrated Arts and Sciences, Hiroshima University T.Takeda,H.Seto,Y.Kawabata,D.Okuhara Hahn-Meitner-Institut T.Krist Institute for Solid State Physics,University of Tokyo M.Nagao,H.Yoshizawa Faculty of Science,Ochanomizu University S.Komura Research Reactor Institute,Kyoto University T.Ebisawa,S.Tasaki Forschungszentrum Jülich M.Monkenbusch	JRR-3M C2-2-2 (NSE)	307
IMT 「T1-3ビーム孔での中性子線束評価」	Institute for Materials Research,Tohoku University K.Ohoyama,K.Nemoto,M.Ohashi, Y.Yamaguchi	JRR-3M T1-3 (HERMES) (KPD)	308
IMT、PONTAの整備 「Ef=14.7meV熱中性子用水平集光型アナライザーの開発」	Neutron Scattering Laboratory,Institute for Solid State Physics,University of Tokyo T.Mori Department of Physics,Tokyo Metropolitan University H.Kadowaki CREST,Japan Science and Technology Corporation K.Kakurai	JRR-3M 5G (PONTA)	309
生体物質の中性子回折による研究 「中性子イメージングプレートの最適化の実証」	Advanced Science Research Center,JAERI Y.Karasawa,N.Niimura	JRR-3M 1G-A (BIX-Ⅰ) T2-3 (BIX-Ⅱ)	310
生体物質の中性子回折による研究 「中性子イメージングプレートを用いたBIX-Ⅰでのバックグラウンド測定」	Advanced Science Research Center,JAERI K.Kurihara,I.Tanaka,Y.Karasawa,N.Niimura	JRR-3M 1G-A (BIX-Ⅰ)	311

中性子散乱
6）装　置

生体物質の中性子回折による研究 「前方ガンマ線からの中性子イメージングプレートの遮蔽」	Advanced Science Research Center,JAERI S.Kumazawa,Y.Karasawa,N.Niimura	JRR-3M 1G-A (BIX-Ⅰ)	312
冷中性子散乱実験デバイスの開発 「低磁場制御磁気多層膜ミラーを用いた中性子偏極実験」	JAERI K.Soyama Research Reactor Institute,Kyoto University M.Hino,S.Tasaki	JRR-3M C2-1 (LTAS)	313
冷中性子散乱実験デバイスの開発研究 「NiCr薄膜の特性測定」	JAERI K.Soyama	JRR-3M C2-1 (LTAS)	314
超低温の導入による中性子散乱の研究 「中性子散乱実験用液体ヘリウムフリー希釈冷凍機の開発」	JAERI Y.Koike,Y.Morii Institute for Solid State Physics,University of Tokyo T.Igarashi,M.Kubota Suzuki Shokan Co.,Ltd. Y.Hiresaki,K.Tanida	JRR-3M T2-4 (TAS-2)	315
高圧下での結晶構造・相変態の研究 「高圧下中性子散乱用サファイアアンビルセル」	School of Engineering Science,Osaka University A.Onodera,K.Furuno JAERI Y.Ishii,Y.Morii	JRR-3M T2-4 (TAS-2)	316

中性子散乱
7）生物学

中性子小角散乱法による昆虫リポホリンの構造解析 「昆虫リポホリンの中性子小角散乱」	Institute of Low Temperature Science, Hokkaido University C.Katagiri Institute for Solid State Physics,University of Tokyo M.Imai Graduate School of Yokohama City University M.Sato Faculty of Liberal Arts and Education, Yamanashi University Y.Ito	JRR-3M C1-2 (SANS-U)	319
リポホリン 「昆虫リポホリンによる炭化水素の取り込み」	Institute of Low Temperature Science, Hokkaido University C.Katagiri Advanced Science Research Center,JAERI S.Fujiwara,I.Tanaka,N.Niimura,S.Koizumi Graduate School of Yokohama City University M.Sato Faculty of Liberal Arts and Education, Yamanashi University Y.Ito	JRR-3M C3-2 (SANS-J)	320
中性子小角散乱によるシャペロニンGro-ELの構造と機能の研究 「シャペロニンGro-ELからの中性子小角散乱」	Department of Physics,Jichi Medical School M.Harada Department of Biochemistry,Dokkyo University School of Medicine K.Ichimura Advanced Science Reserch Center,JAERI I.Tanaka,N.Niimura Physics Laboratory,Kansai Medical University H.Kihara	JRR-3M C1-2 (SANS-U)	321

中性子散乱
7）生物学

中性子溶液散乱法によるカイコ細胞質多角体病ウイルスの構造研究 「中性子小角散乱法によるカイコ細胞質多角体病ウイルスの構造研究」	Graduate School of Integrated Sience, Yokohama City University M.Sato Department of Chemistry for Materials,Mie University M.Tomita Neutron Scattering Laboratory,Institute for Solid State Physics,The University of Tokyo M.Imai Faculty of Bioscience and Biotechnology, Tokyo Institute of Technology N.Tanaka Department of Physics,Faculty of Liberal Arts and Education,Yamanashi University Y.Ito	JRR-3M C1-2 (SANS-U)	322
タンパク質の結晶化機構：オリゴマーの形成とその役割 「サーモライシンの結晶化機構：小角中性子散乱による研究」	Department of Bioapplied Chemistry,Osaka City University H.Ooshima,K.Igarashi,J.Kato JAERI S.Fujiwara,I.Tanaka,N.Niimura	JRR-3M C3-2 (SANS-J)	323
中性子回折による生体物質の構造研究 「pH 4.9で作成したニワトリ卵白リゾチーム単結晶の中性子回折測定」	JAERI S.Fujiwara,Y.Karasawa,Y.Minezaki, I.Tanaka,N.Niimura Tsukuba College of Technology Y.Yonezawa	JRR-3M T2-3 (BIX-Ⅱ)	324
生体物質の中性子回折による研究 「BIX-Ⅱを用いた斜晶系ニワトリ卵白リゾチームのデータ収集」	Advanced Science Research Center,JAERI Y.Minezaki,S.Fujiwara,N.Niimura	JRR-3M T2-3 (BIX-Ⅱ)	325
リン脂質膜構造形成においてコレステロール分子の果たす役割に関する研究 「リン脂質膜構造形成においてコレステロール分子の果たす役割に関する研究」	Department of Applied Physics,Nagoya University H.Takahashi,I.Hatta Institute of Materials Structure Science,High Energy Accelerator Research Organization T.Adachi Institute for Solid State Physics,University of Tokyo M.Imai	JRR-3M C1-2 (SANS-U)	326

中性子散乱
7）生物学

グリセロール水溶液中の短鎖ホスファチジルコリンミセルの構造 「ホスファチジルコリン／グリセロール／水系におけるグリセロール分子の分布」	Department of Applied Physics,Nagoya University H.Takahashi,I.Hatta Neutron Scattering Laboratory,The Institute for Solid State Physics The University of Tokyo M.Imai,Y.Matsushita	JRR-3M C1-2 (SANS-U)	327
ヒトデ生体反応誘起物質(ARIS)の構造 「ヒトデ生体反応誘起物質(ARIS)の構造」	Department of Life Science,Tokyo Institute of Technology M.Hoshi,M.Kawamura Institute of Low Temperature Science Hokkaido University C.Katagiri Institute for Solid State Physics,University of Tokyo M.Imai Faculty of Liberal Arts and Education, Yamanashi University Y.Ito	JRR-3M C1-2 (SANS-U)	328

中性子散乱
8）基礎物理学

冷中性子スピン干渉計の開発とその応用 「冷中性子スピン干渉計を用いた周期的スピン依存場による微弱相互作用の観測」	Research Reactor Institute,Kyoto University T.Ebisawa,M.Hino,T.Kawai,S.Tasaki Department of Nuclear Engineering,Kyoto University D.Yamazaki Department of Physics,Kyushu University N.Achiwa SPring8 The Institute of Physical and Chemical Research Y.Otake	JRR-3M C3-1-2 (MINE)	331
冷中性子スピン干渉計の開発とその応用 「RFスピンフリッパーを利用したスピン干渉計」	Department of Nuclear Engineering,Kyoto University D.Yamazaki,H.Tahata Research Reactor Institute,Kyoto University T.Ebisawa,M.Hino,T.Kawai,S.Tasaki Department of Physics,Kyushu University N.Achiwa	JRR-3M C3-1-2 (MINE)	333
低磁場制御冷中性子パルサーの開発 「多層膜冷中性子パルサーを用いた遅延選択実験」	Research Reactor Institute,Kyoto University T.Kawai,T.Ebisawa,S.Tasaki,M.Hino, D.Yamazaki,Y.Matsumoto Department of Physics,Kyushu University N.Achiwa SPring8 The Institute of Physical and Chemical Research Y.Otake	JRR-3M C3-1-2 (MINE)	334
精密中性子光学実験の基礎と応用の研究 「JRR-3M PNOでの干渉計法によるガリウム同位体の中性子散乱長の精密決定」	Advanced Science Research Center,JAERI H.Tomimitsu,K.Aizawa Faculty of Engineering,Tokyo University Y.Hasegawa,S.Kikuta	JRR-3M 3G (PNO)	335
金属基複合材料の中性子応力測定 「SiC粒子強化アルミニウム合金における相応力の中性子およびX線測定」	Nagoya University Y.Akiniwa,K.Tanaka,T.Takezono JAERI N.Minakawa,Y.Morii	JRR-3M T2-1 (RESA)	337

中性子散乱
9）中性子光学

ラーモア回転による中性子波束のスピン干渉 「中性子スピン干渉による磁気多層膜の動力学回折位相」	Department of Physics,Faculty of Science, Kyushu University N.Achiwa Research Reactor Institute,Kyoto University M.Hino,T.Ebisawa,S.Tasaki,T.Kawai	JRR-3M C3-1-2 (MINE)	341
中性子ラーモア回転によるヘリカル磁性体ホロミウムの動力学回折 「中性子ラーモア回転によるHo単結晶ヘリカル磁場による動力学回折位相」	Department of Physics,Faculty of Science, Kyushu University N.Achiwa Research Reactor Institute,Kyoto University M.Hino,S.Kawano Institute for Solid State Physics,The University of Tokyo K.Kakurai	JRR-3M 5G (PONTA)	343
中性子ラーモア歳差回転によるトンネル時間とラーモア時計の研究 「スピン回転によるファブリペロー磁気膜での中性子束縛状態の測定」	Department of Physics,Faculty of Science, Kyushu University N.Achiwa Research Reactor Institute,Kyoto University M.Hino,S.Tasaki,T.Ebisawa,T.Kawai Department of Nuclear Engineering,Kyoto University D.Yamazaki,H.Tahata	JRR-3M C3-1-2 (MINE)	344
多層膜による非鏡面・干渉性散乱成分の測定 「多層膜による特徴的な非鏡面干渉性反射の測定と解析」	Research Reactor Institute,Kyoto University S.Tasaki,T.Ebisawa SPring8 The Institute of Physical and Chemical Research Y.Otake	JRR-3M C3-1-2 (MINE)	345

中性子散乱
１０）その他

中性子回折による残留応力測定 「ステンレス配管溶接部近傍におけるき裂進展に伴う残留応力再分布の測定」	Mechanical Engineering Research Laboratory, Hitachi (Hitachi) S.Okido Mechanical Engineering Research Laboratory, Hitachi (Tsuchiura) M.Hayashi JAERI Y.Morii,N.Minakawa,Y.Tsuchiya	JRR-3M T2-1 (RESA)	349
超低温の導入による中性子散乱の研究 「中性子回折による超伝導コイルジャケットの残留応力測定」	Naka Fusion Research Establishment,JAERI Y.Tsuchiya,T.Kato,H.Nakajima,K.Ishio, H.Tsuji Advanced Science Research Center,JAERI N.Minakawa,Y.Morii	JRR-3M T2-1 (RESA)	350
原子トンネル効果による極低温化学反応の研究 「1.3K ^{3}He-^{4}He量子液体中でのTとHの再結合反応、T+T→T_2及びT+H→HT_3」	JAERI Y.Aratono,T.Kumada,T.Miyazaki School of Engineering,Nagoya University T.Matsumoto	JRR-3M 2G (TAS-1)	351
実用金属材料の損傷検出に関する研究 「熱処理した鋼管の残留応力測定」	Faculty of Sciences and Technology,Ryukoku University K.Inoue,H.Kawashima,J.Sakaguchi JAERI N.Minakawa,Y.Tsuchiya,Y.Morii	JRR-3M T2-1 (RESA)	353
実用金属材料の損傷検出に関する研究 「直径40mmの鋼丸棒の残留応力測定」	Faculty of Sciences and Technology,Ryukoku University K.Inoue,T.Horikawa,H.Nakamura JAERI N.Minakawa,Y.Morii Department of Materials Science Engineering, Ibaraki University Rudiono	JRR-3M T2-1 (RESA)	354
ジルコニア固溶体の構造相転移のその場観察 「高温における$Zr_{0.3}Ce_{0.7}O_2$の正方から立方への相転移のその場観察」	Department of Materials Science and Engineering Interdisciplinary Graduate School of Science and Engineering,Tokyo Institute of Technolgy M.Yashima,T.Oketani,O.Yokota Institute for Materials Research,Tohoku University M.Ohashi,K.Ohoyama,Y.yamaguchi	JRR-3M T1-2 (KSD)	355

中性子散乱
１０）その他

イオン交換により合成したリチウム遷移金属酸化物の構造 「層状岩塩型リチウム含有鉄酸化物の構造」	Department of Chemistry,Faculty of Science, Kobe University A.Hirano,R.Kanno Osaka National Research Institute,AIST M.Tabuchi Institute for Materials Research,Tohoku University K.Oyama,M.Ohashi,Y.Yamaguchi	JRR-3M T1-3 (HERMES) (KPD)	356

中性子ラジオグラフィ

研究テーマ「表題」	所属 担当者	利用原子炉及び装置名	報告書等	頁
中性子ラジオグラフィによる矩形流路内沸騰二相流のボイド率計測「片面加熱矩形流路内サブクール沸騰時のボイド率計測と最適解析モデルの検討」	原研 伝熱流動研究室 呉田　昌俊 秋本　肇	JRR-3M 7R (TNRF)	本文参照	359
溶融炉心の圧力容器内流動に関する基礎研究「下部ヘッド内挙動に関する水／液体金属二相可視化実験」	原研 原子炉安全工学部 柴本　泰照 中村　秀夫 安濃田　良成	JRR-3M 7R (TNRF)	1. 柴本泰照他２名,「小型容器を用いた溶融炉心下部ヘッド内挙動に関する流動可視化基礎実験」,1998,混相流シンポジウム'98 2. "Visualization of Simulated Molten-Fuel Behavior in the Pressure Vessel Lower Head Using High-Frame-Rate Neutron Radiography" Nakamura 他 1998(投稿中),Nuclear Technology	360
高温融体と冷却材の混合の可視化に関する研究「水蒸気爆発粗混合過程の中性子ラジオグラフィによる可視化」	京都大学 原子炉実験所 三島　嘉一郎 日引　俊 齊藤　泰司 原研 炉心損傷 安全研究室 杉本　純 森山　清史 原研 研究炉技術開発室 松林　政仁 市川　博喜	JRR-3M 7R (TNRF)	1. 三島嘉一郎他４名, Visualization Study of Molten Metal-Water Interaction by Using Neutron Radiography 1997(印刷中),Nuclear Engineering and Design 2. 齊藤　泰司他５名, Application of High-Frame-Rate Neutron Radiography to Steam Explosion Research,1998.3, 3rd International Topical Meeting on Neutron Radiography(Luzerunm Switzerland)	361

中性子ラジオグラフィ

研究テーマ「表題」	所属 担当者	利用原子炉及び装置名	報告書等	頁
研究炉に関する工学的開発研究 「中性子ラジオグラフィに関する開発研究」	原研 研究炉技術開発室 松林 政仁	JRR-3M 7R (TNRF)	1. 松林政仁他1名, 「中性子ビーム線質の規格化の試み」 第2回放射線シンポジウム講演論文集,1997.10, 2. 松林政仁他1名, 「イメージングプレートを用いた文化財非破壊検査技術」,1998, 非破壊検査,第47巻5号 312-314	363
「JRR-3M高束中性子NRシステムによる熱流動現象の可視化と計測に関する研究(II)」	神戸大学 竹中 信幸 浅野 等 小野 厚夫 後 利彦 瀬川 耕司 和田 哲昌 永江 信也 岩谷 淳二 迫田 健吾 浜田 尚志 隅 信介 水端 稔 西岡 聡 荒川 哲矢 小林 幸司 野口 泰幹 木下 泉 西 義久 古谷 正裕 藤江 政武 西村 聡 柴田 豊 関西大学 小澤 守 梅川 尚嗣 松田 健 福田 和将 神戸商船大学 中沢 武 原研 松林 政仁	JRR-3M 7R(TNRF)	本文参照	364

中性子ラジオグラフィ

研究テーマ「表題」	所属 担当者	利用原子炉及び装置名	報告書等	頁
「JRR-3M TNRF2を用いたNRG用電子撮像装置の高解像度化に関する研究」	武蔵工業大学 持木 幸一 村田 裕 宇野 貴之 三野 勉稔 岩田 秀規 原研 松林 政仁	JRR-3M 7R(TNRF)	本文参照	372
「TNRF2およびC2-3中性子ラジオグラフィ用照射場の定量化」	立教大学 小林 久夫 原研 研究炉技術開発室 松林 政仁 神奈川歯科大学 若尾 博美 郵政省 渡辺 茂弥 藤田保健衛生大学 加藤 一夫	JRR-3M 7R(TNRF) C2-3-1 (CNRF)		379
「中性子ラジオグラフィの電池研究への応用」	東京学芸大学 教育学部 鎌田 正裕 京都大学 原子炉実験所 藤根 成勲 米田 憲司 原研 市川 博喜 松林 政仁	JRR-3M 7R(TNRF)		384

即発γ線分析

研究テーマ「表題」	所属 担当者	利用原子炉及び装置名	報告書等	頁
農林水産研究における原子炉中性子即発ガンマ線分析法の利用「中性子即発ガンマ線分析法による農林水産関係試料中のホウ素およびケイ素の定量」	農林水産省 畜産試験場 宮本　進 西村　宏一 農林水産省 遠洋水産研究所 塩本　明弘 農林水産省　農業環境技術研究所 山崎　慎一 原研 分析センター 米沢　仲四郎 松江　秀明 星　三千男	JRR-3M PGA	宮本進他６名, 「中性子即発ガンマ線分析法による羊試料(血液、尿、臓器)中ホウ素の定量」, 1998.7,第35回理工学における同位元素研究発表会要旨集,P168	389
火山岩試料の即発γ線分析「火山岩中ホウ素の高確度即発γ線分析」	学習院大学理学部（現　立正大学地球環境科学部） 福岡　孝昭 京都大学総合人間学部（現　京都大学理学部） 佐野　貴司 東北大学　東北アジア研究センター 長谷中　利昭 原研 分析センター 米沢　仲四郎 松江　秀明 東京大学　原子力研究総合センター 澤幡　浩之	JRR-3M PGA	1. 佐野貴司他５名, 「即発γ線による火山岩中ホウ素の分析：ケイ素を用いた内部標準法」, RADIOISOTOPES(印刷中) 2. 佐野貴司他５名 Accurate and efficient determination of boron content in volcanic rocks by neutron-induced,prompt γ-ray analysis J.Radioanal.Nucl.Chem. (印刷中)	391

即発γ線分析

研究テーマ「表題」	所属 担当者	利用原子炉及び装置名	報告書等	頁
隕石試料の即発γ線分析「コンドライト質隕石のケイ素の分析－即発γ線分析によるコンドライト質隕石のケイ素の定量－」	東京都立大学 大学院理学研究科 海老原　充 S.K.Latif 大浦　泰嗣 G.W.Kallemeyn 中原　弘道 原研 分析センター 米沢　仲四郎 松江　秀明 東京大学　原子力研究総合センター 澤幡　浩之	JRR-3M PGA	S.K.Latif他７名, Prompt gamma-ray analysis (PGA) of meteorite samples, with emphasis on the determination of Si 1998,J.Radioanal.Nucl.Chem. (印刷中)	393
即発γ線分析の大型試料への適用「銅鏡の即発γ線分析」	東京都立大学 大学院理学研究科 中原　弘道 末木　啓介 大浦　泰嗣 齋藤　綾子 慶応大学　文学部 富沢　威 大阪府教育委員会 西川　寿勝 原研 分析センター 米沢　仲四郎 松江　秀明	JRR-3M PGA	中原弘道他８名, Prompt gamma ray anaiysis of archaeological bronze J.Radioanal.Nucl.chem. (印刷中)	394
即発ガンマ線分析(PGA)の化学への応用「即発ガンマ線測定による非破壊状態分析の開発」 (1) テルミット反応生成物のキャラクタリゼーションへの応用 (2)即発γ線線形解析法の改良	大同工業大学 工学部 酒井　陽一 東京大学大学院 理学系研究科 久保　謙哉 原研 分析センター 米沢　仲四郎 松江　秀明 東京大学　原子力研究総合センター 澤幡　浩之 伊藤　泰男	JRR-3M PGA	酒井陽一他７名, Mossbauer characterization and prompt γ-ray analysis of the products of thermit reactions J.Radioanal.Nuclear chemisty,1999,(印刷中)	396

即発γ線分析

研究テーマ「表題」	所属 担当者	利用原子炉及び装置名	報告書等	頁
原子炉冷・熱中性子フルエンスの標準化とその応用に関する研究「球形比例計数管のガス増幅率位置依存性の測定-2-」	電子技術総合研究所 武田 直人 工藤 勝久 原研 分析センター 米沢 仲四郎 松江 秀明 安達 武雄 星 三千男	JRR-3M PGA		397
核反応を利用する分析化学「中性子即発γ線分析の研究」	原研 分析センター 松江 秀明 米沢 仲四郎	JRR-3M PGA	本文参照	398
陽極アルミナ皮膜中の水素含有量と分布「アルミニウム陽極酸化皮膜中の水素の濃度と分布」	東京都立大学 理学研究科 森崎 重喜	JRR-3M PGA	本文参照	400
中性子ガイドビームを用いた中性子吸収反応の核・放射化学への応用「中性子捕獲即発γ線スペクトル中のピーク形状」	熊本大学 工学部 岸川 俊明 野口 悟 原研 分析センター 米沢 仲四郎 松江 秀明 秋田大学教育学部 中村 昭 東京大学 原子力研究総合センター 澤幡 浩之	JRR-3M PGA	本文参照	402

即発γ線分析

研究テーマ「表題」	所属 担当者	利用原子炉及び装置名	報告書等	頁
「固体環境試料および地球化学的試料の即発ガンマ線分析」	東京大学大学院 総合文化研究科 松尾 基之 久野 章仁 大野 渉 久保 健一 原研 分析センター 米沢 仲四郎 松江 秀明 東京大学 原子力 研究総合センター 澤幡 浩之	JRR-3M PGA	本文参照	405

放射化分析

研究テーマ「表題」	所属 担当者	利用原子炉及び装置名	報告書等	頁
ラジオアイソトープ技術者の養成「実習 放射化分析ー貝殻中の銅・ナトリウムの放射化分析ー」	原研 東京研修センター 上沖 寛	JRR-3M 気送管		413
非放射性^{41}Kの長期間追跡のための新たな測定・解析手法の開発「^{41}K存在比の高精度測定と^{41}K追跡法によるカリウムの作物吸収率の算出ー放射化分析利用による安定^{41}Kトレーサ法の開発ー」	農業環境技術研究所 分析法研究室 結田 康一	JRR-3M 気送管	本文参照	414
農林生態系におけるハロゲン元素の動態「世界の土壌・植物系におけるハロゲン元素の含量レベルと動態の解明 ータンザニア国キリマンジャロ州と日本国北海道・九州の土壌ー」	農業環境技術研究所 分析法研究室 結田 康一 元農業技術研究所 井磧 昭	JRR-3M 気送管	本文参照	416
「海洋生物に含まれる微量元素の放射化分析法」	北海道大学 アイソトープ総合センター 大西 俊之 野矢 洋一	JRR-3M HR-1,PN-3		418
「植物の葉に含まれるコバルト分布図の作成」	北海道大学 アイソトープ総合センター 増子 捷二 笠原 茂	JRR-3M PN-1		422

放射化分析

研究テーマ「表題」	所属 担当者	利用原子炉及び装置名	報告書等	頁
惑星物質の元素の移動・分配に関する研究「マグマの希土類元素の組成変化－古富士火山末期から新富士火山にわたるマグマの希土類元素の組成変化－」	地質調査所 富樫 茂子 静岡県農業試験場 海岸砂地分場 宮地 直道 日本大学 文理学部 安井 真也 角田 明郷 朝倉 伸行 遠藤 邦彦 防災科学技術研究所 鵜川 元雄	JRR-3M HR-1,2	1.富樫茂子他６名, 古富士火山末期から新富士火山にわたるマグマの組成変化-富士吉原火山活動観測のボーリングコアの岩石化学的性質,火山42(1997)409-421 2.安井真也他５名, 富士火山・1707年降下火砕堆積物中の斑れい岩質岩片の岩石学的性質とその起源,火山43(1998)43-49	428
惑星物質における元素の移動・濃集機構の研究「堆積岩中の微量元素の挙動－日本で採取された風送塵のSr,Ce,Nd同位体比－」	地質調査所 上岡 晃 気象研究所 五十嵐 康人 広瀬 勝己	JRR-3M HR-1	本文参照	429
伊豆小笠原弧背弧域における火成活動および熱水活動に関する研究「伊豆小笠原弧背弧海山の斑岩銅型鉱化作用－関連火成岩の活動時期－」	地質調査所 石塚 治 湯浅 真人 宇都 浩三 東京大学 海洋研究所 石井 輝秋 University of California,Santa Cruz A.G. Hochstaedter	JRR-3M HR-1	1.石塚治他２名, 伊豆小笠原弧背弧海山の形成史－万治海山潜航調査－13,457-472 2.石塚治他２名, 伊豆小笠原弧背弧海山の低温熱水活動,14(提出中)	430
地球内部物質の放射化分析「海洋島玄武岩類の微量成分元素の挙動と成因 －インド洋モーリシャス島火山岩類の地球化学およびK-Ar年代－」	地質調査所 宇都 浩三 徐 勝 東京大学 地震研究所 兼岡 一郎	JRR-3M HR-2		431

放射化分析

研究テーマ「表題」	所属 担当者	利用原子炉及び装置名	報告書等	頁
「中性子放射化分析による宇宙・火山起源物質の研究」	学習院大学理学部（現 立正大学地球環境科学部） 福岡 孝昭 京都大学 理学部 田澤 雄二	JRR-3M HR-1,2 PN-2,3 JRR-4 PN Sパイプ	本文参照	432
農業環境における原子炉利用新技術の開発と拡大に関する研究 「中性子照射による土壌重金属元素の直接標識化トレーサ利用法の開発－土壌および農業有機資材中元素の直接標識化－」	農業環境技術研究所 櫻井 泰弘 結田 康一 高橋 義明 牧野 知之 上村 順子	JRR-3M 気送管	櫻井泰弘他４名, 「中性子照射による土壌および農業資材中元素の直接標識化」,第35回理工学における同位元素研究発表会,講演要旨p.202(1998.6)	436
新アクチバブルトレーサーをマーカーとした家畜消化管内容物移動の解析手法の開発 「サマリウム、ランタン等をマーカーとした家畜消化管内容物移動の解析」	農林水産省 畜産試験場 松本 光人 宮本 進 山岸 規昭	JRR-3M 気送管		437
高温工学に関する先端的基礎研究 「高温用低原子番号半導体の中性子転換ドーピングの予備試験 －NTDにより生成した単結晶炭化ケイ素中の燐の測定－」	原研 高温照射研究室 馬場 信一 荒井 長利 原研 技術開発課 伊藤 久義 梨山 勇	JRR-3M 気送管	馬場信一他３名, 「中性子転換ドーピングによる高温用SiC半導体の創製に関する予備的検討」, 1998年3月, JAERI-memo-10-087	438
核反応を利用する分析化学 「中性子放射化分析の研究」	原研 分析センター 米沢 仲四郎 松江 秀明	JRR-3M HR-2 PN-1,3	本文参照	439
「食餌中セレンと悪性腫瘍に関する研究」	北里大学 獣医畜産学部 伊藤 伸彦 千田 伸 甲斐 千恵美 田畑 ひとみ 夏堀 雅宏	JRR-3M 気送管	本文参照	440

放射化分析

研究テーマ「表題」	所属 担当者	利用原子炉及び装置名	報告書等	頁
「バルト海産ネズミイルカ (Phocoena Phocoena)の有機態ハロゲン(Cl,Br, I)	愛媛大学 農学部 脇本 忠明 河野 公栄 松田 宗明	JRR-3M 気送管	本文参照	445
「新規な抽出試薬による金属元素の予濃縮－放射化分析」	山形大学 工学部 阿部 重喜 遠藤 昌敏 船田 俊祐 池田 光治	JRR-3M 気送管	本文参照	448
「隕石試料の放射化分析(II)」	日本大学文理学部 永井 尚生 本田 雅健 堂園 克久 東京大学 原子核研究所 今村 峯雄	JRR-3M DR-1	本文参照	453

ＲＩの製造

研究テーマ「表題」	所属 担当者	利用原子炉及び装置名	報告書等	頁
「中性多座配位子を用いるランタニド(Ⅲ)の抽出・選択性」	茨城大学　理学部 井村　久則 大橋　弘三郎 石倉　美保子 亀田　直弘 原研　アクチノイド溶液化学研究グループ 吉田　善行 木村　貴海 目黒　義弘	JRR-3M HR	本文参照	461
「LIX54と中性二座配位子によるランタノイド(Ⅲ)の協同効果抽出」	東北大学 素材工学研究所 武井　周一 秋葉　健一 八戸工業高等専門学校 中村　重人	JRR-3M HR-2 JRR-4 Sパイプ	本文参照	465
非定常放出に対するガスモニタ校正法の開発「放射性ガスのパルス注入に対するガスモニタの応答解析」	原研　線量計測課 大石　哲也 吉田　真	JRR-3M PN-1	1.大石哲也他１名, 第35回日本原子力学会要旨集,第Ⅰ分冊,(1997),p.53 2.大石哲也他１名, 第36回日本原子力学会要旨集,第Ⅰ分冊,(1998),p.134	469

原子炉材料

研究テーマ「表題」	所属 担当者	利用原子炉及び装置名	報告書等	頁
原子力用機能性材料の研究開発「酸化リチウム焼結体からのヘリウム放出挙動」	原研 谷藤 隆昭 八巻 大樹 野田 健治	JRR-2 VT-7 JRR-4 Sパイプ	本文参照	473
原子力用先進機能性材料の研究開発「照射下セラミック材料の電気絶縁劣化特性試験－Al_2O_3,MgO単結晶の中性子およびγ線照射下電気伝導度「その場」測定－」	原研 谷藤 隆昭 片野 吉男 中沢 哲也 野田 健治	JRR-3M BR-2	本文参照	475

核物理

研究テーマ「表題」	所属 担当者	利用原子炉及び装置名	報告書等	頁
アイソトープの核化学的研究「マイナーアクチニドの中性子吸収断面積の測定－^{243}Am(n,γ)^{244}Am反応の中性子吸収断面積の測定－」	原研 核化学研究室 初川 雄一 篠原 伸夫 畑 健太郎	JRR-3M HR	初川雄一他2名, ^{243}Am(n,γ)^{244}Am反応の中性子吸収断面積の測定, Proceedings of the 1997 Symposium on Nuclear Data Nov.27-28 1998,JAERI,Tokai, Japan	479
「^{59}Feをプローブとした強磁性体の超微細相互作用の研究」	新潟大学 理学部 大矢 進 大坪 隆 新潟大学 自然科学研究科 趙 徳濟	JRR-3M HR		480

その他

研究テーマ「表題」	所属 担当者	利用原子炉及び装置名	報告書等	頁
研究炉に関する工学的開発研究「レプリカスーパーミラーの開発」	京都大学 原子炉実験所 川端 祐司 田崎 誠司 梁宮 一政 原研 鈴木 正年	JRR-3M C2-3-4	本文参照	485
フィッション・トラック年代測定における壊変定数を用いた絶対年代較正「標準ガラスによる熱中性子線量の絶対測定－新しい標準ガラスIRMM-540を用いた熱中性子線量測定とフィッション・トラック年代較正－」	㈱京都フィッション・トラック 岩野 英樹 吉岡 哲 檀原 徹	JRR-3M 気送管	本文参照	486
「高速及び熱中性子照射による石英結晶中の点欠陥生成とESR解析」	山口大学 理学部 地球科学教室 福地 龍郎	JRR-3M PN-1,2,3 JRR-4 Tパイプ	本文参照	487
「4πNaI(Tl)γ線検出器による^{166m}Hoの放射能精密測定法の開発」	名古屋大学 工学研究科 宮原 洋 上田 直由 森 千鶴夫 原研 竹内 紀男 大久保 昌武	JRR-3M HR,PN	本文参照	492
「中性子放射化核種のガンマ線エネルギー精密測定法の開発」	熊本大学 工学部 岸川 俊明 上村 実也	JRR-3M,4 気送管	本文参照	496
「LiAlの電気的性質の中性子照射効果の研究」	青森大学 工学部 矢萩 正人 法政大学 工学部 栗山 一男 浜中 廣見 原研 須貝 宏行 棚瀬 正和	JRR-3M HR JRR-4 T-パイプ	本文参照	500

その他

「隕石中の微小構成粒子の同位体・化学組成とその形成環境の研究」	名古屋大学大学院 理学研究科 田中　剛 岩森　光 平原　靖大 矢来　博司 米澤　千夏 C.Dragusann 林　正人 戸上　薫	JRR-3M HR-2	本文参照	504
「低速陽電子ビーム発生の基礎実験」	東京大学　原子力研究総合センター 伊藤　泰男 理化学研究所 伊東　芳子	JRR-4 T-パイプ	本文参照	508
「ランタノイド(Ⅲ)錯体の安定度の順序」	武蔵大学　基礎教育センター 藥袋　佳孝 東京理科大学 理学部 広瀬　彰一 長谷川　佑子 東京大学大学院 理学系研究科 高橋　嘉夫 小橋　浅哉 富永　健	JRR-3M 気送管	本文参照	515

1. Neutron Scattering

1) Magnetism

2) Polymer

4) Superconductivity

8) Fundamental Physics

9) Neutron Optics

10) Etc

4. Neutron Activition Analysis

This is a blank page.

研究成果一覧 (Research Reports)

1. 中性子散乱 (Neutron Scattering)

1) 磁　性 (Magnetism)

This is a blank page.

研究テーマ：(2)強相関電子系の中性子散乱による研究
表題：$CuGe_{1-x}Si_xO_3$の磁気相図

Magnetic phase diagram of $CuGe_{1-x}Si_xO_3$

J. Akimitsu, O. Fujita, M. Nishi[1], K. Kakurai[1], Y. Fujii[1] and S. Katano[2],

Department of Physics, Aoyama-Gakuin University, Chitosedai, Setagaya-ku, Tokyo 157-8572
[1]Neutron Scattering Laboratory, ISSP, The University of Tokyo, Tokai, Ibaraki 319-1106
[2]Neutron Scattering Group, Advanced Science Research Center, Japan Atomic Energy Research Institute, Tokai, Ibaraki 319-1195

The discovery of the compound $CuGeO_3$, which is the first inorganic spin-Peierls (SP) material, stimulated many extensive studies in order to understand its unique physical properties. The coexistence of the SP state and long range antiferromagnetic (AF) order in Zn and Si doped crystals has attracted much attention since it has been naively believed that this cannot occur at the same time in a unique phase. Evidence for the coexistence of the lattice dimerization and the AF order has, however, been revealed by neutron diffraction experiments; both superlattice reflections originated from lattice dimerization and magnetic Bragg peaks are observed below the Néel temperature (T_N) in $Cu_{1-x}Zn_xGeO_3$ and in $CuGe_{1-x}Si_xO_3$. It has also been shown theoretically with phase Hamiltonian technique that disorder induced AF order is possible in the SP state $CuGeO_3$ doped with Si and Zn.

Although several experiments on the doping effect have been performed, there are still some discrepancies. In the present work, hence, the magnetic phase diagram of the Si doped system has been investigated in more detail over a wide range of the doping concentration. The results show that the effects of the Si doping on the magnetic states are rather weak in comparison with those reported in the previous work on the other hand, the effects of Si are a little stronger than those of the Zn doping.

The magnetic moments of Cu^{2+} ions weredetermined by the magnetic intensities observed. The *effective* magnetic moment is 0.21 μ_B for 1.0%, and 0.29 μ_B for 1.8% sample. All the data are presented in Fig. 1 (a). The magnitude of the magnetic moment roughly has a linear relation with T_N. In this figure the concentration dependence of magnetic moments for the Zn doping previously reported[1)] is also shown by the dotted line. The results show a similar tendency for both impurities. The lattice dimerization along the Cu-chain direction is also obtained. Figure 1 (b) shows the dimerization δ

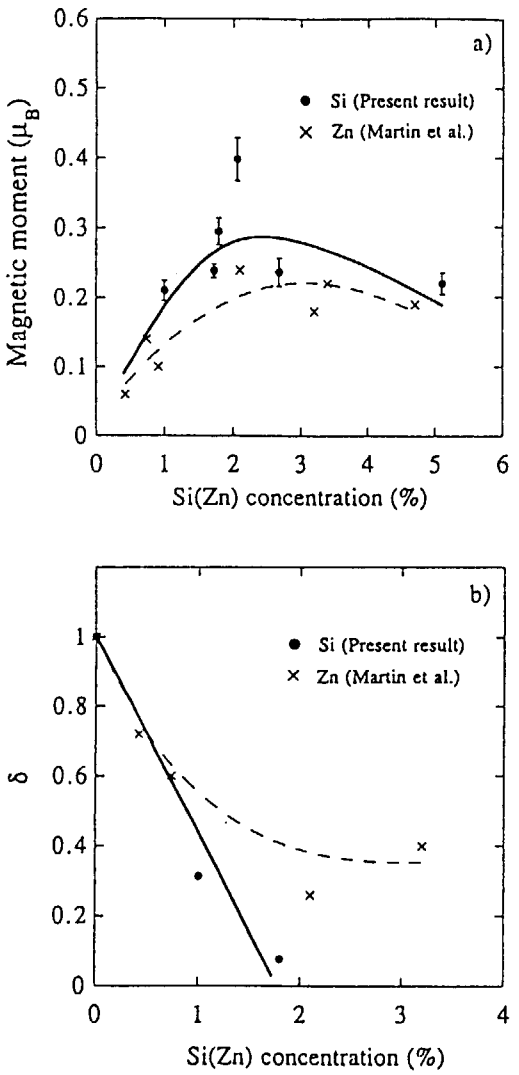

FIG. 1. Magnitude of the magnetic moment (a) and the lattice distortion (b) as a function of the Si concentration. The solid lines are guides to the eye. The dotted lines indicate the data for the Zn doped system observed by Martin *et al.*

at 1.5 K which was normalized by the value of the pure compound. The lattice distortion is greatly suppressed with the Si doping at low temperatures as was mentioned before, and would not be observed over 2.5 % Si. This result is quite different from the work on the Zn doping [1] which is shown by the dotted line in the figure.

Figure 2 shows the magnetic phase diagram as a function of the Si concentration. Comparing with Fig. 1, T_N and T_{SP} are found to have linear relations roughly with the magnetic moments and the lattice dimerization, respectively. The dotted line in this figure shows the results for the Zn doping, and similar discussion mentioned above can be made. For the Si doping, the present result agrees well with the recent work.[2] However, the results show some distinctive discrepancies with those in the previous works[3,4] which is shown by the dash-dotted line. The concentration dependence of T_{SP} reported there is almost twice as large as that of the present result. On this point, a recent report showed that the concentration dependence of these transition temperatures are strongly affected by the preparation temperature for crystals and powdered samples.[5] The discrepancies with the previous results, hence, may be caused by a slight difference of the sample preparation temperatures. As another possibility, the difference in the O_2 deficiency of the samples[5] could be pointed out.

To conclude, the coexistence of the SP and AF states in $CuGe_{1-x}Si_xO_3$ single crystals was carefully examined by neutron diffraction experiments. The Si concentration dependence of the magnitudes of the magnetic moment and the lattice dimerization were presented for a wide range of the concentration.

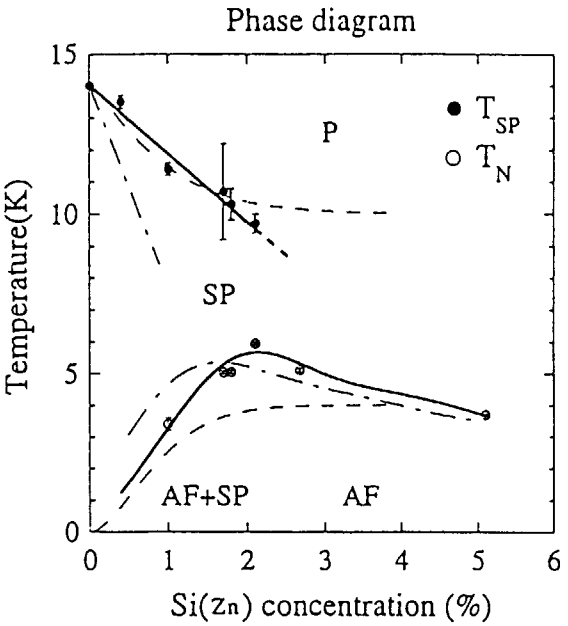

FIG. 2. Magnetic phase diagram as a function of Si concentration. The solid lines are guides to the eye. The dash-dotted lines show the previous results for the Si doped system reported by Renard *et al.*, and the dotted lines represent the data for the Zn doped system observed by Martin *et al.*

References

[1] M. C. Martin, M. Hase, K. Hirota, G. Shirane, Y. Sasago, N. Koide and K. Uchinokura , Phys. Rev. B**56**, 3173 (1997).
[2] K. Hirota, M. Hase, J. Akimitsu, T. Masuda, K. Uchinokura and G. Shirane , J. Phys. Soc. Jpn. (submitted)
[3] J. P. Renard, K. LeDang, P. Veillet, G. Dhalenne, A. Revcolevschi and L. P. Regnault , Europhys. Lett. **30**, 475 (1995).
[4] L. P. Regnault, J. P. Renard, G. Dhalenne and A. Revcolevschi , Europhys. Lett. **32**, 579 (1995).
[5] M. Weiden, R. Hamptmann, W. Richter, C. Geibel, P. Hellmann, M. Köppen, F. Steglich, M. Fishier, P. Lemmens, G. Güntherodt, A. Krimmel and G. Nieva , Phys. Rev. B**55**, 15067 (1997).

研究テーマ：(2)強相関電子系の中性子散乱による研究
表題：梯子格子物質；$Sr_{2.5}Ca_{11.5}Cu_{24}O_{41}$における反強磁性磁気秩序

Hole-induced antiferromagnetic ordering in the spin singlet state of the ladder material : $Sr_{2.5}Ca_{11.5}Cu_{24}O_{41}$

J. Akimitsu, T. Nagata, H. Fujino, M. Nishi[1], K. Kakurai[1], and S. Katano[2]

Department of Physics, Aoyama-Gakuin University, Setagaya-ku, Tokyo 157-8572
[1]Neutron Scattering Laboratory, ISSP, The University of Tokyo, Tokai, Ibaraki 319-1106
[2]Neutron Scattering Group, Advanced Science Research Center, Japan Atomic Energy Research Institute, Tokai, Ibaraki 319-1195

It has long been believed that the ground state of the two-leg ladder system is a singlet state called "the spin liquid state" and this has been confirmed experimentally by the NMR and neutron scattering measurements. From NMR (Knight shift) measurements, spin gap values (ladder) of $Sr_{14}Cu_{24}O_{41}$, $Sr_9Ca_5Cu_{24}O_{41}$ and $Sr_{2.5}Ca_{11.5}Cu_{24}O_{41}$ were reported to be 44 meV, 24 meV and 23 meV, respectively [1]. In inelastic neutron scattering measurements, on the other hand, the spin gap of 32.5 meV, 33.5 meV were observed for $Sr_{14}Cu_{24}O_{41}$ and $Sr_{2.5}Ca_{11.5}Cu_{24}O_{41}$ [2,3].

Recently, however, we observed the magnetic long range order by the heat capacity and neutron scattering measurements. In this paper, we report the neutron scattering measurements on $Sr_{14-x}Ca_xCu_{24}O_{41}$ single crystal at low temperatures around 2 K. Our experiments revealed the new results for the magnetic ground state at high Ca concentration x (x = 11.5) under ambient pressure. From the specific heat results, we observed a magnetic long range order at x ~ 11.5 under fairly low temperatures (T_N ~ 2.1 K) compared with the spin gap value. Magnetic Bragg peaks below T_N were also observed in the neutron scattering measurements on a $Sr_{2.5}Ca_{11.5}Cu_{24}O_{41}$ single crystal.

We performed an elastic neutron scattering for a single crystal $Sr_{2.5}Ca_{11.5}Cu_{24}O_{41}$. From this experiment, we observed a number of Bragg peaks which appeared below 2 K. Figure 1 shows the typical elastic neutron scattering results at (1 0 l), (0 1 l) and (h 0 12), these results were plotted after subtracting the intensity at 5 K from that at 1.4 K. We confirmed that the FWHM of the observed Bragg peaks is nearly the resolution limit. Figure 2 shows the positions of the observed Bragg peaks in the reciprocal lattice space, where the arrow lines and circles correspond to the lines scanned and the Bragg peaks observed, respectively. To clarify whether these Bragg peaks are magnetic or not, we performed the polarized neutron scattering experiments for one of the Bragg peaks, (1 0 12), as shown in figure 3. In both horizontal and vertical field, we observed the spin-flip scattering at 1.4 K. These results clearly show that the

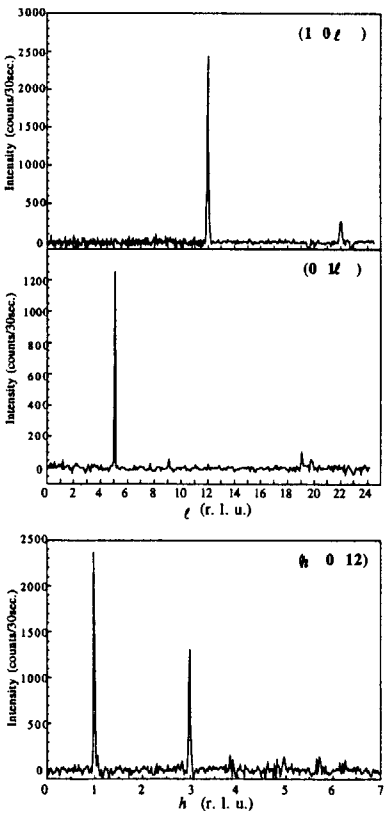

Fig. 1 Typical results by elastic neutron scattering experiments at (1 0 l), (0 1 l) and (h 0 12) of the $Sr_{2.5}Ca_{11.5}Cu_{24}O_{41}$ single crystal, these results were plotted after subtracting the intensity at 5 K from that at 1.4 K.

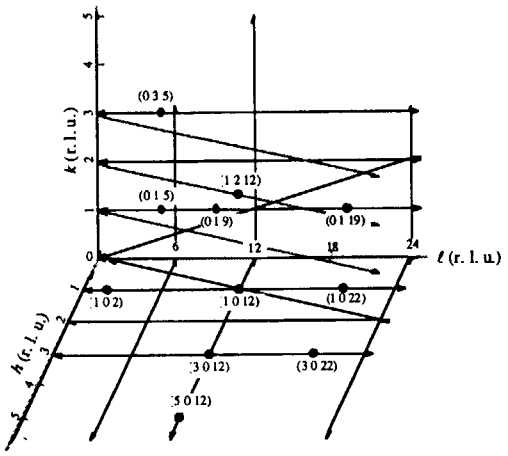

Fig. 2 Positions of the observed Bragg peaks observed by neutron scattering measurements in the reciprocal lattice space of $Sr_{2.5}Ca_{11.5}Cu_{24}O_{41}$ single crystal, arrow lines and circles correspond to the scanned lines and the observed Bragg peaks, respectively.

observed Bragg peak, (1 0 12), is purely magnetic. The static magnetic moments directs almost along the *a*-axis in the ladder planes by taking into account of the scattering vector's direction and the peak intensity at (1 0 12).

Assuming that magnetic spins in the ladders are responsible for the magnetic order, the appearance of (3 0 12) Bragg peak leads to the ferromagnetic order in the *a-c* plane, and this ferromagnetic order aligns antiferromagnetically in the adjacent layers. However, due to the absence of (0 *k* 0) reflection, the possibility of the ferromagnetic or ferrimagnetic order in the plane is excluded. Therefore, we conclude that the spins are antiferromagnetically ordered in the *a-c* plane. However, at present stage, we cannot construct the reasonable magnetic structure in the ladder planes. The final magnetic structure is now under consideration.

We emphasize here the ground state of this system. As described before, inelastic neutron scattering has directly indicated that the spin gap energy for the ladders in the $Sr_{2.5}Ca_{11.5}Cu_{24}O_{41}$, the same material in our present experiment, was found to be 33.5±0.5 meV [3]. Therefore, it is likely that magnetic order is due to some of the unpaired spins, breaking up spin singlet states by introducing the holes into ladders, and these unpaired spins ordered antiferromagnetically at low temperature. Accordingly the ground state of this system at ambient pressure might be one in

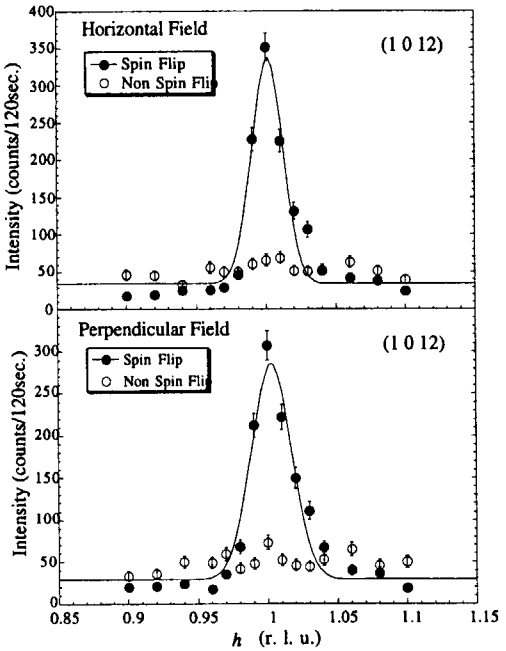

Fig. 3 The experimental results for one of the Bragg peak, (1 0 12) of $Sr_{2.5}Ca_{11.5}Cu_{24}O_{41}$ single crystal at 1.4 K using polarized neutrons. Horizontal field corresponds to the parallel to the scattering vector Q and the vertical field correspond to the perpendicular to the scattering plane at the sample position.

which both paired and unpaired spins coexist and the holes and spins float in a " spin liquid sea " at high temperature. These holes are localized at certain temperature and the spins finally order at $T_N \sim 2.1$ K.

References

[1] K. Magishi, S. Matsumoto, Y. Kitaoka, K. Ishida, K. Asayama, M. Uehara, T. Nagata and J. Akimitsu, Phys. Rev. B **57**, 11533 (1998).
[2] R. S. Eccleston, M. Uehara, J. Akimitsu, H. Eisaki, N. Motoyama and S. Uchida, Phys. Rev. Lett. (to be published).
[3] S. Katano, T. Nagata, J. Akimitsu, M. Nishi and K. Kakurai, preprint.

研究テーマ：強相関電子系の中性子散乱による研究
表題：少数キャリアー物質CePの外場の下における中性子散乱による研究

Neutron Scattering Studies of the Low-Carrier System CeP under External Field

T. Osakabe, M. Kohgi[1], K. Iwasa[1], Y. Haga and T. Suzuki[2]

Advanced Science Research Center, Japan Atomic Energy Research Institute, Tokai, Ibaraki 319-11
[1]Department of Physics, Tokyo Metropolitan University, Hachioji, Tokyo 192-03
[2]Department of Physics, Tohoku University, Sendai 980-77

CeP is a low-carrier-density semi-metallic compound with NaCl-type crystal structure. Recently, Tohoku Univ. group have successfuly made high quallity single crystal samples of CeP. In paticular, the de Haas-van Alphen signal was detected on samples of batch no.2, 3 and 7 (we will abbreviate these to "CeP#2" etc.) It has been revealed by macroscopic measurements such as magnetization or specific heat measurements that CeP#2 and CeP#3 show unusual magnetic phase diagrams under magnetic field or under high pressure[1-3]. Although the static measurements gave no definite information about the datailes of the phass diagrams, our neutron scattering studies revealed that there are actually defferent phases in the diagrams. In this report, we briefly show the recent results of our neutron scattering experiments on CeP#3 and CeP#7 under external field.

Fig. 1 shows the phase diagrams determined by the neutron diffraction experiments on CeP#3 under magnetic field below 6T and under high pressure below 1.7 GPa. The magnetic structures in each phases are schematically shown at the bottom of the phase diagrams, where long and short arrows indicate the Ce ferromagnetic sheets with moment values for each Ce ion to be about 2 and 0.7 μ_B .

These two phase diagrams are quite similar. There is a scalling of 1GPa of pressure to 12T of magnetic field. At zero magnetic field with ambient pressure, CeP#3 show typical type-I antifferomagnetic ordering below the Neel temperature of T_N=10.5K, where each ferromagnetically orderd (001) plane stacks antifferomagnetically with the direction of the magnetic moment perpendicular to the plane. The magnetic moment per Ce atom is estimated to be $0.8\mu_B$+-0.1 μ_B, a value close to that of a Γ_7 crystal field state Ce^{3+} ion (0.7 μ_B).
The most prominat feature of the magnetic structures under magnetic field or under high pressure is that they are composed of two almost independent systems: one is the ferromagnetically coupled 2 μ_B Ce double-layer lattice and the other is the Γ_7 Ce lattice, which is in the crystal field ground state, sandwiched by the 2 μ_B Ce double-layers. The former appers with first order nature below T_{C2} and forms a kind of magnetic frame, while the latter undergoes an antifferomagnetic ordering below around T_{C1} almost independently within the 2 μ_B Ce frame. The interesting point is that many different magnetic phases appers in a quite systematic way under high pressure compared with under magnetic field. This means that the formation of the 2 μ_B Ce double-layer

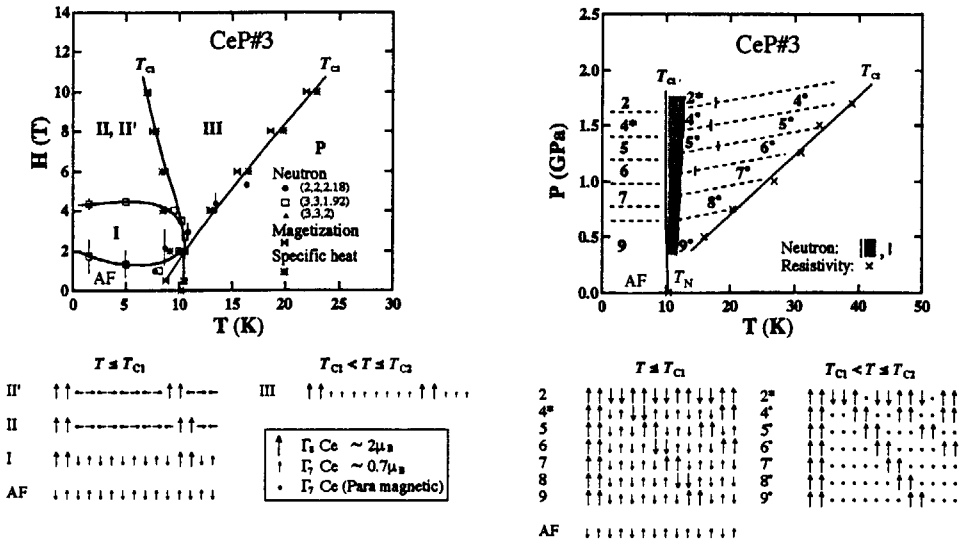

Fig.1 Phase diagrams of CeP#3 under magnetic field and under high pressure.

lattice is more sensitive to high pressure than magnetic field. This is also demonstrated by the fact that, in the magntic diffraction patterns, the widths of satellite peaks which originate from the 2 μ_B double-layer lattice are rather narrower under high pressure than under magnetic field. More detailed discussions concerning the experimental results have already given in separate papers[4-6].

The temperature dependence of the specific heat on CeP#7 was also measured so far. At zero magnetic field with ambient pressure, type-I antifferomagnetic ordering temperature of CeP#7 is identical with those of CeP#2 and CeP#3. Wnen the magnetic field applied, on the other hand, the transition temperature of T_{C2} slightly decreases compared to those of CeP#2 and CeP#3. In addition, the observed peak at T_{C2} is considerably broad, that is, the transition at T_{C2} is not clear in CeP#7. We also carried out the neutron diffraction experiments on CeP#7 under magnetic field below 6T. The results show that there is no such distinct satellite peak as observed in the diffraction patterns of CeP#3. These facts mean that, although the dHvA signal is detected on CeP#7, this sample has less quality for the formation of the 2 μ_B Ce double-layer lattice under magnetic field than CeP#2 and CeP#3. In the work of this year, we have carried out neutron diffraction experiments on CeP#7 under high pressure of 1.2 GPa to investigate the conditon of the formation of the 2 μ_B Ce double-layer lattice.

Fig.2 shows the diffraction pattern of CeP#7 at the pressure of 1.2 GPa. The magnetic structures derived from the diffraction patterns are schmatically shown at the bottom of the figures. It is quit intereiting that, different from the case under magnetic field, the magnetic structures of CeP#7 are identical with those of CeP#3 at the same pressure value of 1.2 GPa.

The above feature of CeP under magnetic field and high pressure can be explaned by the magnetic polaron model proposed by Kasuya et al., in which the combined effect of the Wigner crystallization due to the low carrier density and the Γ_8 p-f mixing stabilizes the magnetic polaron state[7]. The 2 μ_B Ce state observed below T_{C2} can be understood as the polarized 4f Γ_8 state caused by the strong magnetic polaron effect, in which the Γ_8 level is pulled down below the Γ_7 crystal field ground state.

In the framework of the magnetic polaron model, the increase of T_{C2} with increasing magnetic field is clearly due to the Zeeman energy gain of the Γ_8 Ce layers. On the other hand, the successive increase of the ratio of the Γ_8 Ce layers to all Ce layers under high pressure is due to the increase of the carrier (p-hole at Γ point) number as the result of the increase of the p-f mixing caused by applying pressure. Thus, the increas of T_{C2} is due to the p-f mixing energy gain. It is concluded that high pressure more stailizes the magnetic polaron lattice than magnetic field because high pressure is favorable for p-f mixing energy gain. This is also demonstrated by the experimental results on CeP#7.

1) T. Suzuki, JJAP Series 8(1993)267
2) N. Môri, Y. Okayama, H. Takahashi, Y. Haga and T. Suzuki, JJAP Series 8(1993) 183
3) Y. Haga, Thesis, Tohoku Univ.(1995)
4) M. Kohgi et al., Phys. Rev. B49 (1994) 7068
5) T. Osakabe et al., Physica B230-232 (1997) 645
6) M. Kohgi et al., J. Phys. Soc. Jpn.65 (1996) Suppl. B 99
7) T. Kasuya et al., J. Phys. Soc. Jpn.62 (1993)3376; T. Kasuya et al. , Solid State Commun. 93(1995)307

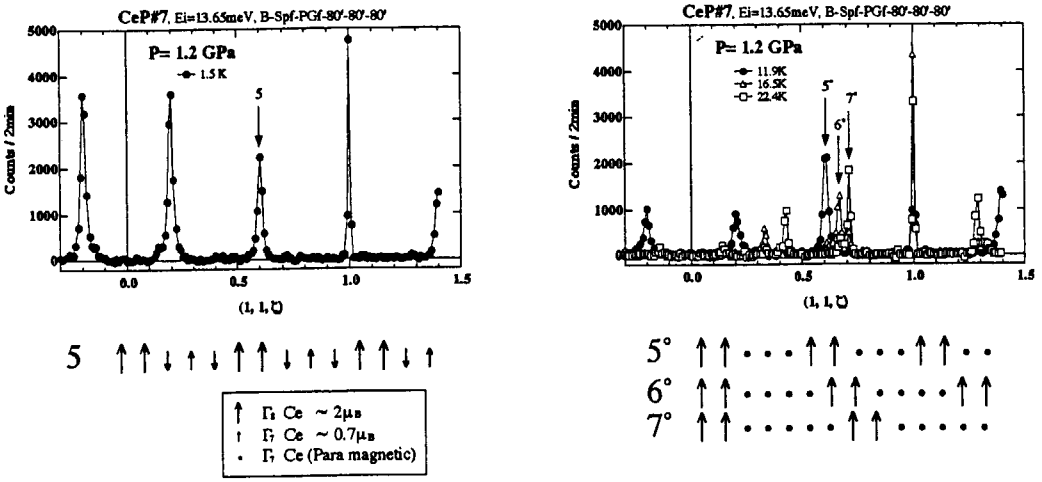

Fig.2 Magnetic diffraction patterns and magnetic structures of CeP#7 under the pressure of 1.2GPa.

原子炉：JRR-3M　　装置：TAS-1(2G)　　分野：中性子散乱(磁性)

研究テーマ : 強相関電子系の中性子散乱による研究
表　　題 : $KCr_3(OD)_6(SO_4)_2$ (Cr-jarosite) の磁気構造

Magnetic structure of $KCr_3(OD)_6(SO_4)_2$ (Cr-jarosite)

T. Inami and Y. Oka[1]

Japan Atomic Energy Research Institute, Tokai, Ibaraki 319-11
[1]*Faculty of Integrated Human Studies, Kyoto Univ., Kyoto 606-8501*

It is theoretically predicted that Heisenberg spins on the kagomé lattice with an antiferromagnetic coupling show large fluctuations at finite temperatures and therefore the ground state of a kagomé lattice antiferromagnet is a main subject of experimental study of low-dimensional magnets. $KCr_3(OD)_6(SO_4)_2$ (abbreviated to Cr-jarosite, it is not a correct name, though) is a model compounds of kagomé lattice antiferromagnet. μSR measurements indicated that spin fluctuation persists even at T=25mK[1], while heat capacity and neutron diffraction experiments suggest that coexistence of weak magnetic order and strong spin fluctuations[2]. In order to elucidate the ground state of Cr-jarosite, we prepared deuterized sample for the sake of reducing incoherent background from proton and carried out detailed powder neutron diffraction experiments.

A powder sample of deuterized Cr-jarosite was synthesized according to procedures described in Ref. 3. Neutron diffraction patterns were collected on the triple-axis spectrometer TAS-2 installed at JRR-3M with 2-axis mode using an ILL-type orange cryostat.

Neutron diffraction patterns measured at 10K are well reproduced by an alunite structure ($R\bar{3}m$) and a small amount of impurity (water). At 1.5K we observed magnetic Bragg reflections and confirmed these peaks disappeared above 4.0K. The peak width is limited by instrumental resolution and thus our sample certainly has a long-range magnetic order. They were indexed on the same rhombohedral unit cell with the chemical one. In this case, there are three independent magnetic moments and, since no (large) net moment was reported for Cr-jarosite from the susceptibility measurements[4], we can employ a so-called 120° structure for a model of the magnetic structure. As shown in fig. 1, there are two types of triads with opposite chirality each other. For the case of (a), magnetic structure factor is a function of the angle ϕ, while for the case of (b) structure factor is independent of ϕ. The observed intensities of the magnetic reflections are well explained by model (a) with ϕ=45° and model (b) (both have the same structure factor). The refined value of the ordered moment was $2.0\mu_B$. It is, however, not easy to construct a spin Hamiltonian whose ground state is model (a) with ϕ=45°. Similarly, for the case of the model (b), there is no adequate reason the magnetic structure lose the trigonal symmetry.

References

[1] A. Keren et al.: Phys. Rev. B **53** (1996) 6451.

[2] A. P. Ramirez et al.: J. Appl. Phys. **73** (1993) 5658.

[3] C. L. Lengauer et al.: Powder Diffraction **9** (1994) 265.

[4] T. Morimoto et al.: private communication.

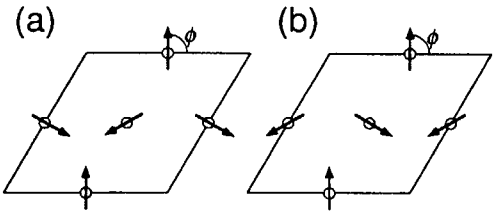

Figure 1: Two possible models of the magnetic structure for $KCr_3(OD)_6(SO_4)_2$

原子炉 : JRR-3M　装置 : TAS-2(T2-4)　分野 : 中性子散乱 (磁性)

研究テーマ : 強相関電子系の中性子散乱による研究
表　　題 : $RbFe(MoO_4)_2$ と $CsFe(SO_4)_2$ の磁気構造

Magnetic structure of $RbFe(MoO_4)_2$ and $CsFe(SO_4)_2$

T. Inami

Japan Atomic Energy Research Institute, Tokai, Ibaraki 319-11

A series of compounds with the chemical formula $A^{I}M^{III}(X^{VI}O_4)_2$ (A : K, Rb, Cs, NH_4, M: Sc, Fe, Cr, Al, rare earth, X: S, Se, Cr, Mo, W) have layered crystal structures.[1] In particular, for molybdates and sulfates (i.e. X=Mo and S), the M ions form a simple hexagonal lattice. Hence, if M is a magnetic ion, it is expected that these compounds are good models of 2-dimensional (2D) triangular lattice antiferromagnets (TAFs). In fact, in high field magnetization measurements on $RbFe(MoO_4)_2$ and $CsFe(SO_4)_2$ a clear evidence of one-third plateau, which is a specific feature of the magnetization process of 2D-TAF, has been observed.[2] In this research, we carried out neutron powder diffraction measurements on $RbFe(MoO_4)_2$ and $CsFe(SO_4)_2$ in order to determine the crystal and ordered magnetic structures of these compounds.

The powdered samples of the molybdate and sulfate were synthesized using a solid state reaction method and dehydration of corresponding alum, respectively. The data were collected on the triple axis spectrometer TAS-2 installed at JRR-3M guide hall. The cryostat was an ILL-type orange cryostat. The observed date were analyzed using Rietveld refinement programs RIETAN and FullProf.

The space group of $RbFe(MoO_4)_2$ is reported as $P\bar{3}m1$.[3,4] Rietveld refinement of neutron powder diffraction patterns at room temperature actually well converges to R_{wp}=7.84% under this space group. We found that a structural phase transition occured at around 200K. The powder patterns measured at 15K is well reproduced by a calculation in which space group $P\bar{3}$ is assumed; R_{wp}= 7.84% was obtained.

A long range magnetic order sets in at T_N=3.7K. The ordered magnetic structure is commensurate in the hexagonal ab-plane and incommensurate along the c-axis. The ordered vector obtained from Rietveld refinement using FullProf is (1/3, 1/3, 1/2-δ) δ=0.052. The observed, calculated and difference patterns measured at 1.5K is shown in Fig.1. The indices of magnetic reflections are shown. The vertical bars indicate nuclear (upper) and magnetic (lower) reflections.

$CsFe(SO_4)_2$ was poor in quality compared with $RbFe(MoO_4)_2$. It should be mentioned that refinement using reported space group $P321$[5] failed. Instead, we used $P\bar{3}$ and obtained rather good convergence R_{wp}=10.49%. Observed magnetic structure is, probably reflecting a imperfection of the lattice, coexistence of commensurate phase whose ordered vector is (1/3,1/3,1/2) and incommensurate one whose ordered vector is (1/3, 1/3, 1/2-δ) δ=0.11. Both magnetic reflections have finite width. The magnetic phase transition is of first order and the transition temperature is 3.6K.

References

[1] S.Oyetola, et al.: Eur. J. Solid State Inorg. Chem. **25** (1988) 259.

[2] T.Inami, Y.Ajiro and T.Goto: J. Phys. Soc. Jpn. **65** (1996) 2374.

[3] P.V.Klevtsov and R.F.Klevtsova: Zhurnal Strukturnoi Khimii **18** (1977) 419.

[4] R.F.Klevtsova and P.V.Klevtsov: Kristallografiya **15** (1970) 953.

[5] J.Bernard et P.Couchot: Comptes rendus **262** serie C (1966) 209.

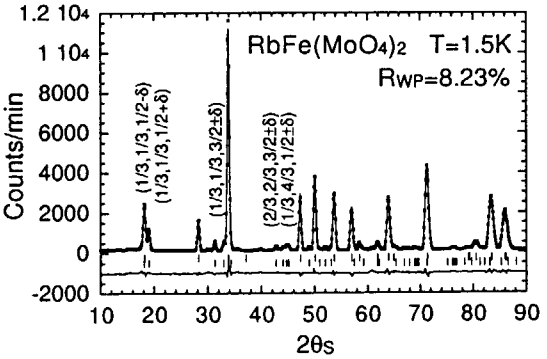

Figure 1: Neutron powder diffraction patterns of $RbFe(MoO_4)_2$ at 1.5K

原子炉 : JRR-3M　装置 : TAS-2 (T2-4)　分野 : 中性子散乱 (磁性)

研究テーマ : 強相関電子系の中性子散乱による研究
表　　題 : Jarosite ($KFe_3(OH)_6(SO_4)_2$) の磁気構造

Magnetic structure of jarosite ($KFe_3(OH)_6(SO_4)_2$)

T. Inami, M. Takano[1] and Y. Oka[2]

Japan Atomic Energy Research Institute, Tokai, Ibaraki 319-11
[1]*Institute for Chemical Research, Kyoto Univ., Uji, Kyoto 611*
[2]*Faculty of Integrated Human Studies, Kyoto Univ., Kyoto 606-8501*

It is well known that the ordering phenomena of a frustrated magnetic system is strongly affected by impurities, dislocations and so on. Jarosite $KFe_3(OH)_6(SO_4)_2$ and related materials are models of a Kagomé lattice antiferromagnet and Wills et al. reported that structural disorder plays an important role for magnetic long range order of these compounds.[1)] They proposed an idea that vacancy at A site (potassium in the case of jarosite) lift the degeneracy of ground states and induce a long range magnetic ordering in this system. We measured three jarosites by means of powder neutron diffraction and report on the crystal, magnetic structure and magnetic phase transition.

Powder specimens of jarosite were obtained by hydrothermal treatment. One sample was prepared by one of the authors (MT) before[2)]. The other two samples (one is normal jarosite and the other is deuterized jarosite) were newly prepared by another author (YO). The deuterized sample was settled in 99.75% D_2O solutions. Neutron diffraction measurements were performed on the powder diffractometer HRPD and triple axis spectrometers TAS-1 and TAS-2 installed at the research reactor JRR-3M.

The susceptibility measurements showed that Takano and Oka samples behave differently near the transition point T_N.[3)] Refinement of nuclear structure shows that indeed the Fe and K sites are not fully occupied and different between samples. The occupation factors, however, are nearly unity and the measurements on magnetic reflection $(11\frac{3}{2})$ showed no significant difference between Takano and Oka samples on T_N (66±1K and 68±1K, respectively) and on temperature dependence of the peak intensities.

The magnetic reflections could be indexed under a rhombohedral unit cell. There are three independent spins and we employed a so-called 120° structure as a feasible model. Refinement using this model successfully converged and the obtained magnetic structure is shown in fig. 1.[4)] The ordered moments are confined in the *ab*-plane. It is noteworthy to mention that the magnetic structure consists of *only* triads of the spins which have clock-wise chirality. In addition, the magnetic structure factor depends on the direction of the triad and weak $(01\frac{1}{2})$ reflection confirms direction of the ordered moments shown in fig. 1. This results can be understood if one consider that there is no trigonal symmetry at the Fe site and straightforwardly we can conclude that the Fe ions have weak Ising-type anisotropy.

References

[1] A.S.Wills and A. Harrison: J. Chem. Soc., Faraday Trans. 92 (1996) 2161.

[2] M. Takano, T. Shinjyo and T. Takada: J. Phys. Soc. Jpn. **30** (1971) 1049.

[3] S. Maegawa et al.: J. Phys. Soc. Jpn. **65** (1996) 2776, Nishiyama et al.: private communications.

[4] T. Inami, S. Maegawa and M. Takano: J. Mag. Mag. Matt. 177-181 (1998) 752.

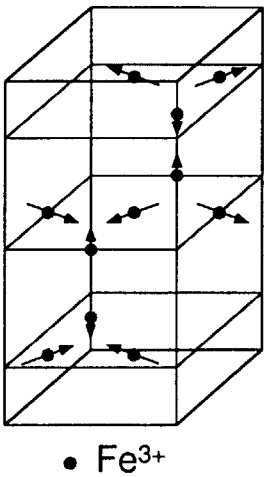

Figure 1: The best model of magnetic structure for jarosite $KFe_3(OH)_6(SO_4)_2$. Only a (lower/upper) half of the unit cell is shown.

原子炉 : JRR-3M　装置 : HRPD(1G)　分野 : 中性子散乱 (磁性)

研究テーマ : 強相関電子系の中性子散乱による研究
表　　題 : Ca_3BMnO_6 (B=Zn,Ni) の磁気構造

Magnetic structure of Ca_3BMnO_6 (B=Zn,Ni)

T. Inami, S. Kawasaki[1] and M. Takano[1]

Japan Atomic Energy Research Institute, Tokai, Ibaraki 319-11
[1]*Institute for Chemical Research, Kyoto Univ., Uji, Kyoto 611*

In recent few years, $A_3BB'O_6$ type oxides (A=Ca, Sr $\cdots$; B=Ni, Cu, Zn $\cdots$; B'=Ir, Pt $\cdots$) with K_4CdCl_6 structure[1)] have been studied from a view point of one-dimensional magnet.[2)] These oxides are composed of alternating chains with face-shared trigonal prisms (BO_6) and octahedra ($B'O_6$), and these chains are isolated by A ions. Here we report on ordered magnetic structures deduced from neutron powder diffraction measurements for two newly synthesized B'=Mn oxides, Ca_3BMnO_6 (B=Zn,Ni).

Polycrystalline samples were prepared using a citrate sol-gel precursor technique and a solid state reaction in air. Neutron diffraction patterns were collected at the temperatures 300K and 10K from 5 to 165° in 2θ with a step interval of 0.05° on the high resolution powder diffractometer HRPD installed at the research reactor JRR-3M with a wave length 2.3005Å. The samples were contained in vanadium cans with a diameter of 10mm with He exchange gas and cooled by a conventional closed cycle ^{4}He refrigerator. All diffraction patterns were analyzed using a Rietveld refinement programs RIETAN and FullProf. Temperature dependence of magnetic Brag reflections was also measured on the triple axis spectrometer TAS-1 installed at JRR-3M.

The neutron diffraction patterns at room temperature could be indexed with space group $R\bar{3}c$. Although a small amount of impurities were observed, refinements under the same crystallographic model of Sr_3NiIrO_6[3)] converged to R_{wp} = 15.78% and R_{wp} = 11.57% for Ca_3ZnMnO_6 and Ca_3NiMnO_6, respectively.

Both compounds show a magnetic long range order at 10K. Magnetic Bragg peaks of Ca_3ZnMnO_6 were indexed with space group $R\bar{3}$. In this space group, we can readily assume two-site collinear antiferromagnetic structure, as shown in fig. 1a. Since (003) reflection is observed, the ordered moments must be contained in the ab-plane, because only the spin component vertical to the scattering vector contributes neutron magnetic scattering. Refinement using this model showed good convergence to R_{wp} = 13.84% and Mn magnetic moment $2.43 \pm 0.15\mu_B$ was obtained. The transition temperature T_N was evaluated to be 25.5K.

The magnetic structure of Ca_3NiMnO_6 is incommensurate and is represented by a single propagation vector (0,0,2+δ). A relative angle between Mn- and Ni-sublattice is required to describe a magnetic structure completely. Since no $(h,k,0)$ reflections were observed, it was found that Ni and Mn moments coupleed almost antiferromagnetically. Here we assumed that Ni and Mn moments were antiparallel. Attempt to refine the incommensurate magnetic structure using FullProf was successful and we yielded R_{wp} = 13.4% and δ = 0.0185(7). The ordered moments lie in the ab-plane and the refined values of Mn and Ni moments are $2.2(2)\mu_B$ and $1.4(2)\mu_B$, respectively. The magnetic structure is illustrated in fig 1b. T_N deduced from (1,1,2+δ) reflection was 19K.

References

[1] G. Bergerhoff and O. Schmitz-Dumont: A. Anorg. Allg. Chem. **284** (1956) 10.

[2] T. N. Nguyen et al.: Science **271** (1996) 489.

[3] T. N. Nguyen and H.-C. zur Loye, J. Solid State Chem. **117** (1995) 300.

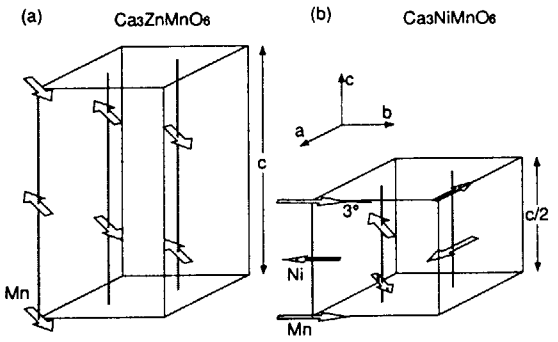

Figure 1: The best models of magnetic structure for (a) Ca_3ZnMnO_6 and (b) Ca_3NiMnO_6.

原子炉 : JRR-3M　装置 : HRPD (1G)　分野 : 中性子散乱 (磁性)

強相関電子系の中性子散乱による研究
層状混合原子価系 $LuFe_2O_4$ の強磁場下の中性子散乱

Magnetic Neutron Scattering Study of Layered Mixed Valence System LuFe2O4 under High Magnetic Field

K. Kitsuta, N. Ikeda, Y. Yamada, T. Inami, and S. Katano

Advanced Research Institute for Science and Engineering, Waseda Univ., Okubo, Shinjuku, Tokyo 169-0072, Japan
Japan Atomic Energy Research Instutute, Tokai, Ibaraki 319-1106, Japan

Hexagonal layered material LuFe2O4 undergoes magnetic phase transition at T=230K to a ferrimagnetic ordered state. Preveous neutron scattering study revealed streak-like diffuse scattering running along [001]-direction on (h/3, h/3, l) (h, l:integers) lines, which persist down to 4K. This suggests that the ordering is formed within each Fe hexagonal layer (2-D ordering), but no correlation between the neibouring layers is developed even at 4K.

One of the possible interpretation of such an extraordinary behavior is that the system can not attain the thermal equillibrium in the cooling process realized in the labolatory time scale. This interpretation is consistent with the hysteresis phenomena observed in magnetization curve M(T): Under zero-field cool (ZFC) condition <M>=0 at 4K, while in FC condition <M>=2 μ_B /Fe ion.

In order to elucidate the properties of the magnetic ordering, especially non-equillibrium nature in ZFC/FC conditions, we carried out neutron scattering exprements under high magnetic field (4T).

(1) ZFC condition : Below T_C , coexistance of Bragg reflections and diffuse streaks are observed on (2/3, 2/3, l)-line where Bragg reflections are indexed as (3/3, 2/3, l/2) (l:integer). Both intensities increases as T is increased.

(2) FC condition : On the same line, the diffuse scattering completely disappeared. Instead, new Bragg reflections appear at (2/3, 2/3, l) (l:integer) while Bragg reflections at (2/3, 2/3, l/2) become relatively weak. The analysis of the magnetic structures under ZFC/FC conditions is now underway.

原子炉：JRR3-M　装置： TAS1(2G)　分野：中性子散乱（磁性）

研究テーマ：電子デバイス材料の構造と物性に関する研究
表題：窒素侵入型化合物$Y_2Fe_{17}N_{3.1}$の中性子回折

Neutron Powder Diffraction Study of Rhombohedral $Y_2Fe_{17}N_{3.1}$

K. Koyama, T. Kajitani[2], Y. Morii[3], H. Fujii and M. Akayama

Faculty of Integrated Arts and Sciences, Hiroshima University, Higashi-hiroshima, 724
[2]Department of Applied Physics, Tohoku University, Sendai 980-77
[3]Advanced Science Research Center, Japan Atomic Energy Research Institute, Tokai, Ibaraki, 319-11

In 1990, Coey and Sun reported that the introduction of nitrogen atoms into R_2Fe_{17} (R=rare earth) compounds led to remarkable increases in the Curie temperature and magnetic moments of the Fe sublattice accompanied by a large increase in unit cell volume (~7%) without the their crystal structures[1]. Since then, many experimental studies have been performed to clarify the basic magnetic properties of interstitially modified compounds $R_2Fe_{17}N_3$. However, in detail, the influence of interstitial N atoms on the Fe magnetic moments in the rhombohedral $Y_2Fe_{17}N_3$ has not been reported yet because of the difficulty to obtain a single-phased sample.

In this work, we carried out neutron powder diffraction study on the rhombohedral $Y_2Fe_{17}N_{3.1}$ with a nonmagnetic Y in the temperature range from 10 to 300 K in order to microscopically clarify the crystallographic and magnetic structures in $Y_2Fe_{17}N_3$.

The host compound Y_2Fe_{17} was prepared by arc-melting under argon atmosphere. After annealing it at 1393 K for two weeks, the ingot was quenched in water. The annealed ingot was pulverized into fine powder less than 20 μm in diameter. The nitride $Y_2Fe_{17}N_{3.1}$ was synthesized by heat treating the powder at 713 K for 24 h under a high N_2-gas pressure of 6MPa. Upon nitrogenation, the lattice parameters a and c, respectively, increase by 2.0% and 2.4% at 310 K without changing the crystallographic symmetry. Neutron diffraction experiment was carried out at the JRR-3M High Resolution Neutron Powder

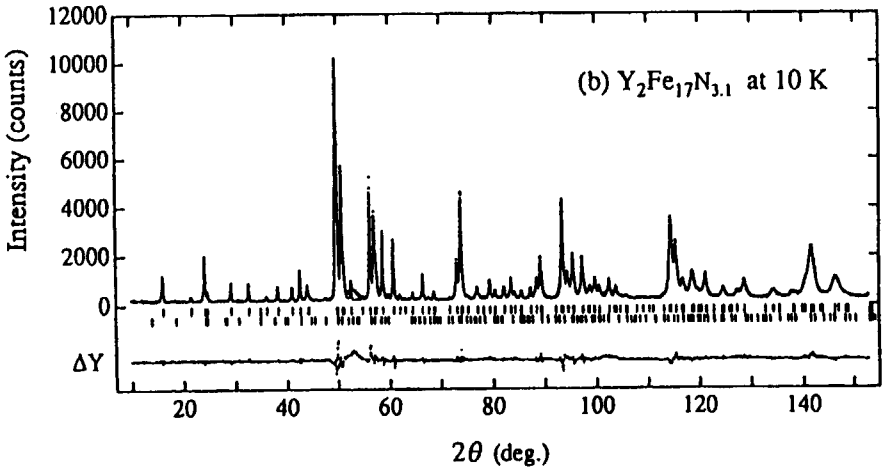

Fig.1. Neutron powder diffraction pattern of $Y_2Fe_{17}N_{3.1}$ at 10 K. The dots and line correspond to the observed and calculated patterns, respectively. The lower part is the difference pattern (observed-calculated).

原子炉：JRR-3M　　装置：HRPD(1G)　　分野：中性子散乱（磁性）

Table 1. Refined parameters of rhombohedral $Y_2Fe_{17}N_{3.1}$ at 10 K. n is the occupation factor; x, y, and z are the fractional coordinates; B is the isotropic thermal parameter (Å); and m is the magnetic moment (μ_B/atom). Numbers in parentheses are the statistical error given by the refinement program.

$Y_2Fe_{17}N_{3.1}$	10 K		R_p=6.21 %			
Rhombohedral		R_I=2.97 %	R_F=1.97 %			
a=8.6710(3) Å		c=12.7241(4) Å				
Atom	Site	n	x	y	z	B	m
Y	6c	1.0	0	0	0.338(1)	0.85(4)	
Fe(1)	6c	1.0	0	0	0.0949(6)	0.202(7)	2.86(5)
Fe(2)	9d	1.0	0.5	0	0.5	0.202	2.12(8)
Fe(3)	18f	1.0	0.2829(5)	0	0	0.202	2.01(4)
Fe(4)	18h	1.0	0.1703(3)	-0.1703	0.4860(4)	0.202	2.41(5)
N(1)	9e	0.995(5)	0.5	0	0	0.65(5)	
N(2)	18g	0.039(2)	0.08(1)0	0.5	0.65		

Diffractometer (HRPD). The diffraction data was analyzed using RIETAN-94, which was developed for application of the Rietveld method[2].

Figure 1 shows the neutron powder diffraction pattern of $Y_2Fe_{17}N_{3.1}$ at 10 K. As is evident from the figure, in the diffraction pattern of $Y_2Fe_{17}N_{3.1}$, a small and broad peak corresponding to α-Fe segregation upon nitrogenation appears around 2θ=53.4°. Therefore, the refinement for the nitride were performed for the data except 2θ range from 52.5 to 54.5°.

The calculated pattern (line) is in very good agreement with the observed pattern (dots), as shown in the figure. The final R factors were R_I=2.97 % and R_F=1.97 %. The result of the refinement at 10 K is summarized in Table 1. Upon nitrogenation, total magnetic moment M increase by 17%, reaching M=38.6(3) μ_B/f.u.[3]. As is evident from Table 1, the site-dependent Fe moments are observed, such that the magnetic moment of the 18f-Fe atoms is the smallest (~2.0 μ_B), while the moment of the 6c-Fe atoms has the largest (~2.9 μ_B). This result could be understood as the differences of environment around the Fe atoms. That is, when the N atoms are introduced into the 9e interstitial site, all the Fe moments probably increase by a reduction in the Fe-Fe overlap caused by the increase in the Fe-Fe distances. In detail, the smallest Fe moment on the 18f sites which are the nearest to the 9e-N atoms is originated in the strong hybridization between the Fe 3d-states and the N 2p-states. On the contrary, the Fe moment on the 6c sites which are the farthest from the 9e-N atoms has the largest in $Y_2Fe_{17}N_{3.1}$.

References

1) J.M.D. Coey and H. Sun, J. Magn. Magn. Mater. **87** (1990) L251.
2) Y.I. Kim and F. Izumi, J. Ceram. Soc. Jpn. **102** (1994) 401.
3) K. Koyama, T. Kajitani, Y. Morii, H. Fujii and M. Akayama, Phy. Rev. B **55** (1997) 11414.

研究テーマ：電子デバイス材料の構造と物性に関する研究
表題：希土類一鉄金属間化合物 Ce_2Fe_{17} の中性子回折実験

Neutron Diffraction Study on Ce_2Fe_{17}

H. Fukuda, Y.Janssen[1], H. Fujii, T. Ekino and Y. Morii[2]

Faculty of Integrated Arts & Sciences, Hiroshima University, Higashi-Hiroshima 739-8521, Japan
[1]Van der Waals-Zeeman Institute, University of Amsterdam,Amsterdam, The Netherlands
[2]Advanced Science Research Center, Japan Atomic Energy Research Institute, Tokai, Ibaraki 319-1195, Japan

In 1997, Janssen et al. reported on the physical properties of Ce_2Fe_{17} with a rhombohedral Th_2Zn_{17}-type structure[1]. Ce_2Fe_{17} showed three different phases in zero field. With decreasing temperature, Ce_2Fe_{17} ordered antiferromagnetically at T_N = 220 K (AF II) and then another antiferromagnetic order (AF I) appeared at T_C = 125 K. Furthermore, Ce_2Fe_{17} showed a giant magnetoresistance GMR at 4.2 K, accompanied by a metamagentic transition from antiferromagnetic to ferromagnetic state with a hysterisis of about 0.2 T. The magnetoresistance effect $\Delta\rho/\rho = (\rho_{AF} - \rho_F)/\rho_{AF}$ reached about 0.85 at 4.2 K. On the other hand, the value of the electronic specific heat coefficinet γ of 351 $mJmol^{-1}K^{-2}$ in zero field decreased about 20% by the metamagnetic transition. This simply suggests that the Ce sublattice does not act an important role for GMR. In order to clarify the mechanism of GMR, we performed the neutron diffraction for Ce_2Fe_{17} with rhombohedral Th_2Zn_{17}-type structure. Detalis of the preparation method of polycrystalline Ce_2Fe_{17} are given in Ref. 1. The neutron diffraction studies were carried out with High Resolution Powder Diffractometer HRPD using thermal neutrons (wavelength λ = 2.30 Å and λ = 2.97 Å) and with Low Energy Triple-Axis Spectometer LTAS using cold neutrons (λ = 4.19 Å) at the JRR-3M.

In Fig. 1, we show the powder diffraction pattern at typical temperatures10 K, 130 K and 300 K obtained by LTAS. We could characterize by rhombohedral Th_2Zn_{17}-type structure on the diffraction pattern at 300 K. We did not observe any extra peak corresponding to α-Fe and hexagonal Ce_2Fe_{17}, indicating that the sample used in this study

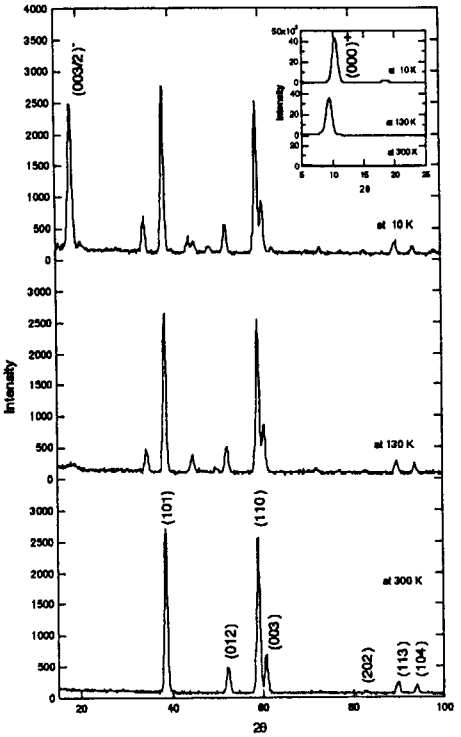

Fig. 1. Powder neutron diffraction pattern at typical various temperatures 10 K, 130 K and 300 K. The inset shows expand one

原子炉：JRR-3M　　装置：HRPD(1G)&LTAS(C2-1)　　分野：中性子散乱（磁性）

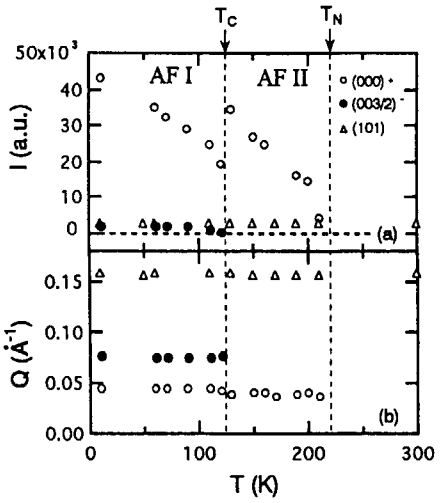

Fig. 2. Temperature variations of integrated intensities (a) and peak positions (b) of the $(000)^+$ and $(003/2)^-$ magnetic reflections for Ce_2Fe_{17}, together with those of nuclear Bragg peak (101).

was single phase. As is obvious in Fig. 1, we can observe some aditional peaks in the diffraction pattern at both 10 K and 130 K without change in the intensity of the nuclear Bragg peaks. Figure 2 shows the temperature variations of the integrated intensities and the peak positions of the two characterictic magnetic peaks $(000)^+$ and $(003/2)^-$, together with those of nuclear Bragg peak (101). As is seen in Fig. 2, the intensity and the peak position of (101) is almost independent of temperature. At T_C, the $(000)^+$ peak position shifts to lower the Q position and the intensity suddenly increases during warming. Above T_C, the $(000)^+$ intensity decreases with increasing temperature and then disappears at about T_N, while the $(003/2)^-$ peak disappears at T_C.We consider that AF II has a helix structure with a propergation vecter τ=0.00372 Å^{-1} along the *c*-axis, where Fe moments lie in a basal *c*-plane and are parallel to each other in the *c*-plane. We estimated the average Fe moment to be about 1.5 μ_B at T_C. On the other hand, the AF I phase has a modified helix structures with τ=0.00435 Å^{-1} along the *c*-axis. This indicates the formation of super-structured magnetic cell, in which the magnetic *c*-parameter is twice as large as the chemical unit cell. The magnetic structure of the AF I phase is completely different from that of the AF II phase. Our results are consistent with the results by Plumier et al.[2] rather than by Givord et al. [3], in which Givord et al. claimed a fan structure below 90 K. So we can simply expect that the magnetic sturecture is the same one as Plumier et al. reported. However, we cannot decide the exact magnetic structure only from these data.

Considering that GMR occured in only the AF I phase, it seems likely that GMR connects to appearence of super-structured magnetic cell in the AF I phase. Hence, we consider that GMR in Ce_2Fe_{17} is mainly caused by the formation of a super-zone gap due to the development of the AF I phase (SDW) of the Fe sublattice. In order to clarify the mechanism of GMR in ditails, it is necessary to determine the exact magnetic structure from the neutron diffraction experiments for Ce_2Fe_{17} single crystal.

References

(1) Y. Janssen et al.: Phys. Rev. B **56**(1997), 13716
(2) R. Plumier & M. Sougi: Proceeding of ICM, Moscow, (1973), 487
(3) D. Givord & R. Lemaire: Proceeding of ICM, Moscow, (1973), 492

課題名：Mn7Sn4の磁気転移の中性子回折による研究
表　題：Mn7Sn4の磁気転移の中性子回折による研究

Neutron Diffraction Study of Magnetic Transition in Mn_7Sn_4

S.Anzai, T.Kobayashi, Y.Yamaguchi[1], M.Ohashi[1], K.Ohoyama[1], and K.Motojima[2]

Faculty of Science and Technology, Keio University
Institute of Materials Research, Tohoku University[1]
Institute for Solid State Physics, University of Tokyo[2]

Mn_7Sn_4 crystallizes in the Ni_2In type of structure in which MnI atoms constitute the simple hexagonal lattice. MnII and vacancies randomely situate on the interstitial sites of the hexagonal lattice [1]. Figure 1a shows the ZFC (zero field cooled) magnetization σ_{ZFC} as a function of temperature at H=0.01T. Between T_C(220-230K) and T_t(100K for y=0 ; 75K for y=0.4), σ_{ZFC} is remarkably higher than that below T_t[2]. At zero field condition, an antiferromagnetic reflection (0 0 1/2) has been observed in our neutron diffraction pattern taken at 10K. However, Fig.1a also shows that below T_t the FC (field cooled) magnetization σ_{FC} is higher than σ_{ZFC} and that it fits the curve extrapolated from the range of $T>T_t$. Moreover, σ_{ZFC} shows a tendency of saturation at 6 K (Fig1b;[2]). Hence, it is of interest to investigate the possibility of a field induced transition characterized by a disappearence of (0 0 1/2) reflection. This is because the (0 0 1/2) reflection is not observed between T_C and T_t.

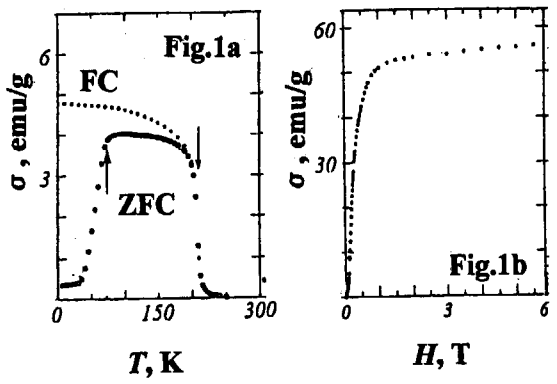

Fig.1 (a) σ_{ZFC} and σ_{FC} as a function of temperature (T) at 0.01T , (b) σ_{ZFC} as a function of magnetic field (H) at 6K.

Powdered sample (12g) was packed in a vanadium cylinder (10mm ϕ). In order to avoid the preferred orientation of sample particles under magnetic field, deuterized methyl alcohol CD_3OD (99.8% purity) was used as the binding regent for particles at low temperatures.

The neutron diffraction patterns of $Mn_{7.4}Sn_4$ were taken with the multi-counter type diffractometer (HERMES, Tohoku University) installed at JRR-3M. The wave length of neutron was 0.18196 nm and the measuring angle of 2 θ is ranging from 3° to 150° . The magnetic field is generated with "ENDOH" superconducting magnet.

Figures 2a-f display the main part of patterns ranging from 3° to 50° . Reflection peaks of solid CD_3OD (indicated by *) are observed, together with $Mn_{7.4}Sn_4$ peaks, at T=6K and H=0T(Fig. 2a).This feature is not changed under 4T; the (0 0 1/2) reflection also appears (Fig.2b). Figure 2c shows the detailed comparison of (0 0 1/2) reflections taken at 0T and 4T. The latter peak is slightly smaller than that of the former one. It is considered that the spin structure of the low temperature phase($T<T_t$) does not change essentially.

Our neutron diffration pattern of $Mn_{7.4}Sn_4$ taken under 0T at the temperatures between T_t and T_C has no magnetic superlattice lines. Then, in order to retain the ZFC condition the sample was held under 0T at 250K($>T_C$). (As seen in Fig.2d, the pattern shows the nuclear peaks of the Ni_2In type structure.) After the thermal agitation at 295K, the neutron diffraction patterns were taken under 0 T (Fig.2e) and 4T (Fig.2f) at 120K. No essential difference is observed between the two patterns. The saturation behaviour in magnetization of $Mn_{7.4}Sn_4$ at 120K is not ascibed to a drastic change of magnetic stucture due to magnetic field.

JRR-3M, HERMES (T1-3), Magnetism

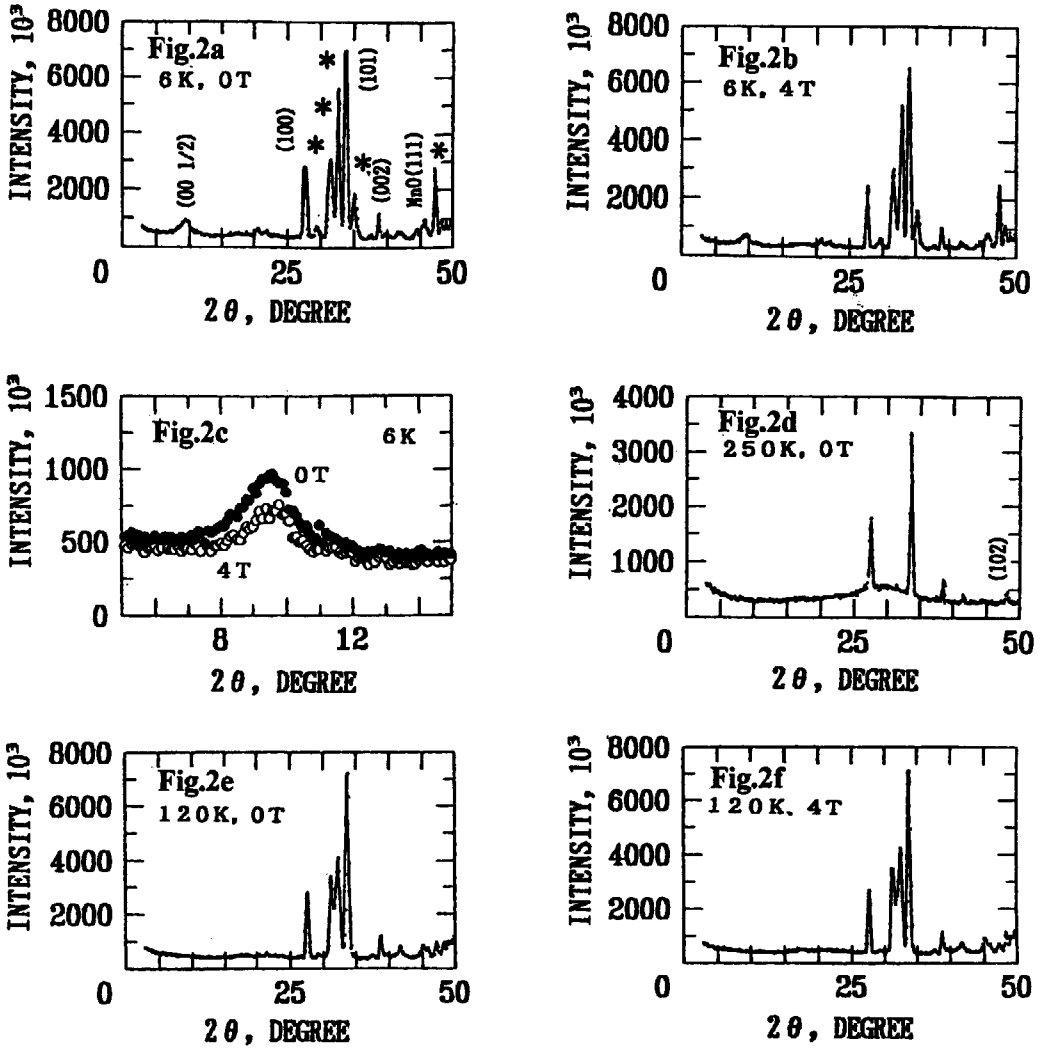

Fig.2 Neutron diffraction patterns of $Mn_{7.4}Sn_4$ taken under zero field and H=4T at various temperatures.

Now we are forwarding the data analysis based on the following starting model. A weak ferromagnetic order is stabilized below T_C. Below T_t, an antiferromagntic order with the period of 8 sheets of Mn basal planes is superimposed on it, and it makes to hard the rotation of ferromagnetic (or ferrimagnetic) domains under field.

References

[1] K.Yasukochi, K.Kanematsu and T.Ohoyama, J.Phys.Soc.Jpn.16(1961)1123.

[2] R.Sugi, T.Shimomura, M.Matoba, S.Matsuzaka, S.Fujii, N.Hagiwara and S.Anzai, Phys.Stat.Sol.(b)189(995)K65.

研究課題：R-Mn-X 系化合物の磁気構造
表題：中性子回折による DyMnSi 磁気相転移の研究

Magnetic Phase Transitions in DyMnSi Studied by Neutron Diffraction

H. Kobayashi[a], M. Ohashi[b], H. Onodera[b], T. Kamimura[a] and Y. Yamaguchi[b]

[a] *Department of Physics, Tohoku University, Sendai 980-8578, JAPAN*
[b] *Institute for Materials Research, Tohoku University, Sendai 980-8577, JAPAN*

RMnSi (R=Dy, Ho) compounds with the orthorhombic TiNiSi-type structure, Pnma, were first synthesized by Nikitin *et al.* ten years ago [1]. They reported that the Néel temperatures of DyMnSi and HoMnSi are 30 and 36 K, respectively. Recently, we have measured the neutron diffraction pattern at 290 K [2]. This pattern is characterized by a occurrence of an additional peak forbidden by the space grope. Then the magnetic ordering temperatures is above room temperature and the Mn atom has a magnetic moment in DyMnSi. In this paper, we report on the magnetic phase transitions in DyMnSi studied by neutron-diffraction experiments

A polycrystalline ingot was made by a conventional argon arc method, followed by vacuum annealing at 900 °C for 100 h. The sample is showed to be the single TiNiSi-type phase by the powder X-ray diffraction. Neutron-diffraction experiments were carried out at the HERMES diffractometer installed at a thermal neutron guide of the JRR-3M reactor in JAERI. A special thin container shaped like double-wall cylinder was used in order to minimize the effect of the large neutron absorption cross section of natural dysprosium.

Figure 1 shows typical three neutron diffraction patters where arrows indicate magnetic peaks. There are three different types of temperature dependence of these intensities. The intensities of peaks indicated by M_1 in Fig. 1 disappear around 55 K. These magnetic lines is probably caused by the ordering of Dy magnetic moments since we have observed the magnetic ^{161}Dy Mössbauer spectra below 53 K. Thus the other peaks indicated by M_2 and M_3 in Fig. 1 are related the ordering of Mn moments. Since the peaks indicated by M_2 are only observed below 180 K, the magnetic structure of Mn sublattice changes around 180 K. The analysis of the data to determine the magnetic structures is in progress.

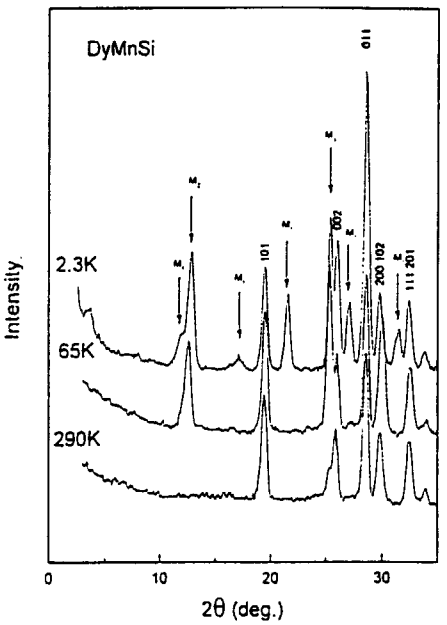

Fig. 1 Neutron diffraction patterns at 2.3, 65, and 290 K. The arrows indicate magnetic reflections.

Reference

[1] S.A. Nikitin, *et al.*; Phys. Met. Metall. 64(1987) 25.
[2] H. Kobayahsi, *et al.*: Activity Report on Neutron Scattering Research 3(1997) 110.

JRR-3M HERMES(T1-3), magnetism

研究テーマ：単結晶$(Fe_{0.98}Ru_{0.02})_2P$の中性子回折
表題：単結晶 Ce_2Fe_{17}の中性子回折

Neutron Diffraction Study of Single Crystal Ce_2Fe_{17}

Y. Uwatoko, E. Matsuoka, T. Ohki, H. Kosaka and K. Motoya*
Department of Physics, Faculty of Science, Saitama University, Urawa 338, Japan
**Science University of Tokyo, Noda 278, Japan*

The physical properties for single-phase Ce_2Fe_{17} with the rhombohedral Th_2Zn_{17} structure revealed that the magnetic phase diagram is reporteds due to two antiferromagnetic transition at 125 K and 215 K, respectively[1]. The binary phase diagram of Ce-Fe indicates a difficulty of growing pure Ce_2Fe_{17}[2]. But, we are growing up a small single crystal Ce_2Fe_{17} with rhombohedral structure by using flux technic. To see the two magnetic phases at low and intermediate temperature, we performed neutron scattering experiments using single crystal Ce_2Fe_{17}.

The neutron diffraction experiments have been carried out by using the HQR diffractometer (T1-1) install at JRR-3M Guide Hall in JAERI (Tokai). An incident neutron with a wave length 2.44 Å obtained by the (220) reflection of PG.

There are no antiferromagnetic refrection at below 90 K. Fig. 1 shows the neutron intensity of Ce_2Fe_{17} along (00*l*) at 100 K. Beside the nuclear reflections at integer position, magnetic reflections may be indicate a helix structure. These magnetic refrections disappear above about T=210 K, which corresponds well to susceptibility measurements, as shown in Fig. 2. The analysis of the data now in progress.

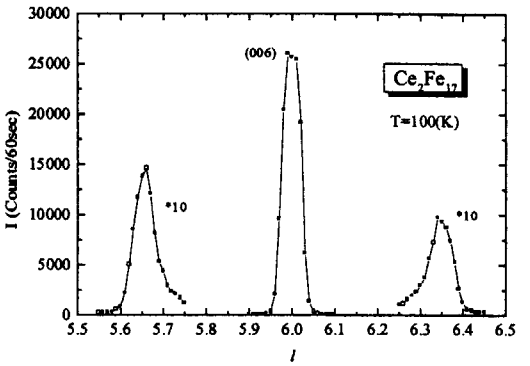

Fig. 1 : The neutron intensity of Ce_2Fe_{17} alog (00*l*) at 100 K.

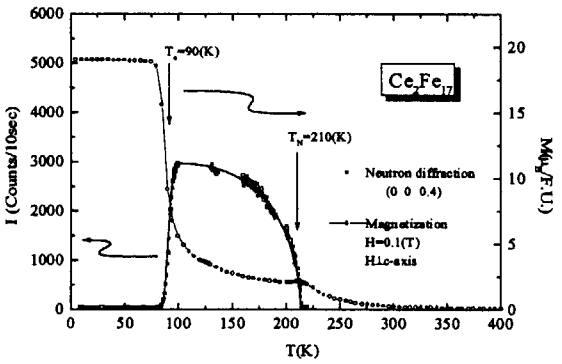

Fig. 2 : Temperature dependence of intensities for helix ordering (0,0,0.4) and temperature dependence of susceptibility along c-axis at H=0.1 T.

References

[1] Y.Janssen et al. Phys. Rev. B, 56 (1997) 13716.
[2]W.Zhang et al., *in Binary Alloy Phase Diagrams, edited by* T. B. Massalski, vol 2 (1992) 1058

JRR-3M, HQR (T1-1), 2. magnetism

研究テーマ：ＥｒＮｉＳｎの磁気構造
表題：ＥｒＮｉＳｎの中性子回折

Neutron Diffraction Study on ErNiSn

Y.Andoh, M.Kurisu[1], G.Nakamoto[1], T.Nobata[1], S.Nakamura[1], R.Hara[1] and S.Kawano[2]
Faculty of Education, Tottori University
[1]*Japan Advanced Institute of Science and Technology*
[2]*Research Reactor Institute, Kyoto University*

The ternary compound ErNiSn crystallizes in the orthorhombic (*Pnma*) TiNiSi-type structure and order antiferromagnetically at T_N=4.0 K [1]. In this report, we performed neutron diffraction investigations on ErNiSn to determine its magnetic structure. Neutron diffraction measurements were performed at the $T_{1\text{-}1}$ beam hole of the JRR-3M reactor of JAERI.

Figure 1 shows the powder neutron diffraction patterns of ErNiSn at 1.45 K and 1.75 K. It is deduced that a magnetic transition occurs between 1.45 K and 1.75 K. The magnetic peaks are indexed with a propagation vector q' = (0.330, 0.494, 0.399) and a spin axis parallel to a-axis at 1.75 K. With decreasing temperature, the intensity of the magnetic peaks originated from q' is decreasing. At 1.45 K, new magnetic peaks are observed. They are indexed with q=(0.285, 0.476, 0.248) and a spin axis inclines to b-axis. These propagation vectors nearly equal to (1/3,1/2,1/3). Neutron diffraction study on isostructual compound ErPdSn suggests that the spin arrangement is described by a sine-modulated spin wave one at high temperature and a squared one at low temperature [2]. However, satellites of higher order were not observed in ErNiSn. Further careful neutron diffraction measurements and analysis are needed to clarify the magnetic structure in the compound.

References

[1] Y.Andoh, M.Kurisu, S.Kawano and I.Oguro, J.Magn & Magn. Mater., **140-144** (1998) 1063.
[2] G.Andre, F.Bouree et al., J.Magn & Magn. Mater., **140-144** (1995) .

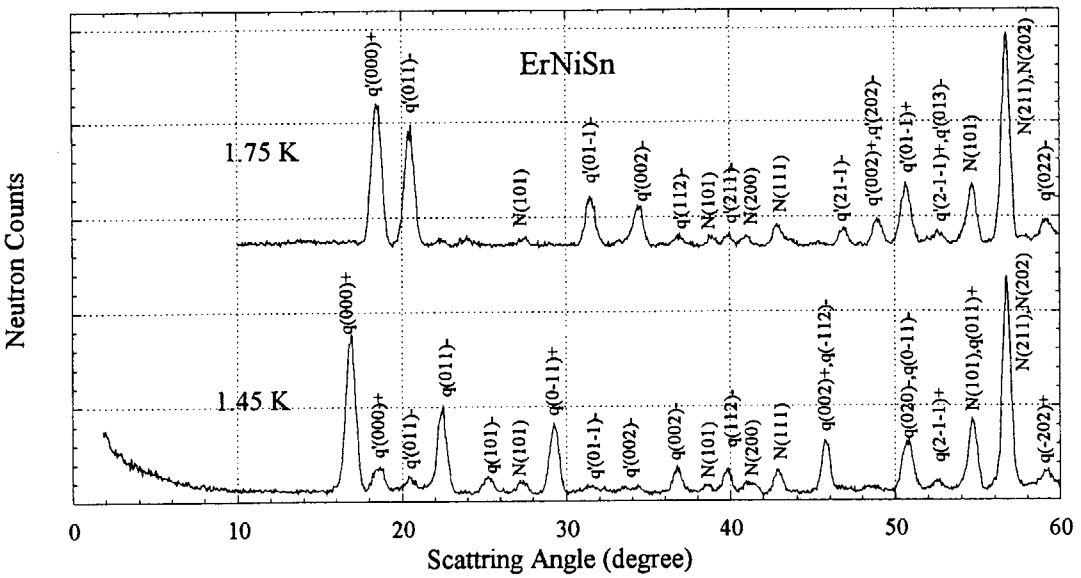

Fig. 1 Powder neutron patterns of ErNiSn at 1.45 K and 1.75 K .

JRR-3M,T1-1,2,magnetism

研究テーマ：$La_xSr_{1-x}MnO_{2.5+0.5x}$の磁気構造
表題：$SrMnO_{2.5}$の中性子回折

Neutron Diffraction Study of $SrMnO_{2.5}$

K.INOUE, T.MORI[1], N.KAMEGASHIRA[1], Y.YAMAGUCHI[2], K.OHOYAMA[2] and M.OHASHI[2]

Fac. Sci. & Tech. Ryukoku Univ. Seta, Otsu 520-2194, Japan
[1]Toyohashi Univ. of Tech. Toyohashi 441-8122 , Japan
[2]IMR Tohoku Univ. Aoba-ku, Sendai 980-8577, Japan

$SrMnO_{2.5}$ has an orthorhombic perovskite structure with ordered oxygen vacancy running for c-direction. Rietveld analysis of powder X-ray diffraction pattern shows that the space group is Pbam and the lattice constants at room temperature are a=5.5197 Å , b=10.7643 Å and c=3.8093 Å. There are two kinds of Mn-O-Mn angle in the c-plane, 180° and 159° . The Mn-O-Mn angle for c-direction is 158° . From magnetization measurements, it is antiferromagnetic with Néel temperature of 375K.

The powder neutron diffraction of this material was done between 20K and 425K. The diffraction patterns obtained at 20K and 425K are shown in Fig.1. It was found that the magnetic structure is antiferromagnetic with two times period for c-direction. Rietveld analysis shows that, in the c-plane, Mn-Mn coupling is ferromagnetic when Mn-O-Mn angle is 180° and is antiferromagnetic when it is 159° . The Mn magnetic moments are along b-axis and the magnitude of them is 3.44 μ_B at 20K. The position of the oxygen vacancy and the direction of Mn moment in the c-plane are shown in Fig.2. The temperature dependence of Mn moment is shown in Fig.3.

The ionic state of Mn in $SrMnO_{2.5}$ is expected to be Mn^{3+} with electron configuration of $t^3_{2g}e^1_g$. The e_g electrons are itinarant because of the hybridization with O 2p states. The experimentally obtained results are consistent with the suppositions that when Mn-O-Mn angle is near 180° the e_g electron transfer is large and the ferromagnetic coupling will appear, and that when the angle is near 150 ° the antiferromagnetic coupling will appear because of strong correlation of e_g electrons. The electrical conductivity is expected not to exist, because Mn-Mn ferromagnetic coupling in the c-plane is isolated.

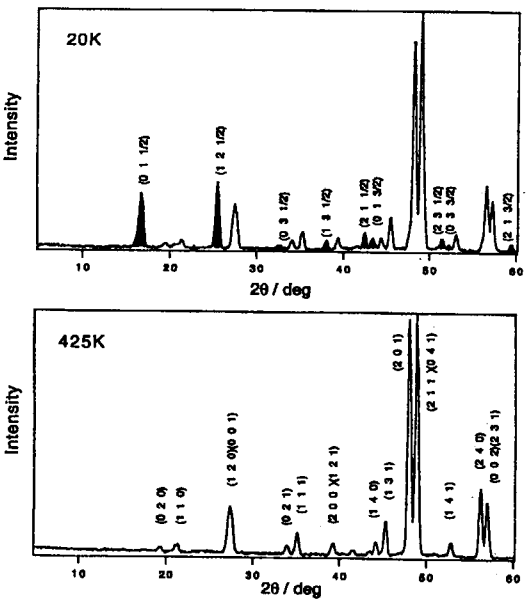

Fig.1 Diffraction patterns at 20K and 425K.

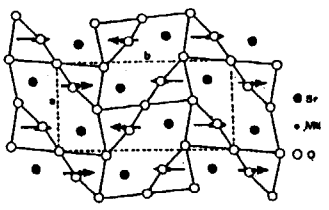

Fig.2 Magnetic structure in the c-plane.

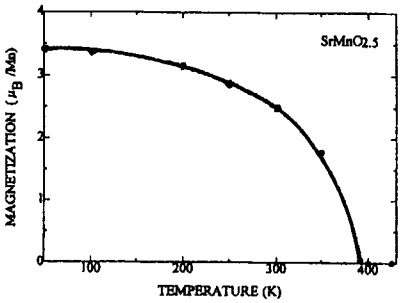

Fig.3 Magnetic moment versus temperature.

JRR-3M, HERMES, 2.magnetism

研究課題：希土類化合物 Nd_7Ni_3 単結晶の磁気構造
表題：希土類化合物 Nd_7Ni_3 の中性子回折

Neutron diffraction studies of rare earth compound, Nd_7Ni_3

S. Kawano[1], T. Tsutaoka[2], T. Kasagi[2], Y. Andoh[3], M. Kurisu[4] and X. Xu[1]
[1]*Research Reactor Institute, Kyoto University, Kumatori, Osaka 590-04, Japan*
[2]*Faculty of School Education, Hiroshima University, Higashi-Hiroshima 739, Japan*
[3]*Faculty of Education, Tottori University, Tottori 680, Japan*
[4]*Japan Advanced Institute of Science and Technology, Ishikawa 923-12, Japan*

The rare earth compound Nd_7Ni_3 crystallizes in the hexagonal Th_7Fe_3-type structure with a space group $P6_3mc$. Magnetization measurements suggest that three magnetic transitions (T_N=29K, T_C=14 K, and T_R=8.7K) occurred below 30K [1]. No other finding about spin configuration has been reported so far. The aim of the present work is to investigate magnetic structural properties of Nd_7Ni_3 by neutron diffraction.

Figure 1 shows the powder neutron-diffraction patterns at 1.7 K and 35 K, well above the Neel temperature obtained using the HQR neutron spectrometer at the $T_{1\text{-}1}$ beam hole of JRR-3M. All the peaks on the 35 K pattern are assigned to the nuclear Bragg reflections for the Nd_7Ni_3 structure and Al reflections from a cryostat. At 1.7 K extra peaks are magnetic Bragg reflections. It is noteworthy of an existence of the magnetic (100) reflection in the figure, which suggests an existence of c-axis ferromagnetic component at 1.7K. The strong $(000)^{\pm}$ reflection suggests that the compound have an antiferromagnetic structure. We, therefore, assume that the Nd moment is helically modulated in the basal plane and along the c-axis ferromagnetic at 1.7 K. The propagation vector of this helical component determined to be $\boldsymbol{k}$ =(0,0,1/3); then the magnetic and crystallographic cells are related as: $a_{magn}=a_{cryst}$ and $c_{magn}=3c_{cryst}$. Using this conical model, we have indexed the magnetic reflections, as shown in Fig. 1.

The temperature dependence of the $(000)^{\pm}$ peak intensity as shown in Fig. 2. The intensity starts to increase slightly from about 8 K. It reaches a maximum around 12 K and vanishes around 25 K, which corresponds to the Neel temperature. The increase from 8 K suggests that the spin configuration change from a *c*-axis conical structure to a helical one. It seems that the intermediate transition temperature by the magnetization measurement corresponds to the temperature showing of the basal moment maximum.

References:

[1] T. Tsutaoka, H. Fukuda, T. Tokunaga, H. Kadomatsu, and Y. Ito, J. Magn. Magn. Mater. **167** (1997) 249.

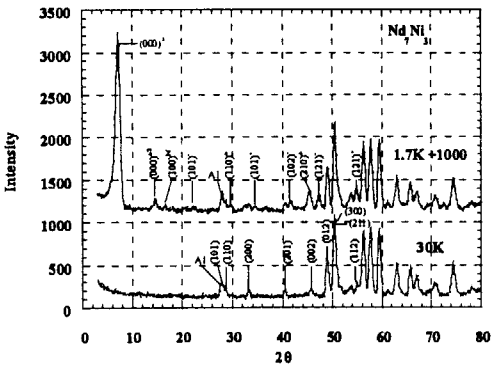

Fig. 1. Powder neutron diffraction patterns of Nd_7Ni_3 at 1.7 K and 35K, well above the Neel temperature.

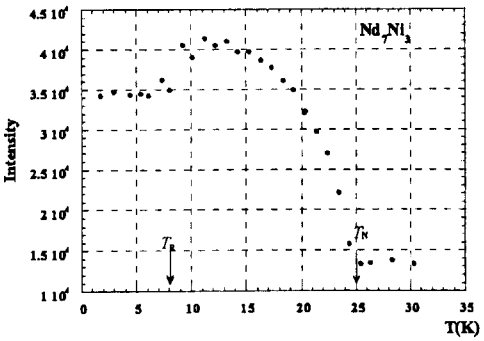

Fig. 2. Temperature dependence of the integerated $(000)^{\pm}$peak intensity.

Reactor: JRR-3M Facility: T1-1 Field: 2. 磁性 magnetism

研究テーマ：希土類金属間化合物ＤｙＣｕＳｉの変調磁気構造と格子変調
表題：ＤｙＣｕＳｉの中性子回折

Neutron Diffraction Study of DyCuSi

K. Ishimoto, S. Takahashi, H. Miki, H. Onodera,
H. Yamauchi, M. Ohashi[1] and Y. Yamaguchi
Institute for Materials Research, Tohoku University, Sendai 980-77, Japan
[1]Faculty of Engineering, Yamagata University, Yanezawa 992 , Japan

DyCuSi has a hexagonal Ni_2In type crystal structure (space group *P63/mmc*) [1]. This crystal structure is stable for other rare earth elements except for Eu. It was reported that GdCuSi and TbCuSi order an antiferromagnetically with T_N = 12K and 11K , respectively [2]. On the other hand, no magnetic orderig were observed in DyCuSi and HoCuSi [2]. Recently, we have observed two magnetic phase transitions in DyCuSi at 5K ($=T_t$) and 10 K ($=T_N$) by means of susceptibility measurement. In order to investigate two magnetic phase transitions in DyCuSi, we have carried out powder neutron diffraction measurement . Neutron diffraction measurement has been performed by using HERMES diffractometer installed at JRR-3M guide hall in JAERI.

Fig.1 shows neutron diffraction patterns at 2.2K , 7K and 20K . The observed pattern at 20K is in good agreement with calculated one of Ni_2In type crystal structure. We can observe additional refrections in data at 2.2K and 7K, which is corresponding to the ordering in the temperature region of $T < T_t$ (low temperature phase) and $T_t < T < T_N$ (high temperature phase), respectively. In both phases magnetic structure can be described by modulating the Dy moments. In the high temperature phase a sinusoidal structure with propagation vector (0 0 0.2) is obtained. Below T_t the magnetic structure becomes commensurate with the lattice and the propagation vector is given by (0 0 1/6). Furthermore the appearance of the third harmonics were observed in the low temperature phase. The magnetic structure changes from incommensurate (sinusoidal) to commensurate (squared-up) at T_t with decreasing temperature. It is necessary for more detail analysis to carry out single crystal measurements.

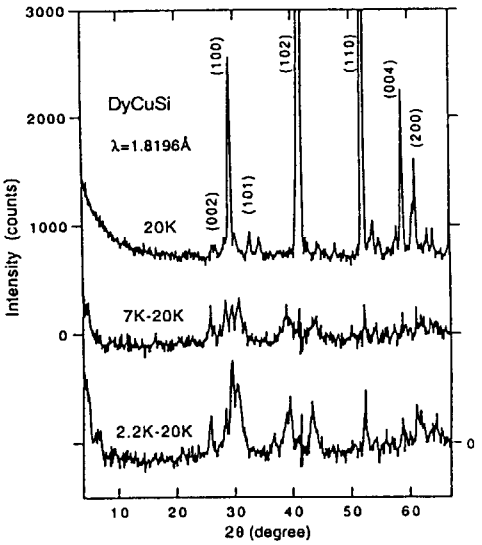

Fig. 1 Neutron diffraction patterns of DyCuSi at 2.2K, 7K and 20K.

References

[1] A. Iandelli : J. Less-Common Met. 90 (1983) 121.
[2] W. Bazela, A. Szytula and J. Leciejewicz: Solid State Commun. 56 (1985) 1043.

JRR-3M, HERMES(T1-3), Magnetism

研究テーマ：重希土類ヘキサボライド（REB_6；RE=Tb, Dy, Ho）の磁気構造の研究
表題：DyB_6の粉末中性子回折

Neutron Powder Diffraction Study of DyB_6

K. Takahashi, H. Nojiri, K. Ohoyama, M. Ohashi, Y. Yamaguchi,
S. Kunii* and M. Motokawa

Institute for Materials Research, Tohoku University, Sendai 980-8577, Japan
**Department of Physics, Tohoku University, Sendai 980-8578, Japan*

DyB_6 is an antiferromagnetic compound with the cubic CaB_6 type structure. Magnetization curves of a single crystal of DyB_6 at 4.2 K show multistep metamagnetic transitions [1]. The magnetic susceptibility and the specific heat shows two anomalies at 26 K and at 32 K [2]. The anomaly at higher temperature has been considered, from the elastic constants measurements [3], to be due to the cooperative Jahn-Teller structural phase transition. The other anomaly at 26 K is considered to be due to the antiferromagnetic ordering.

To investigate magnetic structures and to study the relation between the magnetism and the structure, we have carried out neutron powder diffraction experiments. The powder specimen was prepared by crushing the single crystals which were enriched up to 99.5% in ^{11}B. The experiments were performed using the HERMES diffractometer (λ=1.8187 Å) at JRR-3M in JAERI. Figure 1 shows the diffraction patterns at 2.5 K, 28 K and 34 K. Splittings of nuclear Bragg peaks caused by the structural phase transition are observed at 28 K. The change of nuclear reflection pattern indicates that the structure changes from cubic to rhombohedral symmetry below 32 K (T_S), which is consistent with the results of recent X-ray diffraction measurement [4]. And the fundamental propagation vector of the spin structure at 2.5 K is found to be k = <1/4 1/4 1/2> from the diffraction pattern for the first time.

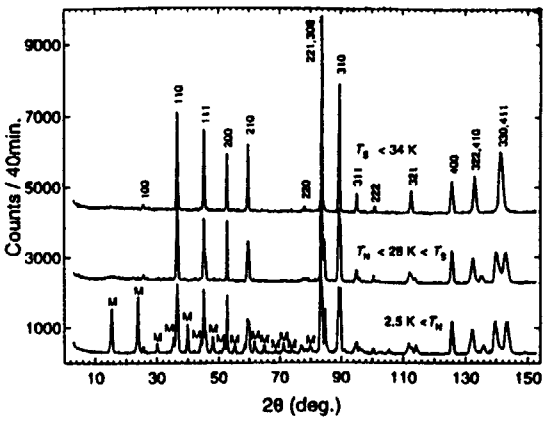

Fig.1 Neutron diffraction patterns of $Dy^{11}B_6$ at 34 K, 28 K and 2.5 K. 'M' indicates magnetic reflections.

References

[1] S. Kunii, K. Iwashita, T. Matsumura and K. Segawa, Physica B 186-188 (1993) 646.

[2] K. Segawa, A. Tomita, K. Iwashita, M. Kasaya, T. Suzuki and S. Kunii, J. Magn. Magn. Mater. 104-107 (1992) 1233.

[3] S. Nakamura, T. Goto, S. Kunii, K. Iwashita and A. Tamaki, J. Phys. Soc. Japan 63 (1994) 623.

[4] T. Kajitani, private communication.

JRR-3M, KPD(HERMES), 2. magnetism

研究課題： HoNiSn 単結晶の中性子回折
表題： HoNiSn の中性子回折

Neutron Diffraction Study on HoNiSn

M.Kurisu, G.Nakamoto, T.Nobata, S.Nakamura, Y.Makihara[1], Y.Andoh[2], and S.Kawano[3]

Japan Advanced Institute of Science and Technology
[1] *Faculty of Engineering, Kyushu Kyoritsu University*
[2] *Faculty of Education, Tottori University*
[3] *Research Reactor Institute, Kyoto University*

It was reported that the RNiSn compounds with R=Gd, Tb, Ho and Dy order antiferromagnetically below 20 K but the other members do not exhibit any magnetic order above 4.2 K [1,2]. We have studied the magnetic properties of RNiSn ternary compounds (R: rare earth) which crystallize in the orthorhombic TiNiSi type [3-6]. Recently, we have elucidated from the detailed magnetic, transport and neutron diffraction measurements on their single crystals that for heavy rare earth RNiSn compounds with R= Tb and Dy their magnetic structure at 1.6 K is described by a squared sine-modulated spin arrangement [3,5]. For other rare earth RNiSn compounds, we have recently found that NdNiSn, HoNiSn and ErNiSn order antiferromagnetically below 4 K with strong magnetic anisotropy [4]. We have also found that all the RNiSn compounds show metamagnetic transitions. The easy axis of magnetization for all the RNiSn except ErNiSn (a-axis) is the b-axis. In the present report, we present the neutron diffraction results on HoNiSn which orders at T_N=3.0 K.

Samples of HoNiSn were prepared by arc-melting the stoichiometric amounts of the elements under pure argon atmosphere. Single crystals were grown by a Czochlalski method. Neutron diffraction measurements were performed at the T_{1-1} beam hole of the JRR-3M reactor of JAERI.

Figure 1 shows the powder neutron diffraction patterns of HoNiSn at 1.4 K. The diffraction at 9.0 K shows only peaks of nuclei. At 1.4 K, we observe the extra magnetic peaks as indicated in fig.1. The magnetic peaks are indexed with a propagation vector q = (0.641, 0.333, 0). No ferromagnetic components are observed on the nuclear positions as reported by Yakinthos and Routsi [2]. Absence of the higher order satellites is not concluded from this powder diffraction experiment. A preliminary single crystal neutron diffraction gave no magnetic reflections in the a^*-c^* reciprocal plane. The magnetic propagation vector for this compound is similar to that for other heavy RNiSn compounds [6], which suggests that the spin arrangement is described by a sine-modulated spin wave one or a squared one. Further careful neutron diffraction measurements in other reciprocal planes are needed to clarify the magnetic structure in the compound.

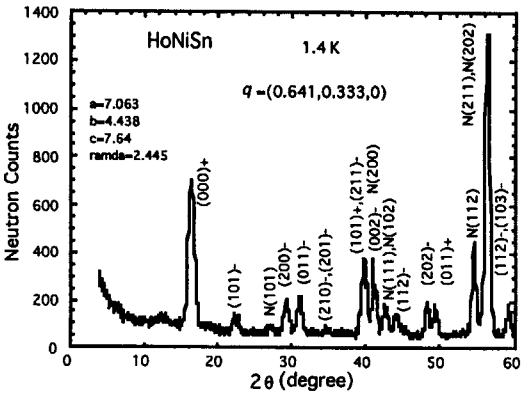

Fig.1 Neutron diffraction patters of HoNiSn at 1.4 K. The magnetic peaks are indexed with a propagation vector q = (0.641,0.333,0).

References

[1] C.Routsi *et al.*, J. Magn. Magn. Mater. **117** (1992) 79.
[2] J.K.Yakinthos *et. al.*, J. Magn. Magn. Mater. **136** (1992) 65.
[3] M.Kurisu *et al.*, Physica B **201** (1994) 107.
[4] Y.Andoh *et al.*, Physica B **237-238** (1997) 575.
[5] Y.Andoh *et al.*, J. Magn. Magn. Mater. **177-181** (1998) 1063.
[6] S.Kawano *et al.*, J. Magn. Magn. Mater. **182** (1998) 393.

JRR-3M, HQR(T1-1), 2. magnetism

研究課題： MnAl 磁石の中性子回折による研究
表 題 ： MnAl 高温相の short range order

Short Range Order in the High Temperature Phase of MnAl Alloy

S. Tomiyoshi[1], H. Odahara[1], M. Ohashi[2] and Y. Yamaguchi[2]
[1]*Faculty of Engineering, Ehime University, Matsuyama 790-8577*
[2]*IMR, Tohoku Univ., Sendai 980-8577*

The τ-phase of MnAl (bct-type structure) is a strong ferromagnet with large magnetic anisotropy. The formation mechanism of the τ-phase which is a metastable one obtained from the high temperature ε-phase is very interesting, but the experimental confirmation of which is not enough. Kojima et al[1] proposed a model that the ε-phase (hcp structure) transforms to the B19 type structure (orthorhombic) and then which transforms martensitically to the τ-phase. Last year we showed by powder neutron diffraction that a short range order of the B19 type is already present in the ε-phase[2].

In the present work we measured the short range chemical order using a single crystal sample of the ε-phase to clarify the presence of the short range order more clearly. The single crystals were grown using Bridgman technique and quenched in water from 1100℃. Neutron diffraction measurement was done using the diffractometer of KSD.

Figure 1 shows a diffraction pattern scanned along (h,0,0) in the hexagonal c-plane at 15K. The sharp peaks at (1,0,0) and (2,0,0) are usual Bragg peaks indexed as the hexagonal closed packed structure, which have very small intensities due to nearly zero matrix alloy. In addition to the ordinary Bragg peaks broad peaks are observed at (1/2,0,0) and (3/2,0,0) positions. We also observed broad peaks with half integer indices in the a*-c* plane, which can be index as the B19 type structure in which like atoms align linearly in the c-plane. Present data shows that the B19 type short range order exists already in the hcp lattice.

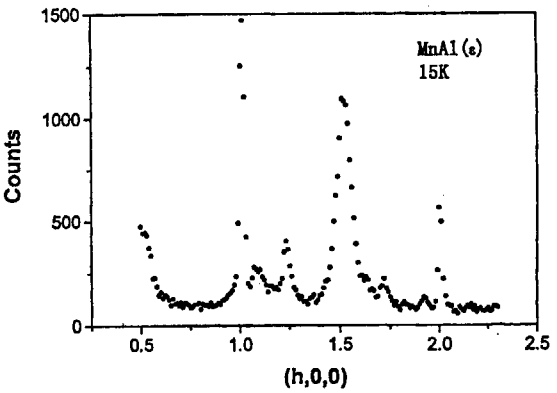

Fig. 1 Diffraction pattern of the ε-phase scanned along (h,0,0) at 15K.

References

1. S. Kojima, T. Otani *et al.*, AIP Conf. Proc., Vol. 24 (1975) 768.
2. H. Odahara, S. Tomiyoshi *et al.*, Memoirs of the Faculty of Engineering Ehime Univ., Vol. 16 (1997) 425.

Reactor: JRR-3M Facility: KSD(T1-2) Field: 2 磁性 Magnetism

課題名：$CePt_2Sn_2$と$NdGa_2$は「量子スピン液体」状態か？

表　題：近藤反強磁性体$CePt_2Sn_2$の中性子回折

Neutron Diffraction Study of the Kondo Antiferromagnet $CePt_2Sn_2$

H. Kadowaki, T. Sasaki, K. M. Kojima,[1] Y. J. Uemura,[1] G. M. Luke,[1] Y. Fudamoto,[1] T Osakabe,[2] Y Koike,[2] N. Metoki,[2] S. Katano,[2] K. Ohoyama,[3] M. Ohashi,[3] Y. Echizen,[4] T. Takabatake[4]

Department of Physics, Tokyo Metropolitan University, Hachioji-shi, Tokyo 192-0397
[1]Department of Physics, Columbia University, New York, NY 10027, U. S. A.
[2]Advanced Science Research Center, Japan Atomic Energy Research Institute, Tokai, Ibaraki 319-11
[3]Institute for Material Research, Tohoku University, Sendai 980
[4]Faculty of Science, Hiroshima University, Higashi-Hiroshima 739

The competition between Kondo spin fluctuation and exchange interactions produce a very heavy electron system of $CePt_2Sn_2$ which is characterized by a very large $\gamma > 3$ J/mole K^2 and a low Néel temperature $T_N = 0.9$ K.[1] Powder diffraction studies were performed to reveal the crystal structure and the magnetic structure using HERMES and TAS-2. The crystal structure is a $CaBe_2Ge_2$-type (P4/nmm) with a small monoclinic distortion. We performed the Rietveld analysis (RIETAN) assuming $P2_1/m$ and $P2_1$ space groups using diffraction data taken at T=1.8 K > T_N. A result for the $P2_1/m$ structure is shown in Fig. 1. One can see that there is certain discrepancy, though quality of fitting is not so bad. Below Néel temperature weak magnetic reflections were observed. Detail of the magnetic profile is being analyzed now. The magnetic structure is a single-k type with a modulation vector (1/3 0 1/2). In Fig. 2 an approximate magnetic structure, i.e., tentative result and to be revised, is illustrated.

Reference

1) W. P. Beyermann et al.: Phys. Rev Lett. **66** (1991) 3289

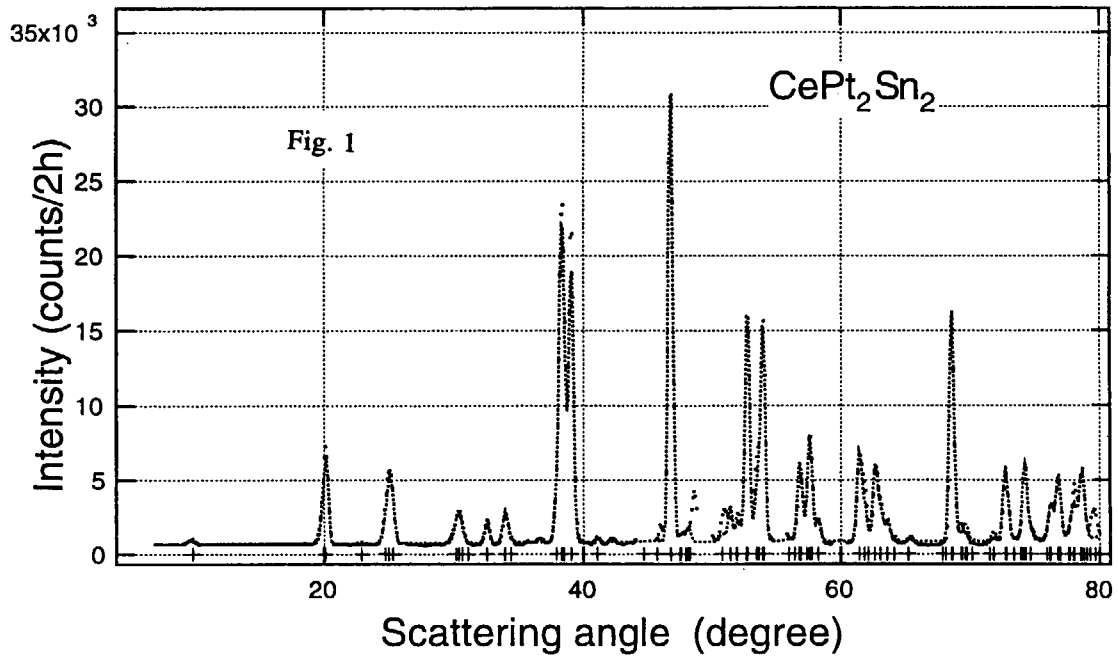

JRR-3M, HERMES(T1-3), magnetism

Fig. 2

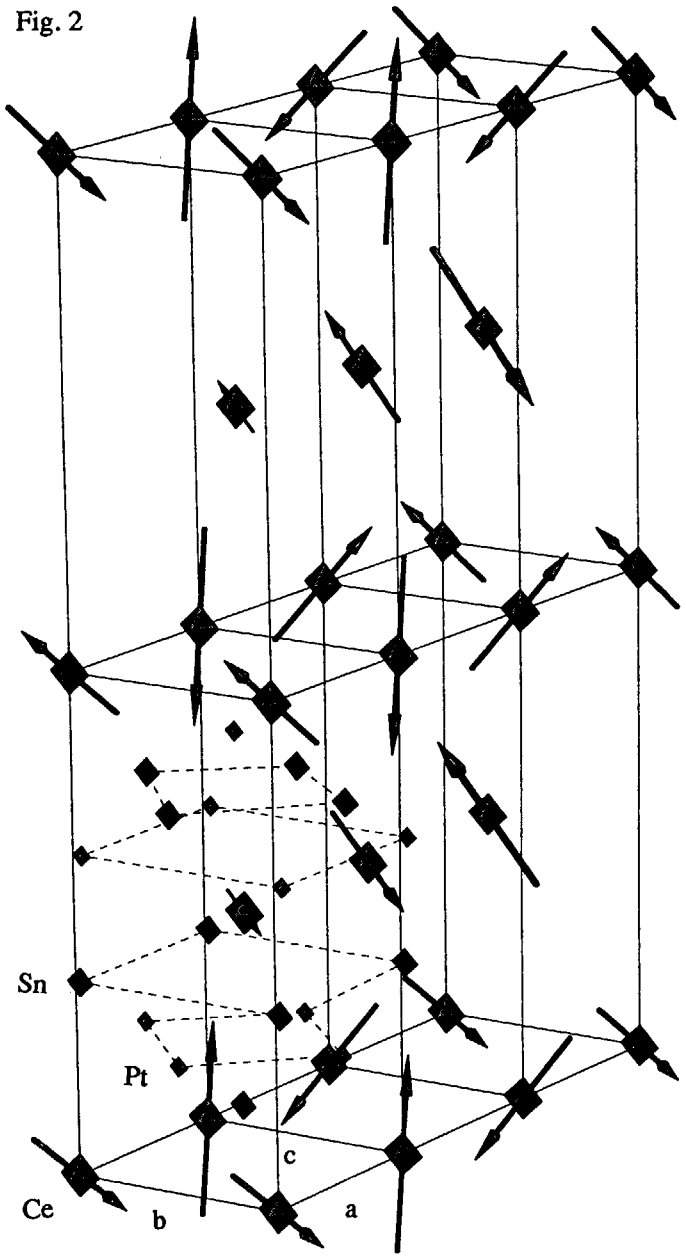

研究テーマ：非晶質ホイスラー合金の磁性
表題：非晶質ホイスラー合金$Cu_2MnAl_{1-x}Zr_x$の中性子回折

Neutron Diffraction of Amorphous Heusler Alloys $Cu_2MnAl_{1-x}Zr_x$

T.Kamimori, Y.Shiraga, K.Konishi, H.Tagne, M.Goto, S.Tomiyoshi[1], K.Ohoyama[2], M.Ohashi[2] and Y.Yamaguchi[2]

Faculty of Science, Ehime University, Matsuyama 790-8577
[1]Faculty of Engineering, Ehime University, Matsuyama 790-8577
[2]Institute for Materials Research, Tohoku University, Sendai 980-8577

A Typical Heusler alloy Cu_2MnAl is well known as a ferromagnet caused by its ordered structure. It arouses an interest of us in magnetism of the alloy in amorphous state. We succeeded to obtain the amorphous Heusler alloy by substitution of Y and Zr for Al[1,2]. The amorphous samples, $Cu_2MnAl_{1-x}Z_x$ (Z = Zr or Y), were prepared by using rapid quench technique. Magnetic measurements show spin glass behavior below T_f ~50K for Z=Y and T_f ~100K for Z=Zr with $x > 0.25$. However, The alloy, $Cu_2MnAl_{0.8}Zr_{0.2}$ shows reentrant spin glass with T_C = 50K and T_f = 10k. The amorphous alloys are paramagnetic above T_f or T_C. However, antiferromagnetic scattering was found for the alloy, $Cu_2MnAl_{1-x}Y_x$, above T_f by neutron diffraction in 1993[2]. The magnetic scattering also was observed at high temperature, 470K that is just below the crystallization temperature. In the present work, Zr was chosen for Z because reentrant spin glass was found for x=0.2 in this alloy system that shows the antiferromagnetic interaction will be weaker in Z=Zr than in Z=Y. The neutron diffraction patterns for x=0.3 were measured at 20K, 120K and R.T. at JRR-3M of JAERI(Tokai). The diffraction pattern shows broad peaks at Q ~1.5, ~3, ~5 and ~6 at R.T. The broad peak at Q ~3 and ~6 corresponds to the one measured by X-ray diffraction. On the contrary, the broad peaks at Q ~1.5 and ~5 do not appear in X-ray diffraction. It shows that the broad peak at Q ~ 1.5 is caused by AF magnetic scattering. The intensity of the AF magnetic scattering is almost the same as that at 20K. This result shows the antiferromagnetic short range ordering is very strong even in Z=Zr. Fig. 1 shows the AF magnetic scattering around Q ~1.5. The magnetic scattering shows that there are 7 types of Mn-Mn coupling. Three broad peaks of Q=1.58, 1.83, 2.00 and 4 narrow peaks of Q=1.455, 1.550, 1.655 and 2.100 are observed. The second and forth ordered ones of these peaks are also observed. As described above, the crystallization temperature of amorphous Heusler alloy is very lower than other amorphous alloys. These narrow peaks will show existence of quasi-crystallites as disordered Heusler alloy.

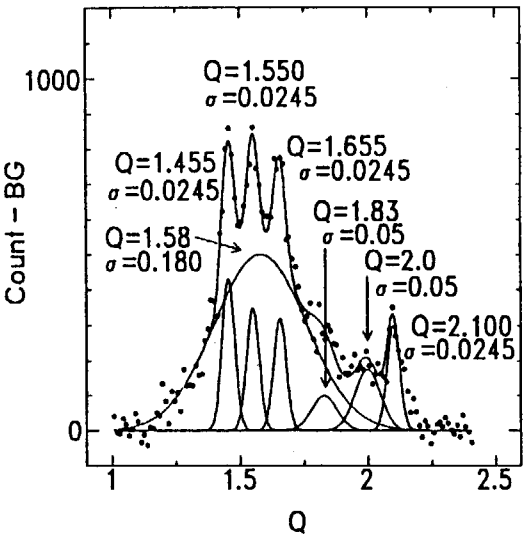

Fig. 1. Magnetic scattering of amorphous $Cu_2MnAl_{0.7}Zr_{0.3}$ at R.T.

References
1) M.Goto, K.Takagi, T.Kamimori and H.Tange; Proceeding of the 2nd International Symposium on Physics of Magnetic Materials. (1992, Beijing, China, International Academic Publications) P.508.
2) M.Goto, T.Kamimori, H.Tange, K.Kitao, S.Tomiyoshi, K.Ohoyama and Y.Yamaguchi; J. Magn. Magn. Mater.,140-144(1995)277.

JRR-3M, KPD-HERMES, magnetism

研究テーマ：ランタノイド複合酸化物の磁気構造
表題：粉末中性子回折による $SrTbO_3$, $BaTbO_3$の結晶構造と磁気構造

Study on the Crystal and Magnetic Structures of $SrTbO_3$ and $BaTbO_3$ by Powder Neutron Diffraction

K. Tezuka, M. Itoh, M. Haga, Y. Hinatsu, Y. Shimojo[1] and Y. Morii[1]

Division of Chemistry, Graduate School of Science, Hokkaido University, Sapporo 060-0810, Japan
[1] *Japan Atomic Energy Research Institute, Tokai-mura, Ibaraki 319-1195, Japan*

We prepared oxygen stoichiometric $SrTbO_3$ and $BaTbO_3$ in which tetravalent terbium ions are stabilized at the *B* sites of the perovskite ABO_3. Magnetic susceptibility measurements have been performed for both the compounds in the temperature range between 4.5K and room temperature. Both the compounds show the antiferromagnetic transition at *ca.* 33K.

In order to determine the crystal and magnetic structures, powder neutron measurements were performed at room temperature and 10K for $SrTbO_3$ and $BaTbO_3$ with a High Resolution Powder Diffractometer (HRPD) in the JRR-3M reactor with a neutron incident wave length ($\lambda = 1.823$Å).

Their crystal structures at room temperature were determined from the Rietveld analysis of these powder neutron diffraction patterns shown in Fig. 1. $SrTbO_3$ has an orthorhombic perovskite-type structure with space group *Pnma* (No. 62) as shown in Fig. 2. On the other hand, $BaTbO_3$ has a rhombohedral structure with space group $R\bar{3}c$ (No. 167).

Both $SrTbO_3$ and $BaTbO_3$ have the orthorhombic perovskite-type structure with space group *Pnma* at 10K and the G-type magnetic structure in which terbium atoms are antiferromagnetically coupled with the six neighboring terbium atoms as shown in Fig. 3. It was found that in $BaTbO_3$ the rhombohedral-to-orthorhombic phase transition occurred when the temperature was decreased from room temperature to 10K, whereas $SrTbO_3$ showed no crystal phase transition in this temperature range.

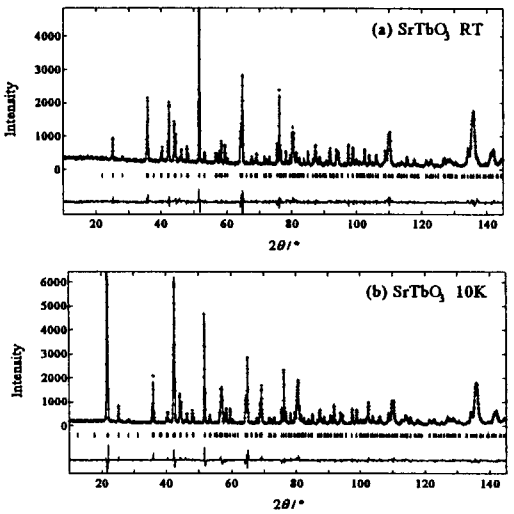

Fig. 1 Powder neutron diffraction pattern fitting for $SrTbO_3$.

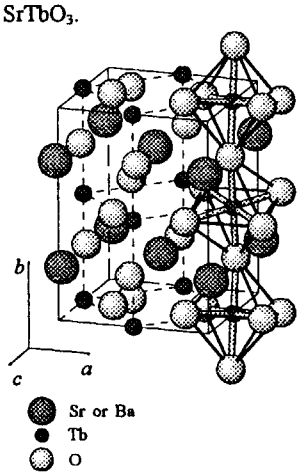

Fig. 2 Crystal structure (orthorhombic *Pnma*) of $SrTbO_3$ at RT and 10K and $BaTbO_3$ at 10K.

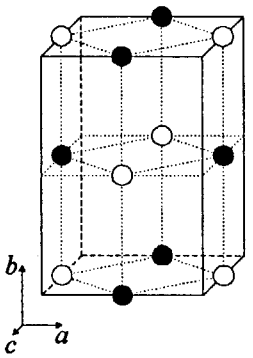

Fig. 3 Magnetic structure for $SrTbO_3$ and $BaTbO_3$ at 10K. O and ● represent directions of magnetic moments of terbium atoms and O is antipararell to●.

原子炉：JRR-3M　　装置：HRPD(1G)　　分野：中性子散乱（磁性）

研究テーマ：ランタノイド複合酸化物の磁気構造
表題：ペロブスカイト $La_{0.85}Sr_{0.15}CrO_3$の中性子回折

Neutron Diffraction Study on Perovskite $La_{0.85}Sr_{0.15}CrO_3$

K. Tezuka, Y. Hinatsu, A. Nakamura[1], T. Inami[1], Y. Shimojo[1] and Y. Morii[1]

Division of Chemistry, Graduate School of Science, Hokkaido University, Sapporo 060-0810, Japan
[1] *Japan Atomic Energy Research Institute, Tokai-mura, Ibaraki 319-1195, Japan*

Magnetic properties of perovskite-type compound $La_{0.85}Sr_{0.15}CrO_3$ have been reported. Their DC magnetic susceptibilities were measured from 4.5K to 320K. The compound showed an antiferromagnetic transition and the Néel temperature was determined to be 270K. Below the Néel temperature, other two magnetic transitions were furthermore observed. One of the transitions occurred at *ca.* 150K. The other magnetic transition was found at *ca.* 20K. The compound showed magnetic hysteresis at 50K.

In order to determine the magnetic structures, powder neutron measurements were performed at room temperature, 250K and 50K with a High Resolution Powder Diffractometer (HRPD) in the JRR-3M reactor with a neutron incident wave length ($\lambda = 1.823$Å).

From the Rietveld analysis of these powder neutron diffraction patterns shown in Fig. 1, it was found that the crystal phase and magnetic transition occurred between 50K and 250K. The crystal structure at room temperature and 250K is rhombohedral with space group $R\bar{3}c$, and it transforms to an orthorhombic structure with space group *Pnma* at 50K. The magnetic structures at 50K and at 250K are both the G-type in which chromium atoms are antiferromagnetically coupled with the six neighboring chromium atoms. The direction of magnetic moments is directed to [111] of the rhombohedral unit cell at 250K and changes to be parallel to the *z*-axis of the orthorhombic unit cell (*Pnma*) at 50K as shown in Fig. 2. In fact, antiferromagnetic moments are not collinear at 50K, because there exists the ferromagnetic component in the magnetic moment of chromium at 50K from the magnetization measurements.

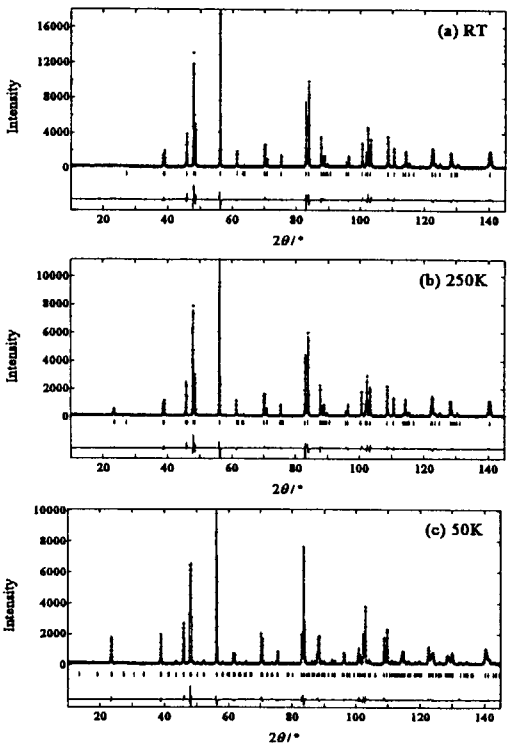

Fig. 1 Powder neutron diffraction pattern fitting for $La_{0.85}Sr_{0.15}CrO_3$.

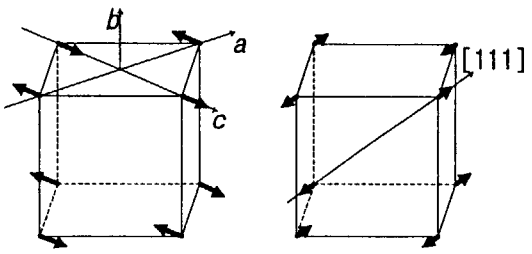

(a) 50K Orthorhombic (*Pnma*) (b) 250K Rhombohedral ($R\bar{3}c$)
Fig. 2 Configuration of magnetic moments of Cr ions in pseudo cubic cell for $La_{0.85}Sr_{0.15}CrO_3$.

原子炉：JRR-3M　　装置：HRPD(1G)　　分野：中性子散乱（磁性）

研究テーマ：量子凝縮相の研究
表　　題：$U_3Pd_{20}Si_6$の結晶及び磁気構造

The Crystal and Magnetic Structure of a Ternary Uranium Compound $U_3Pd_{20}Si_6$

N. Tateiwa[1], N. Metoki[1,2], Y. Koike[2], N. Kimura[3], and T. Komatsubara[1]

[1]Physics Department, Graduate School of Science, Tohoku University, Sendai 980-8545
[2]Advanced Science Research Center, Japan Atomic Energy Research Institute, Tokai-mura 319-1195
[3]Center for Very Low Temperature Science, Tohoku Univeversity, Sendai 980-8545

Uranium compounds attract much attention because of the variety of the magnetic properties. Uranium intermetallics favor itinerant character, since 5f electrons spread out and hybridized with conduction electrons. The itinerant character is revealed by the quantum oscillation experiments in many systems like UGe_3, URu_3, UIr_3 and URh_3. However there is a localized system like UPd_3 which exhibits clear crystal electric field excitation and quadrupole ordering. UPd_3 is so far understood as a rather exceptional case, which has a localized character.

Very recently we have found a new material $U_3Pd_{20}Si_6$ which is an isostructual compound of $R_3Pd_{20}X_6$ (R = rare earth, X = Si, Ge) series[1]. This compound attracts strong interest because of the localized character of 5f electron; The susceptibility obeys the Currie-Weiss law in the wide temperature range (50K < T < 300K) and the effective moment 3.30 μ_B/U is close to the values expected for free uranium ion. The clear anomalies in specific heat at 19K and around 2K indicate the magnetic transitions. The purpose of this study is to reveal the crystal and magnetic structure of $U_3Pd_{20}Si_6$.

Neutron powder diffraction profiles were measured using HRPD (λ = 1.1624 Å). The temperature dependence of the magnetic scattering is measured by a triple-axis spectrometer TAS1. The samples were cooled down to 100 mK by liquid-helium free dilution refrigerator developped by JAERI. Single crystal samples were prepared by the Chochralski pulling method in a tetra-arc furnace.

Fig. 1 shows a neutron powder diffraction spectrum at room temperature. We found that the profile can be well explained by the crystal structure of $R_3Pd_{20}X_6$ as shown in the Fig. 2. There are two different crystallographic sites for uranium atoms; fcc (4a) site and simple cubic (8c) site. Details about the result of the refinement will be published elsewhere.

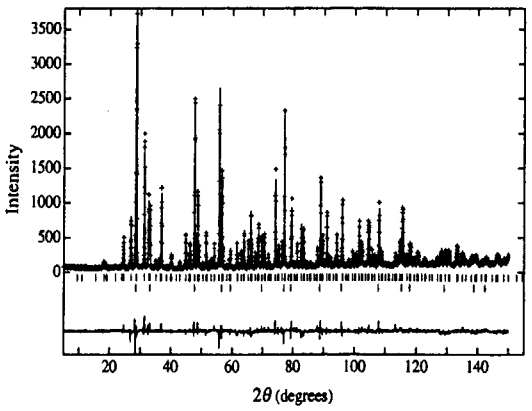

Fig. 1 A neutron powder diffraction spectrum of $U_3Pd_{20}Si_6$ at room temperature.

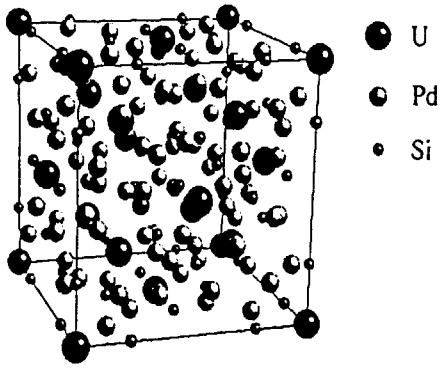

Fig. 2 The crystal structure of $U_3Pd_{20}Si_6$.

Figure 3 shows the result of the spin polarized neutron scattering experiments at the (111) Bragg point. At T = 7K we observed a clear peak in the spin flip (SF) cross section. It indicates the magnetic ordering below the upper transition temperature Tu=19 K. The weak peak in SF at T=21 K is a contamination of the NSF process due to imperfect neutron polarization ratio of our instrument (93%). Figure 4 is the temperature dependence of the SF and non-spin flip (NSF) cross section of the (111) peak. Both SF and NSF cross section exhibits clear increase below Tu=19 K, which is due to magnetic ordering. SF intensities are observed only at (h,k,l)±(1,1,1), where (h,k,l) is the nuclear Bragg point. At the other Bragg points, a small increase of the SF intensity is observed with decreasing temperature below Tu. However it is obviously due to multiple scattering, because this change dissapears, when we measure polycrystalline samples. It is concluded that the magnetic ordering of the type II antifferomagnetic structure of the simple cubic (8c) site, where the propagation vector [111] corresponds to [1/2 1/2 1/2] on the basis of the simple cubic lattice; The periodicity of the simple cubic is half of the unit cell. No magnetic ordering of fcc (4a) site is expected in this temperature range because ferromagnetic component is necessary to explain the increase of the (111) intensity.

Fig. 5 shows the temperature dependence of the (022) intensity below 2K. We observed a continous increase of the peak intensity below the lower transition temperature Tl = 2K. Similar increase was also found in the observed nuclear Bragg peaks. No half order or incommensurate peak was observed. These results indicate the ferromagnetic ordering of the uranium spins on fcc (4a) site. It is consistent with the magnetization and susceptibility measurements. From the intensity calculations, we found that the type II antiferromagnetic ordering of the simple cubic (8c) site is stable for the ferromagnetic transition of the fcc (4a) site. Therefore there is a coexistence of the ferromagnetic and antiferromagnetic ordering below Tl. The detailed analysis of the magnetic structure will be published very soon.

We thank M. Kohgi for the stimulating discussions.

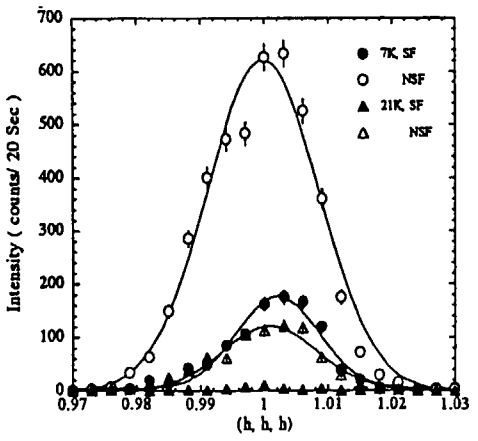

Fig. 3 The result of the spin polarized neutron scattering experiments at the (111) Bragg point.

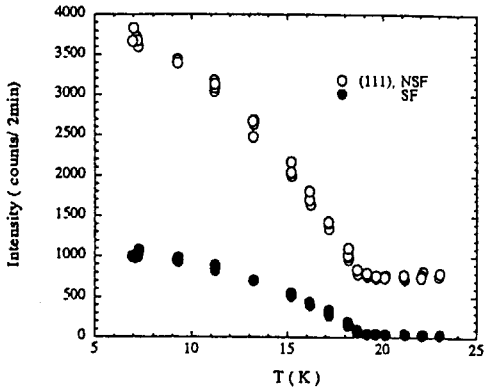

Fig. 4 The temperature dependence of the SF and NSF cross section of the (111) peak.

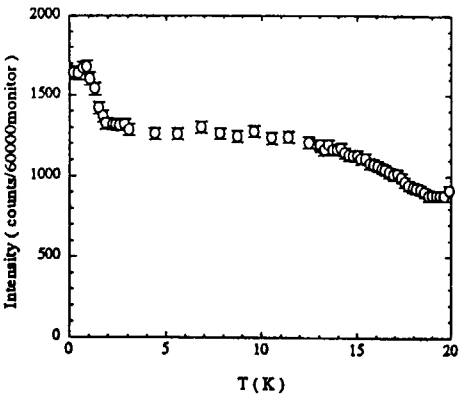

Fig. 5 The temperature dependence of the (022) intensity.

Reference

1) N.Tateiwa, et al., unpubished results.

原子炉：JRR-3M　　装置：HRPD、TAS-1、LTAS　　分野：中性子散乱（磁性）

研究テーマ：量子凝縮相の研究
表　　題：$Nd_3Pd_{20}Ge_6$における磁気転移の研究

Successive Magnetic Sublattice Ordering in $Nd_3Pd_{20}Ge_6$

N. Tateiwa[1], N. Metoki[1,2], Y. Koike[2], M. Nakayama[1], N. Kimura[3] and T. Komatsubara[1]

[1]Physics Department, Graduate School of Science, Tohoku University, Sendai 980-8545
[2]Advanced Science Research Center, Japan Atomic Energy Research Institute, Tokai-mura 319-1195
[3]Center for Very Low Temperature Science, Tohoku University, Sendai 980-8545

Recently the new ternary system $R_3Pd_{20}X_6$ (R: rare earth, X: Si, Ge) has been attracted much interest because of the variety of the physical propeties depending on the rare earth metal. The characteristic feature of this system is the successive magnetic phase transitions. For example, the specific heat and susceptibility measurements[1] of $Nd_3Pd_{20}Ge_6$ show three anomalies at T = 1.75 K, 1.40 K, and 0.54 K. The complicated magnetic phase diagram would be related to the fact that $R_3Pd_{20}X_6$ (space group $Fm\bar{3}m$) has two different crystallographic sites for rare earth atoms ; fcc (4a) site and simple cubic (8c) site. A Donni et al[2] have reported that the magnetic structure at 1.40 K < T < 1.75 K is characterized by the propagation vector [1,1,1]. The purpose of this study is to reveal the antiferromagnetic phases at lower temperatures.

Neutron scattering experiments were carried out using a cold neutron triple-axis spectrometer LTAS installed at JRR-3M. The sample is cooled by a ^{3}He-^{4}He dilution refrigerator. The incident beam (Ei=4.66meV) is monochromatized by a verticaly bent PG with a Be filter. The collimation was 25'-40'-40'-80'. The single crystal was grown by the Chochralski pulling method in a tetra-arc furnace.

Fig. 1 shows the temperature dependence of the (111), (100) and (011) peak intensities. We found that the (111) Bragg intensity increases below 1.75 K, while (100) and (110) peak appear and increase in intensity below 0.54 K. From the crystal structure, we found that the antiferromagnetic ordering at 0.54 K < T < 1.75 K is a type II structure of the Nd sublattice on simple cubic (8c) site, where the propagation vector [111] corresponds to the [1/2 1/2 1/2] on the basis of the simple cubic lattice; The periodicity of the simple cubic is half of the unit cell. No magnetic ordering of fcc (4a) site is expected in this temperature range because ferromagnetic component is necessary to explain the increase of the (111) peak intensity.

The (100) and (011) antifferomagnetic peak below 0.54 K indicates that the antiferromagnetic type I structure of the fcc (4a) site coexists with the type II structure of the 8c site. The magnetic ordering of the fcc (4a) site gives rise to no anomalous behavior of the (111) peak intensity. It means that the type II structure of 8c site is stabe for the magnetic ordering of the 4a site.

The magnetic peak intensity increases gradually below 0.1K. It might be due to the nuclear magnetic ordering of Nd.

No obvious change of the scattering intensity has been observed at the transition around 1.4 K. The origin of this transition remains an open question which should be studied further.

Very recently we found a similar double transition in $U_3Pd_{20}Si_6$. In this compound, surprisingly however, the antiferromagnetic type II structure coexists with ferromagnetic ordering of fcc (4a) site. Anyhow the successive magnetic sublattices ordering would be a charastric feature in $R_3Pd_{20}X_6$ system.

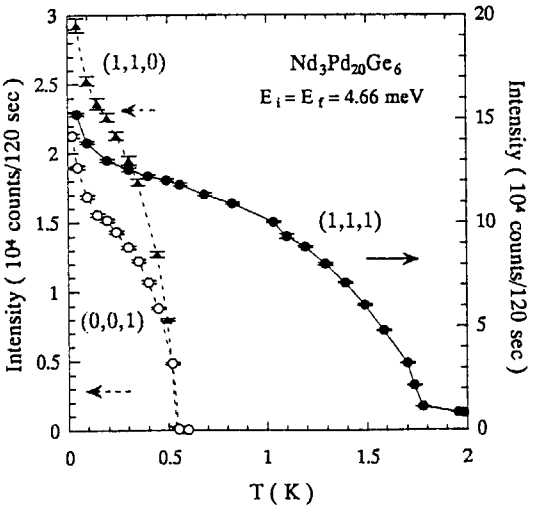

Fig1. The temperature dependences of Bragg intensities of $Nd_3Pd_{20}Ge_6$

References

1) M.Nakayama, et al., unpublished results
2) A.Donni, et al., private communication

原子炉：JRR-3M　　装置：LTAS(C2-1)　　分野：中性子（磁性）

研究テーマ：ErRu2Si2の磁場制御された二重変調磁気構造の研究
表題：ErRu2Si2の磁気構造とメタ磁性の研究

The magnetic structure and the mechanism of the metamagnetism in ErRu2Si2

M.Sato, N.Chigusa, Y.Yamamoto, T.Takeuchi, S.Kawarazaki and Y.Miyako
Department of earth and space science, Osaka University, Toyonaka, Osaka 560-0043

The rare earth ternary intermetallic compounds $RERu_2Si_2$ (RE=rare-earth metal) are classified as a localized-electron magnet except for the Kondo lattice system of $CeRu_2Si_2$. The crystal structure is the tetragonal $ThCr_2Si_2$-type structure (space group I4mmm, body centered tetragonal). They have an ordered state at low temperature and have a strong Ising-type magnetic anisotropy. The magnetic easy axis of them is the c-axis except for $ErRu_2Si_2$

$ErRu_2Si_2$ is antiferromagnetic below 6K, and shows a metamagneitc transition at H_C=0.5T. The previous neutron scattering experiments suggested that the magnetic moment in the ordered state is modurated with a wave vector of (0.2,0,0) and is oriented perpendicular to the c-axis.[1] Recently, our group has performed magnetization measurements changing the direction of the applied field in the c-plane and found that the easy axis is along [110].[2] On the basis of these facts, we have performed neutron diffraction experiments with powder and single crystalline samples and concluded that the magnetic structure is double-q structure as shown in Fig.1.

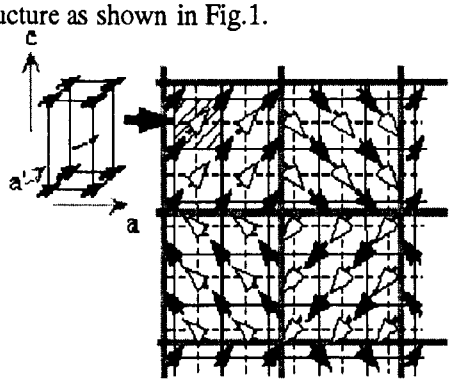

In oreder to understand the metamagnetism of this material on the basis of this double-q structure, we partitioned the pattern of the spin configuration in Fig.1 into four sections in each of which the spins are oriented to the same direction. By assuming that each section responds to magnetic field so that the sum of the anisotropy energy and the Zeeman energy is minimized, we could reasonably explain the observed behavior of the magnetizations.This assumption is also consistent with the results of neutron diffractions with magnetic field as shown in Fig.2.

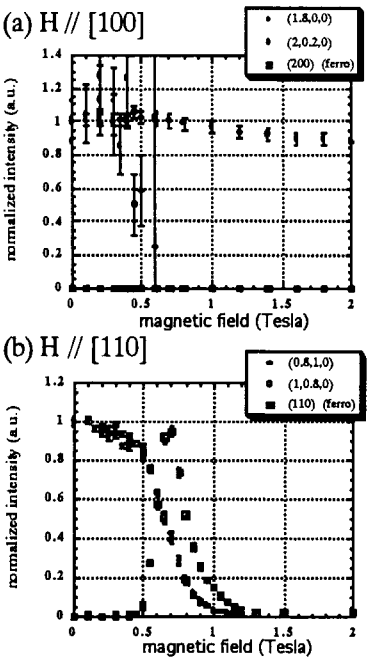

Fig.2 The change of the magnetic scattering intensity by magnetic field. The intensity is normalized by the value of the antiferromagnetic peak at H=0.

References

[1]M.Slaski et al. J.Magn.Magn.Mat.46 (1984) p.114
R.Hamada et al. J.Magn.Magn.Mat. 140-144 (1995) p.907 etc.
[2]T.Takeuchi et al. J.Magn.Magn.Mat. 177-181 (1998) p.1081

研究テーマ：メタ磁性Y2Cu2O5の磁場中磁気構造

表題：メタ磁性Y2Cu2O5の磁場中磁気構造

Metamagnetic transition in $Y_2Cu_2O_5$

M.Motokawa, Y.Matsuoka and K.Kakurai[1]

Institute for materials Research, Tohoku University, Sendai 980-8577, Japan
[1] Institute for Solid State Physics, University of Tokyo, Shirakata, Tokai, Naka, Ibaraki, 319-11 Japan

It is quite strange that $Y_2Cu_2O_5$ shows metamagnetic transitions below T_N=13K, because the anisotropy of Cu^{2+} spin must be much smaller than the antiferromagnetic exchange interactions. When an external field H is applied parallel to the b-axis, the induced magnetization jumps at H_{c1}=3.0 T and H_{c2}=4.8 T, then increases linearly up to the saturation field Hs=8.0 T. The extrapolation of this linear part does not cross the origin, which cannot be explained by the simple molecular-field model. In order to explain these strange behaviors, determination of magnetic structures in a field is important. However, it is very difficult to grow large single crystals of high quality to be used for neutron diffraction experiments. We had to start from synthesis of it and succeeded.

First, we re-examined the magnetization measurements. The magnetization curve for H ∥ b-axis is identical with that obtained by a bundle of tiny needle-like single crystals of which b-axis coincided. The magnetization curves for H ∥ c- and a-axis, which could not be discriminated by the bundle of tiny crystals, increase linearly from the origin and saturate at 11.0 and 10.5 T for H ∥ c- and a-axis, respectively.

We performed neutron diffraction experiments of this compound at temperatures between 2.7 and 30K using PONTA spectrometer in the JRR-3M at JAERI. To look for diffraction peaks of unknown magnetic structure, we used a two-dimensional detector called 'neutron imaging plate', developed at JAERI. The scanning was done from (0, 0, 1) to (0, 0, 3). First we observed the diffraction peaks at zero field. The peaks observed at (0, 0, 1) and (0, 0, 3) are consistent with the structure determined by the powder sample, namely ferromagnetic array along the a- and b-axis and antiferromagnetic array along the c-axis. Next, we applied an external field parallel to the b-axis up to 6 T which covers intermediate parts between H_{c1} and H_{c2} and slightly above H_{c2}. At fields between H_{c1} and H_{c2}, we found new diffraction peaks at (0 1/3, 1) and (0, 1/3, 3), which are completely unexpected positions. If the neutron imaging plate was not employed, it might take a long time to find the diffraction peaks which appear at such unexpected positions. Above H_{c2}, these diffraction peak disappear, while (0, 0, 1 0 and (0, 0, 3) peaks which are observed below H_{c1} revive. The new peaks observed between H_{c1} and H_{c2} mean that the magnetic moments turn from the ferromagnetic array to three lattice period structure along the b-axis keeping ferromagnetic array along the a-axis like Fig.1. Three structures is possible by this results, but the structure shown in Fig.1 is seems to be most probable considering from other experiments[1]. Above H_{c2}, although the intensities of observed peaks is weak, the symmetry is same as that below H_{c1}. These structure changes are completely unexpected and mysterious from the crystallographic point of view.

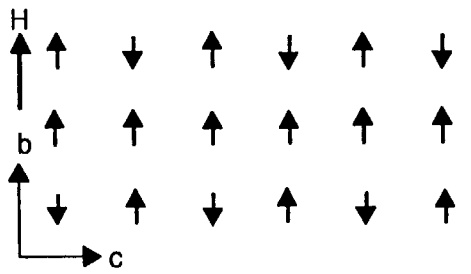

Fig.1 Probable magnetic structure expected by the present experiment.

1) Y.Matsuoka, M.Motokawa, K.Kakurai and B.Lebeck: to be published

JRR-3M, PONTA (5G), Magnetism

研究課題：$(La,Sr)_{n+1}Mn_nO_{3n+1}$のスピン・電荷ダイナミクス
標題：二重層状Mn酸化物$La_{2-2x}Sr_{1+2x}Mn_2O_7$の磁気構造

Magnetic Structure of the Double-Layered Manganite $La_{2-2x}Sr_{1+2x}Mn_2O_7$

M. Kubota[1], H. Fujioka[2], K. Hirota[2], Y. Moritomo[3], H. Yoshizawa[1], and Y. Endoh[2]

[1] *Neutron Scattering Laboratory, Institute for Solid State Physics, University of Tokyo*
[2] *CREST, Department of Physics, Tohoku University*
[3] *CIRSE and Department of Applied Physics, Nagoya University*

The layered perovskite Mn oxide $La_{2-2x}Sr_{1+2x}Mn_2O_7$ has double MnO_2 sheets and $(La_{1-x}Sr_x)_2O_2$ blocking layers stacking alternatively along the c axis. Recently, Moritomo *et al.*[1] have discovered that $La_{2-2x}Sr_{1+2x}Mn_2O_7$ shows a metal-insulator transition accompanied by CMR (colossal magnetoresistance) ; the ratio of magnetoresistance under 7 T to that under zero field at T_C reaches about 20000 %.

We have performed neutron diffraction measurements to investigate how the magnetic structure changes with the hall concentration x $La_{2-2x}Sr_{1+2x}Mn_2O_7$ ($x \sim 0.40$). We have prepared single crystals (x = 0.40, 0.45, 0.48) by the floating-zone method. The magnetic structures were determined using the triple-axis spectrometer TOPAN. The (0 0 2) reflection of pyrolytic graphic (PG) was used to monochromate and analyze the neutron beam, together with two PG filters to eliminate higher order contaminations.

The hall concentration has large effects on the magnetism in $La_{2-2x}Sr_{1+2x}Mn_2O_7$. The ferromagnetic reflection (0 0 2) follows an ordinary power law. However, T_C is strikingly subjective to x (120 K at x = 0.40 and 95 K at x = 0.45) and the ferromagnetism completely disappears at x = 0.48. On the other hand, the A-type antiferromagneitc reflection (0 0 3) shows unconventional exponential temperature dependence below 200 K. We thus define the Néel point T_N at temperature where the (0 0 3) reflection emerges. T_N thus defined is almost independent of x.

Magnetic structure analyses show that the neighboring MnO_2 sheets have planar ferromagnetic components canted with respect to each other along the c axis. The canting angle changes successively (15.7°→57.8°→180°) with the increase of x (0.40→0.45→0.48). The total magnetic moment is about 3.0 μ_B/Mn, which is almost independent of x. We speculate that the moment is less than the full magnetic moment ($4.0-x$ μ_B/Mn) because spins are contracted due to the low dimensionality.

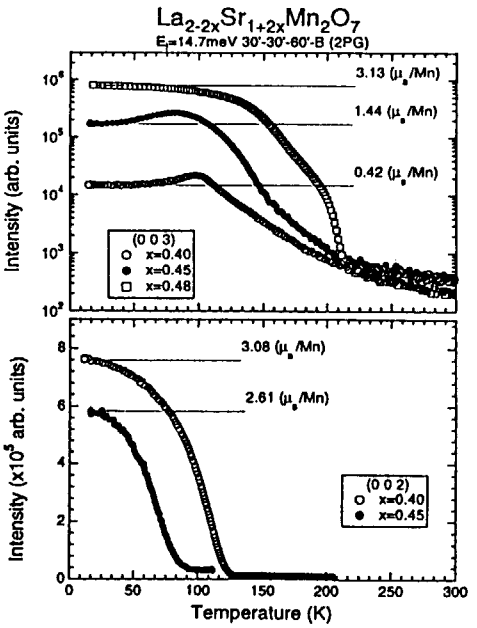

FIG. 1 Temperature dependence of the antiferromagnetic (top) and ferromagnetic (bottom) reflection in $La_{2-2x}Sr_{1+2x}Mn_2O_7$ (x=0.40, 0.45, 0.48).

References

[1] Y. Moritomo *et al.*, Nature (London) **380**, 141 (1996).

Reactor: JRR-3M Facility: TOPAN(6G) Field: 2 磁性 Magnetism

研究テーマ：重い電子系化合物Ce2X(X=Sb, Bi)の磁気構造解析
表題：重い電子系化合物Ce2X(X=Sb, Bi)の磁気構造

Magnetic structures of heavy ferion compounds, Ce_2X (X=Sb, Bi)

K. OHOYAMA, H. HAYASHI, M. OHASHI†, H. ONODERA, Y. YAMAGUCHI, M. KOHGI[1] and T. SUZUKI[2]

Institute for Materials Research, Tohoku University, Katahira, Sendai. 980-77
[1]*Department of Physics, Tokyo Metropolitan University, Tokyo 192-03*
[2]*Department of Physics, Tohoku University, Sendai 980-77*

Ce-based compounds, Ce_2X (X=Sb, Bi), with antifferomanetic ground states($T_N \approx 10K$) exhibit characteristic features of Kondo anomalies and heavy fermion behaviors at low temperautes[1]. Ce_2X has the tetragonal La_2Sb type crystal structure which includes two individual rare earth atom sites, 4e (Ce-I) and 4c (Ce-II), with different local symmetry. Because of the difference of the distance between Ce atoms in this structure, it is expected that the 4f electrons in Ce-I behave like band electrons which are shown in valence fluctuation materials, while the 4f electrons in Ce-II are relatively localised[1]. Therefore, it is interesting to make clear the role of each Ce site for anomalous magnetic behaviours at low temperatures.

We performed neutron powder diffraction experiments on HERMES at the T1-3 hole to determin the magnetic structures of Ce_2X below T_N. From the results of the experiments by HERMES, we found that Ce_2Bi has an antifferomagnetic structure with the propergation vector of $[0,0,\frac{1}{2}]$ below T_N=10.1K. On the other hand, Ce_2Sb has a antifferomagnetic state with the propergation vector of [0,0,1] below T_N=8.2K. Since results of magnetisation measurements indicate that the magnetic moments in Ce_2X are along the c-axis, we determined the magnetic structures as shown in Fig.1; the magnitude of the magnetic moments are given in table.1. Open and closed circles in Fig.1 indicate Ce-I and Ce-II atoms, respectively. A characteristic point is that there exist non-magnetic Ce-atoms at Ce-I in both compounds. We think that the quench of magnetic moments at Ce-I site is due to valence fluctuation behavious of 4f states because of the small distance between Ce-I atoms. On the other hand, Ce-II has a large magnetic moments because the 4f stats are relatively localised.

Table 1: The magnetic moments in Ce_2X

	Ce-I site	Ce-II site
Ce_2Sb	$0.0\pm0.1\mu_B$	$1.5\pm0.2\mu_B$
Ce_2Bi	$0.3\pm0.1\mu_B$	$1.4\pm0.2\mu_B$

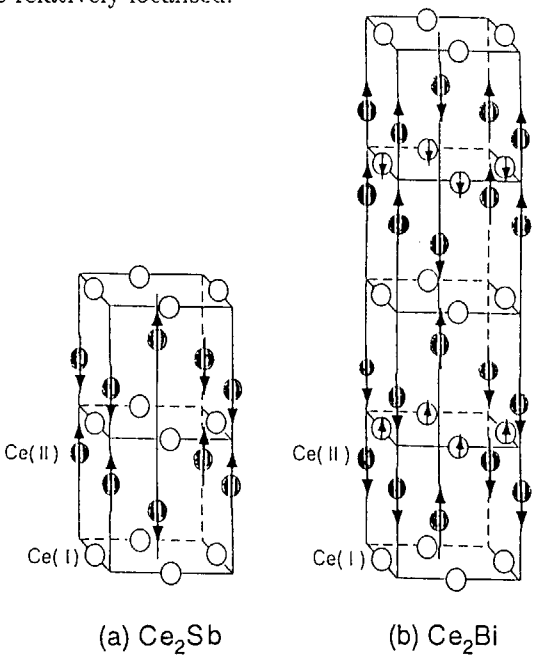

Fig.1 The magnetic structures of Ce_2Sb(a) and Ce_2Bi(b)

References

[1] A. Oyamada, A. Isobe. H. Kitazawa. A. Ochiai, T. Suzuki and T. Kasuya: J. Phys. Soc. Jpn. **62** (1993) 1750.

† Present address: Faculty of Engineering. Yamagata University

JRR-3M, T1-3(HERMES), Magnetism

研究テーマ：正方晶 DyB_2C_2 における四重極相互作用と磁性

表題： DyB_2C_2 の磁気構造

Magnetic structure of DyB_2C_2

H. Yamauchi, H. Onodera, M. Ohashi†, K. Ohoyama, T. Onimaru,
M. Kosaka†† and Y. Yamaguchi

Institute for Materials Research, Tohoku University, Sendai 980-8577

DyB_2C_2 has a tetragonal LaB_2C_2-type crystal structure (space group $P\bar{4}2c$) which is characterised as the layers of -R-(B, C)-R- along the c-axis. Sakai *et al.* reported that DyB_2C_2 is ferromagnetic below 16.4K[1]. On the other hand, in the temperature dependence of the specific heat, a sharp peak at T_t=24.7K is observed in addition to that at T_C=15.3K. In the magnetization measurement, the spontaneous magnetization is observed below T_C. However, there exists no anomaly at T_t in the temperature dependence of magnetic susceptibility, except a very small hump in the magnetic susceptibility along the c-axis. Therefore, the anomaly at T_t is caused by a nonmagnetic phase transition. Since the magnetic entropy is close to Rln2 at T_C and Rln4 at T_t, we think that two Kramers doublets of the ground and first excited states lead to the transitions at T_C and T_t .Fig. 1 shows the H-T phase diagram when the magnetic fields are applied along the a-axis.

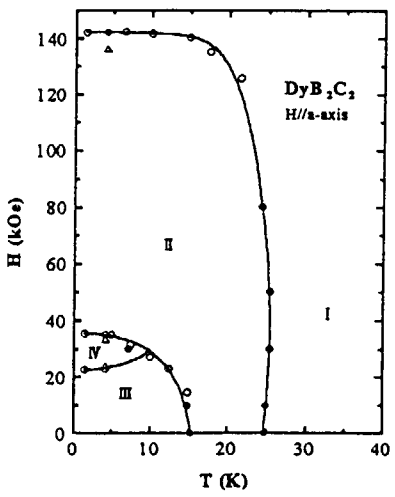

Fig. 1 The H-T phase diagram when the magnetic field is applied along the a-axis determined from the temperature dependence of the specific heat (●) and the differential magnetization (○ and △) measurements, respectively.

In the figure, there exists an unknown phase, phase II, between T_C and T_t while phase III, IV and I are the magnetic long-range ordered states and the paramagnetic state, respectively.

To understand the origin of the phase II and determine the magnetic structure in the phase III, we performed neutron powder diffraction experiments using the powder diffractometer, HERMES (T1-3), installed at the thermal neutron guide of the JRR-3M in JAERI. To optimize the scattering intensity, a double-cylindrical cell with a gap of 0.5mm was used. The duration time of a measurement was about 10 hours.

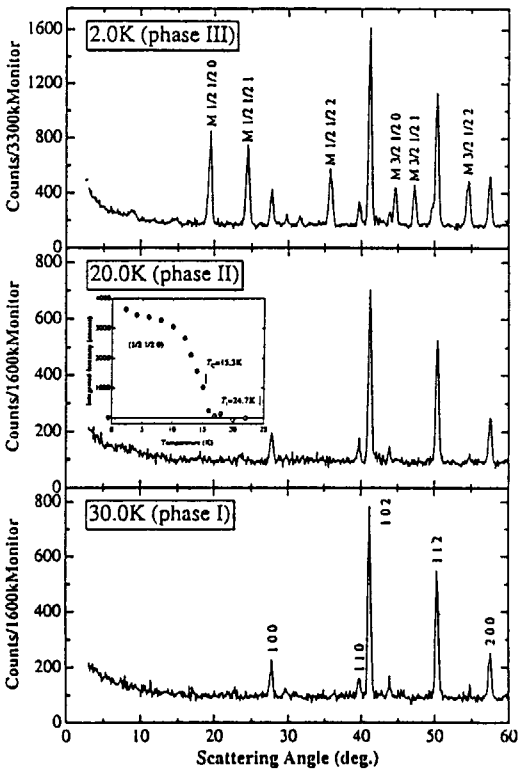

Fig. 2 The temperature dependence of neutron diffraction patterns at 2.0K, 20.0K and 30.0K. The inset gives the temperature dependence of the integrated intensity of the magnetic 1/2 1/2 0 Bragg peak.

JRR-3M, HERMES, 2. magnetism

研究テーマ:正方晶 DyB_2C_2 における四重極相互作用と磁性

表題: DyB_2C_2 の磁気構造

Fig. 2 shows neutron diffraction patterns at 2.0K (phase III), 20.0K (phase II) and 30.0K (phase I). Magnetic reflections are denoted by the letter "M" and the index. The inset gives the temperature dependence of the integrated intensity of the magnetic 1/2 1/2 0 Bragg peak. As shown in Fig. 2, the magnetic reflections in phase III are explained by the propagation vector of Q=[1/2 1/2 1]. Moreover, since no magnetic reflection was observed in the phase II, it is not a magnetic long-range ordered state. This is consistent with the fact that the anomaly at T_t is caused by a nonmagnetic phase transition.

We determined the magnetic structure in the phase III as shown in Fig. 3. Although we do not yet determine the magnitude of the ordered magnetic moments by the neutron diffraction experiments, the value was obtained as $9.1\mu_B$ by the ^{161}Dy Mössbauer spectroscopy.

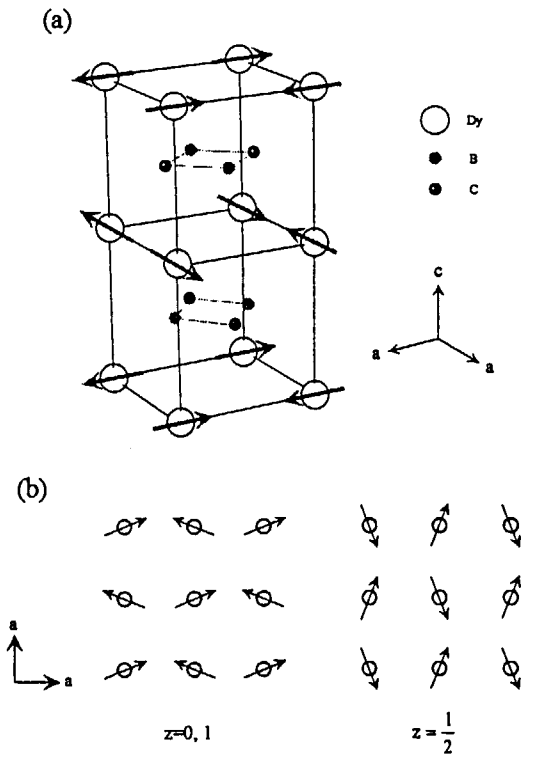

Fig. 3 Magnetic structure of DyB_2C_2 in phase III. (a) The basic antiferromagnetic structure explained by the propagation vector of Q=[1/2 1/2 1]. In this structure, it is neglected that the magnetic moments are canted. (b) The spin arrangement in the c-plane. In this figure, the z-direction is defined as the c-axis.

The magnetic structure is basically an antiferromagnetic one in the c-plane, although the magnetic moments are canted from the a-axis in the c-plane; these canted moments cause the spontaneous magnetization below T_C. Moreover, the magnetic moments are perpendicular to the adjacent magnetic moments along the c-axis. We think that this perpendicular structure, which cannot be explained by the effects of the magnetic exchange interactions, originates from an antiferroquadrupolar (AFQ) ordering structure. Thus, we think that the phase III is a magnetic long-range ordered state with an AFQ ordering. Consequently, we think that T_t is an AFQ transition temperature, T_Q, that is, the phase II is an AFQ ordered state in the paramagnetic region.

Moreover, it should be pointed out that no change of lattice constants was observed at T_t within the experimental errors in the present neutron diffraction experiments. This fact also supports our conclusion that the phase II is an AFQ ordered state. Therefore, we can say that DyB_2C_2 is the first tetragonal compound which undergoes AFQ ordering. To confirm the AFQ ordering at T_Q, other experiments such as ultrasonic-velocity experiments, inelastic neutron scattering and so on are in progress.

Reference

[1] T.Sakai, G. Adachi and J. Shiokawa, Solid State Commun. **40** (1981) 445.

Present address:
† *Faculty of Engineering, Yamagata University*
†† *Department of Physics, Saitama University*

研究テーマ：Pd及びPt合金のフェルミ面効果の研究
表題：Pd及びPt合金の非整合磁気構造

Incommensurate spin modulation in Pd and Pt alloys

R. Abe, N. Hiruma, K. Hirano, K. Fushimi, A. Murakami,
T. Sunaga, T. Ichikawa and Y. Tsunoda

Dep. of Appl. Phys. School of Science and Engineering, Waseda University
3-4-1 Ohkubo, Shinjuku-ku Tokyo 169 Japan

Pd-M and Pt-M (M:3d-element) disordered alloys with M concentration of about 10 at.% were studied by neutron scattering. Satellite diffuse peaks were observed on the [1 0 0] axis around the 1 0 0 reciprocal lattice point for all of specimens. The satellite peak positions depend on the solute element M and its concentration. As the concentration increases, the modulation wave vector Q increases and the satellite peak positions come close to 1 0 0. The satellite peak linewidth is always broad and not sensitive to solute concentration. Although these properties are common for all alloys, the satellite reflections are classified into three groups with different origins. 1) The concentration wave of constituent atoms for non-magnetic alloys (PdV, PtV, PtCr), 2) the spin density wave for spin glass alloys (PdMn, PtMn PdCr) and 3) the transverse wave spin modulation for ferromagnetic alloys (PdFe, PtFe, PdCo, PtCo). Further measurements for PdNi and PtNi alloys show no satellite reflections for both systems. An origin of the these modulation waves in Pd-M and Pt-M alloys is considered to be a reflection of the parallel planes of the Fermi surfaces in these alloys. In the figure, the modulation wave vectors Q determined by the Gaussian fitting for various specimens are plotted as a function of the solute concentration. The concentration dependence is well described by a linear line with positive slope for each system, but zero extrapolations of these lines converge into the same value Q～0.45 in 2π／a unit. Pd and Pt metals have very similar Fermi surfaces and parallel planes normal to the cubic axes with distance of about 0.4 (2π／a unit) are located around the W-point. Furthermore, these surfaces are hole surfaces. When the element with less numbers of d-electrons are introduced to Pd or Pt metals, the diameter of the hole surfaces expands, resulting in increasing of the Q-vector. This is consistent with the present observation.

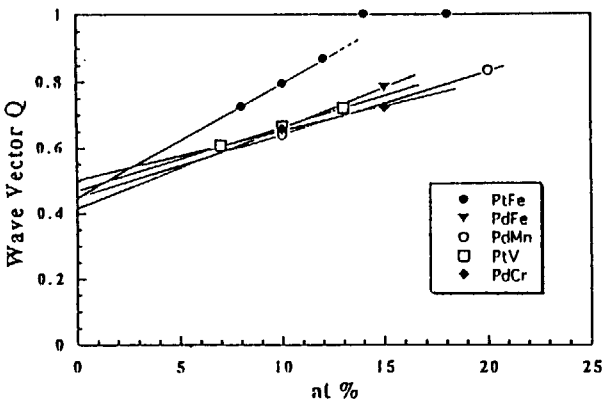

JRR－3M、 T1-1、 Magnetism

課題名：CePの磁気ポーラロン状態の編曲中性子による研究

表　題：CePの磁気ポーラロン状態の磁気構造因子

Magnetic Form Factor of Magnetic Polaron State in CeP

K. Iwasa, M. Kohgi, Y. Haga [1], T. Suzuki [2],
K. Kakurai [3], M. Nishi [3], K. Nakajima [3], P. Link [4], A. Gukasov [4] and J.-M. Mignot [4]

Department of Physics, Tokyo Metropolitan University
Advanced Science Research Center, Japan Atomic Energy Research Institute [1]
Department of Physics, Tohoku University [2]
Institute for Solid State Physics, University of Tokyo [3]
Laboratoire Léon Brillouin, CEA-CNRS, CEA/Saclay, France [4]

Cerium monopnictides CeX (X = P, As, Sb and Bi) are known as systems with low-density carriers (less than 10^{-2} per cerium ion).[1, 2] Among these compounds, CeP is very attractive recently, because it shows the various long-period magnetic structures as functions of magnetic fields or pressures in spite of the simple NaCl-type crystal structure.[3, 4] The structure of phase-I at 2 K and 3 T is composed of a sequence of the double ferromagnetic (001) layers of cerium ions with large moments M_L estimated to be about $2\mu_B$ and the rest nine layers of M_S about $0.7\mu_B$ stacking antiferromagnetically. Thus the structure of phase-I has a period of eleven cerium layers. Without fields, type-I antiferromagnetic (AF) phase with the $0.8\mu_B$ moments appears below 10 K, in which the cerium layers stack antiferromagnetically.

These two kinds of moments M_L and M_S are thought to be ascribed to the 4f-electron crystal field states Γ_8 and Γ_7 under cubic crystal field, respectively from their moment value, where the latter is considered to be the ground state in this compound. The mechanism of appearance of the large moments has been explained by Kasuya et al. theoretically based on the magnetic polaron effect due to combination of strong p-f mixing with localization of low-density holes.[5, 6]

The purpose of this study is to elucidate deirectly wave functions of 4f electrons exhibiting the anomalous magnetic moments.

The measurements of magnetic form factors by polarized neutrons were performed using two spectrometers; PONTA(5G) installed at JRR-3M, JAERI and 5C1 installed at ORPHÉE reactor, Laboratoire Léon Brillouin. The single crystal of CeP was used in this study, which was same as that for neutron diffraction experiments to investigate magnetic structures.[3, 4]

Figure 1 shows the result of magnetic form factor in phase-I as a function of $\sin\theta / \lambda$, where θ is a half of a scattering angle. Vertical axis represents the moment per cerium ion, μ, times form factor, f. The data at $\sin\theta / \lambda = 0$ is quoted from the magnetization measurement. [7] Figure 2 shows the magnetic form factor in type-I AF phase, which was obtained from integrated intensities of unpolarized neutron diffraction. The magnetic form factor in phase-I varies more steeply as a function

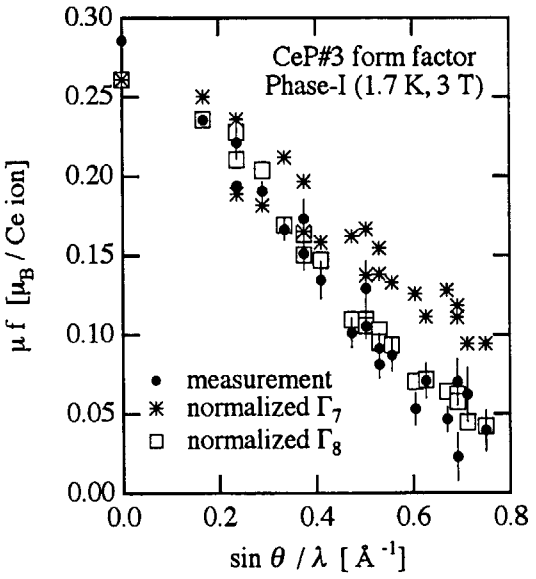

Fig. 1. Magnetic form factor in phase-I. Filled marks with error bars indicate the measured results. Open square marks and crosses indicate calculated results for the crystal field states of Γ_8 and Γ_7, respectively.

JRR-3M, PONTA (5G), Magnetism

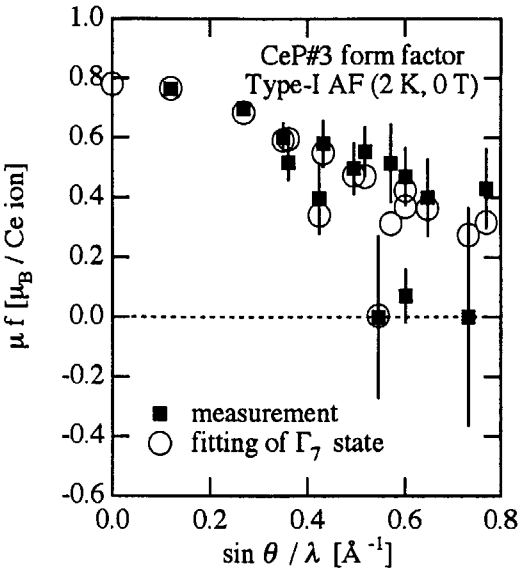

Fig. 2. Magnetic form factor in type-I AF phase. Filled marks indicate the measured results. Open marks indicate the fitted results of calculation for the pure crystal field Γ_7 state.

of $\sin\theta / \lambda$ than that of type-I AF phase. This result shows distinctly the difference between 4f-electron states in phase-I and that in type-I AF phase.

The obtained data are compared to the calculations of magnetic form factors for the crystal field states.[8] The least-square fitting of the form factor of the pure Γ_7 state were performed with the moment value μ as a parameter to the data of type-I AF. In Fig. 2, the results are shown by the open marks, and the obtained moment value is $0.78\mu_B$ per cerium ion. Their variation as a function of $\sin\theta / \lambda$ are very similar to that of the measured data points. It reveals that the 4f-electron state in type-I AF phase is described well by the Γ_7 state. Figure 1 shows the calculated form factor of the Γ_8 state whose moment value is $1.57\mu_B$ as well as that of the Γ_7 state. These are normalized in magnitude. It is clear that the measured form factor in phase-I is very similar to the Γ_8 state one. Since the ferromagnetic component in phase-I is $2 \times M_L - M_S$ per eleven cerium ions, the large moment M_L contributes mainly to the form factor. Therefore, the ordered large moments are described by very similar state as the Γ_8 one. More detailed analysis for the wave functions was performed. The small moment was supposed to be from the pure Γ_7 state. The anomalously polarized cerium ions in phase-I can be expressed by a wave function of $0.948|+5/2\rangle + 0.320|-3/2\rangle$ whose moment value is $M_L = 1.79\mu_B$. It is close to the pure Γ_8 state.

The present study gives the direct evidence that the anomalously polarized Γ_8-like states appear among Γ_7 state cerium ions in phase-I.

Boucherle et al. measured magnetic form factors of CeSb of the ferromagnetic state (4.2 K and 4.65 T).[9, 10] Their analysis shows that the wave function of 4f electrons is $0.995|+5/2\rangle - 0.100|-3/2\rangle$ whose moment value is $2.11\mu_B$. The present estimated M_L in CeP is rather closer to that of the pure Γ_8 state than that of CeSb. This difference of wave functions between CeP and CeSb is considered to be due to that of the extent of magnetic polaron effect which depends on the magnitude of p-f mixing and the carrier numbers.

The precise analysis of the wave function in not only the phases described above but also other phases will be shown elsewhere in near future.

(References)
1) T. Suzuki, Y. S. Kwon, S. Ozeki, Y. Haga and T. Kasuya: J. Magn. Magn. Mater. **90&91** (1990) 493.
2) Y. S. Kwon, Y. Haga, O. Nakamura, T. Suzuki and T. Kasuya: Physica B **171** (1991) 324.
3) M. Kohgi, T. Osakabe, K. Iwasa, J. M. Mignot, I. N. Goncharenko, Y. Okayama, H. Takahashi, N. Môri, Y. Haga and T. Suzuki: J. Phys. Soc. Jpn. **65** (1996) Suppl. B 99.
4) T. Osakabe, M. Kohgi, K. Iwasa, N. Nakajima, J. M. Mignot, I. N. Goncharenko, Y. Okayama, H. Takahashi, N. Môri, Y. Haga and T. Suzuki: Physica B **130-132** (1997) 645.
5) H. Takahashi and T. Kasuya: J. Phys. C, Solid State Phys. **18** (1985) 2697, 2709, 2721, 2731, 2745 and 2755.
6) T. Kasuya and T. Suzuki: J. Phys. Soc. Jpn. **61** (1992) 2628.
7) Y. Haga: Thesis, Tohoku University (1995).
8) E. Balcar, S. W. Lovesey and F. A. Wedgwood: J. Phys. C; Solid State Phys. **3** (1970) 1292.
9) J. X. Boucherle and J. Schweizer: Physica **130B** (1985) 337.
10) J. X. Boucherle, A. Delapalme, C. J. Howard, J. Rossat-Mignod and O. Vogt: Physica **102B** (1980) 253.

研究テーマ：金属相酸化バナジウムの磁気構造と励起
表題 ：金属相$(V_{1-x}Ti_x)_2O_3$の磁気構造と励起

Magnetic Structure and Excitation of Metallic Phase of $(V_{1-x}Ti_x)_2O_3$

K. Motoya, T. Kawasaki and S. Shin[1]

Department of Physics, Faculty of Science and Technology, Science University of Tokyo, Noda 278-8510
[1]Institute for Solid State Physics, The University of Tokyo, Roppongi, Tokyo 106

Elastic and inelastic neutron scattering measurements have been made on a metallic phase of canonical Mott-Hubbard system $(V_{0.95}Ti_{0.05})_2O_3$. The development of an incommensurate antiferromagnetic order has been indicated by the appearance of Bragg peaks characterized by the propagation vector $\mathbf{q}=1.78\mathbf{c}^*$ below T_N=19K. In the temperature range T_R=15K< T < T_N, no magnetic Bragg peak is observed on the (00ξ) reciprocal line. Based on the intensity analysis, we propose a spin-density-wave (SDW) magnetic structure. Below T_R, the direction of the magnetic moments deviate from the hexagonal c-axis by ~60°. In the temperature range $T_R < T < T_N$, the moment direction is parallel to the c-axis. The maximum amplitude of the moment is ~0.5 μ_B at T=8K. Inelastic neutron scattering patterns scanned along the (10ξ) reciprocal line taken at (a) T=9K and at (b) T=30K are shown in Fig.1. Each scan was made with constant energy transfer posted above each curve. Scattering intensity shows peaks at positions corresponding to the magnetic Bragg points observed in the elastic scattering measurements. For small energy transfer scans, the width of the peaks are relatively narrow but much wider than the instrumental energy resolution. The width of the peaks grow wider with increasing energy transfer. Even at T=30K, which is much higher than T_N, scattering pattern still shows clear peaks at magnetic Bragg positions. For small energy transfer scans, peaks around the magnetic Bragg points persist up to T ~$10T_N$, which is much different from normal

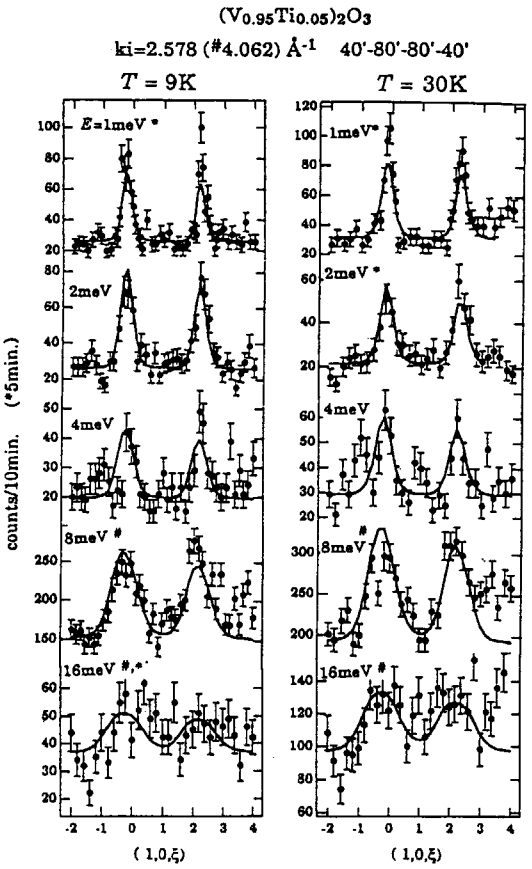

Fig.1.
Inelastic scattering patterns along the (1,0,ξ) reciprocal line with constant energy transfer taken at (a) T=8K and at (b) T=30K. The curves show the results of calculations described in the text.

JRR-3M, T1-1, 4G, magneatism

spin-wave excitation. These characteristics in inelastic scattering properties are similar to those observed in $V_{1.973}O_3$ by Bao *et al.*[1,2] We analyze inelastic scattering spectra based on the self-consistent renormalization (SCR) theory for weakly itinerant antiferromagnet[3] as was done for $V_{1.973}O_3$. In the SCR theory, the imaginary part of the generalized susceptibility is given by

$$\chi''(\mathbf{Q}+\mathbf{q},\omega) = \chi_Q \frac{\hbar\omega/\Gamma\kappa^2}{(\hbar\omega/\Gamma\kappa^2)^2 + \left[1+(q/\kappa)^2\right]^2}$$

where **Q** is the antiferromagnetic wave vector, χ_Q is the static staggered susceptibility, κ is characteristic width in **k** space and Γ is characteristic energy-width. The scattering function $S(q,\omega)$ is related to $\chi''(\mathbf{Q}+\mathbf{q},\omega)$ as

$$S(q,\omega) = \pi^{-1} < n(w)+1 > \chi''(\mathbf{q},\omega),$$

where $n(\omega)$ is Bose thermal factor. The scattering function multiplied by some instrumental factor was convoluted with the resolution function of the spectrometer and the parameters χ_Q, κ and Γ were determined by the least-square fitting procedure. Curves in Fig. 1 represent the fits to the data. In Fig. 2, the temperature variations of these parameters are shown.

The present experiment has shown that a large fluctuating component, which has been observed in the non-stoichiometric system[1,2] is also present in this more "homogeneous" system and of which property can be described in terms of the SCR theory for weakly itinerant antiferromagnet.

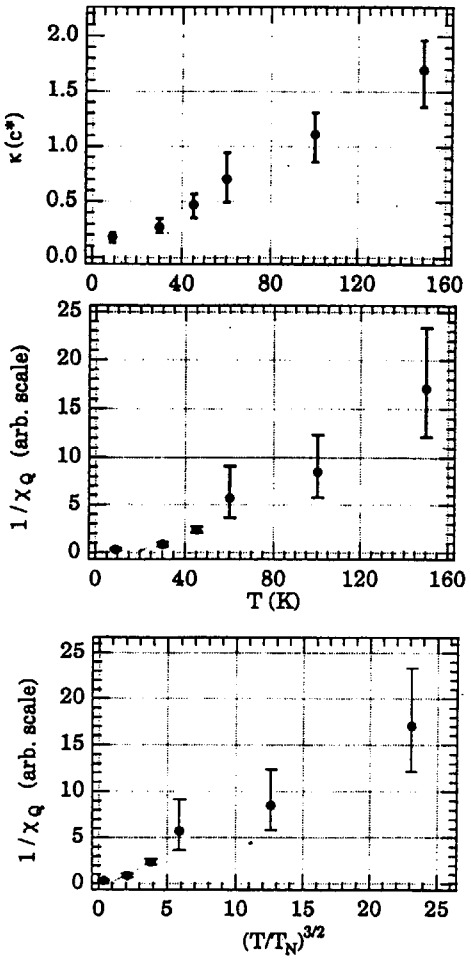

Fig. 2.
Temperature variation of parameters determined by the analysis of inelastic scattering spectra.

References

1) W.Bao, C.Broholm, S.A.Carter, T.F. Rosenbaum, G.Aeppli, S.F.Trevino, P.Metcaf, J.M.Honig and J.Spalek: Phys.Rev.Letters **71** (1993) 766.

2) W. Bao, C. Broholm, J.M. Honig, P. Metcalf and S. F. Trevino, Phys.Rev.B **54** (1966) 3726.

3) K.Nakayama and T. Moriya: J.Phys.Soc.Jpn. **56** (1987) 2918.

研究テーマ: La_2CoO_4のスピンダイナミクスとそのホールドープの効果の研究
表題: La_2CoO_4のスピン波励起

Spin-Wave Excitations in La_2CoO_4

K. Nakajima

Neutron Scattering Laboratory, Institute for Solid State Physics, University of Tokyo
106-1 Shirakata, Tokai, Naka, Ibaraki 319-1106

Layered transition metal oxides, La_2MO_4 have been extensively studied after the discovery of oxide high-T_C superconductors. Since non-doped La_2MO_4 is a good representation of a 2D antiferromagnet (AF), experimental and theoretical interest in a quantum 2D Heisenberg AF has been renewed. Experimental studies on the spin dynamics in La_2MO_4 have been concentrated on mainly M=Cu (S=1/2) and M=Ni (S=1), so far. Then, as natural extension of experimental interest, La_2CoO_4 (S=3/2) is focused on.

In the present work, using a single crystal of La_2CoO_4, inelastic neutron scattering experiment was carried out on a triple-axis spectrometer PONTA. Spin-wave excitations in La_2CoO_4 below Néel temperature (T_N=277.5 K) were measured to determine microscopic parameters, which are indispensable to discuss the 2D spin correlations in this system.

Figure 1 shows results of constant-Q and constant-E scans at the 2D AF zone center, (1, 0, -3) (or (0, 1, -3) due to the crystal twining). The lines represent the results of fits convoluting the instrumental resolution. The gap energies at the zone center were determined to be 9.6±0.2 meV and 17.2±0.5 meV corresponding to in-plane (IP) and out-of-plane (OP) modes, respectively. Note that the OP peak is rather ambiguous since it becomes weak at large Q. To make definite statement, measurement at different Q is required. Excitation gaps are rather large in comparison with those in La_2NiO_4, which indicates large anisotropies in La_2CoO_4. The evidence is consistent to the strong Ising character of spin fluctuations observed near T_N [1]. The inset shows the obtained inter-layer dispersion relation. The results can be accounted by a simple 2D AF spin-wave. From the dispersion up to 35 meV, the inter-layer exchange interaction is determined to be J=9.2±0.3 meV. Preliminary results of the 2D spin correlation length in La_2CoO_4 well agrees with the theoretical calculation using J obtained here without any adjustable parameters [2].

[1]K. Yamada *et al.*: Phys. Rev. B **39** (1989) 2336
[2]K. Nakajima *et al.*: to appear in BENSC Experimental Reports 1998 (Hahn-Meitner Institute Berlin, Germany)

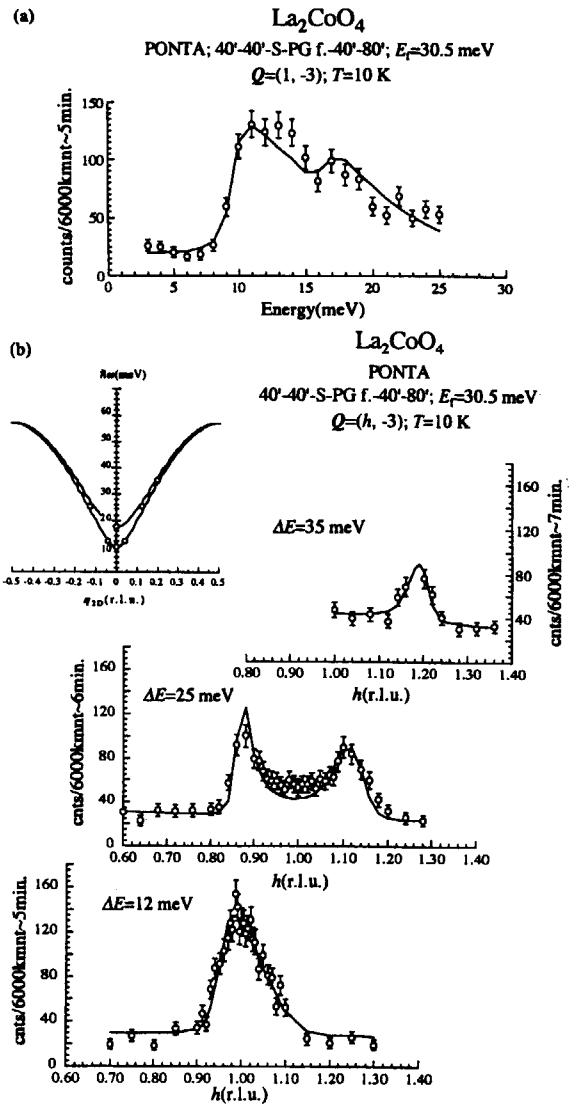

Fig. 1: Result of (a) constant-Q and (b) constant-E scans at the 2D zone center, (1, -3). The Cowley correction have been already made in the figure. Inset shows the obtained intra-layer spin-wave dispersion relation in La_2CoO_4.

研究課題：金属反強磁性体$Nd_{0.45}Sr_{0.55}MnO_3$における異方的スピン波
表　　題：$Pr_{1-x}Ca_xMnO_3$系の電荷秩序および金属・絶縁体転移とスピンダイナミクス

Anisotropic spin waves in a metallic antiferromagnet $Nd_{0.45}Sr_{0.55}MnO_3$

H. Yoshizawa,[1] H. Kawano,[2] . A. Fernandez-Baca,[3]
H. Kuwahara,[4] and Y. Tokura[4,5]
[1]NSL, I.S.S.P., University of Tokyo, Tokai, Ibaraki 319-1106
[2]The Institute of Physical and Chemical Research (RIKEN), Wako, Saitama 351-01
[3]Solid State Division, Oak Ridge National Laboratory, Oak Ridge, Tennessee 37831, U. S. A.
[4]Joint Research Center for Atom Technology (JRCAT), Tsukuba, Ibaraki 305
[5]Department of Applied Physics, University of Tokyo, Tokyo 113-0033

Very recently, we have studied three manganites with $n_h \sim 1/2$, and demonstrated that, instead of the well-known CE-type magnetic structure, some of manganites may have a layered A-type antiferromagnetic (AFM) ordering.[1)] The change of the magnetic structure from a CE-type to an A-type can be interpreted as an effect of widening of the one-electron band width. The behavior of the resistivity of the A-type manganites is distinctly different from those with the CE-type orbital and spin ordering. Based on the detailed study of the lattice and spin structure of the A-type manganites, we suggested the possibility of the *two-dimensional* character in both magnetic and transport properties.[1)]

To examine such a possibility in magnetism, we performed a detailed study of the spin dynamics in $Nd_{0.45}Sr_{0.55}MnO_3$, and found that its spin wave dispersion relation, indeed, possesses a *"quasi"-two-dimensional character*, and this can be understood as a result of underlying orbital ordering. Furthermore, the spin fluctuations in the paramagnetic phase of the A-type $Nd_{0.45}Sr_{0.55}MnO_3$ are dominated by the ferromagnetic (FM) spin fluctuations.

Most of neutron scattering measurements were performed with triple axis spectrometers at the High Flux Isotope Reactor in Oak Ridge National Laboratory. For the scans which require the better energy resolution, we employed a spectrometer HER installed at the cold guide tube in the JRR-3M.

The AFM spin wave excitations were observed at $\sim$ 12 K along the directions parallel and perpendicular to the FM layers. Typical profiles observed at selected reduced wave vectors are illustrated in Fig. 1(a) and (b). By comparing the profiles in Fig. 1(a) and (b), one can easily see that the spin waves propagating within the FM planes have higher spin wave energy.

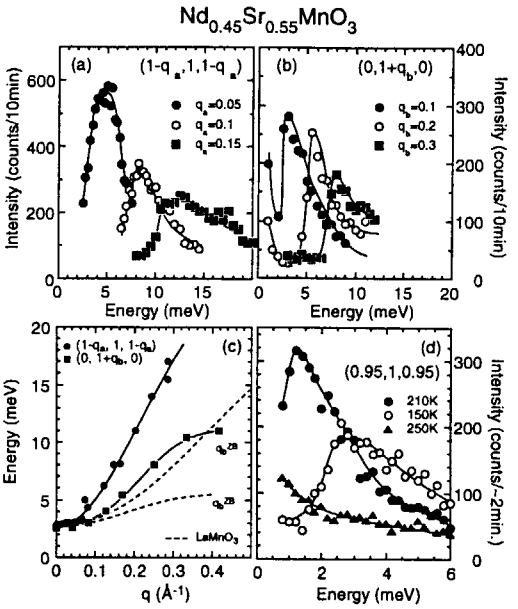

Figure 1: (a) and (b): Spin wave profiles at 12 K. (c): Spin wave dispersion in the A-type AFM $Nd_{0.45}Sr_{0.55}MnO_3$. (d): Spin wave profiles at 210 K and 150 K $< T_N$, and 250 K $> T_N$.

The obtained dispersion relations are depicted in Fig. 1(c), where a clear anisotropy of the excitation energy between the [101] and [010] directions indicates a *quasi-two-*

dimensional feature of the magnetic properties. To parameterize the dispersion relation, we adopted the same spin wave dispersion formula which was employed for the analysis of $LaMnO_3$,[2] and we obtained $8JS = 32.6 \pm 0.9$ meV, $4J'S = -10.1 \pm 0.5$ meV, and $g\mu_B H_A = 0.2 \pm 0.1$ meV. The temperature dependence of the spin wave profiles measured at $Q = (0.95, 1, 0.95)$ are shown in Fig. 1(d). With increase of temperature, the AFM spin wave energy gradually softens, and the AFM spin fluctuations vanish above T_N.

Corresponding to the disappearance of the AFM spin fluctuations above T_N, we find that the intense FM spin fluctuation appears in the paramagnetic phase. At the top panel of Fig. 2, one can see that the diffusive FM spin fluctuation exists in the paramagnetic phase, but the evolution of the peak structure below T_N should be attributed to the AFM spin waves.

The middle panel shows that the diffusive FM component exhibits a sudden decrease below T_N, indicating that the major spectral weight of the spin fluctuations is transferred from the FM component to the AFM component below T_N. The switching of the spin fluctuations due to an orbital ordering is rather common phenomena in the transition-metal oxides with a freedom of the orbitals.

We found that the energy width of the observed FM component in the paramagnetic state is well described by $\Gamma_q = \Lambda q^2$, and obtained $\Lambda \sim 14.1 \pm 1$ meVÅ^2. It should be noted that the Λ is an order of magnitude smaller than the value of the spin stiffness constant $D_{SW} \sim 117$ meVÅ^2 evaluated from the exchange parameters obtained in the present study. The results indicate that the onset of the AFM ordering in $Nd_{0.45}Sr_{0.55}MnO_3$ accompanies with the change of energy scale in spin fluctuations at the same time. The existence of the two energy scales in doped manganites is recently reported by thermopower and resistivity measurements.[3] The reported activation energy of the resistivity is close to the D_{SW}, whereas that of the thermopower is very close to the Λ. The smaller energy scale for the low energy ferromagnetic spin fluctuations in the paramagnetic state is attributed to the hopping of the small polarons.

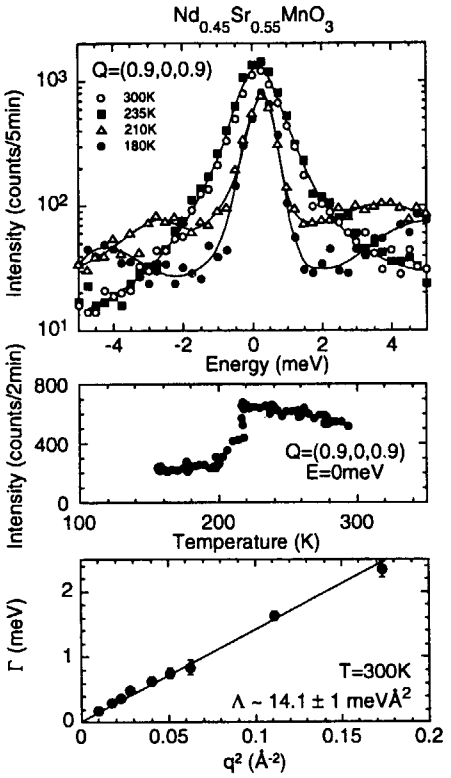

Figure 2: (a): FM scattering observed in $Nd_{0.45}Sr_{0.55}MnO_3$. (b): Temperature dependence of the FM component. (c): Wave vector dependence of the Γ of the FM component at $T = 300$ K.

Part of the work was carried out under the US-Japan Cooperative Program on Neutron Scattering.

References

[1] H. Kawano *et al.*, Phys. Rev. Lett. **78**, 4253 (1997);Physica B (in press); H. Yoshizawa. *et al.*, Phys. Rev. B **58**, (in press).

[2] K. Hirota *et al.*, J. Phys. Soc. Jpn. **65**, 3736 (1996); F. Moussa *et al.*, Phys. Rev. B **54**, 15149 (1996).

[3] M. Jaime *et al.*, Phys. Rev. B **54**, 11914 (1996); B. Fisher *et al.*, Phys. Rev. B **55**, 9227 (1997); T. T. M. Palstra *et al.*, Phys. Rev. B **56**, 5104 (1997).

研究テーマ：2次元ハイゼンベルグフラクトン
表題：2次元パーコレーションハイゼンベルグ反強磁性体のスピン動特性

Spin Dynamics in a Two-Dimensional Percolating Heisenberg Antiferromagnet

S. Itoh, H. Ikeda and H. Yoshizawa[1]

Neutron Science Laboratory, High Energy Accelerator Research Organization, Tsukuba
[1]Neutron Scattering Laboratory, ISSP, The University of Tokyo, Tokai

Recent theories and computer simulations of percolating networks predict the existence of localized fracton excitations with huge oscillation amplitudes [1]. We performed inelastic neutron scattering experiments on a 2D near-percolating antiferromagnet, in order to distinguish fracton excitations from other local excitations. 3D antiferromagnets have at least 6 nearest-neighbors. This makes it rather difficult to distinguish over-damped fractons from Ising-cluster excitations [2]. In this sense, the most ideal system to be examined is a 2D system. The experiments were performed using a single crystal of $Rb_2Mn_{0.598}Mg_{0.402}F_4$ (c_p=0.593 for a square lattice) on the triple axis spectrometer installed at the 4G beam hole at JRR-3M. The spectrometer was operated with a k_f fixed mode (k_f=2.67Å^{-1}). The sample was mounted with its 2D plane to be in the scattering plane. The measurements were performed by constant-Q scans at Q=(q,0,0) at T=4~250K. It is noted that the ordering temperature of this system was measured to be T_N=5K. The over-damped component ($\chi''(q,E)$) of the observed energy spectrum at any q and at any T was well fitted to a damped harmonic-oscillator scattering function $AE\Gamma/\{(E^2-E_p^2)^2+(E\Gamma)^2\}$ (E being the energy transfer). Figure 1 shows the q-dependence of the peak energy (E_p) and the energy width (Γ) obtained by the fitting. At low T, the magnetic response is dispersive and $\chi''(q,E)$ can be described by the predicted functional form of fracton excitations: $E_p(q)\sim\Gamma(q)\sim q^{z_a}$ with the unique exponent z_a [1]. The obtained exponent (z_a=0.9±0.2) is smaller than the predicted value (z_a=2.5), and a similar observation has been reported for the 3D percolating system [2]. As T increases, the q-dependence gradually becomes weaker, and $\chi''(q,E)$ becomes almost independent of q at T>150K. The incoherent character of $\chi''(q,E)$ at high T indicates that collective motions do not exist due to very small thermal correlation lengths. Fracton excitations exist only at low T. At the intermediate temperatures, $\chi''(q,E)$ exhibits a crossover from fracton excitations to incoherent excitations.

References
[1] T.Nakayama, K. Yakubo and R. Orbach, Rev. Mod. Phys. 66 (1994) 381.
[2] H.Ikeda et al., J. Phys.:Condens. Matter 6 (1994) 10543.

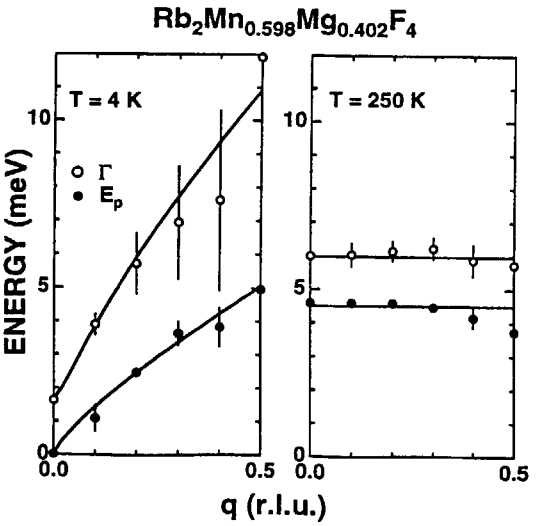

Fig.1 The q-dependence of the peak energy (Ep) and of the energy width (Γ) of the magnetic response $\chi''(q,E)$.

JRR-3M, 4G, 2.magnetism

研究テーマ：スピン・パイエルス化合物 NaV_2O_5の磁気励起
表題： NaV_2O_5のスピン・ダイナミクス —中性子非弾性散乱

Spin Dynamics in NaV_2O_5 – Inelastic Neutron Scattering

Tomoyuki YOSIHAMA[1], Masakazu NISHI[1], Kenji NAKAJIMA[1], Kazuhisa KAKURAI[1,2], Yasuhiko FUJII[1], Masahiko ISOBE[3], Chiharu KAGAMI[3] and Yutaka UEDA[3]

[1] *Neutron Scattering Laboratory, Institute for Solid State Physics, The Univeristy of Tokyo, 106-1 Shirakata, Tokai, Ibaraki 319-1106*
[2] *CREST, Japan Science and Technology Corporation (JST)*
[3] *Material Design and Characterization Laboratory, Institute for Solid State Physics, The Univeristy of Tokyo, 7-22-1 Roppongi, Minato-ku, Tokyo 106-8666*

NaV_2O_5 has been thought to be made up of two kinds of V chains running along the b axis.[1)] One is the V^{4+} (S=1/2) chain and the other is the V^{5+} (S=0) chain, which are aligned parallel to each other by sharing an edge of VO_5 pyramids in the ab-plane as shown in Fig.1. In 1996, Isobe and Ueda[2)] observed an exponential drop in the susceptibility of NaV_2O_5 below T_c (35 K). Fujii *et al.*[3)] found lattice distortion below T_c by means of X-ray diffraction measurement and observed the development of the gap energy of 9.8 meV at $|\mathbf{Q}|$=1.0 Å^{-1} below T_c by means of neutron scattering measurement using the powder sample. These findings have been considered to be a direct evidence that NaV_2O_5 is a spin-Peierls compound, though the low temperature structure has not been determined yet. It should be noted here that an observed gap value (9.8 meV) is significantly large compared to the prediction of 5.3 meV from the BCS-scaling ($2\Delta(T=0\text{ K})/k_BT_c \cong 3.5$), implying that NaV_2O_5 might be a quite unconventional compound as a spin-Peierls system.

Recently the single crystals of NaV_2O_5 were successfully grown by Isobe *et al.*[4)] by a melt growth method using $NaVO_3$ as a flux. The largest one has a dimension of nearly 20 mm × 3 mm × 2 mm. We then carried out inelastic scattering measurements to study the spin dynamics of NaV_2O_5 below T_c using 8 pieces of single cristals (totally 0.5 cm^3).[5)] They were alinged within four degrees so that $(h,k,0)$ zone is mounted in the scattering plane. ISSP-PONTA installed at JRR-3M of JAERI is used in the triple-axis mode of operation with E_i fixed at 30.5 meV and 40'-40'-80'-80' collimations.

We first looked for a magnetic dispersion along the chain-direction (the b-axis). Constant-energy $(3,k,0)$-scans at ΔE=7, 10, 12 and 15 meV at 7 K (below T_c) were carried out. There is only flat background at ΔE=7 meV, while at 10 meV, a gap energy, a strong intensity centered around the 1-D Antiferromagnetic (AF) zone center position k=0.5 r.l.u. can be found. At 15 meV, the two peak structures reflecting the strong AF dispersion along the b*-axis can be observed. These could be well fitted including the resolution effect by a strong 1-D AF dispersion along the b*-axis, with the gap of 9.8 meV and the zone boundary energy of 59.5 meV (from $\frac{\pi J}{2}$ with J=37.9 meV.[6)]).

We next focussed our attention on the spin correlation

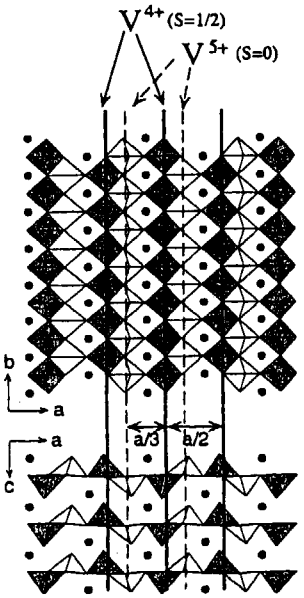

Fig. 1. Crystal structure at room temperature as reported in ref. 1. Two kinds of VO_5 pyramids are running along the b-axis. Filled circles are Na ions. Note that the distance between the V^{4+} chain and V^{4+} chain is $\frac{a}{2}$, while that between V^{4+} chain and V^{5+} chain is $\frac{a}{3}$ and $\frac{a}{6}$.

along the a-axis, where the V^{4+} ($S=\frac{1}{2}$) chain and the V^{5+} ($S=0$) chain share oxygen ions. Energy scans have been carried out at $\mathbf{Q}=(h,0.5,0)$ with $1<h<4$ r.l.u. and we found that, at 7K (below T_c), a single peak structure at the gap energy of 10 meV can be observed when h is an integer, while two peaks can be clearly recognized between $2<h<3$ r.l.u. and $3<h<4$ r.l.u. with the lowest and highest energy position of about 8.5 meV and 11.3 meV, respectively. These peaks vanish at 40K (above T_c) and can hence be associated with the spin-gap formation at T_c. These results indicate that there are two branches along a*-axis, with the energy difference of almost 3 meV, giving an energy scale of the

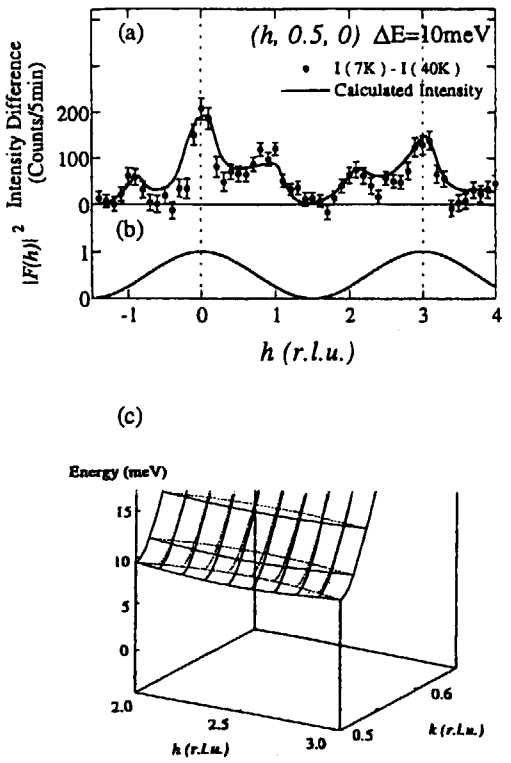

Fig. 2. Filled circles in Fig. 2(a) represent the intensity difference between 7 K (below T_c) and 40 K (above T_c) while scanning along h on the 1-D AF zone center at ΔE=10 meV. The solid line in the Fig. 2(a) is the calculated result assuming the h-dependent structure factor shown in Fig. 2(b) and the dispersion depicted in Fig. 2(c).

interchain interaction along the a^*-axis, much smaller than that of the intrachain b^*-axis direction. In addition to the existence of two modes, we found strong h-dependence of the gap intensity. In the energy scans at $(h, 0.5, 0)$, we observed fairly strong intensities between $2 < h < 4$ r.l.u., while only very weak intensity was observed between $1 < h < 2$ r.l.u. and only the background was observed at $h = 1.5$ r.l.u. In order to discuss this problem more quantitatively, we measured the intensity difference below and above T_c on the 1-D AF zone center (*i.e.* k=0.5 r.l.u.) at ΔE= 10 meV, corresponding to the h-dependence of the magnetic signal, as shown by the filled circles in Fig. 2(a). The strong magnetic intensity observed at $h = 0$ r.l.u. indicates that the magnetic fluctuations in the next-nearest neighbour chains are in phase. Strong intensities were observed at $h = 0$ r.l.u. and 3 r.l.u., indicating that 3 r.l.u. can be regarded as the unit along the a^*-direction. Assuming an h-dependent prefactor ($|F(h)|^2$) in the dynamical structure factor as indicated in Fig. 2(b) and the dispersion with two excitation modes in accordance with the above findings as indicated in Fig. 2(c), the expected intensities including the instrumental resolution for $(h, 0.5, 0)$-scan at ΔE=10 meV can be calculated as depicted with the solid line in Fig. 2(a). In the calculation, the magnetic form factor and the intensity variation along the b^*-direction have been included. The intensity ratio of the lower and upper modes is chosen to be 2:1, as has been suggested from the inelastic results at $\mathbf{Q}=(h, 0.5, 0)$, $2 < h < 3$ r.l.u. However, it should be noted that the change of the ratio (*e.g.* to 1:1) does not essentially affect the calculation. The intensity difference at the two equivalent points, $h = -1$ r.l.u. and $h = 1$ r.l.u., can be explained by the resolution effect. It can then be concluded that the dynamical structure factor $S(\mathbf{Q}, \omega)$ has an h-dependent factor having a periodicity with a unit of 3 r.l.u. Since the distance between the V^{4+} chains is $\frac{a}{2}$ (see Fig. 1), this periodicity is indeed unexpected. One can recognize from Fig. 1 that a clue to our surprising results may be given by the fact that the distance between the V^{4+} chain and the V^{5+} chain is $\frac{a}{3}$ and $\frac{a}{6}$, though the final answer is still now not given.

The above findings indicated that the senario of spin-Peierls transition from the crystal structure as we believed is invalid and soon triggered off a deep reconsideration of the charge arrangement in NaV_2O_5, causing the following stimulating results. Ohama *et al.*[7] carried out ^{51}V-NMR experiment on NaV_2O_5 and discovered that the V sites change its valences at T_c from uniform $V^{4.5+}$ to two different sites of V^{4+} and V^{5+} with a geometrical configuration so that spin-gap is formed. Furthermore, recent theoretical study by Seo and Fukuyama[8], treating NaV_2O_5 as a *quarter-filled spin-ladder system* not as a spin-Peierls system, propose that a zigzag type of charge disproportionation along the ladders of V-ions is stabilized as a ground state due to the intersite Coulomb interaction. We are now considering whether these recent results are consistent with our neutron scattering study, along with more experimental effort to obtain a final understanding of this unique system.

1) A. Carpy and J. Galy : Acta Cryst. **B31** (1975) 1481.
2) M. Isobe and Y. Ueda : J. Phys. Soc. Jpn. **65** (1996) 1178.
3) Y. Fujii *et al.* : J. Phys. Soc. Jpn. **66** (1997) 326.
4) M. Isobe, C. Kagami and Y. Ueda : J. Cryst. Growth. **181** (1997) 314.
5) T. Yosihama *et al.* : J. Phys. Soc. Jpn. **67** (1998) 744.
6) M. Weiden *et al.* : Z. Phys. **B103** (1997) 1.
7) T. Ohama, H. Yasuoka, M. Isobe and Y. Ueda : reported in Technical Report of ISSP, Ser.A 3352 ; submitted to Phys. Rev. Lett.
8) H. Seo and H. Fukuyama : reported in cond-mat/9805185 ; submitted to J. Phys. Soc. Jpn.

研究課題：反強磁性絶縁体$Pr_{1-x}Ca_xMnO_3$系の異常強磁性スピン揺らぎ
表　題：$Pr_{1-x}Ca_xMnO_3$系の電荷秩序および金属・絶縁体転移とスピンダイナミクス

Anomalous ferromagnetic spin fluctuations in an antiferromagnetic insulator $Pr_{1-x}Ca_xMnO_3$

R. Kajimoto,[1] T. Kakeshita,[1] Y. Oohara,[1] H. Yoshizawa,[1]
Y. Tomioka,[2] and Y. Tokura[2,3]
[1]NSL, I.S.S.P., University of Tokyo, Tokai, Ibaraki 319-1106
[2]Joint Research Center for Atom Technology (JRCAT), Tsukuba, 305
[3]Department of Applied Physics, University of Tokyo, Tokyo 113-0033

For hole doped perovskite manganites, the ferromagnetic (FM) metallic state has been qualitatively explained with the double exchange (DE) model. This DE picture implies that, regardless of its FM or AFM ordering in the ground state, the FM spin correlation must be the characteristic feature of spin fluctuations in the paramagnetic state of doped manganites. In order to confirm the existence of the FM spin fluctuations in the paramagnetic state of doped manganites with an AFM ground state, we have studied an *insulating AFM* system $Pr_{1-x}Ca_xMnO_3$.

The insulating AFM $Pr_{1-x}Ca_xMnO_3$ system shows strong *ferromagnetic* (FM) spin fluctuations in the paramagnetic state. Figure 1 shows the profiles of q scans along the $(1,0,l)$ line for the $x = 0.35$ sample. In the paramagnetic phase at 250 K and 200 K, one can see strong diffuse scattering around the FM Bragg point (101), in contrast to no diffuse scattering around the nuclear Bragg point (102) at which the FM structure factor for the Mn ions vanishes. The inset shows the scattering profiles observed at around $(1,0,l)$ with l = odd at 250 K. The diffuse intensity at (101) is strongest, and decreases as Q increases, being consistent with the magnetic form factor. These results lead us to identify that the diffuse scattering observed in the paramagnetic phase originates from the FM spin fluctuations.

Figure 2(a) shows the temperature dependence of the energy spectra of the FM fluctuations in the $x = 0.35$ sample. Solid lines are the fits to the Lorentzian form convoluted with the instrumental resolution. The intense quasielastic scattering is evident in the paramagnetic phase, and it changes over to the AFM spin wave excitations below T_N.

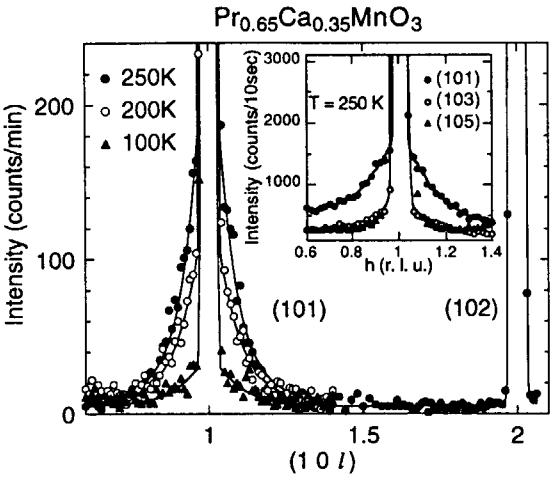

Figure 1: Profiles of Q = (101) and (102) along the [001] direction at 250 K, 200 K and 100 K for $x = 0.35$. Inset: Profiles scanned along the [100] direction near $(10l)$ at 250 K.

In order to quantitatively characterize the FM spin fluctuations, we have studied the q dependence just above T_{CO}. The quasielastic peaks were fitted to a Lorentzian, and the width Γ is plotted against q^2 in Fig. 2(b). For all three samples, Γ shows an excellent linearity on q^2 ($\Gamma = \Lambda q^2$), which indicates that the scattering originates from a spin diffusion-like process. The spin diffusion constant Λ deduced from the fits is practically x-independent for all three samples, yielding 16(4) meVÅ^2 (HWHM) for $x = 0.35$, 13(2) meVÅ^2 for $x = 0.40$, and 16(4) meVÅ^2 for $x = 0.50$, repectively. It should be note that a similar FM component has been re-

cently reported in the *metallic FM* manganites, $La_{0.67}Ca_{0.33}MnO_3$ and $Nd_{0.7}Sr_{0.3}MnO_3$,[1] and a *metallic AFM* $Nd_{0.45}Sr_{0.55}MnO_3$.[2] We would like to point out that the energy scale Λ of such FM fluctuations is anomalously small. For instance, $\Lambda = 15(1)$ meVÅ^2 for $La_{0.67}Ca_{0.33}MnO_3$ and $\Lambda = 14(2)$ meVÅ^2 for $Nd_{0.45}Sr_{0.55}MnO_3$.

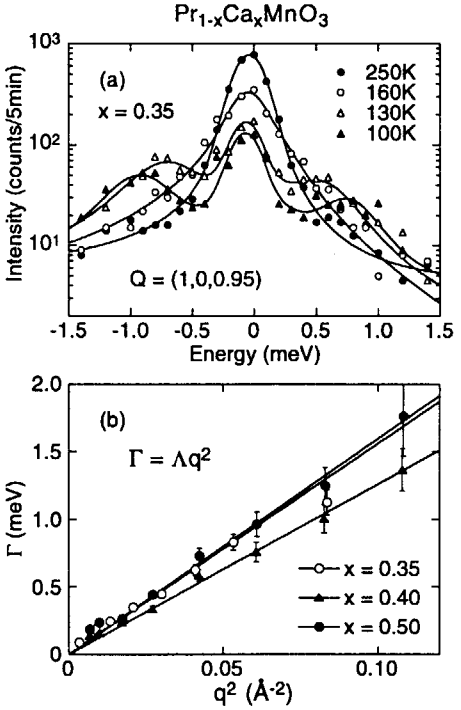

Figure 2: (a) Energy spectra at $Q = (1, 0, 0.95)$ for the $x = 0.35$ sample. (b) Energy widths Γ of quasielastic scattering versus q^2 above T_{CO}; open circle: $x = 0.35$ at (1,0,0.95) and 245 K, triangle: $x = 0.40$ at (0.95,0,0.95) and 250 K, closed circle: $x = 0.50$ at (0.95,0,0.95) and 260 K.

In general, the spin wave stiffness constant D_{SW} and the spin diffusion constant Λ should be of the same order in magnitude when the same exchange interactions control the spin wave propagation as well as the spin diffusion process. The values of D_{SW} in doped manganites found in literature are of the order of 100 meV, and, in fact, the values Λ of the metallic FM samples, $La_{0.8}Sr_{0.2}MnO_3$ and $La_{0.7}Sr_{0.3}MnO_3$, are reported to be of the same order with D_{SW}.[3] We think that the discrepancy of the energy scale between D_{SW} and Λ in $Pr_{1-x}Ca_xMnO_3$ should be attributed to its narrower one-electron bandwidth W. In a system with a small W, the small hopping integral suppresses the mobility of holes, and increases the possibility of the coupling of hole motion with the lattice distortion. It should be note that the existence of the two energy scales in doped manganites is recently pointed out by studies of thermopower and resistivity measurements,[4] and by a neutron scattering study of $Nd_{0.45}Sr_{0.55}MnO_3$.[2] The reported activation energies of the resistivity and thermopower are quantitatively consistent with the spin wave stiffness constant D_{SW} and the spin diffusion constant Λ, respectively. The small energy scale of the thermopower in the paramagnetic state was also attributed to the hopping of the small polarons.

In conclusion, we have demonstrated that the paramagnetic phase in the charge ordered AFM insulator $Pr_{1-x}Ca_xMnO_3$ with $0.35 \leq x \leq 0.5$ is characterized by the anomalous FM fluctuations. For a system with a narrow one electron bandwidth, the energy scale of the FM fluctuations is an order of magnitude smaller than that of the low temperature spin dynamics. These results are compatible with the picture that the spin fluctuations in the paramagnetic state of doped manganites is characterized by the hopping of small polarons.

References

[1] J. W. Lynn *et al.*, Phys. Rev. Lett. **76**, 4046 (1996); J. A. Fernandez-Baca *et al.*, Phys. Rev. Lett. **80**, 4012 (1998).

[2] H. Kawano *et al.*, Phys. Rev. Lett. **78**, 4253 (1997); H. Yoshizawa, H. Kawano *et al.*, Phys. Rev. B **57**, in press.

[3] Y. Endoh and K. Hirota, J. Phys. Soc. Jpn. **66**, 2264 (1997); M. C. Martin *et al.*, Phys. Rev. B **53**, 14285 (1996).

[4] M. Jaime *et al.*, Phys. Rev. B **54**, 11914 (1996); B. Fisher *et al.*, Phys. Rev. B **55**, 9227 (1997); T. T. M. Palstra *et al.*, Phys. Rev. B **56**, 5104 (1997).

研究テーマ：近藤格子上の磁気秩序の研究
表題：Ce(Ru1-1Rhx)2Si2のスピン揺らぎの観測

Observation of the spin fluctuation in $Ce(Ru_{1-x}Rh_x)_2Si_2$ x=0.03, 0.15

M.Sato, N.Chigusa, [A]H.Kadowaki, S.Kawarazaki and Y.Miyako
Department of Earth and Space Science, Osaka University, Toyonaka, Osaka 560-0043
[A]Department of Physics, Tokyo Metropolitan University, Hachioji, Tokyo 192-0397

$CeRu_2Si_2$, which is a moderately heavy Fermion compound, has no magnetic long range order at low temperature. But previous neutron inelastic scattering experiments have revealed that some antiferromagnetic fluctuations develop below 60K.[1] Recently we have reinvestigated the distribution of the generalized susceptibility $\chi(q)$ of this compound in a wide region of the **q**-space. The results indicate that $\chi(q)$ forms a ridge between **q**1=(0.3,0,0) and **q**2=(0.3,0.3,0) on the reciprocal c-plane, and has a peak at **q**3=(0,0,0.35).[2]

$Ce(Ru_{1-x}Rh_x)_2Si_2$ system has the same crystal structure in the whole range of x. An antiferromagnetic phase exists at 0.05>x>0.4, whose ground structure is the spin-density-wave (SDW).[3] The magnetic wave vector is (0,0,0.42) at x=0.15 and becomes larger as x increases. We consider that the fluctuation of $CeRu_2Si_2$ with **q**3 develops into this SDW state due to substitution of Ru with Rh. In order to study the change of the fluctuations in the process of the growth of SDW, we performed neutron inelastic scattering experiments on $Ce(Ru_{1-x}Rh_x)_2Si_2$ x=0.03, 0.15. The experiments were carried out at HER.

The compound of x=0.03 is close to the boundary of the SDW phase. We found that this compound has a short range order with the magnetic wave vector of (0,0,0.35) below 4K, whose magnetic moment is $0.02\mu_B$. The figure shows the results of the q-scans with a finite energy transfer along [100] around the reciprocal point (101) for x=0.00, 0.03, 0.15. One can see in this figure that the fluctuation q1 survives while the fluctuation q3 of x=0.00 grows into SDW of x=0.15 through the short range order of x=0.03. Furthermore, the size of q1 increases in the same way as that of q3.

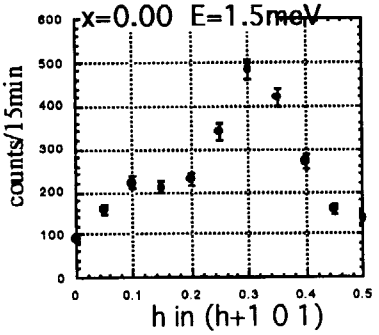

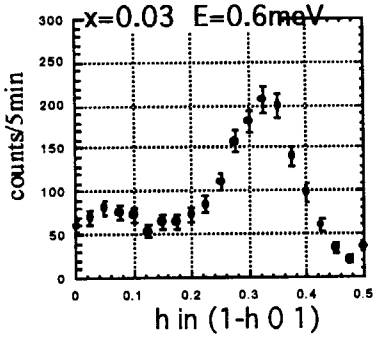

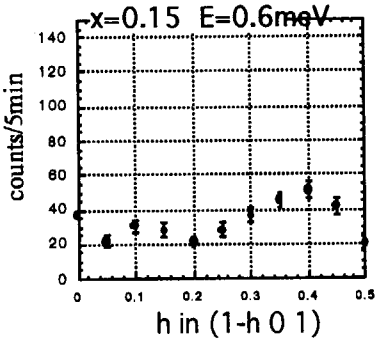

References
[1]L.P.Regnault et al. Phys.Rev.B col.38 no.7 (1988) P.4481 etc.
[2]M.Sato et al. Activity Report on Neutron ScatteringResearch, ISSP, Tokyo vol.4 (1997) p.114
[3]S.Kawarazaki et al. J Phys.Soc.Jpn vol.66 no.8 (1997) p.2473

JRR-3M, GPTAS(4G), HER(C11) , magnetism

研究テーマ：スピングラス$Mn_{0.55}Mg_{0.45}TiO_3$の磁場中における振舞い
表題：スピングラス$Mn_{0.55}Mg_{0.45}TiO_3$の磁場中における振舞い

The behavior of the Spin-glass $Mn_{0.55}Mg_{0.45}TiO_3$ under Magnetic Fields

A. Ito, A. Fukaya[1], K. Kakurai[2], K. Nakajima[2]

Graduate school of Humanities and Sciences, Ochanomizu University, Bunkyo-ku, Tokyo 112-8610 Japan
[1]*The Institute of Physical and Chemical Research (RIKEN), Wako, Saitama, 351-0198 Japan*
[2]*Neutron Scattering Laboratory, Institute for Solid State Physics, University of Tokyo, Shirakata, Tokai 319-1195 Japan*

Spin-glass systems have been extensively studied. However, many basic problems, in particular properties under magnetic fields, remain unsolved. Even the problem whether a real spin-glass(SG) transition occurs not only in zero-field but also in fields has not been solved yet. Generally, a SG system shows different behavior when we perform measurements with different time- and space- scale of observation. Therefore, in order to clarify properties of SG systems, it is necessary to examine the behavior of SG systems by various measurements.

As an objective material, we chose the diluted antiferromagnet $Mn_{0.55}Mg_{0.45}TiO_3$ which shows the spin-glass behavior with the weak uniaxial anisotropy.[1] We have examined the behavior under fields by dc-magnetization, ac-susceptibility and μSR measurements. In Fig. 1, we show the magnetization as a function of temperature under various fields. The behavior changes drastically with increasing field. On the other hand, we have found from the μSR measurements that the behavior is independent of field.

To obtain information on the SG from a different viewpoint, we performed the neutron scattering measurement. We applied the magnetic fields parallel to the hexagonal c-axis

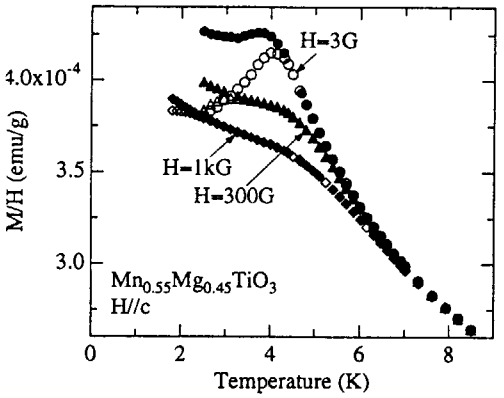

Fig. 1 Magnetization as a function of temperature under the various fields. The open marks show the magnetization under the zero-field-cooled(ZFC) condition and the closed marks under the field-cooled(FC) one.

(spin easy axis) using a cryomagnet with horizontal field.

We show the diffuse scattering intensity as a function of temperature measured at the (2 0 5.08) reciprocal lattice point under a field, H, of 0 or 1.0 T in Fig. 2. In both fields, the diffuse scattering intensity starts to increase at T~20 K, which is much higher than the freezing temperature(T_g=4.5 K at H=3 G) determined by the DC magnetization measurements. The temperature dependence of the intensity for H=0 is almost similar to that for H=1.0 T, which makes a remarkable contrast with the results of

研究テーマ：スピングラス$Mn_{0.55}Mg_{0.45}TiO_3$の磁場中における振舞い
表題：スピングラス$Mn_{0.55}Mg_{0.45}TiO_3$の磁場中における振舞い

the magnetization measurements shown in Fig. 1. The result suggests that the correlation between the spins observed by the time-scale of observation of neutron scattering measurements appears at a temperature much higher than T_g determined by DC magnetization measurements. The correlation between the spins is not affected by the fields at least below 1.0 T.

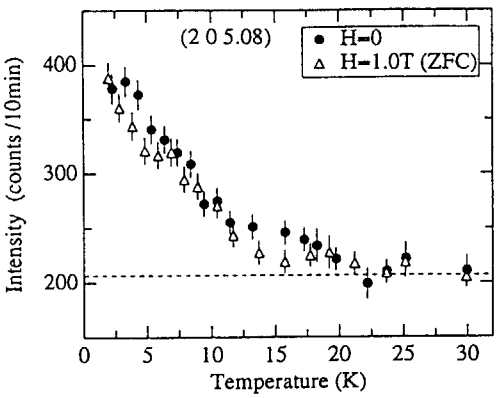

Fig. 2 Diffuse scattering intensity at the (2 0 5.08) reciprocal lattice point under H=0 and 1.0 T.

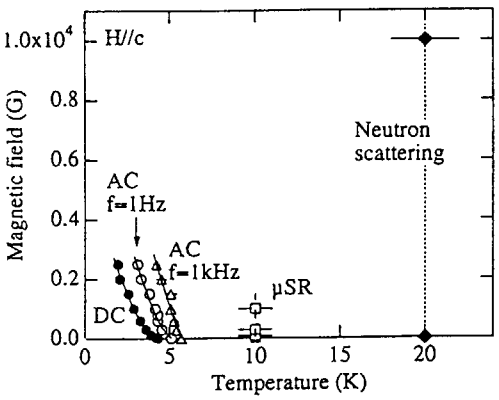

Fig. 3 Magnetic phase diagram in the H-T plane observed by various methods. DC and AC show DC magnetization and AC susceptibility measurement, respectively.

We show the magnetic phase diagram in the H-T plane determined by the neutron scattering measurement in Fig. 3. As a reference, we also show the results observed by DC magnetization, AC susceptibility and μSR measurements. It is clearly seen that the phase diagram strongly depends on the time- and space- scale of the observation.

We also measured the neutron scattering intensity near the (0 0 3) reciprocal lattice point, in which only spin component perpendicular to the c-axis is reflected. In low fields, any magnetic scattering is not observed near (0 0 3). This fact supports that $Mn_{0.55}Mg_{0.45}TiO_3$ is an Ising like spin-glass.[1] When we apply higher fields than 1.0 T, the diffuse scattering intensity at the (0 0 2.88) reciprocal lattice point increases. In the samples with higher Mn concentration which show the antiferromagnetic long range order, a spin-flop transition occurs.[2] Thus, we consider that a spin-flop like transition occurs also in $Mn_{0.55}Mg_{0.45}TiO_3$ and that the correlation between the spins associated with a XY like spin-glass freezing is observed. In other words, the crossover from the Ising spin-glass to the XY like spin-glass occurs. To our knowledge, this study is the first time to observe such a crossover. However, it is not clear whether the formation of the correlation between the spins perpendicular to the c-axis means a real XY like SG transition. To clarify this problem, further studies are necessary.

References

[1] A. Tobo, A. Ito and K. Motoya, J. Phys. Soc. Jpn. 65 (1996) 2249.
[2] A. Fukaya, A. Tobo, A. Ito, H. Aruga Katori and T. Goto, Physica B 201 (1994) 88.

研究テーマ: 準結晶における磁性の研究
表題: Zn-Mg-Ho 系準結晶における異方的な磁気励起

Anisotropic spin correlations in the Zn-Mg-Ho icosahedral quasicrystal

Taku J SATO[1], Hiroyuki TAKAKURA[1,2], An Pang TSAI[1] and Kaoru SHIBATA[3]
[1]*National Research Institute for Metals, Tsukuba 305-0047*
[2]*CREST, Japan Science and Technology Corporation, Saitama*
[3]*Institute for Materials Research, Tohoku University, Sendai*

The Zn-Mg-*RE* (*RE*: rare earth) icosahedral quasicrystal (i-QC) attracts growing attentions recently. Since this system has localized $4f$ magnetic moments on the *RE* sites, it provides an opportunity to study magnetism on the quasiperiodic lattice. To date, the neutron powder diffraction was performed, and suggested a coexistence of the magnetic short-range order (SRO) and long-range order (LRO) at low temperatures, such as $T < T_N \simeq 7$ K for *RE* = Ho [1]. However, the magnetic susceptibility shows no anomaly at T_N, instead, exhibits a spin-glass-like transition at lower temperatures, for example $T_{SG} \simeq 2$ K for *RE* = Ho [2]. Hence, the two results are contradicting. This can probably originate from insufficient sample quality: the previous neutron diffraction experiment used $Zn_{50}Mg_{42}Ho_8$ sample, which is now known to be contaminated by crystalline phases such as the $(Zn_{1-x}Mg_x)_5Ho$ phase.

In the present study, we have performed neutron scattering experiments on powder and single-crystalline samples. The powder experiments are to show the origin of the previously-reported LRO. Whereas the single crystal study is intended to explore the anisotropy of the spin-system, which, if exists, will be the first observation of the anisotropy on the icosahedral quasilattice [3].

Neutron scattering experiments were performed at the triple-axis spectrometer ISSP-GPTAS installed at JRR-3M, JAERI (Tokai), operated in the double-axis configuration. Collimations of 40'-80'-40' or 40'-80'-80' were employed. Incident neutrons of $k_i = 2.67$ Å^{-1} were selected by a vertically-focusing pyrolytic graphite (PG) monochromator, and second harmonics is eliminated by the PG filter.

First, we prepared the single i-phased sample by annealing $Zn_{60}Mg_{30}Ho_{10}$ at 723 K for 200 hrs. The powder diffraction pattern of this sample is shown in Fig. 1(a). The diffraction pattern at $T = 20$ K is shown as a high-temperature reference with only nuclear Bragg peaks. The peaks could be indexed with six indices, confirming the quasiperiodic nature of the sample. The difference of the data between $T = 1.6$ K and 20 K is also displayed to show the development of magnetic scattering intensity at the low temperature. Although the temperature is well below $T_N \simeq 7$ K, there appears to be almost no magnetic Bragg peak, indicating the absence of the LRO in the single-phased sample. Instead, broad peaks appear at $|\boldsymbol{Q}| \sim 0.55, 1.15$ and 2.0 Å^{-1}, and reproduce

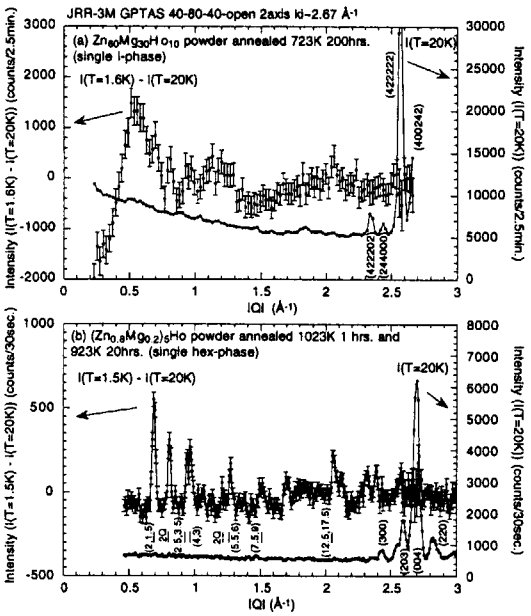

Figure 1: Powder diffraction patters of (a) single i-phase and (b) crystalline contaminant. [3]

the SRO part of the previous report. On the other hand, the powder diffraction pattern of the hexagonal $(Zn_{1-x}Mg_x)_5Ho$ sample, which is the crystalline contaminant of the previously-used sample, is shown in Fig. 1(b). At low temperatures, magnetic Bragg peaks appear at the same positions as the intense LRO peaks in the previous report. These results strongly suggest that the intrinsic magnetism in i-QC is SRO and that the previously-reported LRO can probably arise from the crystalline phase.

Next, we investigated the $\boldsymbol{Q}$ dependence of the diffuse scattering using the single crystal. To see overall feature of the diffuse scattering in $\boldsymbol{Q}$ space, we have made a magnetic-scattering intensity map. Further, to achieve reasonable statistical accuracy within limited experiment time, we measured the intensity in the following procedure. First, the half of the scattering plane, i.e. $Q_x > 0$ and $|\boldsymbol{Q}| < 4$ Å^{-1}, was scanned at $T = 1.3$ and 20 K. After confirming that the subtracted magnetic intensity satisfies the symmetry requirement, we folded the data into a single quadrant of $Q_x, Q_y > 0$. Finally, the quadrant was repeated for all the $|\boldsymbol{Q}| < 4$Å^{-1} space to see characteristics of the intensity distribution.

Figure 2 shows the resulting intensity map of the magnetic contribution. In the map, one can see ridges parallel to the 5f axis, which pass through the intense diffuse peaks. Those ridges appear as the satellites of intense nuclear Bragg reflections. As is well known, the nuclear Bragg reflections of the i-QC can be regarded as projected positions of the six-dimensional (6D) body-centered reciprocal lattice vectors, $\boldsymbol{G}^n_{6D}$, into the three-dimensional (3D) reciprocal space. Since the projection is a linear operation, magnetic diffuse-scattering, appearing as the satellite-ridges in the 3D reciprocal space, also appears as satellite-ridges, elongated along the 5f axis, in the 6D reciprocal space. This suggests that the corresponding spin-correlations can be regarded as *quasi-five-dimensional* in the 6D (real) space. The ridges are found to appear at $\boldsymbol{Q}_{6D} = \boldsymbol{G}^n_{6D} \pm \boldsymbol{q}_{6D}$, where $\boldsymbol{q}_{6D}$ is the magnetic wave-vector: $\boldsymbol{q}^1_{6D} = (x11\bar{1}0\bar{1})_{6D}$ and $\boldsymbol{q}^2_{6D} = (0\bar{1}\bar{1}1x\bar{1})_{6D}$, with x being arbitrary. Since

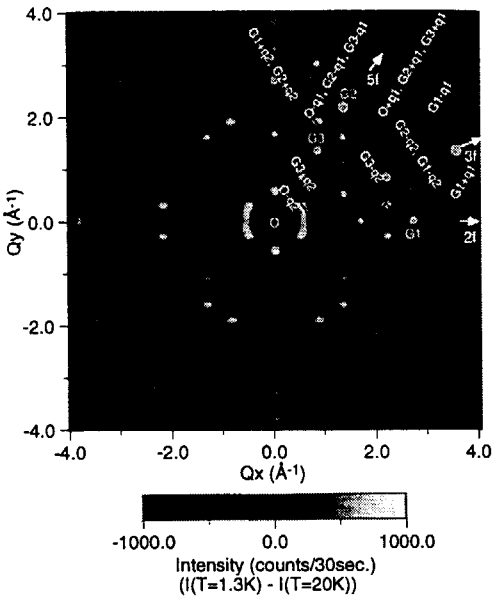

Figure 2: Magnetic scattering intensity-map of the single crystalline Zn-Mg-Ho quasicrystal. A two-fold axis was chosen vertical to the scattering plane. Collimations of 40'-80'-80' were used at ISSP-GPTAS. Dots with G1, G2 and G3 are the positions of intense nuclear Bragg reflections, $\boldsymbol{G}^1_{6D} = (244\bar{2}0)_{6D}$, $\boldsymbol{G}^2_{6D} = (422222)_{6D}$ and $\boldsymbol{G}^3_{6D} = (311111)_{6D}$ [3].

they appear at forbidden nuclear reflection positions, the spin-correlations are antiferromagnetic in nature.

This is the first observation of the ansotropic spin-correlations, which are found to be quite unique as *quasi-five-dimensional*. Further study both experimentally and theoretically is obviously required to elucidate the nature of the anisotropic spin-correlations in the Zn-Mg-Ho icosahedral quasicrystal.

References

[1] B. Charrier *et al.*: Phys. Rev. Lett. **78** (1997) 4637.
[2] Y. Hattori *et al.*: J. Phys.: Condens. Matter **7** (1995) 2313; B. Charrier *et al.*: J. Mag. Magn. Mater. **171** (1997) 106.
[3] T. J. Sato *et al.*: (submitted).

研究課題 二重スピン鎖系 $TlCuCl_3$ のエネルギーギャップと磁気励起
表題 二重スピン鎖系 $TlCuCl_3$ の磁気励起

Magnetic Excitations in Double Spin Chain System $TlCuCl_3$

T. Kato, K. Takatsu, W. Shiramura[1], H. Tanaka, K. Nakajima[2], and K. Kakurai[2]

Department of Physics, Tokyo Institute of Technology, Oh-Okayama, Meguro-ku, Tokyo 152
[1]Department of Physics, Sophia University, Kioi-cho, Chiyoda-ku Tokyo 102
[2]ISSP-NSL, The University of Tokyo, Shirakata, Tokai, Ibaraki 319-11

$TlCuCl_3$ is one of the $KCuCl_3$-family crystals that take an isomorphic structure to $KCuCl_3$. This structure consists of the Cu-Cu dimers which are connected to form double spin chains along the a-axis. The ground state of the crystals is a spin singlet with a finite excitation energy gap E_G. The gap of $TlCuCl_3$ evaluated from the magnetization measurements is 0.65 meV, which is rather smaller than E_G of $KCuCl_3$ (2.74 meV). The temperature T_{max} giving the maximum susceptibility is almost the same value, *i.e.* T_{max} = 38 K for $TlCuCl_3$ and 30 K for $KCuCl_3$. In order to clarify the dependence of three intra-double-chain nearest-neighbor inter-actions and some inter-double-chain inter-actions on E_G and T_{max} in the $KCuCl_3$-family crystals, a systematic study comparing the dispersion curves of $KCuCl_3$ with that of $TlCuCl_3$ must be needed.

We had performed the single-crystal neutron inelastic scattering of $KCuCl_3$ and $TlCuCl_3$. The results for $KCuCl_3$ were published in ref.1. We will mention here the experiment of $TlCuCl_3$. The PONTA spectrometer in JRR-3M at Tokai was used. The final neutron energy was fixed as E_f = 14.7 meV and PRG filter was inserted behind the sample. Collimations were taken as 40'-monochromator-40'-sample-40'-analyser-80'-detector. The $TlCuCl_3$ single-crystal sample was 0.5 cm^3 in volume and had the (0, 1, 0) cleaved plane which was laid in the scattering plane. The excitations for the wavevectors Q = (h, 0, 0) and (h, 0, 1) were researched by some constant-Q and constant-E scans at T = 8 K.

From the constant-Q energy scans in the energy range $1<E<12$ meV, two excitations are observed. Thus, there are two branches in the dispersion relations for the wavevector along the a^*-axis, as shown in Fig.1 with guide curves for the eyes. The lowest energy was too low to observe in the present conditions, but we can guess that the energy for Q = (1, 0, 1) corresponds to the gap.

As for $KCuCl_3$[1], the wavevector giving the gap is the same for $TlCuCl_3$, though only a single branch was observed. The difference in the dispersion of $KCuCl_3$ and $TlCuCl_3$ must come from the different balance of strengths of the exchange interactions, which must be clarified in the next experiments.

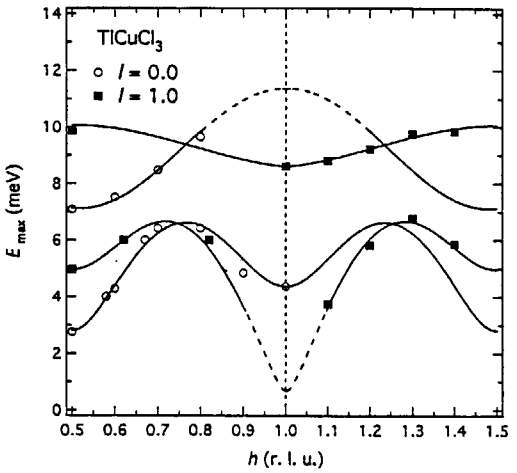

Fig.1. The dispersion of the magnetic excitation in $TlCuCl_3$ along a^*-axis.

Reference

[1] T. Kato, K. Takatsu, W. Shiramura, H. Tanaka, K. Nakajima, and K. Kakurai, *J. Phys. Soc. Jpn.*, **67** [3] (1998) 752-754.

JRR-3M, PONTA(5G), magnetism

研究テーマ：$BaCo_{1-x}Ni_xS_2$ の圧力下における中性子散乱
表題：2次元モット系 $BaCo_{1-x}Ni_xS_2$ の磁気励起

Magnetic Excitation of the 2D Mott System $BaCo_{1-x}Ni_xS_2$

H.Sasaki[1], H.Harashina[1,2], K.Kodama[1,2], M.Sato[1,2], S.Shamoto[3], M.Nishi[4] and K.Kakurai[2,4]

1 Department of Physics, Division of Material Science, Nagoya University, Furo-cho, Chikusa-ku, Nagoya 464-8602
2 CREST, Japan Science and Technology Corporation (JST)
3 Department of Applied Physics, Tohoku University, Aoba, Aramaki, Sendai 980-8577
4 Neutron Scattering Laboratoty, ISSP, the University of Tokyo, Shirakata 106-1, Tokai, Ibaraki 319-1195

$BaCo_{1-x}Ni_xS_2$ has layered structure which consists of alternating stacks of rock-solt-type BaS layers and $Co_{1-x}Ni_xS$ layers, and is expected to have two-dimensional (2D) electronic nature. At $x=0$, the system is in the Mott-insulating state and antiferromagnetic with the Néel temperature T_N ~305 K. The Mott transition can be induced not only by the substitution of Co with Ni but also by applying relatively small external pressure p.[1] Therefore, this compound draws much attention as a typical 2D Mott system. By the Ni-substitution for Co, electrons are introduced and the system becomes metallic when x exceeds 0.22. In the x region around 0.22, the Hall coefficients R_H and the thermoelectric power S have been found to exhibit anomalous behavior similar to that of high-T_c oxides.[2]

For $BaCo_{0.82}Ni_{0.18}S_2$, strong 2D-like magnetic excitation has been observed above T_N, where the system is in the metallic state. Analyzing the data of the inelastic mesurements by using the random phase approximation (RPA), we have found that RPA can explain the experimental results qualitatively well. However, the inverse correlation length κ_{RPA} deduced from the available data within a framework of RPA, does not approach zero as $T \rightarrow T_N$,[3] suggesting that it cannot completly describe the behavior of the present electron system. For $BaCoS_2$, κ_{RPA} approaches zero as $T \rightarrow T_N$.[4] The magnetic excitation of $BaCo_{0.76}Ni_{0.24}S_2$ that does not exhibit Néel order and is in the metallic region has also been studied.

Single crystal of $BaCo_{0.76}Ni_{0.24}S_2$ were prepared by the method described in ref. 2. Neutron measurements were carried out with PONTA(5G) triple-axis spectrometer at JRR-3M of JAERI in Tokai.

Figure 1 shows observed profiles obtained by constant-energy scan at 3 meV at various temperatures. A peak has been observed at $h=1/2$. The dynamical susceptibility $\chi''(q,\omega)$ measured from 2 meV to 18 meV at various temperatures has been analyzed by using the equation

$$\chi''(q,\omega) \propto \frac{\omega \Gamma_0 \chi_0}{\Gamma_0^2 \left(\kappa^2 + q^2\right)^2 \xi_0^4 + \omega^2},$$

where Γ_0 is a characteristic energy of spin fluctuations, χ_0 is the susceptibility of a non-interacting spin system, κ is an inverse correlation length ($=1/\xi$) and ξ_0 is

JRR-3M, PONTA(5G), 2. magnetism

assumed to be unit cell length a. The equation can explain the energy dependence of the full width at half maximum (FWHM) and $\chi''(\omega)$ qualitatively. Then, κ has been caluclated at various temperatures from the experimental value of FWHM. The results are shown in Fig.2. In the present case, κ is almost T-independent at low temperatures. The prediction based on the quantum non-linear σ model gives a better description of the T-dependence of inverse correlation length than RPA. Similar T-dependence of κ was observed in $La_{2-x}Sr_xCuO_4$.[5] They may be able to be argued on a same physical basis.

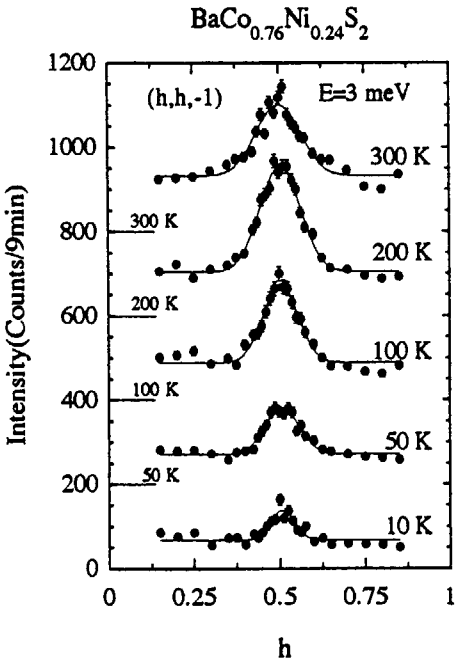

Fig.1. Magnetic scattering intensities of $BaCo_{0.76}Ni_{0.24}S_2$ taken at 3 meV at various temperatures.

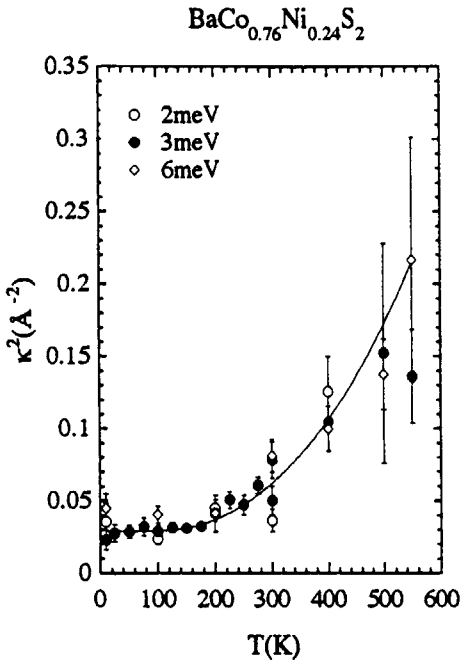

Fig.2 Values of κ^2 deduced from the observed values of FWHM are shown, where Γ_0 is chosen to be 17 meV. The solid line indicates $\kappa = \kappa_0 + \kappa(T)$, where the description of $\kappa(T)$ is given by Hasenfratz and Niedermayer.[6]

References

1) Y.Yasui *et al.*, J. Phys. Soc. Jpn. 66 3194 (1997)
2) J.Takeda *et al.*, J. Phys. Soc. Jpn. 64 2550 (1995)
3) S.Shamoto *et al.*, J. Phys. Soc. Jpn. 66 1138 (1997)
4) H.Sasaki *et al.*, J. Phys. Soc. Jpn. 66 3975 (1997)
5) B.Keimer *et al.*, J. Phys. Soc. Jpn 46 14034 (1992)
6) P.Hasenfratz *et al.*, Phys. Lett. B 268 231 (1991)

研究テーマ：半導体的近藤物質CeRhSbのスピン相関
表題：近藤半導体CeRhSbでの磁気励起

Magnetic excitation in the Kondo semiconductor, CeRhSb

K. Ohoyama, M. Kohgi[1], T. Yoshino[2] and T. Takabatake[2]

Institute for Materials Research, Tohoku University, Sendai, 980-77, Japan
[1]Department of Physics, Tokyo Metropolitan University, Tokyo 192-03, Japan
[2]Department of Quantum Matter, Graduate School of Advanced Science of Matter, Hiroshima University, Hiroshima 724, Japan

The orthorhombic ε-TiNiSi type compound CeRhSb is thought to be a Kondo semiconductor which belongs to the same group as CeNiSn. Transport property measurements indicate that the density of states at Fermi level in CeRhSb becomes extremely small or nearly zero with decreasing temperature below 10 K[1,2]. Moreover, the magnetic susceptibility for CeRhSb is weakly dependent on temperature and exhibits a broad maximum at around 120 K; this behaviours of the susceptibility is quite similar with those in typical valence fluctuation materials[1,2]. To make clear the magnetic response in CeRhSb, we performed inelastic scattering experiments on a polycrystalline sample of CeRhSb using the triple axis spectrometer TOPAN at JRR-3M. The collimation of 30'-60'-S-60'-B, and a fixed final energy of 14.7 meV were used. An neutron powder diffraction pattern from the sample showed only the Bragg peaks of the proper ε-TiNiSi type structure. To decrease the strong absorption effect of Rh atoms, the sample was enclosed in a plate type sample cell(40×40×5mm^3). The plate cell was fixed to be perpendicular to the incident beam.

Fig. 1 shows the temperature dependence of spectra of constant Q scan at Q=1.2Å^{-1} at 1.8 K(open circles) and 30 K(closed circles). Though the observed spectra does not show obvious temperature dependence above 5 meV, the slight temperature dependence at 3 meV may be due to the formation of a gap in the magnetic response[3]. Since the hump at 6 meV was not observed in previous experiments, we do not know the origin at present. Fig.2 shows the temperature dependence of the intensity at 4 meV and 5.5 meV at Q=1.2Å^{-1}. The intensity at 4 meV slightly increases with increasing temperature, while the intensity at 5.5 meV is almost independent of temperature.

To obtain more information at low energy spectra, it is necessary to increase the incident flux. For the high flux experiments, however, the decrease of the γ-ray level is important because Rh is a source of γ-ray when the incident flux becomes large.

JRR-3M, 6G(TOPAN) Magnetism

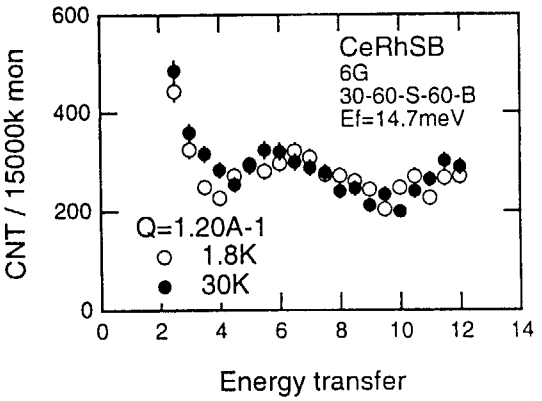

Fig.1 Energy spectra of CeRhSb at 1.8 K(open circles) and 30 K(closed circles) at Q=1.26Å^{-1}

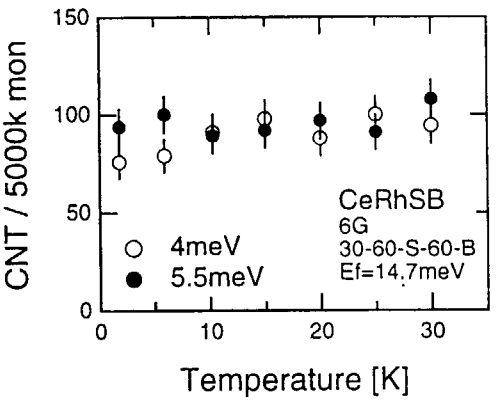

Fig.2 Temperature dependence of the intensity at 4 meV(open circles) and 5.5 meV(closed circles) at 1.2Å^{-1}.

References

[1] S. K. Malik, D. T. Adroja, Phys. Rev. B 43(1991)6277
[2] T. Takabatake, G. Nakamoto, H. Tanaka, Y. Bando, H. Fujii, S. Nishigori, H. Goshima, T. Suzuki, T. Fujita, I. Oguro, T. Hiraoka and S. K. Malik, Physica B 199-200(1994)457
[3] K. Ohoyama, M. Kohgi, T. Yoshino and T. Takabatake, Activity report on neutron scattering research, 4(1997)117

研究課題：$(La_{1-x-y}Y_y)Sr_xMnO_3$の巨大磁気抵抗とスピンダイナミクス
標題：バンド幅を制御したMnペロブスカイト$(La_{1-x-y}Y_y)Sr_xMnO_3$の磁気励起

Magnetic Excitations of Bandwidth-Controlled Mn Perovskite $(La_{1-x-y}Y_y)Sr_xMnO_3$

K. Hirota, A. Nishizawa, and Y. Endoh

CREST, Department of Physics, Tohoku University

The perovskite Mn oxides $R_{1-x}A_xMnO_3$ (R is a trivalent rare-earth ion and A is a divalent alkali ion) have attracted renewed interest recently, due to the discovery of colossal magnetoresistance (CMR) around the Curie temperature T_C. Appearance of the ferromagnetic metallic state in the doped system such as $La_{1-x}Sr_xMnO_3$ has been qualitatively explained by the "double-exchange interactions."[1] Recent investigations on the CMR phenomena, however, have pointed out discrepancies from the simple double-exchange model.[2] To study the effects of band-width on the double-exchange mechanism, spin dynamical behaviors were examined on a series of $(La_{1-x-y}Y_y)Sr_xMnO_3$ single crystals ($y = 0.00, 0.05$, and 0.10) with a fixed hole concentration ($x = 0.20$), where the electronic band-width can be controlled by the average rare-earth ionic radius, i.e., the Mn-O-Mn bond angle. Neutron-scattering measurements were carried out using the triple-axis spectrometer TOPAN.

T_C was determined from temperature dependence of the peak intensity at (1 1 0) in the cubic notation. Thus obtained T_C are summarized along with other parameters in Table 1. Phase transition from the rhombohedral (high temperature) to orthorhombic (low temperature) structure is observed as the appearance of superlattice peak at $(1\ 1\ \frac{3}{2})$ at $T < T_S = 92.5$ K (on cooling) or 112.0 K (on heating) for $La_{0.8}Sr_{0.2}MnO_3$. Upon doping Y, T_S increases drastically; T_S for $y = 0.05$ is higher than the highest available temperature, 330 K. In each sample, the resistivity shows insulator-like upturn with decreasing temperature and reaches maximum around T_C, then drops rapidly and becomes metallic at low temperatures, which is typical of the CMR materials. Polycrystalline samples were measured in comparison, which show a broad maximum at a temperature 50 K lower than that of the corresponding single crystal, indicating that grain boundaries and defects have large effects on electrons and blur the intrinsic properties.

	T_C (K)	D (meVÅ^2)	$T_{C_{MF}}/T_C$
EuO	69	7.4	1.3
Fe	1040	175	2.4
Ni	631	330	4.5
$y = 0.00$	306	102	2.3
$y = 0.05$	281	87	2.3
$y = 0.10$	271	84	2.2
$La_{0.7}Sr_{0.3}MnO_3$	378	114	2.1

Table 1: Dynamical properties of $(La_{1-x-y}Y_y)Sr_xMnO_3$ and some typical cubic ferromagnets. The spin-wave stiffness D is determined at $T/T_C = 0.8$.

The spin-wave dispersion curves for studied $(La_{1-x-y}Y_y)Sr_xMnO_3$ samples show an isotropic behavior in the measured (q, ω) range, $q < 0.40$ Å^{-1} and $\hbar\omega < 20$ meV, and follow well with $\hbar\omega(q) = Dq^2 + E_0$, typical of ferromagnetic spin-wave dispersion in low q and low ω range. In order to study the temperature dependence of spin-wave stiffness D, we have performed constant-Q scans at (1.1 1.1 0) where well-defined peak profiles are obtained in a wide temperature range. Each peak profile was fitted with the spin-wave scattering cross section including the finite life-time h/Γ convoluted with a proper instrumental resolution. Figure 1 shows thus obtained temperature dependence of D.

Decrease of the spin-wave stiffness D upon doping Y is consistent with the double-exchange mechanism. The e_g conduction band is narrowed because the Mn-O-Mn

Reactor: JRR-3M Facility: TOPAN(6G) Field: 2 磁性 Magnetism

bonds are bent by doping Y on La sites, which prevents electrons from hopping between neighboring Mn ions, resulting in diminishing the double-exchange interactions and D. Note that, in small q limit, D is related to the nearest-neighbor exchange interaction (such as the double-exchange interaction) J by $D = zJSd/4$ where S is the spin quantum number and d is the nearest-neighbor distance. We also found that the energy width Γ of spin waves follows $\Gamma(q,T) \propto \{1 - [M(T)/M(0)]^2\}\omega(q,T)$ where $M(T)$ is the magnetic moment at temperature T, as shown in the inset of Fig. 1. This relation is predicted in the double-exchange model.[3] Overall increase of Γ with increasing y is ascribed to random potential introduced by the Y substitution, which shorten the life time of spin waves. It should be pointed out that D scales with T_C as seen in Table 1. Mean-field Curie temperature $T_{C_{MF}}$ is derived from the Heisenberg model with the nearest-neighbor interactions J: $T_{C_{MF}} = 2zJP_s(P_s+1)/3k_B$ where z is the number of nearest neighbors and P_s is the saturation moment. Since D is proportional to J as already mentioned, the scaling of D and T_C supports the above model in the measured Y concentration range, in which the nearest-neighbor interaction, i.e., the double-exchange mechanism, plays a significant role. According to $T_{C_{MF}}/T_C$, which is used for an index of the itinerancy, $(La_{1-x-y}Y_y)Sr_xMnO_3$ is similar to a typical metallic ferromagnet such as Fe. It is interesting that the CMR phenomena appearing in the static properties are not reflected in the spin dynamics.

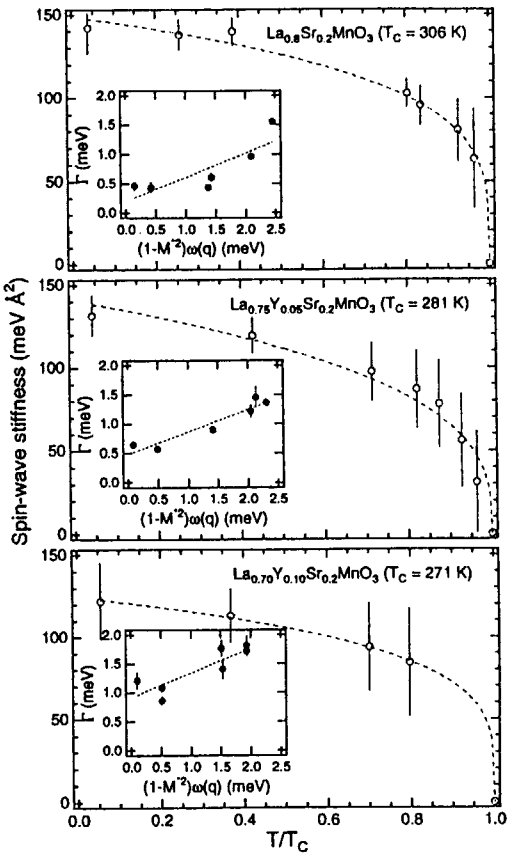

FIG. 1 Temperature dependence of the spin-wave stiffness D. Error bars indicate fitting errors. Dashed lines are guides to the eye. Inset shows a linear relation between $\Gamma(q,T)$ and $(1 - M^{*2})\omega(q,T)$, where $M^* = M(T)/M(0)$.

References

[1] N. Furukawa, J. Phys. Soc. Jpn. **63** (1994) 3214, *ibid* **64** (1995) 2734, *ibid* **64** (1995) 2754, *ibid* **64** (1995) 3164.

[2] A. J. Millis *et al.*, Phys. Rev. Lett. **74** (1995) 5144, *ibid* **77** (1996) 175.

[3] N. Furukawa and K. Hirota (to be published).

研究テーマ：Yb_4As_3のチャージオーダーと重い電子異常
表題： Yb_4As_3のチャージオーダー状態における磁気励起

Magnetic excitations in the charge ordered state of Yb_4As_3

M. Kohgi,[a] K. Iwasa,[a] H. Kadowaki,[a] A. Ochiai,[b] H. Aoki[c] and T. Suzuki[c,#]

[a]*Tokyo Metropolitan University, Hachioji, Tokyo 192-0397, Japan*
[b]*Niigata University, Niigata 950-2181, Japan*
[c]*Tohoku University, Sendai 980-8578, Japan*

Yb_4As_3 is known with its typical heavy-electron-like anomalies at low temperatures in spite that the compound is semimetallic with extremely low carrier density [1]. It undergoes structural transformation at 290 K from the anti-Th_3P_4 type cubic structure to a trigonal one with decreasing temperature. Our polarized neutron diffraction experiment [2] proved directly the existence of the charge ordering in the low temperature phase of Yb_4As_3 where four Yb ions aligned along a [111] direction (Yb_I) become mainly tri-valent whereas the rest of 12 Yb ions (Yb_{II}) in a unit cell are almost di-valent. The inelastic neutron scattering experiments [3] revealed that there exist low energy magnetic excitations which are attributed to the antiferromagnetic coupling in the Yb^{3+} chains. The dispersion relation as well as the spectral shape of the excitations are well explained by the one-dimensional spin-1/2 Heisenberg model. It was also found that, by using the exchange interaction value obtained from the dispersion relation, the model explains the value of C/T at low temperatures as well as the susceptibility anomaly in Yb_4As_3. These results suggest that the heavy-electron behaviors in Yb_4As_3 are strongly related with the formation of the one-dimensional Yb^{3+} chains caused by the charge ordering. However, other anomalous properties such as the heavy electron-like T-square dependence of the electrical resistivity or the steep up-turn of the susceptibility below about 7 K [1] cannot be explained by the simple Heisenberg model. Therefore, it is very interesting to clarify

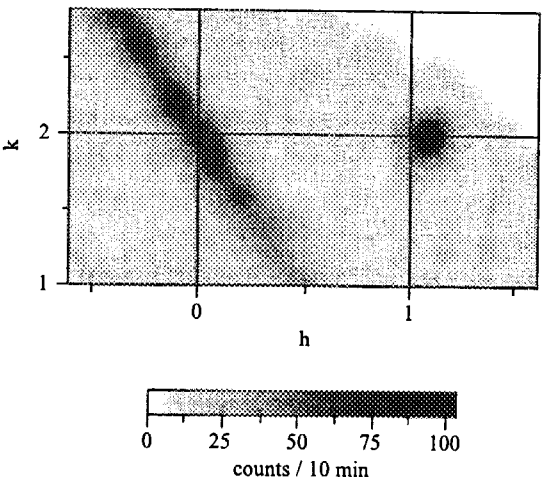

Fig. 1. Intensity map of magnetic response from Yb_4As_3 measured at C11 spectrometer with $\hbar\omega$=0.5 meV at 1.5 K in the (h,h,k) reciprocal lattice plane. Strong peaks near (1,1,2) reciprocal lattice point is due to Bragg contamination from the sample.

Present address: Tsukuba Institute of Science and Technology, Tsukuba 300-0819, Japan.

JRR-3M, C11, 2. magnetism

whether any magnetic response corresponding to these unusual properties, other than that attributed to the one-dimensional property, exists. In order to do that, more detailedneutron inelastic scattering studies of the low energy magnetic excitations in Yb_4As_3 were performed.

The experiments were carried out on the C11 spectrometer using a large analyzer with fixed final energy of 3.1 meV using a single crystal sample of about 2 g. We have done constant-E scans with $\hbar\omega$=0.5 and 0.3 meV in a wide Q range around (0,0,2) in the (h,h,k) reciprocal space, where the [111] direction was settled as the unique axis by utilizing strain-cool technique. Fig. 1 shows the intensity map of the scans with $\hbar\omega$=0.5 meV at 1.5 K. The strong intensity ridge which passes through (002) corresponds to the scattering from the one-dimensional spin excitations around the wave vector $q = \pi/d$ in the one-dimensional representation, where q is measured along the [111] direction and d is the distance of Yb_I ions in the chains. Similar intensity maps were also measured at the IN14 spectrometer at ILL with $\hbar\omega$=2 meV using the fixed incident neutron energy of 14.7 meV. The results indicate that the whole magnetic response from Yb_4As_3 for the energy transfer above about 0.3 meV can be attributed to the one-dimensional antiferro-magnetic coupling in the Yb^{3+} chains, and that there is no clear indication of additional magnetic response which might correspond to the anomalous properties such as the resistivity anomaly or the susceptibility up-turn at low temperatures. Therefore, it is concluded that the energy scale of the heavy-electron anomaly in the transport property specific to the pure material Yb_4As_3 may be very small (less than about 3 K), if its response is sizable, compared to those of spin excitations.

References

[1] A. Ochiai, T. Suzuki and T. Kasuya, J. Phys. Soc. Jpn. 59 (1990) 4129.

[2] M. Kohgi, K. Iwasa, A. Ochiai, T. Suzuki, J.-M. Mignot, B. Gillon, A. Gukasov, J. Schweizer, K. Kakurai, M. Nishi, A. Dönni and T. Osakabe, Physica B 230-232(1997)638.

[3] M. Kohgi, K. Iwasa, J.-M. Mignot, A. Ochiai and T. Suzuki, Phys. Rev. B 56(1997)R11388.

[4] A. Ochiai, H. Aoki, T. Suzuki, R. Helfrich, F. Steglich, Physica B, 230-232(1997)70.

研究テーマ：AV_2O_5(A=Mg,Li,Cs)における量子スピンゆらぎの研究
表題：LiV_2O_5の中性子非弾性散乱による研究

Inelastic Neutron Scattering Study of LiV_2O_5

Y.Takeo[1], T.Yosihama[1], M.Nishi[1], K.Nakajima[1], K.Kakurai[1,2], M.Isobe[3] and Y.Ueda[3]

[1]*Neutron Scattering Laboratory, ISSP, University of Tokyo, 106-1 Shirakata, Tokai, Ibaraki 319-11, Japan*
[2]*CREST, Japan Science and Technology Corporation(JST), Tsukuba, Japan*
[3]*Material Design and Characterization Laboratory, ISSP, University of Tokyo, 7-22-1 Roppongi, Minato-ku, Tokyo 106, Japan*

LiV_2O_5 is the mixed valent (V^{4+}/V^{5+} =1) vanadate of which structural element is the distorted VO_5 pyramid.[i] As can be seen from the structure, the spin system can be regarded as double linear chain consisting of two independent linear chains, zigzag chain or the intermediate model between them, which is called railroad trestle lattice. The magnetic susceptibility of the powder sample of this compound shows good fit to the equation for a S=1/2 Heisenberg antiferromagnetic (1-D HAF) linear chain, although the obtained powder averaged g-factor is 1.8, and that the ground state is not a spin singlet state.[ii] Therefore it is suggested that this magnetic system can be regarded as being highly one-dimensional.

The inelastic neutron scattering experiments on single crystalline samples were performed using triple axis spectrometer PONTA installed at the reactor hall beam line 5G of JRR-3M in JAERI (Tokai). Single crystals (0.6031[g]) were prepared using $LiVO_3$ as a flux. They were aligned with b*(chain)- and c*(stack)-axis in the scattering plane.

Fig.1 shows the **Q**-dependence of scattering intensity along b*-axis around (0,0.5,2) at the constant energy transfer E=12[meV]. This reciprocal lattice point corresponds to the zone center of 1-D HAF linear chain with the lattice constant b. In this Figure, the solid line represents the expected spectrum for a 1-D HAF linear chain model with 2J=308[K] evaluated from magnetic susceptibility measurement. Fig.2 shows the E-dependence of scattering intensity at (0,0.5,1) which is magnetically equivalent to (0,0.5,2) (filled points). The corresponding energy spectrum at (0,0.4,1) (open points) is considered to represent the background including the incoherent scattering from vanadium atoms around energy transfer E=0[meV]. The low energy excitations down to 1[meV] can be clearly observed. We note that there are no excitations observed at around (0,1,0), corresponding to the zone center of a zigzag chain. These neutron scattering results suggest that LiV_2O_5 can be regarded as a S=1/2 1-D HAF linear chain system.

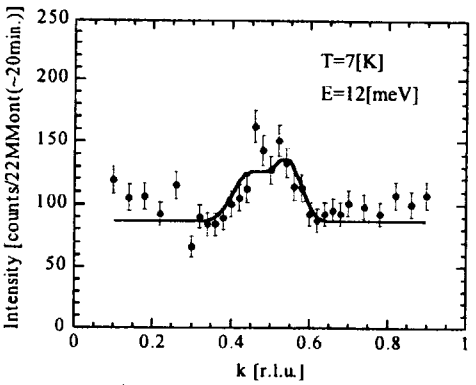

Fig.1: Constant E-scan at (0,k,2).
Instrumental conditions: Ei=30.5[meV] fixed mode and collimations open-PGf-80-S-80-80.

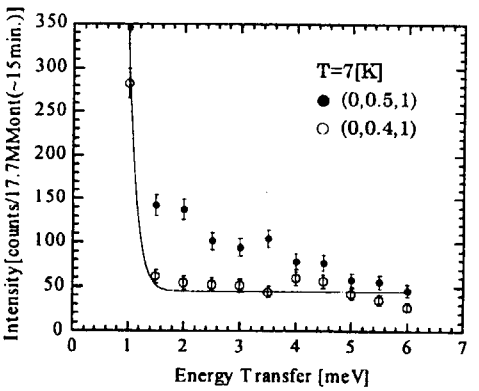

Fig.2: Constant **Q**-scan at (0,0.5,1).
Instrumental conditions: Ei=14.7[meV] fixed mode and collimations open-PGf-40-S-40-80.

[i] D.N.Anderson and R.D.Willett : Acta Crystallogr. Sect.B **27** (1971) 1476.
[ii] M.Isobe and Y.Ueda : J. Phys. Soc. Jpn. **65** (1996) 3142.

JRR-3M、PONTA、2.Magnetism

研究テーマ：AV_2O_5(A=Mg,Li,Cs)における量子スピンゆらぎの研究
表題：SrV_3O_7の中性子磁気散乱による研究

Magnetic Neutron Scattering Study of SrV_3O_7

Y.Takeo[1], T.Yosihama[1], M.Nishi[1], K.Nakajima[1], M.Isobe[2], Y.Ueda[2],
K.Kodama[3,4], H.Harashina[3,4], M.Sato[3,4] and K.Kakurai[1,4]

[1]*Neutron Scattering Laboratory, ISSP, University of Tokyo, 106-1 Shirakata, Tokai, Ibaraki 319-11*
[2]*Material Design and Characterization Laboratory, ISSP, University of Tokyo, 7-22-1 Roppongi, Minato-ku, Tokyo 106*
[3]*Department of Physics, Division of Material Science, Nagoya University, Furo-cho, Chikusa-ku Nagoya 464-01*
[4]*CREST, Japan Science and Technology Corporation(JST), Tsukuba, Japan*

Magnetism of SrV_3O_7 is governed by S=1/2 quantum spins at the vanadium sites in 1/4 depleted square lattice. The structure of this compound is analogous to that of CaV_3O_7, of which the magnetic structure has been recently studied by Harashina et al.[i], although the VO_5 pyramids in SrV_3O_7 are more distorted. From the magnetic susceptibility measurement of the powder sample prepared by solid state reaction, it was confirmed that the magnetic ordering occurs antiferromagnetically and that the Neel temperature T_N is 34.3[K].

Neutron powder diffraction was carried out to determine the spin structure of the ordered phase. In this experiment, we used the triple axis spectrometer PONTA installed at the reactor hall beam line 5G of JRR-3M in JAERI (Tokai). The spectrometer was operated in the double axis mode with Ei=14.7[meV] and collimations:40-PGf-M-Sapphire-40-S-40.

Fig.1 shows the T-dependence of the peak intensity of the (110)(102) reflection group, which has the strongest magnetic scattering intensity. With decreasing T, the magnetic scattering grows in addition to the nuclear scattering below T≃34.5[K], and this is consistent with the magnetic susceptibility measurement.

Fig.2 shows representative magnetic scattering obtained by subtracting the data at 50[K] from those at 7[K]. The integrated magnetic scattering intensities can be well explained assuming the '*stripe order*' spin structure, same as found in CaV_3O_7, but with the spin direction along a(stack)-axis, instead of c-axis for CaV_3O_7. The ordered moment is evaluated to be μ=0.55 $\pm$0.02[μ_B].

In this experiment, the nuclear scattering intensities at T=50[K] were not in complete agreement with the intensities calculated using the previously reported structure data at RT[ii]. A detailed study on nuclear structure is now in progress.

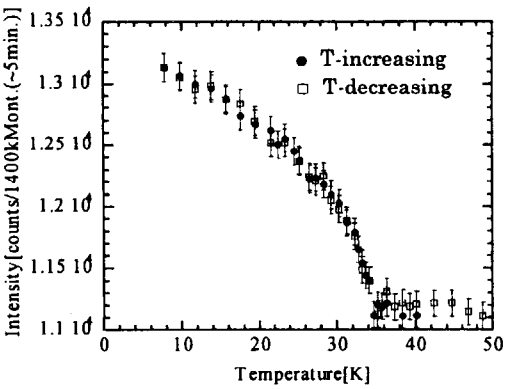

Fig.1: T-dependence of the (110)(102) reflection peak intensity

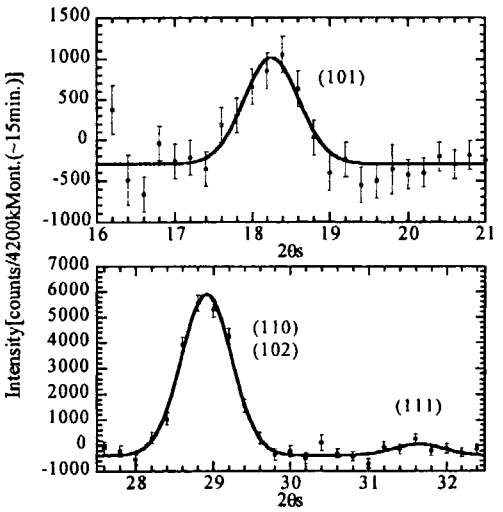

Fig.2: Examples of the magnetic scattering
These spectra are obtained by subtracting the data at 50[K] from those at 7[K]. The solid lines represent the results of Gaussian fits.

[i] H.Harashina et al. : J. Phys Soc. Jpn. **65** (1996) 1570.
[ii] G.Liu and J.E.Greedan : J. Solid State Chem. **103** (1993) 139.

JRR-3M、PONTA、2.Magnetism

研究テーマ： $LiMn_2O_4$の構造と磁気的性質
表題： $LiMn_2O_4$の中性子散乱

Neutron Scattering Measurement of $LiMn_2O_4$

Y.Kasuya, Y.Tsunoda and I.Tomeno*

Department of Applied Physics, School of Science and Engineering, Waseda University
*Advanced Research Center for Science and Engineering, Waseda University**

The spinel-type compound $LiMn_2O_4$ is known to be one of the most promising candidates for cathode materials of rechargeable lithume batteries. The $LiMn_2O_4$ undergoes a Jahn-Teller lattice distortion around 280K, and it makes the rechargeability worse. Thus the structuaral phase transition has been studied by many authors. But very few data were reported on the magnetism of $LiMn_2O_4$ which is a typical manganese oxide.

Previous authors reported that no magnetic long-range order is observed in the data of magnetic susceptibility χ, NMR and neutron diffraction. However we obtained completely different results.

We first studied susceptibility of $^7LiMn_2O_4$ powder sample. Anomalies are seen around 40K and 65K in susceptibility measurement. Neutron diffraction experiments were performed at T1-1 spectromator. Figure 1 shows the observed diffraction pattern at 18K and 45K. A lot of sharp peaks are obtained. Most of them are the magnetic scattering peaks because these are temperature dependent, indicating that there exists a magnetic long-range order at low temperature. Figure 2 shows the temperature dependences of the peak intensities studied at 2θ = 26.1, 30.2 and 33.2 degrees. According to these data, the Neel temperature is estimated to be 65K, and it coincides with one of the anomalies in susceptibility data. On the other hand, there are no remarkable changes in diffraction patterns around 40K, as shown in Fig1. Thus the anomaly at 40K does not look like a magnetic phase transition. Further investigations are going on for this point.

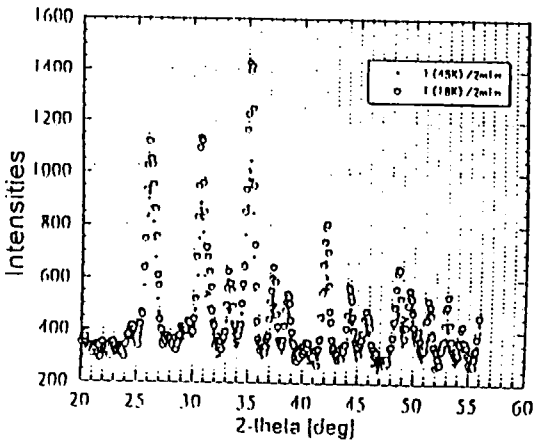

Fig1 $LiMn_2O_4$ powder neutron diffraction

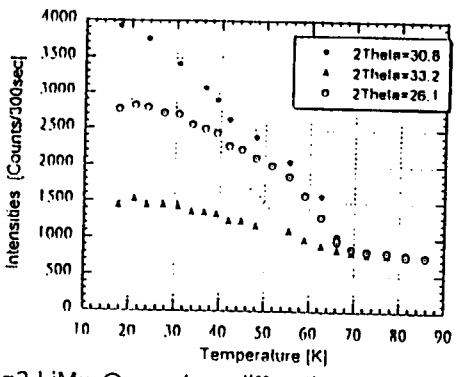

Fig2 $LiMn_2O_4$ neutron diffraction T-dependence

JRR-3M, T1-1, Magnetism

研究テーマ：非フェルミ流体状態におけるCe_7Ni_3の磁気励起
表題 ：Ce_7Ni_3の中性子散乱

Neutron Scattering Study of Ce_7Ni_3

K. Motoya, T. Kawasaki, H. Kadowaki[1], K. Umeo[2],
T. Takabatake[2], H. Okumura[3], K. Kakurai[3] and T. Osakabe[4]

Faculty of Science and Technology, Science University of Tokyo, Noda 278-8510
[1]Faculty of Science, Tokyo Metropolitan University, Hachioji, Tokyo 192
[2]Faculty of Science, Hiroshima University, Higashi-Hiroshima 724
[3]Institute for Solid State Physics, The University of Tokyo, Tokai 319-1195
[4]JAERI, Tokai 319-1195

Ce_7Ni_3 crystallizes in the Th_7Fe_3-type hexagonal structure with three non-equivalent Ce sites. Specific heat and magnetic susceptibility measurements showed that an antiferromagnetic order (T_N=1.8K) coexists with a heavy Fermion state (γ=9 J/K^2 mol f.u.) in this compound[1]. The antiferromagnetic order is suppressed by extremely low pressure (P_c=0.33 GPa) and non-Fermi-liquid (NFL) behavior appears[2]. Taking advantage of the low P_c and the absence of lattice disorder introduced by the alloying, we started neutron scattering study of magnetic excitations from Ce_7Ni_3 accompanied with the magnetic transition and NFL/FL crossover.

Elastic neutron scattering measurements showed that an antiferromagnetic order characterized by the propagation vector $\mathbf{q}$~0.22$\mathbf{c}^*$ appears below T_N=1.8K. Also, a new antiferromagnetic order with the propagation vector $\mathbf{q}$=0.25$\mathbf{c}^*$ appears below T~0.8K, without any appreciable change in the component above mentioned. The SDW magnetic structure deduced from the present measurements is shown in Fig.1, in which moments on Ce-1 (2(b)-site) and Ce-2 (6(c)-site) contribute to the antiferromagnetic order of $\mathbf{q}$~0.22$\mathbf{c}^*$ whereas those on Ce-3 (6(c)-site) contribute to $\mathbf{q}$=0.25$\mathbf{c}^*$. Magnetic field dependence of the magnetic Bragg peak intensity is shown in Fig.2. Antiferromagnetic Bragg peaks observed in zero field disappear above H_c~0.15T. No magnetic Bragg peak is observed except for the ferromagnetic points above H_c.

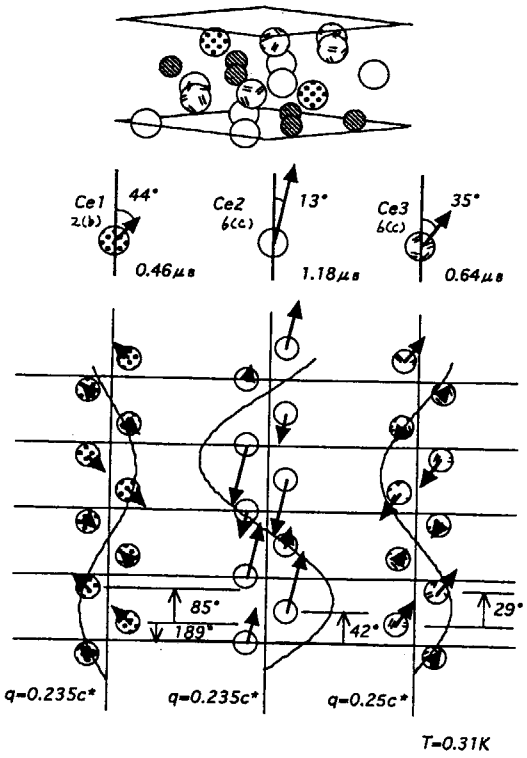

Fig. 1. Magnetic structure of Ce_7Ni_3.

JRR-3M, C1-1, T1-1, 5G, magneatism

Inelastic neutron scattering measurements under the ambient pressure were made on the high nergy resolution spectrometer (C1-1) utilizing a horizontally focused analyzer. In Fig.3, we show the constant energy scans along the (10ξ) reciprocal line taken at T=0.27K. Scattering pattern at E=0.2 meV consists of two components; narrow component starting from antiferromagnetic Bragg points indicated by the arrows, and a slowly varying wide component. The observed pattern suggests that the antiferromagnetic and the ferromagnetic fluctuations coexist in the antiferromagnetic phase. At E=0.3 meV, the scattering pattern consists only of the slowly varying components starting from ferromagnetic Bragg points (100) and (102). Figure 4 shows the scattering intensity map in the (h0k) plane taken at the energy transfer E=0.3 meV. The inelastic scattering measurements under pressure will shortly be started.

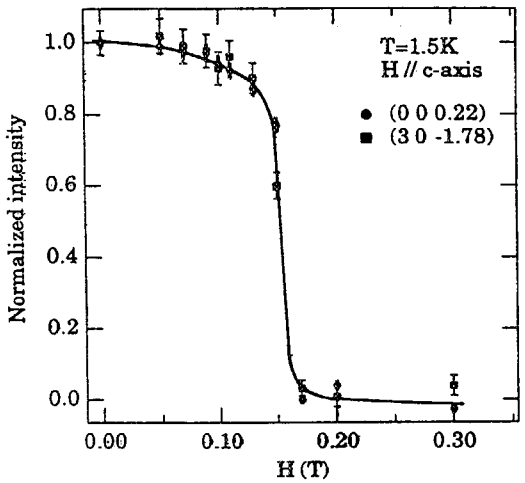

Fig.2. Magnetic field dependence of magnetic Bragg peak intensity.

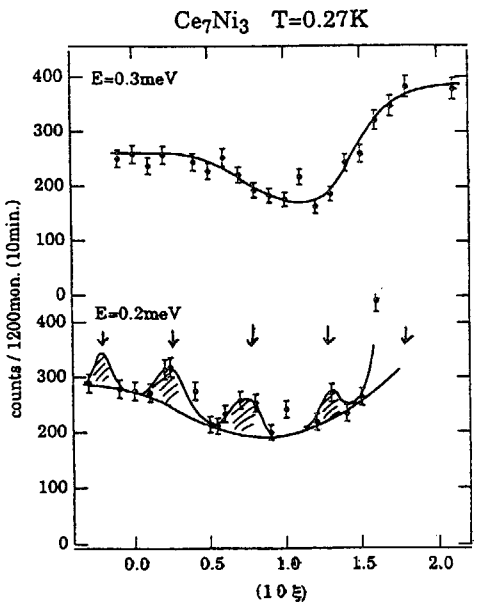

Fig. 3. Inelastic neutron scattering patterns across the (10ξ) reciprocal line.

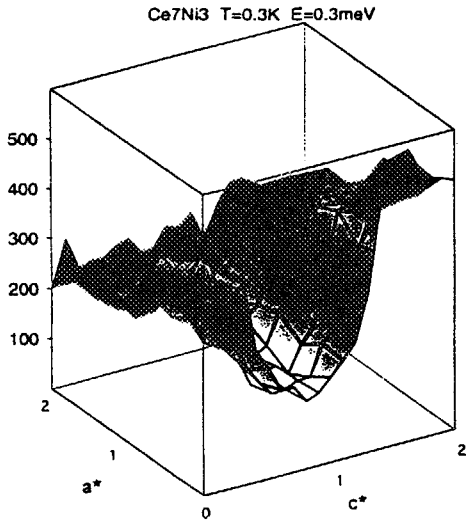

Fig. 4. Inelastic neutron scattering intensity in the (h0l) plane taken at E=0.3meV.

References

1) G.Sereni, O.Trovarelli, J.P.Kappler, C.Paschke, T.Trappmann and H.v.Löhneysen, Physica B 199&200 (1994) 567.
2) K. Umeo, H.Kadomatsu and T.Takabatake, Phys.Rev. B 55 (1997) R692

研究テーマ：$ZnFe_2O_4$ 単結晶の中性子磁気散乱

表題：$ZnFe_2O_4$ 単結晶の中性子磁気散乱

Magnetic neutron scattering of $ZnFe_2O_4$ single crystal

K.Kamazawa, K.Odaka, Y.Tsunoda and K.Kohn

Department of applied physics, School of Science and Engineering, Waseda University
3-4-1 Ohkubo, Shinjyuku-ku, Tokyo169, Japan

The zinc ferrite contains Fe^{3+} magnetic ions only at the octahedral (B) site and for this reason it is simplest magnetic system with spinel structure. However, it is known as an Anderson's frustrated spin system, and hence the antiferromagnetism of zinc ferrite is still not solved. The magnetism in $ZnFe_2O_4$ is investigated by G.V.Bich *et al* [1] and W.Schieel *et al* [2] using powder neutron diffraction. They reported that the center of gravity of the antiferromagnetic short-rang order (SRO) peak shifts towards lower scattering angles as temperature is increased. Below T_N (~10K), the antiferromagnetic SRO and antiferromagnetic long-range order (LRO) coexisted.

We succeeded to grow $ZnFe_2O_4$ single crystal. In the present work, we report neutron scattering data for single crystal $ZnFe_2O_4$. The measurements were performed at the $T_{1\text{-}1}$ triple axis spectrometer installed at the guide hall of JRR-3M in the temperature range from 1.5K to 30K in the 0 0 1 scattering plane. We found that the diffuse magnetic peak is located parallel to the [1 1 0] axis above the Neel temperature (Fig.1).

This means that the one-dimensional antiferromagnetic spin correlation develops parallel to the [1 1 0] axis. The peak position continuously shifts towards small q region as temperature is increased. While the temperature is decreased, the wave vector of the antiferromagnetic SRO peak reaches to 3/4 3/4 0 position, which is commensurate with the lattice periodicity, then, antiferromagnetic long-range order develops. However, the Bragg peaks appear at 1 1/2 0, not at 3/4 3/4 0 (Fig.2). These data suggest that the magnetic structure of $ZnFe_2O_4$ at low temperature is non-collinear spin arrangement.

JRR-3M, HQR(T1-1), 2.magnetism

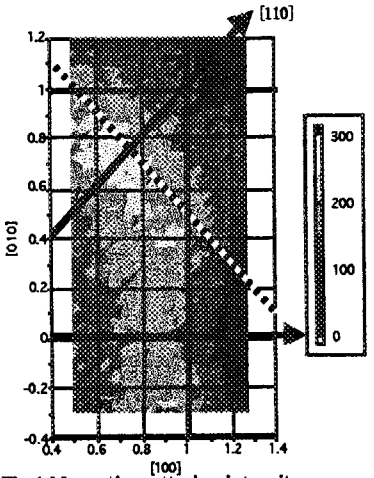

Fig.1 Magnetic scattering intensity map observed at T=15K.

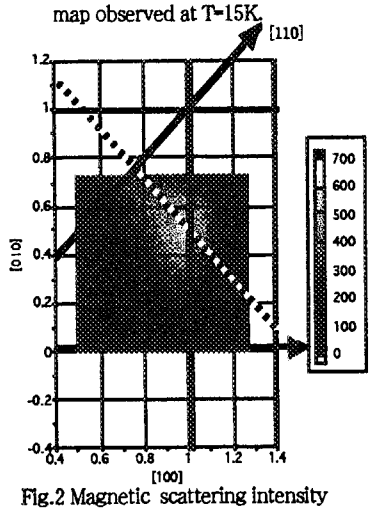

Fig.2 Magnetic scattering intensity map osaerved at T=1.5K.

1) G.V.Bich, A.N.Men', and Yu.A.Petrov, Sov. Phys.Solid State **30**, 1686 (1988).
2) W.Schiessl, W.Potzel, H.Karzel, M.Steiner, G.M.Kalvius, A.Martin, M.K.Krause, I.Halevy, J.Gal, W.Schafer, G.Will, M.Hillberg and R.Wappling, Phys. Rev. **B 53**, 9143 (1996).

研究テーマ：パイライト及びスピネル構造を持つ３d遷移金属化合物の磁性と伝導
表題：$NiS_{2-x}Se_x$の金属絶縁体転移と反強磁性

Metal-insulator transition and antiferromagnetism in $NiS_{2-x}Se_x$

M.Matsuura, H.Hiraka, K.Yamada[1] and Y.Endoh

Department of Physics, Tohoku University, Aramaki, Aoba, Sendai 980-8578

[1]Institute for chemical research, Kyoto University, Gokashou, Uji 611-0011

$NiS_{2-x}Se_x$ is known as a Mott-type metal-insulator transition(MIT) system. Se substitution for S induces MIT at x~0.5. The same type of antiferromagnetic ordering exists in both insulator($0 \leq x < 0.5$) and metal phase ($0.5 \leq x \leq 1.0$) at low temperature. The magnetic moment decreases monotonically across the metal-insulator boundary[1]. For $0.5 \leq x \leq 0.6$, the thermally induced first-order MIT occurs in antiferromagnetic ordering. Recently, we found that there are no appreciable change in the staggered moment at MIT temperature by simultaneous measurements on electrical resistivity and magnetic neutron diffraction. No difference of static magnetic ordering has been observed between insulator and metal phase.

At second stage, we are going to study the dynamical spin fluctuation of this system. Here, we report the first experimental result of inelastic neutron scattering for a single crystal with the volume of 0.1cc ($4 \times 5 \times 5 mm^3$) of x=0.65 in which the magnetic sublattice moment is $0.5\mu_B$/Ni. The single crystal was grown by chemical transport method using Cl_2 gas.

The inelastic neutron scattering experiments were performed with TOPAN spectrometer installed at JRR-3M. The inset of Fig.1 shows the temperature dependence of magnetic Bragg peak intensity at (100) center and electrical resistivity. The Néel temperature is 90K and resistivity increases with rising temperature beyond 90K. The MIT broadens for $0.6 < x < 0.7$. At 60K, resistivity is $10^{-4}\Omega$cm and antiferromagnetic Bragg peak is observed, therefore x=0.65 is antiferromagnetic metal at 60K. Fig.1 shows constant-E scan at ω=3meV along (1,k,0) at 60K. We couldn't observe well-defined signal. We supposed that the sample volume was not enough. However there is a possibility that the magnetic signal may be broad at magnetic Bragg (100). Since a single broad peak at antiferromagnetic Bragg peak position was observed in the inelastic scans on antiferromagnetic metal phase of $V_{2-y}O_3$ system[2]. To get more accurate data, we are now preparing lager size of single crystals.

The work has been supported under the Grant in Aid for the Science Research by the Ministry of Education, Science, Sports and Culture.

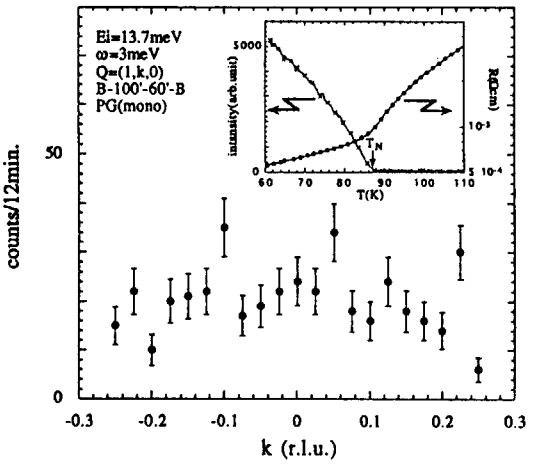

Fig.1 Constant-E scan at ω=3meV along (1,k,0) at 60K. Inset shows temperature dependences of intensity at magnetic Bragg(100) peak center and electrical resistivity.

Reference
[1]T.Miyadai et al.:J.Mag.Mag.Mat. 31-34 (1983) 337.
[2]Wei Bao et al.:Phys.Rev.Lett.71(1993) 766.

Reactor:JRR-3M Facility:TOPAN(6G) Field:Magnetism

課題名：圧力下における２次元強磁性体Cs_2CuF_4および
$(CH_3NH_3)_2CuCl_4$の構造および磁気相転移

表　題：２次元反強磁性体$(C_2H_5NH_3)_2CuCl_4$の圧力誘起弱強磁性

Pressure-Induced Weak Moment in the Two-Dimensional Antiferromagnet $(C_2H_5NH_3)_2CuCl_4$

H. Manaka, M. Nishi[1] and I. Yamada

Department of Physics, Faculty of Science, Chiba University, Yayoi-cho, Inage-ku, Chiba 263-8522

[1]Institute for Solid State Physics, University of Tokyo, Roppongi, Tokyo 106-8666

(Received)

Placing a magnetic compound under a high pressure can yield a change of its magnetism that is strongly correlated with the crystal structure of the compound. Recent investigations of K_2CuF_4 under pressures revealed a drastic pressure-induced transition from ferromagnetic to antiferromagnetic state around 9 GPa,[1)] which is due to the change of orbital ordering of 3d-holes in Cu^{2+} from the antiferrodistortive (AFD) one to the ferrodistortive (FD) one.[2,3)] The pressure-induced magnetic transition similar to that observed in K_2CuF_4 is expected in the series of layered compounds $(C_nH_{2n+1}NH_3)_2CuCl_4$ ($n = 1$ and 2), because the intralayer ferromagnetic exchange interaction in them owes to the AFD orbital ordering of 3d-holes. The spins in each layer in these compounds couple ferromagnetically, while the interlayer coupling of spins is ferromagnetic for $n = 1$ and antiferromagnetic for $n = 2$. The interlayer coupling is some orders of magnitude smaller than that in the layer and the spins align along the a-axis. As revealed by Raman scattering experiments for the $n = 2$ compound,[4)] the crystal structure that results in the AFD disappears around $4 \sim 5$ GPa. Measuring magnetic susceptibility of the $n = 2$ compound at high pressures, Ishizuka *et al.* recently found a ferromagnetic behavior at 1.23 GPa, which is far below the pressure at which the orbital ordering changes. Their preliminary experiment performed with $H = 10$ Oe along the a-axis indicates a ferromagnetic moment induced along the a-axis. On the basis of on this result, we thought that the interlayer coupling probably became ferromagnetic.

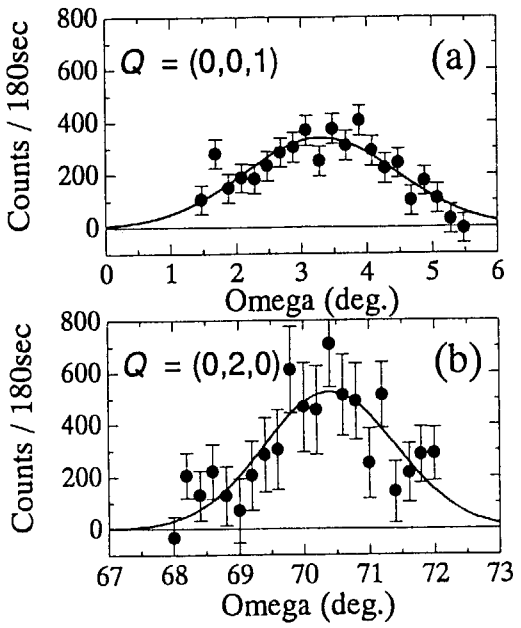

Fig. 1. (a) The magnetic peak that indicates antiferromagnetic coupling of spins in adjacent layers. (b) The ferromagnetic peak, which is not allowed when the spin structure is collinear.

To confirm our expectation of the spin structure around this pressure, we performed neutron diffraction experiments at 2 GPa using the ISSP-HQR spectrometer at JRR-3M in JAERI. As a result, we found that the spins among the layers still couple antiferromagnetically, as shown in Fig. 1 (a), which is contrary to our presupposition. However, we detected a weak magnetic peak that indicates a ferromagnetic moment aligned along the c-axis, which is shown in Fig. 1 (b). These results indicate a collapse of the collinear spin alignment along the a-axis, i.e., spin-canting occurs.

We intend to examine whether the ferromagnetic moment along the a-axis, which was detected by the susceptibility measurement, is surely induced by pressure or not in the next machine time.

We think that the observed weak moment is due to a change of crystal symmetry caused by pressures. As a result of lowering of crystal symmetry by pressure, an antisymmetric exchange interaction becomes to be allowed, and causes a spin canting. Further investigations are now in progress.

1) M. Ishizuka *et al.*: J. Phys. Soc. Jpn. 65 (1996) 1927.
2) M. Manaka *et al.*: J. Phys. Soc. Jpn. 66 (1997) 2989.
3) M. Ishizuka *et al.*: Phys. Rev. B 57 (1998) 64.
4) Y. Morimoto and Y. Tokura: J. Chem. Phys. 101 (1994) 1763.

JRR-3M, T1-1, Magnetism

研究テーマ：TOPAN(東北大学中性子分光器) IMT
表題：$La_{1.95}Sr_{0.05}CuO_4$における準3次元反強磁性秩序

Quasi 3-Dimensional Antiferromagnetic Order in Lightly Doped $La_{1.95}Sr_{0.05}CuO_4$

S. Wakimoto, S. Ueki, K. Yamada*) and Y. Endoh

Department of Physics Tohoku University, Sendai 980-8578, Japan

It is one of the most important subjects among High-T_C researches to clarify correlations between conductivity and magnetism. For $La_{2-x}Sr_xCuO_4$ (LSCO) system, systematic and detailed neutron scattering study for superconducting region ($0.06 \leq x \leq 0.25$) was reported by K. Yamada *et al.*[1] and magnetism in lightly doped region (so-called spin glass region, $0.02 \leq x \leq 0.05$) has been remaining issue. Very recently, T. Suzuki *et al.*[2] and H. Kimura et al.[3] observed elastic sharp q peaks at the incommensurate positions on x=0.12 which must be strongly related with 1/8 problem. Similar sharp elastic peak at commensurate position of x=0.04 was studied by B. Keimer *et al.*[4] In the present paper, we report results of elastic neutron scattering on x=0.05.

Single crystal of x=0.05 was grown by improved travelling solvent floating zone method. Its c-axis lattice parameter suits for a value estimated by interpolation between x=0 and x=0.06. From results of magnetic susceptibility measurements by SQUID, it shows typical spin glass (SG) behavior in a-b plane and SG transition temperature is 4.5K. On the other hand, its interplane magnetic susceptibility deviates from Curie-Weiss law below 20K (Tdv) which is much higher than the SG transition temperature.

Neutron scattering experiments were carried out on triple-axis spectrometer TOPAN installed on thermal neutron beam hole 6G in JRR-3M of JAERI. Collimation set of B-60'-60'-B was utilized.

Fig.1(a) shows magnetic peak observed in *(H, 0, L)* zone. The observed magnetic intensity may be 2-dimensional and there may be intensity rod along c-direction. Although we did not study this intensity along c-direction, this peak means there exists quasi three-dimensional magnetic order, because two-dimensional static order must not be achieved at finite temperatures in this system theoretically due to quantum fluctuations. Fig.1(b) shows temperature

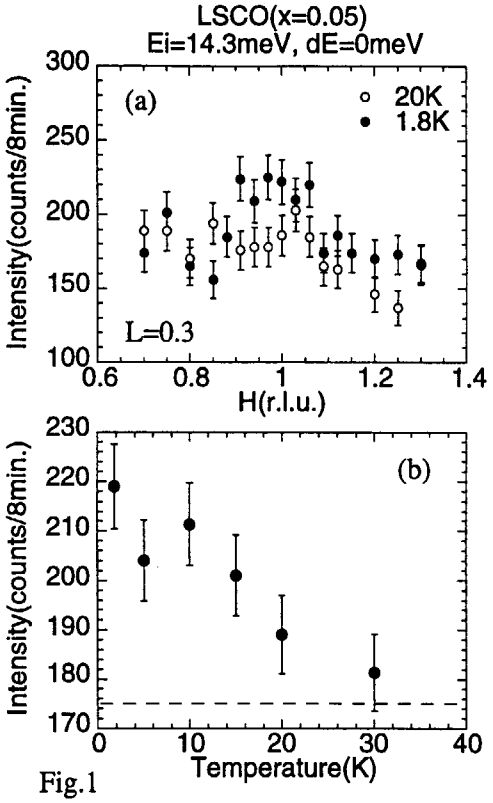

Fig.1

dependence of the magnetic peak intensity. A dashed line in this figure shows back ground level. From this figure, the on-set temperature is about 30K which is higher than T_{dv}. But if we observe this feature with tight energy resolution, the on-set temperature should be lower. We suppose that the deviation of interplane magnetic susceptibility from Curie-Weiss law correlates with this magnetic order. We will study this elastic component systematically on the other concentrations in lightly doped region.

References

[1] K. Yamada *et al.* : Phys. Rev. B57 (1998) 6165
[2] T. Suzuki *et al.* : Phys. Rev. B57 (1998) 3229- 3232
[3] H. Kimura *et al.* : To be published
[4] B. Keimer *et al.* : Phys. Rev. B46 (1992) 14034

*) *Present address : Institute for Chemical Research, Kyoto Univ., Gokasho, Uji 610-0011, Japan*

Reactor : JRR-3M Facility : TOPAN(6G) Field : Magnetism

研究テーマ：三角格子反強磁性体
表題：三角格子反強磁性体$CuFeO_2$の部分秩序相

Partially Disordered Phase in Triangular Lattice Antiferromagnet $CuFeO_2$

S. MITSUDA, T. UNO, M. MASE, N. KASAHARA
Department of Physics, Faculty of Science, Science University of Tokyo, Kagurazaka, Shinjuku-ku, Tokyo 162-8601

We re-investigated successive magnetic phase transitions (T_{N1}~14.0 K, T_{N2}~10.5 K) in a quasi two dimensional triangular lattice antiferromagnet (TLA) $CuFeO_2$ by neutron diffraction measurements at 4G and T1-1 spectrometers using single crystals prepared by floating zone and flux-growth techniques.

Although the magnetic structure in intermediate temperature phase has been identified[1] as 5-sublattice partially disordered (PD) state in which one-fifth of magnetic moments are paramagnetic in magnetic unit cell, it turned out to be incommensurate structure as is seen in the temperature dependence of propagation wave number q shown in Fig.1(a), being consistent with previous powder neutron scattering experiments[2]. Moreover, as is seen in Fig.1(a), with decreasing temperature, full width of half maximum (FWHM) of magnetic Bragg reflection of (q, q, 3/2) start to deviate from resolution limited value below T_{N1} and increases as the wave number q approaches to 1/4, and finally return to resolution limited value below T_{N2}. These feature of FWHM strongly suggests that intermediate phase is not true long range ordered state but quasi-long range ordered state.

By accurate intensity analysis of magnetic Bragg peaks in (h h l) zone, the magnetic structure can be identified as incommensurate Spin Density Wave (SDW) state where the magnetic moment confined along c axis is modulated sinusoidaly along <110> direction within hexagonal c plan and stacked antiferromagnetically along c axis.

With these experimental results in hand, we re-investigated the Monte Carlo (MC) simulation of 2D Ising spin TLA model with $J_2/|J_1| = -0.475$ and $J_3/|J_1| = -0.75$ by Takagi et al.[1,3] in which 9-sublattice PD commensurate state was predicted as thermally induced state above low temperature 4-sublattice state. Note that 3rd neighbor exchange interaction J_3 is necessary to stabilize 4-sublattice state as ground state. In previous MC simulation[3], order parameter with only highly-commensurate structure was surveyed, whereas we simply employed wave vector-dependent-magnetization $M(\mathbf{Q})$ in our MC simulation with system size of 200*200, as shown in Fig.2. Instead of 9-sublattice PD commensurate state predicted in previous MC simulation[3], quasi-long range ordered SDW state with temperature dependent propagation wave vector $\mathbf{Q}=(q,q)$ is well reproduced in our MC simulation, being consistent with present neutron diffraction experimental results, as is clearly seen in Fig.3. Quasi-long range ordered incommensurate SDW state elucidated in present studies forms striking contrast to PD state with temperature independent propagation wavevector $\mathbf{Q}=(1/3,1/3)$ which has been extensively investigated on quasi-1D hexagonal insulators such as $CsCoCl_3$ where 1D magnetic chains can be considered to behaves as a spin on a 2D triangular lattice.

In spite of Heisenberg spin of orbital singlet Fe^{3+} magnetic ions with competing exchange interactions, the feature of Ising spin TLA model with competing interactions up to 3rd neighbors in $CuFeO_2$ is clearly seen in the successive magnetic phase transitions. Noted that growth of 3rd harmonic peak at (1-3q,1-3q) seen in Fig.2 is also confirmed in present neutron experiments as temperature evolution of 3rd harmonic peak at (3q,3q,3/2) is shown in Fig.4.

Reactor:JRR-3M Facility:Triple-axis spectrometer(T1-1,4G) Field:Magnetism

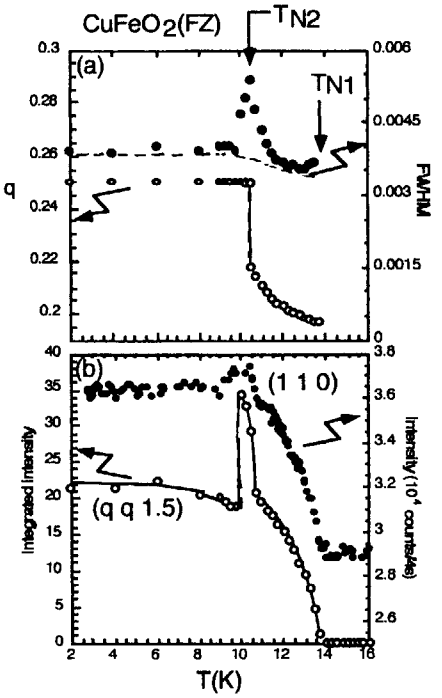

Fig.1 (a) Temperature depndence of propagation wave number q and FWHM of (q q 1.5) magnetic reflection. Resolution limmited value of FWHM interpolated using transverse as well as longitudinal widths of several measureble nuclear peaks in (h h l) zone at T=20K is also plotted(dashed line) (b) Temperature depndence of peak intensity of (110) nuclear refrection and integrated intensities of (q q 1.5) magnetic reflection. Solid lines are guide to eyes.

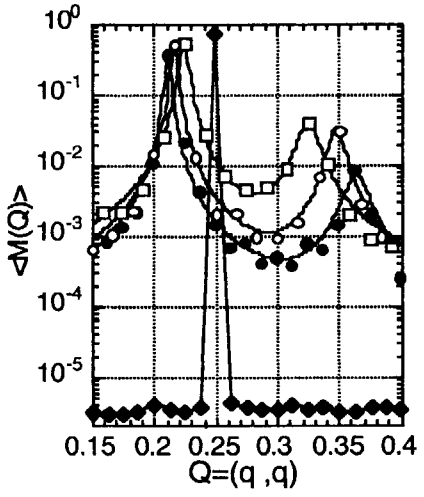

Fig.2 Wave vector dependent-magnetization M(Q=(q,q)) at $\tilde{T} = \frac{k_B T}{|J_1|}$ =0.9(●) ,0.7(○) ,0.5(□) and0.4(◆) calculated by MC simulation of 2D Ising spin TLA model with $J_2/|J_1| = -0.475$ and $J_3/|J_1| = -0.75$.

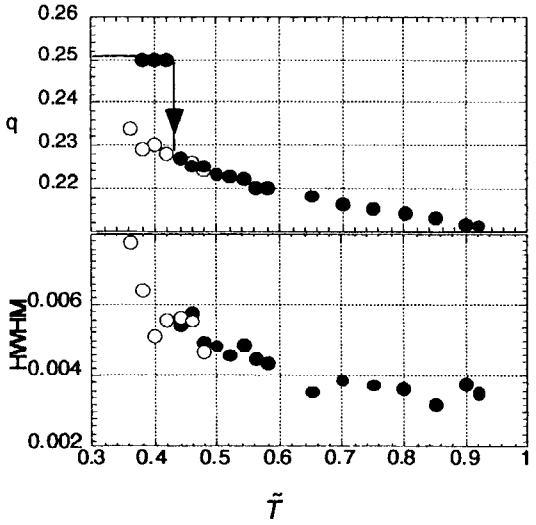

Fig.3 Temperature depndence of propagation wave number q and HWHM of (q, q) peak obtained by MC simulation: heating(●) cooling(○)

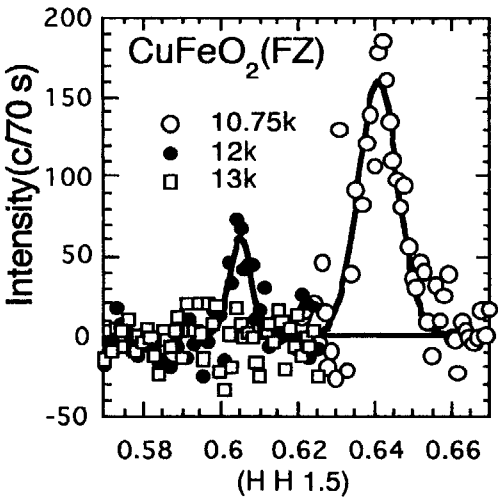

Fig.4 Neutron diffraction profiles of magnetic reflection (3q 3q 1.5) at T=13K, 12K and 10.75 K where difference of intensity form data at T=20K(above T_{N1}~14.0 K).

Reference

1) M. Mekata et al. : J. phys. Soc.Jpn. 62 (1993) 4474.

2) S. Mitsuda et al. : Physica B 213&214(1995) 194.

3) T. Takagi et al. : J. phys. Soc.Jpn. 64 (1995) 4609.

研究テーマ：$U(Ru_{1-x}Rh_x)_2Si_2$における弱い反強磁性スピン揺動を伴う相転移に関する研究
表題：URu_2Si_2における微弱反強磁性モーメントの不純物効果

Effect of Impurity on Tiny Antiferromagnetic Moments of URu_2Si_2

H. Amitsuka, A. Okumura, K. Ikeda, K. Kuwahara and T. Honma[1]

Graduate School of Science, Hokkaido University, Sapporo 060-0810, Japan
[1] *Advanced Science Research Center, JAERI, Tokai, Ibaraki 319-11, Japan*

A puzzling phase transition of URu_2Si_2 at 17.5 K ($\equiv T_o$) is one of the most intriguing subject in heavy fermion physics. A type-I antiferromagnetic (AF) arrangement formed of tiny 5f moments ($\mu_{ord} \sim 0.03(1)\ \mu_B$) below T_o is apparently inadequate to large anomalies in various macroscopic properties, particularly a large entropy reduction.[1)] Failures in various theoretical approaches assuming the dipole to be intrinsic have provoked an alternative hypothesis that some other non-magnetic mechanism drives the phase transition. Interestingly, a recent neutron study has suggested that the onset temperature (T_m) of the magnetic Bragg intensity deviates from the transition temperature (T_o) defined as the midpoint of a jump in C/T.[2)], as a result of the absence of annealing procedure.

Here, we present preliminary results of neutron scattering experiments for the pure and Y 1% doped URu_2Si_2 single crystals. The aim is to study how the tiny moments relate to the transition, by tuning the periodicity in U layers. Both samples were pulled by using a tri-arc furnace, followed by an annealing in evacuated sealed quartz tubes at 850 °C for 5 days. Experiments were made by using the T1-1 triple axis spectrometer at JRR-3M.

Figure 1 shows the temperature variations of (100) magnetic peak intensity I_m normalized by (200) nuclear peak, for each U concentration. For the pure compound, whole feature of I_m is in good agreement with the previous reports for annealed samples. From the best fit to the data by using the relation, $I_m = I(0)(1-T/T_m)^{2\beta}$ for 3D-Ising case ($\beta = 0.31$), we derive $T_m \sim 17.3$ K, which shows good correspondence to T_o. μ_{ord} is roughly estimated to be $\sim 0.02\mu_B$, which also reproduces the previous results.

By substituting Y for 1% of U, μ_{ord} is found to be reduced about half ($\sim 0.008\mu_B$ at 1.6K). This is remarkable, because the total entropy ($\sim 0.2R\ln 2$) released below T_o is unchanged by the doping, ensuring that the ordering is still stable in the static limit. The results thus suggest that the tiny moments are extrinsic to the transition at T_o.

Regarding the separation of T_m and T_o, we may not state the exact onset of I_m because of poor statistics in the present experiments. The above procedure of fitting provides $T_m \sim 13.3$K, which is seemingly lower than T_o (~ 16.5 K). To clarify the point, however, we need careful investigations on the probable tail in I_m. Such experiments are now in progress.

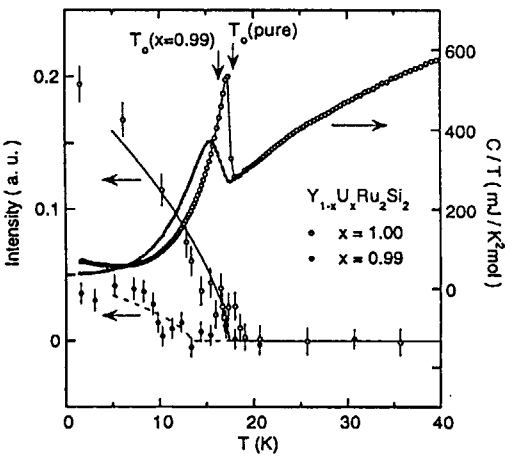

Figure 1: Peak intensity of the (100) Bragg reflection vs. temperature, for $Y_{1-x}U_xRu_2Si_2$ ($x = 1$ and 0.99), shown together with the temperature variations of the specific heat. Solid and broken lines indicate the best fits to the I_m data for each concentration using the relation given in the text.

1) See, e.g.: K. Kuwahara *et al.*, J. Phys. Soc. Jpn. **66**(1997)3251 and its references.

2) B. Fåk *et al.*, J. Magn. Magn. Mater., **154**(1996)339.

JRR-3M, T1-1, 2. Magnetism

研究テーマ: $La_2NiO_{4+\delta}$におけるホールストリップとその磁性への効果の研究
表題: $La_2NiO_{4.125}$における二次元磁気相関におよぼす酸素の秩序化の効果

Oxygen-Ordering Effect on the 2D Spin Correlation in $La_2NiO_{4.125}$

K. Nakajima,[1] S. Hosoya,[2] Y. Endoh[3]
[1]*Neutron Scattering Laboratory, Institute for Solid State Physics, University of Tokyo*
[2]*Institute of Inorganic Synthesis, Yamanashi University*
[3]*Department of Physics, Tohoku University*

Oxygen doping into La_2NiO_4 triggers rich and complicated phenomena, i.e., a phase separation, long range ordering of localized holes and excessive oxygen atoms, a commensurate-incommensurate transition in the magnetic correlations and etc. Since the 2D antiferro-magnetic (AF) spin correlations governs magnetism in this system, the details of the influence on the 2D spin correlations are the one of the most interesting issues of doping problem. The oxygen doped system is affected by holes induced by doped oxygen and the doped oxygen atoms themselves. Our previous study shows that the ordering of doped oxygen atoms drastically changes inter-layer magnetic correlation [1]. Then, it is necessary to obtain the experimental evidence of the effect of oxygen ordering on the 2D spin correlations.

In the present work, we have studied the dynamical 2D spin correlation length in $La_2NiO_{4.125}$ using a single crystal. Experiment was carried out on a triple-axis spectrometer PONTA. In $La_2NiO_{4.125}$, the excessive oxygen develops long range ordering below T_O=304 K. To obtain a disordered state of oxygen atoms, the sample was warmed above T_O and then rapidly cooled by inserting into a pre-cooled *Orange*-type cryostat. Obtained result is compared with the previous one that was taken in the slowly cooled condition [1].

The dynamical intra-layer spin correlation length in quenched $La_2NiO_{4.125}$ is measured by energy-integrated scans. To integrate the signal from the 2D magnetic fluctuations in energy, the spectrometer was operated in the 2-axis mode removing analyzer and scans were performed keeping the final neutron wave vector parallel to the 2D AF ridge. The line width, which corresponds to the inverse spin correlation length, κ was extracted by a fit to a Lorentzian line shape convoluted with the instrumental resolution. Obtained κ and the amplitude, which is roughly proportional to the integrated intensity are represented in Fig. 1 with the previous results from the slowly cooled sample [1]. Here, the intensity is normalized by monitor counts. Both the intra-layer magnetic correlation length and the integrated intensity show no essential difference by oxygen ordering within the experimental error. The result indicates that the intra-layer spin correlations is controlled only by the doped hole [2].

[1] K. Nakajima *et al.*: J. Phys. Soc. Jpn. **66** (1997) 809
[2] K. Nakajima *et al.*: to appear in Physica B

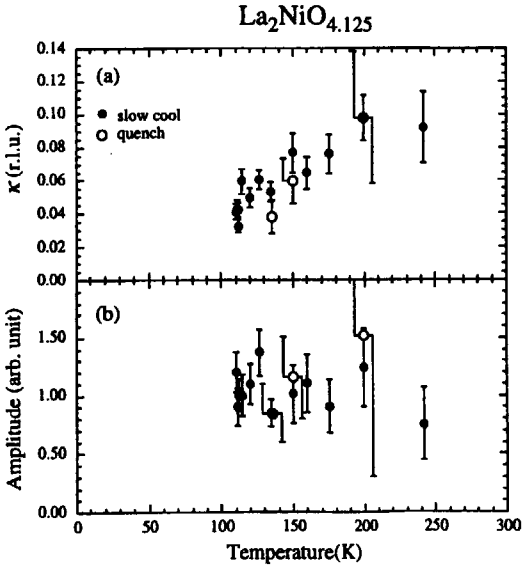

Fig. 1: Temperature evolution of (a) the inverse magnetic correlation length κ and (b) the Lorentzian amplitude of energy-integrated scans for $La_2NiO_{4.125}$.

JRR-3M, 5G, 2. magnetism

研究テーマ: 縮退度の高い非ランダム磁性体におけるスローダイナミックス
表　　題: 擬一次元磁性体 $CoNb_2O_6$ における二次元面間磁気相関緩和

Relaxation phenomena of interplanar magnetic correlations in a quasi-1D magnetic system $CoNb_2O_6$

S. KOBAYASHI, S. MITSUDA, H. YOSHIZAWA[1], M. ISHIKAWA[1], K. MIYATANI[2] and K. KOHN[3].

Dep. of Physics, Faculty of Science, Science Univ. of Tokyo, Kagurazaka, Tokyo 162
[1]*Institute for Solid State Physics, University of Tokyo, Roppongi, Tokyo 106*
[2]*Dep.Materials Sci.&Eng. Ehime University, Bunkyo-cho, Matsuyama 790*
[3]*School of Science and Engineering, Waseda University, Shinjuku-ku, Tokyo 169*

Previous neutron scattering measurements of a deviation of magnetic Bragg scattering function from delta function in a quasi-1D magnet $CoNb_2O_6$ revealed a pronounced 2D magnetic character in antiferromagnetic(AF) phase below T_{N2}~1.9 K.[1),2)] In view of an isosceles triangular arrangement of 1D chains running along c axis, we evidenced that such 2D character results from a cancellation of an exchange field at the apex site from the anti-parallel spins on the base site.[3)] However, it has been unclear why an interplanar inverse magnetic correlation length κ in the a^* direction decreases as the temperature increases. The AF sub-peaks such as (1/2 1/2 0) observed in our recent study[4)] gave a possibility for a non-collinearity of spins on the base sites. Nevertheless, a weakly temperature dependent (1/2 1/2 0) intensity could hardly explain the temperature variation of κ in the AF phase.

In order to verify an origin of such behavior, we performed further single-crystal neutron scattering measurements down to T=1.5 K on the triple-axis spectrometer (4G) installed at JRR-3M in double axis mode with k_f=2.57 Å^{-1}. Since all our previous measurements have been carried out after quenching down to T=1.5 K from paramagnetic state above T_{N1}~3.0 K, we paid attention to two cooling process; slow cooling and quenching from T=4.0 K with a cooling rate of ~0.5K/hour and ~0.05K/sec, respectively.

As clearly seen in (h 1/2 0) scan at T=1.5 K in Fig.1, while the profile of magnetic reflections in the a^* direction for quenching case is broad lorentzian with quite low peak height, that for slow cooling case is sharp lorentzian. The interplanar correlation length $\xi = (2\pi\ \kappa/a)^{-1}$ for slow cooling case is ~57 a, which is four-times longer than that for quenching case of ξ ~15 a. Moreover, as shown in Fig.2, ξ increases with time after quenching down to T=1.5 K. These results conclude that the rapid cooling produces non-equilibrium interplanar magnetic correlations in the AF phase and the anomalous decrease of κ with increasing the temperature might be due to an acceleration effect of relaxation process with a help of thermal fluctuation. Such relaxation phenomena is similar to that observed in a quasi-2D dilute Ising antiferromagnet $Rb_2Co_{0.7}Mg_{0.3}F_4$[5)] and is interpreted as a consequence of a cancellation of interplanar exchange field under the isosceles triangular arrangement of 1D chains which gives rise to a pronounced 2D magnetic character in a quasi-1D magnet $CoNb_2O_6$. Noted that our intensity analysis revealed that the recently observed AF sub-peaks result not from the non-collinearity of spins but from AF domain structures.[6)]

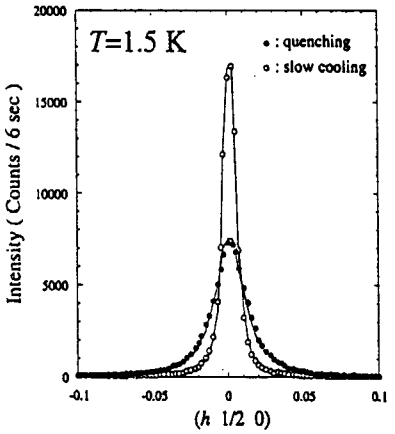

Fig.1 Profiles of magnetic reflections in (h 1/2 0) scan at T=1.5 K for two cooling process.

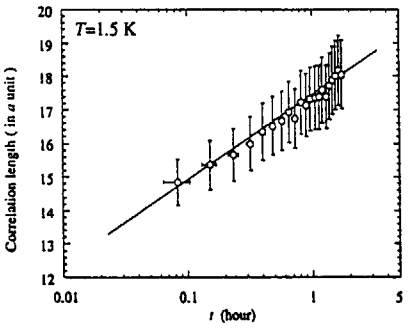

Fig.2 Time dependence of interplanar correlation length obtained after quenching procedure.

Reference

1) S. Mitsuda et al.: J. Phys. Soc. Jpn. **63** (1994) 3568.
2) S. Kobayashi, S. Mitsuda et al.: Physica B **213 & 214** (1995) 176.
3) S. Mitsuda, S. Kobayashi et al.: J. Phys. Soc. Jpn. **64** (1995) 2325.
4) S. Mitsuda et al.: ISSP, Act. Rep. on N. S. Reserch, **3** (1996) 121.
5) H. Ikeda : J. Phys. C **16** (1983) 3563.
6) S. Kobayashi et al.: in preparation.

Reactor: JRR-3M Facility: Triple-axis spectrometer(4G) Field: Magnetism

課題名：重い電子系混合物におけるメタ磁性と反強磁性相関の関係

表　題：CeNi2Ge2における反強磁性相関

Antiferromagnetic Correlation of Heavy Fermion $CeNi_2Ge_2$

H. Kadowaki, T. Fukuhara[1] and K. Maezawa[1]

Department of Physics, Tokyo Metropolitan University, Hachioji-shi, Tokyo 192-0397
[1]Faculty of Engineering, Toyama Prefectural University, Toyama 939-03

The heavy-fermion compound $CeNi_2Ge_2$ has been attracting interest by the metamagnetic behavior at H = 42 T [1] and by non-fermi liquid properties at low temperatures. Purpose of this study is to find antiferromagnetic correlation using single-crystal sample. Inelastic neutron scattering experiments were performed by using 4G-TAS. The energy scale of magnetic excitation is Γ = 4 meV, which was measured by poly-crystal sample [2]. Typical energy scans taken for (h, h, l) scattering zone are plotted in Fig. 1. These spectra show that the energy scale is consistent with the powder data, and that Q-dependence of intensity, that is, antiferromagnetic correlation exists. A few Q-scans are shown in Fig. 2. One can see that peaks at (h, h, l=1/2) indicates doubling of the unit cell of magnetic correlation along the c-axis.

References

[1] T. Fukuhara et al.: J. Phys. Soc. Jpn. **65** (1996) 1559

[2] G. Knopp et al.: J. Magn. Magn. Mater. **74** (1988) 341

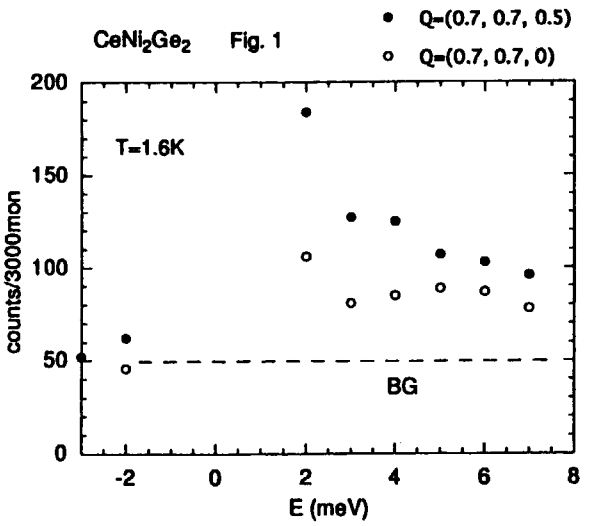

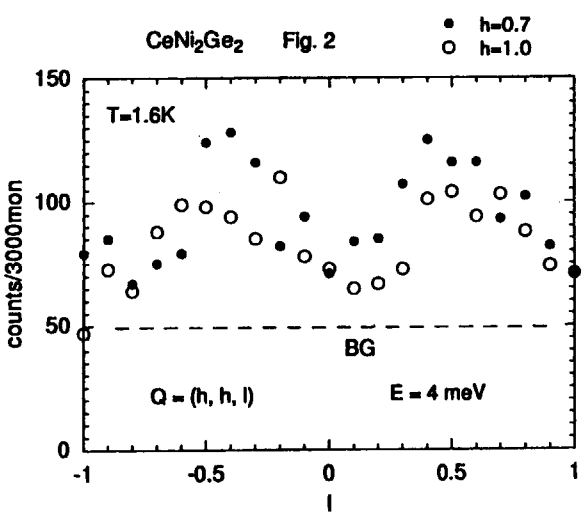

JRR-3M, 4G-TAS, magnetism

研究テーマ：$CsVCl_3$のスピン相関関数
表題：$CsVCl_3$における磁気相関

Magnetic Correlation in $CsVCl_3$

S. Itoh, K. Kakurai[1], Y. Endoh[2], H. Tanaka[3] and K. Nakajima[1]

Neutron Science Laboratory, High Energy Accelerator Research Organization, Tsukuba
[1] Neutron Scattering Laboratory, The University of Tokyo, Tokai
[2] Department of Physics, Tohoku University, Sendai
[3] Department of Physics, Tokyo Institute of Technology

We have been studying the spin dynamics in $CsVCl_3$, an S=3/2, one-dimensional (1D) Heisenberg antiferromagnet, in order to investigate the crossover behavior in the spin dynamics from the quantum (smaller spin) to the classical (larger spin) limits [1, 2]. Classical theory has predicted that the linewidth of the magnetic excitations (Γ) is independent of the 1D momentum transfer (q) and is proportional to the inverse correlation length (κ) at low temperatures, and that Γ is proportional to the temperature (T) as a result of the linear T-dependence of κ. Analyzing the data taken on the chopper spectrometer installed at the spallation neutron source at the Rutherford Appleton Laboratory, we found that, although Γ is independent of q, Γ(T) is different from the classical behavior and it is extrapolated to be finite at low temperatures [2]. In order to obtain an understanding for the behavior of Γ(T), we performed measurements of κ(T).

The neutron scattering experiment was performed on the triple axis spectrometer installed at the 5G beam hole at JRR-3M. The spectrometer was operated in the double-axis mode with E_i fixed to be 30.5 meV using the collimation 15'-20'-20'. The sample was mounted with its 1D reciprocal lattice plane parallel to k_f in order to realize the geometrical condition of the energy-integration at each q. The resolution was measured to be Δq=0.02 r.l.u. (reciprocal lattice unit) at FWHM by removing the PG filter. The q-dependence of the observed intensity was well fitted with the Lorentzian scattering function ($\sim(q^2+\kappa^2)^{-1}$) convoluted with the instrumental resolution. Figure 1 shows κ(T) at T well above the three-dimensional ordering temperature (T_N=13K) obtained by the fitting. In the temperature range ($T>T_N$), the 1D nature can be discussed. As shown in Fig.1, κ(T) is also extrapolated to be finite at low temperatures and behaves classically at high temperatures.

References

[1] S. Itoh, Y. Endoh, K. Kakurai and H. Tanaka, Phys. Rev. Lett. 74 (1995) 2375.
[2] S. Itoh et al., Physica B (1998) in press.

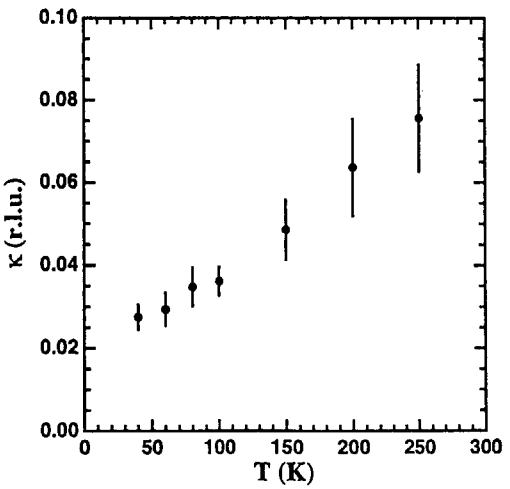

Fig.1 The temperature dependence of the inverse magnetic correlation length in $CsVCl_3$.

研究テーマ：CaV_4O_9、CaV_3O_7の磁気散乱（スピンギャップ研究）
表題：1次元量子スピン系$CuNb_2O_6$のスピンギャップ研究

Study of the Spin-Gap Formation in the Quasi-One-Dimensional Quantum Spin System $CuNb_2O_6$ with Monoclinic Structure

K. Kodama,[1,3] H. Harashina,[1,3] H. Sasaki,[1,3] M. Kato,[1] M. Sato,[1,3]
M. Nishi[2] and K. Kakurai[2,3]

[1]*Department of Physics, Division of Material Science, Nagoya University, Furo-cho, Chikusa-ku, Nagoya 464-8602*
[2]*Neutron Scattering Laboratory, Institute for Solid State Physics, The University of Tokyo, 106-1 Shirakawa, Tokai, Ibaraki 318-011*
[3]*CREST, Japan Science and Technology Corporation (JST)*

$CuNb_2O_6$ has zig-zag chains of edge-sharing CuO_6 octahedra,[1] as shown in Fig. 1, schematically. The chains run along the *c*-axis. The Cu atoms have the valency of +2 and they carry spin S=1/2, forming a quasi-one-dimensional quantum spin system. The system has been reported to have two polymorphs, the orthorhombic (O-) and the monoclinic (M-) phases.[2,3]

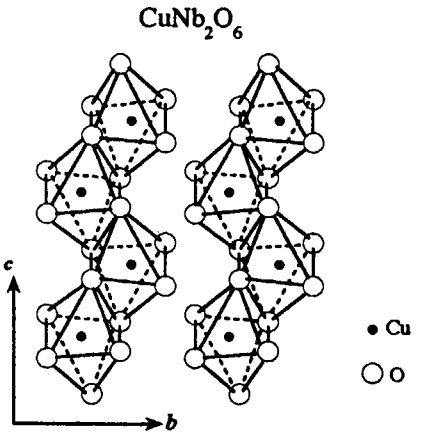

Fig. 1 One-dimensional chains formed of edge-sharing CuO_6 octahedra are schematically shown. Closed and open circle indicate the Cu and O atoms, respectively.

It has been found that the ground state of the M-phase has a spin gap Δ~20 K.[4] We have studied the dynamical magnetic properties of M-$Cu_{1-x}Zn_xNb_2O_6$ (x~0.1) by neutron inelasitc scattering. Because the Zn-substitution does not destroy the spin-gap state,[5] we can discuss the properties by using the results on the Zn-substituted sample.

The measurements were performed on the triple-axis spectrometer ISSP-PONTA at 5G of JRR-3M in Tokai. The dispersion relation of the singlet-triplet excitation along the c^*-direction is shown in Fig. 2. The bottom of the dispersion curve is located at the Q-points with l =0.5, where Q is the scattering vector. This result indicates that the system has ferromagnetic (F)- antiferromagnetic (AF) alternating bond chains. The obtained dispersion curve and the l-dependence of the scattering intensity of the singlet-triplet excitation can qualitatively be explained by a model of the F-AF alternationg bond chain with the exchange parameters determined from the temperature (T) dependence of the magnetic susceptibility χ.

JRR-3M, PONTA (5G), 2. magnetism

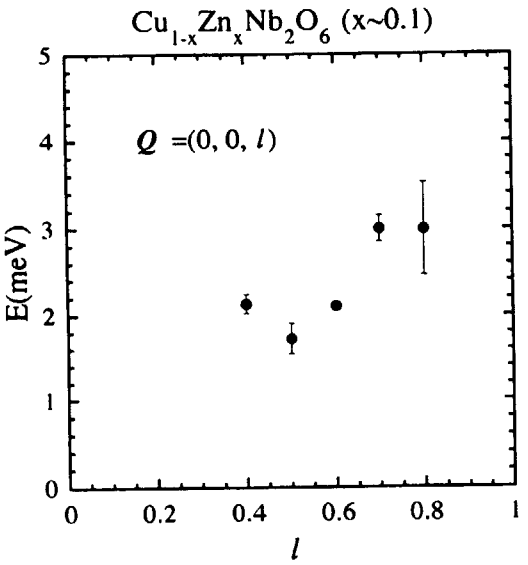

Fig. 2 Dispersion relation along the c^*-(intrachain) direction.

Furtheremore, the another isolated branch with the higher excitation energy was observed. The characterisitcs of the dipersion curve and the l-dependence of the scattering intensity of the higher energy branch can consistently be explained by the exchange parameters state above.[6]

In Fig. 3, the magnetic excitation spectra χ'' at the Q-point where the excitation energy has a minimum value, are plotted as a function of the energy E. The following characteritics of the χ''- E curve can be found : (i) The χ''- E curve becomes concave below about 20 K, which almost corresponds with the characteristic temperture T_0 of the χ-maximum. (ii) The spectral weight softens with decreasing T. The first characteristic indicates that the spin-gap formation (the growth of the singlet correlation) begins at about T_0 with decreasing T. The second one indicates that the antiferromagnetic correlation grows below about T_0 with decreasing T. From these results, it is found that above two kinds of spin correlations, singlet- and AF ones, coexist and grow with decreasing T below T_0.

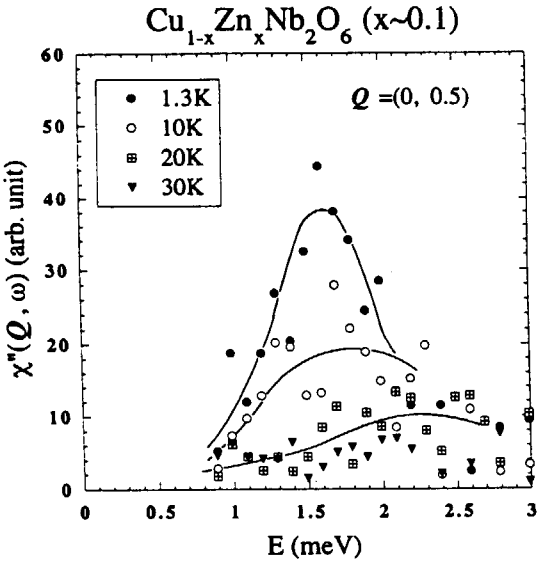

Fig. 3 Magnetic excitation spectra are plotted as a function of E. The data were taken at Q=(0, 0, 0.5), where the excitation energy has a minimum value.

References

1) M. G. B. Drew et al. : J. Mater. Chem. 3 (1993) 889.
2) E. Wahlström et al. : Inorg. Nucl. Chem. Lett. 13 (1977) 559.
3) M. G. B. Drew et al. : J. Mater. Chem. 5 (1993) 1779.
4) K. Kodama et al. : J. Phys. Soc. Jpn. 67 (1998) 57.
5) T. Nishikawa et al. : J. Phys. Soc. Jpn. 67 (1998) No. 6.
6) H. Yokoyama et al. : unpublished data.

課題名：CeNiSnの低エネルギースピンギャップの検証
表　題：近藤半導体CeNiSnのスピンギャップ

Spin Gap of the Kondo Semiconductor CeNiSn

H. Kadowaki and T. Takabatake[1]

Department of Physics, Tokyo Metropolitan University, Hachioji-shi, Tokyo 192-0397
[1]Faculty of Science, Hiroshima University, Higashi-Hiroshima 739

The spin gap of the Kondo semiconductor CeNiSn was clearly observed in the NMR experiment [1] as $1/T_1 \propto T^3$. Since this quantity is essentially the same as zero frequency limit of neutron cross-section, the gap can be measured by neutron [2]. However it is difficult to observe the gap spectrum because of weak signal and strong incoherent elastic scattering of Ni. To reduce incoherent scattering an isotope Ni was used to prepare the sample. Energy spectra have been measured by the cold-guide 3-axis HER with the horizontally curved analyzer configuration [3], which enhances counting rate about an order. Result is shown in the figure. One can see that the spectrum form at T = 1.6 K and the temperature dependence definitely show gap-type features.

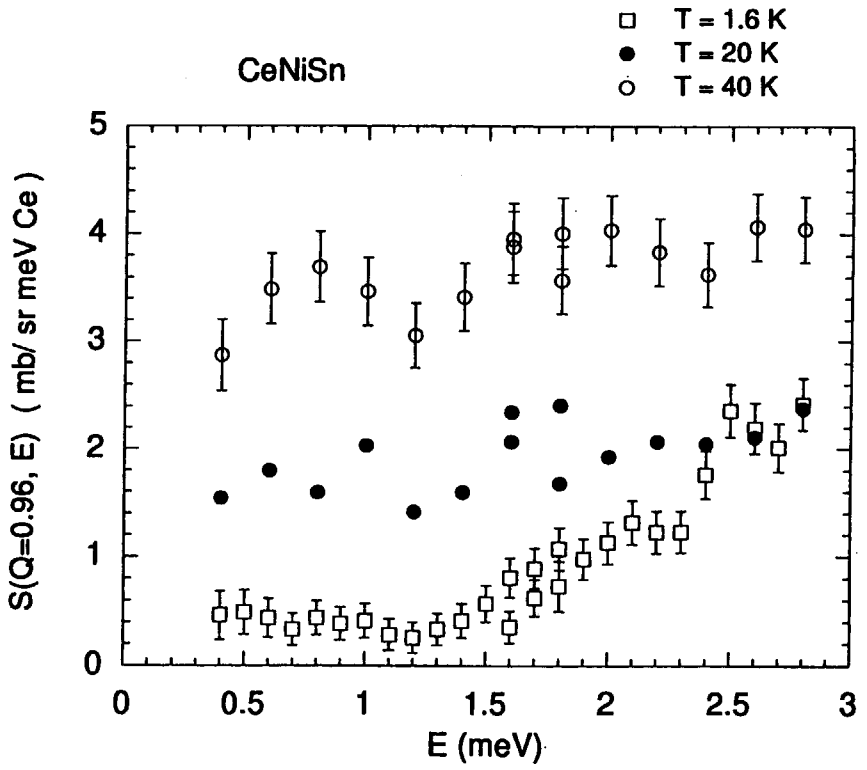

References

[1] M. Kyogaku et al.: J. Phys. Soc. Jpn. **59** (1990) 1728 and **61** (1992) 43
[2] T. J. Sato et al.: J. Phys. Condens. Matter **7** (1995) 8009
[3] H Kadowaki: Activity report on neutron scattering (ISSP-NSLab) **3** (1996) 222 and **4** (1997) 37

JRR-3M, C1-1-HER, magnetism

研究課題：低濃度キャリアー近藤系$Ce_{0.9}La_{0.1}P$の磁気構造に対するLa置換効果
表　題：低濃度キャリアー系$Ce_{0.9}La_{0.1}P$の結晶場の圧力効果

Impact of La substitution on the magnetic structure of a low-carrier-density Kondo system: $Ce_{0.9}La_{0.1}P$

M. Kubota,[1] Y. Oohara,[1] H. Yoshizawa,[1]
N. Mōri,[2] H. Takahashi,[3] A. Uesawa,[4] and T. Suzuki[4]
[1]NSL, I.S.S.P., University of Tokyo, Tokai, Ibaraki 319-1106
[2]I.S.S.P., University of Tokyo, Roppongi, Minato-ku, Tokyo106-0032
[3]College of Humanities and Sciences, Nihon University, Setagaya-ku, Tokyo 156
[4]Department of Physics, Tohoku University, Aoba-ku, Sendai 980-8578

The La substituted system, $Ce_xLa_{1-x}P$ with $x = 0.1$ has been studied and the P–T phase diagram has been established. Figure 1 shows the $P-T$ phase diagram of $Ce_{0.9}La_{0.1}P$. In the overall this phase diagram is very similar to that of CeP. Above the critical pressure P_C ~0.8 GPa, a ferromagnetic component appears in the magnetic structure. The La substitution causes a negative pressure due to the larger radius of the La ion than that of the Ce ion, and this effect well explains the increase of P_C from ~ 0.25 GPa for CeP to ~0.8 GPa for $Ce_{0.9}La_{0.1}P$.[1)] Below P_C, $Ce_{0.9}La_{0.1}P$ has the type–I antiferromagnetic structure "↑↓↑↓", where magnetic moments are ordered ferromagnetically within (100) planes in the x-domain, and such ferromagnetic (100) sheets are stacked antiferromagnetically along the [100] direction. Above P_C, on the other hand, the LPS magnetic ordering coexists with the ferromagnetic component, and its periodicity becomes shorter as the pressure is increased. Above ~2.6 GPa, the magnetic structure converges to the type–IA structure "↑↑↓↓".

As a function of temperature, $Ce_{0.9}La_{0.1}P$ exhibits two ordered phases in the $P-T$ phase diagram; the intermediate (IM) phase below T_{C2} and the low temperature (LT) phase below T_{C1}. Note that we use the same notation of Ref. 2 for the two transition temperatures, T_{C2} and T_{C1}. We also performed ac susceptibility measurements in order to independently determine the transition temperature T_{C2}, and the results were in good agreement with those of neutron diffraction measurements. Although a detailed characterization of the LT phase will be published elsewhere, we emphasize that the transition at T_{C1} in $Ce_{0.9}La_{0.1}P$ is strongly first order.

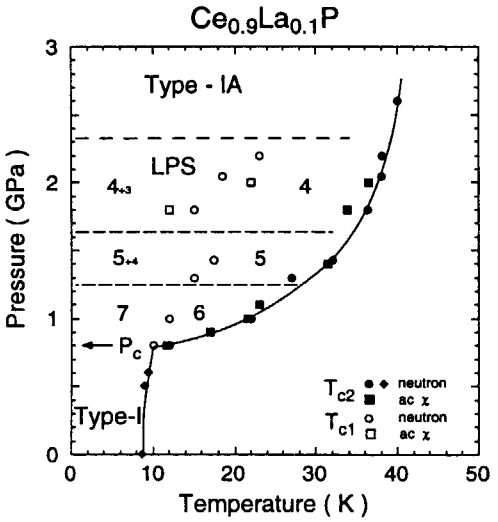

Figure 1: $P-T$ magnetic phase diagram for $Ce_{0.9}La_{0.1}P$. The numbers in the phase diagram denote the period of the LPS structures. The solid curves indicate the phase boundary between the paramagnetic and type-I antiferromagnetic phase below P_C and that between the paramagnetic and IM phase of the LPS ordering above P_C, respectively. The transition temperatures at T_{C2} and at T_{C1} are denoted by filled and open symbols, respectively.

This system exhibits distinct hysteresis upon entering the LT phase, and a few LPS structures coexist at low temperatures. The severe hysteresis prevented us from determining the phase boundary between the IM and LT phases. This should be compared with CeP where the transition to antiferromagnetic ordering on the Γ_7

cites at T_{C1} was reported to be close to second order, and the phase boundary T_{C1} is smooth and is almost parallel to the pressure axis.[2)]

Figure 2 shows typical diffraction patterns along the (h11) direction at selected pressures. These scans provide information on the stacking of the ferromagnetic (100) layers along the [100] direction in the LPS ordering. These patterns indicate that the LPS ordering has a period of 5 layers and 4 layers at 1.4 GPa and at 2.2 GPa, respectively. The insets in Fig. 2 show diffraction patterns along the in-plane direction of the (100) plane. Because the linewidths of the profiles perpendicular and parallel to the (100) plane are resolution-limited, we can establish that the ordering in the IM phase is truly long-range order.

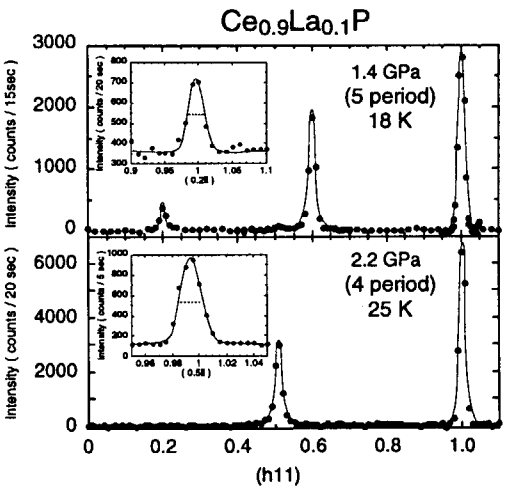

Figure 2: Typical profiles for the LPS ordering in the IM phase at 1.4 and at 2.2 GPa. The curves shown are guides to the eye.

In order to explore the influence of the La substitution on the LPS ordering, we have analyzed the magnetic structures in the IM phase of $Ce_{0.9}La_{0.1}P$, and found that the 5 period LPS structure in the IM phase is close to a sinusoidal modulation, but it is strongly squared up in the LT phase. By evaluating the spin correlation functions, we can further demonstrate that the consecutive paramagnetic layers of the CeP structure do not exist in the IM phase of $Ce_{0.9}La_{0.1}P$. We denote the spin-spin pair correlation function for ferromagnetic layers with the distance δ as $\langle S(\mathbf{o})S(\delta)\rangle$. If there were consecutive paramagnetic layers, the strong condition that $\langle S(\mathbf{o})S(\boldsymbol{a})\rangle \equiv 0$ would always hold for $\delta = \boldsymbol{a}$, where $\boldsymbol{a}$ is a lattice constant. By evaluating the correlation functions for the LPS ordering with the 4- and 5-layer period, we obtained that $\langle S(\mathbf{o})S(\boldsymbol{a})\rangle_4 = 0.20(\pm 0.11)$, and $\langle S(\mathbf{o})S(\boldsymbol{a})\rangle_5 = 0.18(\pm 0.07)$, respectively. Since $\langle S(\mathbf{o})S(\boldsymbol{a})\rangle \neq 0$ for both cases, we exclude the possibility of the consecutive paramagnetic layers in the IM phase of $Ce_{0.9}La_{0.1}P$. Clearly, these results demonstrate that the La substitution causes a drastic change of the actual spin arrangement in the LPS ordering in $Ce_{0.9}La_{0.1}P$.

A natural question one may ask is what determines the periodicity of the LPS ordering. If the competition between the nesting effects and the commensurability is a major driving force for the LPS ordering, it should be possible to continuously change the LPS periodicity in a real material. We observed such a continuous change in the periodicity of the type–IA ordering at 2.2 GPa (not shown). At T_{C2}, the magnetic superlattice peak appears at the incommensurate position. With decreasing temperature, it quickly shifts and is locked in at the commensurate position $h = 1/2$. In the heating process, however, the peak position is completely locked. This result is a clear manifestation of the competition between the Fermi surface nesting effect and the commensurability effect. Considering all available experimental results and existing theories, we conclude that the $p-f$ mixing interaction and the Fermi surface nesting effect are two indispensable ingredients to account for the unusual LPS ordering in CeP and $Ce_{0.9}La_{0.1}P$, but the precise mechanism of the formation of the LPS ordering and especially the origin of the ferromagnetic double layer in the parent material CeP should be further examined.

References

[1] N. Mōri *et al.*, Physica B **186-188**, 444 (1993).

[2] M. Kohgi *et al.*, J. Phys. Soc. Jpn. **65** Suppl.B, 99 (1996); T. Osakabe *et al.*, Physica B **230-232**, 645 (1997).

研究テーマ：CeRh2Si2の圧力誘起超伝導と磁気揺らぎの研究
表題：CeRh2Si2の反強磁性の圧力効果

The pressure dependence of the antiferromagnetism in $CeRh_2Si_2$

M.Sato, N.Chigusa, S.Kawarazaki, Y.Miyako, [A]Y.Koike, [A]N.Metoki and [B]M.Nishi
Department of Earth and Space science, Osaka University, Toyonaka, Osaka 560-0043
[A]Advanced Science Reserch Center, Japan Atomic Energy Research Institute, Tokai, Ibaraki 319-1195
[B]Institute for Solid State Physics, Tokyo University, Tokyo 106-0032

The ternary intermetalic compound $CeRh_2Si_2$ crystallizes in the $ThCr_2Si_2$ -type structure (space group I4mmm, body centered tetragonal). It is an antiferromagnet with two transitions at 36K(T_{N1}) and 25K(T_{N2}). The first phase at $T_{N1}>T>T_{N2}$ has a magnetic modulation with a wave vector **q**1=(0.5,0.5,0). The second phase which appears at $T<T_{N2}$ has two kinds of magnetic modulations at once, whose wave vectors are **q**1 and **q**2=(0.5,0.5,0.5) respectively. In order to determine the ground magnetic structure of the second phase, we reexamined the results of neutron diffraction experiments by comparing them with the recent NMR results[1], and consequently concluded that it consists of three domains which have modulation vectors of **q**1$\pm$=($\pm$0.5,0.5,0) and q2, respectively.[2]

On the other hand, the antiferromagnetism of this compound is sensitive to pressure in spite of its high Neel temperature. Previous electrical resistance measurements under hydrostatic pressure revealed that the transition disappears around P_C=10kbar.[3] The recent topics of this compound is a superconductivity induced by pressure around Pc below T_C=0.4K.[4] But up to now this superconductivity was observed only in polycrystalline samples. In oreder to study what is happening in this compound around the critical pressure, we performed neutron scattering experiments under hydrostatic pressure on single crystalline sample with good quality. The experiments were carried out by using TAS1 and GPTAS. The results shown in figure indicates the pressure-dependence of T_{N1},T_{N2} and saturated value of the magnetic moment. As increasing pressure, the second phase disappears around 7kbar at first, and then the first phase disappears around 11kbar. The value of critical pressure is consistent with the results of previous studies. The magnetic moment decreases as increasing pressure and disappears above 11kbar.

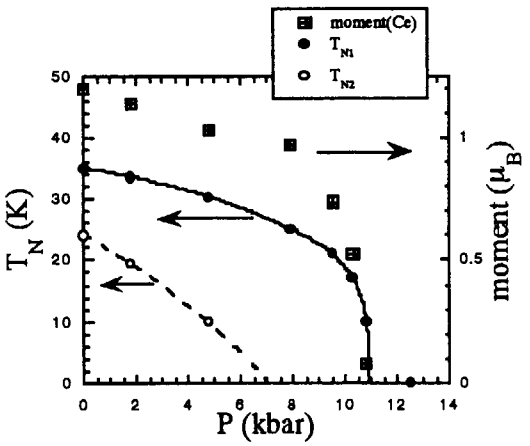

References :

[1]Y.Kawasaki *et al.* unpublished
[2]S.Kawarazaki *et al.* to be published
[3]J.D.Thompson *et al.* J.Magn.Magn.Mat 54-57 (1986) p.377 *etc.*
[4]R.Movshovich *et al.* Physica B 223&224 (1996) p.126

JRR-3M, GPTAS(4G), TAS-1, 2.magnetism

研究課題：磁性体における多重磁気モードの研究
表題：$(Cr_{1-x}Mn_x)_2As$における多重磁気モード

Multi-magnetic-mode in $(Cr_{1-x}Mn_x)_2As$

Y.Yamaguchi,K.Ohoyama,T.Kanouchi,M.Ohashi,and K.Ishimoto
Institute for Materials Research,Tohoku University, Katahira, Sendai 980-77

A series of intermetallic compounds (Cr1-xMnx)2As crystallize in Cu2Sb-type structure in which there are two cation sites, A and B. The magnetic structure of Cr2As is very interesting. Since isotropic exchange interactions cancel out between site-A and B cation and only an anisotropic one remains finite between them. Magnetic moments of site-B Cr align at the Neel temperature. On the other hand those of site-A Cr order below Tt=175K, and that the magnetic anisotropy of site-B Cr becomes very large below Tt through the anisotropic exchange interaction.

Compounds of (Cr1-xMnx)2As show antiferromagnetism, and the Neel temperatures are 393K for x=0.0 (Cr2As) and 430K for x=0.5 (CrMnAs). Magnetic structure, which is denoted by a propagation vector q of the magnetic ordering, is different between Cr2As, q=[0,0,1/2], and CrMnAs, q=[0,0,1]. In the x-dependence of the Neel temperature, there is a minimum around x=0.23. Therefore we expect that a magnetic structural change takes place and some interesting phenomena will appear around this concentration.

In the present investigation, HERMES diffractometer was used on six powder specimens of (Cr1-xMnx)2As with x between 0 to 0.5. Temperature of the specimens was changed using a refrigerator from 15 up to 500K.

On the typical case of x=0.23, diffraction patterns and its temperature dependence indicate that there are three magnetic ordered phases as shown in Fig.1. Below Tt1=170K site-A aligns in a collinear structure with q=[0,0,1/2] whereas site-B takes a spiral structure of q=[0,0,p] with p=0.815 at low temperature and p gradually approaches to 1 at Tt2=190K. Above Tt1 site-A is paramagnetic, while site-B aligns in above mentioned spiral structure and transforms to a collinear structure with q=[0,0,1] at Tt2. This collinear structure continues up to TN=320K.

There are some characteristic features of the magnetic structures observed in (Cr1-xMnx)2As system. First one is independent magnetic ordering between site-A and B cations. Second, magnetic structure of site-B transforms from q=[0,0,1/2] at x=0.0 to q=[0,0,1] at x=0.5 through spiral structures. Third, magnetic structure of site-A is kept in collinear q=[0,0,1/2] mode for the whole region of this system.

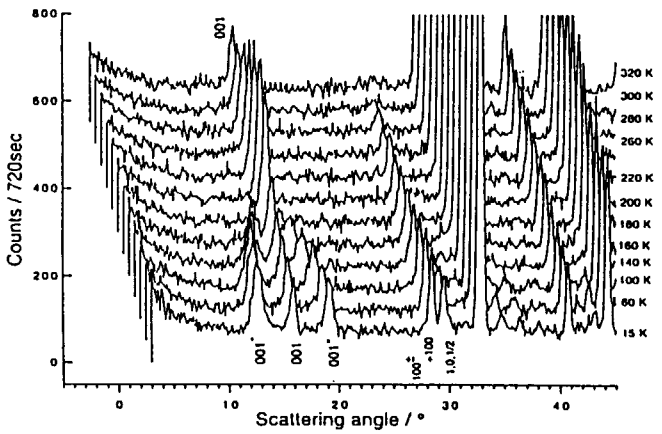

Fig.1
Temperature dependence of neutron diffraction pattern on $(Cr_{0.77}Mn_{0.23})_2As$.

Reactor:JRR-3M Facility: HERMES(KPD) Field: 2.Magnetism

課題名：スピン量子数S=1/2&1スピン交替フェリ磁性鎖の磁性

表　題：スピン量子数S=1/2&1スピン交替フェリ磁性鎖$NiCu(pba)(D_2O)_32D_2O$の研究

Study of an S=1/2 and 1 ferrimagnetic chain compound $NiCu(pba)(D_2O)_32D_2O$

M. Hagiwara[1], K. Kakurai[2], K. Minami[3], Y. Narumi[4,5], K. Tatani[5] and K. Kindo[5,4]

[1]The Institute of Physical and Chemical Research (RIKEN), Wako, Saitama 351-0198
[2] Neutron Scattering Laboratory, ISSP, University of Tokyo, 106-1 Shirakata, Tokai 319-1195
[3]Graduate School of Mathematics, Nagoya University, Nagoya 464-8602
[4]CREST, Japan Science and Technology Corporation (JST), Kawaguchi, Saitama 332-0012
[5]KYOKUGEN, Osaka University, Toyonaka 560-8531

We have investigated magnetic properties of powder samples of $NiCu(pba)(D_2O)_32D_2O$ (pba=1,3-propylenbis(oxamato)) which is one of the prototypical examples of an S=1/2 and 1 ferrimagnetic chain. The plot of magnetic susceptibility (χ) times temperature (T) versus T shows a rounded minimum at about 70 K as shown in Fig.1. The experimental data are compared with a numerical calculation (exact diagonarization 10sites) and the magnitude of the nearest neighbor exchange constant is evaluated as J/k_B=121 K (10.4 meV)[1].

Recent theoretical studies on an S=1/2 and 1 ferrimagnetic chain show that one of the excited branches which is gapped lies higher than that deduced from a conventional spin wave theory. From a reliable calculation, the gap (Δ/J) has been evaluated to be 1.767. In order to verify this theoretical investigation, we performed a neutron scattering experiment on this compound in which the gapped excitaion branch is predicted to exist at about 18.4 meV.

Deutrated powder samples of $NiCu(pba)(D_2O)_32D_2O$ were synthesized according to a reported method[2], and the hydrogen atoms in pba ligand were not replaced by deutron atoms.

Neutron scattering measurements were carried out using ISSP-PONTA spectrometer and the Orange-crio cryostat. Figure 2 depicts the subtracted spectra, I(T=2 K) minus Bose-factor corrected I(T=250K), for designated values of Q ($Å^{-1}$). Since two rounded maxima around 10 meV and 19 meV seem not to vary with the Q values, we can not assign these excitations to be of magnetic origins. Further study using the sample in which all the hydrogen atoms replaced by deutron ones is needed.

[Reference]
1) M. Hagiwara et al. : J. Phys. Soc. Jpn. (in press)
2) Y. Pei et al. : Inorg. Chem. 26 (1987) 138.

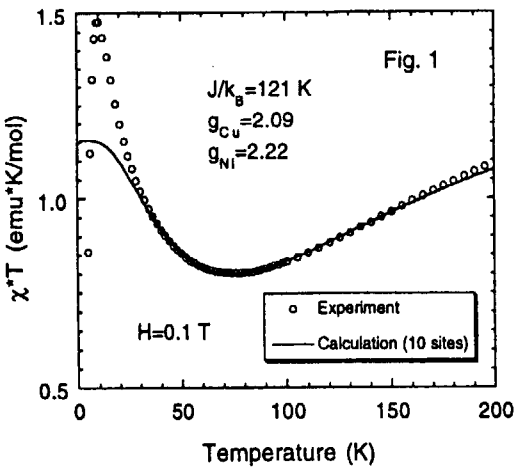

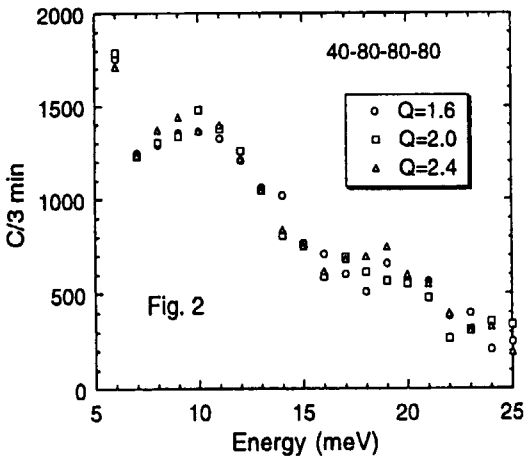

JRR-3M, PONTA (5G), Magnetism

研究テーマ：インターカレーション化合物の結晶構造と磁性
表　　題：Fe_xTiS_2化合物の結晶構造と磁性

Crystal Structure and Magnetic Property of Fe_xTiSe_2 Compounds

M. Shintomi[1], Y. Tazuke[1], H. Takahashi[1], Y. Morii[2] and K. Hojou[2]

[1]Faculty of Engineering, Ibaraki University, Hitachi, Ibaraki 316-8511
[2]Japan Atomic Energy Research Institute, Tokai, Ibaraki 319-1195

$TiSe_2$ consists of repetitions of Se-, Ti- and Se-layers, forming hexagonal CdI_2 structure. 3d transition elements, M, are intercalated in the van der Waals gaps (hereafter called as M-layers) between neighboring Se-layers, forming intercalated compounds M_xTiSe_2.[1,2] $Fe_{0.1}TiSe_2$ is paramagnetic in ref.-1, whereas it showed spin glass behavior in ref.-2. In order to elucidate the discrepancy, we have studied Fe_xTiSe_2 crystallographically and magnetically.

In conventional studies it has been assumed that M-atoms are located in the M-layers and the Ti-atoms are located in the Ti-layers as in pure $TiSe_2$. Since the discrepancy may be due to the difference in crystal structure, it is necessary to verify this assumption, and two experiments have been done. In the first experiment $Fe_{0.1}TiSe_2$ samples were prepared from two kinds of starting materials: a mixture of Fe- and $TiSe_2$-powders as in ref.-1, and a mixture of Fe-, Ti- and Se-powders as in ref.-2. Other conditions of sample preparation were kept identical. No difference was found in the susceptibility in 4.2 K$\leqq T\leqq$300 K. This result have suggested that Ti-atoms are located in the Ti-layers in both kinds of samples.

In the second experiment powder neutron diffraction spectrum of $Fe_{0.2}TiSe_2$ was obtained by HRPD-spectrometer located in JAERI-Tokai at room temperature. Fig. 1 shows obtained spectrum. The sample was prepared from a mixture of Fe-, Ti- and Se-powders and after heat-treatment at 750℃ it was rapidly quenched to room temperature. By this method we can reasonably assume that the metal atoms are randomly distributed in the two possible metal layers. The purpose of the experiment is to discriminate among three possible structures. A-structure : Ti- and Fe-atoms are located in the Ti- and M-layers, respectively. B-structure : Ti- and Fe-atoms are randomly distributed both in the Ti- and M-layers, with the M-layers containing 0.2 moles of metal atoms. C-structure : the M-layers contain 0.2 moles of Ti-atoms and the remaining metal atoms are randomly distributed in the Ti-layers.

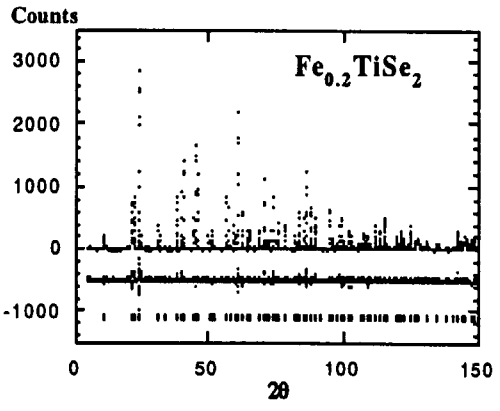

Fig. 1. Neutron diffraction spectrum of $Fe_{0.2}TiSe_2$ at 300K

The reason for selecting the composition of x=0.2 is that we can easily distinguish the A-

structure from B- and C-structures: for the A-structure (001), (111) and several other diffraction lines are expected to be strong, whereas they are expected to be feeble for B- and C-structures. The spectrum shows strong (001) and (111) diffraction lines. Rietveld analyses are done for the three structures by a program presented from Dr. F. Izumi. The A-structure reproduces the spectrum with the R-factor of 0.11 and reasonable values of thermal parameters are obtained. B- and C-structures do not reproduce (001) and (111) lines, and values of thermal parameters are not reasonable.

The results of magnetic experiments and neutron diffraction measurements consistently show that Fe-atoms are intercated into the M-layers. In the subsequent studies, all the powder samples of Fe_xTiSe_2 were prepared from Fe-, Ti- and Se-powders.

Effect of heat-treatment condition on the magnetic property of $Fe_{0.1}TiSe_2$ was Studied. For this purpose the samples were slowly cooled to room temperature after reaction at 750℃, other than rapidly quenching. The rapidly quenched sample showed paramagnetic behavior in 4.2 K≦ T≦300 K. Slowly cooled samples showed susceptibility maximum around 10 K. This temperature is much lower than that, 24 K, reported in ref.-2. The present result has reasonably suggested that in the slowly cooled sample the Fe-atoms are not randomly distributed in the M-layers. Rather, they form clusters, and these clusters give the susceptibility maximum.

Magnetizations were measured for rapidly quenched samples of various compositions x in 4.2 K≦T≦300 K. For 0.15≦x≦0.5 susceptibility maximum was observed. For x=0.15 and 0.2 the forms of the maximum are rounded and below the temperature T_m of the maximum the magnetization was a function of time, suggesting that the susceptibility maximum is due to spin glass transition.[2] For $0.22 \leqq x \leqq 0.5$ the susceptibility maximum is sharp and no time-dependent magnetization was observed. The susceptibility maximum for this composition range may be due to antiferromagnetic transition. Fig. 2 shows tentative T-x magnetic phase diagram.

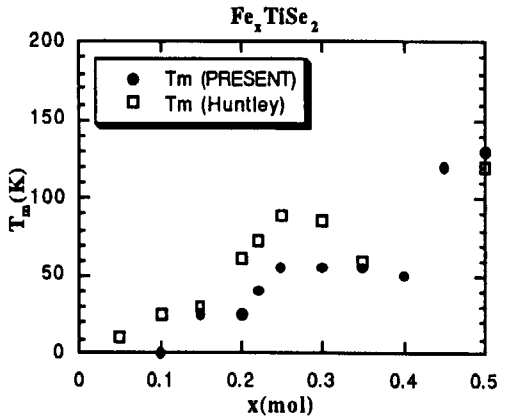

Fig. 2. T-x magnetic phase diagram of Fe_xTiSe_2

Detailed magnetic experiments are in progress. The authors thank Dr. S. Funahashi for neutron diffraction experiment and Miss M. Fukase for magnetic measurements.

References

1) Y. Tazuke and T. Takeyama: J. Phys. Soc. Japan **66** (1997) 827.

2) D. R. Huntley, M. J. Sienko and K. Hiebl: J. Solid State. Chem. **52** (1984) 233.

原子炉：JRR-3M　　装置：HRPD　　分野：中性子散乱（磁性）

研究テーマ：フラストレート磁性体 RMn_2 の磁気構造と格子歪み

表　　題：YMn_2 および関連化合物の磁気構造と格子歪み

The Magnetic Structure and Lattice Distortion of YMn_2 and Related Compounds

M. Shiga, H.Nakamura and N.Metoki[1]

Department of Materials Science and Engineering , Kyoto University, Kyoto 606-8501
[1]Japan Atomic Energy Research Institute, Tokai, Ibaraki 319-11

YMn_2 is an antiferromagnet with a helical modulation of an extremely long period (430Å). The magnetic wave vector can be described as (τ 01) [1]. Recently, we found a substitution of small amount of Tb leads to a change of the direction of the helical modulation from [100] to [110][2]. The origin of such a long period helical modulation has not yet been understood. In order to know the factors to determine the spin structure, we carefully measured the period of helical modulation and degree of the tetrahedral distortion for YMn_2 at several temperatures, and those for $Y_{0.97}Tb_{0.03}Mn_2$, $Y(Mn_{1-x}Al_x)_2$ at 10K by using a high resolution powder diffracto-meter and a low-energy triple-axis spectrometer. We discuss the correlation between these two properties and the origin of helical modulation.

In this year, we measured neutron diffraction of $Y(Mn_{0.03}Al_{0.03})_2$ at 10K and room temperature using HRPD with the wave length of 1.1624Å. However, we were not able to obtain clear results to discuss the helical modulation and tetragonal distortion because each Bragg peak becomes fairly broad by only 3% substitution of Al, suggesting strong disturbance of lattice by substitution Al for Mn. We did not observe splitting of magnetic peaks and (400) nuclear peak, which were clearly observed in YMn_2 and $Y_{0.97}Tb_{0.03}Mn_2$

In this report, we summarize the results so far obtained in the series of the present study and discuss the relation between period of helical modulation and degree of lattice distortion. Figure 1 shows the value of τ vs. 1−a/c of YMn_2 at several temperature and rare earth doped compounds including data obtained by other authors. It is interesting to note that data for Tb and Ce doped YMn_2 lie on the same line with those for YMn_2 at different temperatures. We believe that these observation implies that lattice distortion could be an important factor to determine the helical modulation as proposed by Giebultowicz at al for fcc antiferromagnet[3].

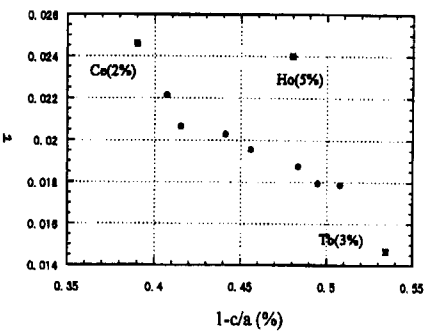

Fig.1 Propagation vector τ against 1-a/c. Closed circles are values for YMn_2 at different temperatures. Closed squares are for rare-earth doped YMn_2 at low temperature

References

[1] R.Ballou et al, J. Magn. Magn. Mater. 70 (1987) 129.
[2] H.Nakamura et al, J. Magn. Magn. Mater. 163 (1996) L1.
[3] C.Ritter et al., Physica B 234-236 (1997) 596.
[4] T.M.Giebultowicz et al., Phys.Rev.B 46 (1992) 1207.

原子炉：JRR-3M　　HRPD(1G)　　分野：中性子散乱（磁性）

研究テーマ： γ-Mn 合金の結晶変態と磁気構造
表題： γ-MnM, (M=Pt, Pd and Rh) 合金の斜方晶相における磁気構造

Magnetic structure of Orthorhmbic Phase in γ-MnM, (M=Pt, Pd and Rh) alloys

T. Hori, Y. Tsuchiya[1], S. Funahashi[1*], Y. Shimojo[1], H. Shiraishi and K. Hojou[1]
Shibaura Institute of Technology, Oomiya, Saitama 330-8570
[1]Japan Atomic Energy Research Institute, Tokai, Ibaraki 319-1106

As is well known, most Mn-rich γ - Mn alloys undergo a distortion from the face centered cubic structure to the face centered tetragonal (f.c.t.) structure with *c/a* < 1 below the Néel temperature. In some cases the distortion to the f.c.t. with c/a > 1 is also observed. In the γ - MnNi alloys, there is a face centered orthorhombic (f.c.o.) region in addition to the f.c.t. regions with *c/a* < 1 and *c/a* > 1 [1]. Recently, the present authors [2] have found that these three regions exist in the γ - MnGa alloys, and determined a non-collinear magnetic structure with 4 sublattices for the f.c.o. phase. The *a*, *b* and *c*-axis components of the magnetic moments, μ_a, μ_b and μ_c are as follows: $\mu_c^2 > \mu_b^2 > \mu_a^2 = 0$ in the f.c.o. structure with $a > b > c$.

We also found that there is the f.c.o. phase in the γ - MnPt with 8 at% Pt, γ - MnPd with 10 at % Pd and γ - MnRh with 10 at % Rh alloys. Neutron diffraction experiments for the powder samples were made by using the HRPD and TAS II diffractometers in the JRR-3M reactor at JAERI. For example, the neutron diffraction pattern using the HRPD at 10 K is shown in Fig. 1. The pattern is explained by assuming the f.c.o. structure with a = 3.807, b = 3.748 and c = A and a non-collinear antiferromagnetic structure with $\mu_a = 0$, $\mu_b = 1.27$ and $\mu_c = 2.38\ \mu_B$ / Mn atom. The angle between the c-axis and magnetic moment, θ, is 32°. We measured the temperature dependence of these lines using the TAS II Although the 110 and 101 reflections for the γ - MnPt with 8 at% Pt were not distinguishably split. We obtained the intensities, I_{110} and I_{101}, by a curve fitting analysis using the double Gaussian functions, and determined the magnetic moment form the I_{110} and I_{101} intensities. The magnetic moment decreases with increasing temperature and vanishes at 510 K which is the Néel temperature. We have also determined magnetic structure for γ - MnPd with 10 at % Pd and γ - MnRh with 10 at % Rh alloys. The results are summarized in table 1.

Jo et al. [3] have proposed a theoretical phase diagram and magnetic structures for various γ - Mn alloys on the basis of Landau expansion of the free energy. For example, three-axis components of the magnetic moments, μ_a, μ_b and μ_c in the f.c.o. structure with $a > b > c$ are as follows; $\mu_c^2 > \mu_b^2 > \mu_a^2$. The results in the present experiments are very consistent with this theory.

Table 1. Magnetic structures

Alloys	Magnetic moments per Mn atom (μ_B) μ_a	μ_b	μ_c	θ
MnPt	0	1.27	2.01	32°
MnPd	0	1.01	1.71	31°
MnRh	0	1.24	2.04	31°

References

[1] N. Honda, Y. Tanji and Y. Nakagawa, J. Phys. Soc. Jpn **41** (1976) 1931
[2] T. Hori, Y. Morii, S. Funahashi, H. Niida, M. Akimitsu and Y. Nakagawa; Physica **B 213&214** (1995) 354.
[3] T. Jo and K. Hirai, J. Phys. Soc. Jpn **55** (1986) 1614.

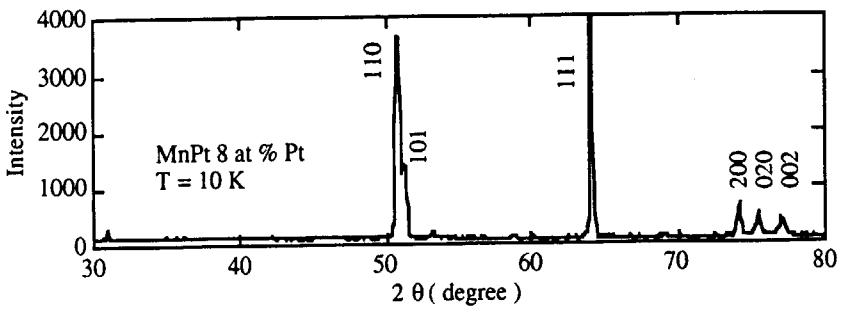

Fig. 1. Neutron diffraction pattern for the γ - MnPt with 8 at % Pt at 10 K.

原子炉：JRR-3M　　装置： HRPD (1G), TAS-2 (2G)　　分野：磁性

1. 中性子散乱 (Neutron Scattering)

2) 高分子 (Polymer)

This is a blank page.

課題名：高分子の結晶構造とダイナミックス

表　題：重水素化ポリエチレンの中性子構造解析

Neutron Structure Analysis of Poly(vinyl Alcohol)

Yasuhiro Takahashi

Department of Macromolecular Science, Faculty of Science,
Osaka University, Toyonaka, Osaka 560, Japan

C. W. Bunn[1] analyzed the crystal structure of atactic poly(vinyl alcohol), in which OH groups are statistically located on both sides of the molecular plane. Thereafter, Sakurada et al.[2] proposed the crystal structure, which is different in the azimuthal angle of the molecular plane and hydrogen bonding network from Bunn's model. In Fig. 1, two crystal structure models are shown. In neutron diffraction, the hydrogen atoms contributes to the diffraction intensity more than X-ray diffraction. Therefore, it may be possible to determine the azimuthal angle more accurately than X-ray diffraction and to clarify the position of the hydrogen atoms associated with hydrogen bonds.

The commercially supplied poly(vinyl alcohol) fibers were used as the sample. Neutron diffraction experiments were made in Japan Atomic Energy Research Institute (JAERI). Intensity distribution on the equator was measured by using λ = 1.8232 A every 0.05° from 2θ = 5° to 165° at 100K, 200K and room temperature. As 2θ increased the inelastic contribution was found to increase, i. e., the peaks not to be indexed appear. Therefore, the intensity distributions from 5° to 100° were used. Integrated intensities were estimated after the indices assigned to each peaks.

First, X-ray structure refinement was carried out under assumption of rigid body, by using the intensity data reported by Nitta et al.[3] The refinement converged to the discrepancy factor R = 10.9 %. The converged structure is shown by broken lines in Fig. 2. The structure is essentially the same as that reported by Nitta et al. which support to the Bunn's model.

The structure refinements under assumption of rigid body were made by using neutron intensity data at 100K, 200K, and room temperature. Here, the hydrogen atoms associated with the hydrogen bonds are not incorporated into the refinements. The discrepancy factors are 28.6 %, 23.9 %, and 29.5 % for the intensity data at 100K, 200K, and room temperature, respectively. The results are shown in Fig. 2. The structures are essentially the same as that obtained by using X-ray diffraction data. This suggests clearly that the Bunn's model is

JRR-3M, HRPD, 6.polymer

correct structure. Furthermore, the difference synthesis (F_o - F_c) synthesis was carried out by using the intensity data at 100K. The contour map is shown in Fig. 3. It is possible to find three peaks on the map which may be associated with the hydrogen bonds. Peak A should be assigned to the hydrogen atom associated with the hydrogen bonds between two molecules faced each other in the unit cell. Murahashi et al.[4] proposed the intramolecular hydrogen bond for isotactic poly(vinyl alcohol). Peak B should be assigned to the intramolecular hydrogen bond in the isotactic sequence of atactic poly(vinyl alcohol). Peak C should be assigned to the intramolecular hydrogen bonds and intermolecular hydrogen bonds between neighboring unit cells.

1) C. W. Bunn, Nature, **161**, 929 (1948).
2) I. Sakurada et al., Bull. Inst. Chem. Res., Kyoto Univ., **23**,78 (1950).
3) I. Nitta et al., Ann. Rep. Inst. Fiber Sci., **10**, 1 (1957).
4) S. Murahashi et al., J. Polymer Sci., **62**, S77 (1962).

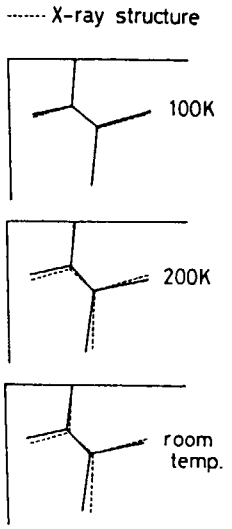

Fig. 2

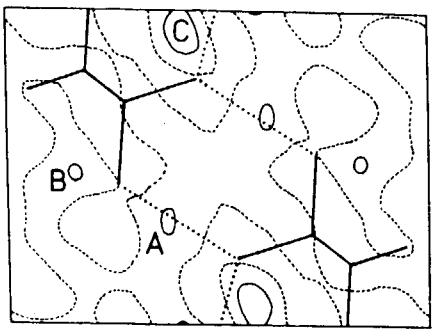

Fig. 3

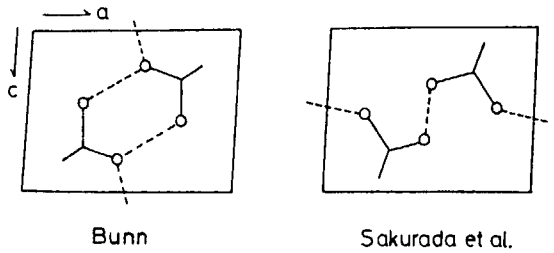

Figure 1. Crystal structure models of atactic poly(vinyl alcohol) proposed by (a) Bunn[1] and (b) Sakurada et al.[2] Broken lines show hydrogen bonds.

課題名：高分子の結晶構造とダイナミックス

表　題：ポリビニルアルコールの中性子構造解析

Neutron Structure Analysis of Deuterated Polyethylene

Yasuhiro Takahashi

Department of Macromolecular Science, Faculty of Science, Osaka University, Toyonaka, Osaka 560, Japan

The crystal structure of polyethylene was reported by Bunn in 1939.[1] Thereafter, many works have been done on the polyethylene. During these works, the accurate crystal structure, the accurate angle φ: the azimuthal angle of the molecular plane with respect to the b-axis, was required. In the present study, the accurate crystal structure analysis of deuterated polyethylene was carried out by neutron diffraction method.

Neutron diffraction experiments were carried out by TAS-2 and HRPD equipped on JRR-3M installed on Japan Atomic Energy Institute.
Intensity distributions on the equator were measured at 10K, 100K, 200K, 300K by using λ = 1.823 Å. The numbers of the observed reflections were 17, 17, 17, and 18 for 10K, 100K, 200K, 300K, respectively.

The accurate unit cell dimensions, a and b, were estimated by the least-squares method (Fig. 1). The standard deviations were about 0.005Å. The rigid-body least-squares refinements were carried out on the c-projection by using the constrained least-squares method,[2] where the bond length and bond angles were fixed, C-C: 0.85Å, C-H:1.09Å, and H-C-H: 110°. The rigid-body temperature factor reported by Pawley[3] was taken into consideration. The values for angle θ, the complement of the angle φ, are shown in Fig. 2. The standard deviations were about 1°. The elements of translational and librational tensors are shown in Fig. 3 and 4, respectively. From the values at 10K, it is concluded that the static disorder of polyethylene is mainly of translational displacements. The librational temperature factor was calculated by using the frequencies of optically active librational motions,[4] 134 (A_g) and 109 (B_{3g}) cm^{-1}, and the equation reported by Cruickshank.[5] The results are given in Fig. 4 as a solid line. The amplitude of the librational motion at 300K are estimated 13.2 °, which is comparable to the values of polyoxymethylene.[6]

1) C. W. Bunn, *Trans. Faraday Soc.*, **35**, 482 (1939).
2) Y. Takahashi et al., *J. Polym. Sci. Polym. Phys. Ed.*. **11**, 233 (1973).
3) G. S. Pawley, *Acta Cryst.*, **17**, 457 (1964).
4) M. Tasumi and T. Shimanouchi, *J. Chem. Phys.*, **43**, 1245 (1965).
5) D. W. J. Cruickshank, *Acta Cryst.*, **9**, 1005 (1956).
6) Y. Takahashi and H. Tadokoro, *J. Polym. Sci. Polym. Phys. Ed.*, **17**, 123 (1979).

JRR-3M, TAS-2, HRPD, 6. polymer

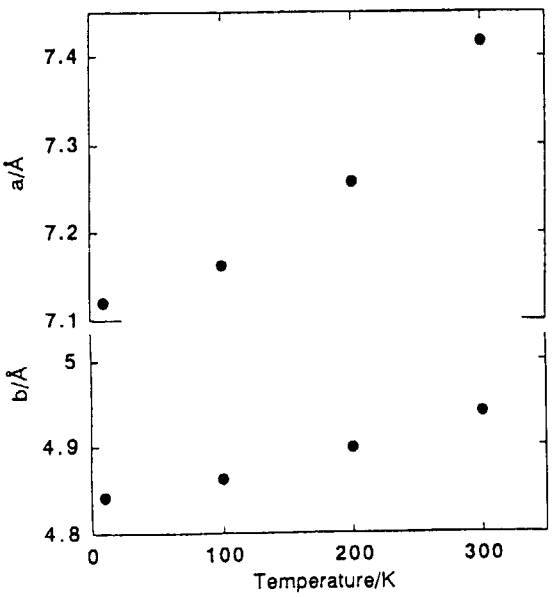

Fig. 1

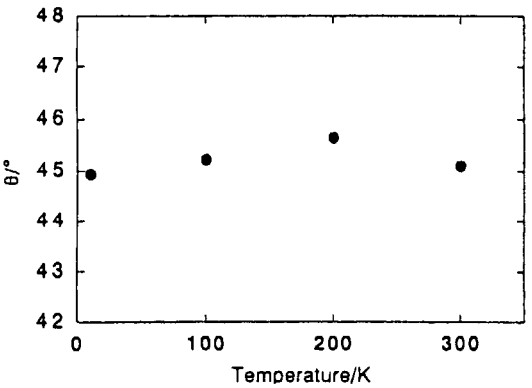

Fig. 2

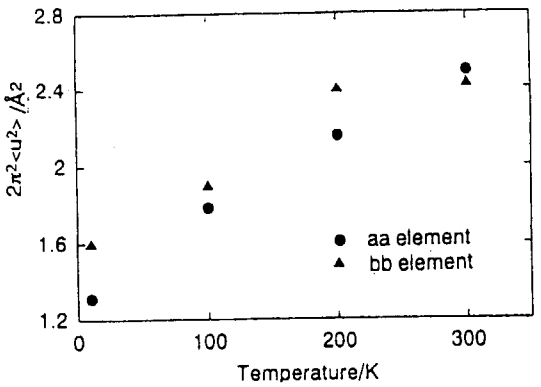

Fig. 3

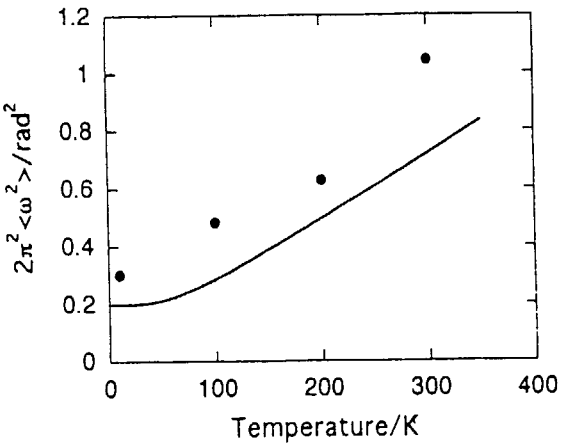

Fig. 4

研究テーマ：アモルファス高分子における非ガウス性の評価
表題：平均２乗変位の分布より見たアモルファスポリマーの動的不均一性

Dynamical Heterogeneity of Amorphous Polymers from the Distribution of Mean Square Displacement

I. Tsukushi, T. Kanaya and K. Kaji
Institute for Chemical Research, Kyoto University, Uji, Kyoto-fu 611-0011, Japan

In order to investigate the dynamical heterogeneity in glass-forming materials, we have evaluated the distribution of mean square displacement (MSD) using an incoherent elastic neutron scattering technique for amorphous polymers.

Assuming that the motion in the individual environment is described under the Gaussian approximation and a distribution of MSD arises from the local heterogeneity, the incoherent elastic scattering intensity of dynamic scattering law $S(Q,\omega)$, which is given by

$$S(Q,\omega=0)=\int_0^\infty \exp\left(-\langle u^2\rangle Q^2\right) g\left(\langle u^2\rangle\right) d\left(\langle u^2\rangle\right) \quad (1)$$

where g(<u2>) is a distribution function. Two distribution functions, normal and log-normal distribution functions, are adopted as g(<u2>).

$$g\left(\langle u^2\rangle\right)=\frac{1}{\sqrt{2\pi\sigma_n^2}}\exp\left\{-\frac{\left(\langle u^2\rangle-\overline{\langle u_n^2\rangle}\right)^2}{2\sigma_n^2}\right\}$$

normal distribution (2)

$$g\left(\langle u^2\rangle\right)=\frac{1}{\sqrt{2\pi\sigma_L^2}}\exp\left\{-\frac{\left(\ln\langle u^2\rangle-\ln\overline{\langle u_L^2\rangle}\right)^2}{2\sigma_L^2}\right\}$$

log-normal distribution (3)

Neutron scattering measurements have been made with a triple axis spectrometer (GP-TAS) in the JRR-3M reactor, Tokai.

Amorphous polymers used in the experiments were poly(methyl methacrylate), poly(vinyl chloride), poly(vinyl acetate), polystyrene, polyisobutylene and polybutadiene.

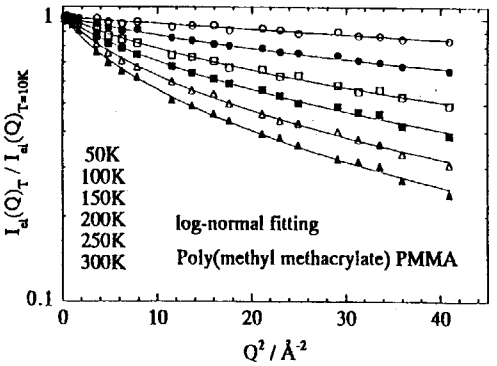

Fig. 1 Logarithm of incoherent elastic scattering intensity $I_{el}(Q)$ versus Q^2 for poly(methyl methacrylate) (PMMA).

Fig. 1 shows the Q^2 dependence of incoherent elastic scattering intensity $I_{el}(Q)$ in a semi-logarithmic form for poly(methyl methacrylate) (PMMA) at various temperatures, where $I_{el}(Q)$ is divided by $I_{el}(Q)$ at 10 K. It is clear that in the wide Q range experiment up to 6.4 Å^{-1}, the Q dependence of $I_{el}(Q)$ can not be described by the Gaussiaan approximation. The solid lines are the results of fit with log-normal distribution, from which the distribution of the MSD were extracted. The deviations of the observed values from the fitting curve with normal and log-normal

JRR-3M, 4G, 6. Polymer

研究テーマ：アモルファス高分子における非ガウス性の評価
表題：平均２乗変位の分布より見たアモルファスポリマーの動的不均一性

distribution are plotted in Fig. 2. The goodness of fit of log-normal distribution is better than that of normal one. This means that the log-normal distribution gives the better reproducibility of the Q-dependence of the elastic scattering.

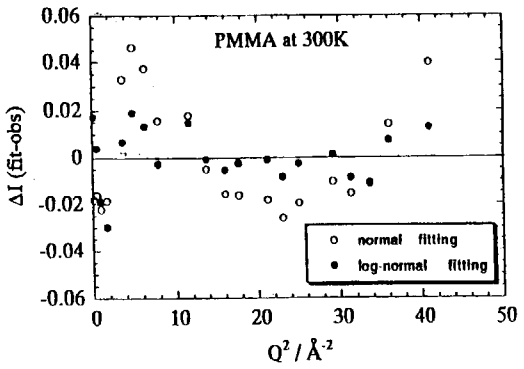

Fig. 2 Differences between experimental and fitted value.

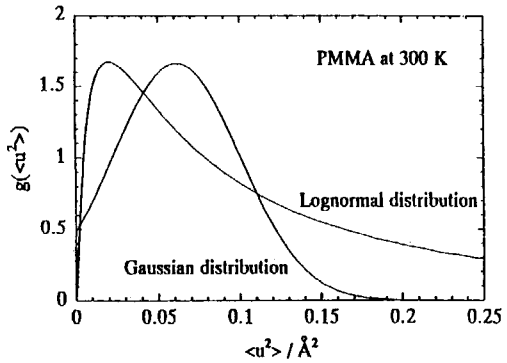

Fig. 3 Normal and log-normal distribution of mean square displacement (MSD) of PMMA at 300 K.

The calculated log-normal and normal distributions of PMMA at 300 K are shown in Fig. 3. The log-normal distribution is broader than the normal one.

JRR-3M, 4G, 6. Polymer

研究テーマ：アモルファス高分子における非ガウス性の評価
表題：アモルファスポリイミドの速いダイナミックスにおける振動ソフトニングの役割

Role of Vibrational Softening in Fast Dynamics of an Amorphous Polyimide

J. Hansen, T. Kanaya, K. Nishida and K. Kaji
Institute for Chemical Research, Kyoto University, Uji, Kyoto-fu 611, Japan

Extensive inelastic neutron scattering studies have revealed that the so-called fast process in picosecond order is commonly observed in most amorphous materials. The recent mode coupling theory (MCT) predicted the fast β-process, which has similar properties with the fast process so that it is often discussed as the MCT β-relaxation process. In contrast to a relaxational viewpoint for the fast process, an alternative explanation has been proposed on the basis of an idea of softening of vibrational modes. The recent vibration-relaxation (VR) model [1] has demonstrated that the softening of the vibrational modes dominates the excess scattering intensity in the quasielastic scattering spectra.

In this study we have performed inelastic neutron scattering measurements on a polyimide (Tg=250 °C) using HER spectrometer and analyzed the results in terms of the VR model to see whether or not the fast process has a relaxational origin.

The results of the fitting with the VR model are shown in Fig. 1; the fit is very good. First we have to emphasize that in the VR model the excess scattering intensity can be mainly explained by the softening of the vibrational motions. The Boson peak frequency ω_b evaluated from the fit is shown in Fig. 2. The softening of the Boson peak is clearly observed at low temperatures. The friction term γ in the relaxationa contribution is also plotted in Fig. 2. The relaxational contribution in the energy range examined is not large. Nevertheless, this contribution is not negligible at high temperatures.

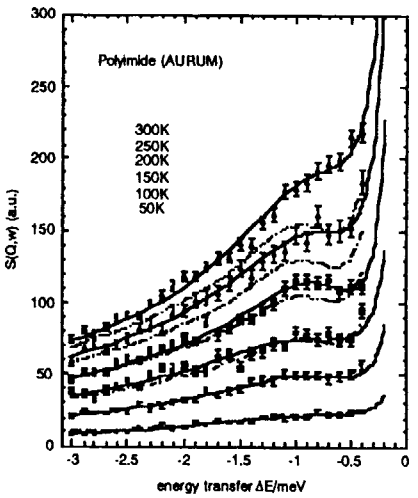

Fig. 1. Results of VR fit (solid lines). Dashed lines are the expected spectra from Bose factor.

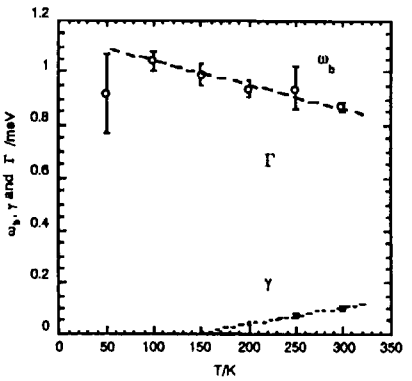

Fig. 2. T-dependence of boson peak frequency and friction term γ in VR model.

[1] U. Buchenau, C. Schoenfeld, D. Richter, T. Kanaya, K. Kaji and R. Wehrmann, Phys. Rev. Lett., **73**, 2344 (1994).

JRR-3M, HER, 6. polymer

課題名：オリゴペプチドの溶液中における会合構造の超二次構造

表　題：オリゴペプチド会合体の溶液中における超二次構造（中性子小角散乱）

Super secondary structure of oligopeptide aggregates in organic solvent

Small-angle neutron scattering study

H. Okabayashi[1], M. Takai[1], M. Ishida[1], M. Furusaka[2] and M. Hirai[3]

Department of Applied Chemistry, Nagoya Institute of Technology[1]
BSF, National Laboratory for High Energy Physics[2]
Department of Physics, Faculty of Social and Information Studies, Gunma University[3]

It is well known that periodicity exists in amino acid sequences for keratin, fibroin, collagen, tropoelastin and other proteins. However, very little is known about the biological role of the repeating oligopeptides. In particular, for the super-secondary structure formed by the repeating oligomers, there is a possibility of presence of an important, presently undefined, biological function. Therefore, further studies on super-secondary structure of model peptides are highly desirable. Detailed studies for aggregation mechanism of oligopeptides will provide basic contributions to the understanding of the super-secondary structure of proteins, which at present remains largely unresolved. In this study, the super-secondary structure of N-acetyl-L-glutamic acid dodecamer α,γ-benzyl ester (A12Z) in organic solvent has been investigated by using the small angle neutron scattering measurements

A12Z was prepared by a stepwise elongation method. Deuterated 1,4-dioxane (DOX-d8, isotope purity 98.5%) was purchased from Aldrich Chemical Company. SANS measurements were carried out using JRR-3M SANS-U (sample to detector distance = 1, 4m, at 298K) with quartz cells (path length = 4mm) filled with sample solutions.

JRR-3M, SANS-U(C1-2), Polymer

Fig.1 shows the SANS spectra of the A12Z/DOX-d8 solutions and the calculated best-fitted profiles at three different concentrations. For calculations of the structure factor, P(Q), the shape of an A12Z molecule was assumed to be disk-like in the aggregated states, because IR spectra of the A12Z solution provide ample evidence that an A12Z molecule takes up an extended β-sheet structure in the aggregated state.

Number-average aggregation numbers, n_n are also inserted in Fig. 1.

It may be concluded that number-average aggregation numbers (n_n) depend upon the concentration and that A12Z aggregate has a stacking structure of the β-sheet.

Fig.1

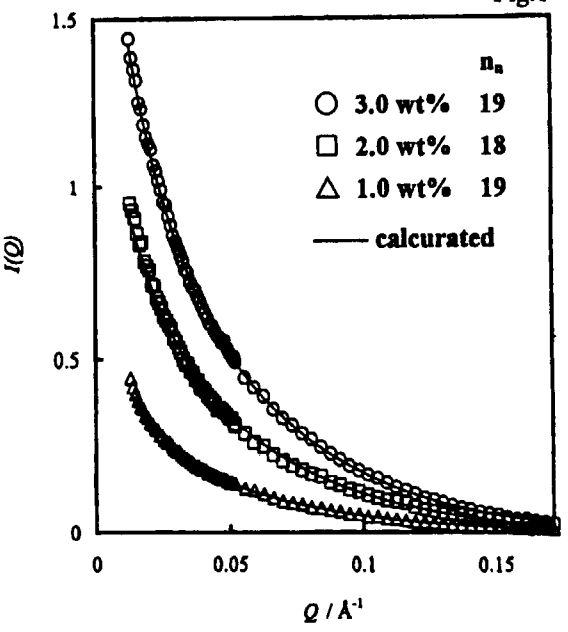

課題名：オリゴペプチドの溶液中における会合構造の超二次構造

表　題：オリゴペプチド会合体の溶液中における超二次構造（中性子スピンエコー法）

Super secondary structure of oligopeptide aggregates in organic solvent

- Neutron spin echo study -

H. Okabayashi,[1] M. Takai,[1] M. Ishida,[1] H. Seto[2] and T. Takeda[2]

Department of Applied Chemistry, Nagoya Institute of Technology[1]

Faculty of Integrated Art and Sciences, Hiroshima University[2]

For N-acetyl-L-glutamic acid octamer α,γ-benzyl ester (A8Z) synthesized by a stepwise procedure, it was found that the IR spectra and the X-ray diffraction powder pattern of the solid sample can be satisfactorily explained in terms of β-sheet structure. The IR spectra of the A8Z dioxane solution were measured at various concentrations. The results showed that the aggregation of the A8Z molecules occurs and the conformation of a A8Z molecule take up a β-sheet structure even in the aggregate.

For the A8Z-dioxane solution (20 wt%) containing the aggregates, the neutron spin-echo (NSE) measurements were made in order to examine the slow dynamics of an A8Z aggregate. The normalized NSE signal amplitude P_{NSE}, which corresponds to the normalized intermediate correlation function $I_N(Q,t)=I(Q,t)/I(Q,0)$, was obtained from the NSE experiments. The relaxation rate $\Gamma(Q)$, obatained using a least – aquares fit of P_{NSE} to the equation $P_{NSE} = A \exp[- \Gamma(Q)\, t]$, increased as Q^2 as shown in Fig. 1. The effective diffusion coefficient D_{eff} was estimated to be $D_{eff} = 1.9\times10^{-7}$cm^2/s using the relation $\Gamma=D_{eff}Q^2$. The NSE measurements for the aggregate solutions of longer oligomers are highly desirable, in order to examine the effect of a size of the aggregate on the slow dynamics of this aggregate particle.

Fig.1

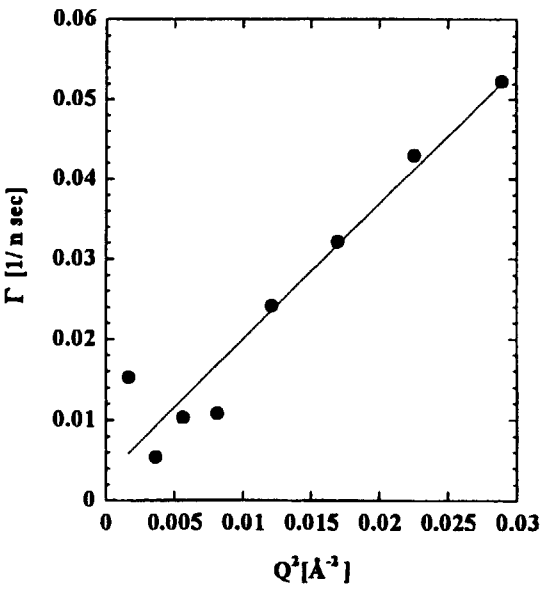

JRR-3M, NSE(C2-2), Polymer

研究テーマ：状態記憶効果を示す高分子ゲルの構造解析
表題：小角中性子散乱による 4-Acrylamido-salicylic acid gel の多重相の研究

SMALL-ANGLE NEUTRON SCATTERING STUDY ON MULTIPLE PHASE BEHAVIOR OF 4-ACRYLAMIDE-SALICYLIC ACID GEL

Masahiko Annaka, Fumiyoshi Ikkai*, Mitsuhiro Shibayama*, and Takayuki Nakahira

Department of Materials Science and Engineering, Chiba University, Inage-ku, Chiba 263-8522, Japan
**Department of Polymer Science and Engineering, Kyoto Institute of Technology, Matsugasaki, Sakyo-ku, Kyoto 606-8585, Japan*

Polymer gels are known to have two phases, swollen and collapsed phases. A volume phase transition occurs between these phases either continuously and discontinuously. Poly(4-acrylamidosalicylic acid) (PASA) gel (Fig.1) exhibited a multiple phase behavior, i.e., existence of more than two different phases depending on their history at a given pH and temperature. Four different phases, i.e., phase 091 (as-prepared), phase 244 (swollen at high pH), phase 064 (heat treated), and phase 233 (swollen at high pH after heat treatment) denoted by their linear swelling ratios in percentage, were clearly resolved. Each of the phases was stable and did not change its swelling ratio with pH or temperature as far as the values of pH or temperature were in the limited ranges. Transition among different phases were discrete and showed hysteresis loop. Here we will investigate the microscopic structure of PASA gel by means of small-angle neutron scattering (SANS) in order to elucidate the nature of multiple phase. The SANS experiment was carried out at the SANS-U, the University of Tokyo.

Fig.2 shows the swelling behavior of PASA gel as functions of pH and Temperature. This series of sewlling experiments leads to following feature in the gel. (1) As the starting point, the gel is in phase 091. (2) It prefers phase 244 at higher pH (i.e., $8 < pH < 10$). (3) A temperature induced transition from phase 0.91 to 0.64 takes place at 50 ℃. (4) However, the memory of phase 064 can be erased by immersing the gel in a reservoir with pH 12. (5) In all of these transitions, there exists a clear hysteresis in each loop.

The open circles in Figure 2 indicate the phases of the samples used for the SANS experiment. The number in the parenthesis indicate the order of sample preparation in the history of pH and/or temperature treatment. The SANS samples are also coded as phase 091, phase 244, etc, according to the result of swelling experiment. Figure 3 shows the reduced scattered intensity functions, $I(q)/[\phi(1-\phi)]$ for the PASA gels in phases 091, 244, 064, 233, and phase 091r. Phase 091r is the re-visited phase of phase 091 after experienced the loop of phase 064 - phase 233 - phase 064 - phase 244. It can be concluded that not only macroscopically but also microscopically, PASA gel goes back to its original state by pH and temperature loop applied here. Details will be discussed elsewhere.

JRR-3M, SANS-U, 6.Polymer

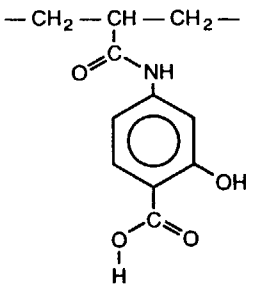

Figure 1. Chemical structure of 4-acrylamidosalicylic acid polymer. They can interact with each other through hydrogen bonding, hydrophobic stacking between benzene rings, or ionic repulsive interaction. Temperature influences the hydrogen bonding and hydrophobic interaction, whereas the pH affects ionization degree and thus the electrostatic interaction. The monomer undergoes ionization process twice, one for carboxyl group and the other for hydroxy group.

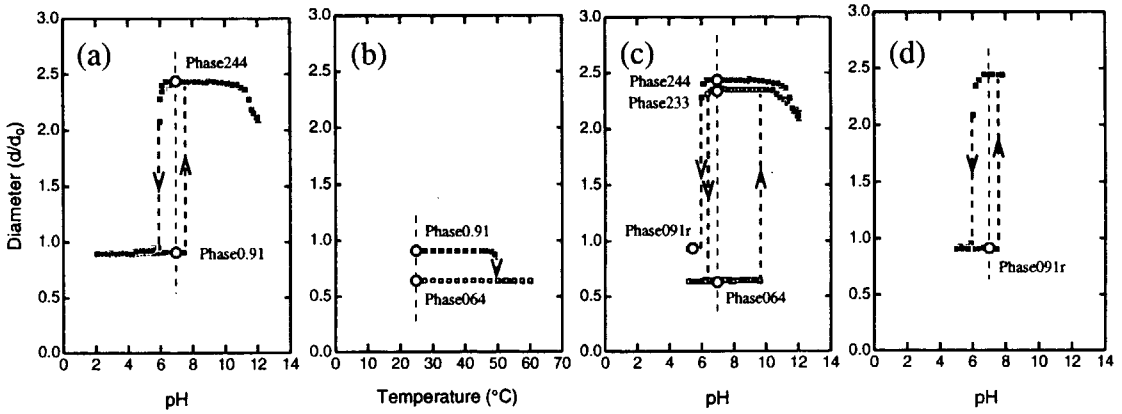

Figure 2. Diameter of 4-acrylamido-salicylic acid gel as a function of pH and temperature. The measurement were carried out on a single gel under a microscope. The sequence of measurement is in a alphabetical order (2a to 2d). The starting point of each diagram is the last point of the previous diagram.

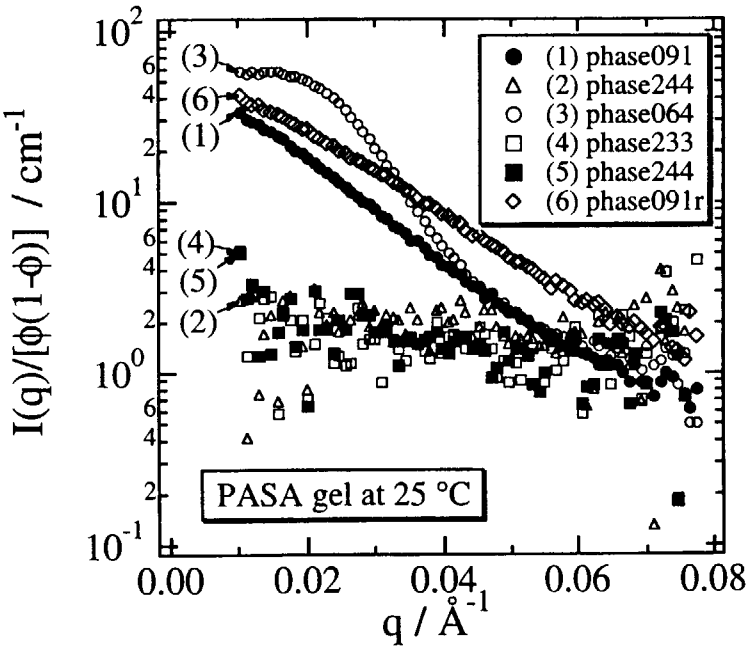

Figure 3. The reduced scattered intensity functions, $I(q)/[\phi/(1-\phi)]$ for the PASA gels in phases 0.91, 2.44, 0.64, 2.33 and 0.91r.

研究テーマ ： 化学架橋ゲルのゲル化過程

表題 ： 時系列小角中性子散乱によるポリN-イソプロピルアクリルアミドのゲル化過程

Time Resolved Small-angle Neutron Scattering Study on the Gelation Process of Poly(N-isopropylacrylamide)

M. Shibayama, T. Norisuye, and S. Nomura

Department of Polymer Science and Engineering,
Kyoto Institute of Technology, Matsugasaki, Sakyo-ku, Kyoto 606-8585, JAPAN

The gelation as well as its temporal control is an attractive problem not only for the chemical and physical viewpoints but also for applications in the industry. Many approaches, such as rheology, viscosity and spectroscopy measurements, have been conducted in the literature. However, none of these techniques provide accurate determination of the gel point and the architecture of chain clusters near the gel point. In our previous work, we have conducted a systematic analysis of gelation for poly(N-isopropylacrylamide) (PNIPA) gels by time resolved light scattering (TRLS).[1] This method involves a monitoring the scattering intensity as the function of time, t, during polymerization and/or gelation. In this work, we report the gelation process of PNIPA gels by time resolved the small angle neutron scattering (TRSANS) in order to clarify the gelation process with more microscopic viewpoint.

PNIPA gels and the corresponding polymer solutions were prepared by redox polymerization. NIPA monomer and N,N'-methylenebisacrylamide (BIS; cross-linker) concentrations were fixed to be 690 and 8.62 mM, respectively. The TRSANS experiments were carried out on the research reactor, SANS, at Institute of Solid State Physics, The University of Tokyo at Tokai. The scattered intensity was collected every 5 min. Figure 1 shows the t dependence of the total scattered intensity for the range of $0.005 \leq q \leq 0.08$ Å^{-1}. Interestingly, an abrupt intensity rise was observed exclusively in the gel sample, followed by a level-off to a plateau intensity. Figure 2 shows the scattered intensity profile, I(q), for PNIPA gels obtained at different t's. Unlike the total intensity, I(q) is not sensitive to the gelation or cluster formation though an increase in I(q) is detected for $q \leq 0.01$ Å^{-1} during the period of $15 < t \leq 20$ min. It was concluded from these experimental findings that the concentration fluctuations by cross-linking are detectable by TRSANS as well as by TRLS.

JRR-3M, SANS-U (C1-2), Polymer

Reference

1) T. Norisuye, M.Shibayama, and S. Nomura, *Polymer*, **39**, 13, 2769 (1998).

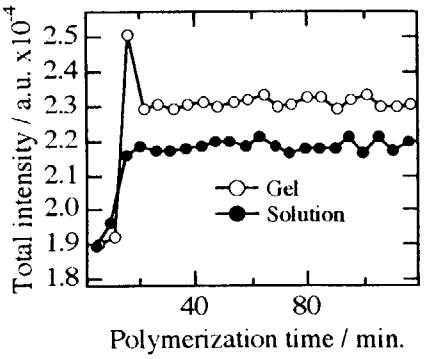

Fig.1 The t dependence of the total scattered intensity.

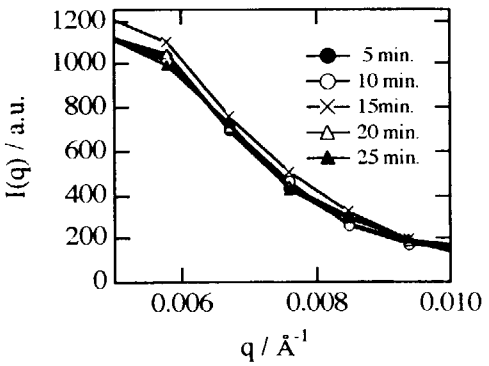

Fig.2 The scattered intensity profile, I(q), for PNIPA gels, obtained at different t's.

研究課題名：高圧によるマイクロエマルジョンの構造相転移、及び双連結構造形成のkinetics
表題：三元系マイクロエマルションにおける圧力誘起構造相転移の中性子小角散乱による研究

A small-angle neutron scattering study of a pressure-induced phase transition in a ternary microemulsion system

M. Nagao[1], H. Seto[2] and D. Okuhara[2]
1 Neutron Scattering Laboratory, Institute for Solid State Physics, The University of Tokyo, 106-1 Shirakata, Tokai, Naka 319-1106, Japan
2 Faculty of Integrated Arts and Sciences, Hiroshima University, 1-7-1 Kagamiyama Higashihiroshima 739-8521, Japan

A mixture of about 20 vol.% of AOT (dioctyl sulfosuccinate sodium salt) and an equal volume fraction of water and oil is believed to form a dense water-in-oil droplet structure at ambient temperature and pressure. A temperature-induced phase transition to a lamellar structure was known[1]. Recently Nagao et al. showed a similar phase transition with increasing pressure by means of small-angle neutron scattering(SANS)[2]. This behavior could be explained that the change of spontaneous curvature with pressure induces the structural phase transition as the case of temperature, however, details of the phase transition is not yet clear.

Therefore, further SANS experiments were performed at the SANS-U of JRR-3M in JAERI, Tokai. 7Å of incident cold neutron was used and a 2-D PSD was placed at 2m from the sample in order to cover a momentum transfer range of $0.01 \leq Q \leq 0.15$[Å^{-1}]. Measurements were performed at pressures between 0.1 and 120 MPa with a step of about 5 MPa. Three samples of 20.9%, 22.4% and 23.0% of purified AOT and the same volume fraction of 99% of *n*-decane and 99.9% of D_2O purchased from Katayama Chemical and Isotec. Inc. were prepared.

In Fig.1, pressure variation of SANS profiles are shown. Open circles and squares indicate the scattering profile from the higher area of the sample cell and full circles and squares from the lower area. The profiles from the higher- and the lower-area were the same at low pressure but not the same at high pressure. This result confirmed that the low pressure phase is uniform and the high pressure phase is two-phase; lower phase is the lamellar and the higher the bicontinuous.

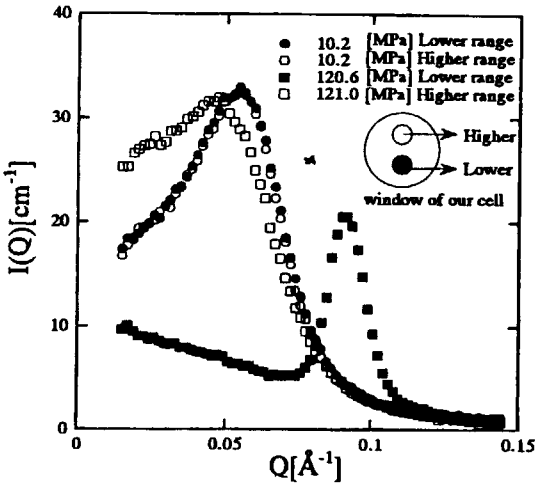

Fig.1: A SANS pattern from the microemulsion system at the low- and the high-pressure range.

In order to explain the scattering profile at low pressure phase and higher area at high pressure phase, we used the Teubner & Strey's formula[3],

$$I(Q) = \frac{1}{A + BQ^2 + CQ^4}, \quad (1)$$

$$d = 2\pi\left[\frac{1}{2}\left(\sqrt{\frac{A}{C}} - \frac{B}{2C}\right)\right]^{-\frac{1}{2}}, \quad (2)$$

$$\xi = \left[\frac{1}{2}\left(\sqrt{\frac{A}{C}} + \frac{B}{2C}\right)\right]^{-\frac{1}{2}}, \quad (3)$$

Reactor: JRR-3M, Facility: SANS-U (C1-2), Field: 6. Polymer

where d and ξ are the characteristic mean repeat distance between water domain and the correlation length of the system, respectively. A function for the lamellar phase was a linier combination of two Lorentzian introduced by Nallet et al[4]. The pressure dependence of d for both the dense droplet and the bicontinuous (subscript m) phase and the lamellar structure (subscript l) were obtained as depicted in Fig. 2. With increasing pressure d_m gradually decreased below P_s, successively it increased drastically and finally it stayed at the constant value above P_f, where P_s and P_f are the transition start pressure and the transition finish pressure.

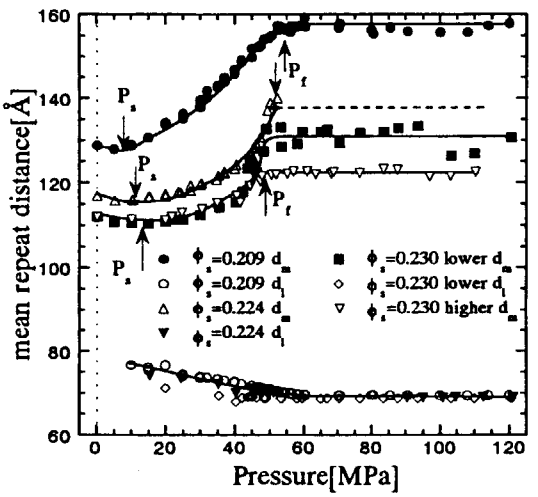

Fig.2: Pressure dependence of d_m and d_l is shown.

In order to characterize the semi-microscopic ordering of oil and water domains, a disorder parameter $1/k\xi$ ($k=2\pi/d$), proposed by Chen et al.[5], was introduced. If the parameter is above 0.446, the structure can be interpreted to be the bicontinuous. In Fig. 3, the pressure dependence of the $1/k\xi$ is shown as a function of P-P_s. All the data follow an universal curve independent of ϕ_s.

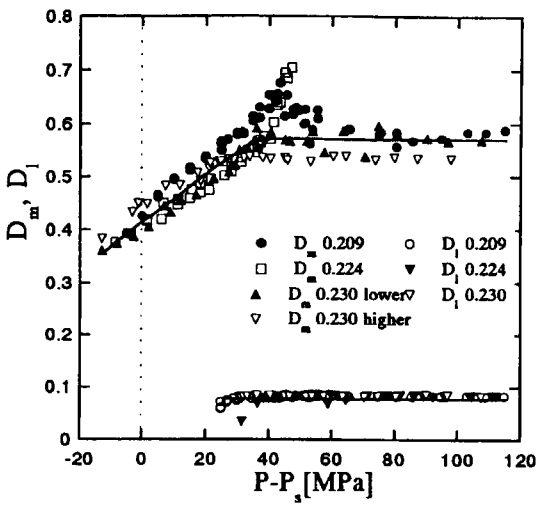

Fig. 3: Pressure dependence of the disorder parameter $1/k\xi$ is shown. The horizontal axes indicates P-P_s.

From these results, we conclude as follows: Below P_s, the phase is uniform and the characteristic repeat distance decreases with increasing pressure and the system becomes more disordered. Between P_s and P_f, highly ordered lamellar structure appears at the lower area of the sample and the characteristic repeat distance of the remaining low pressure phase increases and its semi-microscopic structure becomes disordered. At P_f, the structural change is finished and the coexistence of the ordered lamellar and the disordered phase is stabilized.

References

[1] Kotlarchyk et al., Phys. Rev. A, **46**, 928 (1992).

[2] Nagao et al., Prog. Col. Polym. Sci., **106**, 86 (1997).

[3] Teubner & Strey, J. Chem. Phys., **87**, 3195 (1987).

[4] Nallet et al., J. Phys. France, **51**, 2333 (1990).

[5] Chen et al., Prog. Col. Polym. Sci., **81**, 39 (1990).

研究テーマ：中性子小角散乱法による高分子多成分系の相溶性及び相転移に関する研究
表題：高分子混合系とマイクロエマルジョン系の共連続構造のキャラクタリゼーション

Morphological Characterisation of Bicontinuous Phase-separated Polymer Mixture and Microemulsions

Hiroshi Jinnai[1], Yukihiro Nishikawa[1], Kohtaro Kimishima[1], Takeji Hashimoto[1,2], Satoshi Koizumi[3]

[1]Hashimoto Polymer Phasing Project, ERATO, Japan Science and Technology Corporation, Keihanna Plaza, 1-7 Hikari-dai, Seika, Kyoto 619-0237, Japan
[2]Department of Polymer Chemistry, Kyoto University, 606-8501 Kyoto, Japan
[3]Japan Atomic Energy Research Institute, Tokai, 319-1195 Ibaraki, Japan

Recently, studies of bicontinuous and interpenetrating domain structures developed during phase separation processes, particularly via spinodal decomposition (SD), have been an attractive research theme among researchers dealing with binary mixtures of molecular fluids, binary alloys, and polymer blends over the past decades [1]. Similar kinds of bicontinuous structures have been observed in a water/oil/surfactant three-component microemulsion system in the one-phase region close to the three-phase boundary and in the vicinity of the hydrophile-lipophile balance temperature. It is interesting to examine the common and universal features, if they exist, of the bicontinuous structures observed in phase-separated polymer blends and in microemulsions [2].

In bicontinuous microemulsions, a theory developed by Berk [3] has been used to analyze scattering data and to generate the three dimensional (3d) morphology corresponding to the scattering data. A random Gaussian field that is generated by superposing many isotropically propagating sinusoidal waves with random phases is "clipped" to simulate the two-phase morphology whose essential features depend on the spectral function. Note that this idea was first developed by Cahn for generating the 3d morphology formed SD. Later, Chen et al. [4] proposed a peaked spectral function with a power law decay at large wave numbers which was able to reproduce their SANS intensity distributions from the microemulsions (called a modified Berk "M-B" theory).

We apply the theory to the scattering data from a polymer blend (which is in a non-equilibrium state) in order to see whether or not there are some common features shared by these two dynamically disparate systems. It is worth noting that the two systems have *very* different characteristic lengths: the characteristic length of the phase separated polymer blend used here is of the order of 10 μm, while that of the microemulsion is of the order of 100Å [5].

The polymer blend used in the present study was a near-critical mixture of perdeuterated polybutadiene (dPB) and polyisoprene (PI). Both polymers were synthesized by living anionic polymerization. The number-average molecular weight (Mn) of dPB and PI were, respectively, 61,000 and 141,000. For the microemulsion, ternary mixtures of heavy water (D_2O), n-octane, and tetraethylene glycol monodecyl ether (C4E10) were used. Volume fractions of the surfactant, water, and oil were, respectively, 0.132, 0.434, and 0.434. For the particular concentration of surfactant used here, the bicontinuous region spans the temperature range from about 17.75±0.25 to 22.0±0.5 ° C. The phase separation process of dPB/PI mixture was followed by a time-resolved light scattering (LS) experiment, while small-angle neutron scattering (SANS) measurements were made for the microemulsion using SANS-J instrument at JAERI.

Figure 1 shows the best fits of the M-B theory (solid line) for both the microemulsion at 20.3 ° C (part a) and for the dPB/PI mixture (part b) in log-log plots. An excellent agreement between the SANS profiles and the M-B theory was obtained. It is quite impressive that the M-B theory also reproduced the LS profile (part b) for the dPB/PI blend, especially in the high q-range including the shoulder. However, the fit was not as good in the low q range, i.e. $q < 0.1$ μm. The M-B theories showed shallower slope in this q-range than the experimental data. Furukawa [6] predicted $I(q) \sim q^2$ behavior in $q < q_m$ (q_m is the wavenumber at the maximum scattering intensity), if thermal fluctuations are significant. Hence the discrepancy of the slope in $q/q_m < 1$ between the theories and the LS data may be due to the small effect on the thermal fluctuations to the large scale morphology ($d \sim 7.1$ μm: d is the interdomain repeat distance). On the other hand, sizes of phase separated domains of the microemulsion are much smaller ($d \sim 303$ Å) and interfacial tension lower due to the existence of a surfactant film in the oil-water interface. In the latter case, the thermal noise is expected to have a larger effect on the microstructure, which leads to the weaker q dependence, i.e. $q \sim q^2$. In any event, the fact that the same theory (M-B theory) can reasonably describe scattering behavior of two systems having very different characteristic lengths is remarkable. We therefore conclude that the morphologies of the phase-separated polymer blend and the microemulsions are quite similar except for their length scales.

References

[1] J. D. Gunton, M. San Miguel, P. Sahni: in Phase Transitions and Critical Phenomena, C. Domb and J. L. Lebowitz Eds., Academic Press, New York, 1983, p. 269.
[2] W. Jahn, R. J. Strey: J. Phys. Chem., 92, (1988), 2294.
[3] N. F. Berk: Phys. Rev. Lett., 58 (1987) 93.
[4] S. H. Chen, D. D. Lee, S. L. Chang: J. Mol. Struct., 296 (1993), 259.
[5] H. Jinnai, T. Hashimoto, D. D. Lee, S. H. Chen: macromolecules, 30 (1997), 130.
[6] H. Furukawa, J. Phys. Soc. Jpn., 58 (1989), 216.

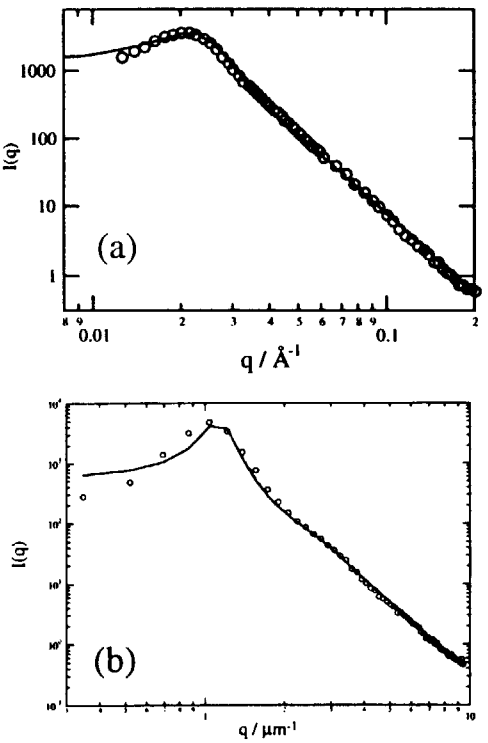

Figure 1. (a) Modified Berk model analysis of SANS profile of the one-phase microemulsion. (b) Modified Berk model analysis of scattering intensity of the dPB/PB blend. Solid lines show the best fit using the M-B therry.

原子炉：JRR-3M　装置：SANS-J(C3-2)　分野：中性子散乱（高分子）

研究テーマ：中性子小角散乱による高分子多成分系の相溶性及び相転移に関する研究
表題：N-イソプロピルアクリルアミドゲルの超小角中性子散乱

Ultra Small Angle Neutron Scattering of N-isopropylacrylamide Gel

T.Okamoto[1], Y.Hirokawa[1], K.Aizawa[2], S.Koizumi[2], and T.Hashimoto[1,3]

[1]Hashimoto Polymer Phasing Project, ERATO, JST,
15 Morimoto-cho, Shimogamo Sakyo-ku, Kyoto 606-0805
[2]Japan Atomic Energy Reserch Institute, Tokai, Ibaraki 319-1195
[3]Graduate School of Engineering, Kyoto University, Kyoto 606-8501

Polymer gels are three-dimensionally cross-linked polymer network containing fluid. They are intriguing materials for polymer science and technologies. The characteristics of gels such as optical, mechanical, thermal properties, and so forth, are related to their inhomogeneities. The inhomogeneities of the gel are essential matters not only for the basic polymer science but also for the technologies. Many studies on the gel have been made so far, however, there are not so many reports relating to the internal structures and inhomogeneities of the gel. In order to understand the characteristics of the gel, it is important to study the internal structures.

The gel used in this work is N-isopropylacrylamide gel. The gel samples were prepared at 24.5°C. The observation of the internal structures of the samples was carried out by means of ultra small angle neutron scattering.

Figure 1 shows the double logarithmic plot of the scattering intensity as a function of the wave number q. The profile shows a maximum at a q value (ca. 0.0004nm^{-1}) corresponding to the spacing of 16μm. The spacing agrees well with that found by the confocal laser scanning microscopy[1]. It has a straight line with a slope of ca. 2.5 over the length scale of 6000 to 600nm, or 6 to 0.6μm, elucidating a fractal-like structure with mass fractal dimension of 2.5.

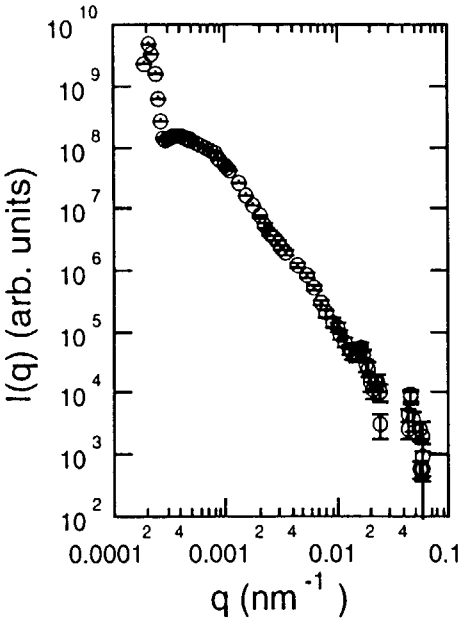

Fig.1 Double logarithmic plot of the scattering intensity as a function of the wave number q.

Reference

1) Hirokawa, Y., Jinnai, H., Okamoto, T., and Hashimoto, T., Polymer Preprints, Japan, **46** (1997) 1918-1919.

原子炉：JRR-3M　　PNO (3G)　　分野：中性子散乱（高分子）

研究テーマ：中性子小角散乱による高分子構造の研究
表題：中性子小角散乱によるセグメント化ポリウレタンのミクロ相分離構造の研究

Microphase Separated Structure of Segmented Polyurethane Studied by Using Small-Angle Neutron Scattering

Sudaryanto and Satoshi Koizumi[1]

National Atomic Energy Agency, Indonesia, Kawasan, PUSPIPTEK, Serpong, 15313, Indonesia.
[1]Japan Atomic Energy Research Institute, Tokai, Ibaraki, 319-1195, Japan

1. Introduction

Segmented polyurethanes (SPU), having hard segment (HS) and soft segment (SS), are known to form a microphase separated structure[1]. This peculiar structure brings SPU to be used in various ways such as biomedical materials, magnetic binders, elastomers, and adhesives.

Many studies have been performed to understand the microphase separated structure of SPU and its effect on various properties [2-6]. It is well known, therefore, that the formation of microphase separated structure highly affects the mechanical properties of SPU as well as their surface properties. Deeper understanding of SPU structure-properties correlation, however, is still needed, owing to their complexity of chemical and physical structures.

Previously, we have studied the relationship between microphase separation and surface properties of SPU[6]. The microphase separation structures were characterized by several methods such as differential scanning calorimetry (DSC), dynamic mechanical analysis, X-ray diffraction, and tensile test measurements. While, the surface properties were studied by X-ray photoelectron spectroscopy (XPS) and contact angle measurements. The results show that the existence of microphase separation results in increase of the surface free energy of SPU, with the soft segment being more predominant on the surface.

The aim of this study is, to investigate quantitatively the effect of the hard segment content and thermal treatment on the microdomain structure of SPU, by using small angle neutron scattering (SANS).

2. Experimental

The studied SPU is composed of 4,4'-diphenylmethane diisocyanate (MDI) and poly (propylene glycol) (PPG), chain extended with 1,4-butanediol (BD). Detailed explanations of samples preparation as well as their thermal, mechanical, and surface properties were reported elsewhere [6].

The SANS measurements were performed by SANS-J instrument (λ=0.6 nm). Samples used in this study were hydrogenated films of thickness of 1 mm and a larger area compared to the neutron beam size. Scattering data of each sample were collected for about 2.5 hours. Effects of thermal treatment were then investigated by placing the sample within a cell which allowed to perform *in situ* experiments at controlled temperature. Profiles of scattering intensity were collected at interest temperature around melting point for about 1 hour.

3. Result and Discussion

Figure 1 shows SANS profiles for three SPUs with various HS contents. q ($=4\pi\sin\theta/\lambda$) is the magnitute of the scattering vector with λ and 2θ being wavelength and scattering angle, respectively. SPU68 (SPU with HS content of 68 wt%) gives the highest intensity over a wide q range, with a sharp maximum at q = 0.33 nm^{-1}. On the other hand, other SPUs have no scattering maximum. SPU56, however, showed higher intensity than SPU32.

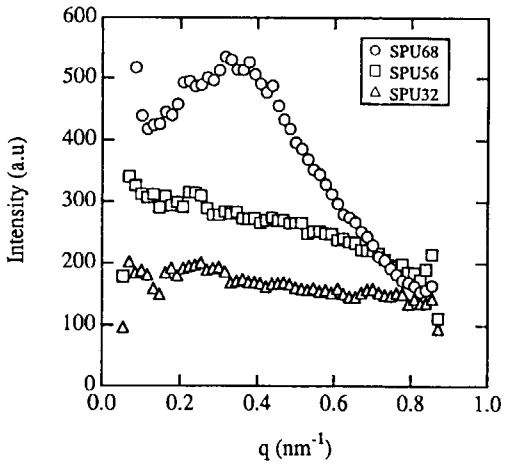

Fig. 1 SANS profiles obtained for SPU with various HS contents.

原子炉：JRR-3M　　装置：SANS-J (C3-2)分野：中性子散乱（高分子）

研究テーマ：中性子小角散乱による高分子構造の研究
表題：中性子小角散乱によるセグメント化ポリウレタンのミクロ相分離構造の研究

According to basic scattering laws, the scattering intensity (I(q)) depends on concentration fluctuation in the system, i.e., the contrast. For a two phase system the contrast value is represented by a mean-square fluctuation. Namely,

$$<\Delta\rho^2> = (\rho_1-\rho_2)^2\varphi_1\varphi_2$$

where ρ_i is the locally averaged scattering length for *i* th phase, and φ_i is the volume fractions for *i* th phase. Since $\varphi_1 + \varphi_2 = 1$, for a given value of $(\rho_1-\rho_2)^2$, the $<\Delta\rho^2>$ becomes maximum when $\varphi_1 = \varphi_2$. In other word, the largest product of $\varphi_1\varphi_2$, among three samples used in this study, must be obtained for SPU with HS content of 56 wt%. While, SPU with HS content of 68 wt% and 32 wt% must have similar values of $\varphi_1\varphi_2$ and $<\Delta\rho^2>$. But the experimental results show an opposite trend from the expected one over the whole q values. According to Chang and Wilkes, these results indicate that microphase separated structure consisting of hard and soft segment domains is formed with increasing HS content[3].

The interdomain distance ($d=2\pi/q_{max}$) formed in this SPU can be estimated to be 19 nm from the position of scattering maximum at q=0.3 nm^{-1}. This value is consistent with result obtained for several other SPU systems by using X-ray scattering, as reported previously[3,4].

These SANS results are well in agree with those obtained by DSC measurement, where the SPU68 has sharp melting peak at 180℃, SPU56 has broad one, and SPU32 had no endhotermic peak, which lead to conclusion that domain formation is clearly observed in the bulk of SPU with high HS content.

Figure 2 shows the SANS profiles of SPU68 with increasing temperature. It is clear that the scattering maximum increased with increasing temperature, which indicates microphase separation between hard and soft segment is developed. The peaks position was also shifted to lower q value with increasing temperature, which corresponds to the decrease in interdomain distance due to enlarging domain size. This result may also be due to the increased mobility of soft segment, which may lead the hard domains to move close each others. The vigorous movement of soft segment may also stimulate in the increase in phase separation.

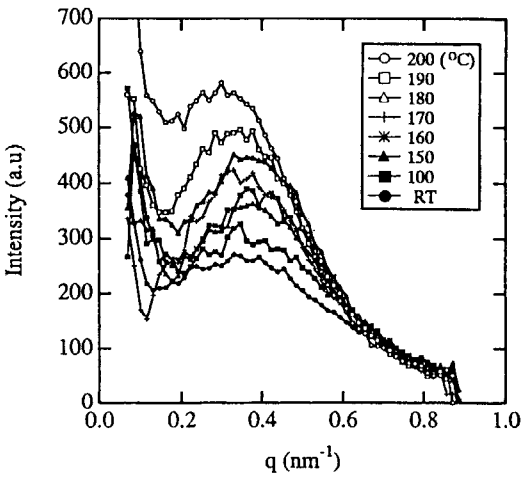

Fig. 2 SANS profiles of SPU68 at with increasing temperature. Each profile was collected at controlled temperature for 1 hour.

4. Conclusion

These SANS measurement support quantitatively the conclusion that microphase separated structure of SPU used in this study can be obviously observed at high HS content, i.e. more than 50 wt%, as determined previously by DSC and X-ray diffraction as well as tensile test measurement. The interdomain distance, was observed to be 19 nm for SPU with HS content 68wt%.

5. References

[1] J.Blackwell and C.D.Lee, in *Advances in Urethane Science and Technology*, K.C. Frisch and D.Klempner, Eds. Technomic, Lancer, PA, 1984, vol.9,pp.25-46.
[2] J.T.Koberstein and R.S.Stein, *J. Polym. Sci.Polym.Phys.Ed.*,21,1439 (1983).
[3] Y.P. Chang and G.L.Wilkes, *J.Polym.Sci. Polym.Phys.Ed.*,13,455(1975).
[4] G.L.Wilkes,S.Abouzahr, *Macromolecules*, 14,456(1984).
[5] J.T.Koberstein and L.M.Leung, *Macromolecules*, 25,6205(1992).
[6] K.Nakamae, T.Nishino, S.Asaoka, and Sudaryanto, *Int'l. J. Adhesion & Adhesive*, 16,233 (1996).

研究テーマ：強相関電子系の中性子散乱による研究

表題：中性子偏極解析によるガラス形成物質の弾性非干渉性構造因子の観察 I.

Direct Observation on Elastic Incoherent Structure Factor of Glass-forming Material by Neutron Polarization Analysis I.

Satoshi Koizumi and Toshiya Inami

Advanced Science Research Center, Japan Atomic Energy Research Institute, Tokai-mura, Ibaraki-ken 319-1195, Japan.

Although the glassy materials have been studied extensively from normal liquids to biopolymers, there still remain several unsettled and attractive topics [1]. In this report, we intend to elucidate an origin of the anharmonic vibrational behavior of glassy materials, employing a unique combination of anisotropic glass-forming copolyester and the neutron polarization analysis [2,3] which allows us to observe the elastic spin incoherent (INC) neutron scattering originating from hydrogen. The elastic incoherent structure factor (EISF), in other words, a long time-averaged self-correlation of local motions, provides information of "*structural cage*" trapping segmental units in a glassy state.

The studied material; thermotropic random copolyester of p-hydroxybenzoic acid (HBA) and 2-hydroxy-6-naphthoic acid (HNA) of 73/27 (mol/mol) having number-average molecular weight of 2.0×10^4, is unique to form an anisotropic glass (or pseudo-hexagonal phase) below T_g (=393K) without perfect crystallization [4,5]. Because of the rigid backbone composed of rigid phenylene and naphtalene groups, which have all hydrogen in a specimen, this material preserves a preferential orientation of rigid chains during a solidification below melting point T_m (=558K). The anisotropic orientation of molecular axis (MA) is greatly advantageous to discuss a relaxational motion in a glassy state.

The neutron polarization analyses have been performed with the polarization triple axis spectrometer TAS-1 at JRR3M at Japan Atomic Energy Research Institute (JAERI) [6]. We employed the Heusler alloys (Cu_2MnAl) as a polarizing monochromator and an analyzer. The spin-flipper was located between the polarizer and the sample position. By using the polarized incident neutron of λ=2.42 A, the polarization of our setup has been determined as 90%±1 as a whole instrument. We fixed the Heusler analyzer at the angle to obtain the elastic scattering (an energy resolution of ca. 0.6mev) and measured the scattered neutron intensity over a wide scattering angle 2θ from 10° to 90°. The scattering q-vector ($q=4\pi/\lambda\sin(\theta)$) was set parallel ($\phi=0°$) or normal ($\phi=90°$) to a direction of the MA (see a inset of Fig. 1). The obtained spectra were corrected for the background scattering. The transmission of the sample specimens was more than 90% so that the effect of multiple scattering was neglected in our data analyses.

Figure 1 shows the elastic scattering profiles of $\phi=90°$ obtained at 300K for both conditions of the spin-flipper *on* and *off*. In the case of spin-flipper *off*, corresponding to spin non-flip process, the intense equatorial reflection (110) of the pseudo-hexagonal phase [5] can be observed at around $2\theta=30°$, while in the case of the spin-flipper *on*, corresponding to spin flip process, the INC scattering can be observed without any reflection.

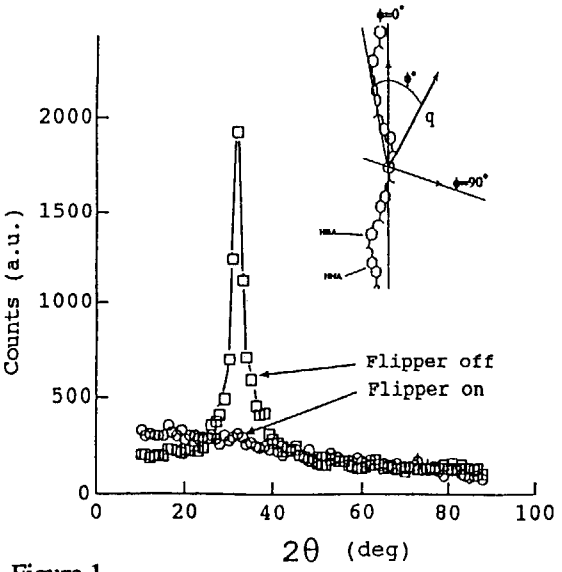

Figure 1

原子炉：JRR-3M　　装置：TAS-1(2G),2(T2-4)　　分野：高分子

The differential scattering cross sections, for conditions of spin *flip* and *non-flip*, can be given as follows [2,3],

$$\left(\frac{d\sigma}{d\Omega}\right)_{sf} \sim \frac{2}{3}\left(\frac{d\sigma}{d\Omega}\right)_{INC}$$

$$\left(\frac{d\sigma}{d\Omega}\right)_{nsf} \sim \frac{1}{3}\left(\frac{d\sigma}{d\Omega}\right)_{INC} + \left(\frac{d\sigma}{d\Omega}\right)_{COH} \qquad (1)$$

where the subscripts refer to spin-flip (sf), non-spin-flip (nsf), coherent (COH) and spin incoherent (INC) scattering. Thus the spin-flop process is composed of the INC scattering, while the non-spin-flop process is composed of both coherent and INC scattering. Taking account into the instrumental inefficiency of polarization, the elastic coherent and elastic incoherent scattering cross sections have been successfully decomposed (see Figure 2). The details of data treatments should be referred in ref.[7]. It should be stressed that the elastic INC scattering cross section provides a long time-averaged self-correlation of local (hydrogen) motions trapped in a structural cage in a glassy or liquid state. We will discuss the details of physical pictures for this study in the following report of part II.

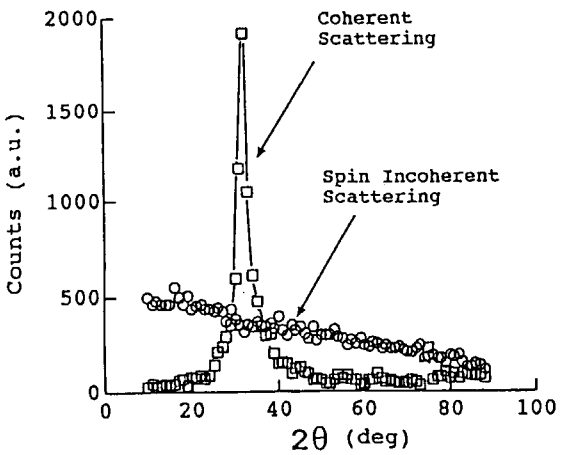

Figure 2

Reference:

[1] C. A. Angell *Science* **267**, 1924 (1995).
[2] R. M. Moon, T. Riste and W. C. Koehler. *Phys. Rev.* **181**, 920 (1969).
[3] W. G. Williams *"Polarized Neutrons"* Oxford Series on Neutron Scattering in Condensed Matter No.1, by Oxford University Press, New York; G. L. Squires "Introduction to The Theory of Thermal Neutron Scattering" Dover Publications, New York.
[4] A. H. Windle, V. Christopher, G. Ruth, M. D. Athene and R. M. Geoffrey *Faraday Discuss. Chem. Soc.* **79**, 55 (1985); J. Blackwell, A. Biswas, A. G. Genaro and R. A. Chivers *Faraday Discuss. Chem. Soc.* **79**, 73 (1985).
[5] D. J. Wilson, C. G. Vonk and A. H. Windle *Polymer* **34**, 227 (1993).
[6\ S. Katano et al. in preparation.
[7] J. C. Dore, J. H. Clarke and J. T. Wenzel. *Nucl. Instrum. Methods* **138**, 317 (1976).

研究テーマ：強相関電子系の中性子散乱による研究

表題：中性子偏極解析によるガラス形成物質の弾性非干渉性構造因子の観察 II.

Direct Observation on Elastic Incoherent Structure Factor of Glass-forming Material by Neutron Polarization Analysis II.

Satoshi Koizumi and Toshiya Inami

Advanced Science Research Center, Japan Atomic Energy Research Institute, Tokai-mura, Ibaraki-ken 319-1195, Japan.

In the report of part I, we demonstrated the useful application of the neutron polarization analysis to observe selectively the elastic spin-incoherent (INC) scattering of a glass-forming copolyester polymer. For next steps, we observed the temperature dependence of the elastic INC scattering. The details of experiments and studied materials are reported in the part I. Figure 1 and 2 show the results obtained for the scattering geometry of $\phi=90^{o}$ (see Fig. 1 of part I).

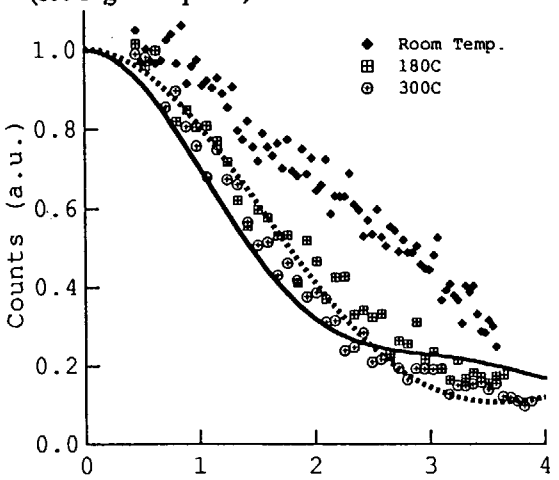

Figure 1

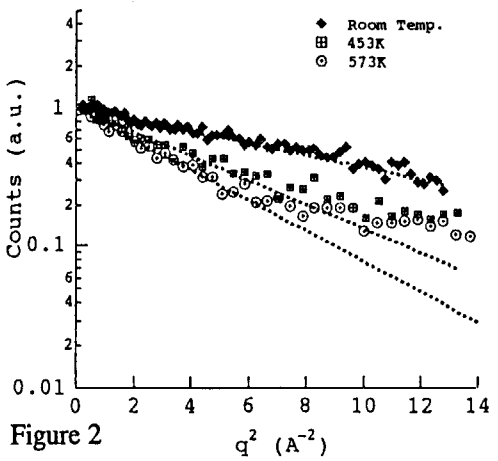

Figure 2

At 300K, the asymptotic q-behavior of INC scattering decrease monotonously as increasing q. On the other hand, at the temperature above Tg (453K and 573K), the asymptotic q-behavior becomes steeper as a function of q, having a minimum at around 2.5 A^{-1}. In Fig. 2 of a logarithmic plot as a function of q^2, we discuss the anharmonic behavior more quantitatively. At the temperature of 453 K and 573 K, the scattering profiles deviate from exponential decay in a q-region higher than 6 A^{-2}, while at 300K the scattering profile decreases exponentially in a whole q-region.

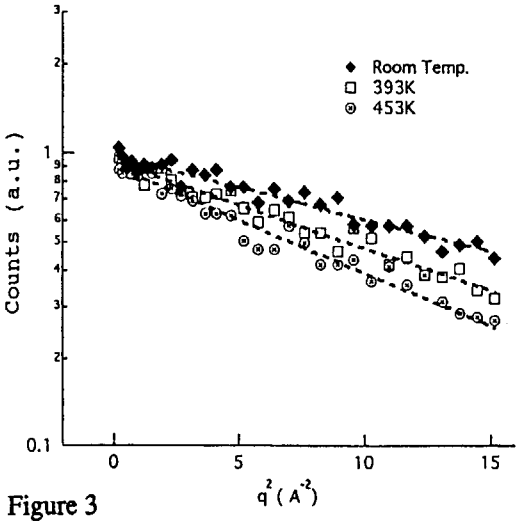

Figure 3

On the other hand, in Fig.3, which obtained for the scattering geometry of $\phi=0^{o}$, the scattering profile decreases exponentially in a whole q-region even for higher temperature above Tg.

From the exponential behavior observed in a low q-region of $q^2<4$ A^{-2}, we estimated an apparent mean square displacement $\langle u^2\rangle_{app}$ through DWF ($\sim \exp(-\langle u^2\rangle_{app} q^2)$). In Fig.4, the filled circles or squares indicate the mean square displacements obtained by using polarized neutron analyses for the scattering

原子炉：JRR-3M　　装置：TAS-1(2G),2(T2-4)　　分野：高分子

geometry of $\phi=0^\circ$ or 90°, respectively. The open circles or squares indicate those estimated by non-polarized neutron, which have been reported in ref. [1]. Both results obtained by using polarized and non-polarized neutron agree well with each other. The increase of $\langle u^2\rangle_{app}$, obtained for $\phi=90^\circ$, is two-steps and linearly as a function of temperature T (K); from 8K to 300K, the harmonic increase of $\langle u^2\rangle_{app} \sim 1.7\times10^{-4}$ T and from 300K to 558K, the anharmonic increase of $\langle u^2\rangle_{app} \sim 7.0\times10^{-4}$ T. The anharmonic increase of $\langle u^2\rangle_{app}$ seems to result from the fast relaxation whose onset temperature is far below Tg. This observation is consistent with the recent studies [2,3]. On the other hand, that for $\phi=0^\circ$ increases more gradually than that for $\phi=90^\circ$ at around Tg. These observations of the anisotropic increase of $\langle u^2\rangle$ suggests that there exists an *anisotropic structural cage* at around Tg.

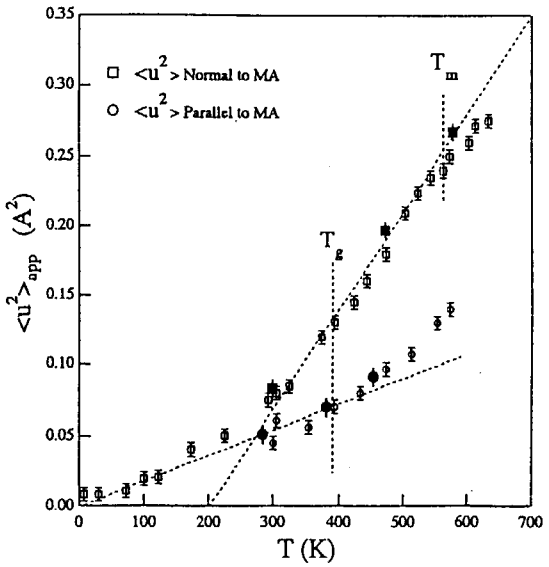

Figure 4

For the scattering geometry of $\phi=90^\circ$, we observed the anharmonic behaviors from two aspects of the increase of $\langle u^2\rangle$ and the q-behavior of INC scattering. We employ a following physical picture of a tight cage and a loose cage, characterizing the anharmonicity [4]. In a low temperature region, the segmental units should be trapped tightly in a glassy state (*tight cage*) where the local vibrational motion is crucial to determine the asymptotic q-behavior for elastic INC scattering through DWF including $\langle u^2\rangle$. As increasing temperature closer to Tg or above Tg, the tight cage might become a *loose cage* so that the additional relaxational process might appear in a loose cage. The segmental units of aromatic groups are covalently connected with each other along a direction of molecular axis (MA), while in a direction normal to MA, a non-covalent interaction is crucial. The cage formed around the segmental units should be *anisotropic*. Therefore, it might be possible for aromatic groups to have a rotational libration or relaxation in an *anisotropic cage*, especially in a direction normal to MA.

According to the proposed picture, the scattering law, for a direction normal to MA ($\phi=90^\circ$), should be given as follows [5],

$$S(q,\omega=0) \sim \exp(-\langle u^2\rangle q^2)[EISF(q,\omega)\delta(\omega)+QEL(q,\omega=0)] \quad (1)$$

which is composed of DWF of a first term and relaxational contributions (EISF and QEL) of a second term. When temperature is low enough, the relaxational contribution of a second term should disappear in a tight cage.

There is a report for isolated glassy polyester that one of the dihedral angle along MA is easy to rotate as a result of two competitive factors, i.e., steric repulsion and resonance stabilization [6]. Thus when temperature is high enough, the rotational motion of aromatic groups about MA must be crucial to describe the local relaxational motion. In a case of the free rotational motion, in which a particle (hydrogen) can move on a circle of a radius r obeying a Fickian diffusion equation, the elastic and quasielastic components in eq.(1) is composed of the Bessel function of the first kind $J_m(x)$ as follows [5],

$$EISF(q,\omega,\phi) \sim J_0^2(qr\sin\phi)$$

$$QEL(q,\omega,\phi) \sim \sum_{m=1}^{\infty} J_m^2(qr\sin\phi)\times\frac{1}{\pi}\frac{D_r m^2}{(D_r m^2)^2+\omega^2} \quad (2)$$

where D_r is a rotational diffusion coefficient and ϕ is an angle between MA and the scattering

vector q. In Fig. 1, we plotted the calculated scattering curve based upon the free rotational model of eq.(2), in which we employed $rsin\phi=1.4$ and considered finite terms from m=1 to m=3 for calculating QEL contributions (see Fig.4). The calculated curve describes well the observed INC (or EISF). A more quantitative analysis of our future work requires to consider the long range [7] or short range [8,9] heterogeneity of a glass state, which results in the distribution of parameters such as rotational diffusion coefficient D_r, angle ϕ and radius r. Thus it is suggested that the appearance of EISF for a rotational relaxation in a loose cage is crucial to contribute on the anharmonic behaviors of increase of $<u^2>$ and the anharmonic q-behavior. In a crossover temperature from a tight cage to a loose cage, the structural cage becomes anisotropic so that the anisotropic motion of segmental units in a direction normal to a local molecular axis, provides the larger increase of $<u^2>$ than that parallel to MA.

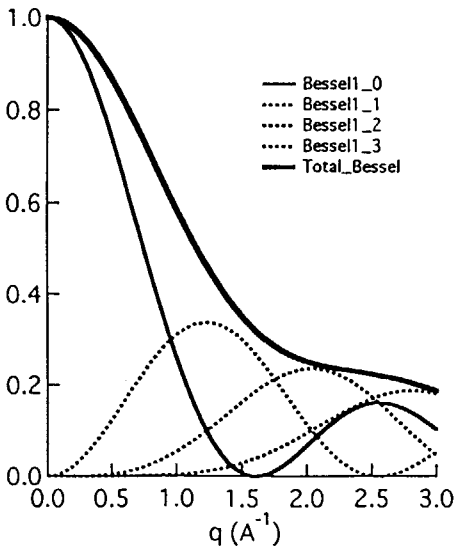

Figure 4 Free rotation model, composed of the Bessel function of the first kind $J_m(x)$. The thin solid line and broken lines indicate the elastic incoherent structure factor (EISF) amd the quasielatic components. The thick solid line shows the total contribution describing the elastic incoherent scattering.

We wish to Dr. T. Shiwaku of Polyplastic Co. Ltd. for supplying a sample specimen. We are also grateful to Professor T. Kanaya of Kyoto Univ. for helpful discussions.

References:

[1] S. Koizumi *J. Chem. Phys.* **107**, 603 (1997).
[2] T. Kanaya, T. Kawaguchi, and K. Kaji *J. Chem. Phys.* **104**, 3841 (1995).
[3] U. Buchenau, C. Schönfeld, D. Richter, T. Kanaya, K. Kaji, and R. Wehrmann, *Phys. Rev. Lett.* **73**, 2344 (1994).
[4] H. Tanaka *J. Chem. Phys.* **105**, 9375 (1996).
[5] M. Bee "*Quasielastic Neutron Scattering: Principles and Applications in Solid State Chemistry, Biology and Materials science*"; Adam Hilger: Bristol, U.K., 1988.; A. J. Dianoux, F. Volino and H. Hervet *Molecular Physics* **30**, 1181 (1975); Bee, M.; Dianoux, A. J.; Volino, F.; *Molecular Physics* **51**, 221 (1984).
[6] A. H. Windle et al. *Macromolecules* **22**, 1129 (1989).
[7] E. W. Fischer *Physica A* **201**, 183 (1993).
[8] R. Zorn *Phys. Rev. B* **55**, 6249 (1997); T. Kanaya, T. Tukushi. and K. Kaji *Prog. Theor. Phys.*, **126**, 133(1997).
[9] S. Koizumi *Physica B* in press.

研究テーマ：高分子多成分系のパターン形成に関する研究
表題：光散乱・中性子散乱による高分子準希薄溶液の構造形成に関する研究

Light Scattering and Small-Angle Neutron Scattering Studies of Shear-Induced Structures in Semidilute Polymer Solutions under Oscillatory Shear Flow

S. Saito, K. Matsuzaka, S. Koizumi[1)], S. Suehiro and T. Hashimoto

Department of Polymer Chemistry, Graduate School of Engineering, Kyoto University
Sakyo-ku, Kyoto 606-8501, Japan
1) Japan Atomic Energy Research Institute, Tokai 319-1106, Ibaraki, Japan

It has been reported that a shear flow, imposed on a semidilute polymer solution in a single phase, enhances concentration fluctuations toward phase separation. This phenomenon is so-called "shear-induced phase separation" and has been studied by light scattering, optical microscopy, and rheology measurement. Here, we report our investigation along this line for a semidilute polymer solution comprised of high molecular weight deuterated polystyrene (d-PS, M_w=3.15×10^6) and dioctyl phthalate (8.0 wt%) by combination of small angle light scattering (SALS) and small-angle neutron scattering (SANS).

On carrying out the SANS experiment, we performed the phase-resolved measurements by using the dynamic data acquisition system (DDAS), which was newly developed in JAERI. A sandwich type shear cell, drived by a servo-controlled hydraulic devise, imposes a oscillatory shear flow on the sample. The incident beam was irradiated along the velocity gradient direction.

Figure 1 shows the SALS and SANS profiles parallel and perpendicular to the flow direction at the representative strain phases ϕ=0° and 90° when an oscillatory shear flow of a strain amplitude γ_0=4.8 and a frequency ω=12.27 rad/s was imposed, where ϕ=0° means the phase at which the magnitude of strain is 0. The solid line indicates the scattering profile at quiescent state, and the dashed line indicates the Ornstein-Zernike function fitted to the experimental data. In higher q-region, the power low of $I(q)\sim q^{-2}$ can be observed, reflecting the form factor of polymer chain at Θ condition. The profiles indicated by symbols are those under shear flow. The open circles denote the scattering profiles parallel to the flow direction, and the closed squares denote those perpendicular to the flow direction. At ϕ=0°, in the lower q-region observed by SANS, the intensity level parallel to the flow is higher than that perpendicular to the flow. This means the existence of the anisotropic structures induced by the oscillatory shear flow. However, in the q-region of SALS, the intensity doesn't depend on the flow direction and the intensity level is higher than the OZ level which corresponds to the scattering from the concentration fluctuation in a single phase. This implies the existence of large scale isotropic inhomogeneity. At ϕ=90°, the SALS intensity parallel to the flow direction increases in the high-q region of SALS. This is caused by the development of the shear-induced structures through the process from ϕ=0° to 90°, which was reported previously.

In both SANS profiles at ϕ=0° and 90°, the power low of $I(q)\sim q^{-4}$ can be observed in the q-region lower than about 0.1 nm^{-1}. This has been known as Porod law, implying the existence of the distinct surface. From this result, we can conclude that the structures induced by oscillatory shear flow are the distinct phase-separated structures rather than the concentration fluctuation in a single phase.

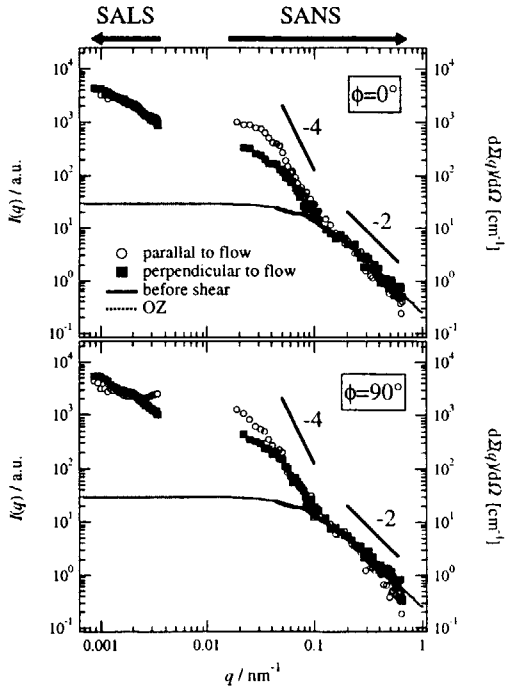

Fig.1 Scattering profiles parallel and perpendicular to the flow direction under oscilltory shear of γ_0=4.8 and ω=12.27 rad/s.

原子炉：JRR-3M　　装置：SANS-J(C3-2)　　分野：高分子

研究テーマ：高分子多成分系のパターン形成に関する研究
表題：強偏斥高分子混合系の界面散乱

Interface scattering of strongly segregated polymer blend.

Hiroyuki Takeno, Takeji Hashimoto, Martin Weber[1]
and Satoshi Koizumi[2]
Kyoto University, Kyoto, 606-8501, Japan
[1]BASF, Germany
[2]Japan Atomic Energy Reserch Institute, Tokai, Ibaraki, 319-11, Japan

Recently numerous studies have been made on phase separation process of polymer blends. In the studies of phase separating structure, it is important to obtain information of the interfacial structure.

In this study, we have investigated the interface scattering for a strongly segregated polymer blend, deuterated polysulfone (dPSU) and polyamide (PA) blend (dPSU/PA) by means of small-angle neutron scattering (SANS). dPSU/PA blend with a composition of 50/50 in weight percent was dissolved in o-chlorophenol at 50 °C and then prepared by precipitation into methanol. The precipitated sample was dried for 24 hours at 100 °C and pressed at 140 °C. The glass transition temperature of dPSU and PA are 180 °C and 110 °C, respectively. The obtained sample was annealed at 240 °C for a given time. SANS was measured as a function of annealing time t_{an}.

Figure 1 shows the scattering profiles of dPSU/PA at various annealing times. In the small-q region (e.g., for t_{an}=74 min. q<0.3 nm^{-1}) the scattering profiles obey Porod law which represents the scattering from sharp interface. {$I(q)=2\pi\Delta\rho^2 S_{sp}$, $\Delta\rho^2$: contrast factor, S_{sp}: interfacial area density} In the high-q(e.g., for t_{an}=74 min. q > 0.3 nm^{-1}), the scattering profiles have almost no q-dependence and the intensity is very weak. The result suggests that there are almost no thermal concentration fluctuations inside the domain because of strong segregation between dPSU and PA. Furthermore, we estimated S_{sp} from Porod law as a function of annealing time (Fig. 2). S_{sp} decreases with time with an exponent of -0.37 ($S_{sp}\sim t^{-0.37}$).

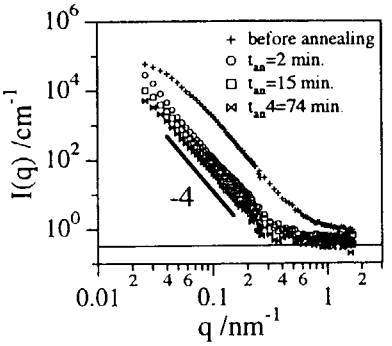

Fig. 1 SANS profile for dPSU/PA blend annealed at 240 °C.

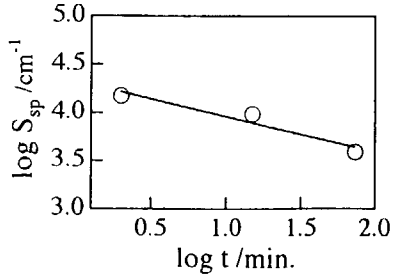

Fig. 2 log S_{sp} vs log t

研究テーマ：高分子多成分系の静的階層構造の研究
標　　題：牛血清アルブミンゲルのPNO研究

PNO Study on Bovine Serum Albumin Gels

Y. IZUMI, K. SOMA, K.AIZAWA[1], S.KOIZUMI[1] AND H.TOMIMITSU[1]

Graduate School of Engineering, Yamagata University, Yonezawa, Yamagata 992-8510
[1]Advanced Science Research Center, JAERI, Tokai, Ibaraki 319-1195

Heat-induced gelation of proteins is very important for commercial production such as foods and pharmaceuticals. For example, some foods of milk and soy proteins have been traditionally manufactured by this principle. To control the process it is essential to understand the fundamental behavior of gelation. Heat-induced gelation is also important in manufacturing lines, because it can cause problems such as the fouling of pipes. Without sufficient imformation about the gelation mechanism, it is almost impossible to deal with such difficulties.

In present work, we intended to investigate the structure of a globular protein gel by PNO measurements. As the globular protein, we selected bovine serum albumin (BSA) by the following reasons. BSA is abundant in blood plasma and also the fifth component in whey protein. The chemical and biological properties have been reported in detail in previous reviews. BSA used was the pure commercial product from Sigma Chemical Co. The solvent used was the heavy water (>99.8%) purchased from CEA. By changing both the gelation temperature (T_{gel}) and the gelation time (G_{time}), three types of heat induced gels were prepared at 0.185M NaCl: gel A (T_{gel}=90°C, G_{tim}=5min), gel B(T_{gel}=80°C, G_{tim}=10min) and gel C (T_{gel}=70°C, G_{tim}=10min). The BSA concentration of the gels was constant (about 17.5wt%). The neutron scattering experiments were performed with the JAERI 3G PNO spectrometer installed at JRR-3M reactor of JAERI (Tokai). The PNO data were obtained at room temperature. The slit height correction has been performed to desmear the effect caused by the vertical divergence of the incident beam. The data is corrected for blank cell background. Data taken at λ=0.25nm cover the q-range 0.0002 nm^{-1} to 0.06nm^{-1}.

Fig. 1 shows the excess scattering curves I(q), radially averaged, in a double log presentation. The Porod behavior of $I(q) \propto q^{-4}$ is observed for each gel. By comparing the data with a monodispersed spheres scattering function, the diameters of junction zone of the present gels can be evaluated. Gel A, B and C correspond to junction zones with diameter of about 0.9, 26 and 32 μm, respectively.

These results indicate that the size of the junction zone decreases and the size distribution broadens as the gelation temperature elevates and that the PNO technique is useful to determine the size of the junction zone of micron order in gels.

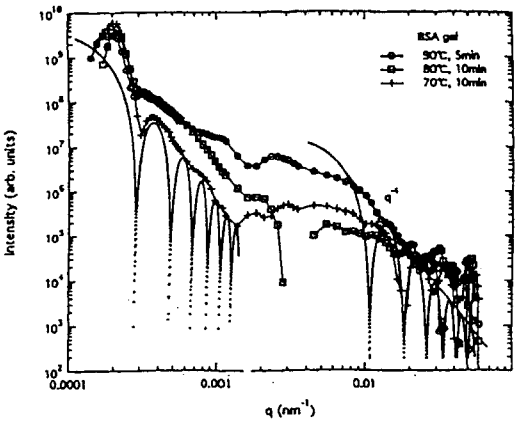

Fig. 1. Log-log plot of intensity vs. q for three gels. 90°C and 5min (gel A), 80°C and 10min (gel B), 70°C and 10min (gel C). The solid lines are guides to the eye. A monodisperse sphere scattering function is shown in gel A and gel C.

References

1) A.Tobitani, Ph. D. thesis, King's College London, University of London (1995).
2) K.Aizawa & H.Tomimitsu, Physica B 213&214(1995)884-886.

原子炉：JRR-3M　　PNO (3G)　　分野：中性子散乱（高分子）

研究課題：二様分子量分布を持つポリスチレン鎖のバルク中の拡がり
表題：低分子量同族体で希釈されたポリスチレンのバルク中の拡がり

Chain Dimensions of Polystyrenes Diluted with Low Molecular Weight Homologues in Bulk

Y.Matsushita,[1] N.Takabayashi, [2] N.Torikai, [3] J.Suzuki, [1] I.Noda[2]
[1]NSL, ISSP, The University of Tokyo, Tokai, Naka, Ibaraki 319-1106, Japan
[2]Department of Applied Chemistry, School of Engineering, Nagoya University
[3]Neutron Science Laboratory, IMSS, High Energy Accelerator Research Organization

Single chain dimensions of polystyrenes diluted with low molecular weight homologues were measured by small-angle neutron scattering to investigate the excluded volume effects generated in amorphous bulk polymer system.

Experiments were actually carried out for three component polymer blend systems, i.e., high molecular weight poly(styrene-d_8)s, poly(styrene-h_8) counterparts and low molecular weight styrene-d_8-styrene-h_8 random copolymer as matrix molecules for each blend. Three sample sets, whose molecular weights are 25K, 120K and 350K, were examined in several matrices, whose molecular weights were ranging from 1.7K to 45.9K. The concentrations of high molecular weight "solute" polymers were 3%, 5%, 10% and 20%. The blend samples were obtained by solvent casting first and successively the films were stacked, moulded and annealed. The sample to detector distances in SANS experiments were 4, 8, 12 and 16m and the wavelength adopted were in the range of 6.0 - 9.5A. Polymer solutions in benzene and styrene monomer were also measured as reference experiments.

It was confirmed that polystyrene chains diluted with low molecular weight homologues were expanded both when the molecular weight of matrices are relatively low and when the concentrations of "solutes" are reasonably low as was the case of the chains in styrene monomer. Further, it was found that the critical degree of polymerization of matrix molecules($N_{m,c}$) which give the excluded volume effects depends on the degree of polymerization of "solutes", but it was also found that the experimental results don't agree with the relationship, $N_{m,c} = N^{1/2}$, which has been predicted by de Gennes .

Reactor: JRR-3M Facility: SANS-U(C1-2) Field: 6. 高分子polymer

研究テーマ：バルク状態並びに溶液中の２元ブロック共重合体の秩序無秩序転移
表題：対称なスチレン－２ビニルピリジンのバルク並びに溶液中の秩序無秩序転移

Order-Disorder Transition of Symmetric Poly(styrene-b-2-vinylpyridine) in Bulk and Solution

Y. Takahashi, S. Kitade, N. Noda, N. Ochiai, I. NODA,
Y. Matsushita[1] and M. Imai[1]

Department of Applied Chemistry, Faculty of Engineering, Nagoya University, Chikusa-ku, Nagoya 464-01
[1]*Institute for Solid State Physics, University of Tokyo, Roppongi, Tokyo 106*

Order-disorder transitions (ODT) of symmetric poly(styrene-b-2-vinylpyridine) in a common good solvent and bulk were determined by dynamic rheological and small-angle neutron scattering (SANS) measurements. Here, we breafly report the SANS results.

Samples used were three symmetric poly(styrene-d8-*b*-2-vinylpyridine) shown in Table I. DP19 and DP20 were measured as α-chloronaphtharene solution while DP17 was measured both in solution and melt. The SANS experiments were performed with the ISSP SANS-U spectrometer installed at JRR-3M reactor of JAERI (Tokai). The wave length was 7 Å.

Table I

Sample code	M_w	M_w/M_n
DP17	1.2×10^4	1.05
DP19	2.0×10^5	1.05
DP20	3.6×10^5	1.08

Figure 1 shows examples of plots of scattered intensity I(q) vs. wave vector q in semidilute solution. It is clear that data in ordered and disordered states are definitely defferent and ODT can be determined without ambiguity. However, the data in concentrated solutions and melt showed relatively small defference in two states. By the analysis of peak position and peak hight, ODT of those samples are also determined. ODT conditions thus determined were consistent with those from rheological measurements. The degree of polymerization dependence of critical volume fraction in solution at almost constant temperature agrees with the theoretical prediction for semidilute solutions. The details are already published in Polymer Journal vol. 30 p.388, 1998.

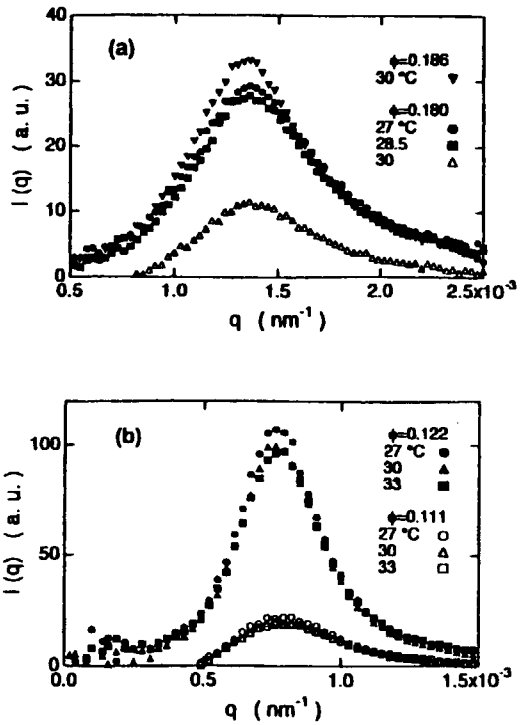

Figure 1. Examples of plots of I(q) vs. q in semidilute solutions (a) for DP19 and (b) DP20. Open and filled symbols show the data in disordered and ordered states, respectively.

研究課題：逆ミセル系の構造形成と構造ダイナミックス
表題：中性子スピンエコー法によるW/O AOTマイクロエマルジョンのダイナミックス研究

Dynamics of w/o AOT Microemulsions studied by Neutron Spin Echo

M. Hirai,[1] H. Iwase,[1] S. Arai,[1] S. Yabuki,[1] T. Takizawa,[1] R. K. Hirai,[2]
T. Takeda,[3] H. Seto,[3] and M. Nagao.[4]

[1] *Department of Physics, Gunma University, Maebashi 371, Japan.*
[2] *Meiwa Women's Junior College, Maebashi, Gunma 371, Japan*
[3] *Faculty of Integrated Arts and Science, Hiroshima University, Higashi-Hiroshima 739, Japan,*
[4] *Institute for Solid State Physics, University of Tokyo, Tokai 106-1, Japan.*

By using neutron spin echo (NSE) we have studied the structural fluctuation of water /sodium bis(2-ethylhexyl)sulfosuccinate (AOT)/ d_{16}-*n*-heptane microemulsion with varying water/ surfactant molar ratio w_0 (=[water]/[AOT]). In our previous synchrotron radiation small-angle X-ray scattering studies we showed that in the w_0 range of 16-50 the obtained structural parameters of the AOT reversed micelle and a linear relation between the water pool radius and the w_0 value are in agreement with those determined by other authors, however we found a serious discrepancy from the linear relation in the w_0 range of $0 < w_0 < 12$, which was understood as a presence of an oligomeric phase. In addition we also found that the enzymatic activity of w/o AOT microemulsions occluding α-chymotrypsins is greatly enhanced in this low w_0 range. However, physicochemical mechanism of appearance of so-called super activity of enzymes entrapped in w/o microemulsion has not been clarified enough. Our recent small-angle neutron scattering experiments with solvent contrast variation method show the change the excluded volume of AOT monomer depending on w_0 value, which would relate to an enhancement of enzymatic activity of proteins entrapped in AOT reversed micelles at low water content since the internal interface of the AOT reversed micelle might play an important role to change an apparent interfacial area of the micelles close to the enzymes.

For clarifying a mechanism of the appearance of super activity, it is essentially important to know dynamics of the interfacial structure of the AOT microemulsion droplets. To observe dynamics of oligomeric phase at low w_0 values, NSE experiments have been carried out by using a NSE spectrometer installed at C2-2 beam port at the research reactor JRR-3M of JAERI. In Figure 1 we show preliminary results obtained by NSE measurements at the film-contrast condition, where the average scattering density of water (98.5%D_2O) is as same as that of d_{16}-*n*-heptane. The reversed micellar solutions were obtained by using an injection method. The w_0 value was selected to be 5, 10 and 20. As shown in Figure 1, the effective diffusion coefficient D_{eff} has a peak around q ~0.075-0.09 Å^{-1}. The position of the peak does not satisfy $qR=\pi$, however it would reflect the oligomers at low w_0 value. Further experiments and analyses are in progress.

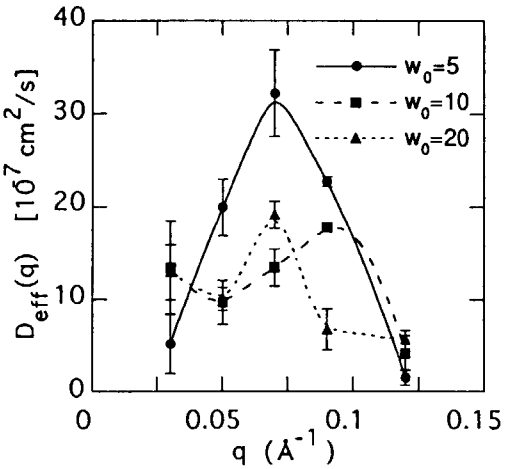

Figure 1 q dependence of effective diffusion coefficient D_{eff} of water/AOT/heptane microemulsion (0.1 M AOT).

Reactor: JRR-3M Facility: NSE(C2-2) Field: 6.高分子Polymer

課題名：ジアルキルホスフェイト分子の非対称と二分子膜形成との相関
表　題：ジアルキルホスフェイト分子の非対称と二分子膜形成との相関（中性子スピンエコー法）

Self-organized structures of Lithium dialkylphosphates a relationship between asymmetric molecular shape and bilayer formation. Neutron spin echo study

H. Okabayashi,[1] N. Hattori[1], S. Sasuga[1], M. Takai,[1] N. Ichiyanagi,[1] H. Seto[2] and T. Takeda[2]

Department of Applied Chemistry, Nagoya Institute of Technology[1]

Faculty of Integrated Art and Sciences, Hiroshima University[2]

Mixed-double chain anionic surfactants (MDAS), (the lithium salts of ethyl (dodecyl)phosphate, butyl(dodecyl)phosphate and hexyl(dodecyl)phosphate), which are asymmetric in the molecular shape, were synthesized and the phase diagrams of the MDAS-water binary systems were determined by using the differential scanning calorimetry and X-ray low angle diffraction methods. The existence of the phase involving a lamellar structure was confirmed for the MDAS-water binary systems.

For the lamellar sample solution (30 wt%) of hexyl(dodecyl)phosphate, the neutron spin echo signals were measured at various Q values (0.03, 0.05, 0.07, 0.09, 0.10, 0.11, 0.13, 0.15, 0.16, 0.17 and 0.18 Å), in order to investigate the slow dynamics of the bilayer structure.

The normalized NSE signal amplitude P_{NSE}, which corresponds to the normalized intermediate correlation function $I_N(Q,t)=I(Q,t)/I(0,t)$, was obtained from the NSE experiments. P_{NSE} against t was best fit to the equation $P_{NSE} = A \exp[- (\Gamma t)^{\beta}]$ as shown in Fig. 1, where the index β obtained from the fitting is 0.665 for Q=0.13Å^{-1}. Zilman and Granek[1)] used the Helfrich bending free energy to describe membrane undulations in sponge and lamellar phases and predicted a stretched exponential relation $I(Q,t)=I(Q,0) \exp[- (\Gamma t)^{2/3}]$.

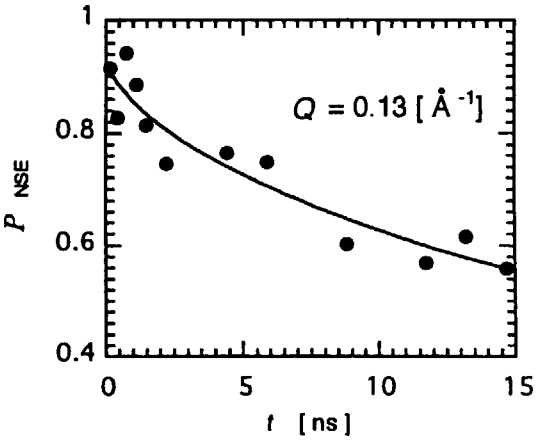

Figure 1 P_{NSE} vs t of HDodPLi-D_2O 30wt% binary system

JRR-3M, NSE(C2-2), Polymer

研究テーマ：高分子ミセルのコロナ部分の分子鎖ダイナミックス
表題：中性子スピンエコー法による高分子ミセルの呼吸モード

Breathing Mode of Polymeric Micelles As Studied by Neutron Spin Echo

T. Kanaya, H. Watanabe, Y. Matsushita[1], T. Takeda[2], H. Seto[2], M. Nagao[1], Y. Fujii[1] and K. Kaji
Institute for Chemical Research, Kyoto University
Institute for Solid State Physics, University of Tokyo[1]
Faculty of Integrated Arts and Science, Hiroshima University[2]

In the previous work [1], we reported the results of neutron spin echo (NSE) measurements on polymeric micelles of deuterated polystyrene (PS) and protonated polyisoprene (PI) diblock copolymers in a selective solvent (n-decane). The core and corona of the polymeric micelles consist of PS and PI, respectively (see Fig.1). The scattering length density of the PS is matched to the solvent so that we see the dynamics of the corona part.

In the present work, we have extended the Fourie time region up to 15 ns using neutrons with longer wavelength (7.1 Å) than the previous measurements [1]. The observed normalized correlation functions $I(Q,t)/I(Q,0)$ are shown in Fig.2 for the 2 % dilute solution, in which the micelles are isolated. For an isolated micelle, we can expected a breathing mode for polymer chains in corona of polymeric micelles [2]. This mode was first formulated by de Gennes [3] and extended to polymer micelles by Farago et al. [2]. The motion is dominated by the osmotic compressibility and the elastic force. Following to Farago et al., we theoretically calculated the normalized correlation functions for the breathing mode and showed the results in Fig. 2 by solid curves. At the high Q values, the agreements are very good, conforming the breathing mode although deviations are observed at the low Q values. This disagreement may be due to lateral modes in the corona part, which was neglected in the theoretical treatment.

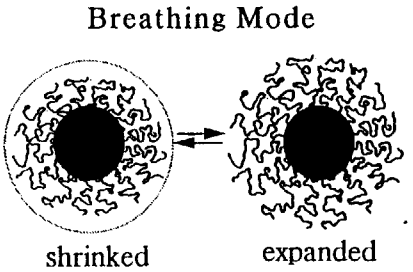

Fig.1. Schematic drawing of breathing mode in an isolated polymeric micelle. The core and corona consist of PS and PI, respectively.

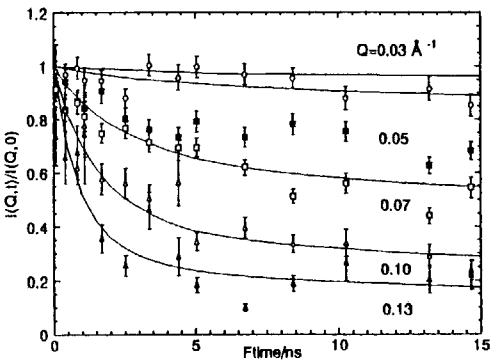

Fig. 2. Normalized correlation functions $I(Q,t)/I(Q,0)$ for the 2% solution. Curves are the theoretical functions. Q values are 0.03, 0.05, 0.07, 0.1 and 0.13 $Å^{-1}$ from top.

1) T. Kanaya et al, Activity Report on Neutron Scattering Research, **4**, 184 (1997).
2) B. Farago et al., Phys. Rev. Lett., **71**, 1015 (1993).
3) P. G. de Gennes, C. R. Acad. Sci. Paris Ser. II, **302**, 765 (1986).

JRR-3M, NSE, 6. polymer

研究テーマ：中性子反射率測定に基づくポリマーブレンド超薄膜中の分子鎖凝集構造評価
表題：中性子反射率測定に基づく2様分子量分布を有するポリスチレンブレンド超薄膜中の分子鎖凝集構造評価

Analysis of Molecular Aggregation State in Polystyrene Film with Bimodal Molecular Weight Distribution by Neutron Reflectivity

Tisato Kajiyama, Keiji Tanaka, Atsushi Takahara, Seiji Tasaki[1], Toru Ebisawa[1], and Yushu Matsushita[2]

Department of Materials Physics & Chemistry, Graduate School of Engineering, Kyushu University, Higashi-ku, Fukuoka 812-8581, Japan

[1]Research Reactor Institute, Kyoto University, Osaka 590-04, Japan,

[2]Neutron Scattering Laboratory, ISSP, The University of Tokyo, Ibaraki 319-11, Japan

Physicochemical properties and aggregation structure of the polymeric solid surface and interface are quite different from those for bulk state.[1-4] The purpose of this study is experimentally to elucidate an effect of the lower molecular weight component on the surface molecular motion and the surface structure, especially the relationship between surface molecular motion and surface aggregation structure for the (PS19.7k/dPS1,000k) film.

Monodisperse PS with Mn of 19.7k (PS19.7k) and dPS with Mn of 1,000k (dPS1,000k) were used for the preparation of blend thin film. The (PS19.7k/dPS1,000k) (5/95 weight/weight) film of ca. 100~200 nm thick were coated from a toluene solution onto a silicon wafer with native oxide layer by a spin-coating method and then annealed under vacuum at 393 K for 24 hrs. Since our main goal is to reveal an effect of lower molecular weight component on the surface molecular motion and the surface structure in the case of the small amount of the lower molecular weight component, the weight fraction of PS19.7k was 5 %. The surface aggregation structure of the (PS19.7k/dPS1,000k) film was evaluated by NR measurements. NR measurement was carried out by using the multilayer interferometer for neutrons (C-3-1-2, MINE). The incident neutrons had a long wavelength of 1.26 nm with wavelength resolution of 3.2 %. The reflectivity was calculated based on the model scattering length density profile along the depth direction by using Parratt's algorithm.

In order to confirm the surface aggregation state of the (PS19.7k/dPS1,000k) (5/95) film, NR measurements were carried out. Figure 1 shows the scattering vector, q [=$(4\pi/\lambda)$ sin θ where λ and θ are the wavelength and the incident angle of the neutron beam] dependence of neutron reflectivity for the (PS19.7k/dPS1,000k) (5/95) film. The solid line denotes the best-fitted reflectivity profile calculated on the basis of the model scattering length density, (b/V) profile along the direction perpendicular to the film surface shown in Figure 2. The model (b/V) profile was drawn on the basis of the dynamic secondary ion mass spectroscopic (DSIMS) measurement by taking account the film thickness and the surface roughness, which were evaluated by ellipsometric measurement and atomic force microscopic observation, respectively. The magnitudes of (b/V) for PS and dPS were 1.41×10^{-4} nm^{-2} and 6.47×10^{-4} nm^{-2}, respectively. Also, the presence of the thin SiO_2 layer of 2 nm thick with (b/V) of 3.48×10^{-4} nm^{-2} was assumed as an oxidation layer at the silicon wafer surface. The film thickness and the surface roughness of were 113.2 nm and 0.33 nm, respectively. Since the calculated reflectivity was in good agreement with the experimental one, it can be consider that the model (b/V) profile shown in Figure 2 corresponds well to the composition profile along the film depth direction of the (PS19.7k/dPS1,000k) film.

Since the magnitudes of (b/V) at both air/polymer and polymer/substrate interfaces were 6.13×10^{-4} nm^{-2} and 5.77×10^{-4} nm^{-2}, respectively, and were small compared with that of the internal region, it seems reasonable to conclude again from the NR measurement that the lower molecular weight PS is preferentially segregated at both interfaces.

The magnitude of (b/V) for the internal region was 6.27×10^{-4} nm^{-2} and was a little smaller than that of pure dPS with (b/V) of 6.47×10^{-4} nm^{-2}. This result indicates that

JRR-3M, C3-1-2 MINE, 6. Polymer

PS19.7k is present in the bulk region as well as at both interfacial regions. Under the assumption of incompressibility for a polymer chain, the magnitude of (b/V) can be expressed as a summation of the magnitude of (b/V) for pure components.[6)]

$$(b/V)(z) = \Sigma (b/V)_i \phi_i(z) \quad (1)$$

$$\Sigma \phi_i(z) = 1 \quad (2)$$

where $\phi_i(z)$ is the volume fraction of i component at z along the direction perpendicular to the film surface. The weight fraction of PS 19.7k at the surface, in the internal region and at the substrate interface calculated with eq. (1) by taking account its density were 6.3 %, 3.7 % and 13.0 %, respectively. Next, the segregation depth range of PS19.7k at both interfaces, which is generally so-called decay length, will be discussed. The decay length can be expressed as a function of exp (-z/ξ) , where ξ is the bulk correlation length. However, since the PS19.7k rich thin layer was observed, here, the segregation depth was defined as the region from the air/polymer or polymer/substrate interfaces to the depth that the maximum slope of (b/V) crossed the bulk (b/V) value. The segregation depth of PS19.7k at the air/polymer and the polymer/substrate interfaces were ca. 13.5 nm and 9.5 nm, respectively. Especially, in the case of the polymer/substrate interface, since the segregation depth is almost comparable to twice the radius of gyration of an unperturbed chain of 7.6 nm, it is likely that the rich layer of PS 19.7k was formed by a PS 19.7k monolayer adsorbed on the silicon wafer surface.

The chain end group with lower surface free energy compared with the main chain part is localized at the film surface and then the free volume fraction at the film surface increases rather than its internal region. Since the concentration of the chain end groups is proportional to 2/N where N is the degree of polymerization, the surface segregation of the lower molecular weight component induces a more excess free volume at the film surface, resulting in more activated surface molecular motion in comparison with the higher molecular weight component. Thus, it seems reasonable to conclude that the surface of the (PS19.7k/dPS1,000k) film is in a glass-rubber transition state at 293 K[4)] due to the surface

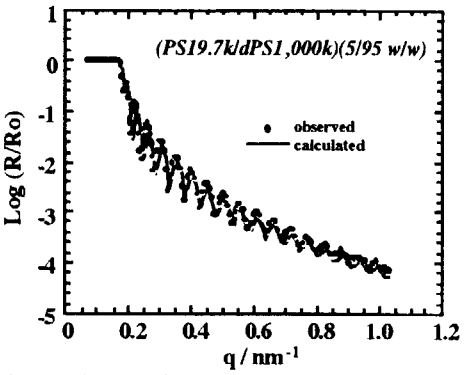

Figure 1 The scattering vector, q dependence of neutron reflectivity for the (PS19.7k/dPS1,000k) (5/95 w/w) film.

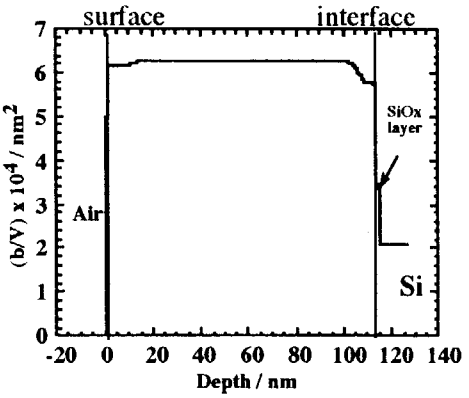

Figure 2. The coherent scattering length density profile along the direction perpendicular film.

localization of the lower molecular weight component, PS19.7k, even though bulk Tg evaluated by DSC is 378 K.

In conclusion, NR reflectivity study of (PS19.7k/dPS1,000k) film revealed that the lower molecular weight component in the PS film with bimodal molecular weight distribution was preferentially segregated at both air/polymer and polymer/substrate interfaces.

References

1) Kajiyama, T.; Tanaka, K.; Ge, S.-R.; Takahara, A. *Prog. Surf. Sci.* **1996**, *52*, 1.
2) Kajiyama, T.; Tanaka, K.; Takahara, A. *Macromolecules* **1997**, *30*, 280.
3) Tanaka, K.; Takahara, A.; Kajiyama, T. *Macromolecules* **1996**, *29*, 3232.
4) Tanaka, K.; Takahara, A.; Kajiyama, T. *Macromolecules* **1997**, *30*, 6626.
5) Russell, T. P. *Mater. Sci. Rep.* **1990**, *5*, 171.
6) Torikai, N.; Noda, I.; Karim, A.; Satija, S. K.; Han, C.-C.; Matsushita, Y.; Kawakatsu, T. *Macromolecules* **1997**, *30*, 2907.

研究テーマ：中性子反射率測定に基づく分子鎖末端構造を制御したブロック共重合体薄膜の凝集構造評価
表題：中性子反射率測定に基づくポリ（スチレンーb－メチルメタクリレート）ブロック共重合体薄膜の凝集構造評価

Analysis of Molecular Aggregation State in Poly(styrene-b-methylmethacrylate) Diblock Copolymer Thin Film by Neutron Reflectivity

Atsushi Takahara, Kensuke Nakamura, Keiji Tanaka, Seiji Tasaki[1], Toru Ebisawa[1], Yushu Matsushita[2], and Tisato Kajiyma

Department of Materials Physics & Chemistry, Graduate School of Engineering, Kyushu University, Higashi-ku, Fukuoka 812-8581, Japan

[1]Research Reactor Institute, Kyoto University, Osaka 590-04, Japan,

[2]Neutron Scattering Laboratory, ISSP, The University of Tokyo, Ibaraki 319-11, Japan

The symmetric A-B diblock copolymer in solid state forms the lamellar structure in the equilibrium state. In the case of symmetric A-B diblock copolymer being composed of components with different surface free energy, it is expected that lamellar orient parallel to the film surface in order to minimize the surface and interfacial free energies. However, little study has been reported on the effect of end group structure on the aggregation structure of diblock copolymer films. In this study, a poly(styrene-d_8-block- methylmethacrylate) diblock copolymer with carboxylated end group [P(dSt-b-MMA)-COOH] was prepared and the neutron reflectivity was measured in order to reveal the effect of introduction of hydrophilic end group on the structure of diblock copolymer thin films.

The sample used was a poly(styrene-d_8-block-methylmethacrylate) diblock copolymer with carboxylated end group [P(dSt-b-MMA)-COOH] synthesized by anionic polymerization of sequential monomer addition. The number average molecular weight and PS weight fraction were 30.5k and 0.4, respectively. The thin film was spin-coated on a silicon wafer and annealed at 423K for a week.

The aggregation structure of the P(dSt-b-MMA)-COOH film was evaluated by NR measurements. NR measurement was carried out by using the multilayer interferometer for neutrons (C-3-1-2, MINE) at the Institute for Solid State Physics, the University of Tokyo. The incident neutrons had a long wavelength of 1.26 nm with wavelength resolution of 3.2 %. The reflectivity was calculated based on the model scattering length density profile along the depth direction by using Parratt's algorithm.

Figure 1 shows the scattering vector, q [=$(4\pi/\lambda)\sin\theta$ where λ and θ are the wavelength and the incident angle of the neutron beam] dependence of neutron reflectivity for the P(dSt-b-MMA)-COOH thin film. The solid line denotes the best-fitted reflectivity profile calculated on the basis of the model scattering length density, (b/V) profile along the direction perpendicular to the film surface shown in the inset of Figure 1. The thickness calculated from Kiessig fringes was ca.71.75 nm which corresponded well with that obtained from ellipsometric measurement. The large maximum of reflectivity observed at ca. $q=0.32nm^{-1}$ corresponded to the long period of lamellar structure. The partial phase mixing was assumed for the calculation of the profile because of the small magnitude of χ between dPS and PMMA. Since the surface free energy of PMMA is greater than that of dPS, the dPS would adsorb at the air interface, on the other hand, PMMA would adsorb on the oxidized silicon substrate. The calculated reflectivity seemed to agree well with the observed one. The result indicated that the introduction of carboxyl group at the end of PMMA block did not influence the aggregation structure of P(dSt-b-MMA)-COOH thin films.

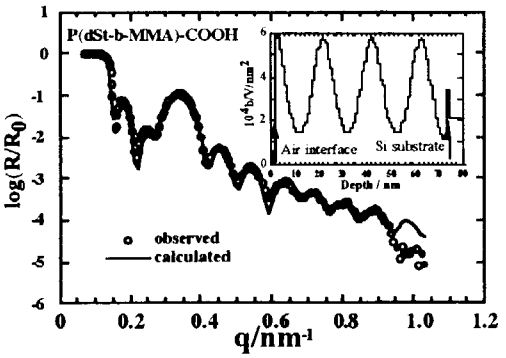

Figure 1 shows the scattering vector, q dependence of neutron reflectivity for the P(dSt-b-MMA)-COOH film. The inset shows the model scattering length density, (b/V) profile along the direction perpendicular to the film surface.

JRR-3M, C3-1-2 MINE, 6. Polymer

研究テーマ：中性子反射率法による固-液界面における両親媒性高分子の形態とその集合状態の解析
表題：中性子反射率法による固-液界面における両親媒性高分子の形態とその集合状態の解析

Determination of the Density Profile of Amphiphilic Polymer Adsorbed at Solid/Liquid Interface by Neutron Reflectometry

H. Endo, K. Kago, K. Matsumoto, H. Matsuoka, H. Yamaoka
Department of Polymer Chemistry, Kyoto University

Polymer surface and interface play important roles in various interface phenomena such as adsorption, adhesion etc. In this study, neutron reflectivity technique (NR) was applied to investigate fine structure of amphiphilic polymer (polyethylene glycol[PEG]) adsorbed at solid/liquid interface. NR technique gives us information about thickness of layers, surface and interface roughnesses with very high resolution (Å order) by *in situ* experiment.

A single-crystal, optically flat silicon slab was used as a substrate in order to achieve acceptable transmission. Solution of 1wt% of polymer in D_2O was introduced into the gap between the silicon block and the Teflon base. The sample was monodisperse PEG (M.W.=50K). The measurement was started more than two hours after the solution was packed in.

The NR measurements were performed at JRR-3 MINE. The wavelength of incident neutron beam was 12.6Å.

The difference of reflectivities between pure water and polymer solution is shown in Figure 1. It can be seen that the reflectivity of pure water is simply decreasing, while the reflectivity of the polymer solution is shown smooth fringes. It is a evidence of the formation of an uniform adsorbed layer.

In the model fitting, we assume the adsorbed polymer layer forms uniform monolayer with the roughness obeys with the Gaussian distribution (we call Gaussian model) or scaling law (see Figure 3). In the scaling theory, the polymer volume fraction, ϕ, is given by the equation

$$\phi(z)=(a/z)^{4/3}$$

where z is the distance from the wall and 'a' is the lowest limit from the wall. It means that polymer segments aggregate and form the uniform layer between wall surface and distance 'a'.

Compared with these two models and experimental data, the scaling theory with parameters are a=50Å and z_{max}=250Å showed better agreement with the experimental data than Gaussian model (see Figure 2).

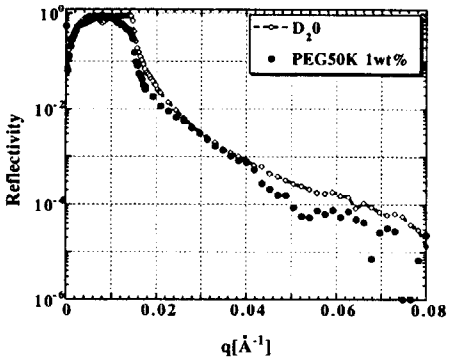

Figure 1. NR curves for pure D_2O and adsorbed layer of PEG50K.

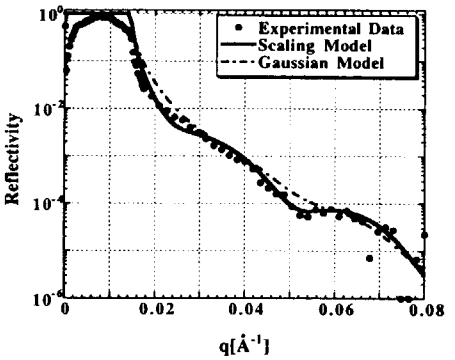

Figure 2. NR profile for PEG50K adsorbed at solid/liquid interface and model fitting curves based on the scattering length density profiles showed in figure 3.

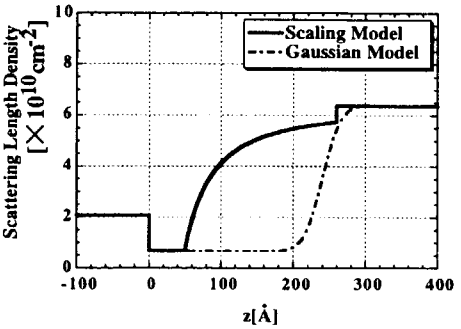

Figure 3. The scattering length density profiles of model fitting.

研究テーマ：ループ状の相図を有するブロック共重合体の相転移に関する研究
表題：ループ状の相図を有するブロック共重合体の相転移

Phase Transition in Block Copolymers with a Looped Phase Diagram

T. Hashimoto, T. Hashimoto, H. Hasegawa, M. Takenaka, M, Sawamoto, M. Nagao[1] and M. Imai[1]

Department of Polymer Chemistry, Graduate School of Engineering, Kyoto University, Sakyo-ku, Kyoto, 606-8501 Japan
[1] Neutron Scattering Laboratory, The Institute for Solid State Physics, The University of Tokyo, Shirakata, Tokai, Naka, Ibaraki, 319-11 Japan

We prepared and investigated by small-angle neutron scattering (SANS) a deuterated polystyrene-*block*- poly(vinyl methyl ether) diblock copolymer (DPS-PVME)[1)] for which a reentrant (circular) phase diagram was predicted.[2)] However, the DPS-PVME with the number-average molecular weight (M_n) of 2.3×10^4 was found to be deep in the disordered state and exhibited the lower-critical solution temperature (LCST) type phase behavior similar to a DPS/PVME blend.

This time we prepared a DPS-PVME sample with much higher molecular weight $M_n = 1.5\times10^5$ and measured its temperature dependence with SANS-U (λ=7.0Å, SDD=4.0m) equipped with the high-temperature cell controlled by TEMCON.

Figure 1 shows the temperature dependence of the small-angle neutron scattering (SANS) profiles from the DPS-PVME sample for the cooling cycle. The scattering profiles are quite unusual for a neat block copolymer. Probablly, homopolymers might have been mixed during the sample synthesis. The asymptote of the scattering profiles with slope -4 (Porod law) suggests the macrophase separation between homopolymer-rich and DPS-PVME-rich domains. The asymptote with slope -2 at higher angles may be due to the scattering from the disordered block copolymer within the macrodomains. On cooling, a peak appeared at q=0.33 nm^{-1}, suggesting the possible ordering at low temperature.

References

1) T. Hashimoto et al., *Macromolecules*, **30**, 6819 (1997).

2) J. Dudowicz and K. F. Freed, *Macromolecules*, **26**, 213 (1993).

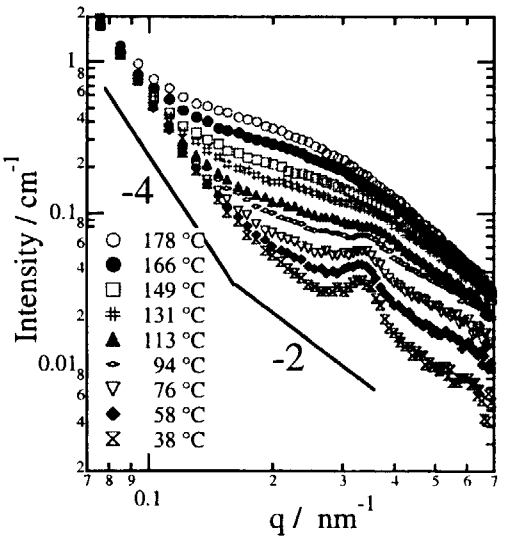

Figure 1 Temperature dependence of the SANS Profiles of the DPS-PVME diblock copolymer in the cooling process.

研究テーマ：ブロック共重合体の秩序ー無秩序転移に関する研究
表題：圧力ジャンプにより誘起された高分子ブロック共重合体の秩序化過程のダイナミックス

Self-Asssembly of Block Copolymers Induced by Pressure Jump

T. Hashimoto, N.SAkamoto, H.Takenak, H. Hasegawa, M. Nagao[1] and M. Imai[1]

Department of Polymer Chemistry, Graduate School of Engineering, Kyoto University, Sakyo-ku, Kyoto, 606-8501 Japan
[1]Neutron Scattering Laboratory, The Institute for Solid State Phyisics, The University of Tokyo, Shirakata, Tokai, Naka, Ibaraki, 319011 JAPAN

Recently, numerous studies have been made on phase transition of complex fluids in various research fields. Small-Angle netron scattering (SANS) has made a great contribution to phase transitiion studies of critical phenomena, miscibility and phase separation processes, etc. As for the studies on the dynamics of the phase separation processes, many experiment on the dynamics phase transition induced by temperature jump. However, it takes some time to reach the target condition by temperature jump and we can not follow the dynamics of a rapid phase transition. On the other hand, since we can attain quick quench by pressure jump, the pressure jumpenables us to follow the dynamics of a rapid phase transition. With this advantage, we investigated the microphase transition processes of Poly(deuterated-butadinen-b-isoprene) (DPB-PI) by using the time-resolved neutron scattering measurement. The number-averaged molecular weight M_n and polydispersity (M_w/M_n) of the DPB-PI are 4.90×10^5 and 1.11, respectively. The volume fraction of DPB is 0.53. Figure 1 shows the chainge in the scattering profiles plotted as a function of wave number q with time after DPB-PI quenched from a disordered state to ordered state by a pressure drop. Pressure was dropped from 80MPa to 0.1MPa at 341.4K. Fluctuation of temperature was within 0.1K during measurement. Surprisingly, at the moment of the pressure jump (t=0), the peak position q_m shifts toward lower q. At later time q_m shifts back to its higher value. The scattered intensity also increases with time. Moreover, the profiles at t>940.02 sec start to exhibit a second-order peak. The appearanc eof the second-order peak implies that ordering into lamella microdomaions started to occur with time. We will analyse the shift of q_m and the change in the scattered intensity in detail.

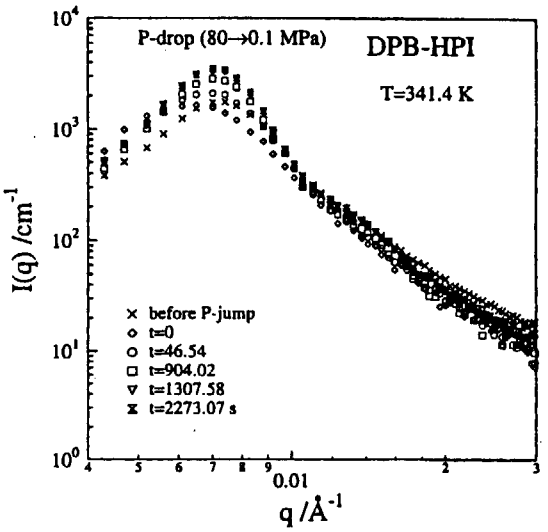

Figure 1 The time change in the scatteredintensity of DPB-PI diblock copolymer induced by pressure jump from 80MPa to 0.1 MPa.

研究テーマ：高分子ブロック共重合体の相溶性に及ぼす圧力効果の研究
表題：高分子ブロック共重合体の相溶性に及ぼす圧力効果

Pressure Effects on the Miscibility of Block Copolymers

H. Hasegawa, N. Sakamoto, H. Takeno, T. Hashimoto, M. Nagao[1] and M. Imai[1]

Department of Polymer Chemistry, Graduate School of Engineering, Kyoto University, Sakyo-ku, Kyoto, 606-8501 Japan
[1] Neutron Scattering Laboratory, The Institute for Solid State Physics, The University of Tokyo, Shirakata, Tokai, Naka, Ibaraki, 319-11 Japan

Most diblock copolymers exhibit the upper critical order-disorder transition temperature (UCODTT) type phase behavior, i.e., they microphase-separate at low temperatures. A typical example is polystyrene-*block*-polyisoprene (PS-PI) and its order-disorder transition (ODT) has been extensively studied. On the other hand, the lower critical order-disorder transition temperature (LCODTT) type phase behavior had not been known until we found it with deuterated polybutadiene *block*-polyisoprene (DPB-HPI) having the microstructures with low vinyl content for both components.[1)] Recently, pressure dependence of the ODT of PS-PI was examined by means of small angle X-ray scattering with synchrotron radiation, and it was found that the UCODTT of PS-PI increased linearly with pressure. Namely, the miscibility of PS-PI decreases with increasing pressure. Therefore, it is interesting to investigate the pressure dependence of LCODTT of DPB-HPI by small-angle neutron scattering (SANS).

SANS-U (λ=7.0Å, SDD=8.0m) was used to obtain the temperature and pressure dependences of the SANS profiles of a DPB-HPI with vinyl contents as low as 5% for both components. We found that the ODT temperature (T_{ODT}) of the DPB-HPI increases linearly with increasing pressure as show in Figure 1. This indicates that the miscibility of DPB-HPI increases by applying pressure in contrast to the case of PS-PI because DPB-HPI has a LCODTT-type phase diagram. In other words, pressure shifts the phase boundary to higher temperatures for both cases.

References

1) H. Hasegawa et al., *Activ. Rep. Neut. Scat. Res., ISSP-NSL*, **2**, 182 (1995).
2) D. A. Hajduk et al., *Macromolecules*, **29**, 1473 (1996).

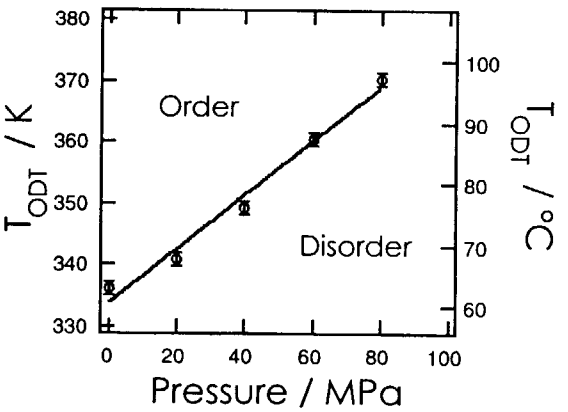

Figure 1 Pressure dependence of order-disorder transition temperature of the DPB-HPI diblock copolymer with the microstructure of low vinyl content for both blocks.

JRR-3M, SANS-U, 6. Polymer

研究テーマ：重水素化ポリブタジエン／ポリブタジエンブレンドの相溶性に及ぼす
圧力効果のミクロ構造依存性
表題：高分子の相溶性およびその圧力依存性におけるミクロ構造の効果

Microstructure Effects on the Miscibility of Polymers and Its Pressure Dependence

H. Hasegawa, N. Sakamoto, H. Takeno, T. Hashimoto, M. Nagao[1] and M. Imai[1]

Department of Polymer Chemistry, Graduate School of Engineering, Kyoto University, Sakyo-ku, Kyoto, 606-8501 Japan
[1] Neutron Scattering Laboratory, The Institute for Solid State Physics, The University of Tokyo, Shirakata, Tokai, Naka, Ibaraki, 319-11 Japan

Miscibility and phase behavior of polydienes, such as polybutadiene and polyisoprene, change dramatically with their microstructure, i.e., the way how the monomeric units are linked together. We have reported that inversion of the phase diagram can be observed for deuterated polybutadiene-*block*-polyisoprene diblock copolymers (DPB-HPI), i.e., lower critical order-disorder transition temperature (LCODTT) type phase behavior for the microstructures both rich in 1,4-linkages and upper critical order-disorder transition temperature (UCODTT) type for those both rich in vinyl linkages.[1)] We have also found that pressure increases the miscibility for the former block copolymer, i.e., the LCODTT increases linearly with increasing pressure. In this study, we examined the effect of pressure on the miscibility of the latter block copolymer.

SANS-U (λ=7.0Å, SDD=4.0m) equipped with the high-pressure cell was used to obtain the pressure dependence of the small-angle neutron scattering (SANS) profiles from the DPB-HPI sample of UCODT-type with the microstrycture of 54 and 72% vinyl linkages for DPB and HPI components, respectively. Figure 1 shows the SANS profiles at room temperature for various pressures. The scattering intensity increases with increasing pressure implying a decrease in the miscibility with pressure, which agrees with the results reported for UCODTT-type block copolymers.

References

1) H. Hasegawa et al., *Activ. Rep. Neut. Scat. Res., ISSP-NSL*, **3**, 187 (1996).

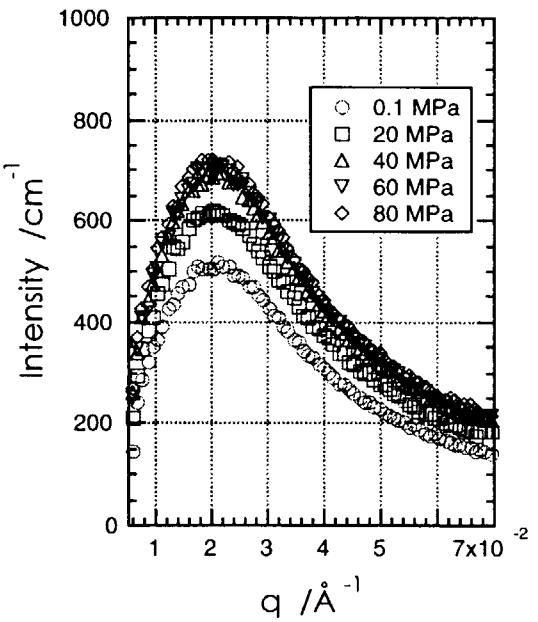

Figure 1 Pressure dependence of the SANS Profiles of the DPB-HPI diblock copolymer with the microstructure of high vinyl content for both blocks at room temperature.

研究テーマ：多糖/水系の高次構造形成と機能発現
標題：生体・高分子のゾルーゲル転移の普遍性

Universality of Sol-Gel Transition in Polymers and Biopolymers

Y. IZUMI, K. SOMA, J. SUZUKI, M. HASHIMOTO[1] AND T. TAKAHASHI[1]

Graduate School of Engineering, Yamagata University, Yonezawa, Yamagata 992-8510
[1]Institute for Solid State Physics, University of Tokyo, Roppongi, Tokyo 106

Thermoreversible sol-gel transition of polymers and biopolymers from solutions is a well-known phenomenon, and it is widely recognized that the gelation takes place as a consequence of three-dimensional network formation by chemical or physical linkage of these polymer chains. Although many efforts have been performed to reveal the mechanisms of sol-gel transition, many unsolved problems have been still remained.

The present work is concerned with the observation of the melting process of the junction zone of micron order in the gels by ULS spectrometer. Polyethylene (Sumikathene G20) characterized by M_n 30,000, M_w/M_n 10-20, the crystallinity 60%, was first used. The solvent used was the deuterated toluene (>99.6%) purchased from CEA. A cooling gel was prepared in a quartz cell of 4mm thickness. The sample was dissolved completely in toluene at an elevated temperature. Then, the gel was formed by standing the hot solution at 24.0℃ for 24h. The concentrations of the gel were 5.1 and 9.7wt%. The neutron scattering experiments were performed with the ISSP C1-3 ULS spectrometer installed at JRR-3M reactor of JAERI (Tokai). The wavelength of the neutron was 4.7309A. The ULS data were obtained over the temperature range between 10C and 70C.

The excess scattering intensity $\Delta I(q)$ at a scattering vector q can be analyzed by the Ornstein-Zernike (OZ) approximation in the slit condition for infinite height:

$$1/\Delta I(q)^2=(1/\Delta I(0)^2)[1+q^2\xi^2] \quad (q\xi<<1),$$

$$1/\Delta I(q)=q\xi/\Delta I(0) \quad (q\xi>>1),$$

where $\Delta I(0)$ is the excess scattering intensity at $q=0$ and ξ is the correlation length of the junction zone.

From the slope and the intercept of OZ plots, the values of $\Delta I(0)$ and ξ are obtained and compiled in Table 1. Using these parameters, all data are scaled as shown in Fig. 1. The figure indicates that $\Delta I(0)/\Delta I(q)=F(x)$ is an universal function of $x=q\xi$. The straight line in the figure has a slope of about 1.0 in agreement with the theoretical prediction. Fig. 1 demonstrates that the melting process can be described by an universality law.

Further studies have been extended to other physical gels including polysaccharides.

Table 1. Evaluated values for $\Delta I(0)$ and ξ.

t (C)	$10^2\Delta I(0)$	$10^{-4}\xi$(A)
c_p=5.1wt%		
12.8	2.78	1.24
39.6	2.55	1.05
52.9	1.78	0.82
58.0	0.29	0.65
65.1	0.20	0.84
c_p=9.7wt%		
32.5	0.28	0.23
46.0	0.25	0.27
55.6	0.18	0.27
60.9	0.10	0.26
64.9	0.04	0.22

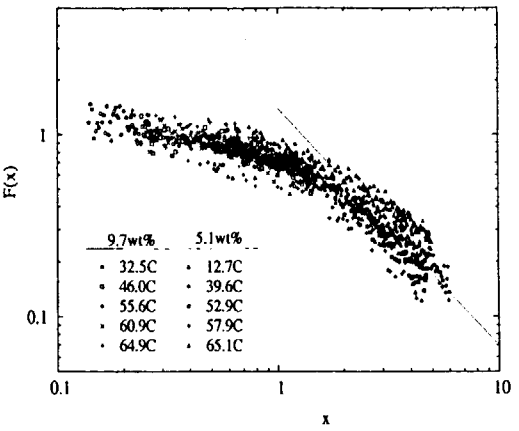

Fig. 1. The scaled plots for the melting process in the branched polyethylene/toluene-d8 gels:

JRR-3M, ULS, 6 polymer

課題名：電解質多糖類カラギーナンのゾルーゲル転移

表　題：κカラギーナンのゲル→ゾル転移における構造変化の観測

Observation of Structural Change of κ-Carrageenan on Gel-to-Sol Transition

M. Sugiyama[a], N. Hiramatsu[b], A. Nakamura[b] and K. Hara[c]

[a]*Department of Physics, Kyushu University, Fukuoka, 812-8581 Japan*
[b]*Department of Applied Physics, Fukuoka University, Fukuoka, 814-0180, Japan*
[c]*Institute of Environmental Systems, Kyushu University, Fukuoka, 812-8581 Japan*

κ-carrageenan is one of typical electrolytic polysaccharide, which includes one sulphate per two galactoses. It is well known that the solution of κ-carrageenan which is neutralized by potassium ions (K-form) makes gelation under the transition temperature and this sol-gel transition is thermo-reversible. In a cross link point of the κ-carrageenan gel, the polymer chains are bound with the potassium ions. Therefore, the gel includes polymer rich regions, which are cross link *regions*, and polymer poor regions, which are solution-like regions.

To observe the structure of κ-carrageenan gel and its change on the gel-to-sol transition, a small-angle neutron scattering (SANS) experiment was carried out with elevating temperature.

The sample of K-form of κ-carrageenan was supplied by Chiba group (Waseda University). The gel sample was made of the heavy water solution with the concentration of 3 wt%. Before a SANS experiment, the gel-to-sol transition temperature was confirmed with a Differential Scanning Calorimeter and then the transition temperature is found to be around 325 K. The SANS experiments were performed in the range of the temperature of 310~340 K with SANS-U of ISSP at JRR-3M of JAERI, Tokai.

As described above, it is deduced that the gel is composed with two regions; polymer rich and polymer poor regions. Therefore, the SANS intensities were piled up with the scattering from these regions and the function of the intensities $I(Q)$ are assumed as,[1,2]

$$I(Q) = I_g(0)\exp\left(-\frac{R_g^2}{3}Q^2\right) + \frac{I_o(0)}{1+\xi^2Q^2}, \quad (1)$$

where R_g and ξ are gyration radius of the polymer rich region and correlation length of polymer poor region, respectively. Figure 1 shows temperature dependence of R_g and ξ, respectively. R_g suddenly became shorter at the gel-to-sol transition temperature, whereas ξ gradually became shorter with elevating temperature. Here, it is considered that shortening of ξ means increase of the polymer chains in the polymer poor regions and that of R_g means extinction of the polymer network at the transition temperature.

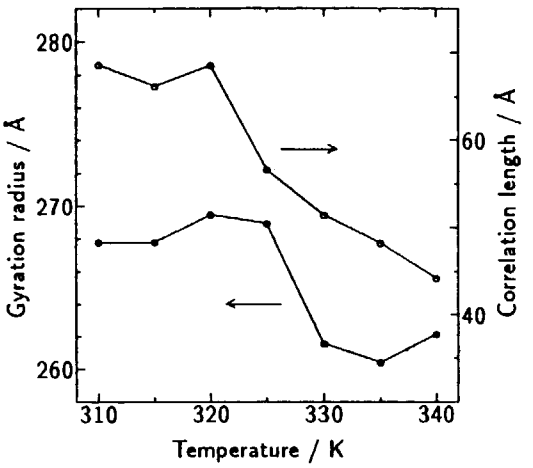

Fig. 1. Temperature dependence of gyration radius and correlation length. The closed and open circles denote gyration radius and correlation length, respectively.

1. S. Mallam, A. M. Hecht and E. Geissler, J. Chem. Phys., **91**(1989)6447

2. S. Mallam, F. Horkay, A. M. Hecht, A. R. Rennie and E. Geissler, Macromolecules, **24**(1991)543

研究テーマ:界面活性剤／水系における立方相ネットワーク構造のゆらぎと成長
表題:流動場下における界面活性剤／水系のモルフォロジー転移

MORPHOLOGY TRANSITION IN A SURFACTANT/WATER SYSTEM UNDER SHEAR FLOW

M.Imai[1], K. Nakaya[1], T. Kato[2], Y. Takahashi[3] and T. Kanaya[4]

[1]*Department of Physics, Ochanomizu University, Bunkyo, Tokyo 112-0012, Japan*
[2]*Faculty of Science, Tokyo Metropolitan University, Hachioji, Tokyo 192-03, Japan*
[3]*Faculty of Engineering, Nagoya University, Chigusa, Nagoya 464-01, Japan*
[4]*Institute for Chemical Research, Kyoto University, Uji, Kyoto 611, Japan*

Amphiphilic molecules will aggregate spontaneously so as to avoid hydrocarbon /water contacts in aqueous solution. The resultant equilibrium structures show a variety of morphologies, such as spherical micelle, cylindrical micelle, cubic lattice, lamellar sheets. These morphologies having strong spatial anisotropy couple with shear flow and modify their static phase behavior. In this study we have investigated the effects of shear flow on the morphology transition in a non-ionic surfactant/water system.

A nonionic surfactant $C_{16}E_7$ was used for the amphiphilic molecule and the sample was prepared at 55 wt% of $C_{16}E_7$ in D_2O. For SANS under shear flow measurements, we used a newly constructed Couette type shear apparatus for SANS-U constructed by Y. Takahashi (one of coauthors). The

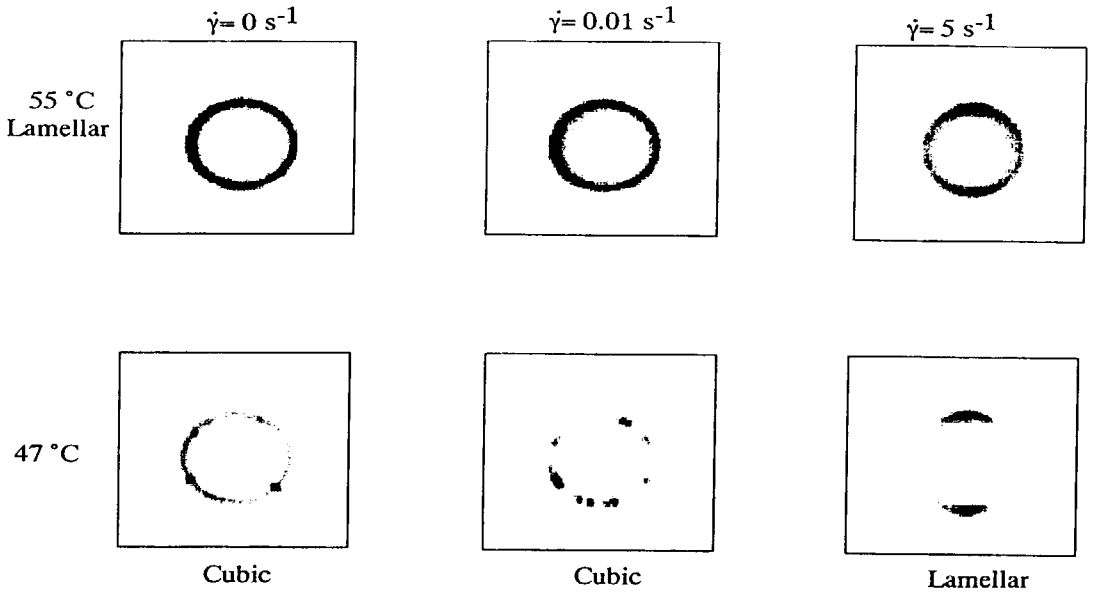

Fig. 1. 2D scattering patterns for the lamellar/cubic transition under various shearing conditions.

Reactor: JRR-3M Facility:SANS-U Field:Polymer

sample is placed between two concentric cylinders and the gap is 1 mm. In SANS under shear flow measurements, the samples were heated to lamellar phase region and then commenced shearing the sample at a predetermined shear rate. We waited for 10 min. for stabilization and then decreased temperature to the cubic phase. The SANS measurements were performed using λ=7Å and sample to detector distance of 1m.

The SANS patterns for lamellar-cubic transition under shear flow are shown in Fig 1. Without shear flow, the isotropic Debye ring scattering pattern transformed into the spotty pattern at 47°C, indicating the lamellar/cubic transition. When we applied shear flow having shear rate of 0.01 s^{-1} to the sample in the lamellar phase, no orientation effects were observed. Decreasing temperature of the sample to 47 °C corresponding to the cubic phase, the scattering pattern showed transition to the cubic phase similar to that without the shear flow, although before the transition there is incubation time. The lamellar phase for shear rate of 5 s^{-1}, the lamellar plane oriented to parallel to the shearing plane. Under this shearing condition, the sample temperature decreased to 47 °C, however, we could not observe the transition to the cubic phase as shown in Fig. 1. This indicates the morphology transition is suppressed by the shear flow. A critical shear rate for suppressing the lamellar/cubic transition was around 1 s^{-1}.

研究テーマ　：　弱荷電高分子ゲルの超構造解析
表題　：　変形下における弱荷電ゲルの構造解析

Structure Analysis on Weakly Charged Gels in Deformed State

M. Shibayama, K. Kawakubo, F. Ikkai, and M. Imai[1]

Department of Polymer Science and Engineering,
Kyoto Institute of Technology, Matsugasaki, Sakyo-ku, Kyoto 606-8585, Japan
[1]Neutron Scattering Laboratory, The Institute for Solid State Physics,
The University of Tokyo, Shirakata, Tokai, Naka, Ibaragi 319-11, Japan

By small-angle neutron scattering (SANS), we confirmed that a weakly charged gel in deformed state shows characteristic two dimensional scattering patterns at different temperatures.

Slab gels were prepared by redox polymerization of N-isopropylacrylamide (NIPA, 668mM) and acrylic acid (AAc, 32mM) in a deuterated water, using N,N'-methylenebis acrylamide (BIS, 8.6mM) as a crosslinker. A disk-shape gel with thickness of 3 mm was punched out from the slab and transferred to a silicon rubber mold. The deformation of the gel was made by compressing the rubber from both sides. The SANS measurements were carried out at the SANS-U spectrometer of the Institute for Solid State Physics (ISSP), The University of Tokyo at Tokai, Ibaragi, Japan.

Figure 1 shows a series of two dimensional SANS intensity profiles of NIPA/AAc gels at 26, 42, and 46 °C. The left and right columns show the profiles for undeformed (λ = 1.07) and deformed (λ = 1.25) gels, respectively, where λ is the deformation ratio along the stretching directions (y axis). At 26 °C where the gel is in a good solvent, the scattered intensity pattern was isotropic even for the deformed gel. When the temperature was increased to 42 °C, the so-called butterfly pattern, i.e., a prolate-shape scattered intensity pattern with respect the stretching direction, appeared in the deformed gels. By further increasing temperature to 46 °C, a scattering maximum was observed. In the undeformed gel, the scattering pattern had a circular maximum with a finite q, where q is the magnitude of the scattering vector. On the other hand, the scattering pattern for the deformed gel became oblate and the scattering peak in the stretching direction moved to the low q direction.

These changes of the SANS intensity patterns were discussed by decomposing it into the thermal fluctuations and the static inhomogeneities and were well reproduced with the Rabin-Panyukov theory for weakly charged gels.[1)]

Reference

1) M. Shibayama, K. Kawakubo, F. Ikkai, and M. Imai, *Macromolecules*, **31**, 2586 (1998).

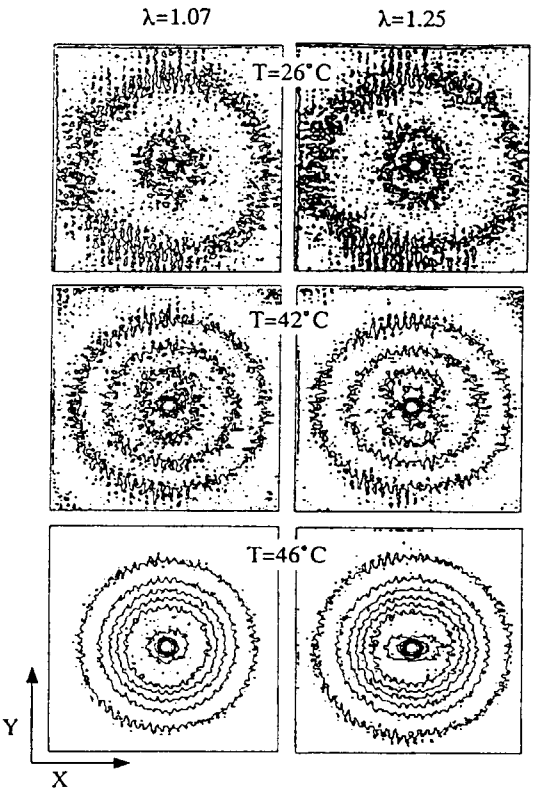

Figure 1 Two dimensional SANS intensity profiles of NIPA/AAc gels at 26, 42, and 46 °C for undeformed (λ = 1.07) and deformed gels (λ = 1.25). The stretching direction is parallel to the y axis.

研究テーマ：多糖類高分子ゲルの構造
表題：微細結晶セルロースの内部構造の観測

Observation of Internal Structure of Microcrystalline Cellulose

M. Sugiyama[a], K. Hara[b], N. Hiramatsu[c], and H. Iijima[d]

[a]*Department of Physics, Kyushu University, Fukuoka, 812-8581 Japan*
[b]*Institute of Environmental Systems, Kyushu University, Fukuoka, 812-8581 Japan*
[c]*Department of Applied Physics, Fukuoka University, Fukuoka, 814-0180, Japan*
[d]*Chemical Technology Department IV, Asahi Chemical Industry Co., Ltd., Nobeoka, Miyazaki 882-0847, Japan*

A microcrystalline cellulose, which has been recently developed by Asahi Chemical Industry Co., Ltd., is a fine particle with the average size of 3 μm. The unique property of this new material is that its aqueous suspension exhibits almost temperature-independent viscosity between 20 and 80°C. However, both the intra- and inter-particle structures are not yet understood; the perpose of our study is to descrive the structure of this thick aqueous suspension of microcrystalline cellulose with small-angle neutron scattering (SANS) technique.

An aqueous suspension of a specially prepared microcrystalline cellulose, which was viscous and opaque, was supplied by Asahi Chemical Industry Co., Ltd, Japan. Two samples were made for the SANS experiments: sample 1 and smaple 2 were aqueous suspensions with the concentration of a microcrystalline cellulose of 10 wt% and 1 wt%, respectively.

The SANS experiments were performed with a SANS-J spectrometer installed at JRR-3M in the Japan Atomic Energy Research Institute, Tokai, Japan. The profiles with a magnitude of the scattering vector (q) ranging from 5×10^{-3} to 5×10^{-2} Å^{-1} were measured with a 6-Å-wavelength neutron beam.

Figures 1 (a) and 1 (b) show double-logarithmic plots for the SANS profiles of samples 1 and 2, respectively. There was no difference in the profile shapes between samples 1 and 2. This result indicades that the observed profiles in the small q region are mainly due to the internal structure of the microcrystalline cellulose particle.

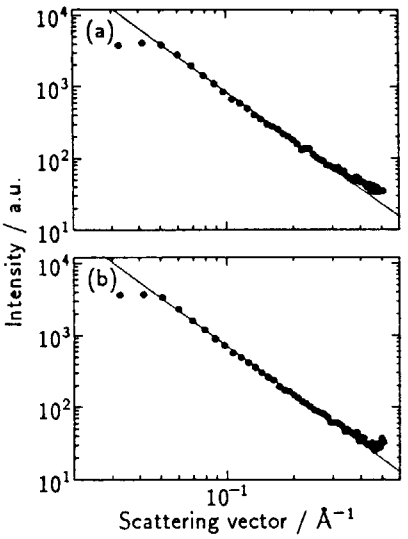

Fig. 1. Double-logarithmic plots of SANS profiles of sample 1 (10 wt%) (a) and sample 2 (1 wt%) (b). The slope of the straight lines in the figures is 2.2.

Moreover, in the q-range from 5×10^{-3} Å^{-1} to 3×10^{-2}, they could be well-fitted by power law curves: $I(q) = I_0 q^{-\alpha}$ with $\alpha = 2.2$. This behavior is characteristic of a fractal structure with a structure factor of $S(q) \propto q^{-D}$ (D is the fractal dimension).[1,2] Therefore, the internal structure of the microcrystalline cellulose particle has a fratcal structure with the dimension of 2.2.

References:

[1] D. W. Schaefer and K. D. Keefer: Phys. Rev. Lett. **56** (1986) 2199.
[2] J. Teixeira: J. Appl. Cryst. **21** (1988) 781.

原子炉：JRR-3M　　装置：SANS-J(C3-2)　　分野：中性子散乱(高分子)

研究テーマ：リエントラント液晶の構造
表題：リエントラント液晶の構造

Structure of a Reentrant Liquid Crystal

O. Oishi, S. Miyajima, M. Nagao[1], and M. Imai[1]

Institute for Molecular Science, Myodaiji, Okazaki 444-8585, Japan
[1]Neutron Scattering Laboratory, The Institute for Solid State Physics, The University of Tokyo, Shirakata, Tokai, Naka, Ibaraki, 319-11, Japan

When conventional liquid loses its isotropic (I) symmetry and assumes uniaxial orientational order, the nematic (N) liquid crystalline state is formed. The smectic A (SA) state is characterized by its one-dimensional translational order in addition to the nematic order. It is therefore natural that the phase transition sequence be I-N-SA on lowering the temperature. However, the present compound, CBOBP (4-cyanobenzoyl-oxy-[4-octyl-benzoyloxy]-*p*-phenylene), exhibits a transition sequence, I-N-SAd-N-SA1 (doubly reentrant sequence) on lowering the temperature. The second N phase is called reentrant nematic (RN), and the SAd to RN transition means that 1-D translational lattice *melts* on lowering the temperature. Due to this peculiarity, the nature of this transition sequence has been one of the interesting topics in recent liquid crystal research [1].

We made neutron diffraction study to clarify the structure of the liquid crystalline phases and hence to clarify the microscopic mechanism of this phenomenon. For this purpose a compound with perdeuterated chain, CBOBP-d17 was prepared. SANS-U instrument was used at an wavelength of 7.0 Å with a velocity selector.

Figures 1 shows the intensity of the smectic primary peak. What is striking is that the peak intensity was very small in SAd phase; smaller than those in N or RN phases, and therefore the reentrant *melting* seems to accompany *increase* in peak intensity. This revealed highly disordered chain structure in the SAd mesophase, in accordance with the deuterium NMR study [1].

[1] S. Miyajima and T. Hosokawa, Phys. Rev. B, 52, 4060 (1995).

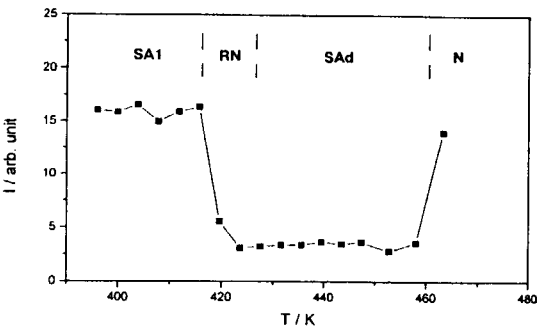

Figure 1. Intensity I of the smectic primary peak as a function of temperature in CBOBP-d17.

JRR-3M, SANS-U (C1-2), Polymer

研究テーマ：超小角中性子散乱法によるコロイド分散液中における合金様結晶構造と相転移の解析
表題：超小角中性子散乱法による分散液中のコロイド結晶の合金様構造と相転移の解析

Ultra-small-angle Neutron Scattering Study of Alloy Structure and Phase Transition in Colloidal Crystals in Dispersion

Hideki Matsuoka, Takashi Ikeda and Hitoshi Yamaoka
Department of Polymer Chemistry, Kyoto University, Kyoto 606-01, Japan
Mitsuhiro Hashimoto, Toshio Takahashi
Institute of Solid State Physics, University of Tokyo, Roppongi, Minato-ku, Tokyo 106, Japan

INTRODUCTION

Previously, we investigated the performance of ULS instrument and shown that it has an enough performance for the USANS(ultra-small-angle neutron scattering) study of the colloidal crystal. In this study, we have tried to observe a colloidal crystal alloy structure in the mixture of two kinds of colloidal particle which are different in size or surface charge by USANS. For the mixture of deuterated and hydrogenated latex particles, USANS experiments with contrast variation technique have been carried out by using D_2O/H_2O mixture as a dispersion medium. In addition, we also have tried to observe the temperature dependence of colloidal crystal.

EXPERIMENTAL

ULS apparatus at Neutron Scattering Laboratory, Institute of Solid State Physics, University of Tokyo, with Bonse-Hart setup was used. Two channel-cut crystals (Si (111)) were used as a monochrometer and analyzer. The FWHM of the rocking curve was 4 sec of arc and its intensity was ca.1000cps. For temperature dependence experiments, the specially designed temperature-control cell was equipped with ULS apparatus.

RESULTS AND DISCUSSION

First, scattering profiles for the mixture of deuterated polystyrene latex (*d*-PS-1, diameter 1510Å) and hydrogenated polystyrene latex (SS-176, diameter 2530Å) were measured by ULS. The mixing ratio of the particles is 80.3:19.7. The USANS profiles were shown in Figure 1. Scattering profile from SS-176 particles was observed in the mixture dispersed in D_2O and scattering profile from *d*-PS-1 particles was observed in the mixture dispersed in H_2O/D_2O (H_2O:D_2O =73.3:26.7) solvent. These data indicate that the smaller particles (d-PS-1) formed crystal-like ordered structure while the larger particles (SS176) arranged randomly in mixed dispersion.

Secondly, the USANS profiles for the mixture of d-PS-1 and SS-176 (mixing ratio of the particle 65.9:34.1) dispersed in D_2O or in H_2O/D_2O (H_2O:D_2O =72.8:27.2) mixture was measured by ULS. The USANS profiles were shown in Figure 2. The scattering profile from the larger particles indicated possibility of crystal-like ordered structure, while the smaller particles seemed to be arranged randomly.

To investigate the temperature-dependence of colloidal crystal, poly-methylmethacrylate (PMMA) latex (MS-32) (diameter 2810Å, volume fraction ca.2.5%) dispersed in D_2O was measured by ULS with changing sample temperature (24℃→70℃→

24℃). The USANS profiles were shown in Figure 3. Melting of crystal structure by raising sample temperature from 24℃ to 70℃ and the possibility of reproduction of colloidal crystal by changing sample temperature(70℃ →24℃) were confirmed.

CONCLUSION

By using the mixture of hydrogenated and deuterated polystyrene latex dispersions, the scattering from each component could be separately obtained by applying contrast variation technique with D_2O/H_2O mixture as dispersion medium. The results obtained here indicate that one component of latex particles forms crystal-like ordered structure. The possibility for formation of colloidal alloy-like structure was certainly observed by ULS.

From the investigation of temperature dependence of PMMA latex(MS-32) dispersed in D_2O, melting of crystal structure has been confirmed by changing sample temperature (24℃→70℃). Reversibility of the structure change was confirmed by experiments with lowering sample temperature(70℃→24℃).

For the experiments for alloy structure at different conditions, such as for different mixing ratio and size ratio of the particles, and temperature dependence of colloidal crystal are planed for the next beam time of neutron.

References

(1) H.Matsuoka, T.Harada, H.Yamaoka ***Langmuir,*** . **10**, 4423-4425 (1994).

(2) H.Matsuoka, T.Harada, K.Kago, H.Yamaoka, ***Langmuir,*** **12**, 5588-5594 (1996)

(3) H.Matsuoka, T.ikeda, H.Yamaoka M.Hashimoto, T.Takahashi ***Langmuir,*** submitted

JRR-3M, ULS, 6. polymer

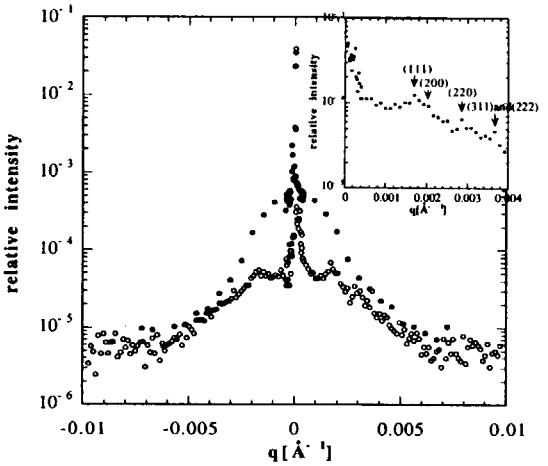

Figure 1 USANS profiles of the mixture of d-PS latex (d-PS-1) and PS latex(SS-176)(mixing ratio 80.3:19.7) in D_2O(filled circle) and in H_2O:D_2O =73.3:26.7 (open circle)

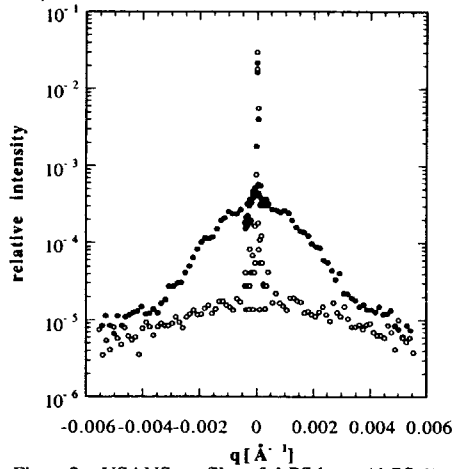

Figure2 USANS profiles of d-PS latex (d-PS-1) and PS latex(SS-176) (mixing ratio 65.9:34.1) in D_2O (filled circle) and in H_2O:D_2O =72.8:27.2 (open circle)

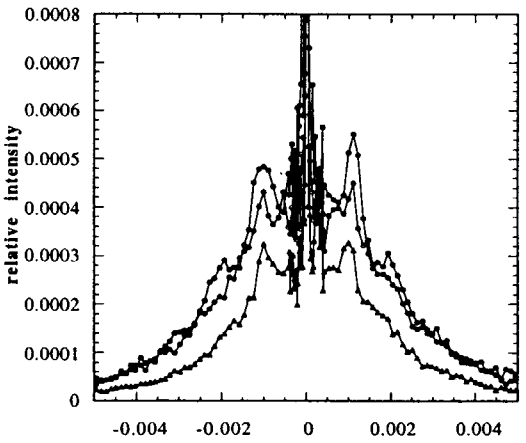

Figure3 USANS profiles of PMMA latex (MS-32) in D_2O at 24℃before heating (filled circle) and at 70℃(triangle) and at 24℃after heating (open circle)

This is a blank page.

1. 中性子散乱 (Neutron Scattering)

3) 構造・励磁 (Structure · Excitation)

This is a blank page.

研究テーマ：コバロキシム錯体結晶の光異性化
表　　題：コバロキシム錯体におけるキラルな1-シアノエチル基の光反転反応のメカニズム

Photoinversion Mechanism of the Chiral 1-Cyanoethyl Group in a Cobaloxime Complex

Takashi Ohhara, Yuji Ohashi, Ichiro Tanaka,[1] Shintaro Kumazawa,[1] and Nobuo Niimura[1]

Department of Chemistry, Tokyo Institute of Technology, Meguro-ku, Tokyo 152-8551
[1]Advanced Science Research Center, Japan Atomic Energy Research Institute, Tokai, Ibaraki 319-11

It was found that the chiral 1-cyanoethyl group bonded to the cobalt atom in some cobaloxime complexes is racemized on exposure to visible light with retention of the single crystal form. Although the relation between the racemization rate and the crystal structure was clearly explained, the mechanism of the racemization has not been clarified. One of four bonds around the chiral carbon atom should be cleaved by photoirradiation in the process of the racemization. The ESR measurement indicated that the Co-C bond was cleaved by photo-irradiation. In order to ascertain the mechanism, the hydrogen atom bonded to the chiral carbon of the 1-cyanoethyl group was replaced with the deuterium atom for the complex of [(*R*)-1-cyanoethyl-d$^{\alpha}$][(*S*)-phenylethylamine]-cobaloxime and the crystal structure after the irradiation was analyzed by neutron diffraction. The analyzed structure showed that the racemization was not observed since the crystal was too large that light cannot penetrate into the crystal. However, the deuterium atom was exchanged with one of the hydrogen atoms of the neighboring methyl group. This suggested that the C-H bond may be cleaved in the process of the racemization.

Another complex with the deuterium-exchanged cyanoethyl group, [(*R*)-1-cyanoethyl-d$^{\alpha}$](pyridine)cobaloxime, was prepared and its crystal strcutre after the irradiation was analyzed by neutron diffraction. The analyzed structure indicated that the chiral cyanoethyl group was partly inverted to the opposite configuration but the deuterium atom bonded to the chiral carbon is not exchanged with the methyl hydrogen atom. This suggests that the Co-C bond is cleaved on exposure to visible light.

In order to make clear which mechanism is true, the complex of [(*R*)-1-cyanoethyl-d$^{\alpha}$]-(piperidine)cobaloxime was prepared and the crystal structure after 1 month exposure was analyzed by neutron diffraction. There are two crystallographically independent molecules in an asymmetric unit. The A molecule is not significantly different from the initial structure, whereas the molecular structures of B before and after the irradiation are different as shown in Fig. 1. The(*R*)-1-cyanoethyl group is partly (45%) inverted to the opposite configuration and the disordered structure of the (*R*) and (*S*) isomers were observed. All the deuterium atom replaced with the hydrogen bonded to the chiral carbon are bonded to the chiral carbon and are not exchanged with the hydrogen atoms of the neighboring methyl hydrogen atoms. This results is the same as that of the pyridine complex examinexd previously.

The exchange process of the deuterium atom bonded to the chiral carbon with the hydrogen of the neighboring methyl group seems to be rare case when the 1-cyanoethyl group is inverted to the opposite configuration. The Co-C bond should be cleaved in the process of photoracemization.

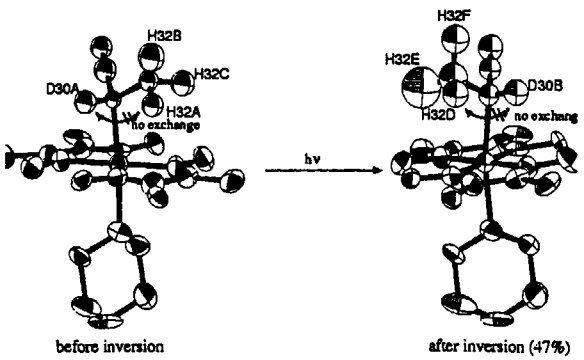

Fig.1

原子炉：JRR-3M　　装置：BIX-1（1G-A）　　分野：中性子散乱（構造）

研究テーマ：コバロキシム錯体結晶の光異性化
表　　題：コバロキシム錯体における3-シアノエチル基3-1光異性化反応のメカニズム

Mechanism of 3 - 1 photoisomerization of the 3-Cyanoethyl Group in a Cobaloxime Complex

Takashi Ohhara, Jun Harada, Yuji Ohashi, Ichiro Tanaka,[1] and Nobuo Niimura[1]

Department of Chemistry, Tokyo Institute of Technology, Meguro-ku, Tokyo 152-8551
[1]Advanced Science Research Center, Japan Atomic Energy Research Institute, Tokai, Ibaraki 319-11

It was found that the 3-cyanopropyl group bonded to the cobalt atom in some cobaloxime complexes is isomerized to the 1-cyanopropyl group in the two step (as shown in the Scheme) on exposure to visible light in the solid state.[1] When the axial base ligand is (*R*)-1-phenylethyl-amine, the 3 - 1 isomerization proceeded with retention of the single crystal form. The structures before and after the change were analyzed by X-rays. The reason why such a large structural change does not destroy the crystal lattice was clearly explained by the reaction cavity for the cyanopropyl group[2]

However, the mechanism of the 3 - 1 isomerization remains equivocal. It must be made clear what is the motive force for the isomerization or why the intermediate structure, 2-cyanopropyl group, was not be observed in the intermediate stages. To examine the mechanism, the complex of (3-cyanopropyl-d^{α},d^{α})[(*R*)-1-phenylethylamine]cobaloxime was prepared. To reduce the background, the hydrogen atoms of (*R*)-1-phenylethylamine and the cobaloxime moities were replaced with the deuterium atoms. A crystal with dimensions 2.0 x 2.0 x 1.0 mm was irradiated with a xenon lamp for 7 days and the crystal strcuture wasanalyzed by neutron diffraction at JAERI.

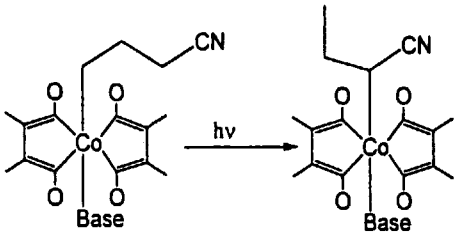

Scheme

Figure 1 shows the molecular strcutures before irradiation. Figure 2 shows the molecular structure after oo hours exposure. Although the conversion rate was about 90 %, the transferred deuterium atoms are clearly assigned. One of the deuterium atom bonded to the carbon atom of the 1 position of the 3-cyanopropyl group is transfered to make a bond with the carbon atom of the 2 position. This indicates that the 2-cyanopropyl group should be made in the process of the 3 - 1 isomerization.

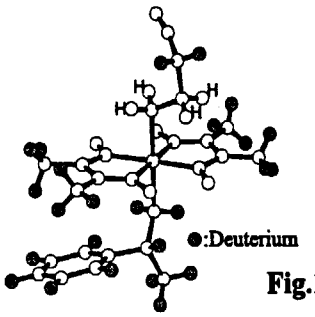

Fig.1

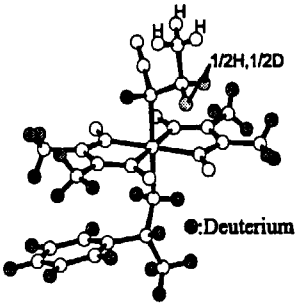

Fig.2

References

[1] F. Kurashima, N. Takatsu, K. Ishida, Y. Arai, S. Takeuchi and Y. Ohgo, Annual Meeting of the Chemical Society of Japan, Kyoto, Abstract I, 290 (1995).
[2] M. Yoshiike, Master Thesis, Tokyo Institute of Technology, 1998.

原子炉：JRR-3M　　装置：BIX-1（1G-A）　　分野：中性子散乱（構造）

研究テーマ：コバロキシム錯体結晶の光異性化
表　　題：$TaCp_2(H)(SiMe_2H)_2$の構造

The Classical Structure of $TaCp_2(H)(SiMe_2H)_2$

R. Bau, I. Tanaka[1], T. Ohhara[2], N. Niimura[1], Y. Ohashi[2], Q. Jiang[3] and D.H. Berry[3]

Dep. of Chem., Univ. of Southern California, Los Angeles, CA 90089, U.S.A.
[1]Advanced Science Research Center, JAERI, Tokai, Ibaraki 319-1195, Japan
[2]Dep. of Chem., Tokyo Insitute of Technology, Meguro, Tokyo 152-8551, Japan
[3]Dep. of Chem., Univ. of Pennsylvania, Phyladelphia, PA 19104, U.S.A.

After the agostic C-H-M interaction was first demonstrated to exist, by neutron diffraction, in the compound $\{Fe(\eta^3\text{-}C_8H_{13})[P(OMe)_3]_3\}^+$, there were numerous attempts to search for analogous Si-H-M systems. Such species are of interest because of their suspected role in hydrosilations and other catalytic reactions involving metallo-silicon compounds. In 1982, Schubert and co-workers published the first (and to date the only) neutron diffraction study of a bona fide Si-H-M agostic (or non classical) interaction in $Mn(H)(SiPh_2F)(C_5H_4Me)(CO)_2$. Since then, other investigators have succeeded in characterizing Si-H-M interactions with X-ray diffraction methods, for example the Si-H-system in $TiCp_2(SiH_2Ph_2)(PMe_3)$.

A large single crystal of $TaCp_2(H)(SiMe_2H)_2$ (0.8x0.8x4.0mm) was grown via recrystallization from toluene/hexane[1)] and sealed in quartz cap under a nitrogen atmosphere. Neutron diffraction data were collected at room temperature at JRR-3M reactor of JAERI using the BIX-I single-crystal diffractometer,[2)] equipped with two area detectors. A neutron difference-Fourier map, phased by the positions of the non-hydrogen atoms (and the calculated C-H hydrogen atoms) derived from the X-ray analysis,[1)] yielded only one large peak corresponding to the unique hydride ligand. Exhaustive least-squares refinement yielded final agreement factors of R=8.9% and Rw=9.5% for all 1295 reflections in the data set.

A plot of $TaCp_2(H)(SiMe_2H)_2$ is given in Figure 1. Within experimental error, the unique hydride ligand is symmetrically located between the two silicon atoms: the Ta-H distance is 1.785(15)Å, the non-bonding H...Si distances are 2.18918) and 2.190(17)Å, and the H-Ta-Si angles are 55.2(5)° and 55.5(5)°. All distances and angles in the molecule are quite normal: the afore-mentioned Ta-H distance agree quite well with that found in TaH_3Cp_2 [average 1.774(3)Å], [3)] while both single-bonded Si-H distances (of the $SiMe_2H$ ligands) have the expected value of 1.48(2)Å.

The classical structure of $TaCp_2(H)(SiMe_2H)_2$ reported here is consistent with the NMR spectrum of the compound, which essentially shows the two dimethylsilyl ligands as being equivalent.[1)] Our result does not, of course, imply that all complexes of this type $MCp_2(H)R_2$ (M=Nb, Ta) are classical, although we note that one other compound originally thought to have an unsymmetrical geometry, $NbCp_2(H)(SiMe_2Cl)_2$, has recently had its structure revised in favor of a symmetrical one.

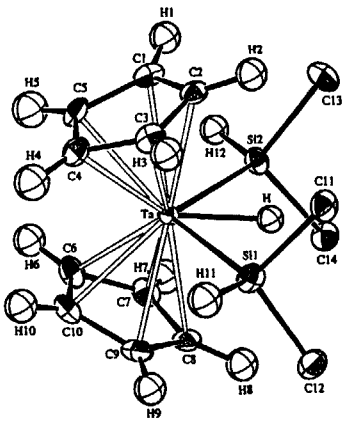

Fig. 1 Molecular plot of $TaCp_2(H)(SiMe_2H)_2$, with hydrogen atoms of the methyl groups removed for clarity.

References

[1] Q. Jiang, P.J. Carroll and D.H. Berry , Organometallics **10** (1991) 3648.
[2] N. Niimura, I. Tanaka and *et al.* , Physica **B 213&214** (1995) 786.
[3] R.D. Wilson, T.F. Koetzle, R. Bau and *et al.*, J. Am. Chem. Soc. **99** (1977) 1775.

原子炉：JRR-3M　　装置：BIX-1（1G-A）　　分野：中性子散乱（構造）

研究テーマ：プロトン及びイオン伝導機構の結晶学的研究
表　　題：プロトン伝導性酸化物の中性子回折

Neutron Diffraction Study of Proton-conducting Oxides

T. Nagasaki, N. Noda, Y. Ishii[1], T. Matsui and Y. Morii[1]

Graduate School of Engineering, Nagoya University, Nagoya 464-8603
[1] Japan Atomic energy Research Institute, Tokai, Ibaraki 319-1195

Such perovskite-type oxides as $SrCeO_3$ and $BaCeO_3$ doped with, e.g., Yb_2O_3 show protonic conductivity in hydrogen or water vapor atmosphere. Hydrogen (proton) sites in these materials, however, still seem to be an open question. The purpose of the present study is to identify the hydrogen sites in them by using neutron powder diffraction and to thereby cast light on the conduction mechanism.

In the present study, we used $SrTi_{0.97}Sc_{0.03}O_3$ as a sample material because it has a simple crystal structure (perovskite type, Pm3m) at ambient temperature as well as relatively high hydrogen solubility.

Powders of $SrCO_3$, TiO_2, and Sc_2O_3 were mixed and pressed into pellets, which were then heated at 1673 K for 40 h in air for reaction and ground into powder again. We heated some of the powder at 873 K for 30 h in the air flow containing D_2O vapor of 50 kPa. (We refer to this process as D_2O treatment.) This D_2O treatment dissolves 1-2 mol% deuterium atoms in $SrTi_{0.97}Sc_{0.03}O_3$.[1)] We measured the diffraction patterns for the samples with HRPD.

The peak intensity for the sample with the D_2O treatment was different from that for the sample without it. The difference was very small, yet was well above the purely statistical fluctuation. We determined relative changes in the observed intensity and compared them with those in structural factors calculated assuming various occupation sites for deuterium atoms. The results are shown in fig. 1. In the models a)-e), we assumed that the deuterium atoms reside a) in the middle of O-O atoms, c) in the middle of O-Sr atoms, d) in the center of O-O-O triangles, and e) in the middle of O-Ti atoms, respectively. Sata et al.[1)] have concluded that

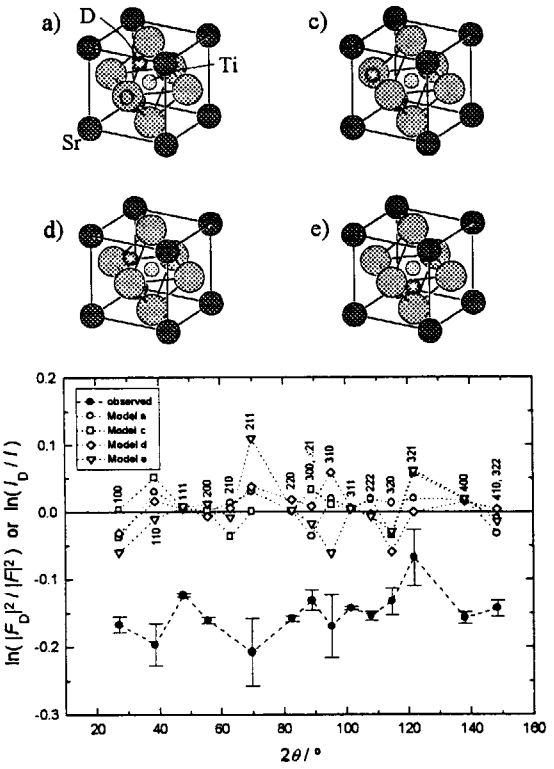

Fig. 1 Comparison of the relative changes due to deuterium dissolution in the observed intensity I with those in the structural factors F; various deuterium sites a)-e) were assumed in calculating F.

deuterium atoms occupy the sites slightly shifted from the sites a), analyzing their neutron diffraction data for single crystals. None of the models, however, can explain the present experimental results satisfactorily. Further analysis is now in progress.

Reference

[1] N. Sata, K. Hiramoto, M. Ishigame, S. Hosoya, N. Niimura, and S. Shin, Phys. Rev. B **54** (1996) 15795.

原子炉：JRR-3M　　装置：HRPD (1G)　　分野：中性子散乱（構造）

研究テーマ：プロトン及びイオン伝導機構の結晶学的研究
表　　題：CuClTe の中性子回折

Neutron Powder Diffraction of CuClTe

M. Hirota, T. Sakuma, H. Takahashi[1], Y. Onoda[2], Y. Ishii[3]

Department of Physics, Faculty of Science, Ibaraki University, Mito 310
[1]Applied Physics Group, Faculty of Engineering, Ibaraki University, Hitachi 316
[2]National Institute for Research in Inorganic Materials, Tsukuba 305
[3]Japan Atomic Energy Research Institute, Tokai 319-11

A group of ternary copper compounds of the composition CuXTe (X = Cl, Br, I) with high copper-ionic conductivity was synthesized by Rabenau et al .[1] These compounds have the tetragonal symmetry in the space group $I4_1/amd$. They clarified a statistical distribution of Cu^+ ions.

It has reported by specific heat measurements that CuBrTe and CuITe show the phase transition at 230 K and 347 K and 281 K, respectively, but CuClTe doesn't show the phase transition below the melting point 400℃.[2] Hitherto, the structural studies of the respective phases of CuBrTe and CuITe have been carried out, but those of CuClTe haven't been done very much.

We performed the neutron powder diffraction study on CuClTe to decide the temperature dependence of the structural parameters of CuClTe. Neutron diffraction measurements were collected from a powder CuClTe at 10 K, room temperatur, 200℃ and 360℃ with a triple-axis spectrometer TAS-2 installed at JRR - 3M in Japan Atomic Energy Research Institute. The incident neutron wavelength of 1.4361 Å was used . The range of diffraction angle covered by the spectrometer was 5° - 100°. Fig.1 shows the result of the double-axis measurement of CuClTe at 10K.

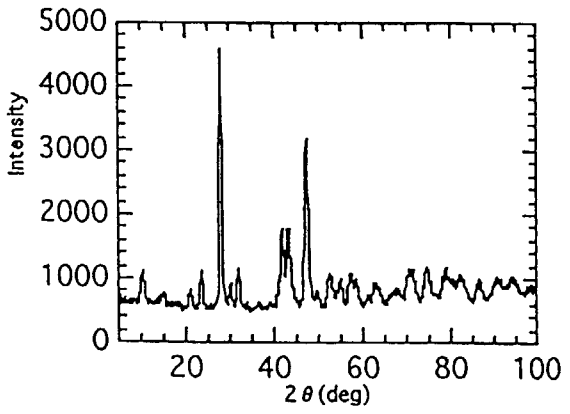

Fig.1. Neutron diffraction pattern of CuClTe at 10 K.

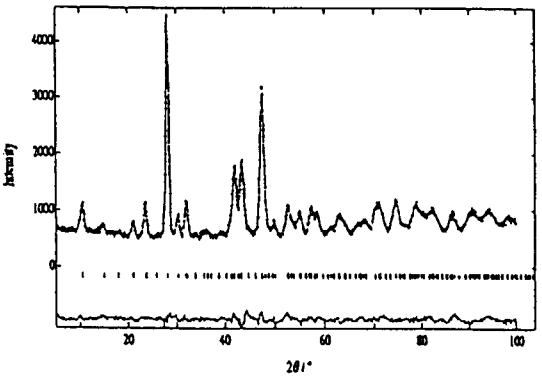

Fig.2. Result of Rietveld refinement of CuClTe at 10 K.

Rietveld analyses were performed with the neutron diffraction data.[3] Fig.2 shows the result of the diffraction pattern at 10 K. *R*- factors for 10K, room temperature, 200℃ and 360℃ were 2.65%, 3.64%, 6.07% and 6.27%, respectively. It was found from the refined parameters that one of Cu^+-sites exhibited peculiar behavor with the temperature change. We are going to perform conductivity measurement of CuClTe to research the relation with the temperature dependence of the structural parameters.

References

1) A. Rabenau, H. Rau and G. Rosenstein : Z. anorg. Chem. **374** (1970) 43
2) T. Sakuma, T. Kaneko, H. Takahashi and K. Honma : J.Phys. Soc. jpn. **60** (1991) 1136
3) Y.-I. Kim and F. Izumi : J.Ceram. Soc. Jpn. **102** (1994) 401

原子炉：JRR-3M　　装置：TAS-2　　分野：中性子散乱(構造)

研究テーマ：中性子散乱による$Li_2Ge_7O_{15}$の強誘電相転移に関与するソフトフォノンの研究
表題：中性子散乱による$Li_2Ge_7O_{15}$の強誘電相転移に関与するソフトフォノンの研究

Soft Phonon Associated with Ferroelectric Phase Transition of $Li_2Ge_7O_{15}$ by Neutron Scattering

M. Wada Takeda, Y. Noda[1], T. Yamaguchi[2], and Y. Iwata[3]

Department of Physics, Faculty of Science, Shinshu University, Matsumoto 390-8621
[1]Department of Physics, Faculty of Science, Chiba University, Chiba 263-8522
[2]Department of Electrical Engineering, College of Science and Engineering, Meisei University, Hodokubo, Hino 191-8506
[3]Reserch Reactor Institute, KyotoUniversity, Kumatori-cho, Sennan-gun, Osaka 590-0400

$Li_2Ge_7O_{15}$(LGO) undergoes a ferroelectric phase transition at T_C = 283.5K. The space group in paraelectric phase belongs to *Pbcn* and the ferroelectric phase to $Pbc2_1$ with spontaneous polarization along the c-axis. The crystal structure is constructed strongly puckered layers of GeO_4-tetrahedra linked by GeO_6-octahedra to form a three-dimensionally bridged framework. The Li atoms occupy the positions in the vacant channels extending three-dimensionally.

LGO has attracted intense interest because of its peculiar behavior that in the phase transition the dielectric critical slowing-down is observed as well as the soft phonon. The purpose of this study is to confirm at which point the polar phonon softens. The phonon dispersion in the LGO single crystals has been measured around the transition temperature T_c by the inelastic neutron scattering. The (300) and (500) Bragg reflection appear abruptly under T_c. The detail temperature dependence of both elastic and inelastic components of the (500) reflection were measured (Fig. 1). The typical softening of a transverse optic phonon mode at Γ point was observed around T_C (Fig. 2). The temperature dependence of frequency of soft phonon shows a good agreement with that observed by Raman scattering and far-infrared measurements. The measurement of detail temperature dependence of the soft phonon branch is now under progress.

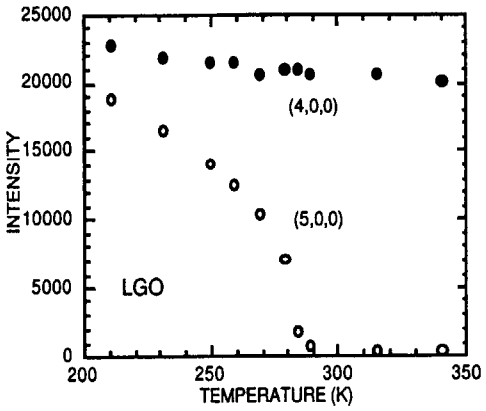

Fig.1 Temperature dependence of (500) and (400) reflections of LGO.

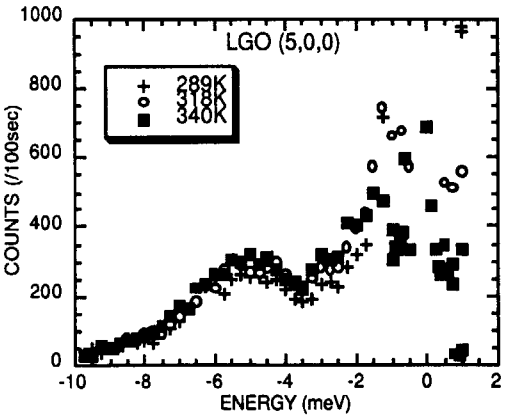

Fig.2 Temperature dependence of the inelastic scattering spectra around (500) of LGO.

JRR-3M, 4G, Structure

研究テーマ：圧力下におけるA_2BX_4型強誘電体の単相-双晶相転移とソフトフォノン
題　　目：Rb_2ZnBr_4の相転移における静水圧効果

Effects of Hydrostatic Pressure on the Phase Transitions in Rb_2ZnBr_4

H. Shigematsu, M. Kubota[1], M. Nishi[1], H. Mashiyama[2] and T. Matsui

Department of Quantum Engineering, Graduate School of Engineering, Nagoya University, Nagoya 464-8603, Japan
[1]*Neutron Scattering Laboratory, I. S. S. P., University of Tokyo, Tokai, Ibaraki 319-1195, Japan*
[2]*Department of Physics, Faculty of Science, Yamaguchi University, Yamaguchi 753-8512, Japan*

Many of the A_2BX_4-type ferroelectrics, for example, Rb_2ZnCl_4, K_2ZnCl_4 and K_2CoCl_4, undergo successive phase transitions from a paraelectric normal phase (phase I, space group *Pmcn*) to an incommensurate phase (phase II) and to a ferroelectric phase (phase III, $P2_1cn$), which is followed by a monoclinic phase ($C1c1$). In Rb_2ZnBr_4, there is another intermediate phase (phase IV, T_4 (76 K) < T <T_3 (112 K), with a twined structure), which is characterized by an extra symmetry operation.[1)]

In this report, we will show the results of the hydrostatic pressure effect on this intermediate phase. Hydrostatic-pressure technique was used to obtain an additional information on the existence of the twin-structure and the extra symmetry operation.

The measurements were performed by using the triple-axis spectrometer 4G and C1-1 at JRR-3M of JAERI. Energy scans were done with the fixed incident neutron wave number k_i=2.57 Å^{-1} for 4G and k_i=1.55 Å^{-1} for C1-1. Hydrostatic pressure was generated by a clamping-type high pressure cell.

Figure 1 shows the temperature dependence of the integrated intensities of the (5/2 3/2 0) superlattice reflection and the (1 4 0) Bragg reflections on heating under pressure of about 1.5 kbar. Although the phase transition temperature T_4 decreased with increasing pressure, the reflection condition did not seem to change, and the relation between the magnitude of four structure factors $|F(\pm h \pm k\, 0)|$ persisted in phase IV. The low-frequency excitation which softened at T_3 was observed above T_3 (see Fig. 2). On the other hand, no hardening mode was recognized below T_3. The same results were obtained under uniaxial stress along [0 0 1] direction.

In conclusion, the structure of phase IV under hydrostatic pressure was caused by the partial remnant of these extra symmetries which corresponded to the 2_1-screw axis, *c*-glide or *n*-glide plane of phase III, almost exactly. Furthermore, the domain ratio was almost 1:1 even under hydrostatic pressure or uniaxial stress.

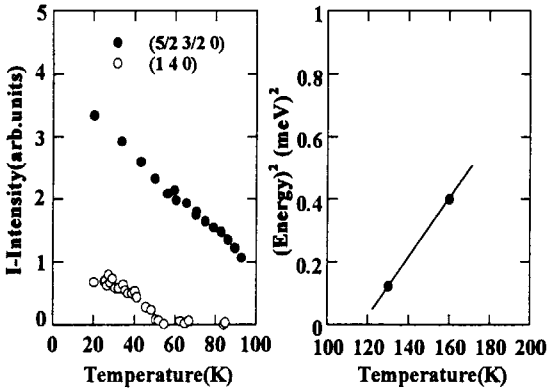

Fig.1　　Fig. 2

Fig. 1 Temperature dependence of the integrated intensity on heating.
Fig. 2 Temperature dependence of square of the energy transfer of soft phonon at *S* point.

1). H. Shigematsu, H. Mashiyama, Y. Oohara and K. Ohshima: to be published in J. Phys. :Condensed Matter (1998).

Reactor: JRR-3M　　Facility: GPTAS(4G), HER(C1-1)　　field: structure

研究テーマ： A_2BX_4型強誘電体の多形転移と格子振動
表題：中性子非弾性散乱で調べたK_2ZnBr_4のα-β転移の音響フォノンモードの異常

ACOUSTIC PHONON MODE ANOMARY OF α–β TRANSITION IN K_2ZnBr_4 STUDIED BY INELASTIC NEUTRON SCATTERING

H. Mashiyama[1], M. Takesada[2] and H. Shigematsu[3]

[1] *Department of Physics, Yamaguchi University, Yamaguchi 753, Japan*
[2] *Research Institute for Electronic Science, Hokkaido University, Sapporo 060, Japan*
[3] *Department of Quantum Engineering, Nagoya University, Nagoya 464-01, Japan*

The K_2ZnBr_4 crystal takes the monoclinic structure (α phase) at room temperature. With increasing temperature the α phase transforms to the β phase of a orthorhombic structure at about 460K as α–β phase transition. The virtual intermediate state model (VIS model) has been proposed as a mechanism of the α–β transition.[1] The VIS model indicates that the transition is accompanied with large atomic displacement parallel to almost the a axis. The purpose of the present study is to investigate anisotropy of the temperature dependence of acoustic phonon modes as precursor phenomena of the transition by using inelastic neutron scattering.

A single crystal was mounted in a furnace for a high temperature range or in a closed-cycle cryostat for a low temperature range. Inelastic neutron scattering experiments within the (a*, c*) scattering plane were performed by using a triple-axis spectrometer installed at C1-1 (HER) of JRR-3M in JAERI (Tokai). Energy scans were done with fixed incident neutron k_i of 1.76A^{-1} in open-open-80'-80' collimation. The energy resolution was 0.35meV (FWHM).

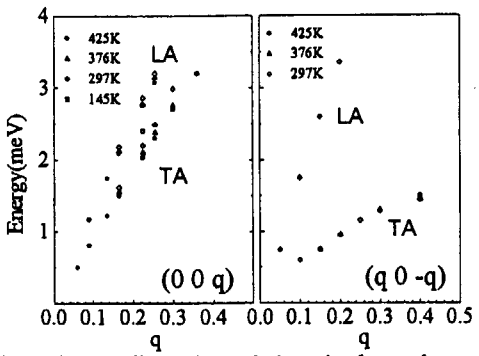

Fig.1 Phonon dispersion relations in the a phase of K_2ZnBr_4 along (0 0 q) and (q 0 –q) at 425, 375, 297 and 145K.

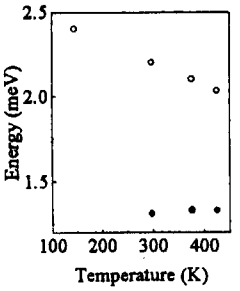

Fig.2 Temperature dependence of the energy shift of TA mode. Open and close circles show the modes along c* axis at q=(0 0 0.225) and a*-c* at q=(0.3 0 –0.3), respectively.

Inelastic neutron scattering intensity was investigated on the lines (2 0 -2)-(2 0 -1) and (4 0 -1)-(3 0 0). The dispersion relations along (0 0 q) and (q 0 –q) are obtained as shown in Fig. 1. By comparing the temperature dependence of the TA phonon branch along (0 0 q) and that along (q 0 -q), it is clear that the TA phonon mode along (0 0 q) has a tendency of softening with increasing temperature as shown in Fig. 2. This anisotropic temperature dependence in the TA mode is discussed by using the VIS model as the following. The observed phonon branches along (q 0 -q) and (0 0 q) are related to the atomic motions along the [1 0 1] and [1 0 0] directions, respectively. According to the VIS model, K^+ ions and $ZnBr_4^{2-}$ tetrahedra should shift mostly to the [1 0 0] direction at the transition. That is, the stronger temperature dependence of the TA mode along (0 0 q) than along (q 0 -q) can be explained as an effect of a motion related to the transition. The results support the VIS model.

[1]M.Takesada and H.Mashiyama: J. Phys. Soc. Jpn. 63, 2618 (1994).

JRR-3M, TAS(4G), HER(C1-1); 1. Structure

研究テーマ：KDPの臨界散漫散乱の新しい見地からの測定
表題　　：ヌルマトリックスにしたKDPの散漫散乱とLOフォノン

Diffuse Scattering and Anomalous LO phonon of Null-Matrix KDP

Y. NODA and K. SANO

Faculty of Science, Chiba University, Yayoi, Inage, Chiba 263

The idea of the present work is based on that the intensity from hydrogen atoms in KH_2PO_4 (KDP) can be diminished if hydrogen atoms(H) are partially replaced by deuterium atoms(D) since a H-atom has negative scattering amplitude and a D-atom has positive one. Such a sample is usually called a null-matrix one. Our interest in this material is the role of the hydrogen atoms and PO_4 groups for the phase transition to the ferroelectric phase. Concerning the neutron scattering experiments, diffuse scattering of d-KDP was reported[1], whose intensity map was very characteristic. The result was interpreted by a dipole-dipole interaction, but the role of an ice-rule was not clear from the experiments. Recently, anomalous LO phonon around 30meV was found[2] in d-KDP, but the displacement pattern of individual atoms is not clear yet. The purpose of the present experiments is that we synthesize a null-matrix KDP and observe diffuse scattering associated with the phase transition. Further, we observe the LO phonon to study the nature of the contributing atoms.

We have crystallized d-KDP whose T_c was determined to be 221K by X-ray and neutron scattering experiments. The crystal size was $39x36x15mm^3$. We also crystallized a null-matrix KDP whose size was $33x62x155mm^3$. The chemical formula of a null-matrix sample must be $K(H_{0.641}D_{0.359})_2PO_4$. The observed T_c was 160K and this value is good enough compared with the expected one.

Neutron experiments was performed at 4G of JRR3M. First, we observed diffuse scattering of d-KDP. Fig.1 shows the intensity map around 303 reflection at 222K, 1K above T_c. The intensity distribution is essentially the same with the reported one. Then we measured the diffuse scattering with the null-matrix sample, ending in failure. The background intensity due to the incoherent scattering of H-atoms were strong as was predicted, but the problem was absorption effect. The main Bragg intensity itself reduced tremendously and the sample size did not work effectively. We also observed the LO phonon around 30meV with the null-matrix sample at 100K, 60K below T_c. Well defined phonon peak was found, and it indicates the LO phonon includes the displacement pattern of PO_4 molecules.

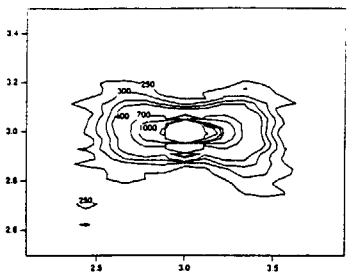

Fig.1 Diffuse scattering around 303 in d-KDP at 222K

Reference

1) J. Skalyo et al.: Phys. Rev. **3 5**(1970)4603.

2) I. Tamura et al.: Physica. B219&220(1996)608.

Reactor : JRR-3M　　Facility : GPTAS (4G)　　Field : structure

研究テーマ：カルコゲン化合物半導体の強誘電相転移
表題：中性子散乱によるTlGaSe2の構造相転移の研究

Neutron Scattering Study of the Successive Phase Transitions in TlGaSe2

S. Kashida(1), Y. Kobayashi(1) and Y. Tsunoda(2)

(1) Department of Environmental Science, Niigata University, Ikarashi 8050, Niigata, 950-21
(2) Graduate School of Science and Engineering, Niigata University, Ikarashi 8050, Niigata,
(2) School of Science and Engineering, Waseda University, Okubo, Shinjyuku, Tokyo, 169

$TlGaSe_2$ and $TlInS_2$ are ternary semiconductors which have layer structures. The phase transitions in these thallium compounds have been studied for more that two decades. From dielectric and optical studies, it was found that the compounds undergo successive phase transitions. Neutron diffraction studies have shown that the lowest temperature phase is commensurate and the intermediate phase is incommensurate. In submillimeter dielectric studies, soft ferroelectric modes are observed to follow the phase transitions.

The present study is aimed to clarify the mechanism of the successive incommensurate phase transitions. Neutron scattering experiments were done using the triple axis diffractometers T1-1 and C1-1.

The intensity of the superlattice reflections was scanned in the **a*-c*** plane, in order to search for the modulation wave vector which characterizes the incommensurate phase. In Fig. 1, the obtained intensity maps are shown as a function of the temperature.

As the temperature is decreased below about 117.5 K, the satellite reflections appear at incommensurate positions. In the low temperature commensurate phase below abot 106K, the satellite reflections appear at commensurate positions **q**= (4,0,-6.75) and (4,0,-7.25). These two reflections have a local center of symmetry at **q**= (4,0,-7).

In the intermediate phase between 106K and 117.5K, the satellite reflections shift to **q**= (3.97,0,-6.75) and (4.03,0,-7.21).

It will be noticed that these two satellite reflections are lacking the local center of symmetry. The lack of the center of symmetry will suggest that the modulation which characterizes the intermediate phase is not of the usual sine wave type.

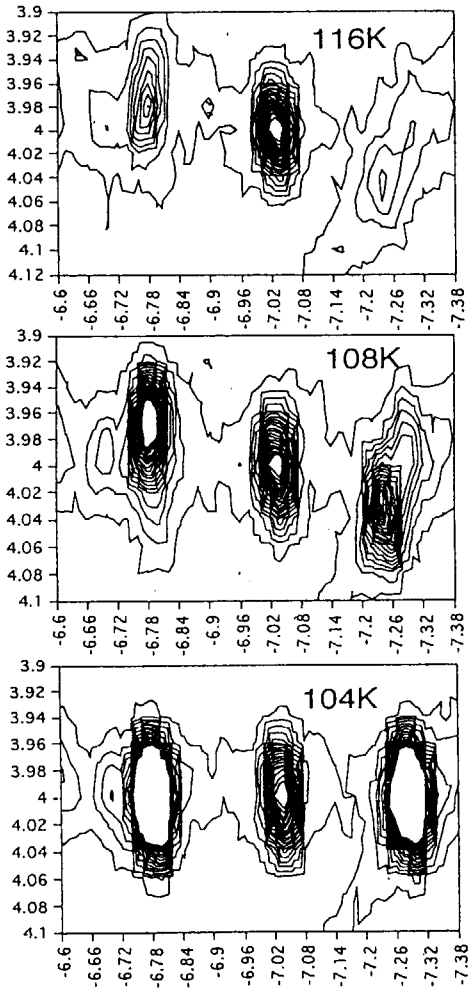

Fig. 1 Contour maps of the satellite reflections taken around q=(4,0,-7)

Reactor:JRR-3M Facility: T11, C11 Field:1.Structure

研究テーマ：誘電体の低温での構造相転移の研究
表題　　：hex-$BaTiO_3$の低温相の構造

Structural Study of Low Temperature Phases of hex-$BaTiO_3$

Y. Noda, K. Akiyama, T. Shobu, Y. Morii[1] and H. Yamaguchi[2]

Faculty of Science, Chiba University, Yayoi, Inage, Chiba 263
[1]JAERI, Advanced Science Research Center, Tokai, 319-11, Japan
[2]Electrotechnical Laboratory, Umezono, Tsukuba 305, Japan

A hexagonal type $BaTiO_3$ undergoes successive phase transitions from the prototype hexagonal phase (phase I) to phase II and phase III on cooling at 222K and 74K respectively. The intermediate phase II was extensively studied, and the space group of phase II is $C222_1$. The phase III is a ferroelectric phase, and detailed structures of the low temperature phases are not known. At the present work, we studied the structure of phase II and phase III to know the mechanism of the phase transition of h-$BaTiO_3$.

Structures of the low temperature phases were studied by neutron powder diffraction at HRPD in JRR3M. In addition, we have preferred a high resolution powder diffraction experiment by using SPring-8 synchrotron radiation to determine the symmetry of phase II and III. The unit cell and the space group of phase II was confirmed to be the orthorhombic and $C222_1$, and the symmetry in phase III was newly determined as monoclinic with the deformation of the γ-angle. The most possible symmetry in phase III is $C112_1$, or equivalently $P112_1$ as a crystallographic conventional unit cell. We have performed neutron powder experiments with the wave length 2.3A and 1.16A. The preliminary results of 2.3A one was already published. Fig. 1 shows the obtained and calculated diffraction profiles, taken in phase I, II and III. Since we used shorter wave length 1.16A, remarkable change of the pattern was found around 80 and 120 degrees, which was not seen in 2.3A experiments. The shift patterns of atoms in phase II and phase III were determined. The atomic shift in phase II is well explained by a soft phonon mode condensation, but the shift pattern in phase III was much more complicated and composed a shift of oxygen atoms.

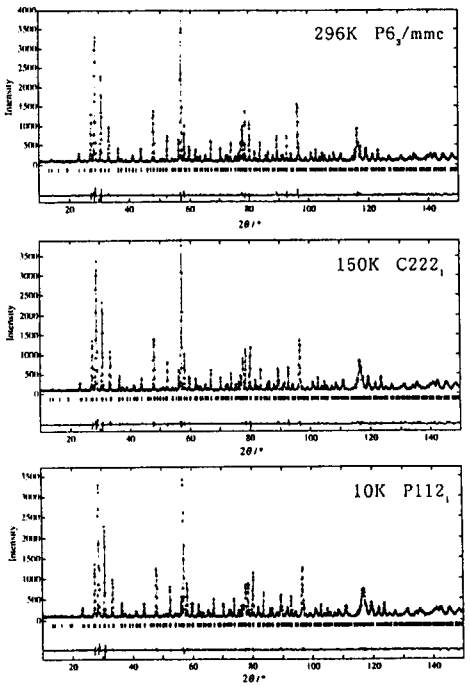

Fig.1 Observed and calculated diffraction profiles.

原子炉：JRR-3M　　装置：HRPD (1G)　　分野:中性子散乱（構造）

強相関電子系の中性子散乱による研究
$Pr_{1-x}Ca_x MnO_3$ の電荷秩序

Charge Ordering in $Pr_{1-x}Ca_xMnO_3$

H. Hino, N. Ikeda, Y. Yamada,T. Inami, S. Katano

Advanced Research Institute for Science and Engineering, Waseda Univ., Okubo, Shinjuku, Tokyo 169-0072 Japan

Japan Atomic Energy Research Instutute, Tokai, Ibaraki, 319-1106, Japan

Recently, provskite type doped manganese oxides have attracted attentiions du to extraordinary magneto-transport properties such as CMR phenomena.

One of the important aspects is the transition to charge-magnetic ordered states. $Pr_{1-x}Ca_x MnO$ (x=0.3) is reported to transform to the charge ordered state with the chage /hole configuration on ab-plane as shown in Fig. 1. However, the nominal hole concentration for the postulated charge structure is n=1/2, which is far from the x-value (x=0.3) of the observed system. One of the possibilities to reconcile the discrepancy would be that the correct structure is an alternative stacking of layers with n=1/2 and n=0 along the c-axis, which is consistent with the x-value of x=0.25.

In order to investigate this possibility, we studied the charge ordering in Pr Ca MnO . Preliminary electron diffraction study has shown that satellite reflections appear at (h/2 k/2 l/2), which indicates that the lattice is doubled along the orthorhombic c-axis. Neutron scattering studies have been carried out to investigate temperature dependence of the satellite intensity. As shown in Fig. 2, it shows extraordinary behavior : After reaching the maximum value at T (magnetic transition temperature), it starts to decrease upon decreasing temperature. This seems to suggest the competition between charge ordering vs. magnetic ordering. Detailed analysis of the charge structure is now underway. .

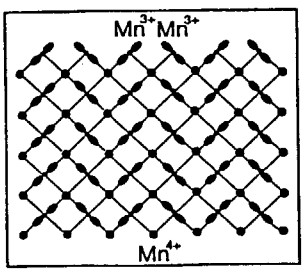

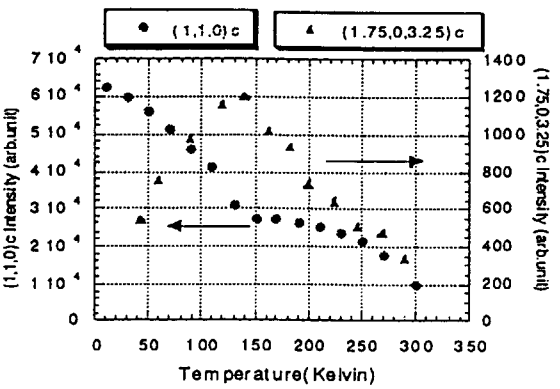

原子炉：JRR3-M　装置：TAS-1(2G)　分野：中性子散乱（構造）

研究テーマ：高圧下での結晶構造・相変態の研究

表題：$Ti_{50}Ni_{30}Cu_{20}$合金におけるマルテンサイト変態の前駆段階の中性子散乱による研究

A Neutron Scattering Study of the Premartensitic State in $Ti_{50}Ni_{30}Cu_{20}$ Alloy

X. Ren, K. Taniwaki, N. Miura, K. Otsuka, Y. Morii[1], Yu.I. Chumlyakov[2]

Institute of Materials Science, University of Tsukuba, Tsukuba, Ibaraki 305-8573, Japan

1. Japan Atomic Energy Research Institute, Tokai, Ibaraki 319-1195, Japan

2. Siberian Physical Technical Institute, Tomsk 634050, Russia

The origin of martensitic transformation (MT) has remained unclear for nearly one century, despite that great technological success has been achieved utilizing MT to harden steels and to develop shape memory alloys. An important step towards understanding the reason why MT needs to occur in a certain alloy was made by Zener[1)] over 50 years ago, who pointed out that MT is closely related to the softening of the resistance to the shear of close-packed plane {110} along <1-1 0> direction, which is reflected by a softening in elastic constant c'. In 60's and 70's, the discovery of soft mode and its success in explaining 2nd order displacive transitions in ferroelectric materials cast new light on the similar MT, and then many researchers tried to find similar mode-softing in martensitic alloys. However, the results were quite puzzling: in most cases {110}<1-1 0> TA2 transverse mode softens prior to MT, but it never go to zero like 2nd order transitions. This feature is now recognized to be common for all 1st order displacive transitions. Then we have to answer why a partially soft mode can induce MT. Recent theoretical studies using Landau-type model suggest that if two (maybe more) order parameters become correlated, a 1st order MT can occur without complete mode-softening. If we go a little further, we can deduce that multiple order parameter is the origin of the 1st order character of MT. It is apparent that there exist many possible order parameters for MT, because MT is a strain transition and there exist many possible strain modes acting as potential order parameters. This may be the reason why MT has frequently been found to exhibit multi-step transition, with each step characterized by different order parameters. Our recent work on elastic constants measurement on TiNiCu alloys gave direct support to this view[2,3)].

The purpose of the present study is to use neutron scattering technique to study phonon mode anomaly prior to MT for a $Ti_{50}Ni_{30}Cu_{20}$ alloy which exhibit B2-B19 martensitic transformation. Compared with elastic constants measurement which can explore only modes near BZ center, neutron inelastic scattering has the advantage of being able to obtain information on the whole BZ, so that we may observe many strain /shuffle modes and their relation to the martensite structure may be understood. In the present study, we pay much attention to the possible multiple mode softening, which has not been reported in the previous studies.

Single crystal sample with a size of $9*9*6mm^3$ was mounted on a triple axis spectrometer TAS-2 with a temperature controlling system. The incident neutron energy was 14.7mV (wavelength 2.35A) , a PG filter was used to reduce higher order reflection, the collimations were 17'-40'-40'-40'. It should be pointed out that Ti-Ni based alloys appear to exhibit strong incoherent scattering, which makes the background very high, thus the accurate determination of peak position is difficult, especially around BZ boundary. We tried to solve this problem by sampling over a wide ΔE range for several times and determine peak position with Guassian fitting.

The main results are as follows:

(1) TA2 phonon branch exhibits two dips, one is around $q_{max}/3$, another one is at $q_{max}/2$ (Fig.1). The phonon energy of both dips become further decreased with approaching transformation temperature, but appear unlikely to reach zero at M_s. Surprisingly, it is found that the former dip is deeper than the latter, although the latter dip is related to B2-B19 transformation.

(2) $q_{max}/3$ dip is appreciably shifted from exact 1/3 position, it is around $0.375q_{max}$.

(3) We also observed elastic scattering along <110> direction and its temperature dependence (Fig.2). We found that no obvious elastic peak exists around $q_{max}/3$and $q_{max}/2$. However, an elastic peak was found around $0.67q_{max}$, but showed little temperature dependence down to M_s. This suggests that $q_{max}/3$ and $q_{max}2/3$ are not equivalent. This is difficult to understand at present.

To summarize, we found that a double mode-softening in $Ti_{50}Ni_{30}Cu_{20}$ alloy prior to B2-B19 martensitic transformation, despite that only one of them is related to the observed martensitic transformation. The other soft mode is related to the R phase (a different martensite) which is not realized in this alloy. This result seems to suggest that the observed MT is merely the winner of several possible candidates, which is characterized by different modes or order parameters. The competition in harmonic and anharmonic energy among them determines which should show up.

Finally, we would like to point out that further experiment should be done in order to verify the above interesting results.

References:

1. C. Zener, Phys. Rev., 71(1947), 846.
2. X. Ren and K. Otsuka, Scripta Mater., 38(1998), in press .
3. X. Ren, K. Taniwaki, K. Otsuka, T. Suzuki, K. Tanaka, Yu.I. Chumlyakow, and T. Ueki, Philo. Mag. A, 75(1998), in press.

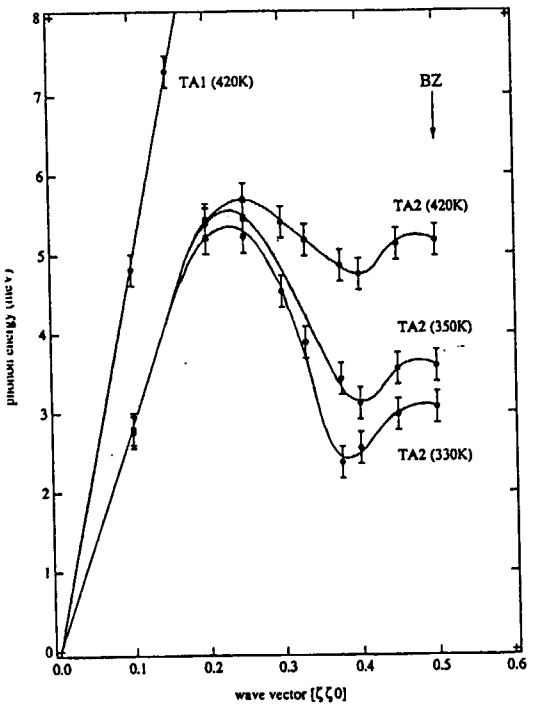

Figure 1. TA2 phonon dispersion relation

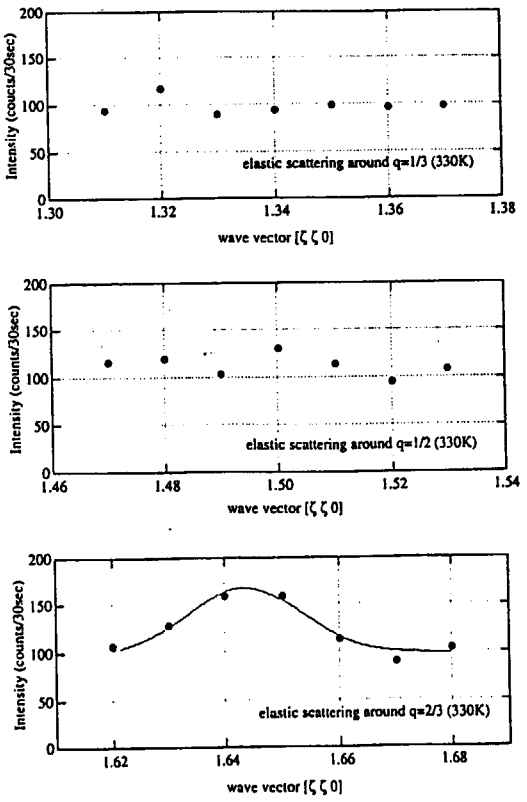

Figure 2. Elastic scattering along <ζζ0>

研究テーマ：中性子散乱によるアルカリ金属挿入層状珪酸塩の研究
標題：アルカリ金属挿入バーミキュライトの格子動力学

Lattice Dynamics of Alkali-Metal Intercalated Vermiculite

N. Wada, K. Nakajima[1], and K. Kakurai[1]

Toyo University, Fac. of Engineering, Kujirai, Kawagoe City, Saitama, 350-8585 Japan
[1] Neutron Scattering Laboratory, The Institute for Solid State Physics
The University of Tokyo, Shirakata, Tokai, Naka, Ibaraki, 319-11 Japan

Recently, vapor-phase intercalation of alkali metals to layered silicates has been successfully carried out and the structural and electrical properties of the new intercalation compounds have been investigated.[1,2] There, the observation of a drastic increase in the conductivity upon intercalation is particularly noteworthy. Here, our interest centers around studying the phonon dynamics of Rb vermiculite, especially the intercalant-host interactions.

A single crystal of "Kenya" vermiculite (~2 grams with a mosaic spread of ~4 °) was cation-exchanged in a RbCl water solution for months. Then the crystal (the ideal chemical composition is $Rb_x(Si_{4-x}Al_x)Mg_3O_{10}(OH)_2$ with x~0.9) was studied at room temperature using the triple-axis spectrometer PONTA (5G).

Figure 1 shows the observed LA phonon energies as a function of the wave vector **q** parallel to the c axis. The published data for mica (the ideal composition is $K(Si_3Al)Al_2O_{10}(OH)_2$) by N. Wada and W. Kamitakahara[3] is also shown for comparison. As seen from the figure, the c-axis LA phonon energies in Rb vermiculite appears to be less than those in mica, more so near the zone boundary. We think that this phonon softening may be strongly related to the interaction between the Rb intercalant layer and the host silicate layer.

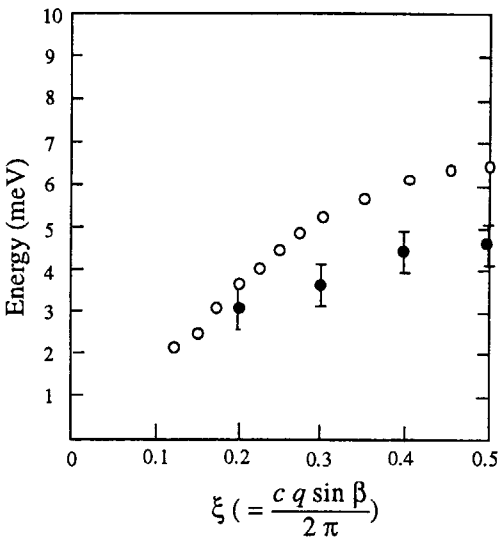

Fig. 1 LA phonon energies as a function of the wave vector **q** along the c axis in Rb vermiculite. Our data points are indicated by filled circles. The data of Reference 3 for mica are also shown by open circles.

Fig. 2 shows the measured dispersion points for the b-axis LA and $TA_{||}$ (polarization in the plane) phonons. It is noticed that the $TA_{||}$ phonons observed in Rb vermiculite exhibit higher frequencies that those in mica. It is difficult to discuss the LA phonons, however, because of the limited data at this time.

Our preliminary experiments suggest that (1) further inelastic scattering data are needed

JRR-3M, PONTA, 1. structure

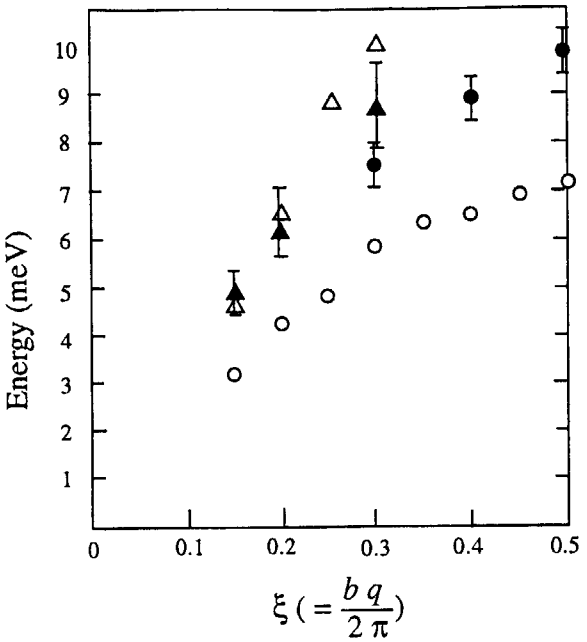

Fig. 2 LA (noted by filled triangles) and $TA_{\parallel}$ (noted by filled circles) phonon energies as a function of the wave vector **q** along the b axis in Rb vermiculite. The data of Reference 3 for mica are also shown by open triangles for the LA phonons and open circles for the $TA_{\parallel}$ phonons.

to clarify the phonon dispersion curves in Rb vermiculite, and (2) inelastic scattering experiments on the sample intercalated by the vapor transport method will contribute to further understanding the intercalant-host layer interactions and the mechanism for the intercalation.

REFERENCES

1. N. Wada, H. Okui, Y. Omura, A. Fujiwara, H. Suematsu, and Y. Murakami, Mat. Res. Soc. Symp. Proc. **453** (1997) 95-100.

2. N. Wada, Y. Omura, Rev. of High Press. Sci. and Tech., Vol. **7** (1998) 727-729.

3. N. Wada and W.A. Kamitakahara, Phys. Rev. **B** 43, 2391 (1991).

研究テーマ：中性子散乱による応力測定の研究
表　　題：VAMAS標準試料内部ひずみ分布の測定

The internal residual stress measurement for VAMAS Round Robin Sample by neutron diffraction method

N. Minakawa, Y. Morii, Y. Tsuchiya, M. Hayashi[1], S. Ohokido[1], K. Tanaka[2]、 Y. Akiniwa[2]
JAERI, 1. Ech. Eng. Res. Lab., Hitach Ltd., 2. Nagoya university

1, The outline

VAMAS is the abbreviated designation of Versailles Project on Advanced Materials and Standards. It aims at the international standardization of the residual stress measurement by the neutron diffraction method. VAMAS made a standard sample and it has around in every country organization and which degree was the similar strain distribution gotten or measured in the comparison. This time, we measured VAMAS standard sample by RESA at JRR-3 in Guide Hall and the excellent result could be gotten.

2, The standard sample

Outer ring diameter is 50mm and ring caliber is 25mm with a column plug diameter is 25mm which was manufactured by aluminum 7050. These are put in to each other at the liquid-nitrogen temperature, after that returning the room temperature, the stress occurs to the boundary surface by the thermal expansion. It measured the internal residual strain distribution of $\Delta d/d$. A sample size is shown in Figure -1.

3, The measurement condition

The measurement position was used the direction of Figure-1 and measured RADIAL, HOOP and AXIAL planes. The condition of the equipment and neutron beam is shown next.

The monochromator crystal : Si(311)
The mosaicnes of the crystal : 0.22°
Scattering angle of monochromator crystal : $2\theta M = 79.75°$
The neutron wavelength : 0.20995 nm
The insident and reflection beam slit size : measurement of Radial and Hoop 3 mm (width) x 10mm (Height)
measurement of Axial 3mm(Width) x 3mm(Height)
Beam Collimation : 0.2° - 0.33° - 0.33°
Neutron detector : Zero dimensional ^{3}He detector

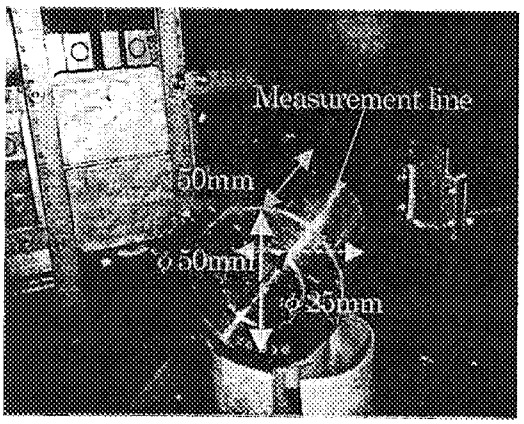

Fig-1 RING & PLUG SAMPLE

4, The measurement procedure

(1) To look for the lattice constant of the material, it measured plug material by neutron diffraction.
(2) It measured texture to know the nature of the material and decision of the measurement Miller index. It was measured based on the neutron diffraction result of (1), it used χ, ϕ

axis - goniometer at the plug (111), (200) and (220).

(3) It fixed a measurement Miller index from the result of the neutron diffraction and the result of the texture measurement. It installed a plug sample in 3 axis (X,Y,Z) goniometer and based on the arrow marking which is written in the sample surface, it fixed the measurement surface of RADIAL, HOOP, AXIZL. Every direction was measured by θ -2 θ scan method, it measured each index in d_0(h,k,l).

(4) It installed a ring and a plug sample on the 3 axis goniometer and it was selected the neutron diffraction measurement which is the index, (111), (200), (220). The ring and plug (111) strain distribution is shown in Figure-2.

5, The consideration

The purpose of VAMAS measurement is to make the standard of the standardization by measuring the same sample with the equipment of every country organization and comparing it. The measurement result by RESA agreed with the strain distribution over each American and European organization approximately. It is possible to say that it is the strain distribution which is quite near the result which was computed by the finite element method. Because we weren't informed of a value with Young's modulus and Poisson's ratio every each index of aluminum 7050, we could not done calculation.

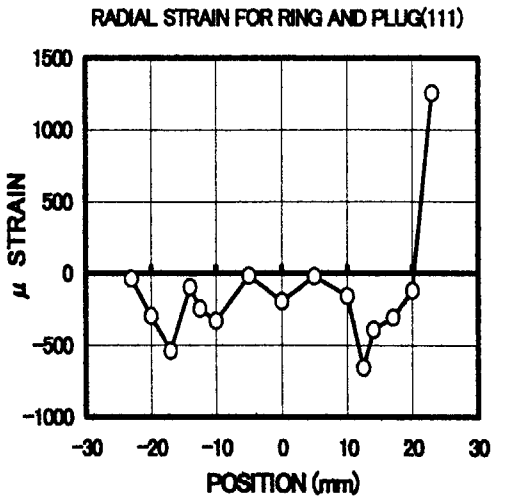

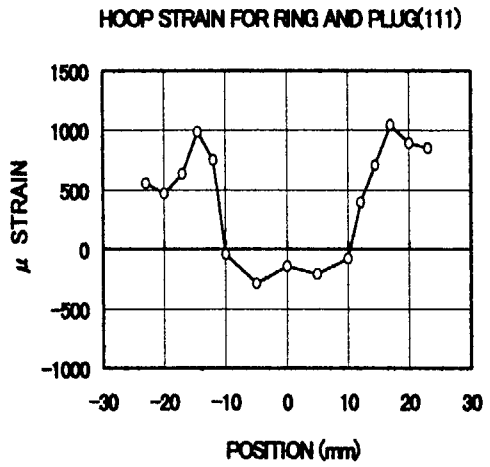

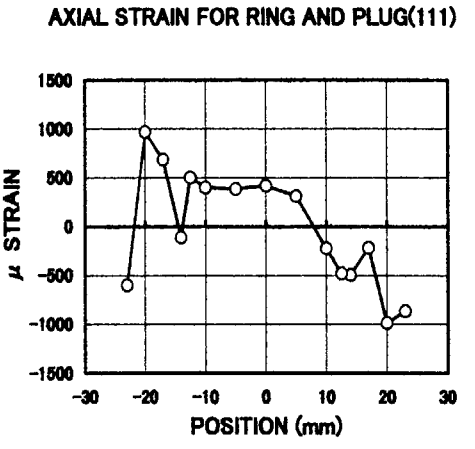

Fig-2 Distribution of Strain for VAMAS Ring & Plug (111)

研究テーマ：アニオン配座を中心とした多元系金属酸化フッ化物の構造の精密化
表題：$Nd_2Ln_2O_3F_6$ (Ln: Y, Eu, Gd) 中でのアニオン配座の電気化学特性への影響

Influence of Anion Arrangement in $Nd_2Ln_2O_3F_6$ (Ln: Y, Eu, Gd) on Electrochemical Property

M.Takashima, S.Yonezawa, T. Tanioka and Y. Nakajima

Department of Materials Science and Engeneering, Faculty of Engineering, Fukui University, 3-9-1 Bunkyo, Fukui 910-8507

Binary rare earth oxide fluorides, $LnLn'O_xF_y$ (Ln,Ln':rare earth elements), have been prepared by solid-solid reaction between rare earth oxide and fluoride. $LnLn'O_xF_y$s are the solid electrolyte in which oxide ion can be transferred. Especially, Nd contained compounds, $Nd_2Ln_2O_3F_6$, have higher conductivity of $\sim 10^{-2}$ S m^{-1} among them. Though there is fluoride ion in these compounds, alomost all charge are carried by oxide ion.[1] In this study, the anion arrangements in $Nd_2Ln_2O_3F_6$(Ln:Y, Eu,Gd) are discussed by X-ray powder diffraction measurement (XRD), Neutron diffraction measurement (ND) concerning with the difference of their conductivities.

The powder samples of $Nd_2Ln_2O_3F_6$ (Ln;Y, Eu, Gd) were synthesized by the solid-solid reaction between 1 mol Nd_2O_3 and 2 mol LnF_3 at 1100 ~ 1200 °C in the driest possible atomosphere (Ar). XRD (Shimadzu XD-3As) and ND (JRR-3MT1-3)(monitor count : 3300, setp : 0.05°, range : 5 ~ 154°, λ = 0.1817 nm) measurements were carried out. The powder sample was formed into pellet and the electric conductivity was measured.

Among $Nd_2Ln_2O_3F_6$ samples, $Nd_2Eu_2O_3F_6$ gave the highest conductivity of 3.5 Sm^{-1} at 600 °C under P O_2= 0.4 Pa. The transport numbers of the oxide ion and the electron were measured to be around 0.9 and less than 0.05, respectively, at a temperature ranging from 500 to 700°C [2]. The conductivity of each $NdLnO_3F_6$ was in the order of Ln=Eu, Y, Gd (almost same for Y and Gd) at 700°C. As the results of XRD-Rietveld refinement, the crystal structure of $Nd_2Eu_2O_3F_6$ was found to be expressed by the monoclinic lattice (P 1 2/c 1, a_0 = 0.396 nm, b_0 = 1.13 nm, c_0 = 0.562 nm, β = 134.84° [R_F = 3.33]). The molecular number, Z was calculated to be one from the density data (measured; 6.98 kg m^{-3}, calculated; 6.96 kg m^{-3}). As shown in Fig.1, three oxide ions occupy the six corners of an octahedron (2e sites), which is surrounding a fluorite like cluster consist of EuF_2, in its occupancy of 0.5, while that containing Nd consists of $NdO_{0.5}F$. Four corners (2f sites) of a cube surrounding Nd are occupied with 4 F ions and 2 O^{2-} ions (2f sites, y=0.01) occupy the other four corners of it in the occupancy of 0.5. Oxide ion in $Nd_2Eu_2O_3F_6$ would be supposed to be conductible to migrate through the vacant sites (2f) in the y = 0.01 plane and 2e sites at which the site occupancy of O^{2-} is 0.5. From the results of XRD and ND - Rietveld refinement, the anion arrangement in $Nd_2Y_2O_3F_6$ must be different from that of $Nd_2Eu_2O_3F_6$. Some F^- must occupy 2f site which contains the O^{2-} vacants. Since O^{2-} could be transferred through these vacants, $Nd_2Y_2O_3F_6$ must have lower electric conductivity than $Nd_2Eu_2O_3F_6$. In case of Gd, the anion arrangement in it would be similar to that in $Nd_2Y_2O_3F_6$ (XRD). This might be the reason why $Nd_2Gd_2O_3F_6$ has the similar conductivity to $Nd_2Y_2O_3F_6$ which is lower than that of $Nd_2Eu_2O_3F_6$ while Gd^{3+} has very close ionic radius to Eu^{3+}.

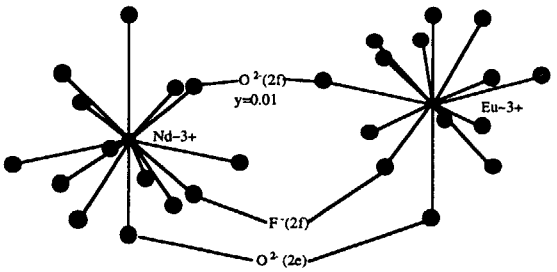

Fig.1 Anion arrangement around Nd and Eu in $Nd_2Eu_2O_3F_6$. The thick line corresponds to the bond between the metal ion and the anion at 2f site

JRR-3M, T1-3 Hermes, 1.structure

References

1) M. Takashima, S. Yonezawa, K. Horita, K. Ohwaki and H. Takahashi, *J. Mater. Chem.*, **6**, 795 (1996).
2) M. Takashima, S. Yonezawa and U. Ukuma, *J. Fluorine Chem.*, **87**, 229 (1998).

研究テーマ：スカンジウム含有リチウムリン酸塩の構造とイオン伝導性
表題：スカンジウム含有リチウムリン酸塩の構造とイオン伝導性

Structure Refinement of Lithium Ion Conductors $Li_3Sc_2(PO_4)_3$ and $Li_{3-2x}(Sc_{1-x}M_x)_2(PO_4)_3$ (M=Ti, Zr) with x=0.10 by Neutron Diffraction

Takahito Suzuki, Kenji Yoshida, Kazuyoshi Uematsu, Tatsuya Kodama, Kenji Toda, Zuo-Guang Ye, Masayoshi Ohashi[1] and Mineo Sato

Department of Chemistry and Chemical Engineering, Faculty of Engineering, Niigata University, Ikarashi 2 no-cho 8050, Niigata 950-2181, Japan
[1]Institute for Material Research, Tohoku University, katahira 2-1-1, Aoba-ku, Sendai 980-0812, Japan

Lithium superionic conductors exhibiting an enough high ionic conductivity at ambient temperature are expected in order to develop new rechargeable lithium battery systems. The crystal structures of $Li_3Sc_2(PO_4)_3$ and $Li_{3-2x}(Sc_{1-x}M_x)_2(PO_4)_3$ (M=Ti, Zr) with x=0.10, lithium ion conductors, were refined by the Rietveld analysis for neutron diffraction patterns in order to confirm the site location and site occupancy for Li ions.

The powder neutron diffraction experiments were carried out by using the HERMES diffractometer installed at the T1-3 beam port of the T1 thermal neutron beam guide of JRR-3M. In Table 1 the crystallographic data of $Li_3Sc_2(PO_4)_3$ and $Li_{3-2x}(Sc_{1-x}M_x)_2(PO_4)_3$ (M=Ti, Zr) with x=0.10 are given. The monoclinic phase and orthorhombic phase of $Li_3Sc_2(PO_4)_3$ have almost the same crystal structure, the crucial difference between both phases is the distribution of lithium ions. Our results obtained in this study confirm again the above results concerning with the monoclinic phase, but somewhat differ in the lithium location in the orthorhombic phase, where all the lithium sites are partially occupied. Such partial occupancy behavior over the whole lithium sites is also seen in the Ti- and Zr-substituted samples, where the occupancy ratio at Li(1) site is a little greater than that for the orthorhombic phase of the unsubstituted sample.

The Rietveld refinement confirmed clearly that a much high disorder was introduced to the three kinds of Li sites in the orthorhombic superionic conduction phase of $Li_3Sc_2(PO_4)_3$. The orthorhombic phase was stabilized at room temperature by substituting Ti^{4+} or Zr^{4+} for Sc^{3+} sites. The stabilized materials was also found to have such a high disorder over the Li sites. The improvement of the ionic conductivity can be ascribed to the stabilization of the orthorhombic phase by the introduction of small amounts of Ti^{4+} and Zr^{4+} ions and to the creation of a number of vacancies on the available lithium sites, coupled to the substitutions.

Table 1 Characteristics of neutron experiment and unit cell parameters of $Li_3Sc_2(PO_4)_3$ and $Li_{3-2x}(Sc_{1-x}M_x)_2(PO_4)_3$ (M=Ti, Zr)

Compound	Space group	*a* (Å)	*b* (Å)	*c* (Å)	γ (°)	V (Å^3)
$Li_3Sc_2(PO_4)_3$ (298K)	$P2_1/n$	8.8483(4)	12.2737(5)	8.7959(4)	90.015(6)	955
$Li_3Sc_2(PO_4)_3$ (573K)	*Pbcn*	12.3998(6)	8.8352(4)	8.8270(4)	———	967
$Li_{3-2x}(Sc_{1-x}Ti_x)_2(PO_4)_3$ x=0.10 (298K)	*Pbcn*	12.3332(4)	8.7829(3)	8.8067(3)	———	954
$Li_{3-2x}(Sc_{1-x}Zr_x)_2(PO_4)_3$ x=0.10 (298K)	*Pbcn*	12.3542(5)	8.7947(4)	8.8202(4)	———	958

JRR-3M, KPD VS. HERMES, 1. Structure

研究テーマ： $(La,Sr)_{n+1}Mn_nO_{3n+1}$のスピン電荷ダイナミクス
表題: マンガン酸化物における反強磁性金属状態

Antiferromagnetic metallic state in doped manganites

Y. Moritomo, T. Akimoto, Y. Maruyama, A. Nakamura, K. Hirota[1], K. Ohoyama[2], and M. Ohashi[2]
CIRSE, Nagoya University, Nagoya 464-01, Japan
[1]*Department of Physics, Tohoku University, Sendai 980-77, Japan*
[2]*Institute for Materials Research, Tohoku University, Sendai 980-77, Japan*

The doped manganites show much more multifarious properties in the heavily-doped region ($x \geq 0.5$). Here, we have investigated the electronic and magnetic properties for $La_{1-x}Sr_xMnO_3$, especially for the heavily-doped region.

We show in Fig.1 temperature dependence of resistivity ρ and magnetization M for crystals of $La_{1-x}Sr_xMnO_3$ (x=0.0) at x=0.50 and 0.54. At x=0.50, the $\rho - T$ curve steeply decreases below T_C(=360 K; downward arrow) down to $\sim 5\times10^{-5}\Omega$cm at 5 K. By contrast, the x=0.54 compound shows a ferromagnetic-to-antiferromagnetic transition at T_N=200 K (see the lower panel of Fig.1), accompanying a slight increase of the ρ-value. Nevertheless, the resistivity for x=0.54 remains low ($\sim 4\times10^{-4}\Omega$cm at 5 K) even in the antiferromagnetic phase, indicating that the hole-doping procedure beyond $x \sim 0.5$ alters the ground state for $La_{1-x}Sr_xMnO_3$ from the FM state to the AFM state. A similar AFM state is observed also for x=0.57 (not shown). For x=0.60, however, ρ-value steeply increases below T_N=250 K.

To investigate the spin structure for the AFM state, neutron diffraction measurements were performed with Kinken Powder Diffractometer for high efficiency and high resolution measurements, HERMES, installed at the JRR-3M reactor in Japan Atomic Energy Research Institute, Tokai, Japan. Neutrons with wave length 1.819Å were obtained by the (331) reflection of Ge monochromater, and a combination of 12′-∞-Sample-18′ collimator. Melt-grown crystal ingots were crushed into fine powder and were sealed in a vanadium capsule with helium gas, and mounted at the cold head of the closed-cycle He-gas refrigerator. The nuclear Bragg reflections in the papramagnetic state (330 K) are well reproduced with the orthorhombic structure (*Pbnm*; Z=4) with lattice constants of a=5.4329(7)Å, b=5.4470(8)Å and c=7.7556(9)Å. Figure 2 shows the powder pattern for $La_{0.46}Sr_{0.54}MnO_3$ (x=0.54, z=0.0) in the antiferromagnetic phase at 10 K. The observed magnetic superlattice reflections (indicated by hatching) can all be indexed by the A-type antiferromagnetic structure.

The key factor that realizes the AFM state is considered to be the anisotropy of the two e_g orbitals, i.e., the two-dimensional $d_{x^2-y^2}$ state and the one-dimensional $d_{3z^2-r^2}$ state. Reflecting the anisotropy of the e_g orbitals, the electron transfer integral t_{ij} between the i- and j-sites strongly depend not only on the orbital species but also on the relative direction $\vec{r}_j - \vec{r}_i$. The e_g-electron system gains the maximum kinetic energy when the $d_{x^2-y^2}$ orbitals forms a pseudo-2D band. If such a pseudo-2D band were realised, the in-plane exchange interaction would be ferromagnetic mediated by the itinerant $d_{x^2-y^2}$-electrons (DE interaction), while the antiferromagnetic superexchange interaction should dominate along the z-direction because of negligible t_{ij}-value.

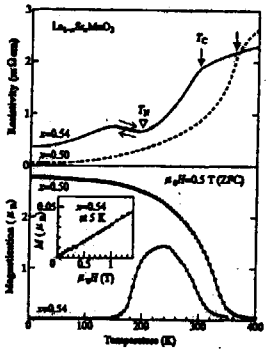

FIG. 1. Temperature dependence of resistivity (upper panel) and magnetisation (lower panel) for crystals of $La_{1-x}Sr_xMnO_3$. Solid curves are for x=0.54 and broken curves for x=0.50. Arrows and triangles represent the Curie temperatures (T_C) and Neel temperatures (T_N), respectively. Inset shows magnetisation curve at 5 K for x=0.54.

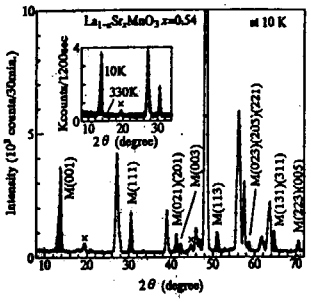

FIG. 2. Neutron powder profiles for $La_{0.46}Sr_{0.54}MnO_3$ (x=0.54) at 10 K. Shaded areas indicate magnetic superlattice reflections, which are indexed in the *Pbmn* setting. Inset shows temperature dependence of the powder neutron profiles: open and closed circles are at 330 K ($> T_C$) and at 10 K ($< T_N$). Small impurity peaks (cross) are originated hexagonal $SrMnO_3$.

JRR-3M, KPD, 1.crystal structure・excitation

研究テーマ： $(La,Sr)_{n+1}Mn_nO_{3n+1}$のスピン電荷ダイナミクス
表題: $La_{0.5}Sr_{1.5}MnO_4$の電荷整列転移における格子効果

Lattice effects on charge-ordering transition in $R_{0.5}Sr_{1.5}MnO_4$

Y. Moritomo, A. Nakamura,S. Mori[1], N. Yamamoto[1], K. Ohoyama[2], and M. Ohashi[2]
CIRSE, Nagoya University, Nagoya 464-01, Japan
[1] *Deaprtment of Physics, Tokyo Institute of Technology, Tokyo 152, Japan*
[2] *Institute for Materials Research, Tohoku University, Sendai 980-77, Japan*

Crystal of $La_{1-x}Sr_{1+x}MnO_4$ (x=1/2) shows the charge-ordering (CO) transition, i.e., real-space ordering of the doped carriers, at T_{CO}=230 K. Here, we report a significant suppression of the CO transition in layered manganites $R_{0.5}Sr_{1.5}MnO_4$ with decrease of the averaged radius r_R of R^{3+} (*chemical pressure*), which makes a sharp contrast with the layered nickelates.

Lattice constants were obtained by Rietveld analysis of powder X-ray diffraction patterns, and are listed in Table I together with the ratio of the lattice constant c/a. With decreasing r_R, $d_{Mn-O(in)}(\equiv 2/a)$ steeply decreases from 1.932Å for R=La to 1.916Å for R=Sm. Accordingly, the ratio c/a increases from ≈3.218 for R=La to ≈3.230 for R=Sm, suggesting the increasing static JT distortion of the MnO_6 octahedra along the c-axis. To determine the magnitude of the JT distortion, neutron powder diffraction measurements were performed at 300 K for $La_{0.5}Sr_{1.5}MnO_4$ and $Nd_{0.5}Sr_{1.5}MnO_4$ with Kinken Powder Diffractometer for high efficiency and high resolution measurements, HERMES, installed at the JRR-3M reactor in Japan Atomic Energy Research Institute, Tokai, Japan. Neutrons with wave length 1.819Å were obtained by the (331) reflection of Ge monochromater, and a combination of 12′-∞-Sample-18′ collimator. Melt-grown crystals were crushed and were sealed in a vanadium capsule with helium gas. Results of Rietveld analysis are summarized in Table II. Substitution of the smaller Nd^{3+} ions for larger La^{3+} ions increases the out-of-plane bond length $d_{Mn-O(out)}$, and hence increases the static out-of-plane JT distortion ($\Delta \equiv d_{Mn-O(out)}/d_{Mn-O(in)}$) from Δ ≈1.04 for R=La to ≈1.05 for R=Nd.

In Fig.1 are plotted the critical temperatures for CO transition for $R_{0.5}Sr_{1.5}MnO_4$ as a function of $d_{Mn-O(in)}$. T_{CO} was determoned from suppression of in-plane component χ_{ab} of magnetic susceptibility. With decreasing $d_{Mn-O(in)}$, the CO state (the hatched region) is suppressed and finally disappears around $d_{Mn-O(in)}$ ≈1.922Å. This observation indicates that repulsive interaction between the e_g-electrons (or the small polarons) is not the dominant driving force of the CO transition, since such an interaction is expected to enhance with decrease of the inter-site distance.

The suppression of T_{CO} with decreasing $d_{Mn-O(in)}$ implies that the e_g-orbital degree of freedom plays an important role in the transition, since the increasing static out-of-plane JT distortion of the MnO_6 octahedra stabilizes the $d_{3z^2-r^2}$ state and changes the character of the e_g-orbital. It is probable that the charge-ordered state in layered manganites is stabilized by concomitant cooperative JT distortion within the MnO_2-sheet, or equivalently the orbital-ordering. Murakami *et al.* proposed that the charge-ordering of the layered manganites accompanies an orbital-ordering with wave vector (1/4, 1/4, 0). According to this scenario, the observed suppression of the CO transition (see Fig.1) is interpreted as follows. For R=La with smaller static JT distortion along the c-axis, the charge- and orbital-ordered state is easily realized with slight modification of the in-plane oxygen positions. With decreasing $d_{Mn-O(in)}$, however, the orbital-ordered state within the MnO_2-sheet is difficult to be realized, since the e_g-electrons are dominated by the $d_{3z^2-r^2}$ character.

TABLE I. Lattice constants for $R_{0.5}Sr_{1.5}MnO_4$ at 300 K.

R	a(Å)	c(Å)	a/c
La	3.8632(6)	12.430(1)	3.2175
$La_{0.5}Nd_{0.5}$	3.8524(3)	12.4097(5)	3.2213
$La_{0.25}Nd_{0.75}$	3.8490(3)	12.4080(3)	3.2237
Nd	3.8405(3)	12.3955(6)	3.2275
Sm	3.8309(2)	12.3751(5)	3.2303

TABLE II. Typical bond lengths for $R_{0.5}Sr_{1.5}MnO_4$ at 300 K.

R	$d_{Mn-O(in)}$(Å)	$d_{Mn-O(out)}$(Å)	$d_{Mn-O(out)}/d_{Mn-O(in)}$
La	1.9316(3)	2.00(1)	1.04
Nd	1.9203(2)	2.01(1)	1.05

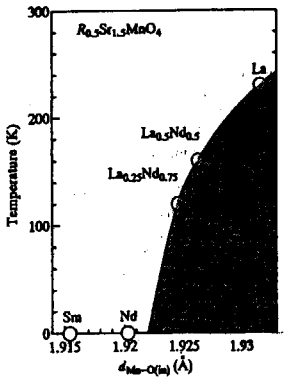

FIG. 1. Electronic phase diagram for $R_{0.5}Sr_{1.5}MnO_4$ as a function of the in-plane Mn-O bond length $d_{Mn-O(in)}$. Solid curve is a guide to the eyes. Hatching represents the charge-ordering state.

JRR-3M, KPD, 1.crystal structure・excitation

研究題目：粉末中性子回折装置HERMES (IMT)
表題：新しい超伝導体$Li_{0.16}ZrNCL$とその母相βZrNClの構造研究

Structure study on novel layered superconductor $Li_{0.16}ZrNCl$ and its parent ß-ZrNCl

S. Shamoto, T. Kato, Y. Ono, T. Kajitani, K. Ohoyama[A], M. Ohashi[A*], and Y. Yamaguchi[A]

Dept. of Applied Physics, Tohoku University, Sendai 980-8579, Japan
[A]Institute for Materials Research, Tohoku University, Sendai 980-8577, Japan
**(present address: Faculty of Engineering, Yamagata University, Yonezawa)*

Structures of ß-ZrNCl and superconducting $Li_{0.16}ZrNCl$ (T_c=15K) are determined by powder neutron diffraction using JRR3M-HERMES. Unit cells of ß-ZrNCl and $Li_{0.16}ZrNCl$ have same space symmetry of $R\bar{3}m$ (No.166) type. ZrN bilayer in $Li_{0.16}ZrNCl$ is found to form almost perfect double honeycomb lattice, in which ZrN satisfies an "isosteric" principle with h-BN as AB/8e$^-$. In addition, slip of $[ZrNCl]_2$ slab layers by intercalation is observed.

ß-ZrNCl was prepared by the reaction of ZrH_2(99.7%) with NH_4Cl(99.5%) at 650°C for 30min under the flow of NH_3 gas (99.9%, 20-50cc/min). The product contains ß-ZrNCl and baddeleyite-type impurity phases. ß-ZrNCl phase was purified, and separated from the mixture by a chemical vapor transport as described in the literature [1]. In the purified ß-ZrNCl, however, hydrogen was remained, which gives high background for neutron diffraction data by incoherent neutron scattering.The lithium intercalation was carried out by dispersing the sample in 15% *n*-butyllithium solution in hexane in an Ar-filled glove box for one day. The Li concentration x of our sample is expected to be the same as those (x=0.16) in ref. 2, because of the same sample preparation procedure and the same superconducting transition temperature. The samples with the weight of 3.78g and 2.68g were sealed in Al cans filled with He gas for ß-ZrNCl and $Li_{0.16}ZrNCl$ respectively. The sample can with $Li_{0.16}ZrNCl$ was reserved into liquid nitrogen, until neutron diffraction measurements were performed, in order to prevent the sample from delithiation, which easily occurs even in Ar atmosphere at room temperature (R.T.). Neutron measurements were carried out with the monochromatized neutron radiation of λ = 1.8196Å. The scattered intensity was collected from 5° to 154.9° in 2θ by 150 counters stepped by 0.1°. The results obtained by neutron diffraction were refined using the Rietveld analysis computer program RIETAN[3]. The refined structural parameters are listed in Tables I and II. The space group $R\bar{3}m$ (#166) was successfully assigned for the refinement rather than the space group of $P\bar{3}m1$ (#164) [1]. The Zr, N and Cl occupation factors agreed with the chemical analysis (Zr:N:Cl=1:1:1) of ß-ZrNCl [1]. Zr atom is located at 6*c* site with z~0.12 while N is at 6*c* site with z~0.20 for ß-ZrNCl but Zr and N atoms swap their sites in the lithium system. This site exchange causes distinguishable differences in the X-ray and neutron diffraction patterns. Figures (a) and (b) show determined structures of ß-ZrNCl and $Li_{0.16}ZrNCl$, respectively. Zigzag Zr-N double layered local structure in the parent crystal becomes almost flat in the lithium system. We wish to term this flat local structure as a " double honeycomb lattice". Above stated structure modes are different from the one proposed by Yamanaka et al. [4] but may be isomorphic with those of ß-HfNCl and its lithium (as well as other alkaline earth metals) intercalated superconductor with T_c = 25K[5] , respectively.

研究題目：粉末中性子回折装置HERMES (IMT)
表題：新しい超伝導体$Li_{0.16}ZrNCL$とその母相βZrNClの構造研究

Table I. Structural parameters ofß-ZrNCl at T=4K

Space Group $R\bar{3}m$; a=3.5974(2) Å, c=27.548(2) Å

atom	site	g	x	y	z	B_{eq}/Å^2
Zr	6c	1.0	0	0	0.1208(1)	3.6(2)
N	6c	0.99(1)	0	0	0.1984(1)	4.4(1)
Cl	6c	0.99(2)	0	0	0.3876(1)	4.0(2)

R_I=3.04%, R_p=8.19%, R_{wp}=11.17%, R_e=3.29%

Table II. Structural parameters of$Li_{0.16}ZrNCl$ at T=4K

Space Group $R\bar{3}m$; a=3.6016(4) Å, c=27.694(6) Å

atom	site	g	x	y	z	B_{eq}/Å^2
Zr	6c	1.0	0	0	0.2076(3)	2.4(2)
N	6c	0.94(3)	0	0	0.1307(3)	3.3(1)
Cl	6c	1.00(3)	0	0	0.3883(2)	3.5(2)
Li	3a	0.32(fix)	0	0	0.0	0.8(fix)

R_I=5.35%, R_p=10.07%, R_{wp}=13.50%, R_e=3.62%

References

[1] M. Ohashi, S. Yamanaka, M. Sumihara and M. Hattori : J. Solid State Chem. 75 (1988) 99.
[2] H.Kawaji, K.Hotehama and S.Yamanaka : Chem. Mater. 9 (1997) 2127.
[3] F. Izumi: "The Rietveld Method", ed. by R. A. Young, Oxford University Press, Oxford (1993), Chap. 13; Y.-I. Kim and F. Izumi: J. Ceram. Soc. Jpn., 102 (1994) 401.
[4] S.Yamanaka, H.Kawaji, K.Hotehama and M.Ohashi: Adv. Mater. 8(1996) 771.
[5] S.Yamanaka, K.hotehama and H.Kawaji : Nature 392 (1998) 580.

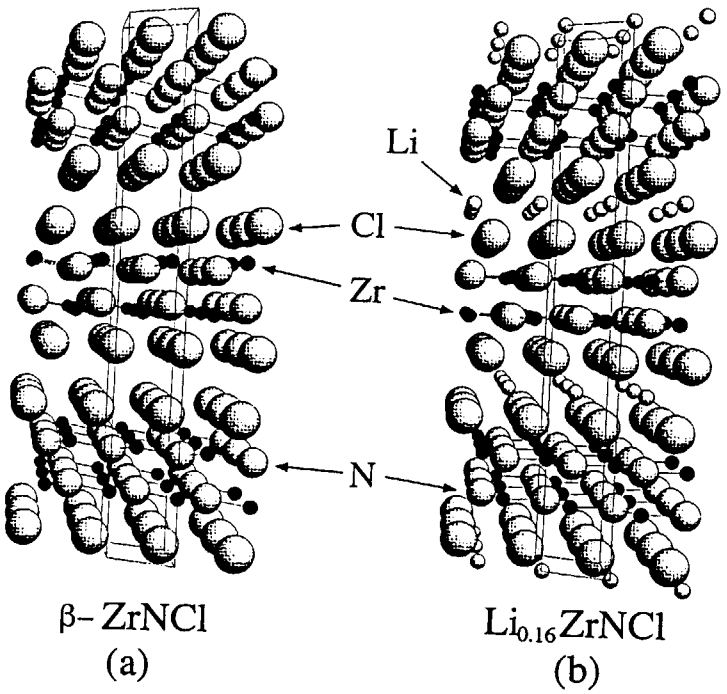

研究テーマ：水素結合中の水素原子核のイメージング
表題：KDPの水素結合における水素原子核のイメージングの中性子粉末回折法による研究

Neutron Powder Diffraction Study for Imaging of Hydrogen Nucleus in the Hydrogen Bond of KDP

Shigefumi YAMAMURA, Shintaro KUMAZAWA[1], Eiji NISHIBORI[2], Masaki TAKATA[3], Makoto SAKATA[2], Yoko SUGAWARA, Yoshinobu ISHII[1] and Yukio MORII[1]

Department of Physics, School of Science, Kitasato University, Kanagawa 228-8555, Japan
[1]Advanced Science Research Center, JAERI, Tokai, Ibaraki 319-1106, Japan
[2]Department of Applied Physics, School of Engineering, Nagoya University, Nagoya 464-8603, Japan
[3]Department of Material Science, Interdisciplinary Faculty of Science and Engineering, Shimane University, Shimane 690-8504, Japan

In order to explore the nature of hydrogen bond, it is important to examine distribution of hydrogen nucleus together with electron distribution. For first step of this study, we have already performed electron density studies for KDP(KH_2PO_4) and ADP($NH_4H_2PO_4$) by Maximum Entropy Method (MEM) using synchrotron radiation powder diffraction data[1,2]. We have revealed from the electron distribution that the hydrogen bond in O–H–O had a covalent character. For second step of this study, we carried out MEM analysis for KDP using neutron powder diffraction data collected by HRPD diffractometer at JAERI with wave length of neutron, 1.823 Å[3]. It was found that resolution i.e. number of data was not enough to obtain precise distribution of hydrogen nucleus because of relatively long wave length of neutron. In this report, we carried out neutron powder diffraction study at 10 K for KDP using short wave length of neutron, 1.16 Å.

Neutron powder diffraction experiments were performed using HRPD diffractometer at JRR-3M. In order to improve profile shape of powder pattern, data collection range for each detector was overlapped. The powder diffraction data up to 2θ = 140° include 448 reflections, which corresponds to 0.62 Å resolution in real space.

The structure refinement by Rietveld method was performed using the computer program RIETAN-98, which is now in developed by Dr. F. Izumi (NIRIM). By using this program, integrated intensities for the MEM analysis can be precisely calculated from the overlapped measurement data of HRPD. Fitting result of the powder pattern is shown in Fig. 1. The reliable factor for pattern fit, R_{wp}, was 2.50 % and that for integrated intensities, R_I, was 2.45 %. These values were showing fairly good fit comparing with the values, R_{wp} = 2.76 % and R_I = 4.98 % for conventional Rietveld method. The positional parameters for hydrogen atom showed ordering of the hydrogen atom in the hydrogen bond.

MEM analysis for imaging of hydrogen nucleus from the obtained powder data is in progress.

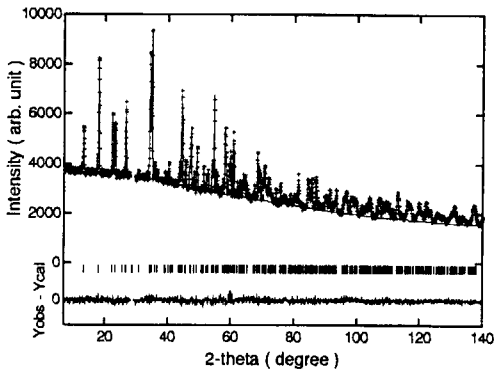

Fig. 1. Fitting result of neutron powder diffraction pattern for KDP at 10 K by Rietveld analysis.

References

1) S. Yamamura et al., Photon Factory Activity Report **14** (1996) 186.
2) S. Yamamura et al., Photon Factory Activity Report **15** (1997) in press.
3) S. Kumazawa et al., JAERI NSL Report April 1995 - March 1996, 99.

原子炉：JRR-3M　　装置：HRPD(1G)　　分野：中性子散乱（構造）

課題：半磁性半導体 $Zn_{1-x}Mn_xTe$ の非弾性散乱
表題：$Zn_{0.568}Mn_{0.432}Te$ の冷中性子散乱

Cold neutron scattering study of $Zn_{1-x}Mn_xTe$ with x=0.432

T.Kamiya,Y.Ono,T.Sato[1],Y.Oka[1] and T.Kajitani

Department of Applied Physics, Graduate School of Engineering,Tohoku University, Sendai 980-8579

[1]*Reseach Institute for Scientific Measurements,Tohoku University,Sendai 980-8577*

Diluted magnetic semiconductor, $Zn_{1-x}Mn_xTe$with $x \leqq 0.6$, undergoes spinglass transition at low temperatures below 30K. Giebultowicz *et al.* observed the damped magnon-like dispersion along [110] and [210] directions at 4.2 K in $Cd_{1-x}Mn_xTe$ with x=0.6 despite the absence of long range spin order. [1]

Several single crystals of $Zn_{1-x}Mn_xTe$ ($0<x<0.6$) were grown by conventional Bridgeman method. In this system, the lattice parameter linearly increases with increasing Mn concentration. We estimated the Mn concentrations based on the accurately determined lattice parameters. The spingalss transition temperature, T_g=17 K, was determined from the magnetization measurement using SQUID magnetometer. In order to study spin dynamics above and below T_g, we carried out cold neutron scattering experiment using TOF-type spectrometer AGNES, installed in the guide hall of the JRR-3M at JAERI.

The sample with x=0.432 and T_g=17K was selected in the present study. Cold neutron scattering intensities were measured at 10K,17K,30K and 293 K, respectively. Figure 1 shows incident and scattered neutron wave vectors, $\mathbf{k}_i$ and $\mathbf{k}_f$,respectively in the (0 0 1) resiprocal lattice plane . Cold neutron spectra observed around the reciprocal lattice point 1 1/2 0 are shown in Fig.2.

Sharp elastic peak (Δ E=0) and additionalbroad Lorentzian tail appears at 17K and 30K. This is probably the critical magnetic scattering arising from the spin fluctuation. Weak inelastic peak is noticed at Δ E=-1meV in the spectra at 17 K and 10 K. This energy transfer is smaller than the magnon-like peak energy (2-4 meV) at 1 1/2 0 observed in $Zn_{1-x}Mn_xTe$ with x=0.65. [1]

Reference [1] T.M.Giebultowicz *et al.*, Phys. Rev. B39, 6857 (1986)

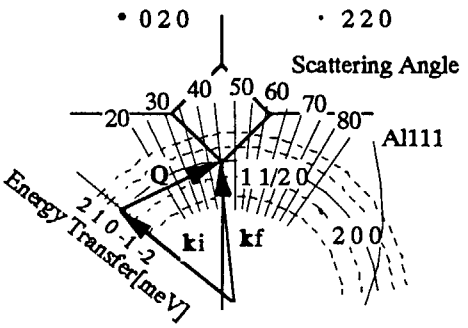

Fig.1 Scattering condition.

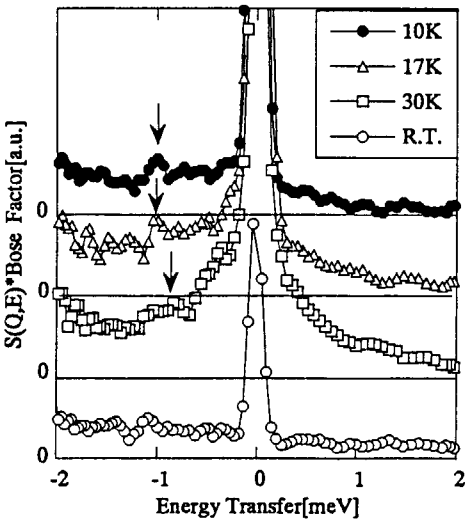

Fig. 2 Temperature dependent change of cold neutron spectra.

研究テーマ：超低温の導入による中性子散乱の研究
表題：Fe-Cu合金の析出現象の中性子小角散乱による研究

SANS Study of precipitation phenomena of Fe-Cu alloy

K. Aizawa, A. Iwase, T. Tobita and M. Suzuki

Japan Atomic Energy Research Institute, Tokai, Ibaraki 319-1195, Japan

There are many studies for precipitation phenomena in the Fe-Cu alloy system. In order to understand the relation of hardening and precipitate during thermal aging for dilute copper concentration in this system, we studied Fe-0.6at%Cu alloy by small-angle neutron scattering (SANS).

Samples were solution-treated at 1123 K for 2 hours and they were quenched in water. Then they were aged at 773K from 8h to 1000h. Each sample dimension is about $10\times10\times2mm^3$. SANS measurements were performed using SAN-J instrument at JRR-3M in JAERI. The covered q-range ($q=2\pi\theta/\lambda$, θ : scattering angle, λ : neutron wavelength) is from 0.02 to $2nm^{-1}$.

Except very early stage of thermal aging, it is well known that the chemical composition of precipitate is almost identical that of pure copper. Because of low copper concentration, we can treat the SANS profile as form factors of copper precipitates with particle size distribution. All SANS intensities showed independent component about aging with nearly q^{-6} behavior in the very low-q region. This may be attribute the contribution such as grain boundary or large scale inhomogeneity that doesn't relate to copper precipitation. So we subtracted that component from SANS intensities to extract the cross section of copper precipitate.

Figure 1 shows the aging time dependence of SANS cross section of copper precipitate. In the case of 100h aging, the SANS cross section shows q^{-1} dependence clearly. In this case, the scattering body has dimension considerably larger along one axis than along the other two. Therefore we assume that the shape of the precipitate is a ellipsoid of rotation with a : a : av (a : radius of the minor axis of precipitate, v : ratio of the major axis and the minor axis) during thermal aging. We assume the major axis and the minor axis have Gaussian distribution also.

Figure 2 shows the aging time dependence of the major axis and the minor axis obtained by least square fitting of the above model. The minor axis grows with the aging time monotonously. On the other hand, the major axis grows up to 100h aging, then it shrinks with the aging time. In the case of 1000h aging, the shape of copper precipitate tends to spherical.

We measured the Vickers hardness of this sample to compare SANS results. The hardness of the as quenched sample is about 80 DPH. Then the hardness gradually increases and the profile of hardness forms a peak around 100h aging with about 110 DPH. The time to the maximum of the major axis about thermal aging corresponds to that to the maximum of hardening by Vickers hardness measurement.

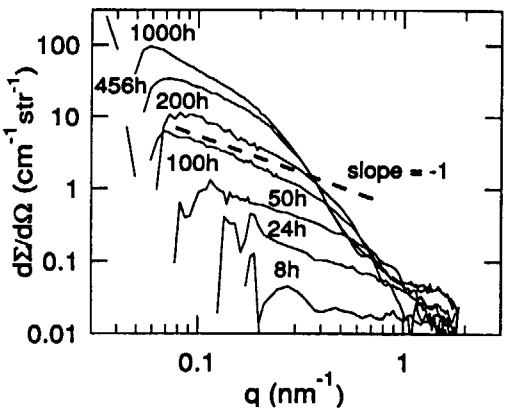

Fig. 1 The aging time dependence of SANS cross section of Fe-0.6at%Cu alloy.

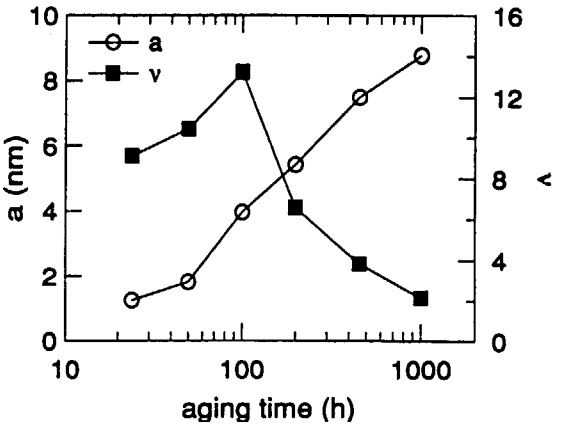

Fig. 2 The aging time dependence of the major axis and the minor axis obtained by least square fitting of Fe-0.6at%Cu alloy.

原子炉：JRR-3M　　装置：PNO (3G)　　分野：中性子散乱（構造）

研究テーマ：精密中性子光学実験法によるNi基超合金単結晶の観察
表題：クリープ損傷を施したNi基超合金CMSX-4の構造評価

Characterization of single-crystal Ni-base superalloy CMSX-4 with creep damage (II)

K. Aizawa, H. Tomimitsu, H. Tamaki[1] and A. Yoshinari[1]

Japan Atomic Energy Research Institute, Tokai, Ibaraki, 319-11
[1]Hitachi Research Laboratory, Hitachi, Ltd., Hitachi, Ibaraki, 317

In order to check the possibility of nondestructive testing to the expected life of operated blades made from Ni-base superalloy, we have applied small-angle neutron scattering (SANS) experiments to the CMSX-4 superalloy with creep damage as a model case. We reported the morphological change with creep damage caused by tensile stress of that sample in previous report[1]. The range of observation corresponded to that of less than 30% to creep rupture time. The purpose in this article is to show the morphological change up to near creep rupture.

The sample is a single crystal CMSX-4. In the case of as heat-treatment sample, the morphology observed by SEM is aligned cuboidal precipitate of γ' phase in γ matrix. It was loaded tensile stress to introduce creep damage with 14kgf/mm^2 at 1313K. The stress direction was parallel to <001> direction of a sample. In this case, the morphology observed by SEM is lamella structure of γ and γ' phases with normal direction being parallel to stress. Samples were cut into 30mm×19mm×2mm^t. The SANS measurements were carried out using PNO instrument with the q-range ($q=2\pi\theta/\lambda$, θ : scattering angle, λ : neutron wavelength) of 2×10^{-4}-6×10^{-2}nm^{-1} at JRR-3M in JAERI. This instrument is a double crystal SANS machine using Si perfect crystal with (5,-5) setting. Incident neutron beams were parallel to <100> direction of a sample.

Figure 1 shows the smeared SANS intensity of single crystal CMSX-4 with damage rate from 10% to 85% to creep rupture time. The q-vector is parallel to stress direction. The 1st peak from lamella structure is clearly shown. It shifts to lower q with increasing creep damage. This means the average distance of lamella structure grows with increasing creep damage. So that is a good parameter to describe the morphological change due to creep damage. After desmearing the data for infinite slit height system, we obtained that parameter by least square fitting of 1st peak from lamella structure, assuming Gaussian peak shape.

The average distance of lamella structure as a function of creep rate for rupture time is shown in fig. 2. It gradually increase up to 54% creep damage, then rapidly grows. The SANS results is good agreement with SEM observation.

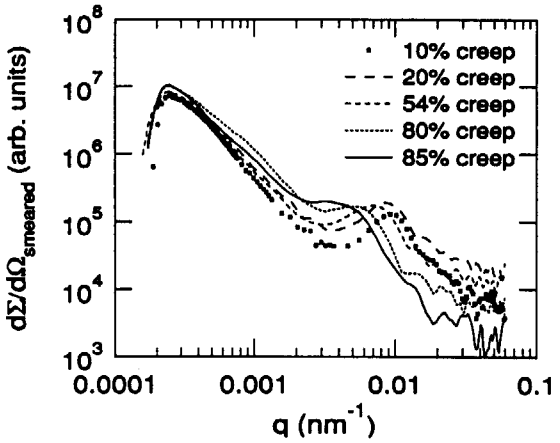

Fig.1 The dependence of SANS cross section for damage rate to creep rupture time.

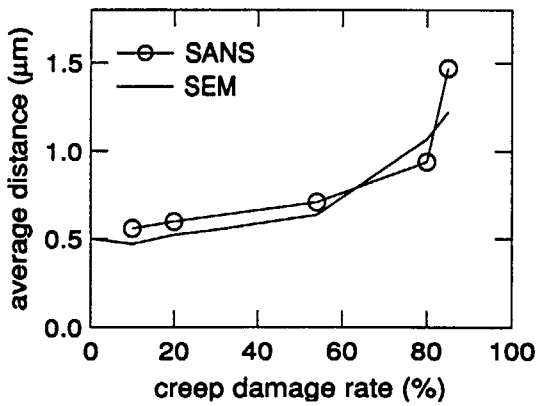

Fig. 2 The dependence of the average distance of lamella structure as a function of damage rate to creep rupture time.

References

[1] K. Aizawa, H. Tomimitsu, H. Tamaki and A. Yoshinari: (PROGRESS REPORT ON NEUTRON SCATTERING RESEARCH, April 1, 1996-March 31, 1997, 54

原子炉：JRR-3M　　装置：PNO(3G)　　分野：中性子散乱（構造）

ウランおよびランタノイド複合酸化物の合成、構造と磁気的性質

Preparation, Structure, and Magnetic Properties of Uranium and Lanthanide Complex Oxides

北海道大学大学院理学研究科化学専攻　日夏幸雄
Division of Chemistry, Graduate School of Science,
Hokkaido University, Yukio Hinatsu

1. はじめに

アクチノイド系、ランタノイド系を体系化している5f電子、4f電子の固体結晶中での基礎的挙動の理解を深め、これら電子の挙動に起因する特異な現象の発見と解析することを目的とする。

この研究では、

① アクチノイド系では、遷移金属を含む三元系ウラン複合酸化物CoU_2O_6、NiU_2O_6の合成とその磁気的性質

② ランタノイド系では、安定な+3価以外に異常な酸化状態として+4価をとり得るプラセオジムを含むペロブスカイト酸化物$BaPrO_3$, $SrPrO_3$について、その結晶構造と磁気的性質について調べた。

2. 研究経過

① アクチノイド系

試料の合成は以下の方法で行なった。

[CoU_2O_6]　まずCoOとU_3O_8を秤量、摩砕、混合後、空気中1000℃で1日加熱反応させ、$CoUO_4$を合成した。次に$CoUO_4$とUO_2を等量秤量し、石英反応管に熔封し、800℃で1日加熱反応させ、CoU_2O_6を得た。

[NiU_2O_6]　CoU_2O_6と同様の方法では合成できず、この合成には、NiO、UO_2、UO_3を等量秤量し、摩砕、混合後、石英反応管に熔封し、800℃で1日反応させ、NiU_2O_6を得た。

磁化率の測定には、SQUIDを用い、その温度依存性（4.2 K～室温）、磁場依存性を測定した。

CoU_2O_6については、粉末中性子回折を行い、波長λ=1.823Åの中性子を用い、温度はネール温度(T_N=32.5K)前後である10 K、100 Kで測定を行なった。

② ランタノイド系

$BaPrO_3$、$SrPrO_3$は、$BaCO_3$ ($SrCO_3$) とPr_6O_{11}を出発物質として酸素気流雰囲気中1300℃で加熱することにより合成できた。$BaPrO_3$は高温で加熱することにより一部酸素を失うので、酸素定比化合物を得るためには一旦1000℃で24時間保持することが必要であったが、$SrPrO_3$ではさらに750℃で48時間加熱することを要した。

磁化率の測定には、SQUIDを用い、電子スピン共鳴吸収スペクトル（ESR）測定は4.2 Kで行った。

3. 研究成果

① アクチノイド系

粉末X線回折の結果から、CoU_2O_6、NiU_2O_6はいずれも六方晶系Na_2SiF_6構造を持つことがわかった。格子定数はそれぞれ、a = 9.1124、c = 4.9987; a = 9.0215、c = 5.0219Åである。

磁化率の温度変化（図1）から、いずれの化合物についても低温（32.5 K、35.3 K）で反強磁性転移することを見い出した。この転移温度は磁場の強さに依存しないこともわかった。CoU_2O_6の磁化率は、120 Kから室温の温度範囲でCurie-Weiss則が成立したが、NiU_2O_6については大きな温度に依存しない磁化率(χ_o)のため、成立せず、磁化率はχ=1.21/(T+6.9)+1.1×10^{-3}(emu/mole)に従うことがわかった。表1には、磁化率測定から得た主なデータを記した。有効磁気モーメントの解析から、CoU_2O_6、NiU_2O_6中のウランは＋5価の酸化状態にあることがわかった。

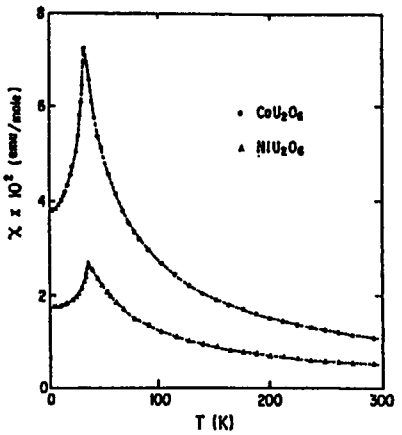

図1　CoU_2O_6、NiU_2O_6の磁化率の温度変化

JRR-3M　HRPD　アクチノイド、ランタノイドの固体化学

表1　CoU_2O_6、NiU_2O_6の磁性データ

Compounds	T_N(K)	$\mu_{eff}(\mu_B)$	θ(K)	χ_0(emu/mole)
CoU_2O_6	32.5	5.27	−27.8	—
NiU_2O_6	35.3	3.11	−6.9	1.1×10^{-3}

100 Kでの中性子回折のデータから、格子定数、原子位置等、結晶構造の精密化を行なったが、X線回折と同様の結果であった。

中性子回折による磁気ピーク（図2）の位置を合わせるには、波数ベクトル（0,0,1/6）が最適であり、磁気構造の大きさは結晶格子の6倍の大きさであることがわかった。磁気モーメントの大きさは（001）面内で変わり、磁気構造は6つの（001)面の繰り返しで表わすことができることがわかった。結晶構造の面からは、磁性イオンであるCoとUを含むC軸に垂直な面には2種類あるので、結局CoU_2O_6の磁気構造は、z=0、z=1/2のそれぞれ6つの面で表わすことができることがわかった。図3には、z=0面およびz=1/2面でのCoとUの磁気モーメントの向き、CoU_2O_6の正弦波的磁気構造を示した。

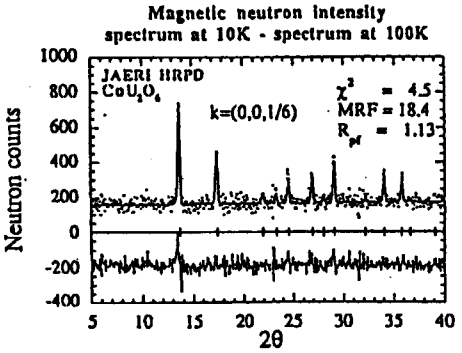

図2　CoU_2O_6の磁気ピーク

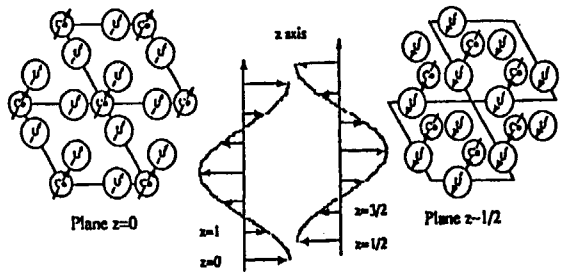

図3　CoU_2O_6の磁気構造

② ランタノイド系

X線回折から、$BaPrO_3$、$SrPrO_3$いずれも斜方晶ペロブスカイト構造（空間群Pbnm）を持つことがわかった。$BaPrO_3$では11.5 Kで反強磁性転移したが、$SrPrO_3$では4.2 Kまで常磁性挙動を示した。結晶構造解析を行うと、$BaPrO_3$ではほぼ直線であったPr-O-Prの並びが、$SrPrO_3$では直線状から大きく逸脱し、このため酸素を介した超交換相互作用が起こりにくくなったためだと考えられる。

Pr^{4+}のESRスペクトルは、反磁性体である$BaCeO_3$、$SrCeO_3$にドープし、4.2 Kで測定した。^{141}Prの核スピン(I = 5/2)との相互作用による超微細構造が見られ、$Pr^{4+}/BaCeO_3$のスペクトル（図4）では、許容遷移に加え、禁制遷移も測定できた。

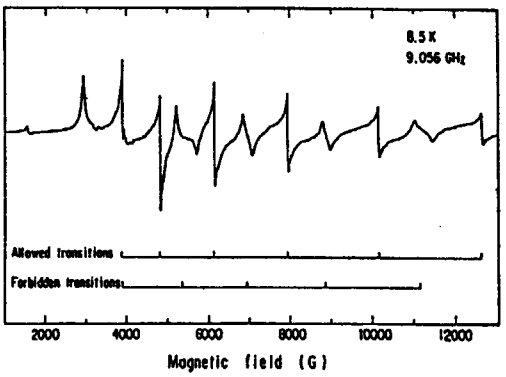

図4　$Pr^{4+}/BaCeO_3$のESRスペクトル

$Pr^{4+}/BaCeO_3$では、Pr^{4+}の周りの最近接酸素イオンによる結晶場はオクタヘドラル対称として扱え、解析により|g| = 0.741, 超微細結合定数A =0.0609 cm^{-1}を得た。g値は、基底状態J=5/2のΓ_7状態のみから計算される -10/7 の絶対値よりはるかに小さく、このことから4f電子には結晶場効果が著しく働くことがわかった。図5には、$BaCeO_3$中のPr^{4+}イオンのゼーマン分裂の様子を示した。

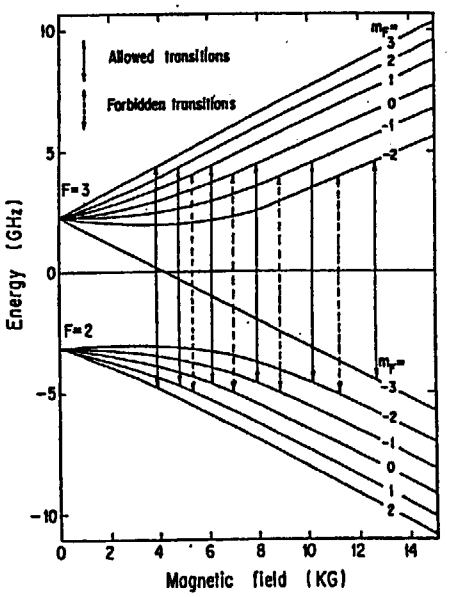

図5　$BaCeO_3$中のPr^{4+}のゼーマン分裂

$Pr^{4+}/SrCeO_3$のESRスペクトル（図6）では異方性が見られた。これは$BaCeO_3$と比べ、$SrCeO_3$の結晶ではより斜方に歪んだ構造を持つため、セリウムサイトに入るPr^{4+}の周りの最近接酸素イオンによる結晶場の対称性がオクタヘドラルから著しく歪んでいることに対応している。図6下部にはsimulationにより求めた$Pr^{4+}/SrCeO_3$のスペクトルを示した。

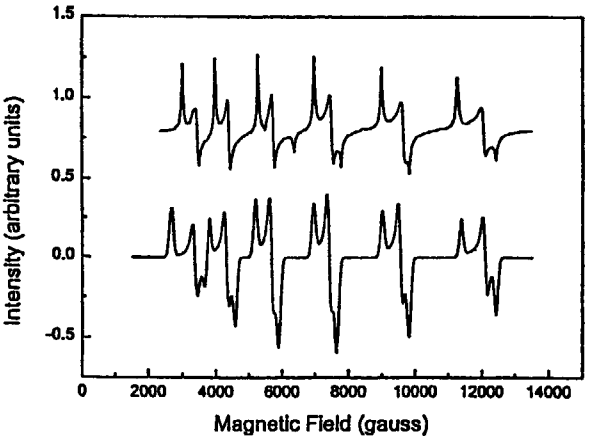

図6　$Pr^{4+}/SrCeO_3$のESRスペクトル

This is a blank page.

1. 中性子散乱 (Neutron Scattering)

4) 超伝導現象 (Superconductivity)

This is a blank page.

研究テーマ：(2)強相関電子系の中性子散乱による研究
表題：梯子格子物質；$(Sr_{2.5}Ca_{11.5})Cu_{24}O_{41}$におけるスピンギャップ

Neutron Scattering Study of the Spin Gap in the Hole-Doped Spin Ladder System $(Sr_{2.5}Ca_{11.5})Cu_{24}O_{41}$

J. Akimitsu, T. Nagata, S. Katano[1], M. Nishi[2], and K. Kakurai[2],

Department of Physics, Aoyama-Gakuin University, Setagaya-ku, Tokyo 157-8572
[1]Neutron Scattering Group, Advanced Science Research Center, Japan Atomic Energy Research Institute, Tokai, Ibaraki 319-1195
[2]Neutron Scattering Laboratory, ISSP, The University of Tokyo, Tokai, Ibaraki 319-1106

Recently, theoretical prediction has been made that a two-leg ladder, coupling of two spin-1/2 Heisenberg chains, leads to a singlet ground state with a spin gap and a finite correlation length at $T = 0$. The existence of a spin gap is obvious in the limit that exchange interaction along the rung is much larger than that along the leg, since the ground state is then simply a collection of singlets along the rungs. For a general ratio, the ground state is a resonating valence bond state.

Experimentally, it is intriguing that the spin gap value vs. number of holes and the existence of the spin gap in the superconducting state. In this report, we summarize the present situation of the spin gap in the two-leg ladder $(Sr,Ca)_{14}Cu_{24}O_{41}$.

Figure 1 shows the inelastic neutron scattering intensity – the difference between the intensity measured at around the antiferromagntic zone center (0.5 0 1.5) and the background intensity measured at the reciprocal lattice point (1.5 0 1.36) – at 7 K obtained with the constant-Q method. As shown in the figure, the intensity is distributed over a wide energy range beyond the energy resolution. A broad but clear peak in the intensity was, however, observed at 33.5 ± 0.5meV for the zone center (0.5 0 1.5). This energy can be assigned to be the spin gap energy of this heavily doped compound. The inset presents the scattering intensities with this energy along the c^* direction. These intensities were peaked at (0.5 0 1.5) and also at (0.5 0 2.5), which clearly shows that the spin gap observed here has the periodicity of the ladders and, thus, is certainly originated from the ladders of this material. Very recently, neutron scattering experiments for a single crystal showed that the spin gap of the parent material $Sr_{14}Cu_{24}O_{41}$ is about 32.5 meV [1]. Therefore, within the experimental accuracy, the spin gap of the doped compound does not change even if Ca is substituted up to 11.5 (Fig. 2). The present result

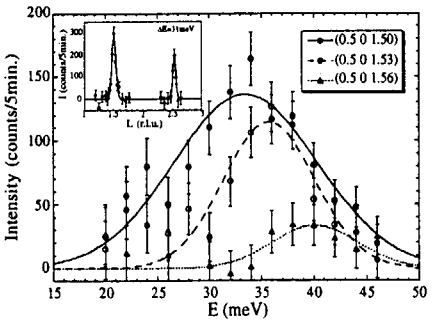

Fig. 1. Inelastic neutron scattering intensities after the subtraction of the background intensity for the constant-Q scans. The solid line shows the spin excitation at the antiferromagnetic zone center, showing the spin gap energy of 33.5±0.5 meV. The inset shows the intensities with this energy along the c^* direction. The dotted lines show the spin excitations at the reciprocal lattice point apart from this zone center. The lines are the results of the Gaussian fitting.

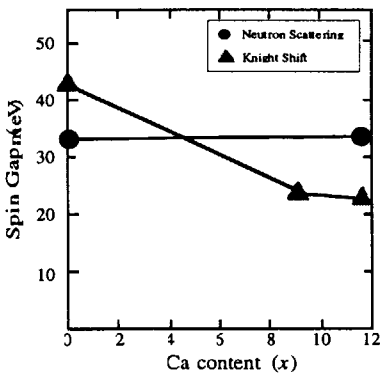

Fig. 2. Spin gap as a function of the Ca content. The circles show the results from neutron inelastic scattering experiments. The triangles are the results of the Knight shift in the NMR experiments in Ref. 4.

is initially unexpected since the transport property of the system is drastically changed from an insulator to a metallic state with the Ca doping. Holes doped by the Ca substitution would affect the spin liquid state of the system. Some theories actually suggested that the spin gap decreases with increasing the Ca content [2,3]. The results obtained here, thus, indicate the necessity of theories that explain the magnetic excitation properties in this spin ladder system.

Fig. 3 (a) shows the constant energy scans with Δ = 34,40,50.5 meV. With departing from the zone center, the excitation energy increases greatly, indicating a dispersive character. The dispersion relation derived from the constant-E scans in Fig. 3 (a) is displayed in Fig. 3 (b). Here, the scans were fitted to Gaussian profiles.

Since the energy is limited up to 55 meV in the present work, the data is not enough to discuss the exchange couplings in the system. However, the dispersion obtained can be explained with large exchange energies of the order of 100 meV. The dotted line is the dispersion curve represented using the exchange constants which was recently obtained by Eccleston *et al.* for the parent compound - the exchange constants along the legs $J_{\parallel}$=130 meV and along the rungs $J_{\perp}$=72 meV [1]. It is clear that to get the whole dispersion curve and then to discuss the exchange interactions precisely, experiments at higher energies up to 200 meV are required. Such experiments are now being planned using a spectrometer on a spallation neutron source.

The inset of Fig. 3 (b) shows an intensity contour map obtained in the present experiments. Strong intensities are concentrated around the antiferromagnetic zone center, and are spread over the wide range of the energies around the spin gap excitation energy of 33.5 meV. This intensity distribution might be a distinctive feature of this system, and should be understood in the future work.

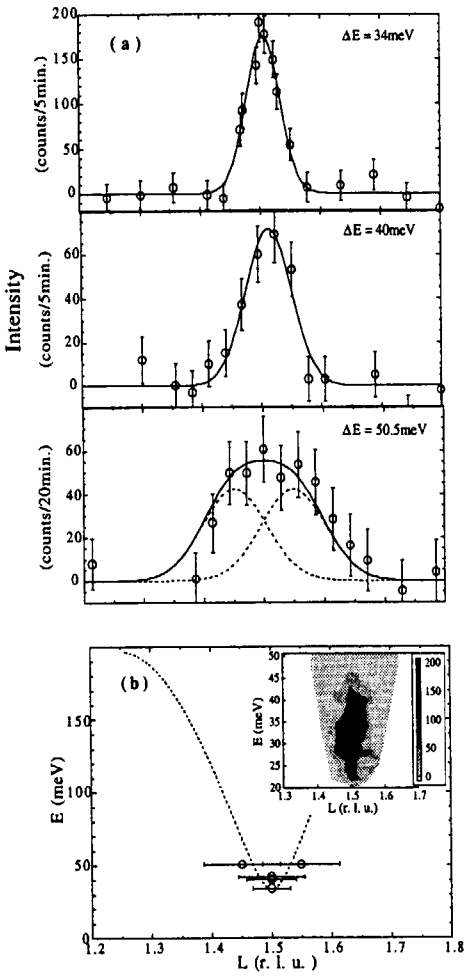

Fig. 3 (a) Inelastic neutron scattering intensities for the constant-E scans. The lines are the results of the fits to a Gaussian, or the sum of two Gaussians displaced equally from the zone center. (b) Dispersion relation at 7 K. The horizontal bars represent the full width at half maximum (FWHM) derived from Gaussians fits to the data shown in (a). The dotted line shows the dispersion relation with the exchange constants along the legs $J_{\parallel}$=130 meV and that along the rungs $J_{\perp}$=72 meV which were proposed for the parent compound. The inset shows the intensity contour map obtained from the present experiments.

References

[1] R. S. Eccleston, M. Uehara, J. Akimitsu, H. Eisaki, N. Motoyama, S. Uchida, (to be published in Phys. Rev. Lett.)

[2] E. Dagotto, J. Riera, and D. Scalapino, Phys. Rev. B**45**, 5744 (1992).

[3] D. Poiblanc, H. Tsunetsugu, and T.M. Rice, Phys. Rev. B**50**, 6511 (1994).

[4] K. Magishi, S. Matsumoto, Y. Kitaoka, K. Ishida, K. Asayama, M. Uehara, T. Nagata, and J Akimitsu, Phys. Rev. B**57**, 11533 (1998).

研究テーマ：強相関電子系の中性子散乱による研究
表題：中性子小角散乱法を用いた$NdBa_2Cu_3O_{7-d}$のメゾスコピック構造の観察

Observation of Mesoscopic Structure in $NdBa_2Cu_3O_{7-d}$ by Small Angle Neutron Scattering Measurement

K.Osamura, S.Miyata, J.Suzuki[1], K.Kuroda[2] and N.Koshizuka[2]

Department of Materials Science and Engineering, Kyoto University, Kyoto 606-8501, Japan
[1]Advanced Science Research Center, Japan Atomic Energy Research Institute, Ibaraki 319-1195, Japan
[2]Superconductivity Research Laboratory, International Superconductivity Technology Center, Tokyo 135-0062, Japan

$NdBa_2Cu_3O_{7-d}$ (Nd123) is a member of $REBa_2Cu_3O_{7-d}$ family of high-T_c superconductors and have also the quite high transition temperature beyond 90K. It was noticed that Nd123 has high critical current density of 70000A/cm^2 at 77K as reported by Ting *et al*[1]. The critical current of bulk type-II superconductors are produced by vortex pinning in the peak effect, seen in, for example, magnetization measurements. In order to clarify the origin of the peak effect of this material, we performed small angle neutron scattering measurements which give the information of the structure of nano meter scale, which coincides with the scale of important factors like as coherence length, penetration depth, typical vortex spacing and so on. It is necessary that the scale of the pinning potential is the same order of the coherence length to effect a vortex, and also necessary that the pinning potential is distributed as the same order of the vortex spacing and penetration depth to pin vortices collectively.

Small angle neutron scattering measurement was performed with SANS-J apparatus at JRR-3M reactor in JAERI-Tokai. Incident beam was parallel to the c-axis of the crystal and neutron wavelength was selected ranging from 0.6 to 1.5nm. All measurements were performed in room temperature.

Scattering patterns for the sample (Lot.No. 0729-4) with neutron wavelength of 1.5nm obtained on the 2-dimensional position sensitive detector is shown in Fig.1. It can be seen the cross-shaped patterns with its arms stretching along a- and b-axes and it is seen in all other experimental conditions. And it can be seen also weak but apparent four spots in 110 directions.

The cross shaped pattern suggest that the structure with sharp boundaries normal to a- and b-axes, i.e., rectangles and/or squares of nano scale order is distributed in the samples. On the other hand, four spots lead to the existence of periodic structure along 110 crystal direction in the sample. In Y123, twin structure arranging along 110 direction (twin boundaries spread also in 110 planes) is observed by TEM[2]. In Nd123 sample used in this experiments, twin structure is also observed by TEM. Such a spot like pattern is seen in only the sample of 0729-4. The 0729-4 sample heat treated as " 900°C×100hrs+quench / 500°C×100hrs+quench / 320°C×330hrs " shows the largest critical current density calculated from magnetization measurement in all samples with different heat treatments.

In I(q)-q radial average functions which is given by averaging intensities as to absolute value of q, lower q component than around 0.04nm^{-1} seems to grow up in 0729-4 sample. It indicates that, in real space, structures of larger scale than 150nm grows up in 0729-4 sample.

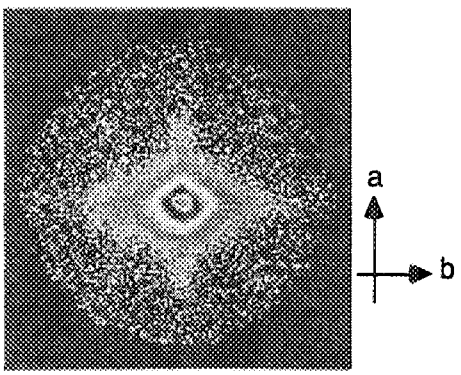

Fig.1 Scattering pattern for 0729-4 sample in room temperature and no applied field obtained on 2-D PSD.

References

1) Wu Ting, T.Egi , K.Kuroda and S.Tanaka, Appl. Phys. Lett., 70(1997), 770-772.
2) C.S.Pande, A.K.Singh, L.Toth, D.U.Gubser and S.Wolf, Phys. Rev B, 36(1987), 5669-5671.

原子炉：JRR-3M　　装置：SAS-J(C3-2)　　分野：中性子散乱（超伝導）

研究テーマ：強相関電子系の中性子散乱による研究
表題：中性子小角散乱法を用いた非双晶$YBa_2Cu_3O_{7-d}$における磁束格子観察

Attempt to Observation of Vortex Lattice in Twin-Free $YBa_2Cu_3O_{7-d}$ by Small Angle Neutron Scattering

K.Osamura, S.Miyata, J.Suzuki[1], S.Okayasu[2]

Department of Materials Science and Engineering, Kyoto University, Kyoto 606-8501, Japan
[1]Advanced Science Research Center, Japan Atomic Energy Research Institute, Ibaraki 319-1195, Japan
[2]Department of Materials Science, Japan Atomic Energy Research Institute, Ibaraki 319-1195, Japan

$YBa_2Cu_3O_{7-d}$ (YBCO), which has high critical point (Tc) beyond the liquid nitrogen temperature, is the one of the most famous superconductors in the application research. As much as the critical point, pinning characteristics is also important for the applications. As YBCO (or 123-family) is the tetragonal structure at high temperature and transforms the orthorhombic structure at low temperature including superconductivity region, so twin structure is formed in the samples . Though the twin structure is thought to play a important role of vortex pining, pinning characteristics of the sample is ,in general, complicatedly composed by different many mechanisms, and it is difficult to estimate the contributions of the elements either qualitatively or quantitatively. For the observation of the vortex pattern by small angle neutron scattering (SANS) measurement, four spots indicating the periodic potential along 110 directions are observed and it is explained that vortices is trapped by twin plane by Forgan *et al.*[1] but, on the other hand, the similar scattering pattern is explained as the result of the effect by vortex core structure by Keimer *et al.*[2]

Recently, "twin-free" YBCO prepared by cooling under the uniaxial pressure has been used in some experiments. As to M-H hysteresis loop in magnetization measurements, it is reported that the magnetic hysteresis disappears at low field and "reentrant" peak effect appears at relatively high field by Nishizaki *et al.* and Okayasu *et al.*

In this experiment, we try to obtain more intrinsic information of the vortex structure free from twin in this "twin-free" YBCO and discuss the contribution of the twin structure to the pinning characteristic by comparison with conventional twinned YBCO. The sample used in this experiment is about 0.5*0.5*0.1 mm^3 (70μg). SANS measurement is performed with SANS-J apparatus at JRR-3M reactor in JAERI-Tokai. Neutron wavelength is selected in 1.0nm and $\Delta\lambda/\lambda$=24.4%. Sample-to-detector is 10m.

In general, due to weak contrast of magnetic induction in mixed state scattering intensity is very weak in high-Tc superconductors. To extract the signal from scattering data, background scattering is measured at zero field and subtracted from raw data. But we failed to find the effective data in it.

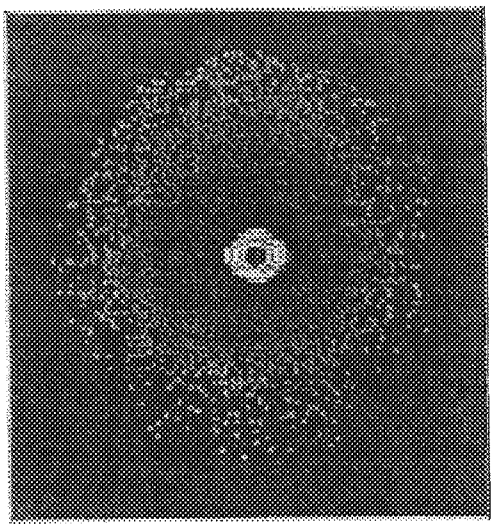

Fig.1 Scattering pattern from twin-free YBCO at 5K and 656G.

References

1) Forgan et al., Physica C, 185-189(1991), 247-252.
2) Keimer et al., Phys. Rev. Lett., 73(1994), 3459-3462.

原子炉：JRR-3M　　装置：SANS-J(C3-2)　　分野：中性子散乱（超伝導）

研究テーマ：強相関電子系の中性子散乱による研究
表題：$La_{2-x}Sr_xCuO_4$における中性子小角散乱強度の温度依存性と緩和現象

Temperature Dependence and Relaxation Phenomenon of Small Angle Neutron Scattering Intensity on $La_{2-x}Sr_xCuO_4$

K.Osamura, S.Miyata, J.Suzuki[1], T.Sasagawa[2] and K.Kishio[2]

Department of Materials Science and Engineering, Kyoto University, Kyoto 606-8501, Japan
[1]Advanced Science Research Center, Japan Atomic Energy Research Institute, Ibaraki 319-1195, Japan
[2]Department of Superconductivity Engineering, University of Tokyo, Tokyo 113-8656, Japan

On observations of vortex lattices in high-T_c superconductors by the neutron scattering, only a little signal can be detected due to the weak contrast of magnetic induction in the sample. It is, therefore, very important to subtract the background scattering produced by inhomogeneities in the sample from row data. Though it has been considered that the scattering from inhomogeneities is almost temperature independent by now, it turned out to be strongly dependent on the history of temperature in $La_{2-x}Sr_xCuO_4$ (LSCO). In order to investigate the behavior of scattering intensities to the temperature history, we performed small angle neutron scattering (SANS) measurements with $La_{2-x}Sr_xCuO_4$ sample.

The sample is synthesized by traveling solvent floating zone (TSFZ) method and the content of Sr is x=0.20 ($La_{1.8}Sr_{0.2}CuO_4$, T_c=30K). SANS measurements were performed with SANS-J apparatus at JRR-3M reactor in JAERI-Tokai. The total scattering intensity in no field is shown in Fig.1 in a function of temperature. It apparently increases at around 30K and shows irreversible behavior in cooling and warming process. Keeping the temperature at a constant lower than around 30K, the relaxation phenomenon that total intensity increases as time was observed. This phenomenon was enhanced by the applied field and didn't saturate in about ten hours. It should be noticed that this relaxation phenomenon was observed in no applied field. Even though in the field, it wasn't changed. So this case of relaxation is different from typical flux creep relaxations seen as the response to the change of the applied field.

About the origin of additional scattering, it is considered as follows. [1] magnetic induction, [2] atomic spin interaction, [3] nuclear interaction to be the potential for the neutron. For [1], though applied field is indeed zero, some gauss of residual field is detected around the sample. As the observation of Bitter pattern is reported in Bi2212[1)] and Y123[2)] at 8 [G] and 5.5 [G] respectively. So it is though to be possible in also LSCO. But the radial distribution function (I(q)-q profile) is not consistent with existence of vortices, because there is no signal of spatial correlation (even short range correlation) in it. For [2], antiferromagnetic ordering of Cu spins are, in general, thought to be broken in the over-doped region. For [3], tetra-ortho phase transition point is comparable to this anomalous point (30K). In fact, such a phenomena of increasing of intensity and relaxation were not observed in the under-doped sample (x=0.136), which tetra-ortho transition point is quite high temperature far above 30K.

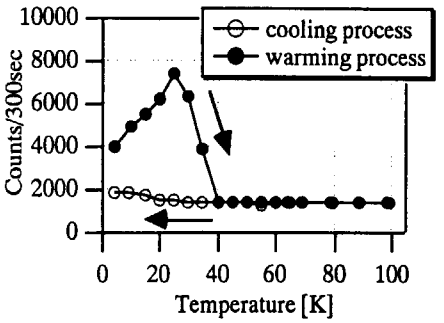

Fig.1 Temperature dependence of total counts of neutrons scattered from LSCO(x=0.20) sample in no field. It icreases apparently at low temperature (under around 30K).

References

1) D.J.Bishop *et al.*, Science, 255(1992), 165-172.
2) K.Sasaki *et al.*, Jpn J. Appl. Phys., 32(1993), L990-L993.

原子炉：JRR-3M　　装置：SAS-J(C3-2)　　分野：中性子散乱（超伝導）

研究テーマ：強相関電子系の中性子散乱による研究
表題：(Nd,Ce)2CuO4+d の小角散乱実験

Small-Angle Neutron Scattering Study of Vortices in a Strongly Anisotropic $(Nd,Ce)_2CuO_{4+\delta}$ Superconductor

J.Suzuki[1], S.Miyata[2], and K.Hirata[3]

[1]Advanced Science Research Center, Japan Atomic Energy Research Institute, Tokai, Ibaraki 319-1195
[2]Department of Materials Science and Engineering, Kyoto University, Kyoto 606-01
[3]National Research Institute for Metals, Tsukuba, Ibaraki 305-0047

The $(Nd,Ce)_2CuO_{4+\delta}$ known as a electron-doped superconductor[1] shows strong superconducting anisotropy. We carried out the small-angle neutron scattering (SANS) experiments on this material in order to observe the Josephson vortices[2-3], which is expected to be seen in strongly anisotropic layered superconductors. The evidence of the Josephson vortices was not obtained in this study, but flux creep phenomenon and irreversible behavior were observed at low temperatures.

The single crystal of $Nd_{1.85}Ce_{0.15}CuO_4$ has a volume of 1.126×1.006×2.282 mm^3 and a mass of 18.1 mg. The mosaic spread obtained from the (200) and (006) reflections is less than 0.17°. The SANS experiments were performed using a SANS-J instrument at the JRR-3M reactor in JAERI. The neutron wavelength was 1 nm. A magnetic field was applied along the crystalline a-axis, nearly parallel to the beam direction.

The q dependence of the SANS from the sample follows a power law of $I(q) \propto q^{-3}$ at low temperatures. Figure 1 shows the temperature dependence of the intensity integrated over the whole q range. Its temperature variation shows thermal hysteresis. When the sample was cooled under the field of 5 Gauss (remanent field at the sample position), the integrated intensity gradually increases. On the contrary, during the heating process, the intensity reveals maximum around 25K. This irreversible feature indicates that a flux motion like a flux creep becomes quite slow at low temperatures. Figure 2 shows the time development of the integrated intensities at 3.5 and 20 K. The increase of the intensity obeys a power law $At^{\alpha}+B$ (α=0.82 at 3.5K, and 0.77 at 20K). This formula does not include a time constant, but the SANS result shows that the relaxation time to reach a equilibrium vortex state becomes longer at the lower temperature. These results are similar to the SANS results for $(La,Sr)_2CuO_{4+\delta}$, and $NdBa_2Cu_3O_y$[4]. A study to clarify this relaxation mechanism observed in some oxide high-T_c superconductors is in progress.

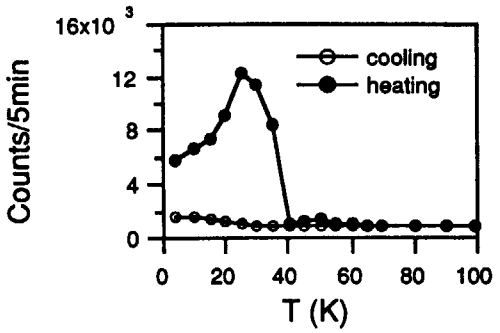

Fig. 1 Temperature dependence of the total scattering counts. Below 40K, the irreversible behavior is observed.

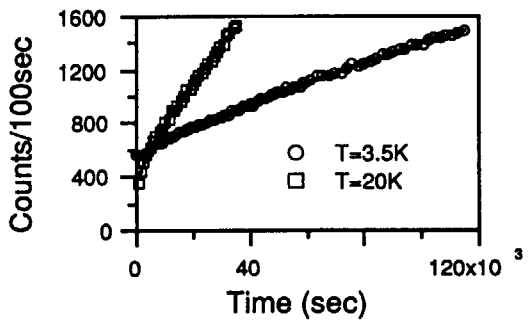

Fig. 2 Time development of the total counts at low temperature. The relaxation follows power laws.

References

[1] Y.Tokura et al., Phys. Rev. Lett. **62** (1989) 1197.
[2] L.N.Bulaevski, Sov. Phys. JETP **37** (1973) 1133.
[3] L.N.Bulaevski, and J.R.Clem, Phys. Rev. B **44** (1991) 10234.
[4] S.Miyata, K.Osamura, J.Suzuki, K.Kuroda, and N.Koshizuka, JAERI Review **97-012** (1997) 45.

原子炉：JRR-3M　装置：SANSJ(C3-2)　分野：中性子散乱(超伝導)

研究テーマ：強相関電子系の中性子散乱による研究
表題：双晶YBa2Cu3O7の小角散乱実験

Small-Angle Neutron Scattering Study of Twinned $YBa_2Cu_3O_y$

M.Watahiki[1,2], J.Suzuki[1], S.Miyata[3], and M.Murakami[4]

[1]Advanced Science Research Center, Japan Atomic Energy Research Institute, Tokai, Ibaraki 319-1195
[2]Japan Science and Technology Corporation, Kawaguchi, Saitama 332-0012
[3]Department of Materials Science and Engineering, Kyoto University, Kyoto 606-01
[4]Superconductivity Research Laboratory, International Superconductivity Technology Center, Koto-ku, Tokyo 105-0023

In conventional type-II superconductors, when an applied field is above the lower critical field (H_{c1}) but below the upper critical field (H_{c2}), flux lines penetrate into the superconductor as quantum flux lines. It is well known that the flux lines in the type-II superconductors form a hexagonal or tetragonal lattice. The small-angle neutron scattering (SANS) technique has been used directly to observe the structure of flux line lattices (FLL) in traditional superconductors[1]. It is not easy to detect the scattering signal from the FLL of high-T_c superconductors due to the large value of a penetration depth. However, extensive researches have been performed in order to investigate the novel properties and phases of the vortex systems of various high-T_c superconductors[2-5]. Forgan et al. have observed the tetragonal lattice in twinned $YBa_2Cu_3O_y$ (Y-123) crystals in an applied field parallel to the crystalline c-axis. When the sample was rotated away from the c-axis, the FLL changed into a hexagonal lattice[3]. The superconducting properties of Y-123 strongly depend on the oxygen content, which affects the anisotropy and doping level. The doping level can be controlled by changing the annealing temperature. The anisotropy parameter estimated from magnetic measurements increases with decreasing the oxygen content. Therefore, it is interesting to study how the anisotropy of Y-123 affects the structure of the FLL. We performed SANS measurements at 4.2K in order to investigate the FLL structures in Y-123 single crystals.

Single crystals of Y-123 used in the present study were grown by the flux method and were post annealed at 430°C for ten days. SANS measurements were performed at SANS-J of the JRR-3M reactor in JAERI using cold neutrons with a wavelength of 1 nm. A magnetic field was applied along the c-axis direction, nearly parallel to the neutron beam. Scattering patterns were observed after cooling through T_c in the applied field (H_{FC}).

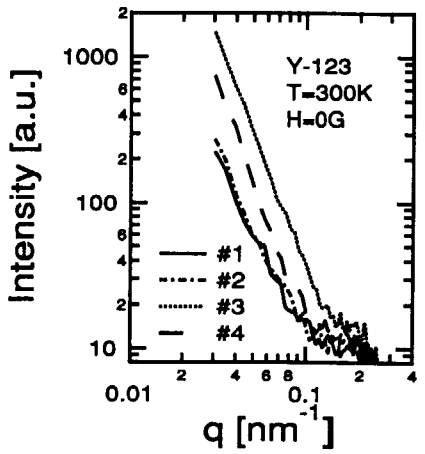

Fig.1 The averaged intensities in a radial direction in Y-123 at T=300 K and zero field. The signal indicates only the scattering from the sample itself without vortices.

Firstly, we have to select the best sample with the lowest background scattering at above T_c. The measurements were performed for four samples grown by different heating cycles. Figure 1 shows the averaged intensities in a radial direction at room temperature and zero field. These signals reveal the scattering from the crystal imperfection of the samples such as twin boundaries, compositional fluctuation, defects, and so on. We then adopt one sample giving the lowest background scattering for low temperature experiments. Figure 2 shows a typical scattering pattern at T=4.2 K and H_{FC}=656 Gauss. If the FLL is well ordered, the diffraction from the FLL should give either the 4-fold or 6-fold symmetric Bragg spots (they are usually distorted)[3]. However, we could not

原子炉：JRR-3M　装置：SANS-J(C3-2)　分野：中性子散乱(超伝導)

研究テーマ：強相関電子系の中性子散乱による研究
表題：双晶YBa2Cu3O7の小角散乱実験

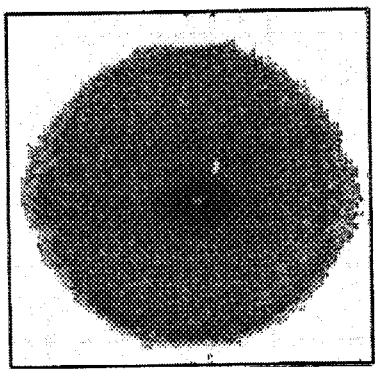

Fig.2 The scattering pattern from Y-123 at T=4.2 K and H_{FC}=656 Gauss. The Bragg spots from a FLL are not observed.

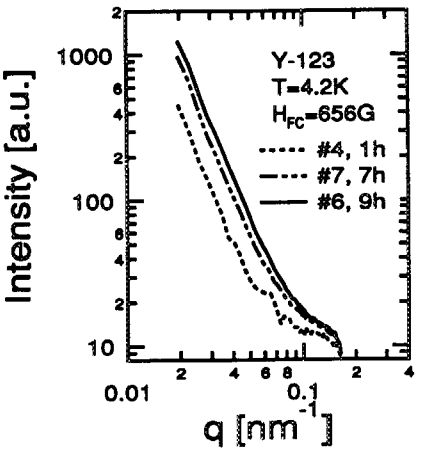

Fig.3 The averaged intensities in a radial direction in Y-123 at T=4.2 K and H_{FC}=656 Gauss. The intensity increases with increasing the time after cooling process.

observe any Bragg spots from the FLL, although the time dependence of the intensity was detected. The imperfection of the sample is thought to make the FLL a less ordered structure and relax the vortex system to a state with a lower free energy. Figure 3 shows the averaged intensities in a radial direction under various measuring times. Increasing the time after cooling the sample, the scattering intensity gradually increases. This time dependence is similar to the results obtained by Miyata et al.[6] for $NdBa_2Cu_3O_y$ and $(La,Sr)_2CuO_{4+\delta}$, and by Suzuki et al. for $(Nd,Ce)_2CuO_{4+\delta}$[7], which also give no Bragg scattering from the FLL. The origin of the time dependence is not clear, but it seems quite important for the observation of the FLL to reduce the sample imperfection resulting in the relaxation effect on the scattering intensity.

References

[1] J.Schelten, G.Lippmann and H.Ullmaier, J. Low Temp. Phys. **14** (1974) 213-226.
[2] E.M.Forgan, D.Paul, H.A.Mook, P.A. Timmins, H.Keller, S.Sutton and J.S.Abell, Nature **343** (1990) 735-737.
[3] E.M.Forgan, D.Paul, H.A.Mook, S.L.Lee, R.Cubitt, J.S.Abell, F.Gencer and P.A.Timmins, Pysica C **185-189** (1991) 247-251.
[4] R.Cubitt, E.M.Forgan, G.Yang et al, Nature **365** (1993) 407-411.
[5] M.Yethiraj, H.A.Mook, G.D.Wignall, R. Cubitt, E.M.Forgan, D.M.Paul and T.Armstrong, Phys. Rev. Lett. **70** (1993) 857-860.
[6] S.Miyata, K.Osamura, J.Suzuki, K.Kuroda and N.Koshizuka, JAERI Review **97-012** (1997) 45-45.
[7] J.Suzuki, S.Miyata and K.Hirata, in this report.

原子炉：JRR-3M　装置：SANS-J(C3-2)　分野：中性子散乱(超伝導)

研究テーマ：強相関電子系の中性子散乱による研究
表題：中性子回折によるLaBa2(Fe1-xCux)3Oyの研究

Neutron Diffraction Study on $LaBa_2(Fe_{1-x}Cu_x)_3O_y$

T. Ishigaki, K. Kitaguchi, T. Futase and Y. Tsuchiya[1]

Department of Materials Science and Engineering, Muroran Institute of Technology, Muroran, Hokkaido, 050-8585, Japan
[1]Japan Atomic Energy Research Institute, Tokai, Ibaragi, Japan

Since the discovery of the superconductor $YBa_2Cu_3O_{7-y}$, intensive works in substitution effect of transition metals for Cu site in order to make clear the mechanism have been made. In Fe substitute system $YBa_2(Cu_{1-x}Fe_x)_3O_{7+y}$, the substitution limit of iron for copper is less than 0.33. It is well known that Fe atoms occupy the Cu(1) site (chain site) by Neutron diffraction[1]. On the other hand, ^{57}Fe Mössbauer spectroscopy suggested that Fe occupy both the Cu(1) and Cu(2) site[2]. There are different results for the occupation site of Fe.

Hung *et al.* succeeded in synthesis $YBa_2Fe_3O_8$[3]. Its crystal structure was similar to tetragonal $YBa_2Cu_3O_{7-y}$ with full occupation in basal oxygen. Our group also has been succeeded synthesis La substituted $LaBa_2Fe_3O_y$. In this experiment, we have investigated the crystal structure of $LaBa_2(Fe_{1-x}Cu_x)_3O_y$ especially the substituted site of Cu atom in place of determine the Fe substituted site in $YBa_2(Cu_{1-x}Fe_x)_3O_{7+y}$, .

Samples x=0.0 , 0.05 and 0.10 were prepared by the conventional solid state reactions. The oxygen contents determined by Iodometry. Neutron diffraction measurements were performed at Room Temperature and about 10 K using High resolution Powder Diffractometer HRPD at JRR-3M of JAERI. The profile analyses were done using the Rietveld Program RIETAN[4]. Initial structural model were based on $YBa_2Fe_3O_8$ reported by Hung *et al.* The results of idometry suggested the existence of excess oxygen, we add O(4) site on La plane (0, 0, 1/2). Diffraction patterns shows that the samples were consisted with two phase which have different oxygen contents, data were analysed using the feature of multi-phase refinement in RIETAN.

We allocated Cu atoms to both Fe sites at first. In course of refinements, occupation factors showed that Cu atoms preferentially occupied Fe(2) (FeO_5 pyramid) site.

Fe^{3+} ion in pyramid site was easily replaced by Cu, which shows the octahedral oxygen arrangement for Fe^{3+} is more stable than pyramid stie. It seem to be consistent with Fe atom preferentially occupy Cu(1) site in Fe doped YBCO system which is able to be eight coordination according to incorporate excess oxygen.

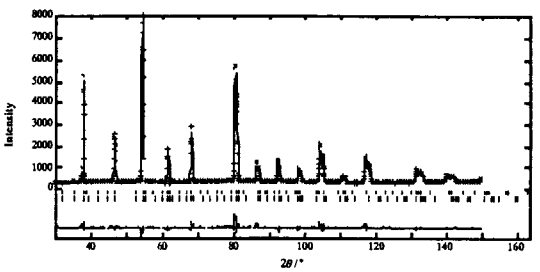

Fig. 1 Neutron diffraction Pattern of $LaBa_2(Fe_{1-x}Cu_x)_3O_y$ (x=0.1) at RT

References

1) T. Kajitani et al., Jpn. J. Appl. Phys. (1988) L354
2) T. Tamaki et al., Solid State Comm., 65 (1988 43.
3) Q. Hung et al., Phys. Rev. B 45 (1992) 9611-9619.
4) F. Izumi, in; The Rietveld Method, ed. R. A. Young (Oxford University press), Oxford, 1933 chap 13.

原子炉：JRR-3M　　装置：HRPD(1G)　　分野：超伝導

研究テーマ：ウラン化合物における超伝導の研究
表題：URu_2Si_2における微少磁気モーメントの異常な温度依存性

Unusual Temperature Dependence of the Tiny Moment in URu_2Si_2

T. Honma[1], Y. Haga[1], E. Yamamoto[1], N. Metoki[1], Y. Koike[1], H. Ohkuni[2] and Y. Ōnuki[1,2]

[1]Advanced Science Research Center, Japan Atomic Energy Research Institute, Tokai, Naka, Ibaraki 319-1195, Japan
[2]Graduate School of Science, Osaka University, Toyonaka 560-0043, Japan

URu_2Si_2 is a fascinating compound in which superconductivity coexists with antiferromagnetic ordering. Previous neutron scattering experiments revealed that a weak antiferromagnetic state with 0.02-0.04 μ_B/U develops below 17.5 K[1,2]. To shed more light on the interplay between magnetism and superconductivity, we have done neutron scattering experiments in the temperature range of 100 mK to 5 K. In this paper, we show an unusual temperature dependence of the antiferromagnetic Bragg peak intensity.

Single crystals were grown by the Czochralski pulling method in a tetra-arc furnace under the pure argon gas atmosphere. The typical size of the ingots was 3-4 mm in diameter and 40 mm in length. The samples were annealed at 1000°C for one week, which were wrapped in Ta and Zr foils and sealed in a quartz tube under vacuum of 1×10^{-7} torr.

The resistivities show a sharp peak at 17.5 K, which is reminiscent of a spin density wave antiferromagnet Cr. We observed an onset superconducting transition at 2.5 K and resistivity zero at 1.4 K. The residual resistivity ratio (RRR = ρ_{RT}/ρ_0) was 41.8.

Neutron scattering experiments were carried out by using a cold neutron triple-axis spectrometer LTAS installed in the research reactor JRR-3M at Japan Atomic Energy Research Institute. The neutron beam was monochromatized by a PG monochromator. The fixed incident neutron energy of 4.768 meV was used with a Be filter cooled down to 10 K.

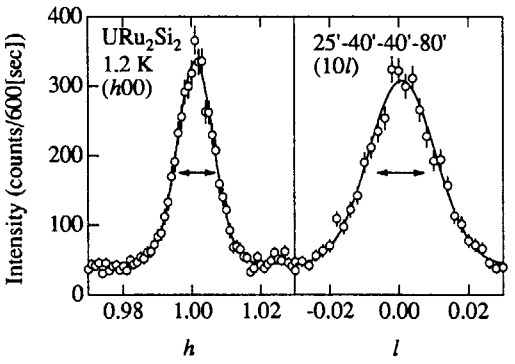

Fig.1 Profiles of the (1 0 0) magnetic Bragg peaks along the longitudinal and transverse directions at 1.2 K in URu_2Si_2. The solid lines are the results of least-square fit by the Gaussian function.

Figure 1 indicates the scattering profiles of the (1 0 0) magnetic Bragg peak along the longitudinal and transverse directions at 1.2 K. The profiles are described by a Gaussian line shape with a constant background. The linewidth is broader than the resolution in both directions indicated by arrows in Fig. 1. The spin correlation lengths are ξ_a=640±50Å and ξ_c=500±30Å, respectively, which are consistent

原子炉：JRR-3M　　装置：LTAS(C2-1)　　分野：中性子散乱（超伝導）

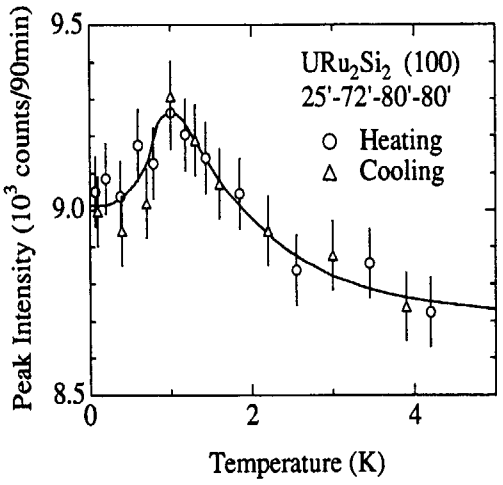

Fig. 2 Temperature dependence of the (1 0 0) magnetic Bragg peak intensity in URu_2Si_2. A solid line connecting the data is a guideline.

with previous studies within experimental errors[2,3]. We determined the magnitude of the ordered moment as $\mu_{ord} \sim 0.02\ \mu_B/U$ at 1.2 K, by comparing the integrated intensity with the one of the (1 0 1) nuclear Bragg peak. It is also in good agreement with previous results[2].

Figure 2 shows the temperature dependence of the peak intensity I(1 0 0). The intensity increases with decreasing the temperature. However, it shows a peak around 1 K which corresponds to the superconducting transition temperature T_c. Below 1 K, the intensity decreases rather steeply. The magnitude of the intensity reduction is about 2% of the maximum. From the magnetic structure of URu_2Si_2, it is clear that this anomaly cannot be explained by redistribution of the magnetic domains. It is thus concluded that the magnetic order parameter is coupled to the superconducting one. Similar results have been reported in other heavy fermion superconductors; UPt_3 (reduction rate of 5-10%, an ordered moment of 0.02 μ_B/U), UNi_2Al_3 (3%, 0.2 μ_B/U) and UPd_2Al_3 (1%, 0.85 μ_B/U)[4-6]. The coupling of the order parameters would be a characteristic feature in this system.

In conclution, we measured the temperature dependence of the (1 0 0) mangetic Bragg peak intensity in the temperature range of 100 mK to 5 K. We observed a steep decrease of the peak intensity below about T_c. This result indicates the interplay between magnetism and superconductivity in URu_2Si_2.

References

1) T. E. Mason et al., Phys. Rev. Lett. **65** (1990) 3189.

2) B. Fåk et al., J. Magn. Magn. Mater. **154** (1996) 339.

3) C. Broholm et al., Phys. Rev. B **43** (1991) 12809.

4) G. Aeppli et al., Phys. Rev. Lett. **63** (1989) 676.

5) N. Metoki et al., J. Phys. Soc. Jpn. **66** (1997) 2560.

6) N. Metoki et al., Phys. Rev. Lett. **80** (1998) 5417.

研究テーマ：ウラン化合物における超伝導の研究
表題　　：重い電子系超伝導体UBe_{13}における磁気秩序の欠如

Absence of magnetic ordering in a heavy fermion superconductor UBe_{13}

Y. Haga[1], Y. Koike[1], N. Metoki[1], E. Yamamoto[1], T. Honma[1] and Y. Ōnuki[1,2]

Japan Atomic Energy Research Institute, Tokai, Ibaraki 319-1195, Japan
Graduate School of Science, Osaka university, Toyonaka, Osaka 560-0043, Japan

In the heavy fermion superconductors such as UPt_3, URu_2Si_2 and UPd_2Al_3, antiferromagnetic (AF) ordering coexists with superconductivity. Magnetic interaction between 5*f* electrons plays a crucial role to form anisotropic superconducting state such as *d*- or *p*- wave pairing.

UBe_{13} with cubic structure is a candidate of a *p*-wave superconductor[1]. However, there is no evidence for magnetic ordering in UBe_{13} down to 25 mK in spite of a large paramagnetic Curie temperature θ_p of -100 K determined from magnetic susceptibility[2]. Specific heat is, however, reported to deviate from a power law behavior below 50 mK[2]. In order to clarify the origin of this anomaly, we performed a neutron scattering experiments on UBe_{13} in very low temperatures.

Polycrystalline sample of UBe_{13} was synthesized by arc-melting U and Be in an argon gas atmosphere. The sample were cooled by a ^{3}He-^{4}He dilution refrigerator down to 20 mK.

Neutron scattering experiments were performed using a cold neutron triple-axis spectrometer LTAS in JAERI with E_i = 4.674 meV.

Figure 1 shows elastic scattering profiles from UBe_{13} taken at 0.02 K and 0.77 K as well as the difference between them. Sharp nuclear Bragg peaks (200) and (222) are observed at both temperatures. Additional Bragg peaks such as (100), (110) or (111) indicated by arrows were not observed within an experimental error.

In order to examine a ferromagnetic ordering, we measured a temperature dependence of the (200) nuclear Bragg peak intensity, as shown in Fig. 2. The peak intensity increases gradually with decreasing temperature. However, there is no clear magnetic transition around 0.02 K. It is also noted that the intensity does not change upon superconducting transition at 0.8 K.

Lower limit of the detectable ordered moment size in the present experimental condition is estimated to be 0.3 μ_B/U for a simple antiferromagnetic ordering with $\boldsymbol{k}$ = (001). Since the experimental accuracy is not optimum, magnetic ordering with extremely small magnetic moment would not be detected. However, the anomaly in the specific heat below 50 mK is presumably attributed to nuclear quadrupole splitting of Be and additional magnetic contribution is extremely small[3]. Therefore, we conclude that magnetic ordering is absent in UBe_{13} down to 20 mK.

References

1) D.Einzel et al.: Phys. Rev. Lett. **56** (1986) 2513.
2) E.A. Schuberth: Int. J. Mod. Phys. B **10** (1996) 357.
3) W.G. Clark, et al.: J. Mag. Mag. Mat. **63-64** (1987) 396.

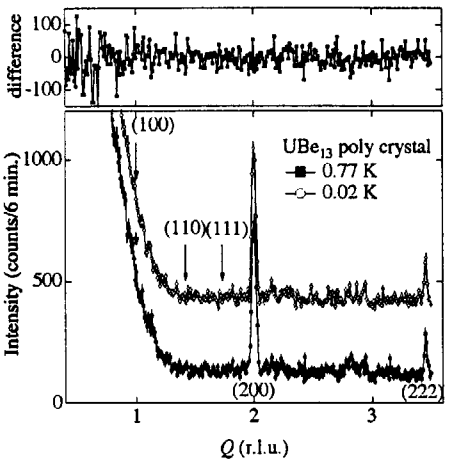

Fig. 1 Neutron diffraction profile for polycrystalline UBe_{13} taken at 0.77 K and 0.02 K (lower panel). Upper panel shows the difference between them.

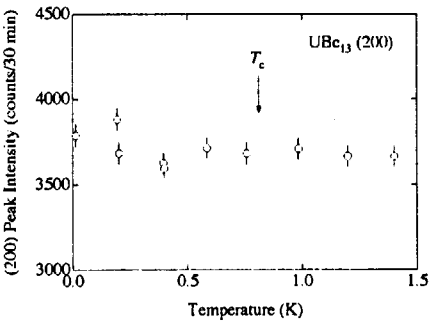

Fig. 2 Temperature dependence of (200) Bragg peak intensity for UBe_{13}.

原子炉：JRR-3M　　装置：LTAS (C2-1)　　分野：中性子散乱（超伝導）

研究テーマ：量子凝縮相の研究
表　　題：重い電子系超伝導体UPd_2Al_3における異方的超伝導ギャップ

Anisotropic Superconducting Gap in a Heavy Fermion Superconductor UPd_2Al_3

N. Metoki[A], Y. Koike[A], Y. Haga[A], and Y. Ōnuki[A, B]

[A]*Advanced Science Research Center, JAERI, Tokai, Ibaraki 319-1195*
[B]*Graduate School of Science Department of Physics, Osaka University, Toyonaka, Osaka 560*

Anisotropic superconductivity in heavy fermion superconductor is one of the most exciting topics in the field of condensed matter physics. Recent intensive neutron scattering study on a heavy fermion superconductor UPd_2Al_3 revealed that the superconducting gap appears in the spin excitation spectra, indicating that the superconductivity is magnetic origin [1,2]. Since the *d*-wave pairing is reported by NMR studies [3,4], it is of particular interest to reveal the anisotropy of the superconducting gap. In this paper we report the result of the low energy spin excitation measured by neutron scattering.

Neutron scattering experiments were carried out using a cold neutron triple-axis spectrometer LTAS at the Japan Atomic Energy Research Institute (JAERI). The signal is integrated in a certain q-range using curved analyzer crystal. The single crystal sample, which is the same as measured before, is cooled in a liquid-helium-free ^{3}He-^{4}He dilution refrigerator down to 100 mK.

Figure 1 shows the result of the constant-E scan with the energy transfer ΔE = 0.6 meV at 0.1 K (a) and 2.1 K (b), below and above the superconducting transition temperature T_c = 1.9 K, respectively. Below T_c we found a clear peak around the (0.5 0 0.5) reciprocal lattice point. The intensity at low Q region is the background. The constant-Q profile with Q = (0.5 0 0.5) (Fig. 2) shows a weak but clear inelastic peak at ΔE = 0.7 meV. The spin excitation gap of about 0.7 meV ≈ 4 $k_B T_c$ is in the same order of the superconducting energy gap. This energy gap is a little larger than the one at (0 0 0.5), where we observed the gap of 0.36 meV ≈ 2.2 $k_B T_c$. This difference would be due to the anisotropy of the superconducting gap.

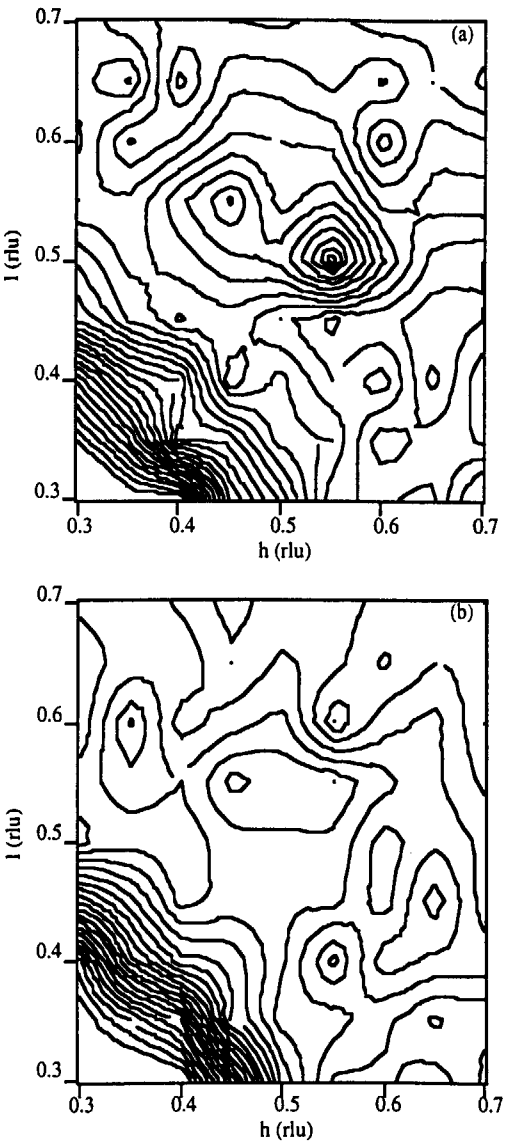

Fig. 1. The contour map of the constant-E profile of UPd_2Al_3 with ΔE = 0.6 meV at 0.1 K (a) and 2.1 K (b), respectively.

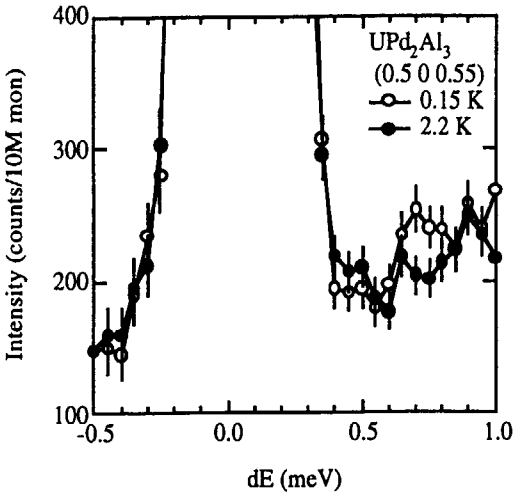

Fig. 2. The neutron inelastic scattering profile of UPd_2Al_3 at (0.5 0 0.5).

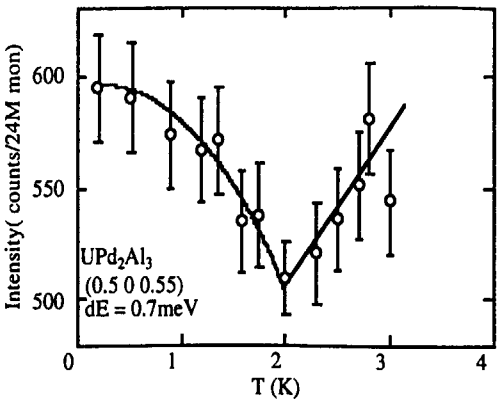

Fig. 3. The temperature dependence of the scattering intensity at (0.5 0 0.5) with ΔE = 0.7 meV. The solid line is guide for the eyes.

Figure 3 is the temperature dependence of the scattering intensity of this peak. Above T_c the intensity decreases with decreasing temperature. Below T_c, the intensity increases like superconducting order parameter. This temperature dependence is very similar to the one of the inelastic scattering peak observed at (0 0 0.5). See figure 3(b) in Ref. 1.

It is often observed that antiferromagnetic correlation with several independent modes coexists in heavy fermion systems like $CeRu_2Si_2$ [5]. Heavy fermion superconductor UPt_3 exhibits (1/2 0 1) antiferromagnetic peak below 5 K, while the (001) out-of-plane antiferromagnetic correlation coexists with a typical energy scale of 10 meV [6]. In addition to the antiferromagnetic ordering in URu_2Si_2, short range correlation around (1, 0.4 0) was reported [6]. It should be noted that in case of UPd_2Al_3 the (0 0 0.5) and (0.5 0 0.5) antiferromagnetic correlation strongly couple to the superconductivity, which makes this compound unique. The next step is to reveal the structure of the anisotropic superconducting gap.

We would like to thank M. Tachiki, M. Kohgi, and S. Koh for stimulating discussions.

References

[1] N. Metoki et al., J. Phys. Soc. Jpn. **66** (1997) 2560.
[2] N. Metoki et al., Phys. Rev. Lett. **80** (1998) 5417.
[3] M. Kyogaku et al., J. Phys. Soc. Jpn. **61** (1992) 2660.
[4] H. Tou et al., J. Phys. Soc. Jpn. **64** (1995) 725.
[5] L.P. Regnault et al., Phys. Rev. B**38** (1988) 4481.
[6] A.I. Goldman et al., Phys. Rev. B**36** (1987) 8523.
[7] G. Aeppli et al., Phys. Rev. Lett. **63** (1989) 676.
[8] W.J.L. Buyers et al., Physica **B199-200**, 95.

研究テーマ：YBCO B_{2u}モード(24meV)異常と磁気励起との関係

表題：B_{2u}フォノン測定による擬ギャップ形成研究

Pseudo Gap Formation Studied by B_{2u} Phonon Measurements

H. Harashina,[1,2] H. Sasaki,[1] K. Kodama,[1,2] M. Sato,[1,2] S. Shamoto,[3] K. Kakurai [2,4] and M. Nishi [4]

[1]*Department of Physics, Division of Material Science, Nagoya University, Furo-cho, Chikusa-ku, Nagoya 464-8602*
[2]*CREST, Japan Science and Technology Corporation (JST)*
[3]*Department of Applied Physics , Faculty of Engineering, Tohoku University, Aoba, Aramaki, Sendai 980-8577*
[4]*Neutron Scattering Laboratory, Institute for Solid State Physics, The University of Tokyo, Shirakata 106-1 Tokai, Ibaraki 319-1195*

In $YBa_2Cu_3O_{6+x}$ with T_c ~ 60K, a gap-like structure seems to appear in the spectral function of the magnetic excitation, $\chi''(q, \omega)$ with decreasing T at around the temperature T_0, below which various physical properties behave anomalously. This pseudo gap formation has been studied by neutron measurements of the magnetic excitations[1,2] and B_{2u} phonons[3,4], in which the O(2) and O(3) atoms within a CuO_2 plane have out-of-phase motions perpendicular to the plane. It has been reported that the pseudo gap behavior is caused by the formation of singlet pairs with the same symmetry as that of Cooper pairs ($d_{x^2-y^2}$-like).[3,4] Here, we report data of the B_{2u} mode ($\hbar\omega$~ 24meV) in $YBa_2Cu_{2.9}Zn_{0.1}O_{6.75}$. Neutron scattering measurements were performed with the ISSP-PONTA(5G) spectrometer in JRR-3M at Tokai.

Figures 1 and 2 show the T-dependence of energies $\hbar\omega$ and profile widths w, respectively, for $YBa_2Cu_{2.9}Zn_{0.1}O_{6.75}$ ($T_c \lesssim$10K) and $YBa_2Cu_3O_{6.7}$ (T_c ~ 62K). The similar T-dependence of $\hbar\omega$ and w of $YBa_2Cu_{2.9}Zn_{0.1}O_{6.75}$ and $YBa_2Cu_3O_{6.7}$ suggests that the pseudo gap formation survives almost intact even after the Zn-doping. In the magnetic excitation spectra $\chi''(\omega)$ measured for the present Zn doped crystal, a gap-like structure can be seen in the low energy region at around 200K, while at low temperatures the low energy excitation spectra increase and the gap-like structure disappears.[2] This behavior is considered to be caused by the electron localization: The loss of the

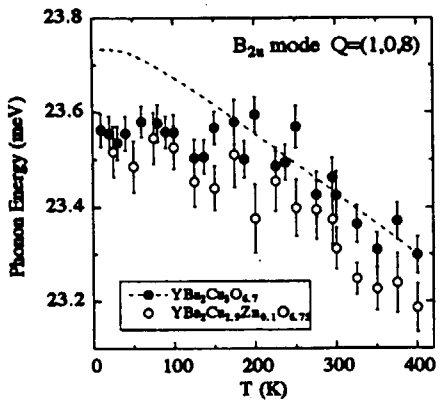

Fig. 1 Energies of the B_{2u} mode are plotted as functions of T taken for $YBa_2Cu_{2.9}Zn_{0.1}O_{6.75}$ and $YBa_2Cu_3O_{6.7}$. The dashed line shows the T-dependence expected from the ordinary anharmonic effect.

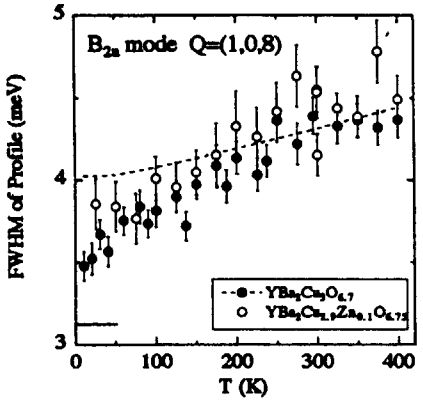

Fig. 2 Full widths at a half maximum of the profiles of the B_{2u} mode plotted against T for $YBa_2Cu_{2.9}Zn_{0.1}O_{6.75}$ and $YBa_2Cu_3O_{6.7}$. The dashed line indicates the extrapolation of the profile width from the high temperature region. The instrumental resolution width is also shown by the horizontal line.

itinerant nature due to the electron localization seems to have a serious effect on the formation of the pseudo gap, and the localized spins at Cu sites tend to approach a Neel ordered state. The difference between the impurity effects on the B_{2u} phonon and the magnetic excitation can be explained by considering that the pseudo gap has the (x^2-y^2)-like symmetry. The B_{2u} phonon is expected to have the strong coupling to the electrons in the k-region where the order parameter Δ with (x^2-y^2)-like symmetry is large. The observed insensitivity of the B_{2u}-phonon anomalies to the Zn-doping indicates that the order parameter in the k-region does not suffer significant effects of the doping. The magnetic excitation around $q=(\pi/a, \pi/a)$ is, on the other hand, severely affected by the doping.

References

1) B. J. Sternlieb, G. Shirane, J. M. Tranquada, M. Sato and S. Shamoto: Phys. Rev. B47 (1993) 5320.
2) H. Harashina, S. Shamoto, T. Kiyokura, M. Sato, K. Kakurai and M. Nishi: J. Phys. Soc. Jpn. 64 (1995) 1462.
3) H. Harashina, K. Kodama, S. Shamoto, M. Sato, K. Kakurai and M. Nishi: J. Phys. Soc. Jpn. 64 (1995) 1462.
4) H. Harashina, K. Kodama, S. Shamoto, M. Sato, K. Kakurai and M. Nishi: Physica C263 (1996) 257.

JRR-3M, PONTA(5G), 3. supercon.

研究テーマ：IMT、日米協力
表　　題：Zn及びNdのドープされたLSCOの中性子散乱研究

Neutron Scattering Study of Zn- and Nd-doped LSCO

J.M. Tranquada[1], N. Ichikawa[2] and K. Kakurai[3]

[1] *Physics Department, Brookhaven National Laboratory, Upton, NY 11973, U.S.A.*
[2]*Superconductivity Research Course, The University of Tokyo, 2-11-16 Yayoi, Tokyo 113, Japan*
[3]*Neutron Scattering Laboratory, ISSP, University of Tokyo, 106-1 Shirakata,Tokai 319-11, Japan*

The interplay between charge and spin correlations turns out to be relevant in many investigations of transition-metal oxides, especially of the copper-oxide high-Tc superconductors. Recent neutron diffraction studies of $La_{1.6-x}Nd_{0.4}Sr_xCuO_4$ with x=0.12 have shown that an elastic magnetic component develops in the so-called low-temperature tetragonal (LTT) phase at the same position as the dynamic magnetic scattering observed in samples without Nd-doping[1]. In this context it is of interest to study the charge and spin correlations in the Zn-doped LSCO in comparison to the Nd-doped LSCO.

Neutron scattering investigations of $La_{1.88}Sr_{0.12}Cu_{0.98}Zn_{0.02}O_4$ (LSCZO) and $La_{1.48}Nd_{0.4}Sr_{0.12}CuO_4$ (LNSCO) samples were performed on PONTA (5G) spectrometer.

LSCZO

The magnetic peaks were measured using E_i=14.7meV, 40'-40'-80'-80' and a PG filter before the monochromator. Scans along Q=(1/2,1/2+ξ,0), in tetragonal notation, at T=1.5K are shown in Fig.1. The average value for the peak splitting is ε=0.121. The temperature dependence of the magnetic signal measured at (0.5,0.625,0) is shown in Fig.2. The signal at the peak position becomes comparable with the background near 20K. Although quite a bit of time was spent to observe charge-order peaks, sofar no signs of them have been detected. The strength of the magnetic scattering in this Zn-doped compound is approximately 5 times smaller than that of the Nd-doped sample studied here.

LNSCO

The magnetic peaks in this crystal showed an average splitting of ε=0.118, consistent with the earlier results. The charge-order peak at (0,2+2ε,0) was also observed, consistent with the previous results. (Ei=14.7meV;open-80'-80'-80') The modulation of the charge-order intensity along *l*, as indicated by the recent X-ray studies[2], was looked at by tilting the sample to vary *l*. Only a weak modulation was observed in integrated intensities. If the spin and charge modulations were 2D rather than locally 1D, the magnetic peaks are expected to appear along (1/2+ξ,1/2+ξ,0) and charge-order peaks at (ε,2+ε,0). Neither of them have been observed in this Nd-doped sample.

Acknowledgements: This study was carried out within the U.S.-Japan Cooperative Program on Neutron Scattering, a Grant-in-Aid for Scientific Research from the Ministry of Education, Science and Culture, Japan.

Reference

[1] J.M. Tranquada et al., Nature 375 (1995) 561.
[2] M.V. Zimmerman et al., Europhys. Lett. 41 (1998) 629.

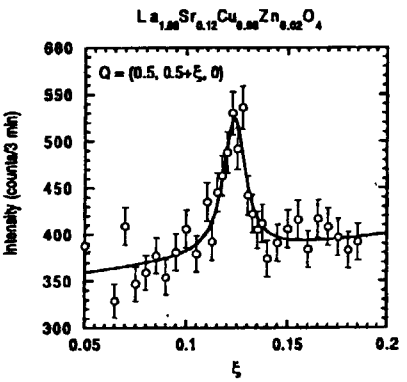

Fig.1: The magnetic peak seen in LSCZO along Q=(1/2,1/2+ξ,0) at T=1.5K.

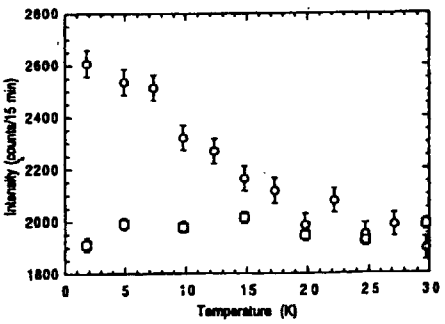

Fig.2: Temperature dependence of the magnetic signal in LSCZO (open points). Square points indicate the background.

Reactor : JRR-3M　　Facility : PONTA (5G)　　Field : Superconductivity

研究テーマ：$La_{2-x}Sr_xCuO_4$のスピン揺動
表題：$La_{2-x}Sr_xCuO_4$(x=0.12, 0.18) のCuO_6八面体の傾きに関係した構造不安定性

Structural Instability Associated with the Tilting of CuO_6 Octahedra in $La_{2-x}Sr_xCuO_4$

H. Kimura, C. -H. Lee, K. Yamada, and G. Shirane[1]

Department of Physics, Tohoku University, Sendai 980-8578, Japan
[1]Department of Physics, Brookhaven National Laboratory, Upton, New York 11973-5000, U. S. A.

It is well known that there exists a strong coupling between the lattice and electronic systems in the superconductivity of high-T_c cuprates with La_2CuO_4-type structure. In this point of view, low energy phonon excitations play important roles in superconductivity. In fact, recently Lee *et al.*[1] studied the anomalous behavior of *Z*-point phonon near the T_c, which associate with the tilting of CuO_6 octahedra, in optimally hole-doped $La_{1.85}Sr_{0.15}CuO_4$. They claimed that the *Z*-point phonon, which goes soft with decreasing temperature, starts saturating below T_c. This experimental facts suggest a strong electron-lattice coupling in this system. In this present study, we extend the similar measurements to x=0.12 and x=0.18 in order to study the overall property of the phonon softening in wide range of Sr (hole) concentration. Furthermore we also tried to examine the diffuse scattering in the high-temperature tetragonal phase.

Neutron scattering experiments were carried out on the triple-axis spectrometer of Tohoku University installed at JRR-3M in JAERI. The initial or final energy of neutron were fixed at 14.1 meV. The (0 0 2) Bragg reflection of Pyrolytic Graphite (PG) were used in order to monochromatize and analyze neutron beam. PG filters were put for initial or final beam to reduce the higher-order contaminations. The reciprocal space is described using reciprocal lattice unit in the *Bmab* coodinates system.

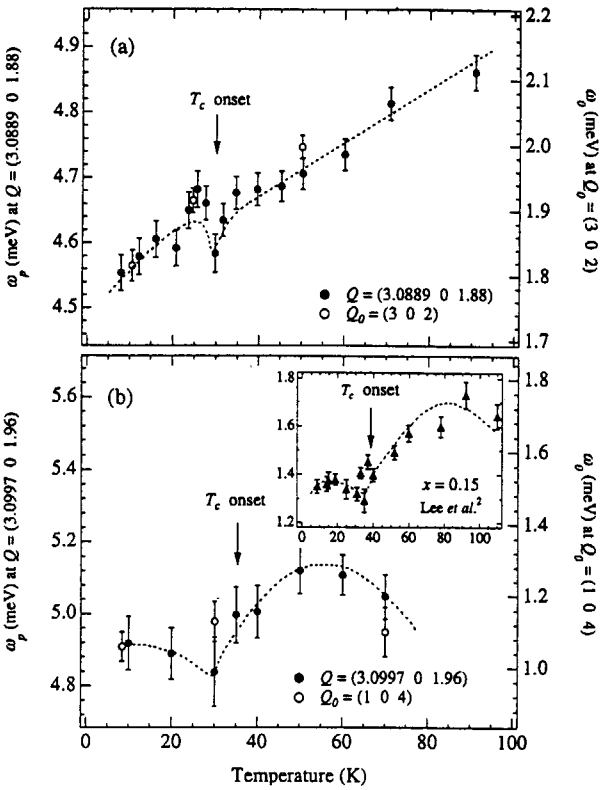

Figure 1

A. Soft phonons through T_c.

The *Z*-point phonon around Q_0=(3 0 2) was studied as a function of temperature. We measured at $Q=Q_0+q$ where the instrumental resolution focuses most effectively on the dispersion of phonon, which can be written as $\omega_p^2(q) = \omega_0^2 + Aq^2$. Therefore we can measure the relative change in the phonon frequency ω_0 at Q_0 more accurately, which is based on the assumption

JRR-3M、TOPAN(6G)、3. 超伝導　supercon.

that A is weakly temperature dependent.

Temperature dependence of the soft phonon frequency on x=0.12 and 0.18 are shown in Fig.1(a) and (b), respectively. It is very remarkable that whereas the softening of phonon start breaking with appearing superconductivity in x=0.18 as Lee *et al.* reported, however in x=0.12, the softening once stops at T_c but starts softening again at lower temperature. As for the line-width of x=0.12, similar temperature dependence to that of x=0.15 was observed.

It is important to investigate whether the absence of the softening phonon *saturation* might be a specific phenomenon for the x~1/8 or commonly occurs for the underdoped samples. As one possibility, we can speculate that the remaining of phonon-softening in the superconducting state is one of the characteristic properties around x=1/8.

B. Lattice Modulation in Tetragonal Phase

The tetragonal-to-orthorhombic structural phase transition occurs with decreasing temperature in this system. At structural transition temperature T_s, (0 k l) (k=*odd*, l=*even*) superlattice reflection starts appearing on cooling. In this section, the results of the temperature dependence above T_s of the superlattice peak at (0 3 2) is described. We newly found that above T_s, the residual week diffuse peak starts splitting into two incommensurate positions (0 3±δ 2) for both x=0.12, 0.18. As shown in Fig.2, the incommensurate diffuse peaks are clearly seen at much higher temperature than T_s for x=0.12. Both the two spectra of x=0.12, 0.18, are fitted with the two Lorentzian quite well. The temperature dependence of the incommensurability δ was also measured for both the samples (Fig.3). As for x=0.18, δ increases with temperature and saturates into δ~0.12 (r. l. u.) which value is very close to the incommensurability δ of the elastic and inelastic

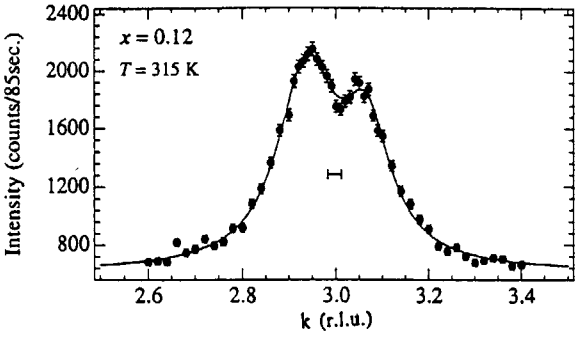

Figure 2

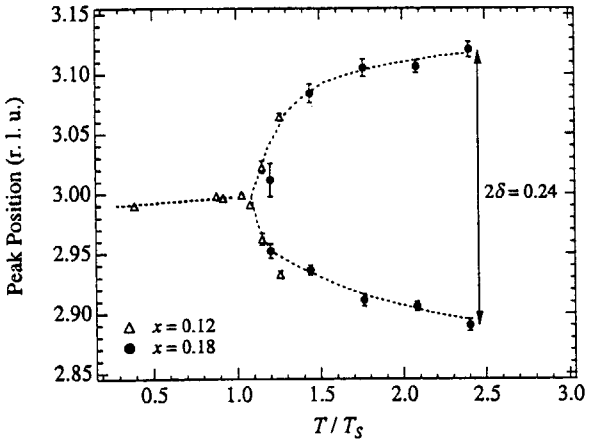

Figure 3

magnetic peaks seen in this system around (π, π). Furthermore, it is remarkable that both δ can be almost scaled by T_s . As for the origin of these incommensurate diffuse peak, there are some possibilities but they are not still confirmed. Further systematic studies for the wide range of Sr concentration are required at this moment. We will proposed the new structural model for HTT phase.

References

1. C. -H. Lee, *et al.* Phisica C **257**, 264 (1996).

研究題目:BEDT-TTF化合物の中性子散乱による研究
表題：BEDT-TTF塩の中性子散乱研究

Neutron Scattering Study on BEDT-TTF Salts

T.Kajitani, S.Shamoto, Y.Ono, M.Yamada, S.Takashima

Department of Applied Physics, Graduate School of Engineering, Tohoku University, Aoba 08, Aobaku, Sendai 980-8579, Japan

Superconducting κ-(BEDT-TTF)$_2$Cu(SCN)$_2$ and metallic α-(BEDT-TTF)$_2$KHg(SCN)$_4$ have been studied by means of the cold neutron inelastic scattering measurement at temperatures below 100K. The generalized phonon density of states , g(ω), were measured for both system. An appreciable decrease of the g(ω) was noticed at temperatures below superconduction critical temperature, T_c= 9.6 K, at the energy range of E $\fallingdotseq$ 2.8 meV which corresponds to the superconduction gap energy, $2\Delta = 3.52\ k_B T_c$ (BCS) = 2.9 meV, of the κ-phase cuprate. This phenom-enon reflects enhanced electron-phonon coupling at E = 2Δ below T_c. Antiferromagnetic transition is proposed for the α-(BEDT-TTF)$_2$KHg(SCN)$_4$ at 8K previously. New inelastic neutron scattering peak was found in the range from 2.1 to 2.45 meV below T_N, possibly an indication of the gap formation there. Figure shows obtained generalized phonon density of states, GPDOS, of κ-(BEDT-TTF)$_2$Cu(SCN)$_2$ at temperatures from 1.5K to 50K. The spectra are calculated from the neutron energy loss side of the data. A broad peak seen in the range of E= -0.5 ～-1.5 meV is by the aluminum heat shield of the cryostat. In the case of κ-(BEDT-TTF)$_2$-Cu(SCN)$_2$, appreciable decrease of GPDOS at E= - 2.8 meV below T_c = 9.6 K is seen. The energy can be compared with the superconduction gap, 2Δ, estimated from the weak coupling theory , namely, $2\Delta = 3.52 k_B T_c$ = 2.9meV. The phonon density of state in the range close to 2Δ becomes lowed by the appreciable phonon-electron coupling below T_c, since the energy of the phonon modes at just above or beneath the 2Δ increase or decrease , respectively. Similar decrease of the GPDOS was found previously at E = -4.8meV of V_3Si below T_c.

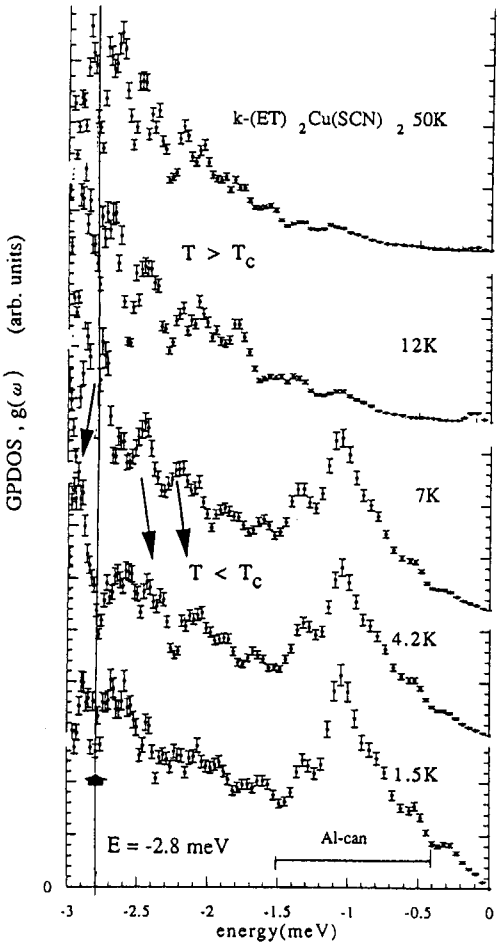

GPDOS of κ-(BEDT-TTF)$_2$Cu(SCN)$_2$.

研究テーマ：超低温の導入による中性子散乱の研究
表題：超低温における UPt_3 の反強磁性秩序の中性子散乱による研究

Neutron scattering study of the antiferomagnetic ordering in UPt_3 at ultralow temperatures

Y. Koike[a], N. Metoki[a], N. Kimura[b], E. Yamamoto[a], Y. Haga[a], Y. Ōnuki[a,c] and K. Maezawa[d]

[a] Advanced Science Research Center, Japan Atomic Energy Research Institute, Tokai, Naka, Ibaraki 319-1195, Japan

[b] Center for Low Temperature Science, Tohoku University, Sendai 980-0845, Japan

[c] Graduate School of Science, Osaka University, Toyonaka 560-0043, Japan

[d] Faculty of Engineering, Toyama Prefectural University, Toyama 939-0398, Japan

It is widely accepted that the magnetic ordering in UPt_3 plays an important role for the unconventional superconducting natures. However the origin of the magnetic correlation with a tiny magnetic moment ($0.02\mu_B$/U) is still an open question. The antiferromagnetic ordering was observed by muon spin resonance[1], neutron [2,3] and magnetic X-ray scattering measurements [4], while no trace of the magnetic transition was reported in specific heat[5], static susceptibility[6], and NMR[7] measurements. It is interpreted that the antiferromagnetic ordering is not true static and long range ordering but dynamical fluctuation. Meanwhile the anomaly observed in the specific heat[8,9] and thermal expansion measurements [10] at about 18 mK is suspected to be a signature of the long range ordering. To shed more light on this subject, the neutron scattering experiments have been carried out in order to study the antiferromagnetic correlation at ultralow temperatures.

Neutron scattering experiments were carried out using a cold neutron triple-axis spectrometer LTAS at the Japan Atomic Energy Research Institute (JAERI). The single crystal sample (3 x 3 x 30 mm^3) was cooled down in a ^{3}He-^{4}He dilution refrigerator below 20 mK. This ultralow temperature was obtained by a very good contact of the sample onto the OFC (oxygen free copper) sample holder attached on the mixing chamber. Details of the set up are described in ref. 11.

Figure 1 shows the temperature dependence of the scattering profile of a (0.5 0 1) antiferromagnetic peak. We observed the clear antiferromagnetic peak down to 20 mK. The peak intensity exhibits no significant change within an experimental accuracy (10%). However we found the remarkable temperature dependence of the linewidth. At 570 mK, for example, the linewidth of this peak 0.022 $Å^{-1}$ and 0.011 $Å^{-1}$ for the longitudinal and transverse directions, respectively, is broader than the resolutions (denoted by arrows in Fig. 1). The spin correlation length is estimated as 290 ± 50 Å and 550 ± 40 Å, respectively, which is in good agreement with the previous reports[2-4]. At 20 mK, however, almost a resolution limited peak was observed in both directions.

Figure 2(a) shows the temperature dependence of the longitudinal linewidth ($W_{//}$) of (0.5 0 1) peak profiles observed with the collimations of 26'-40'-20'-72'. The resolution of this condition is higher than the previous study[11]. The linewidth is steeply decrease below 50 mK and becomes a resolution limited below 20 mK. In Fig. 2(b), we show the temperature dependence of the spin correlation length ($\xi_{//}$). A finite spin correlation length is observed down to 20mK, but below 20 mK, the correlation length increases divergently.

The presence of the antiferromagnetic peak down to 20 mK is quite surprising. It means that the dynamical spin fluctuation exists at ultralow temperatures. The spin correlation length of about 400 Å, which is much longer than the one in the

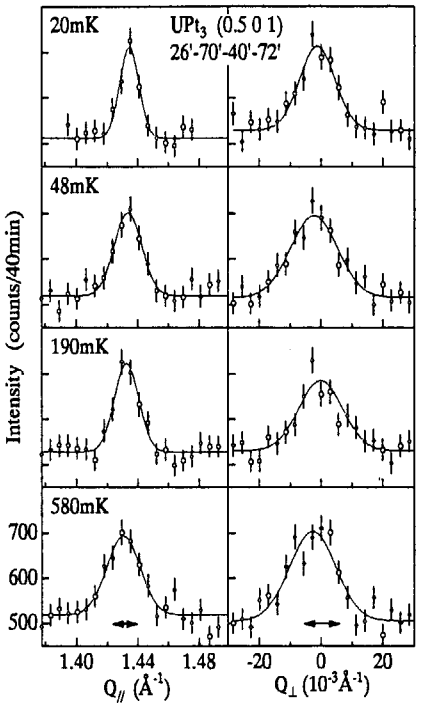

Fig. 1. Temperature dependence of the scattering profile of the (0.5 0 1) peak in the longitudinal ($Q_{//}$) and transverse ($Q_{\perp}$) directions for UPt_3. The arrows indicate the resolution.

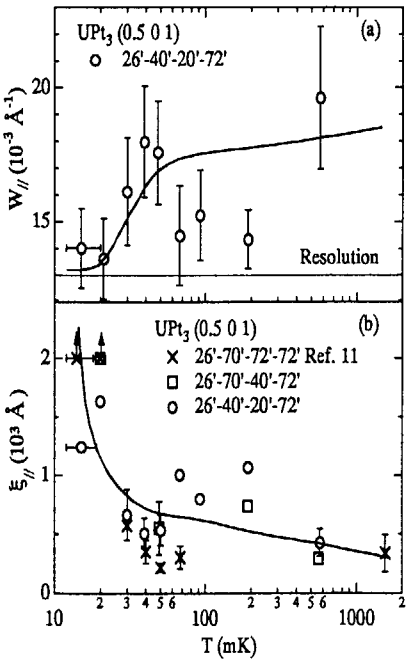

Fig. 2. (a) Temperature dependence of the linewidth ($W_{//}$) of (0.5 0 1) peak profile and (b) of the spin correlation length ($\xi_{//}$) in UPt_3. The crosses indicate the previous data shown in ref. 11. Solid lines are guide for the eyes.

short-range correlation system, is also very unusual. The steep increase of the correlation length below 20 mK suggests the static antiferomagnetic ordering at lower temperatures. It is quite interesting that this result corresponds to the anomalies in the specific heat[8,9] and thermal expansion [9]. The origin of this unusual magnetic fluctuation is unclear, and must be studied theoretically[13,14].

In conclusion, we found the long-range antiferromagnetic correlation in the heavy fermion superconductor UPt_3 below 20 mK in the neutron scattering experiments.

We would like to thank A. Sawada, T. C. Kobayashi, and K. Miyake for stimulating discussions.

References

[1] R. H. Heffner et al., Phys. Rew. B39 (1989)11345.
[2] G. Aeppli et al., Phys. Rev. Lett. 60 (1988) 615.
[3] G. Aeppli et al., Phys. Rev. Lett. 63 (1989) 676.
[4] E.D. Isaacs et al., Phys. Rev. Lett. 75 (1995) 1178.
[5] A. de Visser et al., Physica B147 (1987) 81.
[6] P.H. Frings et al., J. Magn. Magn. Mater. 31-34 (1983) 240.
[7] H. Tou et al., Phys. Rev. Lett. 77 (1996) 1374.
[8] E.A. Schuberth et al., Phys. Rev. Lett. 68 (1992) 117.
[9] E.A. Schuberth, Int. J. Mod. Phys. B10 (1996) 357.
[10] A. Sawada et al., Czech. J. Phys. 46 (1996) S2 803.
[11] Y. Koike et al., J. Phys. Soc. Jpn. 67 (1998) 1142.
[12] For example, I.A. Fomin and J. Flouquet, Solid State Commun. 98 (1996) 795.
[13] Y. Okuno et al., Meeting Abstracts of J. Phys. Soc. Jpn. Vol. 52 Issue 2, Part 3 (1997) p. 476.

This is a blank page.

1. 中性子散乱 (Neutron Scattering)

5) 非晶質・液体 (Amorphous · Liquid)

This is a blank page.

研究テーマ: 非弾性中性子散乱法による $[CH_3)_nNH_{4-n}]Cl$ のメチルアンモニウム分子回転
表題: 非弾性中性子散乱法による $[CH_3)_3NH]Cl$ 結晶におけるトリメチルアンモニウム分子のフラストレイト回転

A frustrated rotation of trimethylammonium molecule in $(CH_3)_3NHCl$ studied by inelastic neutron scattering

Norio Achiwa, Toshihiro Oya and Hiroyuki Takakura

Department of Physics, Faculty of Science, Kyushu University, Hakozaki, Fukuoka, 812, Japan

Trimethylammonium chloride, $(CH_3)_3NHCl$ (TMACl), has a phase transition at T_c=308K below wh5ch the structure belongs to the space group $P2_1/m(Z=2)$[1] and above wh5ch it is tetragonal $P4/nmm(Z=2)$[2], implying a dynamic disorder of the TMA molecule around their three fold axis. In order to study the reorientations in TMACl, quasielastic neutron scattering[3] and recently, molecular dynamics simulation[4] by one of the present authors were reported.

According to our previous X-ray study, electron density of a TMA molecule[2] on ab plane in the high temperature phase clearly shows four fold symmetry distribution. In the low temprature phase, the reorientation of TMA molecule is frozen where the three C atoms of TMA molecule form a deformed triangle. The symmetry of a TMA molecule in free state is C_{3v} which is incompatible with the local symmetry of C_{4v}. In order to study the frustration effects in the reorientational motion of TMA molecule in the high temperature phase, inelastic neutron scattering exeperiment has been performed using a TOF-type cold neutron spectrometer, AGNES at JAERI with an incident neutron energy of 4.59meV. Temperature dependence of scattering law S(Q, ω) is shown in fig. 1, where quasielastic scattering apears above T_c.

The phonon density of states g(ω) at various temperatures is shown in fig. 2. Sharp libration modes of TMA molecule at 9meV and 12meV below the T_c change to broad peaks and shift to lower energies above the T_c. The softening of livration modes at high temperature phase is due to the soft potential of C_{4v} symmetry.

The phonon dispersion curve below 5meV changes from a concave to a convex curve across the T_c with increasing temperature. The ratio of g(ω) above and below the T_c shows a peak around 2meV without correction for the softening effect of the lattice phonon density. This boson like peak would be the contribution of translational and rotational mode coupling of trimethylammonium molecule.

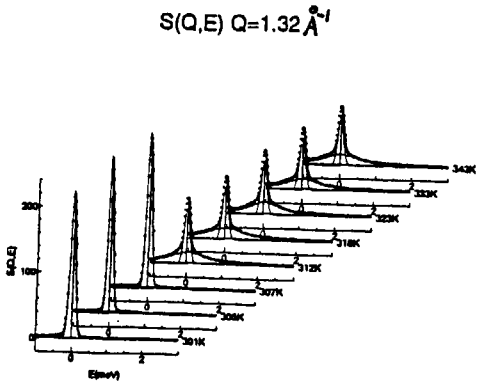

Fig.1 The observed scattering low S(Q, ω) of TMACl below and above T_c=308K.

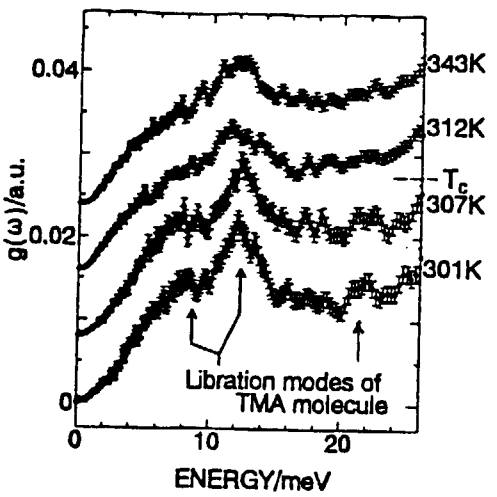

Fig.2 The observed phonon density of states g(ω) of TMACl below and above T_c=308K.

References

[1] J. Lindgren and I. Olovsson, Acta Cryst. **B24**, 554.
[2] M. Sugiyama, M. Machida, N. Koyano and Y. Iwata, J. Korean Phys Soc. **29**, S537(1996).
[3] M. Schlaak, J. C. Lassegues, A. Heidemann and R. E. Lechner, Mol. Phys. **33**, 111(1977).
[4] J. Kido and M. Machida, J. Korean Phys. Soc. **29**, S542(1996).

JRR-3M, AGNES(C3-1), Amorphous

研究テーマ：サイズを精密に制御された空間内における水分子集団の動力学
表題：中性子散乱による MCM-41 細孔内水分子のダイナミクスに関する研究

Neutron Scattering Study on Dynamics of Water Molecules in MCM-41

Shigeharu Kittaka,[a] Shuichi Takahara,[a] Yasushige Kuroda,[b] Toshinori Mori,[b] Hideaki Hamano,[b] Toshio Yamaguchi,[c] Tsuyoshi Kajitani[d]

[a] *Department of Chemistry, Faculty of Science, Okayama University of Science, 1-1 Ridaicho, Okayama 700, Japan*
[b] *Department of Chemistry, Faculty of Science, Okayama University, Tsushima, Okayama 700, Japan*
[c] *Department of Chemistry, Faculty of Science, Fukuoka University, Nanakuma, Jyonan-ku, Fukuoka 814-80, Japan*
[d] *Graduate School of Engineering, Tohoku Univ.Sendai 980-77, Japan*

Families of MCM-41, which were developed by Beck *et al.* in 1992,[1] are one of the most suitable model samples for the study on the properties of confined liquid, because they contain highly controlled cylindrical channels with very narrow pore size distribution. In the present study, we have investigated dynamics of water molecules confined in MCM-41 by quasi-elastic neutron scattering (QENS).

Three kinds of siliceous MCM-41 samples (C10, C14 and C18) were prepared by the method of Beck *et al.*[1] using alkyltrimethylanmmonium bromide with alkyl chains of 10, 14 and 18 carbon atoms, respectively. The pore diameters calculated from the N_2 adsorption isotherms were 2.14 (C10), 2.84 (C14) and 3.74 nm (C18). Adsorption isotherms of water were measured in the temperature range 283-303 K to confirm the capillary condensation of water and to use for adjustment of water contents in the samples. The sample pores were filled with water at the relative pressure range 0.6-0.8. Melting behaviors of water in the MCM-41 samples were studied by differential scanning calorimetry (DSC) after cooling down to 130 K at a heating rate of 5 K min^{-1}. A broad endothermic peak due to the melting of frozen water was observed at 221 (C14) and 242 K (C18), while no peak was observed for C10 sample.

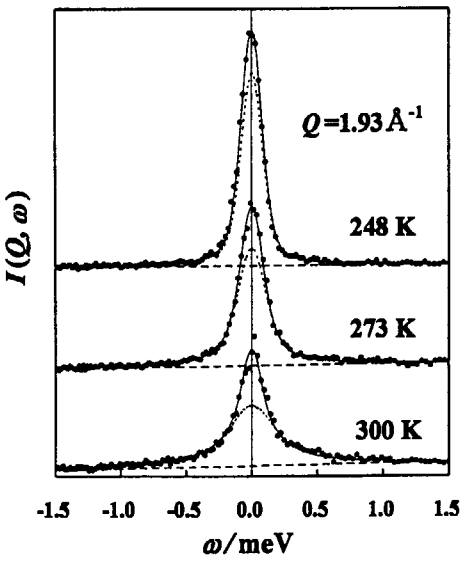

Figure 1. Temperature dependence of neutron scattering spectra for the water-filled C10 sample at Q = 1.93 $Å^{-1}$. Closed circles indicate the experimental data. Solid, dotted and broken lines represent the total fit with eq 1, the quasi-elastic component and the baseline, respectively.

QENS measurements of the water-filled samples were carried out on the time-of-flight type spectrometer AGNES[2] installed at the JRR-3M reactor of Japan Atomic Energy Research Institute. The wavelength of neutron beam was 4.22 Å, the momentum transfer (Q) range 0.61-2.38 $Å^{-1}$, and the temperature range 200-300 K.

Typical examples of the neutron scattering spectra of the water-saturated samples are shown in Figure 1. In the present study, the QENS spectra are ascribed mostly to the scattering from protons (more than 90 %). The observed spectra were analyzed by a least-square fitting procedure using the program KIWI.[3] In fitting the data, the scattering law $S(Q,\omega)$ convoluted with the resolution function was used. The $S(Q,\omega)$ employed is

$$S(Q,\omega) = A\left(\frac{1}{\pi}\cdot\frac{\Gamma}{\omega^2+\Gamma^2}\right)+(1-A)\delta(\omega) \qquad (1)$$

Here, ω is the energy transfer, A and Γ are the fraction and the half-width at half-maximum (HWHM) of a Lorentzian component, respectively, and $\delta(\omega)$ is a δ-function. The first term of the scattering law corresponds to the quasi-elastic component ascribed to the translational diffusive motion of water molecules in the cylindrical channels. On the other hand, the second term corresponds to the elastic component which may be due to the confined geometry effect[4] on the diffusive motion and the existence of "static" protons such as of the surface silanol groups and of the water molecules physisorbed on the pore walls. The Γ values obtained

JRR-3M, AGNES, 4. amorphous

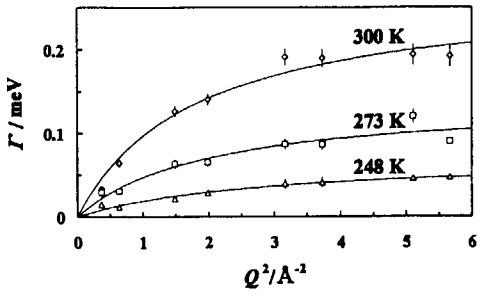

Figure 2. Q^2-dependence of Γ (HWHM of Lorentzian component) for the water-filled C10 sample. The error bars represent estimated standard deviations. Solid lines represent the fitted lines according to the jump diffusion model.

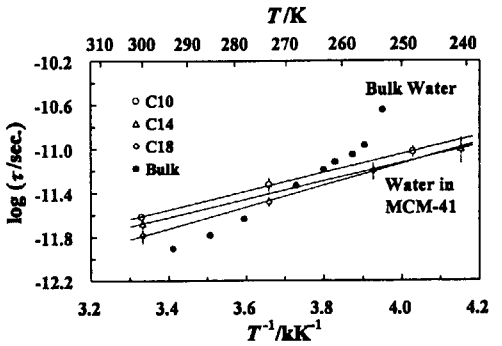

Figure 3. Arrhenius plot of the residence time τ for the confined water (opened symbols). The error bars represent estimated standard deviations. Literature values of bulk water[6] (closed circles) are plotted for comparison.

are plotted against Q^2 for the C10 sample and shown in Figure 2 as an example. Accurate Γ values were not determined from the spectra measured at temperatures below the melting point because their line widths were significantly narrower than the HWHM of the resolution function of the instrument (ca. 60 μeV).[2] QENS of C18 sample adsorbing only monolayer water were also measured, but the line widths of the spectra were too narrow to analyze. This result suggests that the water molecules physisorbed on the pore walls move much slowly, compared with the capillary condensed water.

The Q^2 - Γ data for the capillary condensed water were fitted by using the jump diffusion model;[5]

$$\Gamma = \frac{DQ^2}{1+DQ^2\tau} \qquad (2)$$

where D is the self-diffusion coefficient and τ the residence time. It should be pointed out that the D values obtained contain rather large errors because D is mainly determined from Γ values less than 1 $Å^{-1}$ at small Q where Γ contains large ambiguity. Thus, the D values were not discussed in detail in the present study. Figure 3 shows an Arrhenius plot of τ for the confined water and for bulk water in ref. 6. The τ values of protons of confined water was longer than that of bulk water at room temperature but increased slowly with decrease in temperature to cross the line for bulk water. The former result was explained by an activation entropy decrease due to the impermeable pore walls, while the latter by an activation energy decrease due to destruction of hydrogen bond network by surface field. In addition, the fact that the smaller the pore size, the larger the τ values at room temperature can reasonably be explained by an increase in amount of water molecules neighboring the silica surface. In this report, contribution of rotational motion of water molecules to $S(Q,\omega)$ was neglected. More detailed analysis taking account of this contribution is now in progress.

References

1 Beck, J. S.; Vartuli, J. C.; Roth, W. J.; Leonowicz, M. E.; Kresge, C. T.; Schmitt, K. D.; Chu, C. T-U.; Olson, D. H.; Sheppard, E. W.; McCullen, S. B.; Higgins, J. B.; Schlenker, J. L. *J. Am. Chem. Soc.* **1992**, *114*, 10834.

2 Kajitani, T.; Shibata, K.; Ikeda, S.; Kohgi, M.; Yoshizawa, H.; Nemoto, K.; Suzuki, K. *Physica B* **1995**, *213&214*, 872.

3 A fit program for quasi-elastic data analysis, "KIWI ver.1.01" made by Fanjat, N.

4 Bellissent-Funel, M.-C.; Chen, S. H.; Zanotti, J.-M. *Phys. Rev. E* **1995**, *51*, 4558.

5 Egelstaff, P. A. *An Introduction to the Liquid State*; Academic Press: London and New York, 1967.

6 Teixeira, J.; Bellissent-Funel, M.-C.; Chen, S. H.; Dianoux, A. J. *Phys. Rev. A* **1985**, *31*, 1913.

研究テーマ：低分子ガラスの低エネルギー励起の空間スケール
表題：３－メチルペンタンガラスのボゾンピークに関する散乱ベクトル依存性

Scattering-Vector Dependence of the Boson Peak in Glassy 3-Methylpentane

O. Yamamuro, I. Tsukushi [1], T. Kanaya [1], and T. Matsuo

Department of Chemistry, Graduate School of Science, Osaka University, 1-1 Machikaneyama-cho, Toyonaka, Osaka 560-0043, Japan
[1] Institute for Chemical Research, Kyoto University, Uji, Kyoto 611-0011, Japan

The low energy excitation in amorphous materials is one of the current topics in condensed matter physics [1]. We have studied this phenomenon on the hydrocarbon glasses with simple molecular structures [2-5]. The hydrocarbon glasses can be regarded as the van der Waals glass which is frequently treated in the theoretical and molecular dynamics studies. So far, we have focused our attention into the energy spectra neglecting the scattering-vector (Q) dependence; all of the data with different Q values were summed up to improve counting statistics. In the present study, we measured the Q dependence of the boson peak intensity. The work similar to the present one have been done only for some polymer glasses [6-8]. We expect that the present data will provide useful information on the mechanism of the boson peak.

The samples examined in this study were 3-methylpentane [$CH_3CH_2CH(CH_3)CH_2CH_3$ M = 60] This material can be vitrified easily by liquid-quenching. The glass transition temperature T_g is 77 K A commercial reagent of 3-methylpentane, which was purchased from Tokyo Kasei Kogyo Inc., was purified by fractional distillation and checked by gas chromatography.

Inelastic neutron scattering experiments of 3-methylpentane were performed with a high energy resolution triple-axis spectrometer HER (C3-1-1) installed at the cold neutron source of JRR-3M (Tokai, Japan). The k_i scan with constant k_f was performed using a horizontally curved analyzer.

The liquid 3-methylpentane was confined in a concentric double-cylinder aluminum can (35 mm in height, 14.5 mm in outer diameter of the outer cylinder, 13.6 mm in outer diameter of the inner cylinder, 0.25 mm in thickness of both cylinders) using an indium gasket. The volume and thickness of the sample were 0.3 cm^3 and 0.2 mm, respectively. The transmission of neutron beam was estimated to be about 90 %. The Q scan was performed at elastic position (ΔE = 0) in the Q range of 0.4—2.1 $Å^{-1}$ and at the boson peak energy of 3-methylpentane (ΔE = 2.5 meV [8]) in the Q range of 0.5—2.4 $Å^{-1}$. The step of Q was 0.1 $Å^{-1}$ for every scan. The data were collected at several temperatures in the temperature range 10—90 K.

Figure 1 shows the Q dependence of the boson peak intensity at several temperatures. The data were fitted to the equation for the incoherent neutron scattering of a harmonic oscillator:

$$I_{inel} = I_b + AQ^2\exp(-Q^2\langle u^2\rangle),$$

where I_b is the background, $\langle u^2\rangle$ the mean square displacement of the vibration, and A the constant. These three parameters were determined by the fitting. The data at every temperature were fitted well, indicating that the boson peak of 3-methylpentane can be treated as a single oscillator.

Figure 2 shows the elastic intensity at temperature T divided by the data at 10 K. The data were plotted in logarithmic scale and against Q^2. Since the elastic intensity is proportional to the Debye-Waller factor $\exp(-Q^2\langle u^2\rangle)$, the slope of each plot corresponds to $\langle u^2\rangle(T)$-$\langle u^2\rangle$(10 K). We evaluated $\langle u^2\rangle(T)$ by fitting each data to a straight line.

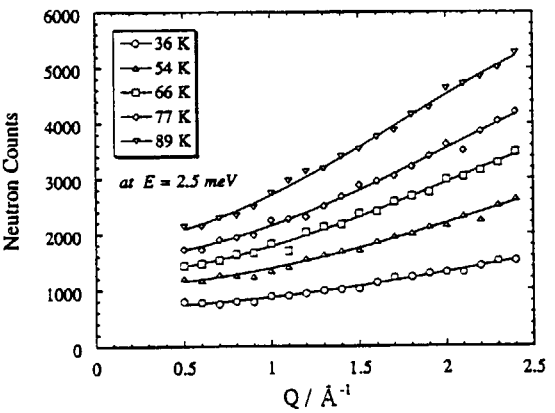

Fig. 1 Q dependence of the boson peak intensity (ΔE = 2.5 meV) of 3-methylpentane.

The temperature dependence of the mean square displacement obtained in this study is summarized in Fig. 3. The $<u^2>$ values from the elastic data (open circles) are smaller than those from the inelastic data (triangles). This is because the former represents as the average of all the vibrations including the intramolecular ones while the latter only the soft vibration associated with the boson peak. The similar results have been obtained for the polymer glasses [8]. The present results are quite consistent with our model for the boson peak of molecular glasses; i.e., the origin of the boson peak is the rotational vibration (libration).

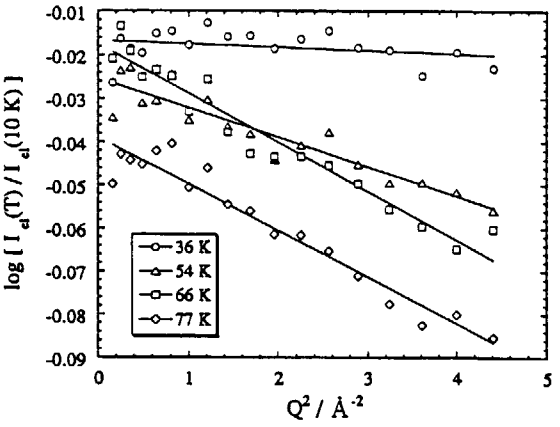

Fig. 2 Q dependence of the elastic peak intensity of 3-methylpentane.

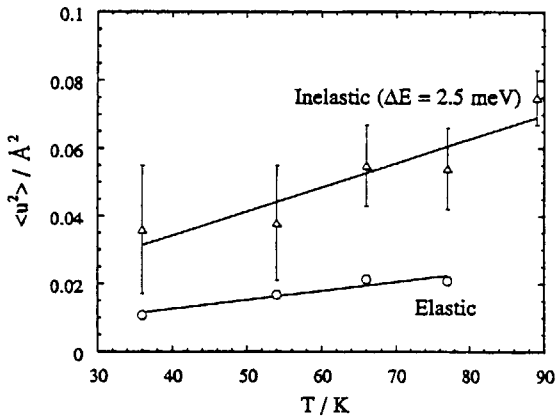

Fig. 3 Temperature dependence of the mean square displacement obtained from the elastic peak (circles) and boson peak (triangles).

References

[1] For example; U. Buchenau, in *Dynamics of Disordered Materials*, edited by D. Richter, A. J. Dianoux, W. Petry, and J. Teixeira (Springer, Berlin, 1989).
[2] O. Yamamuro, T. Matsuo, K. Takeda, T. Kanaya, T. Kawaguchi, and K. Kaji, J. Chem. Phys. **105** (1996) 732.
[3] O. Yamamuro, I. Tsukushi, T. Matsuo, K. Takeda, T. Kanaya, and K. Kaji, J. Chem. Phys. **106** (1997) 2997.
[4] A. Lindqvist, O. Yamamuro, I. Tsukushi, and T. Matsuo, J. Chem. Phys. **107** (1997) 5103.
[5] O. Yamamuro, I. Tsukushi, T. Matsuo, K. Takeda, T. Kanaya, and K. Kaji, Prog. Theor. Phys. suppl. **126** (1997) 89.
[6] B. Frick and D. Richter, Phys. Rev. B **47** (1993) 14795.
[7] K. Linder, B. Frick, and U. Buchenau, Physica A **201** (1993) 112.
[8] U. Buchenau, C. Pecharroman, R. Zorn, and B. Frick, Phys. Rev. Lett. **77** (1996) 659.

研究テーマ：分子性ガラスの低エネルギー励起に及ぼす分子間水素結合効果
表題：単価および多価アルコールガラスのボゾンピーク

Boson Peaks in Mono- and PolyAlcohol Glasses

O. Yamamuro, K. Harabe, K. Takeda [1], I. Tsukushi [2], T. Kanaya [2], and T. Matsuo

Department of Chemistry, Graduate School of Science, Osaka University, 1-1 Machikaneyama-cho, Toyonaka, Osaka 560-0043, Japan
[1] Department of Chemistry, Naruto University of Education, Naruto, Tokushima 772-8502, Japan
[2] Institute for Chemical Research, Kyoto University, Uji, Kyoto 611-0011, Japan

For most of amorphous solids, a broad excitation peak is observed at 2—5 meV in their Raman and neutron scattering spectra. This phenomenon, which is called boson peak from the temperature dependence of the intensity, is one of the current topics in condensed matter physics. Various types of amorphous materials have been studied and several models have been proposed to reproduce the experimental results [1]. However, the origin and the microscopic mechanism of the low energy excitation have not been explained with sufficient generality.

We have studied this phenomenon using the hydrocarbon glasses with simple molecular structures [2-5]. The hydrocarbon glasses can be regarded as the van der Waals glass which is frequently treated in the theoretical and molecular dynamics studies. It is also advantageous that the molecular mass can be changed systematically in a homologous series. In this study, we measured inelastic neutron scattering (INS) of mono- and polyalcohol glasses. The alcohol glasses have intermolecular hydrogen bonds and so have more rigid and ordered local structures than the hydrocarbon glasses. We expected that the comparison between the hydrocarbon and alcohol glasses would provide useful information on the mechanism of the boson peak.

The samples examined in this study were propanol [$CH_3CH_2CH_2OH$, M = 60, T_g = 96 K], ethylene glycol, [$CH_2(OH)CH_2OH$, M = 62, T_g = 153 K], glycerol [$CH_2(OH)CH(OH)CH_2OH$, M = 92, T_g = 184 K], and threitol [$CH_2(OH)CH(OH)CH(OH)CH_2OH$, M = 122, T_g = 229 K], where M is the molecular mass and T_g the glass transition temperature. Propanol is a mono alcohol with only one OH group while other three alcohols are polyalcohols with one OH group at each carbon atom. These samples (purity: > 99 %) were purchased from Tokyo Kasei Kogyo Co. Ltd. and used without purification. For ethylene glycol, about 10 % of glycerol was doped to suppress the crystallization.

INS experiments were performed with a direct geometry chopper-type TOF spectrometer AGNES (C3-1-1) installed at the cold neutron source of JRR-3M (Tokai, Japan). The wavelength of the incident neutron (selected by PG(002) monochromater) was 4.22 Å^{-1} (4.59 meV), corresponding to the energy resolution of 0.1 meV and the energy window of < 20 meV. In our experiment, 61 ^{3}He tube counters were installed at 2θ = 20—34°, 45—60°, 70—84°, and 95—109° with the step of 1°. This counter arrangement covers the scattering vector Q region of 0.5—2.4 Å^{-1}.

The liquid samples were confined in the concentric double-cylinder aluminum can (35 mm in height, 14.5 mm in outer diameter of the outer cylinder, 12 mm in outer diameter of the inner cylinder, 0.25 mm in thickness of both cylinders) using an indium gasket. The volume and thickness of the sample were 1.4 cm^3 and 1 mm, respectively. The transmission of neutron beam was about 60 %, producing the multiple scattering of about 20 %. Thus, we used rather large quantity of the sample to obtain good counting statistics sacrificing the accuracy since our main purpose was the comparison among several alcohol samples.

The raw scattering data, neutron counts (I) against time-of-flight (t_f), were processed into the dynamic structure factor $S(Q,\omega)$ by correcting for the effects of the background, counter efficiency, Jacobian $dt_f/d\omega$, etc. as usual. The observed $S(Q,\omega)$ was dominated by incoherent scattering from hydrogen atoms of the alcohol molecules. We calculated the density of states $G(\omega)$ from $S(Q,\omega)$ by assuming one phonon scattering process.

Figure 1 shows the $S(Q,\omega)$ of the four alcohol glasses observed at 100 K. All of the data with different Q values were summed up to improve counting statistics; the average Q value is 1.5 Å^{-1}. The data were scaled by dividing the integrated intensity for each sample. A broad but clear excitation peak (boson peak) was observed at 2—5 meV in every sample.

Figure 2 shows the density of states (divided by ω^2) calculated from $S(Q,\omega)$. The

data were multiplied by the molecular mass to normalize the state density to a molecule. The peak intensities of the three polyalcohols are similar to each other while that of propanol (monoalcohol) is much larger than those of the polyalcohols.

The boson peak energy of $S(Q,\omega)$ is plotted in Fig. 3 as functions of inverse square root of molecular mass. The literature data for the hydrocarbon glasses [2-7] and methanol [8] and ethanol [9] are also plotted for comparison. For the hydrocarbon glasses, the data lie on a straight line implying the simple mass dependence of a harmonic oscillator with the same force constant. However, the alcohol glasses have a quite different mass dependence from that of the hydrocarbon glasses. From these results, we guess that the boson peak energy of the hydrocarbon glasses is dominated by the molecular mass while that of the alcohol glasses by the intermolecular interactions. As is well known, the hydrogen-bond interaction in the alcohol glasses is much larger than the van der Waals interaction in the hydrocarbon glasses.

From the systematic molecular-mass dependence of ω_{bp}, one can visualize the boson peak of the molecular glasses as arising from the overall motion of the molecules, probably the rotational vibration (libration). Previous heat capacity data [2-5] allowed us to deduce that this vibration occurs cooperatively in domains composed of several molecules . The alcohol glasses may have larger domains than the hydrocarbon glasses and propanol glass may be intermediate between them.

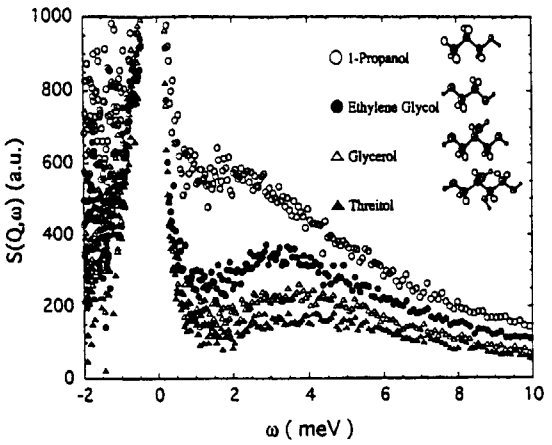

Fig. 1 $S(Q,\omega)$ spectra of several mono- and polyalcohol glasses.

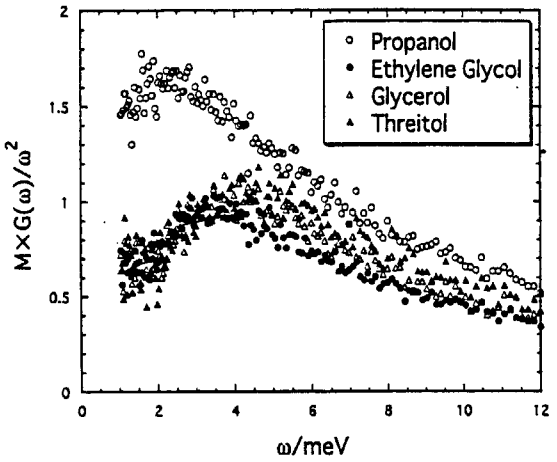

Fig. 2 Density of states divided by ω^2.

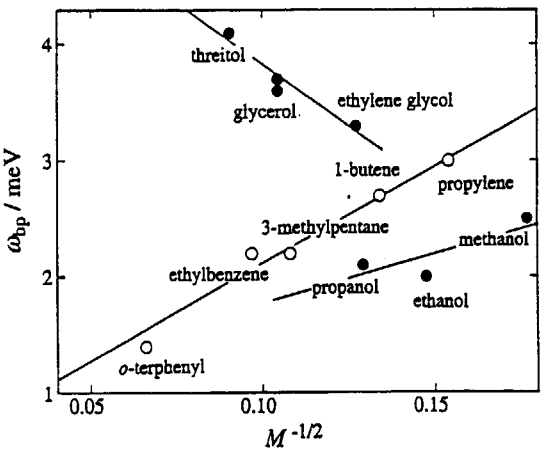

Fig. 3 Molecular mass dependence of the boson peak energy. Open and closed circles denote the data of hydrocarbon and alcohol glasses, respectively.

References

[1] For example; U. Buchenau, in *Dynamics of Disordered Materials*, edited by D. Richter, A. J. Dianoux, W. Petry, J. Teixeira (Springer, Berlin, 1989).
[2] O. Yamamuro, T. Matsuo, K. Takeda, T. Kanaya, T. Kawaguchi, K. Kaji, J. Chem. Phys. **105** (1996) 732.
[3] O. Yamamuro, I. Tsukushi, T. Matsuo, K. Takeda, T. Kanaya, K. Kaji, J. Chem. Phys. **106** (1997) 2997.
[4] A. Lindqvist, O. Yamamuro, I. Tsukushi, T. Matsuo, J. Chem. Phys. **107** (1997) 5103.
[5] O. Yamamuro, I. Tsukushi, T. Matsuo, K. Takeda, T. Kanaya, K. Kaji, Prog. Theor. Phys. suppl. **126** (1997) 89.
[6] B. Frick, J. Williams, S. Trevino, R. Erwin, Physica **B213&214** (1995) 506.
[7] J. Wuttke, M. Kiebel, E. Bartsch, F. Fujara, W. Petry, H. Sillescu, Z. Phys. **B91** (1993) 357.
[8] F. J. Bermejo, J. Alonso, A. Criado, F. J. Mompeán, J. L. Martínez, M. García-Hernández, A. Chahid, Phys. Rev. B **46** (1992) 6173.
[9] M. A. Ramos, S. Vieira, F. J. Bermejo, J. Dawidowski, H. E. Fischer, H. Schober, M. A. González, C. K. Loong, D. L. Price, Phys. Rev. Lett. **78** (1997) 82.

研究テーマ：ガラスの中範囲秩序と物性
表題：鉛メタケイ酸塩ガラスの中範囲秩序

Intermediate-Range Order in Lead Metasilicate Glass

K. Suzuya, D.L. Price[1], M.L. Saboungi[1] and H. Ohno

Japan Atomic Energy Research Institute, Sayo, Hyogo 679-5143, Japan
[1]Argonne National Laboratory, Argonne, Illinois 60439-4814 U.S.A

The nature of intermediate-range order in glasses remains one of the outstanding problems in condensed matter physics[1]. The most general and persistent evidence of intermediate-range order is the first sharp diffraction peak (FSDP), the feature observed at low wave vector in the structure factor $S(Q)$ of many systems, including oxide and chalcogenide glasses and complex liquids[2,3]. The wave vector Q_1 of the FSDP corresponds to a length scale $L_1 = 2\pi/Q_1$ on the order of 2.5 r_1 (r_1 is the nearest-neighbor distance in the glass), greater than the dimensions of the nominal building blocks of the glasses[3,4]. One of the features, the generality of which has not been emphasized in earlier work, is that the position of the first peak corresponds closely to that of a strong diffraction peak in a related crystalline phase and, therefore, to associated Bragg planes. We believe this to be an important clue to the origin of the FSDP.

We investigate this relationship by neutron diffraction (ND) studies of lead metasilicate ($PbSiO_3$) glass and crystal. The ND measurements for $PbSiO_3$ glass and crystal were done on the GLAD (IPNS, ANL) and on the TAS-1 (JRR-3, JAERI), respectively. Figure 3 shows ND data for $PbSiO_3$. (a) and (b) are original neutron weighted $S(Q)$'s for $PbSiO_3$ crystal and glass, respectively, which has been Fourier transformed to the 1-D real space correlation function $G(r)$. (c) and (d) are backtransformed $S(Q)$'s which are obtained from the $G(r)$ of $PbSiO_3$ crystal associated with truncation at two values R_{max}. For R_{max} = 7 Å, the FSDP is unrecognized, but for R_{max} = 9 Å, the FSDP is reproduced at Q = 1.2 Å^{-1}, a value similar to that of the original $S(Q)$ for $PbSiO_3$ glass. This shows, with little ambiguity, that a intermediate-range structure in $PbSiO_3$ glass consistent with FSDP can be specified by the $G(r)$ of the crystal extending to values of $r \sim 9$ Å.

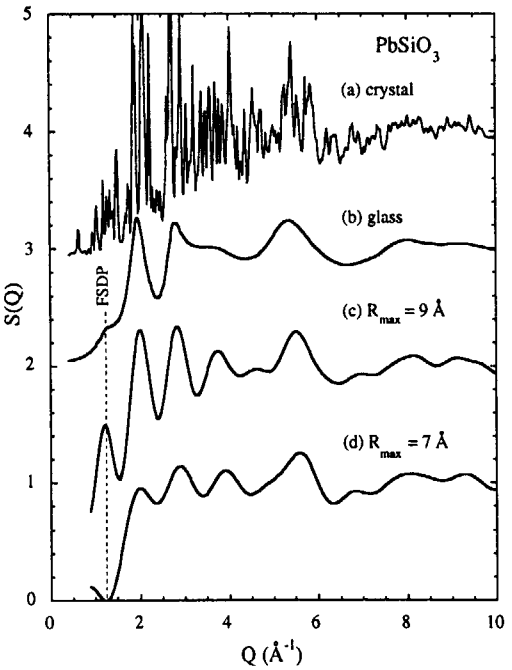

Fig. 1 Experimental neutron structure factor $S(Q)$ for $PbSiO_3$ crystal (a) and $PbSiO_3$ glass (b), and back Fourier transforms $S(Q)$ of the reduced pair correlation function $G(r)$ for $PbSiO_3$ crystal obtained by a transforms of experimental neutron $S(Q)$, associated with truncation at R_{max} = 9 Å (c) and 7 Å (d). Each $S(Q)$ plot is displaced by 1.0 for clarity.

References

[1] S.R. Elliott, Nature 354 (1991) 445-452
[2] S.C. Moss and D.L. Price, in: Physics Disordered Materials, eds. D. Adler, H. Fritzsche and S.R. Ovshinsky (Plenum, New York, N.Y., 1985) p. 77-95.
[3] D.L. Price, S.C. Moss, R. Reijers, M.-L. Saboungi and S. Susman, J. Phys. Condens. Matter 1 (1989) 1005-1008
[4] P.H. Gaskell, M.C. Eckersley, A.C. Barns and P. Chieux, Nature 350 (1991) 675-677

原子炉：JRR-3M　　装置：TAS-1（2G）　　分野：液体・不規則性物質

研究テーマ：プロトン及びイオン伝導機構の結晶学的研究
表　　題：AgI-Ag_2O-V_2O_5系ガラスの短距離および中距離秩序

Short- and Medium-range Order of AgI-Ag_2O-V_2O_5 Glass System

H. Takahashi, K. Shishitsuka, T. Sakuma[1], Y. Shimojo[2] and Y. Ishii[2]

Faculty of Engineering, Ibaraki University, Hitachi 316 Japan
[1]Faculty of Science, Ibaraki University, Mito 310, Japan
[2]Japan Atomic Energy Research Institute, Tokai 311-19, Japan

It is well known that AgI-Ag_2O-V_2O_5 system has wide glass forming region. The purpose of the present investigation is to clarify the short- and medium-range order in silver vanadate glasses. In order to get information about the medium-range order, the first sharp diffraction peak (FSDP) in the low-Q region for $(AgI)_{0.5}((Ag_2O)_{1-X}(V_2O_5)_X)_{0.5}$ glasses is examined by X-ray and neutron diffraction. Raman scattering experiment is also performed to determine the V-O network structure.

Raman scattering peaks for silver vanadate glasses are assigned using the results of those for alkali vanadate crystals. It is concluded that the network structure for metavanadate glass (X=0.5) is mainly composed of one dimensional VO_4 tetrahedral chain, and that for pyrovanadate (X=0.33) glass consists of the $V_2O_7^{4-}$ structure unit similar to other alkali and alkaline earth vanadate glasses. In 0.5>X>0.33 glasses, Raman profiles continuously change from that of metavanadate to pyrovanadate. It is considered that the average VO_4 chain length systematically varies in these composition range. On the other hand, Raman profiles for glasses having X>0.5 resembles each other. Since the ratio of the bridging oxygen to the non-bridging oxygen increases with increasing X, gradual change from VO_4 linear chain to connected two dimentional VO_4 network would form with increasing X.

Figure 1 shows the neutron and X-ray diffraction profiles in the low-Q range. FSDP could not observe for the representative composition by neutron diffraction, while FSDP is detected for all the glasses by X-ray diffraction. It is concluded that FSDP originates from V-O and V-V correlation. The composition dependence of the peak position corresponds to the network structure investigated by Raman scattering. The shift of the peak position to higher Q value means decrease of the interchain correlation length. The change of the correlation length mainly results from the variation of network structure from VO_4 linear chain to $V_2O_7^{4-}$ unit. It seems that FSDP shift reflects the morphological degree of freedom depending on the length of structure unit.

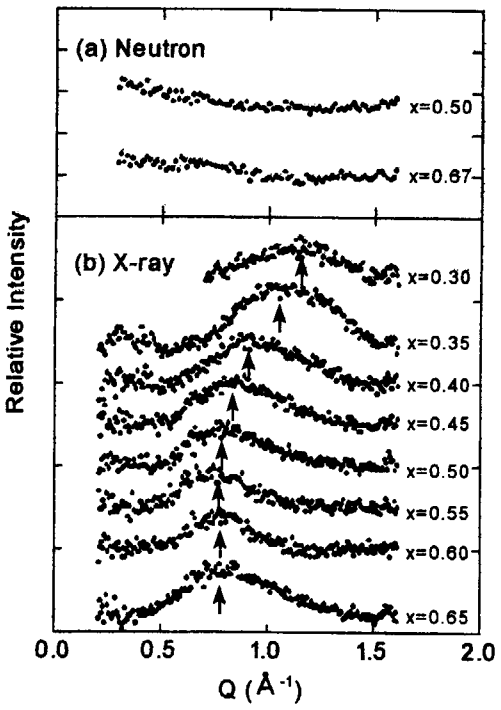

Fig. 1 Neutron and X-ray diffraction profiles for $(AgI)_{0.5}((Ag_2O)_{1-X}(V_2O_5)_X)_{0.5}$ glasses in low Q range.

原子炉：JRR-3　　TAS-2(T2-4)　　分野：中性子散乱（液体・不規則物質）

研究テーマ：メカニカルミリング法によって得た分子性アモルファス固体の低エネルギー励起
表題：メカニカルミリング法によって得たアモルファストリメチル-β-シクロデキストリンの
低エネルギー励起

Low-Energy Excitation of Amorphous Tri-*O*-methyl-*β*-cyclodextrin Produced by Mechanical Milling

I. Tsukushi, T. Kanaya and K. Kaji
Institute for Chemical Research, Kyoto University, Uji, Kyoto-fu 611-0011, Japan

Solid state amorphization by mechanical milling by a ball mill and irradiation of high energy neutron or electron beam is an unique method to produce the amorphous state. These are processes in which energy is supplied to a crystalline material to disturb the equilibrium structure and freeze it in an energized metastable amorphous state, whereas, in the more traditional procedures of liquid quenching and vapor deposition, the energy is removed from the sample as rapidly as possible. We have measured the incoherent inelastic and quasielastic neutron scattering of tri-*O*-methyl-*β*-cyclodextrin (TMCD) by a time of flight (TOF) spectrometer, AGNES in order to compare the mechanical milling amorphous (MMA) state with the liquid-quenched glassy (LQG) state from the dynamic view point.

Fig. 1 shows the dynamic scattering law $S(Q,\omega)$ of MMA, LQG of TMCD at 100 K. A broad peak at around 1 ~ 2 meV was observed for both amorphous states. This peak is the so-called boson peak which is usually observed in amorphous materials. In the present stage, there is no difference in the peak position, the broadness and the intensity between MMA and LQG. The different path to the amorphous state does not much affect to the dynamics of amorphous state, at least in the energy region examined.

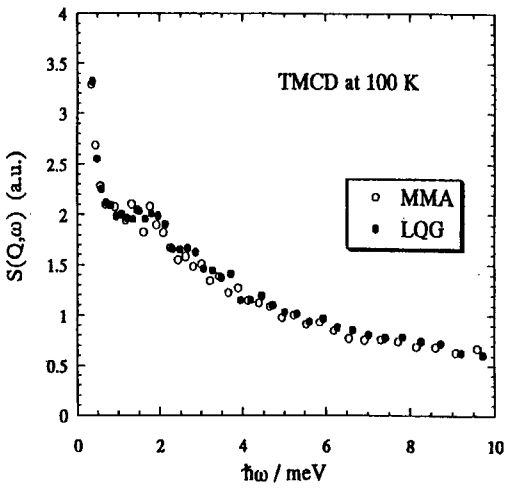

Fig. 1 Dynamic scattering law $S(Q,\omega)$ of tri-*O*-methyl-*β*-cyclodextrin (TMCD) at 100 K.
O: Mechanical milling Amorphous (MMA)
●: Liquid-quenched glass (LQG)

研究課題：両親媒子系複雑液体のスローダイナミックス

表題：中性子スピンエコー法による両親媒子系複雑液体のスローダイナミクス

Neutron Spin Echo Investigation on the Slow Dynamics in Complex Fluids Involving Amphiphiles

T. Takeda, Y. Kawabata, H. Seto, S. K. Ghosh, S. Komura[1], M. Nagao[2]

Faculty of Integrated Arts and Sciences, Hiroshima University, Higashi-Hiroshima 739-8521

1 Faculty of Science, Ochanomizu University, Ootsuka, Tokyo 112-8610

2 Institute for Solid State Physics, University of Tokyo, Tokai, Naka Ibaraki 319-1106

We have studied slow dynamics in complex fluid systems such as the shape fluctuation of microemulsion droplets, membrane undulation in lipid-bilayers and bicontinuous microemulsions using the neutron spin echo spectrometer(NSE) at C2-2 port of JRR-3M, JAERI[1]. The ternary system non-ionic surfactant $C_{12}E_5$/ n-octane / water at equal volume fraction of octane and water for volume fraction 0.2 of $C_{12}E_5$ represents a sequence of microemulsion / lamellar / microemulsion phase with increasing temperature. The intermediate correlation functions $I(Q,t)$ obtained from our NSE experiments were well fitted to the following equation,

$$I(Q,t) = I(Q,0)\exp[-(\Gamma t)^{2/3}] \quad , \qquad (1)$$

in the bicontinuous microemulsion and the lamellar phases of the $C_{12}E_5$/n-octane/water system and also in the lamellar phase of the dipalmitoylphosphatidyl-choline(DPPC)-water-$CaCl_2$ system. The relaxation rate Γ obtained from the fitting to Eq.(1) increased as Q^3 at higher Q as shown in Fig. 1. These results support the theory presented by Zilman and Granek[2]. They used the Helflich bending free energy to describe membrane undulations in sponge and lamellar phases and predicated a stretched exponential relaxation of Eq.(1), where Γ increases as $\varkappa^{-1/2}Q^3$. $\varkappa$ is bending modulus. We estimated $\varkappa$ in the bicontinuous microemulsion phases and the lamellar of the $C_{12}E_5$/n-octane/water system using their theory as shown in Fig. 2. $\varkappa$ in 5wt% DPPC-D_2O with Ca^{2+} of 7mM at 45°C was estimated to be 6.3×10^{-20} J.

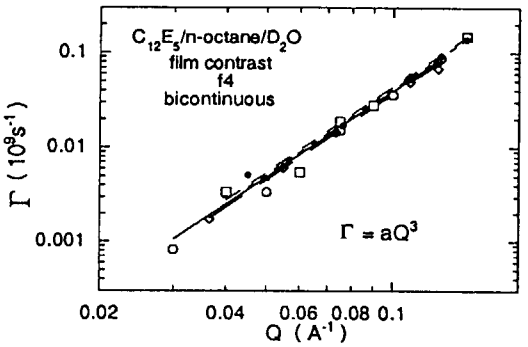

Fig.1 Q dependence of Γ obtained using the fitting to Eq.(1) in higher temperature bicontinuous microemulsion phase (f4) of the film contrast sample of the $C_{12}E_5$/n-octane/water system.

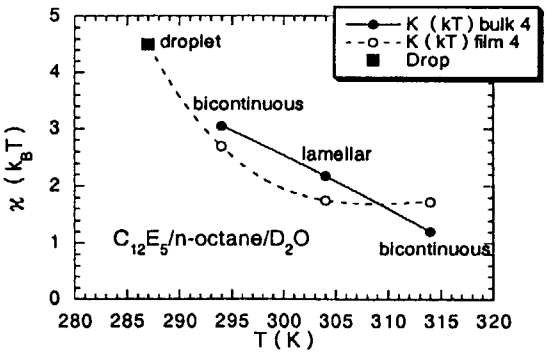

Fig.2 Bending modulus $\varkappa$ obtained from NSE experiments in the $C_{12}E_5$/n-octane/water system.

1) T.Takeda et al; J. Phys. Soc. Jpn. 65 Suppl.A (1996) 189-194.
2) Zilman & Granek: Phys. Rev. Letters 77 (1996) 4788-4791.

Facilities and Instruments　　Research field

研究課題：マイクロエマルジョンの構造の違いによる界面活性剤膜の運動状態
表題　　：紐状ミセルネットワークの中性子スピンエコー実験 II

A Neutron Spin Echo Study of Network of Wormlike Micelles II

H. Seto, T. Kato[1], T. Takeda, M. Nagao[2], Y. Kawabata, D. Okuhara, S. Komura[3]
Faculty of Integrated Arts and Sciences, Hiroshima University
Department of Chemistry, Tokyo Metropolitan University[1]
Institute for Solid State Physics, The University of Tokyo[2]
Faculty of Science, Ochanomizu University[3]

Aqueous solutions of non-ionic amphiphile $C_{16}E_7$ are known to form "wormlike micelles". When temperature is increased from 10 °C up to about 50 °C, hydrodynamic radius of micelles increases from about 30 Å to 200 Å drastically and this behavior is interpreted that a shape of micelles grows from globular to tubular. In semi-dilute and concentrated solutions, wormlike micelles form a network structure whose static propertyies are analogously understood as chain-like polymers. However, their dynamical properties are not equal to the case of polymers because the micelles entangle and fuse each other. Recently Kato et al. investigated their dynamical properties by NMR and LS, and showed that the dynamics in semi-dilute concentrations could be understood by the "living polymer" model, and in concentrated solutions the fusion of wormlike micelles occurs.

In this study, collective motions of wormlike micelles are investigated by means of neutron spin echo spectroscopy at NSE spectormetor at JRR-3M, JAERI, Tokai, in the momentum transfer range of $0.03 < Q < 0.2$ ($Å^{-1}$). A concentrated solution, 20% of $C_{16}E_7$ was selected as a sample. The sample was contained in a niobium cell with a quartz window whose thickness was 4 mm. In Fig. 1, a typical intermediate correlation function obtained by the NSE experiment is shown as a function of the

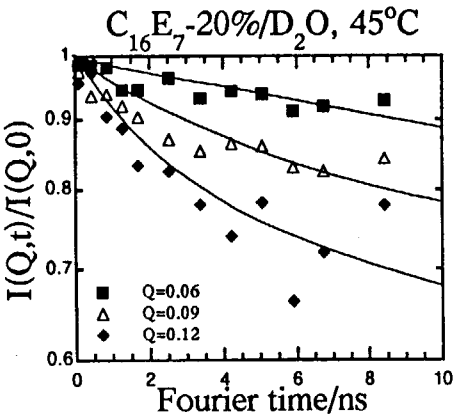

Fig. 1 A typical example of the observed intermediate correlation function at T = 45 °C.

Fourier time t. We assume that its t dependence is explained by a linier combination of two exponentials,

$$I(Q,t)/I(Q,0) = f_1 \exp(-\Gamma_s t) + (1-f_1)\exp(-\Gamma_f t)$$

The first term corresponds to a "slow relaxation" originated from collective motion of micelles and the second comes from a "fast relaxation" of the diffusion of amphiphile molecules. Therefore, the relaxation rate Γ_f of the second term was calculated assuming the dynamical scaling and only Γ_s was a fit parameter. Solid lines in Fig. 1 are the results of fitting. From the fitting, Q-dependence of an effective diffusion constant D_{eff} ($= \Gamma_s / Q^2$) was obtained. The values were around 1.0×10^{-11} (m^2/s), almost the same for all the observed Q, and increased with increasing temperature.

Reactor: JRR-3M　　Facility: NSE (C2-2)　　Field: 非晶質、液体 amorphous

研究テーマ：炭化フッ素系界面活性剤水溶液における2次元方向へのミセル成長
表題：ペルフルオロオクタン酸セシウム水溶液における2次元方向へのミセル成長

Micellar Growth along Two Dimensions in Aqueous Solutions of Cesium Perfluorooctanoate

T. Kato, H. Iijima, H. Yoshida[1], and M. Imai[2]

Department of Chemistry, Tokyo Metropolitan University
1 Department of Industrial Chemistry, Tokyo Metropolitan University
2 1 Institute for Solid State Physics, University of Tokyo

It is well known that micelles grow if required conditions are satisfied. Under the restriction that all the head groups are exposed to water and that there is no space that is not filled with hydrophobic chains in a micellar core, micelles grow along one dimension (to rod) or two dimensions (to disk). However, there has been no report showing existence of bidimensional aggregates directly except for mixed short-chain lecithin/long-chain lecithin aggregates. In the present study, we have measured small angle X-ray and neutron scattering (SAXS and SANS, respectively) on H_2O solutions of cesium perfluorooctanoate (CsPFO) at different surfactant concentrations. For 0.1 and 0.3 M solutions, SANS has been measured for various D_2O/H_2O mixed solvents.

SANS measurements were performed on the JRR-3M SANS-U. The sample-detector distance and the wavelength of neutrons were 2m and 0.7nm, respectively. Observed scattering curves have been analyzed with a double-layered ellipsoid form factor combined with the rescaled mean spherical approximation for the intermicellar structure factor.

Figure 1 shows observed SANS profiles for CsPFO-H_2O solutions at different concentrations of CsPFO. The scattering curves can be fitted well with both prolate (a) and oblate (b) ellipsoid models. However, the semiminor axis of micellar core, R_c, obtained for the prolate ellipsoid is much longer than the extended length of the fluorocarbon chain which is close to the R_c obtained for the oblate ellipsoid (13.0Å). As the surfactant concentration increases, the aggregation number of micelles increases from 50 to 132 as the concentration increases from 0.063 to 0.5 M. At the same time, the degree of counter ion binding increase from 0.61 to 0.85. These results suggest micellar growth along two dimensions.

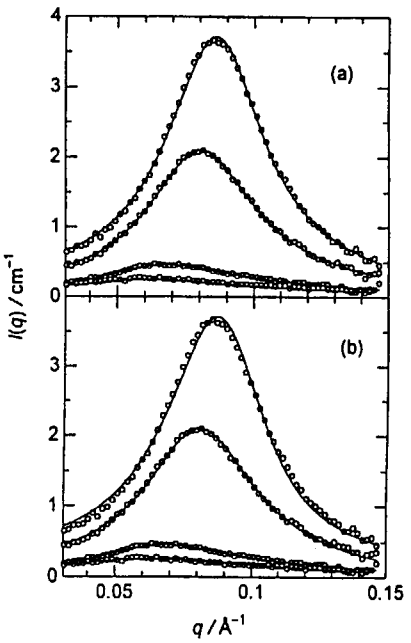

Figure 1 SANS data and best fits using prolate (a) and oblate (b) ellipsoid models for 0.06, 0.10, 0.31, and 0.50 M (from the bottom) CsPFO in H_2O.

JRR-3M, SANS-U, 4. 非晶質、液体

研究課題：液体カルコゲンの中性子小角散乱
表題：液体セレンの中性子小角散乱測定

SANS Measurements of Liquid Se

M. Inui, K. Maruyama[1], Y. Kawakita[2], S. Takeda[2], S. Tamaki[1*] and M. Imai[3**]

Faculty of Integrated Arts and Sciences, Hiroshima University, Higashi-Hiroshima 739-8521, Japan
[1] *Faculty of Science, Niigata University, Niigata 950-2181, Japan*
[2] *Faculty of Science, Kyushu University, Ropponmatsu, Fukuoka 810-8560, Japan*
[3] *The Institute of Solid State Physics, The University of Tokyo, Tokai 319-1195, Japan*
* *present address: The College of Biomedical Technology of Niigata University, Niigata 951-8122, Japan*
** *present address: Faculty of Science, Ochanomizu University, Tokyo 112-0012, Japan*

Liquid (l-) Se has two-fold coordinated chain structure where atoms are covalently bonded. Near the melting temperature, chain molecules in l-Se are known to consist of 10^4 - 10^5 atoms and l-Se shows semiconducting properties. The results of viscosity, magnetic susceptibility and NMR measurements suggest that the chain becomes short with increasing temperature. It is noteworthy that there appears metallic Se in the supercritical region at high temperature and pressure, where the average chain length is about 10. Large density fluctuation and very short chain molecules in the supercritical fluid are considered to induce the metallic state.

It is interesting to study the correlation between chain length and density fluctuation in l-Se. Small angle neutron scattering (SANS) is a useful probe of observing density fluctuation in such liquid. We have carried out SANS measurements on l- and amorphous Se for the first time[1]. In this work, SANS experiments in smaller Q region were carried out to investigate the origin of the cluster formation.

SANS measurements were performed using the spectrometer (SANS-U) of the Institute of Solid State Physics, the University of Tokyo, installed at the beam line of a cold source in JRR-3M. The camera lengths in this work were 4m and 12m, and I(Q) spectra are deduced from the subtraction of the background of dark counts and that from a quartz empty cell with the absorption correction for the sample.

Figure 1 shows I(Q) of l-Se at 270°C where the result from the camera length of 4m is denoted by open circles and that from 12m by solid squares. Although the net SANS intensity from l-Se is very small, we believe that this is real one after careful treatment of the data. $I(Q)$ slightly increses with decreasing Q down to 0.02Å^{-1}. The slope changes around 0.02Å^{-1} and $I(Q)$ becomes large down to 0.01Å^{-1}. In the last report, there may appear a broad peak around 0.01Å^{-1} in $I(Q)$ and it seems to be reproduced. It is, however, difficult to determine if the peak exist or not at the present stage. Further measurements such as the temperature dependence are necessary to confirm it.

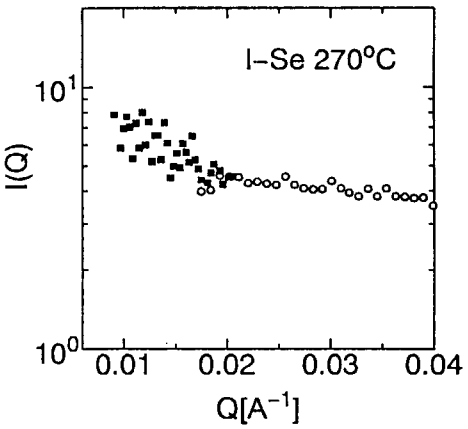

Figure 1: The SANS intensity profile $I(Q)$ of l-Se at 270°C

Reference

[1] M. Inui et al., Physica **B 213 & 214** (1995) 552.

Reactor : JRR-3M　Facility : SANS-U(C1-2)　Field : 4. 非晶質，液体 amorphous

課題名：溶融IIIb-Te混合系

表　題：液体In-Te混合系の局所構造

Local Structures of Liquid In-Te Mixtures II

S. Takeda, Y. Kawakita, S. Yoshioka, H. Nakashima, I. Hiraishi

Department of Physics, Faculty of Science, Kyushu University,

Ropponmatsu, Fukuoka 810-8560, JAPAN

In-Te system is well known to have a strong compound-forming character even in the liquid state around the stoichiometric composition of In_2Te_3. Conductivity [1] and magnetic susceptibility [2] measurements show a deep minimum value at this composition just above the melting point, which implies the localization of conduction electrons. However these electronic properties exhibit an anomalous temperature dependence [1,2] around the In_2Te_3 composition. With increasing temperature, the composition of minimum magnetic susceptibility moves from In_2Te_3 to In_2Te and conductivity minimum around the composition In_2Te_3 tends to disappear. The observed specific heat of liquid In-Te mixtures have large values over a wide temperature range from the melting point (667°C) to 800°C[3] and this suggests the occurrence of some structural change such as the dissociation of chemical complex in the liquid state.

We reported the local structural of In_2Te_3 and its temperature dependency in Activity Reports vol. 4[4]. The network structure of the triangular pyramidal units which is composed of one In atom and three Te atoms bonding to it is expected as the model of liquid In_2Te_3 just above the melting point. With increasing temperature, the three-fold coordinated In atoms become unstable by thermal agitation, and this unit is easily distorted or destroyed.

In this paper, we will report the concentration dependence of the structure of liquid In-Te system. Neutron diffraction measurements were performed using the TAS instrument of The University of Tokyo, at the JRR-3RM reactor. Experimental conditions and data analysis were the same as previously reported [4]. The obtained pair distribution functions are shown in Figure 1. The first peak including much contribution from In-Te covalent bond is located at 2.9Å for the compositions less than 40 at.%

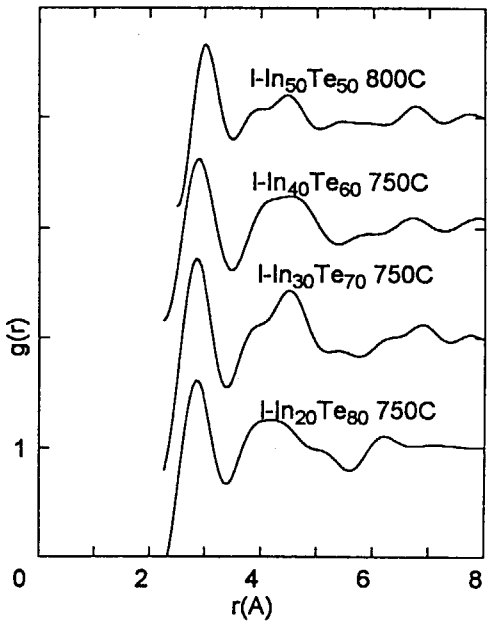

Figure 1. Pair distribution functions of liquid In-Te mixtures.

In and elongated significantly to 3.0Å for liquid $In_{50}Te_{50}$. The second peak around 3.9Å for liquid $In_{20}Te_{80}$ is considered as the contribution of tellurium interchain correlation. This contribution disappears for $In_{40}Te_{60}$ and another hump around 4.55Å appears which may correspond to Te-Te correlation in the $InTe_3$ unit.

[1] Y. Ninomiya, Y. Nakamura and M. Shimoji: Phil. Mag. 26 (1972) 953.

[2] Y. Tsuchiya, S. Takeda, S. Tamaki, Y. Waseda and E.F.W. Seymour: J. Phys. C:Solid State Phys. 15 (1982) 2561.

[3] S.Takeda, H. Okazaki and S. Tamaki: J. Phys. C:Solid State Phys. 15 (1982) 5203.

[4] S. Takeda, Y. Kawakita, R. Matsubara, H. Nakashima and A. Hiramatsu: Activity Reports vol. 4 (1997) 165.

JRR-3M, 4G, Amorphous & Liquid

研究テーマ：ランタノイド（III）有機化合物錯体の構造と溶媒和
表題：中性子回折法による塩化物イオン水溶液におけるランタンの水和構造

Hydration Structure of Lanthanum Ion in Aqueous Chloride Solution Determined by Neutron Diffraction Method

T. Yaita, S. Suzuki, H. Narita, S. Tachimori and Y. Ishii
Japan Atomic Energy Research Institute, Tokai, Ibaraki 319-1195, Japan

Introduction

Recently the hydration of lanthanide (III) ions in aqueous solution has been studied using X-ray and neutron diffraction[1], XAFS[3] and NMR[2]. Since these studies provide us several interesting results, for example, the hydration number changing in going from the lighter to the heavier lanthanides in the series; it is very important for separation chemists to elucidate separation behavior of these elements in solvent extraction and ionic exchange processes. However, the above methods can not provide us positions of hydrogen. Neutron diffraction is a unique tool for probing the structure of materials containing hydrogen, such as water and aqueous solutions. Accordingly, in this study, we determined the hydration structure of aqueous lanthanum chloride solution by neutron diffraction.

Experimental Methods

Sample solutions were prepared with heavy water (99.9% D) in order to eliminate the strong incoherent scattering of protons. The ^1H content of the final solution was checked by ^1H-NMR. To prepare the salt sample solution, we dissolved $LaCl_3$ salt into the D_2O solution. The neutron experiment was carried out with TAS-1 of JRR-3(2G) at Japan Atomic Energy Research Institute by using about 1-Å neutrons. The samples were contained in a quartz tube. The measured intensities were corrected for D_2O-D_2O background. In this way, the correlations of the solutions, namely, Cl-D_2O and Cl-Cl did not cancel, therefore, this result included these interactions.

Results and Discussion

The radial distribution function (Fig.1) shows that the first hydration sphere of water molecules around a lanthanum ion is almost defined. Since the peaks in the distribution function are quite well separated, it is possible to make an estimate of hydration structure. The first peak at 2.55-Å is attributed to oxygen of water. The previous x-ray diffraction study[1] reported that the bond distance between lanthanum and oxygen of water is 2.58-Å, and is approximately equal to this work's result. The second peak at 3.24-Å arises from deuterium of water, suggesting that water molecules orient themselves about ionic core. The third broad peak around 5.0-Å arises from chloride ion. Chloride ion exist outside the primary coordination sphere and isolate the hydrated lanthanum from the bulk structure of water by braking hydrogen bonds around hydrated waters. This result agreed with the ^{139}La NMR results[2].

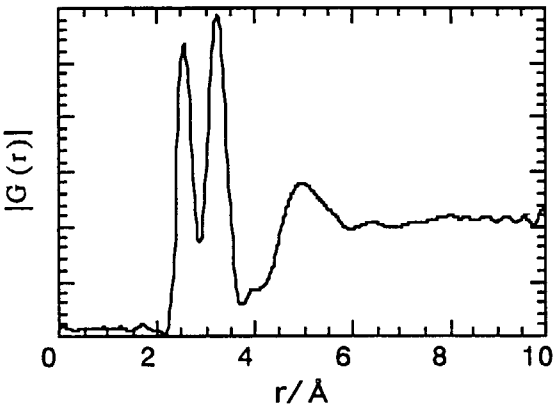

Fig.1
Radial distribution function in $LaCl_3$-D_2O system

References

1)A. Habenschuss and F. H. Spedding, J. Chem.
Phys., **70(8)**,3758 (1979).
2)T.Yaita, D.Ito, S.Tachimori, J. Phys. Chem., **102(20)**, 3886(1998).
3)T.Yaita et al., J. Radioanal. Nucl. Chem. in press.

原子炉：JRR-3M　　装置：TAS-1(2G)　　分野：液体・不規則性物質

1. 中性子散乱 (Neutron Scattering)

6) 装　置 (Instrument)

This is a blank page.

研究テーマ：研究炉利用高度化の技術開発
表　　題：中性子散乱実験用多重極限条件発生装置の性能試験

Performance Test of a System for Simultaneously Generating Triple Extreme Conditions for Neutron Scattering Experiments II

A. Moriai, S. Ichimura, A. Ohtomo, S. Kawano[1], A. Onodera[2]

Department of Research Reactor, JAERI, Tokai, Naka, Ibaraki, 319-1112
[1] Research Reactor Institute, Kyoto University, Kumatori, Sennan, Osaka, 590-0451
[2] Faculty of Engineering Science, Osaka University, Toyonaka, Osaka, 560-0043

In recent years neutron scattering studies of condensed matters have shown predominant trend of studies of under extreme conditions such as low temperature, high magnetic field and high pressure. These parameters of temperature, pressure and magnetic field have been selected as independent thermodynamic variables for sample environment. However, those parameters have been only selected as a single-variable or a double-variables at most in neutron scattering so far because of various technological difficulties existing in the development of a system available for simultaneously controlling those three parameters.

As previously reported, we have developed a cryomagnet system with a high pressure cell[1], and carried out several tests for the system to verify its performance. The present article represents the results of one of related experiments derived from measuring magnetic phase transition for $TbNi_2Si_2$ rare-earth compound under triple extreme conditions by neutron scattering. The $TbNi_2Si_2$ compound crystallizes in a tetragonal $ThCr_2Si_2$-type structure, which undergoes two successive magnetic transitions: an amplitude modulated antiferromagnetic structure with a propagation vector $\boldsymbol{Q}_1=(1/2\pm\tau, 1/2\mp\tau, 0)$ with $\tau=0.075$ for $9K<T<T_N(=15K)$ and a simple antiferromagnetic structure with $\boldsymbol{Q}_2=(1/2, 1/2, 0)$ for $T<9K$[2]. For another interesting respects, the compound exhibits typical multi-step metamagnetic phase transitions in a external field: at 4.2K six long period modulated structures are induced in the *c*-axis magnetization process up to 5T[2]. It is, therefore, interesting to observe pressure effect of those structure, since several numbers of intermediate phases will be imply comparable free energy between those field-induced structures.

The neutron scattering experiments were carried out in the $\boldsymbol{a}^*$-$\boldsymbol{b}^*$ reciprocal lattice plane with a triple axis spectrometer, TAS-2 installed at the $T_{2\text{-}4}$ beam port of JRR-3M in JAERI, and wavelength of incident neutrons was 2.44Å. Pressure was generated hydrostatically and was measured by the change of lattice constant of NaCl single crystal placed together with $TbNi_2Si_2$ single crystal in the cell. Magnetic field was applied along the *c*-axis up to 5T.

Figure 1 shows the field dependence of several magnetic Bragg peaks under ambient pressure at 1.7K. At low fields below about 1.5T the magnetic structure of this compound changes with a simple commensurate antiferromagnetic structure with a propagation vector $\boldsymbol{Q}_2=(1/2, 1/2, 0)$. On the other hand, four intermediate phases III, IV, V and VI associated with each propagation vectors appear and then vanish successively with increasing

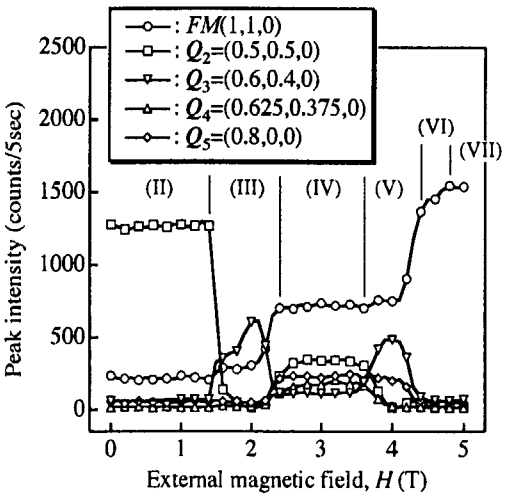

Fig. 1 Field dependence of several magnetic Bragg peaks of $TbNi_2Si_2$ under ambient pressure at 1.7K.

原子炉：JRR-3M　　装置：TAS-2(T2-4)　　分野：中性子散乱(装置)

field as well as ferromagnetic component (phase VII) grows step by step.

Figure 2 shows the schematic drawing of the magnetic Bragg peaks in the a^*-b^* reciprocal plane under ambient pressure and under 0.7GPa in various fields at 2K. In an ambient pressure, while according to Blanco *et al.*[3], two intermediate phases (corresponding to phases III and V in Fig.1) under zero-pressure at 1.7K

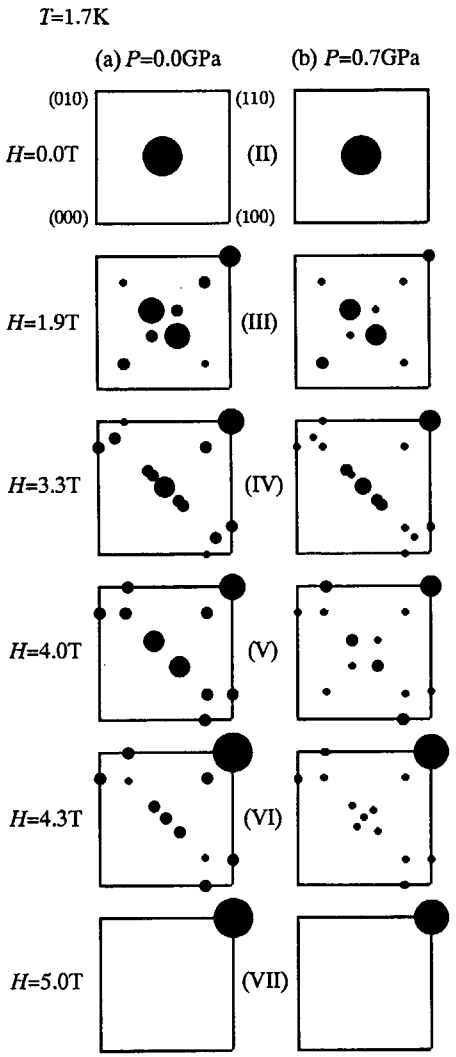

Fig. 2 Schematic drawing of the magnetic Bragg peaks in the a^*-b^* reciprocal plane under ambient pressure (a) and under 0.7GPa (b) in various fields at 1.7K

exists, we found new two phases (phases IV and VI) beside them. The phases III and V are characterized by vanishing of the peaks associated with propagation vector Q_2=(1/2, 1/2, 0) and by the appearance of four peaks with the vector Q_3=(1/2±τ, 1/2∓τ, 0) with τ=0.1 together with its higher harmonics. Particularly in the phase V the four peaks along the <110> direction vanishes except for an additional four peaks related to Q_5=(±0.8, 0, 0) and Q_5'=(0, ±0.8, 0). The phases IV and VI are characterized by the peaks associated with the same propagation vector Q_3, Q_5 and Q_5'. No peaks exhibits along <110> direction in both phases. For the phase IV the difference is the existence of another four peaks associated with Q_4'=(1/2±τ, 1/2∓τ, 0) with τ=0.125 together with its harmonics.

For pressure up to 0.7GPa in Fig. 2(b), no significant changes were shown up to 3.3T on the spin structure and the propagation vectors for the phases II, III and IV, but in the phases V and VI above 4T additional peaks were observed along <110> direction. The four peaks are indexed with Q_3' for the phase V in 4T, while the peaks for the phase VI in 4.3T are indexed with difference propagation vector Q_4'=(1/2±τ, 1/2∓τ, 0) with τ=0.125. The resurgence of the four peaks along <110> direction suggests that two independent domains are present. Expected domains include a single-Q magnetic structure and a double-Q one in this view point. In the case of the former, the domain is characterized by D_1 associated with Q_3, or the domain D_2 associated with Q_3', while for the latter both the domains appear[3]. Pressure seems to stabilize the other domain in relatively high fields.

Reference(s)

1) S. Kawano *et al.*, Physica B (1998) in press.
2) H. Fujii, T. Shigeoka, J. Magn. Magn. Mat. **90 & 91** (1990) 115-120
3) J. A. Blanco *et al.*, J. Magn. Magn. Mat. **97** (1991) 4-14

研究テーマ：　中性子スピンエコー分光器　（ＩＭＴ）

表題　：　改３号炉C2-2中性子スピンエコー分光器の改良

Improvement of Neutron Spin Echo Spectrometer at C2-2 of JRR-3M

T. Takeda, H. Seto, Y. Kawabata, D. Okuhara, T. Krist[1], M. Nagao[2], H. Yoshizawa[2], S. Komura[3],T. Ebisawa[4], S. Tasaki[4], M. Monkenbusch[5]

Faculty of Integrated Arts and Sciences, Hiroshima University, Higashi-Hiroshima 739-8521

1 Hahn-Meitner-Institut, Glienicker Str. 100, D-14109 Berlin, Germany

2 Institute for Solid State Physics, University of Tokyo, Tokai, Naka Ibaraki 319-1106

3 Faculty of Science, Ochanomizu University, Ootsuka, Tokyo 112-8610, Japan

4 Research Reactor Institute, Kyoto University, Kumatori, Sen-nan, Osaka, 590-04

5 Forschungszentrum Jülich,D-52428 Jülich, Germany

We have been improving a neutron spin echo spectrometer(NSE) at C2-2 cold neutron guide port of JRR-3M, JAERI[1]. We fabricated a new monochromater with the wavelength of λ = 7.14 A^{-1} which is a double reflection supermirror monochromator of Soller slit type like old one with λ = 5.9 A^{-1}. The monochromator consists of 12 supermirrors with the dimension of 76x112 mm^2. Each mirror is a sheet of silicon wafer with alternating layers of Ni and Ti metal sputtered on the wafer in Berlin and has a reflectivity of 60～90% over an angular range $\Delta\theta/\theta$ of about 35～42%. Performance tests of the monochromator at $2\theta_M$ =7.00° have been carried out after careful alignments. The polarized neutron flux was 4.2x10^5/cm^2s at the sample position when the neutron path in the first precession coil with the collimation of 30ϕmm is evacuated. λ = 7.14 A^{-1} and FWHM of its resolution $\Delta\lambda/\lambda$ = 18% were estimated from the neutron spin echo signal profile. The maximum Fourier time *t* grew up to 15 ns using the new monochromater as shown in Fig. 1.

In order to gain more neutron intensity, we replaced the spiral coils for the beam cross section of S = 30ϕmm with one for S = 50ϕmm and have prepared the spiral coils for S = 70ϕmm and S = 100ϕmm and a detector system with an assembly of 8 one-dimensional PSDs.

We improved the dancing floor in order to drive smoother the table for the 2nd precession coil, analyzer and detector and to set the scattering angle at the sample $2\theta_S$ by a computer control.

1) T.Takeda et al; J. Phys. Soc. Jpn. 65 Suppl.A (1996) 189-194.

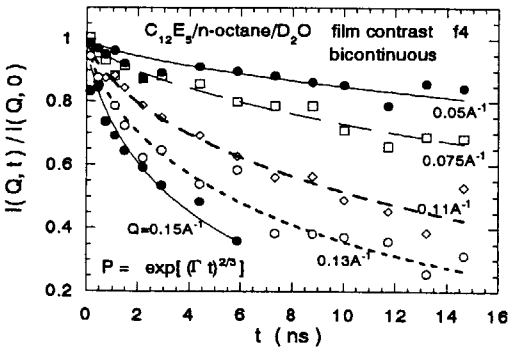

Fig. 1 Intermediate correlation functions $I(Q,t)$ obtained from our NSE experiments at JRR3 in the higher temperature bicontinuous microemulsion phase of the film contrast sample of the $C_{12}E_5$/n-octane/water system.

Facilities and Instruments
JRR-3M　N S E (C2-2)

Research field
9.装置技術　instrum.

研究テーマ：IMT
表題：T1-3ビーム孔での中性子線束評価

Estimation of the neutron beam flux at T1-3

Kenji OHOYAMA, Keiji NEMOTO, Masayoshi OHASHI† and Yasuo YAMAGUCHI

Institute for Materials Research, Tohoku University, Katahira, Sendai, 980-77

For evaluation of the performance of HERMES at the T1-3 hole, we estimated the neutron beam flux, Φ, by two different methods: measurremsnts of the direct beam and the incoherent scattering from a standard vanadium rod.

Open circles in Fig.1 show the intensity of the direct beam per 60 s versus the thickness of attenuators of acrylic plates at the sample position. The beam size was S=2 mm×20 mm=0.4 cm^2 at the sample position using a beam narrower. The wave length of the incident neutron is 1.8196 Å. The solid line in Fig.1 shows the result of the fitting procedure using the usual dumping function, $I_{obs} = I_0 Exp[-\alpha t]$. Here, α and t are the dumping factor and thickness of the attenuators, respectively. From the fitting procedure, the parameters are determined as I_0=6.5×10^5 n/60s and α=0.32 mm^{-1}, respectively. Since a ^{3}He detector (ϕ10mm, 8atm) was used for the measurements, the counting efficiency of the detector is roughly estimated as η=0.64 at λ=1.8196 Å. Thus, we calculated the beam flux at the sample position of HERMES, Φ_{direct}, as 4.2×10^4 n sec^{-1} cm^{-2} from I_0, S, and η.

Figure 2 indicates the 2θ dependence of scattering intensity of a standard vanadium rod whose diameter and effective length are ϕ5 mm and 20 mm. The absorption effect of the sample was corrected. The duration time of this measurement for each point was 19760 s. Some Bragg peaks of vanadium itself were observed which are denoted by the index in Fig.2. The increase of the intensity at low angle is due to air scattering. Since the incoherent scattering cross section of vanadium and the effective solid angle of a detector are 5.1 b[1] and 8.8×10^{-4} sr., the beam flux, Φ_v, was estimated as 2.7×10^4 n sec^{-1} cm^{-2}.

Φ_{direct} and Φ_v are consistent quite well. It should be pointed out that these values are the lower limit of the estimation because η is the higher limit of the detector efficiency. Therefore, although the estimation in this paper is too simple to obtain the accurate beam flux. the neutron flux of the monochromated beam at T1-3 is estimated as at least 3-4×10^4 n sec^{-1}cm^{-2}.

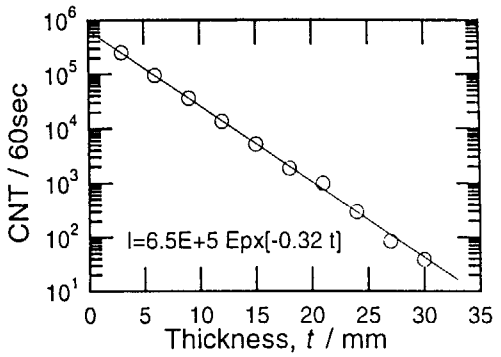

Figure 1: The intensity of the direct beam at T1-3

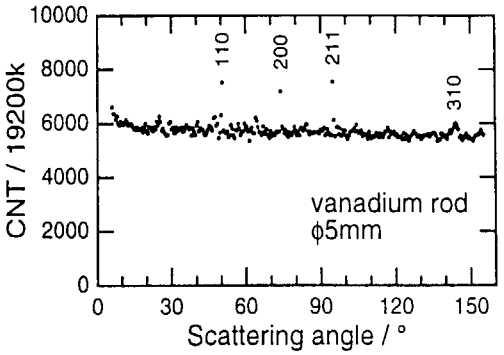

Figure 2: A scattering pattern of a standard vanadium($\phi = 5mm$) using HERMES.

References

[1] *Neutron diffraction* by Hishino in Japanese

† Present address: Faculty of Engineering. Yamagata University

JRR-3M, T1-3(HERMES), Instrument

研究テーマ：IMT、PONTA の整備
表　　題：Ef=14.7meV 熱中性子用水平集光型アナライザーの開発

Construction of Horizontally Focusing Analyzer for E_f=14.7 meV Thermal Neutrons

T. Mori[1], H. Kadowaki[2] and K. Kakurai[1,3]

[1]*Neutron Scattering Laboratory, ISSP, University of Tokyo, 106-1 Shirakata,Tokai 319-11, Japan*
[2]*Department of Physics, Tokyo Metropolitan University, Hchioji, Tokyo 192-0397, Japan*
[3]*CREST, Japan Science and Technology Corporation (JST), Tsukuba, Japan*

A fixed, horizontally focusing analyzer for thermal neutrons with 14.7meV energy has been designed and constructed. This type of analyzer allows one to gain intensity by sacrifying the Q-resolution, but retaining the original energy resolution. Hence it is suited for a Q-independent excitations, like e.g. crystal field excitations.

The design parameters are determined using computer simulations. The final design parameters for 14.7meV neutrons are:

Pyrolytic graphite (PG) crystals:

Size: 40x40 mm surface and 2mm thickness
Mosaicity: 2 degrees
Number of PG crystals: 15
Tilt angle for the horizontal focusing:±1.27 degrees from one column to the next.
Tilt angle for the vertical focusing: ±10 degrees for upper and lower row crystals.

The 15 PG crystals (PGC-X20) were purchased from Matsushita Electric and checked individually by neutron diffraction.

The desired tilt angles are realized by fixing the PG crystals on the precision machiened surfaces of the Cd-coated Aluminum columns. (see picture)

The preliminary test result using Vanadium incoherent scattering is shown in Fig.1. Fig.1a) shows the incoherent scattering measured with the only vertically bent analyzer.

Fig.1b) shows the same scattering measured using the new horizontally and vertically focusing analyzer under the same collimation condition. A gain in the intensity by a factor of ~4.3 can be observed without loss in the energy resolution.

Acknowledgements: We would like to thank Dr. Nishiki of Matsushita Electric for supplying us with numerous test crystals.

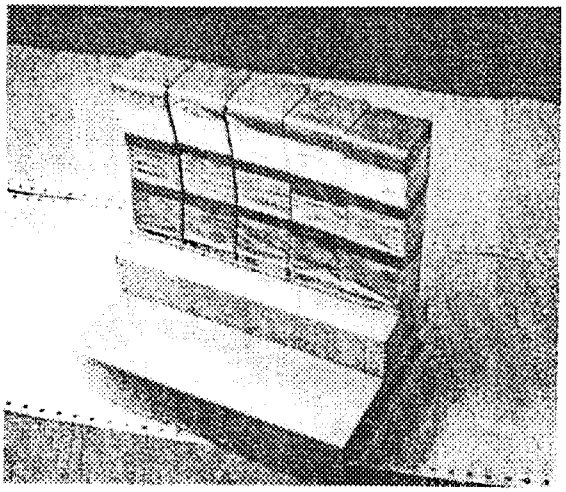

Picture: The horizontally focusing analyzer for E_f=14.7meV thermal neutrons.

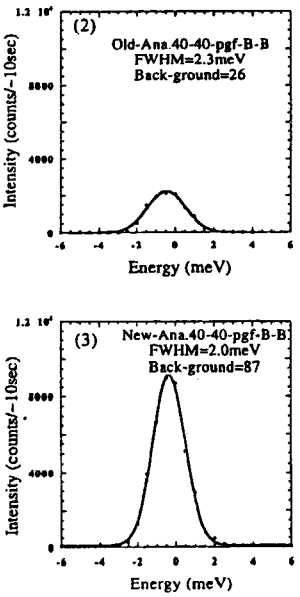

Fig.1: Incoherent scattering of Vanadium measured a) with the old, only vertically bent analyzer, and b) with the new horizontally focusing analyzer.

Reactor : JRR-3M　　Facility : PONTA (5G)　　Field : Instrumentation

研究テーマ:：生体物質の中性子回折による研究
表題：中性子イメージングプレートの最適化の実証

The actual proof of the optimization of Neutron Imaging Plate

Y.Karasawa and N.Niimura
Japan Atomic Energy Research Institute, Tokai, Ibaraki 319-1195, Japan

We have optimized the neutron imaging plate (NIP) by estimating a color center creation efficiency(ε_{cc}) experimentally and have already reported the preliminary results[1]. In case of the NIP Gd doped, the optimized NIP is realized when the thickness is 200μm, the molar ratio of PSL material (ϕ_{PSL}) is 0.6 at neutron wavelength 2Å . However, in the estimation of ε_{cc}, gamma-ray effect has not been considered even though it is rather large when ϕ_{PSL} is high.

The optimization of the NIP (Gd doped) was again tried. This time the gamma-ray effect has been carefully considered in the experimental arrangement. The BIX-1 was used for the experiment. In order to reduce the gamma-ray contribution as much as possible, the neutron beam, which was monochromatized by Si(111) firstly and diffracted by PG (004) secondly, was prepared. By irradiating this neutron beam on the NIP, ε_{cc} was estimated as previously reported[1] and the result is shown with the old one in Fig.1.

The old ε_{cc} increases monotonously with ϕ_{PSL}, but the present ε_{cc} tends to saturate around ϕ_{PSL} 0.5. Neutron sensitivity has been calculated by using the new ε_{cc}, and the optimized NIP is given, that is, ϕ_{PSL} is 0.5 when thickness is 200 μm and neutron wavelength is 2.1Å .

The actual proof for the optimization was examined by observing the Bragg reflections on the three different kinds of the NIPs which ϕ_{PSL} = 0.25, 0.5 and 0.75, respectively. Thickness of the three NIPs are the same and are 200μm. The Bragg reflections from a tetragonal hen egg-white lysozyme were measured with the above mentioned NIPs at BIX-II. The exposure time was two hours, neutron wavelength was 2.16Å and the distance between the NIP and the crystal was 30cm.

The results are as follows:
1) The obtained numbers of Bragg spots, whose intensities are higher than 2σ, are 20, 11 and 7 on the NIP of ϕ_{PSL} 0.5, 0.25 and 0.75, respectively.
2) Fig.2 shows the integrated intensity of the four Bragg spots taken on the NIPs of the different ϕ_{PSL} 0.25, 0.5 and 0.75.
It was proved that the optimized NIP provided the best diffraction pattern from the protein single crystal.

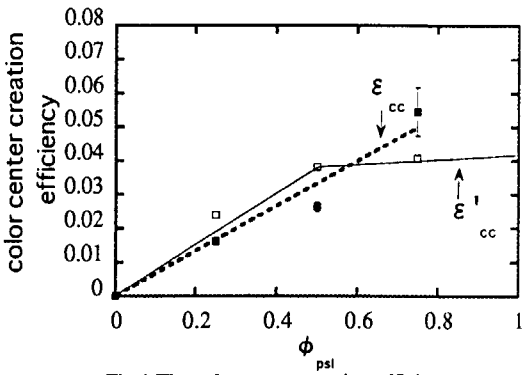

Fig.1 The color center creation efficiency
ε_{cc}: not corrected gamma-ray effect
ε'_{cc}: corrected gamma-ray effect

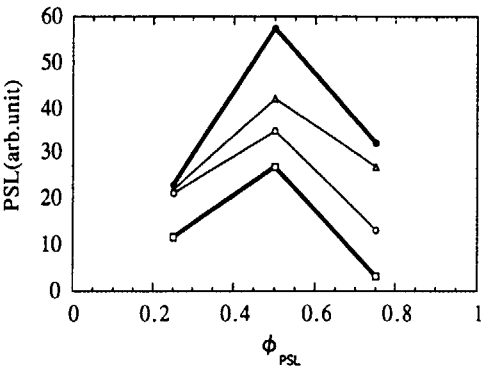

Fig.2 The integrated intensities of HEW-lysozyme Bragg spots

Reference

[1] Y.Karasawa, N.Niimura, A.Moriai, J.Miyahara, K.Takahashi, S.Tazaki, NSL -report 1996

原子炉：JRR-3M　　装置:BIX-I(1GA),BIX-II(T2-3)　　分野:中性子散乱(装置)

研究テーマ:生体物質の中性子回折による研究
表題:中性子イメージングプレートを用いたBIX Iでのバックグラウンド測定

Measurement of background at BIX I site using Neutron Imaging Plate

K. Kurihara, I. Tanaka, Y. Karasawa, N. Niimura

Advanced Science Research Center, Japan Atomic Energy Research Institute, Tokai, Ibaraki 319-1195

We are planing to replace the detector of BIX I in the reactor site of JRR-3M to a neutron imaging plate (NIP) which has been developed by our group[1]. We have measured background contributing to the NIP around the BIX I in order to shield the NIP effectively. The background comes from various origins: incoherent scattering neutron from a sample, air scattering of direct beam, leak from other diffractometers, and so on. We have measured the background in various kinds of conditions and evaluated the components of background.
50% of Gd doped 200μm thick NIP was put at the detector position and at 2θ = 40° and the distance from a sample was 200mm. The wavelength of neutron was 1.06Å. A tetragonal lysozyme crystal grown from D_2O solution was used as the sample whose volume was 4×3×3 mm^3.

The total background at the detector position was classified into four groups for the convenience of the planing of shielding method. The first one (B1) comes from the environment radiation. The second one (B2) consists of leak from other diffractometers and spectrometers. The third one (B3) is composed of leak from a flight tube at BIX I site and scattering of direct beam at a beam narrower and the air. The forth one (B4) comes from the sample itself. B1 was measured during suspension of the reactor. To determine the background of each group the NIP was exposed under three conditions such as 1) neutron beam on and with the sample, 2) neutron beam on and without the sample, and 3) neutron beam off.

The results are summarized in Table 1. B1 was 0.1 PSL/h/mm^2. Under the first condition the intensity of the total background (B1+B2+B3+B4) was measured to be 15.9 PSL/h/mm^2. B1+B2+B3 was obtained to be 13.4 PSL/h/mm^2 under the second condition. B1+B2 was determined to be 1.8 PSL/h/mm^2 under the third condition. According to these results B1, B2, and B3 were determined to be 1.7, 11.6, and 2.5 PSL/h/mm^2, respectively.

Shielding from γ-ray must be taken into account because NIP is sensitive to γ-ray. B1 could be restrained by shielding the diffractometer with B_4C and Pb bricks. 20mm thick B_4C reduces neutron background to 0.1%[2] and 30mm thick Pb does γ-ray background to 10%[3]. These bricks could also shield the NIP from the background originated from the beam narrower and the flight tube. The neutron background from the air scattering of direct beam might be repressed by putting a cylinder containing He gas just behind a sample on the way of direct beam. To reduce the forward direction γ-ray background we plan to attach 1mm thick Pb film in front of the NIP, which effect has been well proved[4, 5].

Experimental condition			Source	Intensity (PSL/h/mm^2)
No.	Sample	Beam		
1	with	on	B1-B4	15.9
2	without	on	B1-B3	13.4
3		off	B1,B2	1.8
			B1	0.1

Table 1 The experimental conditions and corresponding sources of the backgrounds and their intensities.

References

1) N. Niimura et al., Nucl. Instr. Methods **A349** (1994) 521-525.
2) Y. Karasawa, Master Thesis, Tohoku University (1995).
3) Y. Karasawa et al., This report **12** (1997) 91-92.
4) Y. Karasawa, Doctor Thesis, Tohoku University (1998).
5) S. Kumazawa et al., This report (1998).

原子炉:JRR-3M　　装置:BIX I(1GA)　　分野:中性子散乱(装置)

研究テーマ　：　生体物質の中性子回折による研究
表　　題　：　前方ガンマ線からの中性子イメージングプレートの遮蔽

Shielding Neutron Imaging Plate from Forward Direction γ-ray

S.Kumazawa, Y.Karasawa and N.Niimura
Advanced Science Research Center
Japan Atomic Energy Research Institute, Tokai, Ibaraki 319-1195, Japan

We have developed a neutron imaging plate (NIP), which has been widely adapted in the fields of neutron diffractometry and radiography. The NIP is superior to the conventional 2-dimensional ^{3}He type detector with respect to high spatial resolution, wide dynamic range, high capture efficiency for thermal neutrons, a wide sensitive area. There is, however, a problem to be overcome, when the NIP is applied in case that the background of γ-ray is comparable to that of neutrons. The NIP is sensitive to not only neutron but also γ-ray which becomes a background noise. The NIP can not discriminate γ-ray from neutrons, since the NIP is an integration type detector. For example, the background of γ-ray in the reactor site is about 10 times larger than that in the guide hall. It must be considered that the NIP is shielded from γ-ray in order that the neutron signal is effectively captured on the NIP.

For the environment γ-ray, the effective shield can be achieved by enclosing the NIP with Pb bricks of an appropriate thickness. For the γ-ray coming from a sample direction, the background noise of γ-ray will not be avoided by the above method. One of the improvement way is to put a thin Pb foil on the NIP surface. The Pb foil has high transparency for the neutron signal and dumps low energy γ-ray by the absorption effect. In this study, the effect of γ-ray shielding by using the various thick Pb foils is examined.

Diffraction spots, which consist of neutrons, and background around the spots, which consist of both neutron and γ-ray, were measured with the BIX-I diffractometer. The sample was hen egg-white lysozyme crystal and the exposure time of one frame was 20 min. The integrated intensities of several diffraction spots and the background intensities of corresponding spots were sampled. The integrated intensities of neutron diffraction spots do not depend on the thickness of Pb foil so much. The reduction of neutron intensities is about 3 % even if the thickness of Pb foil is 3 mm. On the other hand, the background intensities are exponentially dumped with increasing the thickness of Pb foil. Fig. 1 shows the neutron signal ratio to the background intensities. As shown in the figure, the ratios tend to saturate, when the Pb foil is thicker than 1.5 mm.

It is concluded that the signal to noise ratio is improved about twice, when a 1.5 mm thick Pb foil is put on the NIP surface.

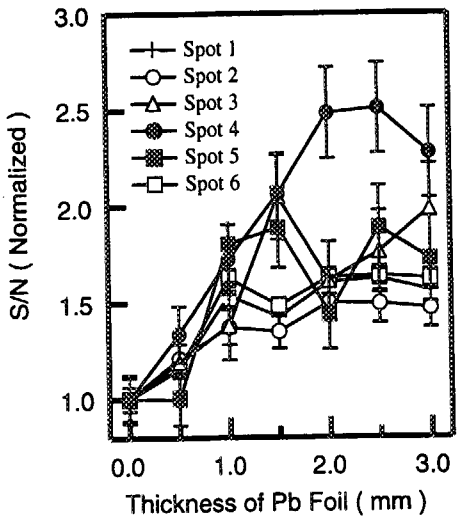

Fig.1 S/N ratios plotted against thickness of Pb foil.

原子炉：JRR-3M　　装置：BIX-I(1GA)　　分野：中性子散乱（装置）

研究テーマ：冷中性子散乱実験デバイスの開発

表題：低磁場制御磁気多層膜ミラーを用いた中性子偏極実験

Polarized Neutron Option using Multilayer Polarizer Controlled under a Very Low External Magnetic Field

K Soyama, M. Hino[1] and S. Tasaki[1]

Japan Atomic Energy Research Institute, Tokai, Ibaraki 319-11
[1]Research Reactor Institute, Kyoto University, Kumatori, Osaka 590-04

A polarized neutron experiment system has been developed to perform the neutron optics experiment and polarized neutron reflectometry at the reflectometer installed on the cold neutron triple-axis spectrometer (LTAS, C2-1) at JRR-3M.

A multilayer of Permalloy/Ge, which was coated in a magnetic field and can work under an external magnetic field less than 50 gauss[1)], was chosen as a spin polarizer and analyzer, because it can be set in a restricted space and control the neutron spin state easily and precisely.

The polarized neutron experiment system consisted of a spin polarizer, a π-flipper coil of Mezei type, and a spin analyzer. Each coil for the polarizer and analyzer consisted of a pair of solenoids : each was made from 200 turns of copper wire of 0.78mm^2 cross section and a inside diameter of solenoid was 90mm. The π-flipper coil consisted of a precession coil and a cancel coil of guide field. The guide coil consisted of a pair of multiwires : each was made from 20 turns of copper wire of 0.78mm^2 and had an area 700mm × 400mm. The current to produce the each magnetic field was controlled by a VAX computer (VAX-2600) which was connected with a remote computer.

Preliminary polarizing efficiency measurement of the multilayer polarizer was performed. Schematic draw of an experimental set-up is shown in Fig. 1. Monochromatic 3.6 Å neutrons were provided by a pyrolytic graphite monochromator (α=0.5°). The collimation of the beam was achieved by a couple of B_4C slits placed at a distance of 0.3 mm to 1.5 m a part. The magnetic field of 20 Gauss was produced at the polarizer and analyzer site between two solenoids, and 5 Gauss was produced at the central site of the guide coil. The polarized neutrons were detected by a position- sensitive proportional counter (ORDELA Moder-1150N) with a spatial resolution, FWHM of 1.0mm. The distance from the center of the polarizer to the detector was 765mm. The polarizing efficiency is defined through the following relation,

$$P = (N_{off} - N_{on}) / (N_{off} + N_{on})$$

where, N_{off} and N_{on} are the number of neutrons which are detected when the spin-flipper are on and off. The first obtained polarizing efficiency was 60%. The coil configuration and magnetic field at each polarizing component are being optimized to enhance the polarizing efficiency.

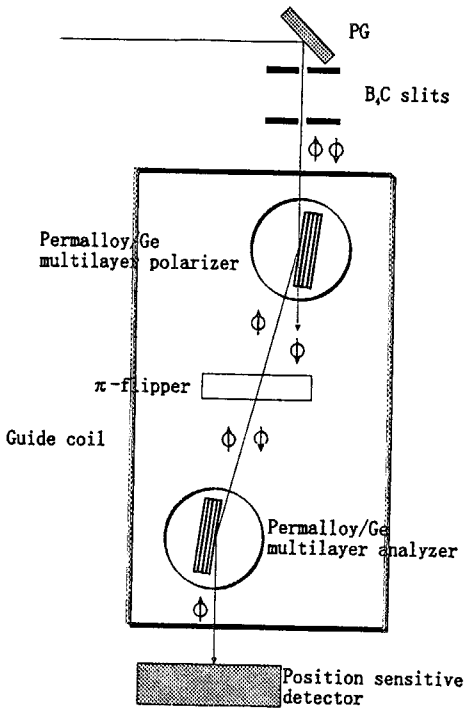

Fig.1 Schematic draw of an experimental set-up for polarization measurement

Reference

[1] T. Kawai, T. Ebisawa, S. Tasaki, T. Akiyoshi, M. Hino, N. Achiwa, Y. Otake and H. Funahashi, J. Phy. Soc. Jpn. **65** (1996) Suupl.A pp.245

原子炉：JRR-3M　　装置：LTAS(C2-1)　　分野：装置

研究テーマ：冷中性子散乱実験デバイスの開発研究

表題：NiCr 薄膜の特性測定

Characterization of NiCr Thin Film

K. Soyama

Japan Atomic Energy Research Institute, Tokai, Ibaraki 319-11

In order to enhance the reflectivity of Ni/Ti multilayer mirrors, many improvements have been conducted to decrease the interface roughness of Ni/Ti multilayers, because the large grained Ni layers with a structure of columnar growth lead to rough interfaces with an increase in the number of layers and decrease the reflectivity. In this study, the decrease of crystallization of Ni has been carried out by mixing chromium atoms to Ni layers.

NiCr monolayers with a thickness of 2000Å were deposited with changing Cr mixing ratios in Ni layers. The mixing ratios were 10%, 20%, 30%, 40% and 50%, which were determined by an electron spectroscope for chemical analysis (SHIMADZU ESCA-850). They were coated on Si substrates using an ion beam sputtering technique. The crystal structure and the critical angle of external total reflection of each NiCr monolayer were studied by high angle X-ray diffraction measurements and the neutron reflectometry.

X-ray measurements were performed in a θ-2θ mode using CuK_α radiation (λ=1.54Å). Figure 1 shows the observed patterns from the NiCr monolayers as a function of the Cr mixing ratio. At a mixing ratio of 10%, the Ni(111), Ni(200) and Ni(220) textures are clearly observed. The NiCr layer remains crystalline, and forms the cubic structure. At a mixing ratio of 20%, the intensity of the Ni(111) and Ni(200) peaks are reduced. On the other hand, the intensity of Ni(220) peak increases. At mixing ratios of 30% and 40%, Ni(220) orientation are still observed. The shift of Ni(220) peak to lower angle may be due to the solid solution of chromium atoms into Ni layers and the Ni(220) intensity reduction may be due to Ni alloying or amorphization. At a mixing ratio of 50%, Ni crystalline is not observed, and Cr_3Ni_2 (Tetragonal) peaks are recorded.

The critical angles of external total reflection of the NiCr monolayers were determined by neutron reflectivity measurements. They were performed in a θ-2θ mode using the reflectometer installed on the cold neutron triple-axis spectrometer (LTAS, C2-1) at JRR-3M. The wavelength was 3.8Å and the wavelength resolution was 1%. The dimension of the beam was 0.2mm in width and 10mm in height, and the collimation of the beam was achieved by B_4C and Cd slits placed at a distance of 1.5m apart. The obtained critical angles of total reflection were 0.0182Å^{-1}, 0.0176Å^{-1}, 0.0164Å^{-1}, 0.0156 Å^{-1} and 0.0144Å^{-1} as for the Cr mixing ratios of 10%, 20%, 30%, 40% and 50% respectively. The critical angle of total reflection is given by $\phi_c = \lambda(Nb/\pi)^{1/2}$, where N is the average number of atoms per unit volume and b is the bound coherent scattering length. Then Nb were 6.58E+10 cm^{-2}, 6.16E+10 cm^{-2}, 5.38E+10 cm^{-2}, 4.83E+10 cm^{-2} and 4.14E+10 cm^{-2}, which were derived from above mentioned results. They are decreased with an increase in the Cr mixing ratio.

From Fig. 1, it is clearly observed that the Ni(111) and Ni(200) textures are reduced, then it is expected to decrease the interface roughness of Ni/Ti multilayers by adding chromium atoms.

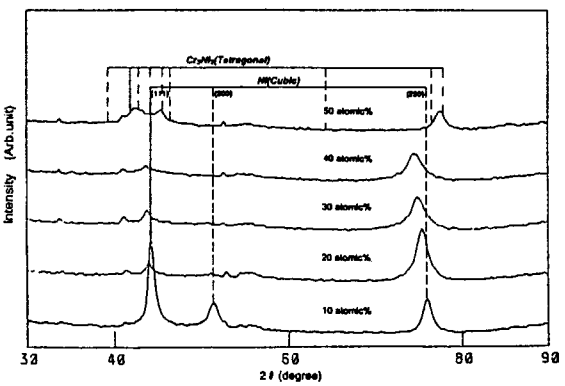

Fig. 1 X-ray diffraction patterns from the NiCr monolayers as a function of Cr mixing ratio.

原子炉：JRR-3M　　装置：LTAS(C2-1)　　分野：装置

研究テーマ：超低温の導入による中性子散乱の研究
表題：中性子散乱実験用液体ヘリウムフリー希釈冷凍機の開発

Development of liquid-He-free dilution refrigerator for the neutron scattering

Y. Koike[1], Y. Morii[1], T. Igarashi[2], M. Kubota[2], Y. Hiresaki[3] and K. Tanida[3]
1 Japan Atomic Energy Research Institute, Tokai, Ibaraki 319-1195, Japan
2 Institute for Solid State Physics, University of Tokyo, Roppongi 7-22-1, Tokyo 106-8558, Japan
3 Suzuki Shokan Co., Ltd. Kawagoe, Saitama 350-0833, Japan

We have developed a liquid-He-free dilution refrigerator named mK cryocooler[1] which is composed of a pulse-tube/GM hybrid cryocooler[2] and a JT dilution refrigerator unit[3].

Figure (a) shows the precooling process by the hybrid cryocooler. Typically, we precooled the cryostat to 4 K in about 1 day . As shown in Fig. (b), it took about 8 hours to cool down from 4 K to the lowest temperature, 77 mK in a preliminary experiment. At the lowest temperature, the ^{3}He circulation rate was estimated to be 1 x 10^{-4} mol/s from the flow rate of the rotary pump. The still temperature was about 0.8 K. The cooling power was 22 μW at 100 mK.

We used the mK cryocooler in the neutron scattering experiments at JRR-3M to study rare-earth compounds and uranium compounds. The lowest temperature achieved in the study was 41 mK.

The obtained lowest temperature will be lowered by improving the heat exchanger. For example, we are planing to install the step heat exchangers. The precooling time of one day to reach 4 K was too long. We installed the liquid N_2 pot on the pulse tube flange for quick precooling. At present, the gas handling system is operated manually. This causes another time consumption for researchers. Therefore, we will make a new gas handling system in order to control it by a computer, i.e. mK temperature can be achieved only by pushing a start switch. The two stage pulse tube refrigerator is preferred for our mK cyocooler because it has no mechanical vibration at all. We have a plan to replace the hybrid cryocooler by the two stage pulse tube refrigerator at the final phase of the development if a suitable cooling power become available.

We believe that the mK cryocooler benefit not only neutron scattering researcher but also any researchers in the various scientific fields.

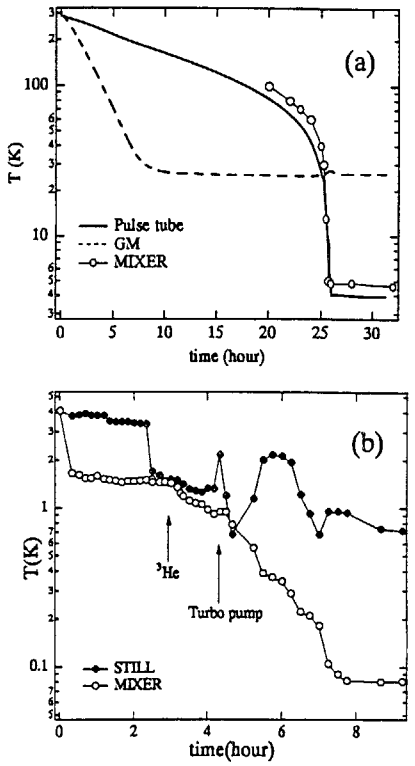

Fig. (a) Cooling test to 4. 2K and (b) condensation time of mixture gas and cooling test to the lowest temperature.

References

[1] Y. Koike et al., to be published in Proceedings of ICEC17 (1998).
[2] K. Tanida et al., Proceedings of ICEC16/ICMC (1996) 303.
[3] M. Sawano et al., Proc. 3. Japan-Sino Joint Seminar on Small Refrigerators and Related Topics, Okayama (1989) 27.;M. Kubota et al.,to be published in Proceedings of ICEC17 (1998).

原子炉：JRR-3M　　装置：TAS-2(T2-4)　　分野：中性子散乱（装置）

研究テーマ：高圧下での結晶構造・相変態の研究
表題：高圧下中性子散乱用サファイアアンビルセル

Sapphire-Anvil Cell for Neutron Scattering at High Pressure

A.Onodera, K.Furuno, Y.Ishii[1] and Y.Morii[1]

School of Engineering Science, Osaka University, Toyonaka, Osaka 560-8531, Japan
[1]Japan Atomic Energy Research Institute, Tokai, Ibaraki 319-1106, Japan

Recent development in high-pressure technique, that of diamond-anvil cell (DAC) in particular, has enabled to reach static pressure as high as 500 GPa. X-ray diffraction investigations of pressurized solids are now being carried out up to about 200 GPa. This owes to a combination of the synchrotron source and imaging plate, which permits to study a sample with a volume in the order of 10^{-3} mm^3. Such a small volume will not basically allow neutron scattering measurement where, normally, a volume larger than 10 mm^3 is needed. In fact, this requisite volume can be achieved with a piston-cylinder type apparatus as exemplified by our design [1].

Although the volume requirement can be answered, the highest attainable pressure is limited to a level of a few GPa as far as the piston-cylinder type apparatus is used. To reach higher pressure, opposed anvil designs, DAC for instance, should be employed. With DAC, however, the volume of the sample to be studied is very small. Enlarging the volume within DAC, in turn, costs extraordinarily high.

An alternative way is to use sapphire as the anvil material. The mechanical properties of sapphire are inferior to those of diamond, but the maginitude in the mechanical differences is about an order. In addition, for the same sizes, sapphire is less expensive than diamond by about one order of magnitude.

Under the backgrounds described above, we have designed a sapphire-anvil cell (SAC) for neutron scattering. The cell simply consists of a minipress and a pair of opposed sapphire anvils. A sample with a volume of 2 mm^3 can be studied. The volume is believed to be adequate for neutron scattering to be performed if supermirror is installed at the neutron facility. The pressure attainable with this specific SAC has not been assessed. Instead, we have undertaken prototype studies using small-sized anvils.

The prototype anvil measures 5 mm in diameter and 3 mm in height. The volume of the sample studied is about 10^{-2} mm^3. In principle, the pressure attainable with the opposed anvils is governed by the mechanical strength of the material employed for the anvil, the area of top face, the angle for taper from the top face down to the flank, the mechanical properies of the gasket, and some other issues. Of these, the most important is the taper angle. By fixing the top face at 1 mm in diameter, by aligning the compression axis parallel to the crystallographic *c*-axis, and by using enrolled Cu plate as the gasket, we have studied five different designs with different taper angles. The attainable pressures for each anvil design was known by monitoring the pressure from shift of fluorescence of ruby which was incorporated into the sample space.

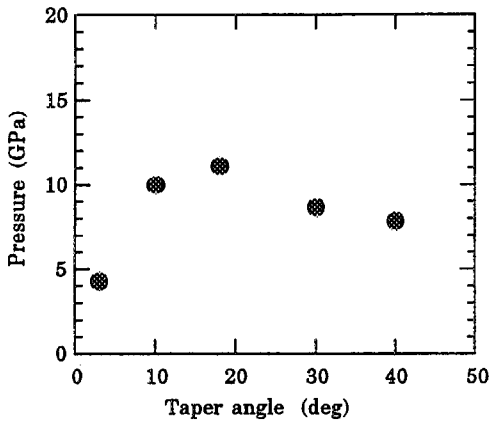

Fig. 1. Pressure generation with different tapers.

Figure 1 shows average of maximum pressure obtained from total of at least five experiments for each anvil design. It appears that the tapering angle is optimized between 10 and 18°. This experimentally derived optimization turned out to be in good agreement with our finite-element analysis. The optimum angle can change relative to the gasket as well as the sample materials.

Reference

[1] A.Onodera *et al.*: Jpn.J.Appl.Phys., 26 (1987) 152.

原子炉：ＪＲＲ－３Ｍ　装置：ＴＡＳ－２(Ｔ２－４)　分野：中性子散乱(装置)

1. 中性子散乱 (Neutron Scattering)

7) 生物学 (Biology)

This is a blank page.

課題名：中性子小角散乱法による昆虫リポホリンの構造解析
表　題：昆虫リポホリンの中性子小角散乱

Small-Angle Neutron Scattering of Insect Lipophorin

C. KATAGIRI, M. IMAI*, M. SATO† and Y. ITO§

Institute of Low Temperature Science, Hokkaido University, Sapporo 060
**Institute for Solid State Physics, University of Tokyo, Tokai, Naka, Ibaraki 319-11*
†Graduate School of , Yokohama City University, Yokohama, Kanagawa 236
§Faculty of Liberal Arts and Education, Yamanashi University, Koufu 400

Lipophorin is a major lipoprotein in insect blood and serves as a reusable shuttle to transport various lipids such as diacylglycerol and hydrocarbons between tissues. In resting adult locusts, lipophorin usually exists as high-density lipophorin (HDLp, r=1.10g/ml), a spherelike particle with a particle weight of about 6.0×10^5 and contains two apoproteins and 40% (w/w) lipid. At the commencement of long-distance flight, adipokinetic hormone is released from the corpus cardiacum and stimulates diacylglycerol uptake from the fat body by HDLp. Diacylglycerol is utilised as fuel for long-distance flight. Simultaneously, about 9 molecules of a third apoprotein associate with HDLp, which results in the transformation of HDLp to low-density lipophorin (LDLp, r=1.05g/ml). The LDLp contains about five times more diacylglycerol than HDLp. In HDLp, diacylglycerol locates at the middle layer of the particle surrounded by a spherical micellar arrangement of the outer hydrophilic surface[1,2,3]. The detailed knowledge of the molecular organisation (particularly location of diacylglycerol) of the LDLp is essential to understand the mechanism of the transformation of HDLp to LDLp. The small-angle neutron scattering study with H_2O/D_2O contrast variation was performed on the locust LDLp. Fig. 1 demonstrates Guinier plots of the scattering curves of LDLp of which diacylglycerol were deuterated or not.

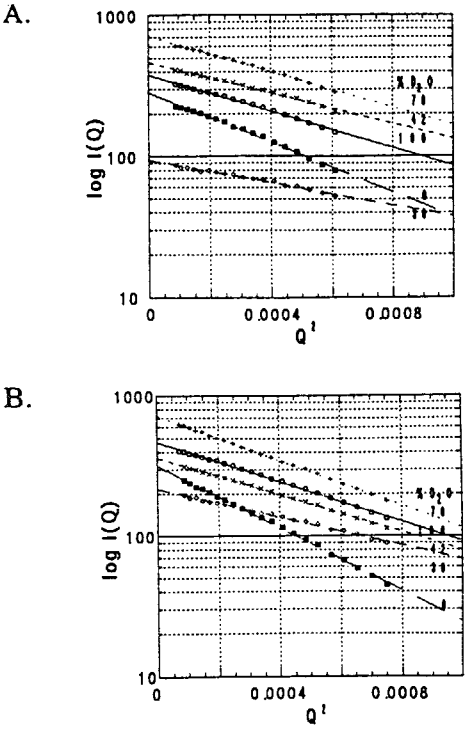

Fig. 1 Guinier plots of small-angle neutron scattering curves of locust LDLp of which diacylglycerol was deuterated (A) or not (B).

References

1)C. Katagiri *et al.*, *Biochem.* **30** (1991) 9675.
2)C. Katagiri, *J. Crystallographic Soc. Jpn.* **36** (1994) 162 [in Japanese].
3)C. Katagiri *et al.*, *Activity Report on Neutron Scattering Research* 3 (1996) 208.

Reactor: JRR-3M　Facility: SANS-U(C1-2)　Field: 5.生物 Biology

研究テーマ：リポホリン
表題：昆虫リポホリンによる炭化水素の取り込み

Uptake of Hydrocarbons by Insect Lipophorin

C. Katagiri, S. Fujiwara[1], I. Tanaka[1], N. Niimura[1], S. Koizumi[1], M. Sato[2] and Y. Ito[3]

Institute of Low Temperature Science, Hokkaido University, Sapporo 060-0842
[1]Advanced Science Research Center, JAERI, Tokai, Ibaraki 319-1195
[2]Graduate School of Yokohama City University, Yokohama, Kanagawa 236-0027
[3]Faculty of Liberal Arts and Education, Yamanashi University, Koufu 400-0016

Since lipids are not water soluble, they are carried in blood as lipoproteins, macromolecular particles in which the lipids are complexed with a variety of apoproteins. Lipoproteins from different animals have basically a common molecular architecture. The surface is covered with hydrophilic groups of phospholipids and apoproteins, whereas the core contains apolar lipids. Despite the common structural organisation, lipoproteins vary in physiological function, chemical composition, and metabolism. Mammalian lipoproteins transport mainly triacylglycerol and cholesterol esters and are metabolised in peripheral cell and liver. An insect lipoprotein, lipophorin, works as a reusable shuttle to transport diacylglycerol and hydrocarbons from the sites of synthesis, absorption, and storage to sites of utilisation. Diacylglycerol is utilised as a fuel for flight. Hydrocarbons protect insects from desiccation at the cuticular surface.

Lipophorin forms a sphere-like particle of about 170-Å diameter with a particle weight of about 6.0×10^5. All phospholipid constituents of the lipophorin are located in the outer surface with apoprotein. The hydrocarbon component is located in the core of the particle. In the present study, we aimed to observe the process of the transportation of hydrocarbons by the lipophorin. For this purpose, we purified the silkworm pupal lipophorin which does not contain hydrocarbons, and incubated it with the cockroach integument, the site of hydrocarbon synthesis. The structural changes from the hydrocarbon-free to hydrocarbon-containing lipophorin were detected by time-resolved small-angle neutron scattering apparatus (SANS-J). Although the hydrocarbon-free lipophorin is known to take hydrocarbons up *in vitro* from cockroach integument, appreciable changes including profiles (Fig. 1) and Rg (data not shown) were not found during incubation. To overcome this problem, we are currently attempting to modify the incubation procedures.

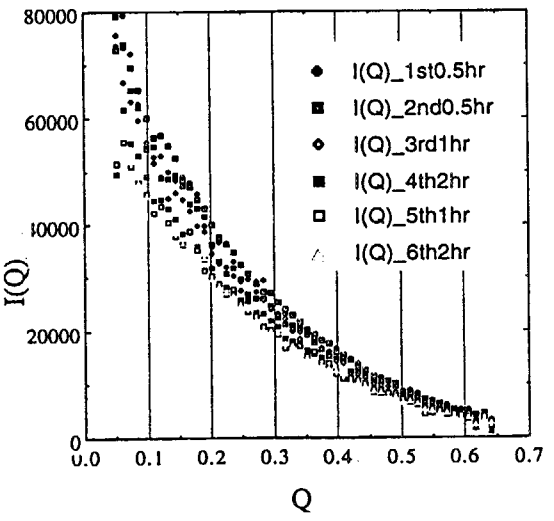

Fig. 1 Time-reolved small-angle neutron scattering profiles of hydrocarbon-free lipophorin which was incubated with cockroach integument.

原子炉：JRR-3M　装置：SANS-J (C3-2)　　分野：中性子散乱(生物)

課題名：中性子小角散乱によるシャペロニンGro-ELの構造と機能の研究

表　題：シャロペニンGro-ELからの中性子小角散乱

Small Angle Neutron Scattering from chaperonin Gro-EL

M. Harada, K. Ichimura*, I. Tanaka#, N. Niimura#, H. Kihara†

Department of physics, Jichi Medical School, minamikawachi-machi, Tochigi 329-04, Japan

*Department of Biochemistry, Dokkyo University School of Medicine, mibu, Tochigi 321-02, Japan**

Advanced Science Reserch Center, Japan Atomic Energy Research Institute, Tokai, Ibaraki 319-11, Japan#

Physics Laboratory, Kansai Medical University, Hirakata 573, Japan†

Chaperonins are proteins that mediate the folding of denatured protein or help the newly synthesized polypeptides to fold. Gro-EL, the chaperonin of *Escherichia coli*, consists of 14 subunits of relative molecular weight 57,000. These subunits are arranged in two heptameric rings stacked back to back. The ring has an outer diameter of 137Å and the combined cylindrical particle has a length of 146Å. The central cavity has a circular mouth of 45Å in diameter.[1] The binding site of the substrate protein has not been yet identified. Contrast variation methods using a small-angle neutron scattering(SANS) are very effective to determine the substrate-binding site on the partially deuterated complex of Gro-EL with substrate protein.

The SANS experiments on Gro-EL were carried out in the 100%,75%,25% and 0%D_2O solutions at 20°C. The sample solution contained the purified Gro-EL(9.0mg/ml), 100mM KCl and 50mM Tris-Cl (pH7.4). Figure 1 shows Guinier plots for Gro-EL in the 100%D_2O solutions. The least-squares fitting for the100%, 75%, 25% and 0%D_2O solutions showed 62.5(0.5)Å, 62.5(0.5)Å, 67.5(2.8)Å and 63.9(1.4)Å of the radius of gyration(Rg). These values are consistent with the calculated Rg of 63.6Å from the crystal coordinates.[1] For the scattering curves in the 100%D_2O solution, model fitting was done by assuming the right hollow cylinder. The parameters evaluated by a least squares fitting were height H=120.9Å, outer radius R_1=69.5Å and inner radius R_2=15.5Å. The calculated scattering curve is shown in Fig.2(solid curve). The another model in which the cylindrical cavity was partially filled with a plug was also examined. The parameters evaluated with this model were height H=130.3Å, outer radius R_1=65.9Å , inner radius R_2=30.5Å and the plug length L=58.4Å. The calculated scattering curve is also shown in Fig.2(dotted curve). Of the two models, the model that the cylindrical cavity was partially filled with the plug showed a good agreement with the experimental data.

Reference

1) K.Braig, et al., Nature, Vol.371, 578-586 (1994)

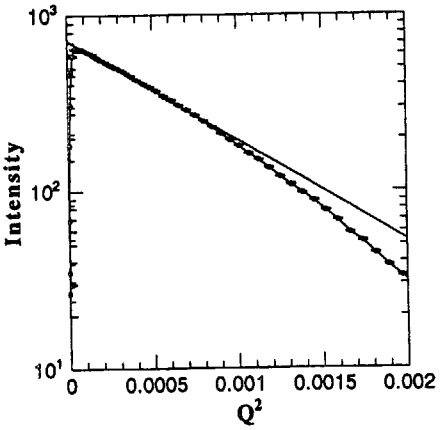

Fig. 1 Guinier plot for chaperonin Gro-EL

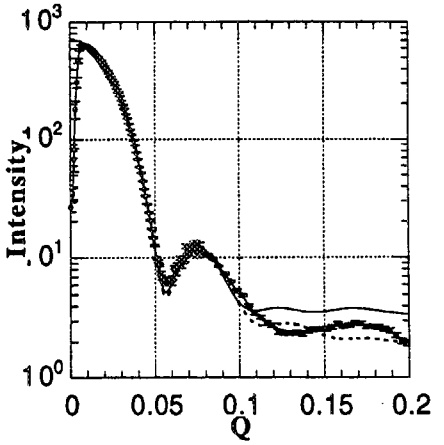

Fig.2 Small-angle neutron scattering from chaperonin Gro-EL.

Facilities and Instruments
JRR-3M SANS-U (C1-2)

Research field
biology

研究テーマ：中性子溶液散乱法によるカイコ細胞質多角体病ウイルスの構造研究
表題：中性子小角散乱法によるカイコ細胞質多角体病ウイルスの構造研究

Small-Angle Neutron Scattering Study on Bombyx mori Cytoplasmic-Polyhedrosis Virus

M. Sato, M. Tomita[1], M. Imai[2], N. Tanaka[3], and Y. Ito[4]

Graduate School of Integrated Science, Yokohama City University
Department of Chemistry for Materials, Mie University[1]
Neutron Scattering Laboratory, ISSP, The University of Tokyo[2]
Faculty of Bioscience and Biotechnology, Tokyo Institute of Technology[3]
Department of Physics, Faculty of Liberal Arts and Education, Yamanashi University[4]

Bombyx mori cytoplasmic-polyhedrosis virus (BmCPV) is characterized by the production of hexahedral/icosahedral occlusionbodies, where thousands of BmCPV particles are included. BmCPV is a biological supramolecular particle with a molar mass of about 10^8 and consists of RNA and protein. Elucidation of the structure-function relationship of the virus particle awaits the structural analysis by small-angle neutron scattering (SANS) using the contrast variation method.

SANS experiments were carried out by SANS-U, installed at the C1-2 beam port of the JRR-3M reactor, in 0%, 50%, 75% and 100% D_2O solutions with a virus concentration of 6.5mg/ml. The temperature of the solutions were kept at at 6℃. Wavelength of neutron, λ is 7 A ($\Delta\lambda/\lambda = 0.1$). 2D-PSD was located at the positions of 4 and 12m. The two data-sets obtained with the different PSD positions were merged together, after subtracting background scattering, to cover a q range from 0.002 to 0.08A^{-1}. The merging-R values lay between 0.029 to 0.058. The merged data were then corrected for measurement time, transmission, sample-cell thickness and virus concentration.

The Guinier plot of each data-set is linear, showing that BmCPV particle is homogeneous with respect to the size and shape of the virus. The Linear $I(0)^{1/2}$- D_2O% plot estimates that the mean scattering density of the particle is corresponding to 49.3% D_2O level, which is supported experimentally by the fact that 50% D_2O data showed no significant scattering. Since the mean scattering densities of RNA and protein are corresponding to 40% and 65% D_2O levels, respectively, the estimated mean scattering density means that the virus contains almost equal amounts of RNA and protein.

Figure shows the SANS profiles measured at 0%, 75%, and 100% D_2O concentrations. 50% D_2O data-set was omitted due to the fairly weak scattering. The facts that the shapes of the profiles differ from each other in D_2O content and have four or five subsidary maxima reflects inhomogenious scattering density distribution within the particle. The Stuhrmann plot gives a linear relationship with a negative slope, indicating that the center of mass coincides with that of the particle and scattering density of the peripheral region is lower than that of the central region. This means the lower scattering density region corresponds to the protein and the central higher density region to RNA.

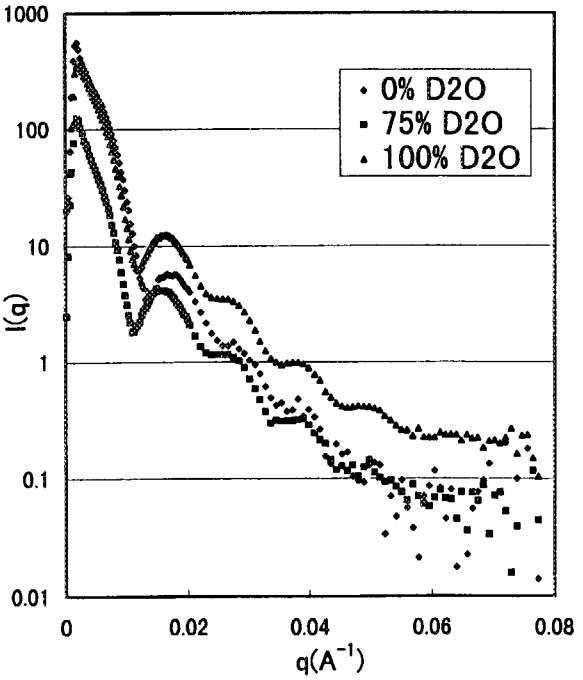

Figure SANS Profiles of BmCPV in 0%, 75% and 100% D_2O Solutions.

JRR-3M, SANS-U (C1-2), Biology

研究テーマ： タンパク質の結晶化機構：オリゴマーの形成とその役割
表題： サーモライシンの結晶化機構：小角中性子散乱による研究

Mechanism of Crystallization of Thermolysin: A Small Angle Neutron Scattering Study

H. Ooshima, K. Igarashi, J. Kato, S. Fujiwara[1], I. Tanaka[1] and N. Niimura[1]
Department of Bioapplied Chemistry, Osaka City University, Osaka 558-8585, Japan
[1]Japan Atomic Energy Research Institute, Tokai, Ibaraki 319-1195, Japan

The crystallization of protease thermolysin proceeds through two step; formation of primary particles (oligomers) and crystal growth by highly ordered aggregation of the primary particles [1]. In the present work, size of the primary particles and its distribution were investigated by small angle neutron scattering (SANS).

SANS experiments were performed at 5 °C for supersaturated and undersaturated thermolysin - D_2O solution. Supersaturation was varied with pH. Wavelength of neutron was 7 Å.

Figure 1 presents a Guinier-plot obtained for the undersaturated solution (3 mg/mL, pH 12.5). Rg was estimated as 16.8 Å, which corresponds to the size of monomeric molecule. This means that thermolysin was dissolved completely in the undersaturation condition. For the super-saturated solution (3 mg/mL, pH 7.5), a different scattering pattern was obtained as shown in Figure 2, indicating the presence of oligomers with uniform size. The estimated Rg was 75.5 Å. The size corresponds to the size of three unit cells (36 thermolysin molecules). This result suggests that growth unit in the crystallization of thermolysin is the oligomers with 75.5 Å of Rg.

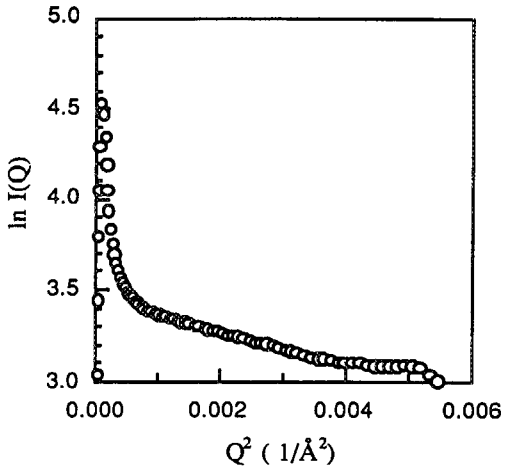

Fig. 1 a Guinier plot of scattering data (thermolysin: 3 mg/mL, pH 12.5)

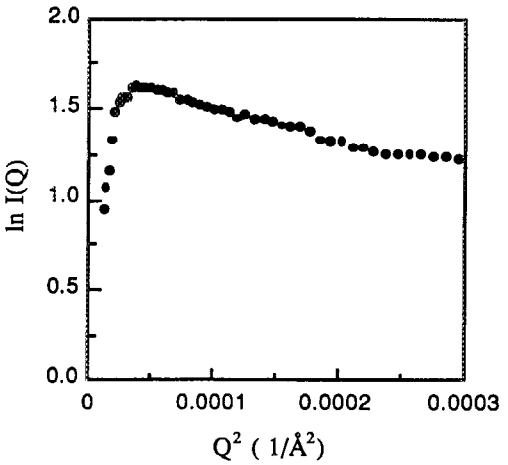

Fig. 2 a Guinier plot of scattering data (thermolysin: 3 mg/mL, pH 7.3)

Reference(s)

[1] G. Sazaki et al., Journal of Crystal Growth, 130, 357-367 (1993).

原子炉：JRR-3M　　装置：SANS-J(C3-2)　　分野：中性子散乱（生物）

研究テーマ：中性子回折による生体物質の構造研究
表題：pH 4.9 で作成したニワトリ卵白リゾチーム単結晶の中性子回折測定

Neutron Diffraction Measurements of Single Crystrals of Hen Egg-White Lysozyme grown at pH 4.9

S. Fujiwara, Y. Yonezawa', Y. Karasawa, Y. Minezaki, I. Tanaka, and N. Niimura

Japan Atomic Energy Research Institute, Tokai, Ibaraki 319-1195
'Tsukuba College of Technology, Tsukuba, Ibaraki 305-0821

Hydrogen atoms in a protein play an essential role in performing specific functions of the protein, as well as contribute through hydrogen-bond network to the stability of the protein. Particularly, it was suggested from calorimetry measurements that pH dependence of charge distribution of the protein may have important effects on thermodynamic characterization of the proteins[1]. It is thus important to study the pH dependence of protonation of amino acid residues in the protein, in order to elucidate the relationship between structural data and thermodynamic data. Neutron diffraction is unique and powerful in locating the positions of the hydrogen atoms in the protein. We have started a project which explore the protonation of amino acid residues in the protein at various pH.

We chose hen egg-white (HEW) lysozyme as a model protein. Crystals of HEW lysozyme were grown in D_2O at various pH with a concentration gradient method[2]. It was found that the crystals can be grown at pH between 3 and 7. The space group of the crystals was $P4_32_12$, and the cell parameters were a=b=7.91nm and c=3.66nm. Quality of the crystals was checked extensively by measuring the neutron diffraction patterns with BIX-2[3]. The best crystal of HEW lysozyme grown at pH 4.9 was selected as a starter, since the optimum pH of lysozyme activity is 5.0. (The structure of the protein at pH 7 was solved with Laue method[4].) The size of the crystal was about 2 mm×1mm×1 mm.

Data collection of neutron diffraction is the most time-consuming step, so an efficient data-collection strategy should be considered. The strategy could be different in different samples. We measured the neutron diffraction patterns of the lysozyme crystal using the oscillation method with the oscillation range of 0.2, 0.4, and 0.6 degrees. The data that covered the range of 2.4 degrees were collected. We analyzed these data with DENZO and SCALEPACK[5]. It was found that the number of independent reflections was the largest in the data obtained by 0.4 degrees' oscillation. We thus employed the oscillation method of 0.4 degrees to collect the data from the HEW lysozyme crystal. We have started the data collection, and the measurement is now under progress. So far, about 1500 independent reflections were collected.

References

1) S. Kidokoro: Personal communication.
2) M. Ataka and T. Katsura: JAERI Memo 61 (1992) 92-213.
3) S. Fujiwara et al.: Physica B (in press)
2) N. Niimura et al.: Nature Struc. Biol. 4 (1997) 909-914.
5) Z. Otwinowski and W. Minor: Methods Enzym. 276 (1997) 307-326.

原子炉：ＪＲＲ－３　　BIX - II（Ｔ２－３）　　分野：生物

研究テーマ：生体物質の中性子回折による研究
表題：BIX-IIを用いた斜晶系ニワトリ卵白リゾチームのデータ収集

Data collection of triclinic hen egg-white lysozyme by BIX-II

Y.Minezaki, S.Fujiwara, N.Niimura

Advanced Science Research Center, Japan Atomic Energy Research Institute, Tokai, Ibaraki, 319-11

We have already reported the neutron crystal structure analysis of tetragonal hen egg-white (HEW) lysozyme, and the positions of 960 hydrogen atoms in the protein and 157 bound water molecules were determined[1]. The discussion of the nature of the bound water molecules of HEW lysozyme is now under way. It is very interesting to know how many bound water molecules among 157 determined are inherent in HEW lysozyme. The neutron crystal structure analysis of triclinic HEW lysozyme (P1, a=27.2A, b=31.9A, c=34.2A, alpha=88.4, beta=108, gamma=111.7) might provide the answer. We have planned the neutron crystal structure analysis of triclinic HEW lysozyme for that purpose and tried the data collection by using BIX-I and BIX-II. In this report, we will show the preliminary results of data collection method of triclinic HEW lysozyme by using BIX-II.

We have used a single crystal, the size of which was 1.5*1.5*1.5 mm3. The crystal was kindly provided by Harata Group of NIBHT. The very high resolution X-ray structure analysis of triclinic HEW-lysozyme has been already reported by his group[2].

One example of the diffraction pattern obtained by BIX-II for 16 hours exposure time is shown in Fig.1. The minimum d-spacing among the observed diffraction spots is 1.8 A. In order to estimate the proper exposure time for the measurement, we collected images of one hour exposure time 20 times separately. We added two images, three images, and so on till 20 images in the computer. Each resultant corresponds to the image of two hours exposure data, three hours and so on to 20 hours, respectively. From these resultants images we concluded that the minimum exposure time to obtain the maximum number of Bragg reflections is 4 hours.

We have examined the scan condition for the data collection. Four kinds of method, A) 0.2 degree step scan method (where the sample is still during the measurement and after the measurement the sample is rotated by 0.2 degree), B) 0.2 degree sample oscillation during the measurement, C,D)1.0 degree oscillation and E) 1.6 degree oscillation, have been tried. In each measurement, the total sample crystal rotation angle was 2.0 degree and total measurement time of 2.0 degree was kept constant. All the data reduction processes were carried out by using Mac-Denzo. The parameter 'mosaicity' was chosen as 2.0 degree or 1.3 degree. Total number of the collected Bragg reflections and I/s were summarized in Table 1.

It is concluded from the Table that for the triclinic HEW lysozyme; 1) the smaller the sample oscillation is, the higher I/s is and the more the obtaied number of Bragg reflections is., and 2)there is not so much difference between 0.2 degree step scan method and 0.2 degree sample oscillation method.

Table 1

set name	scan method	mos.	total	mean-I	mean-s	mean-I/s
A-set	0.2 step		763	15989	1436.7	10.8
B-set	0.2 osc.	2.0	712	16204	1436.7	10.6
C-set	1.0 osc.	2.0	675	11325	1553.6	7.34
D-set	1.0 osc.	1.3	605	11186	1403.8	7.61
E-set	1.6 osc.	1.3	579	10640	1527.2	6.94

References

[1] N.Niimura, Y.Minezaki, et al., NATURE structural biology 4 11 (1997) 909-912.
[2] K. Harata, et al., PROTEINS:Structure, Function, and Genetics 30 (1998) 232-243.

Fig.1

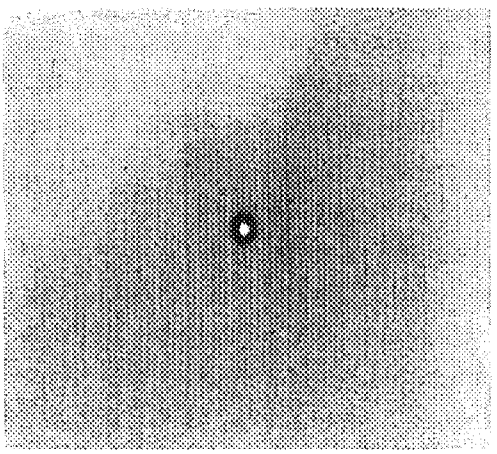

原子炉：JRR-3M　　装置：BIX-II(T2-3)　　分野：中性子散乱（生物）

研究テーマ： リン脂質膜構造形成においてコレステロール分子の果たす役割に関する研究
表題： リン脂質膜構造形成においてコレステロール分子の果たす役割に関する研究

Study on Cholesterol's Roles of a Structure Formation in Phospholipid Membranes

T. Adachi#, H. Takahashi, M. Imai* and I. Hatta

Department of Applied Physics, Nagoya University, Chikusa, Nagoya 464-8603, Japan
**Institute for Solid State Physics, University of Tokyo, Tokai, Naka, Ibaraki 319-1195, Japan*
#Institute of Materials Structure Science, High Energy Accelerator Research Organization, Tsukuba, Ibaraki 305-0801, Japan

A ripple phase is well known in phospholipid systems, especially in dipalmitoylphosphatidylcholine (DPPC). The ripple structure exhibits a periodic undulation of a bilayer, but its detailed structure has not yet been determined. Incorporation of cholesterol into a phospholipid bilayer affects the nature of the bilayer. It has been reported that the periodic spacing of the ripple structure increases as cholesterol concentrations rise. Although several explanations of this mechanism have been proposed, it has still not elucidated. The most important point to understand the cholesterol effect on the ripple structure is to determine the distribution of cholesterol in the bilayers. Thus, in order to make clear the cholesterol distribution in the ripple structure, small angle neutron diffraction experiments were performed on a DPPC-cholesterol system.

We investigated the DPPC bilayers containing 0, 5, 10 and 15 mol% cholesterol. Four samples were prepared.

Small-angle scattering intensity was proportional to about Q^{-2} as shown in Fig. 1. It suggests that a scatterer takes 2-dimentional structure, and the slope undergoes a change by the cholesterol concentration. Two reflections were observed around Q=0.04 and 0.09 $Å^{-1}$ as shown in Fig 2. These two peaks come from a ripple structure and a lamellar structure, respectively. The detailed analysis is now in progress.

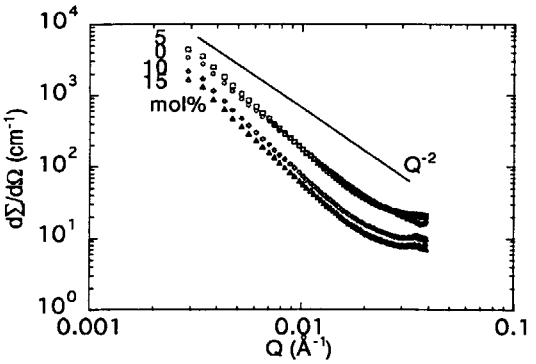

Fig. 1 Small-angle neutron scattering from DPPC-d62/cholesterol systems.

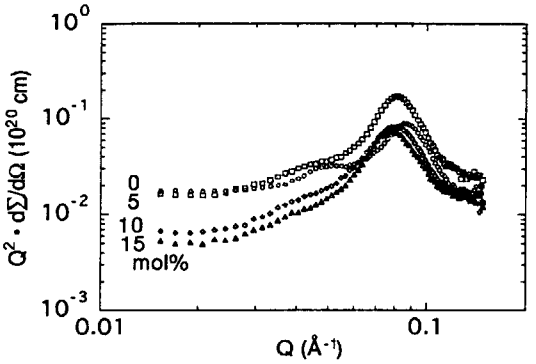

Fig. 2 Reflections from a ripple structure and a lamellar structure of DPPC-d62/cholesterol systems.

JRR-3M, SANS-U, 7. biology

研究テーマ：グリセロール水溶液中の短鎖ホスファチジルコリンミセルの構造
表題：ホスファチジルコリン/グリセロール/水系におけるグリセロール分子の分布

Distribution of Glycerol Molecules in Phosphatidylcholine/Glycerol/Water System

H. Takahashi, M. Imai[1], Y. Matsushita[1], and I. Hatta

Department of Applied Physics, Nagoya University, Chikusa-ku, Nagoya, 464-8603 Japan
[1]Neutron Scattering Laboratory, The Institute for Solid State Physics
The University of Tokyo, Shirakata, Tokai, Naka, Ibaraki, 319-1195 Japan

Glycerol protects living organisms and tissues from cryoinjury. It is generally believed that an important site of action of glycerol is cell membranes where phospholipid bilayers are a fundamental structure. Hence, the interaction between glycerol and phospholipid bilayers has been extensively studied to explore the molecular mechanisms of cryoprotective function of glycerol. In this study, by means of small-angle neutron scattering (SANS), we investigated whether glycerol molecules do not distribute homogeneously around phosphatidylcholine bilayer membranes. For this purpose, we measured the scattering profiles from palmitoyl-oleyl-phosphatidylcholine (POPC) membranes in four component glycerol-water mixtures (deuterated glycerol (glycerol-d_8), normal glycerol, H_2O and D_2O) which have the same neutron scattering length density (5.29×10^{-6} Å^{-2}) but have different compositions.

The glycerol water mixture with molar ratio of glycerol : water = 4.7 : 95.3 was used. Membrane vesicle samples were obtained by sonication using a Branson tip-type sonicator (about 10 min). The metal from the tip was removed from the solution. SANS measurements were performed at 25 °C with the SANS-U spectrometer of the Institute for Solid State Physics (ISSP) of the University of Tokyo in JRR-3M at Tokai. The radius of gyration R_t of a single membrane was determined using an IQ^2 versus Q^2 plot [1], where I is the scattering intensity and Q is the scattering vector.

It was found that the values of R_t of POPC membranes are not constant for five different composition samples with the same neutron scattering length density (Fig.1). This result indicates that glycerol molecules do not distribute in a homogenous manner in glycerol/water region around POPC membranes. Further analysis is now in progress.

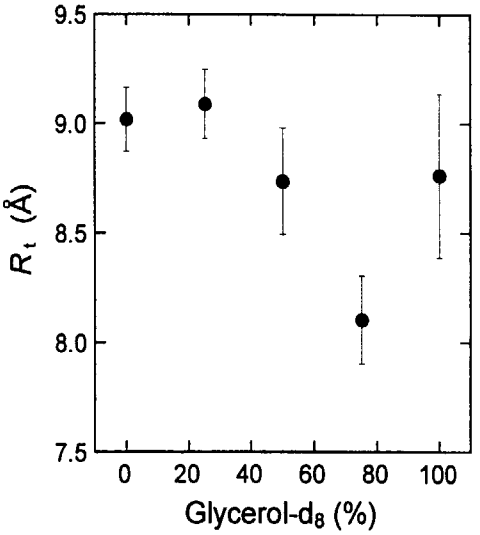

Figure 1 Plot of the radius of gyration R_t of a single POPC membrane in glycerol/water mixtures as a function of percentage of deuterated glycerol (glycerol-d_8) in total glycerol.

Reference

1. D.A. Sadler and D. L. Worcester (1982) *J. Mol. Biol.* 159,485-499.

課題名：ヒトデ生体反応誘起物質(ARIS)の構造
表　題：ヒトデ生体反応誘起物質(ARIS)の構造

Structure of Acrosome Reaction-Inducing Substance in Egg-Jelly of Starfish

M. HOSHI, M. KAWAMURA, C. KATAGIRI*, M. IMAI† and Y. ITO§

Department of Life Science, Tokyo Institute of Technology, Yokohama 227
*Institute of Low Temperature Science, Hokkaido University, Sapporo 060
†Institute for Solid State Physics, University of Tokyo, Tokai, Naka, Ibaraki 319-11
§Faculty of Liberal Arts and Education, Yamanashi University, Koufu 400

Acrosome reaction-inducing substance (ARIS) is a component in egg jelly of starfish, *Asterias anurensis*, and is a key molecule of triggering the acrosome reaction (1). The acrosome reaction is defined as exocytosis of acrosomal vesicle of a sperm, when a sperm makes contact with an egg. Starfish eggs are covered with extracellular jelly coat which contains three groups of molecules responsible for triggering the acrosome reaction. However, ARIS alone induces the acrosome reaction in high calcium or high pH seawater. ARIS is a highly sulfated fucose-rich glycoprotein and the activity of ARIS is species-specfic. The activity of ARIS depends on a unique sulfated saccharide chain. Although we elucidated the structure of its main saccharide chains (2), its molecular weight has not been determined yet because of the huge mass. It is also still unkown how ARIS is recognized by the receptor of the sperm head. To elucidate this phenomenon, the whole structure of ARIS will be required. For this purpose, its small-angle neutron scattering analysis was attempted in various D_2O concentration (3). However, the results were ambiguous for the strucural analyses. Therefore, we subjected ARIS in different pH buffers to small-angle neutron scattering measurements. Wavelength of neutron was 7A and the camera length was 12m. Fig. 1 shows that the scattering functions obtained at pH 5 and 8 were not different and suggests that we need the data at lower Q range for obtaining Rg.

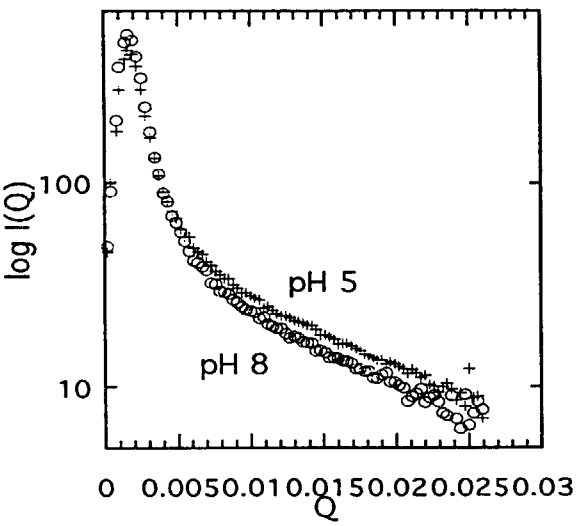

Fig. 1. Small-angle neutron scattering of ARIS at pH 5 and 8.

References

(1)M. Hoshi *et al.*, *Int. J. Dev. Biol.* 38 (1994) 167
(2)S. Koyota *et al.*, *J. Biol. Chem.* 272 (1997) 10372
(3)M. Hoshi *et al.*, *Activity Report on Neutron Scattering Research* **4** (1997) 212.

Reactor: JRR-3M　　Facility: SANS-U(C1-2)　　Field: 5.生物 Biology

1. 中性子散乱 (Neutron Scattering)

8) 基礎物理学 (Fundamental Physics)

This is a blank page.

研究課題: 冷中性子スピン干渉計の開発とその応用
表題: 冷中性子スピン干渉計を用いた周期的スピン依存場による微弱相互作用の観測

Observations of Very Weak Interactions between Neutron Spin and Spin Dependent Periodic Field Using a Cold Neutron Spin Interferometer

T. Ebisawa, D. Yamazaki[1], M. Hino, T. Kawai, S. Tasaki, H. Tahata[1], N. Achiwa[2] and Y.Otake[3]

Research Reactor Institute Kyoto University
Department of Nuclear Engineering Kyoto University[1]
Department of Physics, Kyushu University2
SPring8 The Institute of Physical and Chemical Research[3]

We observed very weak interactions between neutron spin and spin dependent periodic field using a cold neutron spin interferometer with two radio-frequency $\pi/2$ flippers (RF flipper) at MINE of JRR-3M[1]. The arrangement of the experimental set up is shown in Fig. 1.

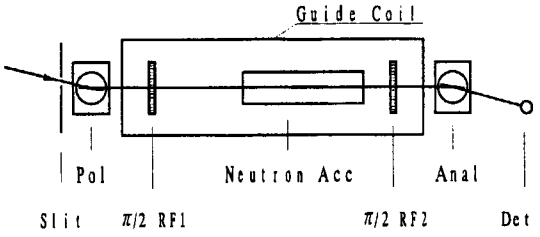

Figure 1: The arrangement of the experimental setup, which consists of a couple of polarizer and analyzer mirrors, a couples of the identical RF-$\pi/2$ flippers driven at the same frequency, a spin dependent neutron accelerator, a guide field and a detector. A time dependent periodic field with uniformity in space is applied to the spin dependent accelerator.

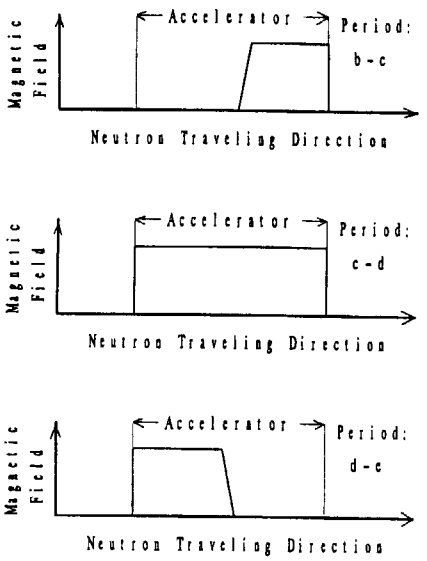

Figure 2: Neutron timing passing through the accelerator. Periodic rectangular pulses with 4 msec width were applied to the accelerator. Neutron experiences the potential with uniformity in space and the phase shift between the neutron partial waves is produced according to the neutron timing.

The first RF-$\pi/2$ flipper splits the polarized state $|z+\rangle$ of neutron into $|z+\rangle$ and $|z-\rangle$ states, which is given by

$$|z+\rangle = 1/2\{|z+\rangle + e^{i(\omega t+\Delta_0)}|z-\rangle\} \qquad (1)$$

where ω is the frequency of the flipper, t the time after the neutron passing the first flipper and Δ_0 the phase of the oscillation field applied to the first RF-flipper. The second RF-$\pi/2$ flipper compensates the phase shift of ωt_0 between the split states, where t_0 is the neutron traveling time between the two flippers. We measure a neutron time spectrum by a time analyzer, which is triggered by the same start signal with that of the two RF flippers. As a result the measured neutron time spectrum shows a constant value with the constant phase of Δ_0 for all channels.

When we apply a periodic magnetic field with rectangular shape, as shown in Fig.2, parallel to the guide field as the spin dependent neutron acceleration field, the neutron experiences a potential of μB in the oscillating field, but not receive any force because of the uniform potential in space[2].

The length of the accelerator is 32 cm and the neuron speed is 320 m/sec(λ = 12.5Å) with velocity resolution of 3.5 %(FWHM). It takes 1.0 msec for the neutron to pass through the accelerator. A periodic magnetic

field with a time width of 2 msec was applied to the accelerator. The neutrons experience the following periodic potential according to the neutron timing passing through the accelerator. (1)In periods of a-b and e-f, neutron does not feel magnetic field. So, No phase shift is observed in these periods. (2)In period b-c, neutron experiences the uniform potential of $\pm\mu B$ by the magnetic field in the exit side and the phase shift between the two eigenstates is produced in spite of no force by the magnetic field in the accelerator. At the exit edge of the accelerator, neutron is accelerated or decelerated according to the spin state. (3)In period c-d, neutron experiences the uniform potential of $\pm\mu B$ through the accelerator, and is accelerated or decelerated at the both edge of the accelerator according to the spin state. This case is equivalent to conventional Larmor precession of neutron spin and the phase shift between the two eigenstates is produced by their momentum differences in the accelerator. It should be noted that selecting period of the potential less than passing time through the accelerator, we can observe only quantum mechanical phase shift no force in the accelerator. (4)In period d-e, neutron experiences the uniform potential in the entrance side, and is decelerated or accelerated at the entrance edge according to the spin state.

In the periods of b-c and d-e, the neutron partial waves are accelerated or decelerated according to their spin states. We, however, can not observed their effect in terms of any phase shift, because the phase shift caused by their energy difference of $\pm\omega t$ is completely compensated by that caused by their momentum difference according to the acceleration and deceleration. As a result we can observe only the quantum mechanical effect caused by the periodic potential, which has no force to the neutron in the accelerator.

A time spectrum measured for the above periodic field is showed in Fig.3.

Taking t the time width of the oscillation, the phase shift in the period c-d is given by $2\mu Bt/h$, which should be equivalent to the measured phase shift. We, therefore, can evaluate the weak interaction from the measured phase shift. In the case of Fig.2, the applied magnetic field B and potential energy $2\mu B$ were 0.83 μT and 10^{-13} eV, respectively. Evaluated phase shift from the applied magnetic field was 0.15(rad.). On the other hand, the measured phase shift was evaluated to be ϕ_s=0.174 $\pm$ 0.004(rad.). Both results agree qualitatively each other. The discrepancy may be due to the not so good accuracy of measured magnetic field. This measurement shows an energy sensitivity of about 10^{-14} eV, which is improved in proportion to neutron wavelength and the length of the accelerator. We could detect a small interaction of 10^{-16} eV for a neutron wavelength of 300 Åand an accelerator length of 1 meter.

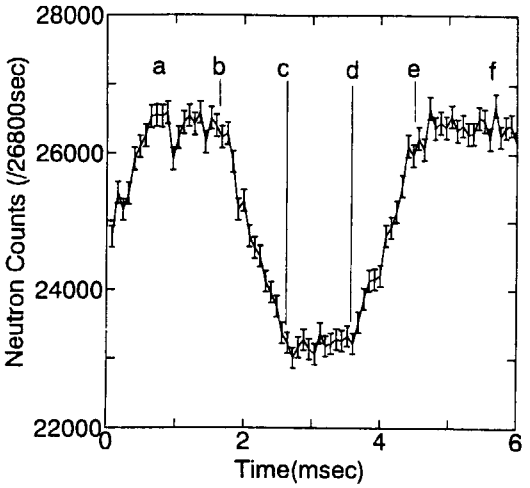

Figure 3: Measured neutron time spectrum. The ordinate indicates neutron counts, which correspond to the phase shift. a - f indicate neutron timing passing through the accelerator, which are illustrated in Fig.2.

This periodic potential method for detection of very weak potential has an unique advantage that the measurement accuracy is free from time dependent fluctuation of the experimental conditions.

The above discussion is applicable to the other periodic fields such as uniform electric field and uniform electric voltage. Applying an periodic electric field to neutrons, the potential energy corresponds to the Schwinger interaction for a free neutron, which is given by $\mu \cdot E \times V$, where E is the electric field and V the neutron velocity. In case of voltage, assuming spin dependent neutron charge $\pm e_n$ according to their spin states. neutron experiences uniform periodic potential of $e_n \cdot V$. This situation is analogous to conventional accelerators for charged particles.

References

[1] T.Ebisawa, D.Yamazaki, S.Tasaki, T.Kawai, M.Hino, T.Akiyoshi, N.Achiwa, Y.Otake, J. Phys. Soc. Japan, **67**, (1998) 1569.

[2] G.Badruk, H.Weinfurter, R.Gähler, A.Kollmar, A. Wehinger, A.Zeilinger, Phys. Rev. Lett., **71**, 1993 307.

冷中性子スピン干渉計の開発とその応用
表題：RF スピンフリッパーを利用したスピン干渉計

A Neutron Spin Interferometer using RF Spin Flippers

D. Yamazaki, T. Ebisawa[1], M. Hino[1], T. Kawai[1], S. Tasaki[1], H. Tahata and N. Achiwa[2]

Department of Nuclear Engineering, Kyoto University, 606-8501, Japan
[1]Research Reactor Institute, Kyoto University, 590-0494, Japan
[2]Department of Physics, Kyushu University, 812-8581, Japan

A new neutron spin interferometer have been developed using radiofrequency spin flippers (RF flippers) at MINE of JRR-3M. This interferometer, which is composed of a polarizer, two RF–$\pi/2$ flippers and an analyzer mirror (only five elements!), provided time dependent interference patterns (quantum beat signals) with high visibility (> 0.85) and with high resolution of phase shift ($< 1\%$).

The arrangement of this spin interferometer is shown in Figure 1. The first RF–$\pi/2$ flipper split the polarized

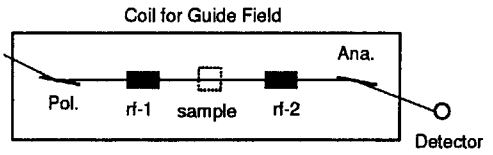

Figure 1: The arrangement of the spin interferometer with RF spin flippers. Optical elements are placed at the "sample" position. An accelerator coil is placed there in the performance test.

state $|z+\rangle$ of neutron into $|z+\rangle$ and $|z-\rangle$ states. Interacting with sample (spin dependent optical devices), the two spin eigenstates get different phases through spin dependent interactions and are superposed at the second RF–$\pi/2$ flipper. Taking frequencies of the two RF flippers ν_1 and ν_2, we have an energy difference $h(\nu_1 - \nu_2)$ between the two states after the superposition at the second RF and can observe time dependent interference pattern (quantum beat signal [1][2]) with frequency of $\nu_1 - \nu_2$ when the reflected beam by the analyzer mirror is detected. The spin-dependent interactions with samples (optical elements) are observed as a phase shift of the quantum beat signal. When frequencies of the two RF flippers are equal, the phase shift due to spin-dependent interactions are observed as a change of neutron counts because there is no energy difference between the two states superposed at the second RF flipper.

This interferometer enables us to obtain a high visibility of the interference pattern because almost no momentum-dependent phase, which often spoils visibility of interference signals owing to the momentum dispersion of neutron beam, is generated until they are superposed. And it is applicable to more versatile spin dependent interference phenomena in comparison with the former spin interferometer using Mezei-type spin flippers [3].

A performance test of this interferometer was carried out using a time analyzer, which was triggered by the same start pulses with that of the RF flippers. We observed phase shifts of quantum beat signals through an interaction with additional magnetic field (parallel to the guide field) by an accelerator coil. Frequencies of the RF flippers were set at $\nu_1 = 25.52$kHz, $\nu_2 = 25.72$kHz and the RF flippers with these frequency generate quantum beat signal of 200Hz. The experimental data is displayed in Figure 2.

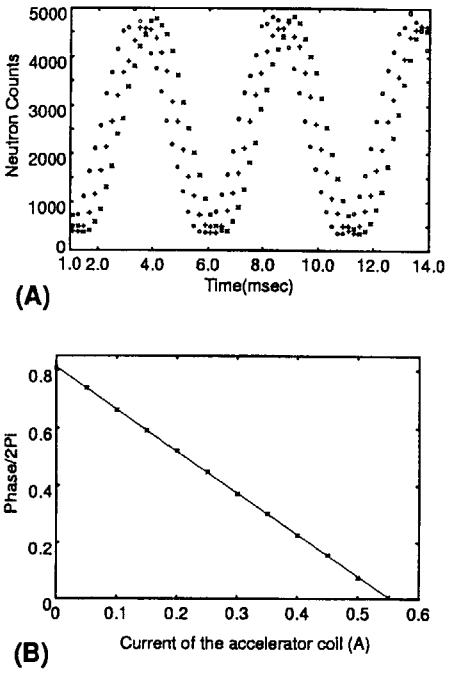

Figure 2: (A): Quantum beat signal when I=0(✖), 0.05(✚) and 0.10 A (o) of current for accelerator coil. (B): Phase shift of quantum beat with I=0 ~ 0.55 A.

Beat signals with high visibility more than 0.85 were obtained and the phase shift was determined within 1%. This interferometer can be used to detect spin-dependent interactions with optical devices such as multilayer magnetic thin films and coils [4].

An RF–π flipper placed between the two RF flipper may be useful when a phase echo or spin echo conditions are required.

References

[1] T.Ebisawa *et al.*: J. Phys. Soc. Jpn. **67** (1998) 1569.
[2] D. Yamazaki *et al.* : Physica **B** (1998) in press.
[3] T. Ebisawa *et al.* : Phys. Rev. **A57** (1998) 4720.
[4] T. Ebisawa *et al.* : in this report.

研究テーマ: 低磁場制御冷中性子パルサーの開発
表題: 多層膜冷中性子パルサーを用いた遅延選択実験

Delayed choice experiment using a multilayer cold neutron pulser

T. Kawai, T. Ebisawa, S. Tasaki, M. Hino, D. Yamazaki, Y. Matsumoto, N. Achiwa[1], Y. Otake[2]

Research Reactor Institute, Kyoto University, Osaka, 590-0494, Japan
[1]*Department of Physics, Kyushu University, Fukuoka, 812-8581, Japan*
[2]*Spring-8, Institute of Physical and Chemical Research, Kamigori, Hyogo 678-12*

In 1978, J.A.Wheeler presented the delayed choice thought-experiment to verify Bohr's view concerning the propagating behaviour of a photon after being split through a semi-reflecting mirror. In that experiment, it is required to establish the condition of whether the second wave splitter is introduced or not at the point of intersection of the two partial waves split by the first wave splitter. The switching function of a cold neutron pulser could be used for that purpose, that is, as a neutron optical switch. We call "a multilayer polarizing neutron mirror placed in the pulsed magnetic field" a multilayer cold neutron pulser, or in abbreviation a cold neutron pulser.

A delayed choice experiment was done using the cold neutron spin interferometer of Jamin type arrangement which is installed at the JRR-3M of JAERI. A pair of identical composite neutron mirrors composes the pair of the wave splitters of the interferometer. The composite neutron mirror consists of a Ni/Ti multilayer((Ni:85 Å/Ti:85 Å)x5(layers)), a Ge gap layer(4000 Å), and a Permalloy/Ge multilayer((Permalloy:85 Å/Ge:85 Å) x5(layers))(PGM), evaporated in series on the single Si wafer in a magnetic field of 130 Gauss. The top PGM functions as a wave splitter for a polarized neutron and the Ge gap layer takes the role of a phase shifter. The pair of identical composite neutron mirrors was set at parallel positions about 40 cm apart. Polarized 12.6 Å neutrons with a FWHM bandwidth of 3.5 % is incident on the first composite mirror and divided into two coherent partial waves. The phase difference between the two partial waves induced through the first composite mirror is compensated by the second one because the two partial waves are superposed upon each other at the second mirror. When the second composite mirror rotates by a small angle $\delta\theta$ on a vertical axis parallel to the mirror surface, the phase difference changes, and interference fringes are observed by varying $\delta\theta$.

In the case of the delayed choice experiment, the second composite mirror was placed in the pulsed magnetic field of 15 Gauss for producing the conditions of whether the second wave splitter is introduced or not when a polarized neutron reaches the second wave splitter. In the first "delayed choice", the PGM of the second mirror(the second wave splitter) is not placed when the neutron reaches the first mirror, and it is introduced after the neutron passed through the first mirror. Whether the second wave splitter is placed or removed is decided after the neutron passed through the first mirror. This is the meaning of "delayed choice". In the second "delayed choice" mode, the second wave splitter is placed when the neutron reached the first mirror, and it is removed after the neutron passed through the first mirror. In the first mode, the interference fringe was obtained in the same manner as the case of the Jamin type interference fringe. In the second mode, the interference fringe disappeared as shown in Fig. 1 in which other cases are also indicated. It was shown that whether the interference fringe is obtained or not depends only on whether the second wave splitter is introduced or not, after the neutron passed through the first one. Delaying choice has no effect on the interference. From this result we could deduce that the neutron wave propagates both ways with equal probability after being split by the first wave splitter and does not choose one of the two ways, as explained by quantum mechanics. The two-channel oscillator is used to provide accurate synchronization and timing for the π-flipper and the pulsed magnetic coil in order to insure clear discrimination between the two-modes operation.

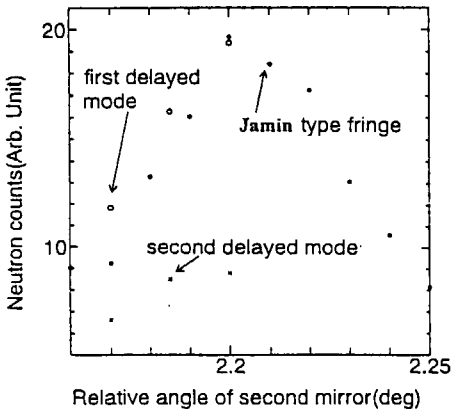

Figure 1: The interference fringe observed by changing the relative angle between the first and the second composite mirror(Jamin type fringe). Interference fringe appeared in the first delayed mode, and disappeared in the second delayed mode.

[1] JRR-3M, MINE, 8, Fundamental physics

研究テーマ：精密中性子光学実験の基礎と応用の研究

標　　題：JRR-3M PNOでの干渉計法によるｶﾞﾘｳﾑ同位体の中性子散乱長の精密決定

Precise Neutron Scattering Lengths of Gallium-Isotopes Obtained by Interferometry at PNO in JRR-3M

Hiroshi Tomimitsu, Yuji Hasegawa1, Kazuya Aizawa and Seishi Kikuta1

Advanced Science Research Center, JAERI, Tokai, Ibaraki, 319-1102 Japan
1Faculty of Engineering, Tokyo University, Hongo, Bunkyo, Tokyo, Japan

As the neutron scattering lengths of elements or isotopes are very important as the basic quantity, many values measured by various methods have been tabulated1). Some of them, however, seem to be made much more accurate. We determined the accurate of gallium isotopes with the interferometry at the PNO-apparatus.

^{69}Ga of 99.7% purity and ^{71}Ga of 99.6% purity were used as the specimen. They were melt and put in a flat glass cell, respectively. The thickness was 2.000 mm for both specimen. Those isotopes stayed in the liquid state during all the measurements at the room temoerature.

Neutron interferometry was carried out at the PNO. With the beam-collimator of 30min. of arc., the wavelength was selected as 0.15123nm. The cross section of the neutron beam was restricted to 2mm in width and 4mm in height. An LLL-type Si interferometer was used. Because of their small amount, the specimens were set so as to receive the transmitted-beam only behind the 1'st reflecting plate(splitter) of the interferometer.

We measured the oscillation of the intensities with the specimen-rotation within ±30 deg. of arc. or so. Measurements were repeated ten times for both specimens, and very similar curves were obtained, respectively. Fig.1 shows the typical example of the measured oscillation curves of ^{69}Ga, with the least square fits on the experimental data.

Next, we analyzed the experimental data following the equation;

$$I=A\cos(B/\cos(\omega+C)+D)+E, \quad \cdots\cdots(1)$$

where the parameters mean as following;
ω: the amount of specimen rotation from the original angular position,
A: apparent amplitude of the intensity-oscillation,
B: this includes all of the physical meanings as

$$B=-N\lambda tb, \quad \cdots\cdots(2)$$

with N=atomic density of the specimen,
λ=wavelength of the neutron used,
t=thickness of the specimen, and
b= the coherent scattering length to be determined;
C: amount of the angular mis-setting from the ideal origin of the specimen,
D: intrinsic phase term of the interferometer, and
E: apparent back-ground part in the intensity-oscillation including all of the imperfectness of the experimental condition, respectively.

In this study, we determine the coherent neutron scattering length in four significant figures, because the B-value, the atomic weight and the specimen thickness are known to four figures or less. Then, we should take account of the effect of the glass cell containning the specimen and of the air excluded by the specimen and cell from the neutron path. Eq.(2) is , thus, modified as follows;

$$B=(B_s-B_a)+(B_c-B_a)$$
$$=-\{(N_sb_s-N_ab_a)\lambda t_s-(N_cb_c-N_ab_a)\lambda t_c\}$$
$$=-\{b_s-b_a\times(1+t_c/t_s)N_a/N_s\}N_s\lambda t_s+B_c, \quad \cdots\cdots(2')$$

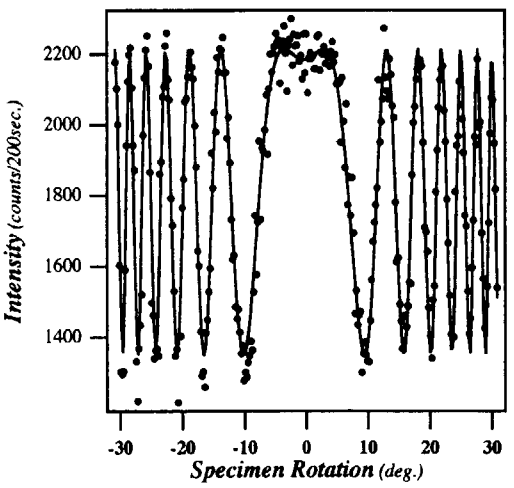

Fig.1 Example of the Intensity Oscillation Curve of ^{69}Ga

原子炉：JRR-3M　　装置：PNO(3G)　　分野：中性子散乱（基礎物理）

where suffixes s, c and a mean the specimen, the glass cell and the air, respectively.

With a conventional least square method, we analyzed all the experimental curves, as already shown in Fig.1, and obtained the B's for the Eq.(2'). Thus, we obtained the coherent neutron scattering length as;

b=8.051 fm for ^{69}Ga, and
b=6.173 fm for ^{71}Ga,

respectively, after reducing the effect of the glass cell and the air. Here, Bc for the glass cell was determined by measuring the empty cell. ba was estimated as 12.52 fm by assuming the air composion of 20.9 % O_2 with b=5.83 × 2 fm, 78.1 % N_2 with b=6.44 × 2 and 1.0 % Ar with b=2.07. The atom number density of the air was estimated as 2.488×10^{19} atoms/cm^3 with the relation of density=V/N_A, with V=RT/p = 2420.7 cm^3 with pressure p=1 atm., T=295 K and the gas constant R=82.0567 cm^3 × atm/K.

As the first stage, we refined the b-values of the gallium isotopes, by taking the effect of the impurities into account. The total effects of the "pure" impurities, except for the isotopic mutual contamination of ^{69}Ga and ^{71}Ga, were estimated as 0.002 fm for ^{69}Ga and 0.003 fm for ^{71}Ga, respectively, making use of the tabulated b-values of the impurity atoms[1]. Accordingly, the b-values were slightly modified to be 8.049 fm and 6.170 fm for ^{69}Ga and ^{71}Ga, respectively.

As the next step, the effect of the isotopic mutual contamination was resolved by solving a simple set of the linear equations with two variables as follows:

$$0.996 \times b^{(69)} + 0.003 \times b^{(71)} = 8.049$$
$$0.004 \times b^{(69)} + 0.995 \times b^{(71)} = 6.170,$$

because ^{69}Ga was contamined by 0.3% ^{71}Ga and ^{71}Ga by 0.4% ^{69}Ga, respectively. $b^{(69)}$ and $b^{(71)}$ temporally stand for the final b-values, b0, to be determined here for ^{69}Ga and ^{71}Ga, respectively, and both right side members are the b-values just obtained. The b-values for the two isotopes were finally determined as:

b_0 = 8.063 fm for ^{69}Ga, and
b_0 = 6.169 fm for ^{71}Ga, respectively.

In the final stage, we estimated the uncertainties of the b-values determined above. Uncertainties of the Avogadro constant, the density and the wavelength are so small compared to the others that they can be neglected. For the sake of a reasonable estimation of other uncertainties, we explicitly treated B-value as $B=B_0(1\pm\beta)$, the atomic number density as $N=N_0(1\pm\nu)$ and the thickness as $t=t_0(1\pm\tau)$. The ambiguity of the b-value, db, can be written, then, as $\delta b = b_0(\beta+\nu+\tau)$, where, for example, B_0 means the main B-value derived in the curve-fitting and β means the ratio of the ambiguity of the B-value to the main B-value, and so on. In the present analysis, these errors can be estimated for both isotopes, $\tau = \delta t/t_0 = 0.0005/2.000 = 0.00025$ and $n = (\delta N_A/N_A + \delta\rho/\rho + \delta A/A) \fallingdotseq \delta A/A = 0.005/69.72 = 0.00007$. As b is equal to 0.0017 in the case of ^{69}Ga, δb was estimated as 0.016 fm. Since b equals to 0.0021 in the ^{71}Ga case, on the other hand, δb was estimated as 0.015 fm. Accordingly, we conclude the final b-values their uncertainties as follows:

b = 8.063±0.016 fm for ^{69}Ga, and
b = 6.169±0.015 fm for ^{71}Ga,

respectively.

Results, determined above, were significantly different from the known values obtained by other method, i.e., the former is larger by about 2% and the latter is less by about 4% compared with the tabulated values[1], respectively. On the other hand, the values of the high purity aluminum, niobium and natural gallium, which were also measured as the standard specimens in the present experiment, were almost the same as the known values.

The coherent neutron scattering lengths of ^{69}Ga and ^{71}Ga were, thus, successfully obtained by the neutron interferometry at the PNO[2].

References

1) L.Koester, H.Rauch and E.Seymann: Atomic Dta and Nuclear Data Tables 49(1991) 65.
2) This work will be published in NIM-A.

研究テーマ：金属基複合材料の中性子応力測定
表題：SiC粒子強化アルミニウム合金における相応力の中性子およびX線測定

Neutron and X-ray Diffraction Study of Phase Stresses in SiC Particulate Reinforced Aluminum Alloy

Yoshiaki AKINIWA, Keisuke TANAKA, Takuya TAKEZONO,
Nobuaki MINAKAWA[1], and Yukio MORII[1]

Nagoya University, Nagoya 464-8603, Japan
[1]Japan Atomic Energy Research Institute, Tokai, Ibaragi 319, Japan

Aluminum alloys reinforced with silicon carbide particles (SiCp) have several advantages in structural applications such as nearly isotropic mechanical properties, high specific stiffness and strength, and high wear resistance. Since the strength of the composites depends on that of matrix and particles, it is important to evaluate the stress state of each material under loading. The neutron and X-ray diffraction methods can detect separately the stress in each constituent phase of the composite. The neutron and X-ray diffraction methods were used to measure the phase stresses in the aluminum alloy reinforced by SiCp under uniaxial loading. The measured phase stresses were compared with the predicted values calculated by Eshelby's inclusion models[1].

The experimental materials used were monolithic aluminum alloy (Al2024) and aluminum alloy reinforced by silicone carbide particles (SiCp/Al2024). The volume fraction of SiC particles of the composite is 20% and their average size is 3 μm. An extruded rod of the composite was heat-treated under T6 conditions. The grain size of the matrix is about 5 μ m. On the other hand, the grain size of the unreinforced material is 5～10 μm in the rolling direction and about 5 μm in the transverse direction.

The X-ray diffractions from Al 222 and SiC 116 by Cr-Kα radiation were used for X-ray stress measurement. The stress was evaluated by the 2θ-$\sin^2\psi$ method obtained from the specimen strained to several known stresses by using a specially designed four point bending device under the iso- or side-inclination condition along parallel and perpendicular direction to the loading axis, respectively. For the diffraction of SiC 116, the stress constant (S=-1880 MPa/deg), Young's modulus (E=433 GPa) and Poisson's ratio (ν=0.129) were calculated by using Krö ner's model from the elastic constants of single crystals. The measured X-ray elastic compliances agree well with the predicted values calculated by using Krö ner's model [2]. The phase stress measured by the X-ray method in matrix and SiC particles of composite increased in proportion to the applied stress. The macrostress calculated from the phase stress by using the rule of mixture was equal to the applied stress.

The neutron stress measurement was performed for the same diffraction planes as the X-ray stress measurement with the RESA (REsidual Stress Analyze equipment) at JAERI. The specimen was uniaxially strained with a hydraulic tensile testing equipment. The wave length used was 1.8065Å. The direction of the lattice strain measured was parallel and perpendicular to the loading axis. The strain was calculated on the basis of the initial lattice spacing at σ_A=0. The phase stress measured by the neutron method in the matrix is nearly equal to that by the X-ray method, and is less than the theoretical prediction using the self-consistent model and Eshelby-Tanaka-Mori model [3]. For the case of SiC particles, measured phase stress is close to the theoretical prediction.

References

[1] J. D. Eshelby, Proc. Roy. Soci. London, A241 (1957), 376.
[2] E. Krö ner, Einkristalls, Zeitschrifts f. Phys., 151 (1958), 504.
[3] T. Mori and K. Tanaka, Acta Met., 21, (1973), 571.

原子炉：JRR-3M　　装置：RESA（T2-1）　　分野：中性子散乱（基礎物理）

This is a blank page.

1. 中性子散乱 (Neutron Scattering)

9) 中性子光学 (Neutron Optics)

This is a blank page.

研究テーマ: ラーモア回転による中性子波束のスピン干渉
表題: 中性子スピン干渉による磁気多層膜の動力学回折位相

Dynamical Diffraction Phase through Magnetic Multilayer Film by Neutron Spin Echo Interferometer

Norio Achiwa, Masahiro Hino[1], Toru Ebisawa[1], Seiji Tasaki[1], Takeshi Kawai[1]

Department of Physics, Faculty of Science, Kyushu University, Hakozaki, Fukuoka, 812, Japan
[1]Research Reactor Institute, Kyoto University, Kumatori, Osaka, 590-04, Japan

[1]

We have proposed that dynamical diffraction phase through a magnetic multilayer film at Bragg condition should be observed by the shift of Larmor precession of transmitted neutron and a preliminary result was shown by using transverse neutron spin echo(NSE) instrument[1]. The shift of Larmor precession is given by the phase difference of ↑ and ↓ neutron wave functions through the magnetic multilayer. According to our previous paper[1], we need to deal only wave number $k_\perp$ perpendicular to the surface plane of the multilayer and one dimensional periodic rectangular potential for ↑ and ↓ spin neutrons. That is, the ↑ spin neutron goes through the periodic potential of 316neV-0neV for the permalloy45 ($Fe_{55}Ni_{45}$:55Å)-titanium(Ti:54Å)(abbreviated as PA/Ti) multilayer of 15 bilayers while the ↓ spin feels 124neV-0neV potential in it. In each magnetic layer, the wave number is given by $k_\pm = \frac{\sqrt{2m(E-(U\pm|\mu B|))}}{\hbar}$, $E = \frac{(\hbar k_\perp)^2}{2m}$, U the nuclear potential and B the magnetic induction of 1.6T in the permalloy45. By solving Schrödinger equation on the one dimensional periodic rectangular potential for ↑ and ↓ spin neutrons, the wave function in the j-th multilayer in the state of Larmor precession is given by,

$$\psi_{j\pm}(r) = A_{j\pm}\cdot e^{ik_{j\pm}r} + B_{j\pm}\cdot e^{-ik_{j\pm}r}. \quad (1)$$

If we represent $\psi_{j\pm}(r)$ by a vector $\binom{A_{j\pm}}{B_{j\pm}}$, at the first interface $\psi_{0\pm}(r_0) = \binom{1}{r_\pm}$ and at the last interface $\psi_{j\pm}(r_j) = \binom{t_\pm}{0}$, using the reflection and the transmission coefficients $r_\pm$ and $t_\pm$. These are related by a transfer matrix $M_\pm$[2] as

$$\begin{pmatrix} 1 \\ r_\pm \end{pmatrix} = \begin{pmatrix} M_{11\pm} & M_{12\pm} \\ M_{21\pm} & M_{22\pm} \end{pmatrix} \begin{pmatrix} t_\pm \\ 0 \end{pmatrix}. \quad (2)$$

Solving Eq. (2), one can obtain transmission coefficients as $t_\pm = \sqrt{T_\pm}e^{i\Delta\phi_\pm}$, where $\Delta\phi_\pm$ are the additional phase across the multilayer and $T_\pm$ the transmission probabilities. Then we get the extra Larmor precession $\Delta\phi = \Delta\phi_+ - \Delta\phi_-$ through a magnetic multilayer as follows.

$$\langle S_x\rangle = \hbar\cos(\Delta\phi_+ - \Delta\phi_-)\frac{\sqrt{T_+T_-}}{T_+ + T_-}, \quad (3)$$

$$\langle S_y\rangle = -\hbar\sin(\Delta\phi_+ - \Delta\phi_-)\frac{\sqrt{T_+T_-}}{T_+ + T_-}, \quad (4)$$

$$\langle S_z\rangle = \frac{\hbar}{2}\frac{T_+ - T_-}{T_+ + T_-}. \quad (5)$$

Then, the amplitude of the NSE signal, P can be expressed by the transmission probabilities $T_\pm$ as

$$P = P_0\frac{|\langle S_{x,y}\rangle|}{|\langle S_{x,y}\rangle| + \frac{1}{2}|\langle S_z\rangle|} \quad (6)$$

$$= P_0\frac{4\sqrt{T_+T_-}}{4\sqrt{T_+T_-} + |T_+ - T_-|}, \quad (7)$$

where P_0 is the NSE signal in the absence of the magnetic layer.

The experiments were carried out with transverse NSE instrument inserting the magnetic PA/Ti multilayer in one of the Larmor precession fields. The wavelength resolution with polarizer was 12.6±0.44(FWHM)Å and the divergent angle was 0.7×10^{-3} rad. As shown in Fig. 1, the transmission probability through the magnetic PA/Ti multilayer for ↑ and ↓ spin of neutrons were measured and

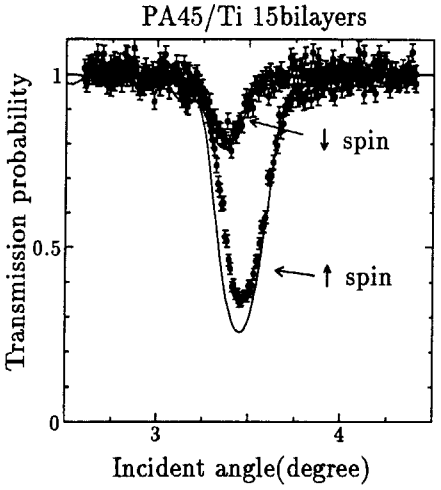

Figure 1: Transmission probabilities of ↑ (•) and ↓ (○) spin neutrons through permalloy45(55Å)-Ti(54Å) multilayer of 15 bilayers as a function of incident angle for the wavelength of 12.6Å. The solid lines are the calculated transmission probabilities based on one-dimensional Schrödinger equation with periodic rectangular potentials for ↑ and ↓ spins.

[1]JRR-3M, MINE, 8, Neutron Optics

the Bragg angle for the ↑ spin is higher than that for the ↓ spin. This is due to the difference of wave number $k_{\pm}$ for them.

The shift of Larmor precession versus incident angle was measured across the Bragg condition. At the Bragg condition an anomalous oscillatory phase shift of Larmor precession was observed as shown in Fig. 2. At the Bragg condition the ↑ spin neutron

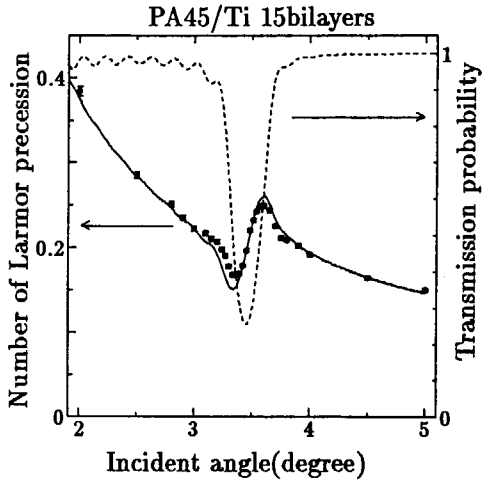

Figure 2: The shift of NSE signals as well as transmission probability through permalloy45(55Å)-Ti(54Å) multilayer of 15 bilayers as a function of incident angle for the wavelength of 12.6Å. The solid line is the calculated Larmor precession as well as the broken line the calculated transmission probability across the Bragg condition as a function of incident angle, on the basis of solving Shrödinger equations for one dimensional periodic potential of rectangular type for ↑ and ↓ spins.

is split into the reflected H-wave and the transmitted O-wave. The transmitted O-wave ↑ spin recombined with the transmitted ↓ spin gives extra-Larmor precession.

The Schrödinger equation of each ↑ and ↓ spin neutron for the one dimensional periodic rectangular potential was solved by a matrix method[2]. The phase difference between ↑ and ↓ spin wave functions calculated are plotted against the crystal angle in Fig. 2. The anomalous phase shift which was observed across the Bragg reflection is qualitatively reproduced by the simulation. The main contribution of the Larmor shift comes from the phase shift of ↑ spin wave function at the Bragg condition because the phase shift of the ↓ spin wave function is smaller.

The anomalous phase shift which is observed at the Bragg condition is similar to the phase shift in the region of Darwin table width[3] in a perfect crystal as a dynamical diffraction effect which can be measured by interferometer.

The forward diffracted Larmor precession will give a new method to observe the phase shift of neutron wave function through a magnetic crystal.

This work was supported by a Grant-in-Aid for Scientific Research from the Japanese Ministry of Education, Science and Culture(No. 06220203, No. 07209202) and Yamada Science Foundation.

References

[1] N. Achiwa, M. Hino, S. Tasaki, T. Ebisawa, T. Akiyoshi and T. Kawai, J. Phys. Soc. Japan, **65** Suppl. A (1996) 183.

[2] S.Yamada, T.Ebisawa, N.Achiwa, T.Akiyoshi and S. Okamoto, Annu.Rep. Res.React. Inst. Kyoto Univ. **11** (1978) 8.

[3] V.K.Ignatovich, D.Protopopescu and M. Utsuro, Phys. Rev. Lett. **77**(1996) 4202.

研究テーマ: 中性子ラーモア回転によるヘリカル磁性体ホロミウムの動力学回折
表題:中性子ラーモア回転によるＨｏ単結晶ヘリカル磁場による動力学回折位相

Neutron Spin precession due to Dynamical Diffraction Phase through Helical Magnetic Crystal of Holmium

Norio Achiwa, Masahiro Hino[1], K. Kakurai[2], S. Kawano[1]

Department of Physics, Faculty of Science, Kyushu University, Hakozaki, Fukuoka, 812, Japan
[1]Research Reactor Institute, Kyoto University, Kumatori, Osaka, 590-04, Japan
[2]Institute for Solid State Physics, The University of Tokyo, Shirakata, Tokai, Naka, Ibaraki, 319-11 Japan

[1]

Spin precession of neutron due to dynamical diffraction effect through a helical magnetic crystal of holmium have been re-observed using a forward scattering neutron spin echo technique, when an external magnetic field is parallel to the helical axis. The spin precession of the transmitted neutron is considerably enhanced near a magnetic Bragg reflection in rocking curve but the shift of Larmor precession is both plus direction when the magnetic $(000)^{\pm}$ Bragg is approached from left or right side in the rocking curve, against to the prediction by Nityananda et al. [1]. For the reflected neutrons, the spin echo signal disappeared, then, we can conclude that there exists no coherency between the ↑ and ↓ spin neutron wave functions reflected by the left and the right handed helical domains, respectively.

The transmission behavior of spinor wave function of neutrons passing through a helical magnetic field have been extensively studied theoretically [1][2][3][4]. The Larmor precession state of neutron is considered as a superposition of ↑ and ↓ neutron wave functions in each of the two spin eigenstates. The Larmor precession is interpreted as the phase differences between the two wave functions.

When the Larmor precessing neutron passes through the crystal in the vicinity of the $(000)^{+}$ or $(000)^{-}$ magnetic Bragg condition, only the component of the ↑ or ↓ spin neutron interacts with one of the left or right handed magnetic induction of the helical domains. Then a part of, for example, ↑ spin neutron is divided into H-wave and O-wave. The transmitted ↑ spin neutron, that is, the O-wave, recombines with ↓ spin neutron giving extra Larmor precessions. The amount of the extra-Larmor precessions are proportional to the strength of the magnetic induction and the thickness of the crystal. Figure 1 shows the Larmor precession of the transmitted neutrons against the rocking crystal angle near the $(000)^{\pm}$ magnetic satellite when the external field is parallel to the helical axis. Sign of the phase shift is same across the Bragg condition of the crystal angle. Usually it is not easy to observe the dynamical diffraction effect of magnetic Bragg reflection by neutron diffraction because a perfect magnetic crystal is difficult to be grown up. On the while, the Larmor precession passing through the helical crystal depends on a beam divergence and the Larmor shift is an average of the spin precession for every path lengths in the crystal.

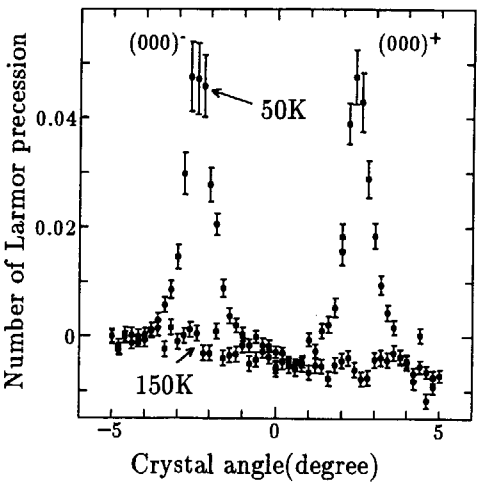

Figure 1: The shift of NSE signals of forward scattering (Q=0) neutrons through a holmium single crystal plate with thickness of 1.6mm across $(000)^{-}$ magnetic reflection by ω scan at 50K (•)(below T_N) and at 150K(○)(above T_N). The external field is applied along the helical magnetic axis parallel to the c-axis. The beam divergence is 0.63×10^{-3}radian.

References

[1] R.Nityananda and S.Ramaseshan, Solid State Commu. **9** (1971) 1003.

[2] G.Eder and A. Zeilinger, Nuovo Cim. B **34** (1976) 76.

[3] Ch.Scwink and O.Scharph, Z. Physik, B **21** (1975) 305.

[4] M.Calvo, Phys. Rev. B **18** (1978) 5073.

[1]JRR-3M, PONTA 8, Neutron Optics

研究テーマ: 中性子ラーモア歳差回転によるトンネル時間とラーモア時計の研究
表題: スピン回転によるファブリペロー磁気膜での中性子束縛状態の測定

Measurement of quasibound states of neutron in Fabry-Perot magnetic resonator using spin precession

M. Hino, N. Achiwa[1], S. Tasaki, T. Ebisawa, T. Kawai, D. Yamazaki[2], H. Tahata[2]

Research Reactor Institute, Kyoto University, Osaka, 590-0494, Japan
[1]Department of Physics, Kyushu University, Fukuoka, 812-8581, Japan
[2]Department of Nuclear Engineering, Kyoto University, Kyoto, 606-8501, Japan

Quasibound states of neutron in matter were observed for the first time with ultracold neutron by Steyerl and co-workers[1] and Mâzza estimated neutron lifetime in quasibound states[2], however, none has observed quasibound states using Larmor precession. Therefore we measured Larmor precession angles of neutron spins transmitted through double-hump or triple-hump potential barriers for ↑ spin neutrons[3]. The double-hump and triple-hump potential barriers were created by a sequence permalloy45(PA)–Ge–PA films and PA–Ge–PA–Ge–PA deposited on flat silicon wafers, respectively. Here an ↑ spin neutron wave feels double-hump or triple-hump potential barriers and a ↓ one feels almost a small rectangular potential. These multilayers are called Fabry-Perot magnetic thin film resonator, and the layer thickness of each films was measured by a quartz crystal oscillator during deposition. The measured thicknesses of permalloy45($Fe_{55}Ni_{45}$) films for double-hump type were 150Å and those for triple-hump were 100Å, and the thicknesses of all germanium films were 800Å, respectively.

By inserting the Fabry-Perot resonator into the second spin precession field of a neutron spin interferometer(NSI)[4] installed at the cold neutron guide tube(C3-1-2) of the JRR-3M reactor at JAERI, we could observe quasibound states of ↑ spin neutron in the Fabry-Perot resonator using Larmor precession, which is shown by the shift of neutron spin echo(NSE) signals. In this experiment, the NSI is considered as a miniature of a transverse NSE instrument, and the wavelength resolution and the divergent angle are 12.6Å±0.44Å(FWHM) and 0.7×10^{-3}rad, respectively.

As shown in Fig. 1, the Larmor precession angles versus the incident angles show sinusoidal oscillations and the oscillation is well reproduced by the theoretical phase difference of ↑ and ↓ spin neutron wave functions calculated with one-dimensional Schrödinger equation for triple-hump potential barrier. The smaller the incident angles, the bigger and sharper the sinusoidal oscillations are. The incident angles of the maximum and the minimum shifts of the sinusoidal oscillation don't correspond to the incident angles of peaks of transmission probability, but

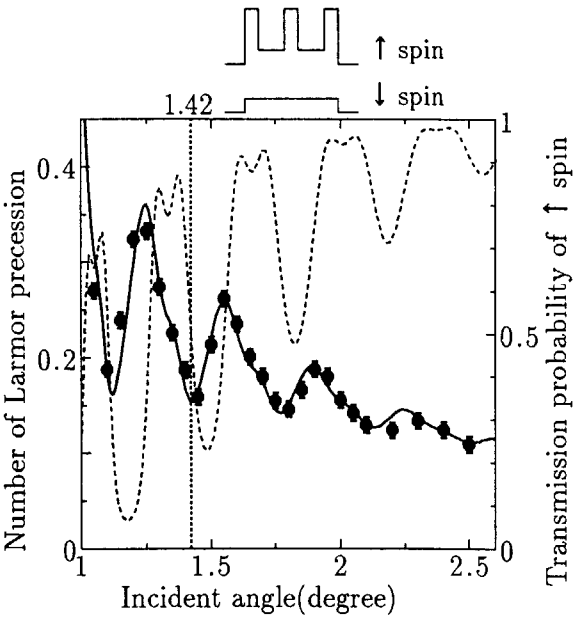

Figure 1: The shift of NSE signals(closed circles and solid line) and transmission probability(broken line) of ↑ spin neutron through the PA-Ge-PA-Ge-PA Fabry-Perot resonator as a function of incident angle.

the centers of sinusoidal oscillation correspond to the angle of the peaks. The Larmor precession rotates regardless of magnetic or non-magnetic field, then we can not use the Larmor precession as an ordinary Larmor clock.

References

[1] A.Steyerl, T.Ebisawa, K.A.Steinhauser and M.Utsuro, Z. Phys. B. 41(1981)283.

[2] M.Maaza, B.Pardo, J.P.Chauvineau, A.Raynal, A.Menelle, F.Bridou, Phys. Lett. A223(1996)145.

[3] M. Hino, N. Achiwa S.Tasaki, T. Ebisawa, T. Kawai and T. Akiyoshi, Physica B, in press.

[4] T. Ebisawa, H. Funahashi, S.Tasaki, Y.Otake, T. Kawai, M. Hino, N. Achiwa and T. Akiyoshi, J. Neutron Research vol 4, 157(1996).

JRR-3M, MINE, 8, Neutron Optics

研究課題: 多層膜による非鏡面・干渉性散乱成分の測定
表題: 多層膜による特徴的な非鏡面干渉性反射の測定と解析

Measurements and analysis of non-specular coherent scattering from multilayers

S.Tasaki, T.Ebisawa, Y.Otake[1]
Research Reactor Institute Kyoto University
SPring8 The Institute of Physical and Chemical Research[1]

Interface roughness is one of the main cause of reduction of neutron reflectivity in multilayer mirrors, and it also induces diffuse and off-specular scattering. In this study, we made measurements on a off-specular coherent scattering from multilayer neutron mirrors with different interface roughness.

Off-specular coherent scattering is caused from correlation of roughness profiles between layers.[1] The scattering cross section is described by Sinha, with Born approximation[2]. In a very simple case, where all the roughness profile is duplicated perfectly from layer to layer (perfect correlation), above equation can be modified as follows,

$$\left(\frac{d\sigma}{d\Omega}\right) = \frac{2\pi N^2 b^2}{A} L_x F_L \frac{\lambda^4 \exp\left(-\frac{(\theta-\theta_B)^2}{2A}\right)}{256\pi^4(\theta_B)^4}, \quad (1)$$

where θ_B, L_x, F_L, N and b are Bragg angle of this multilayer for neutron wavelength λ, Laue factor, atomic number density and coherent scattering length of multilayer material.

We prepare two samples, i.e. multilayer evaporated on smooth and rough substrate. The smooth substrate is a Si wafer for semiconductor and its surface roughness is estimated as 2Å rms. The rough substrate is a polished Si wafer with surface roughness of 11.6Å rms. Multilayers consisting of Ni and Ti (100Å d-spacing, 50 bilayers) are stacked on both substrates using vacuum evaporation.[3]

Measurements of off-specular coherent scattering intensity were performed with 12.6Å-neutron reflectometer at JRR-3M reactor in Japan Atomic Energy Research Institute.[4] Since the reflectometer is so called θ-2θ type, 'first order' off-specular peak appears at almost constant position independent from neutron incident angle θ to the sample. Hence in the measurements, we scanned the neutron detector around the first Bragg peak position for each θ. After the scan, we integrate the off-specular peak. Incident neutron beam collimation is 1/1000rad. Detector slit width is 2mm.

The plots of off-specular peak intensity vs. $\theta - \theta_B$ are shown in Fig.1, where θ_B is Bragg angle for these multilayers. For the rough sample a large peak of off-specular reflection appears, whereas for the smooth sample, no such peak is observed.

The measured data for the rough sample agrees well with the calculation. The agreement implies that roughness between layers correlates and correlation function obeys Gaussian in the rough multilayer.

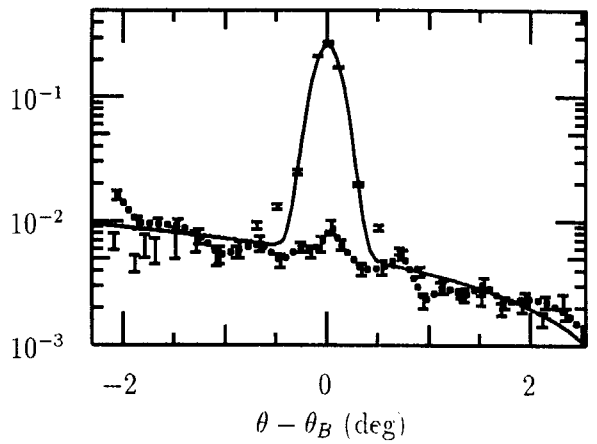

Fig.1 Intensity of non-specular component vs. incident angle to the multilayer.

References

[1] D.E.Savage, J.Kleiner, N.Schimke, Y.-H.Phang, T.Jankowski, J.Jacobs, R.Kariotis and M.G.Lagally, *J. Appl. Phys.*, **69** (1991) 1411

[2] S.K.Sinha, *Mat. Res. Soc. Symp. Proc.*, **376** (1995) 175

[3] S.Tasaki, T.Ebisawa, T.Akiyoshi, T.Kawai, and S.Okamoto, *Nucl. Inst. Meth. Phys. Res.*, A**355** (1995) 501

[4] T.Ebisawa, S.Tasaki, Y.Otake, H.Funahashi, K.Soyama, N.Torikai, Y.Matsushita, *Physica B* **213&** **214** (1995) 901

JRR-3M, MINE, 8, Neutron Optics

This is a blank page.

1. 中性子散乱 (Neutron Scattering)

10) その他 (Etc)

This is a blank page.

研究テーマ：中性子回折による残留応力測定
表　　題：ステンレス配管溶接部近傍におけるき裂進展に伴う残留応力再分布の測定

Measurement for Redistribution of Residual Stress with Crack Progress near the Weldment on Stainless Steel Pipe.

S. Okido, M. Hayashi*, Y. Morii**, N. Minakawa** and Y. Tsuchiya**

Mechanical Engineering Research Laboratory, Hitachi, 3-1-1 Saiwai, Hitachi, Ibaraki 317-8511
* Mechanical Engineering Research Laboratory, Hitachi, 502 Kandatsu, Tsuchiura, Ibaraki 300-0013
**Japan Atomic Energy Research Institute, Tokai, Ibaraki 319-11

The distribution of welding residual stress is known to change when cracks occur. The welding residual stress distributes along not only the surface but also the cross section of the structural components. The change in residual stress distribution in the cross section is important in evaluating the fracture caused by crack growth, because crack growth behavior is affected by changes in residual stress distribution.

Change in residual stress distribution in the cross section were examined using a method for neutron diffraction method of welded stainless steel pipe.

An apparatus for measuring neutron diffraction was used residual stress analyzer (RESA) established in JRR3M. The neutron wavelength λ was 0.199 nm. A Cd slit was used to limit the area for measurement to 2×2 ×4 mm. The lattice strains were measured based on (200) diffraction. Stresses were calculated using Hooke's law from the lattice strain values measured in three directions. In the calculation, the elastic constant E was 134 GPa and Poisson's ratio ν was 0.34.

The circumferentially butt-welded pipe specimen was made of type 304 stainless steel, which had an outer diameter of 114.3 mm, a thickness of 8.6 mm and a 10 mm wide weld line. Measurements were taken 1 mm away from the fusion line at a 1mm deep pitch in the thickness direction. A circumferential defect simulating inner surface crack, that was 2mm deep and 16mm long, was notched by an electric discharge machine 1 mm away from the fusion line.

The distribution of longitudinal residual stress was measured using the neutron diffraction method before and after notching of the defect. The data obtained are plotted in Fig.1. The residual stress in the region from the inner surface to the tip of the notch was found to be relieved by this notching of the defect. The values for residual stress distribution before and after notching of the defect were almost the same, in spite of near the defect tip. The residual stress distribution was not changed by the present of the defect. This suggests that the defect may have been too small to disturb the residual stress field.

The distribution of the residual stress in the cross section of welded pipe is recognized as measurable by the neutron diffraction method. We plan to measure a welded pipe specimen having a larger notch in order to examining the change in residual stress distribution.

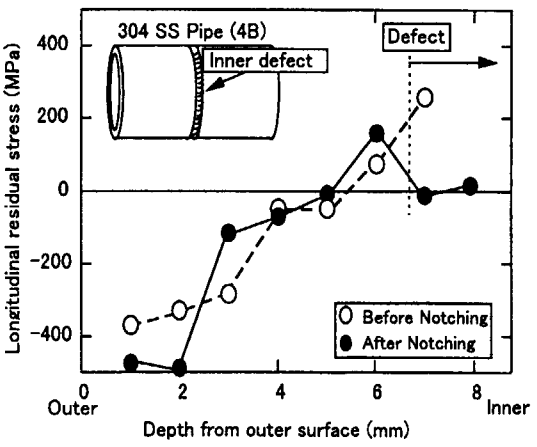

Fig. 1　Distribution of longitudinal residual stresses 1 mm away from fusion line

原子炉：JRR3M　　装置：RESA(T2-1)　　分野：中性子散乱（その他）

研究テーマ：超低温の導入による中性子散乱の研究
表題：中性子回折による超電導コイルジャケットの残留応力測定

Residual Stress Measurement of Superconducting Coil Jacket by Neutron Diffraction

Y. Tsuchiya, N. Minakawa[1], Y. Morii[1], T. Kato, H. Nakajima, K. Ishio, and H. Tsuji

Naka Fusion Research Establishment, Japan Atomic Energy Research Institute, Ibaraki 319-01 Japan
[1]Advanced Science Research Center, Japan Atomic Energy Research Institute, Ibaraki 319-11 Japan

Some improvements on neutron spectrometer for residual stress analysis (RESA) installed at JRR-3M reactor in JAERI were made recently. Monochrometor system of bent Si single crystals was adopted to RESA instead of a pyrolytic graphite monochrometor. The monochrometed neutron beam was converged at the position of the sample by the monochrometor system. As an other improvement, a conventional ^{3}He detector was installed to RESA besides an one-dimensional position sensitive detector (PSD). A solar collimator can be set into the diffracted beam line when the conventional detector is used. Using the improved RESA, internal residual stress measurement of a superconducting coil jacket was performed.

A sample is a jacket of a superconducting central solenoid coil (CS coil) for international Thermonuclear Experimental Reactor (ITER). The jacket material, INCOLOY 908, is a nickel-iron based precipitate hardening type alloy. INCOLOY908 has a possibility of fracture due to Stress Accelerated Grain Boundary Oxidation (SAGBO) in the region of tensile residual stress above 200MPa. It is advisable that the residual stress of the jacket is to be a value below 200MPa to avoid the SAGBO cracking.

The square cross section of the coil jacket was 45 × 45 mm^2 and the inside diameter of about 35 mm. The sample jacket tube enclosed a bundle of Cu wire of 35mmϕ instead of Nb^{3}Sn superconducting wire to reproduce a condition of the actual use. The coil was cut to a length of about 150mm for a neutron diffraction measurement. The sample was confirmed to be FCC single phase by neutron diffraction measurement. A solid solution of INCOLOY 908 was used as the standard sample of stress-free condition. The thickness of the jacket material for the measurement is about 4.5 mm.

The incident beam wave length of 2.0995Å was used. In order to define the sampling volume within the sample, incident beam and scattering beam were restricted for 2 × 4mm^2 of cross section by Cadmium masks before and after the sample. Zero-dimensional counter was used and a collimator of 20' was set before the counter. For the three principal orientations x, y and z corresponding to longitudinal, transverse and vertical directions of the sample, (111) plane spacings were measured scanning from outer surface of the jacket to inside every 1mm in depth. The residual stress distributions of the CS coil jacket that were obtained in this study are shown in fig. 1. These spatial distributions of the residual stress show the same tendency as the data by PSD mode. A peak/background ratio was improved successfully by using modified RESA.

Reference

Y. Tsuchiya, et al. Physica B 241-243 (1998) 1264-1266

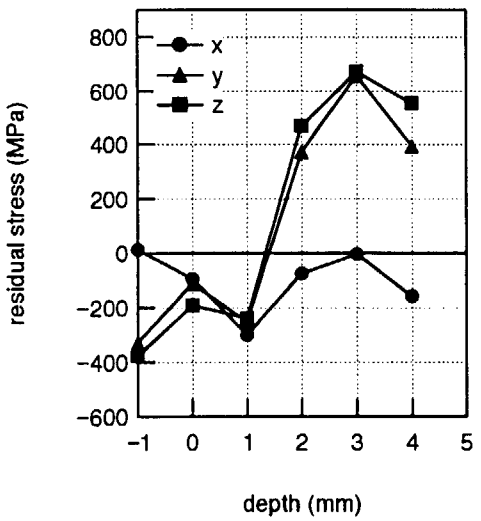

Fig.1 The residual stress distributions of the CS coil jacket for three orthogonal direction, x, y and z.

原子炉：JRR-3M　　装置：RESA（T2-1）　　分野：中性子散乱（その他）

研究テーマ：原子トンネル効果による極低温化学反応の研究
表題：1.3 K ^{3}He-^{4}He量子液体中でのTとHの再結合反応，T + T → T_2及びT + H → HT，

Recombination Reactions of T + T → T_2 and T + H → HT in Quantum Liquid of ^{3}He-^{4}He Mixtures at 1.3 K

Y. Aratono,[1] T. Matsumoto,[2] T. Kumada[1] and T. Miyazaki[1,2]

[1]Japan Atomic Energy Research Institute, Tokai-mura, Ibaraki-ken 319-1195, Japan
[2]School of Engineering, Nagoya University, Furo-cho, Chikusa-ku, Nagoya 464-8603, Japan

Liquid helium shows very significant quantum effect such as superfluidity due to its small mass and very weak van der Waals interaction. The authors proposed that the liquid helium can be used as a new medium for the investigation of low temperature chemistry in the quantum medium, expecting the unique chemical reactions arising from the quantum characters of the medium.[1,2] During the course of the studies using the liquid ^{3}He-^{4}He mixture as the reaction medium, the authors found the preferential formation of HT over T_2 in the recombination reactions of T + T → T_2 and T + H → HT, where T and H are produced through ^{3}He(n, p)T.

Recent progress of laser techniques has been stimulating the spectroscopic studies of the structures of bubbles formed by electron and neutral atom and of snowball formed by positive ions, which are characteristically observed in the liquid helium.[3-5] Though the optical spectroscopic method has been successfully applied to the study of physicochemical properties of electron, helium ion, neutral and charged metal atoms and some their dimers, no experimental investigation has been performed on the characteristics of the hydrogen isotopes in the liquid helium as well as on their chemical reactions. This is due to the difficulties of the introduction of the isotopes into the liquid helium and of no suitable methods for observation.

The authors proposed the nuclear activation method for study of T reactions in the ^{3}He-^{4}He mixture.[2] According to the phase diagram of the ^{3}He-^{4}He mixture,[6] we can choose the superfluid state at the ^{3}He(0.280)-^{4}He(0.718) mixture or the normalfluid state at the ^{3}He(0.670)-^{4}He(0.330) mixture at 1.3 K. T atom produced by the nuclear reaction of ^{3}He(n, p)T has an initial kinetic energy of 192 keV and is thermalized very efficiently prior to the reaction through the successive collision with surrounding helium atoms. Thermal neutron irradiation was performed at TAS-1 of JRR-3M(Japan Research Reactor No. 3M) for about 10-20 hrs at 1.30± 0.02 K. Since the irradiation port was designed for neutron scattering experiment, γ-ray dose rate was very low and thus the secondary effect caused by γ-ray could be neglected. The thermal neutron flux measured by Au-foil activation method was typically 3.1×10^{11} m^{-2} sec^{-1} but changed from sample to sample because of the difficulty of the setting the sample exactly at the same geometrical position. The reaction products, HT and T_2, were analyzed by radio-gaschromatography.

Table 1 shows the mol % yields of HT(Y_{HT}) and T_2(Y_{T_2}). The values are the average of the twice experiments. A very large difference is seen between Y_{HT} and Y_{T_2}.

The following reactions will occur in the system.

$$H + H \rightarrow H_2 \quad (1)$$
$$T + H \rightarrow HT \quad (2)$$

原子炉：JRR-3M　　装置：TAS-1（2G）　　分野：その他（放射化学）

$$T + T \rightarrow T_2 \qquad (3)$$

Table 1 mol % yields of HT(Y_{HT}) and T_2(Y_{T_2})

^{3}He : ^{4}He	state	Y_{HT}(%)	Y_{T_2}(%)
0.282:0.718	s	99.05 ± 0.09	0.95 ± 0.09
0.670:0.330	n	99.53 ± 0.05	0.47 ± 0.05

[a] s: superfluid, n: normal fluid.

Since the reactions (1)-(3) are generally considered as the barrier-free radical reactions, the reaction rate is controlled by the diffusion behaviors of H and T. In such a case, the rate constant(k_D) for the above reaction can be written as follows,[7]

$$k_D=[2k_BT(r_A+r_B)^2]/[3\eta(T)r_Ar_B], \qquad (4)$$

where k_B, T, η (T), r_A, and r_B represent Boltzmann constant, temperature, coefficient of viscosity, and atomic radii of A and B atoms. The eq. (4) shows that the reaction rates for (1) - (3) are identical each other because the atomic radii of H and T are same and that, therefore, Y_{HT} should be equal to Y_{T_2}. However, the experimental results shown in Table 1 are different from the theoretical prediction by eq. (4).

The definite conclusion cannot be obtained on the controlling mechanism leading to the preferential formation of HT over T_2. However the following is considered to be responsible for this at the present stage of the experiment. It is well known that the electron and the neutral atoms form the bubble due to the strong Pauli repulsive short-range force between He and them. This suggests that the effective atomic radii and masses of H and T change. No report has been published on the bubble structure of H and T but can be predicted to be 1 - 1.7 nm from the radii of Cs bubble[8] and electron bubble.[9] As for the effective masses, both the experimental results and the theoretical calculation predict to be about 10 for H, D and T.[10,11] Moreover, the recombination reaction in the gas phase at around 1 K is reported to be strongly affected by the difference of the energy level structure at low temperature between hydrogen isotopes.[12] Based on these experimental results and theoretical prediction, it seems reasonable that the rate constants for the reactions (1) - (3) cannot be predicted by the simple diffusion model such as eq. (4). They will be controlled by the unique processes arising from quantum properties of the liquid helium.

References

[1] Y. Aratono, "Chemistry in Liquid Helium" (in Japanese), Houshasenkagaku(Radiation Chemistry), **64**(1997), 7-16 .

[2]Y. Aratono, T. Matumoto, T. Kumada, K. Komaguchi, and T. Miyazaki, J. Phys. Chem., A, **102**(1998), 1501-1506.

[3]"Proceedings of the 128th WE-Heraeus-Seminor on Ions and Atoms in Superfluid Helium" Zeitschrift fur Physik B **98**(1995).

[4]A. Fujisaki, K. Sano, T. Kinoshita, Y. Takahashi, and T. Yabusaki, Phys. Rev. Lett., **71**(1993), 1039-1042.

[5]M. Takami, Comments At. Mol. Phys., **32**(1996), 219-231.

[6] "Chemical Kinetics and Dynamics" ed J. I. Steinfeld, J. Francisco, and W. L. Hase, Prentice Hall, Inc., Englewood Cliffs, New Jersey (1989) Chap. 4, P. 162.

[7] D. O. Edwards and M. S. Pettersen, J. Low. Temp. Phys., **87**(1992), 473-523.

[8]H. Bauer, M. Beau, B. Friedl, C. Marchand, and K. Miltner, Phys. Lett., A., **146**(1990), 134-140.

[9]C. C. Grimes and G. Adams, Phys. Rev. B, **41**(1990), 6366-6371.

[10]M. Saarela and E. Krotscheck, J. Low Temp. Phys., **90** (1993), 415-449.

[11]M. E. Hyden and W. N. Hardy, J. Low. Temp. Phys., **99** (1995), 787-849.

[12]M. Arai and T. Mizusaki, Private communication.

研究テーマ：実用金属材料の損傷検出に関する研究
表題：熱処理した鋼管の残留応力測定

Residual Strain Measurements of a Heat Treated Steel Pipe

K.INOUE, H.KAWASHIMA, J.SAKAGUCHI, N.MINAKAWA,[1] Y.TSUCHIYA[1] and Y.MORII[1]
Fac. Sci. & Tech. Ryukoku Univ. Seta, Otsu 520-2194, Japan
[1]*Japan Atomic Energy Research Institute, Tokai-Mura, Ibaraki 319-1195, Japan*

The 13% Cr steel pipe for the oil well is heat treated after plastic rolling, to obtain the desired strength. The pipe with diameter of 73mm and the thickness of 5.51mm, used for this experiments, was quenched from 900℃ to the room temperature by spraying the water on the outer surface. The crystal structure of the material becomes bcc, owing to the martensitic transformation. As the rate of cooling is different at each position of the wall thickness, the residual stress appears.

To know nondestructively the residual stress at each position, we have made the neutron diffraction study and observed a small change of the lattice spacing at intervals of 1mm of the wall thickness. RESA, installed at T2-1 port in JRR-3M was used. As a vertically focussed monochromator, (004) reflection of three pieces of pyrolytic graphite was used.. The wave length of the neutron beam was 2.1034 Å. The (110) reflection from each position of the pipe was observed. To see a small area of the x(radial) and y(hoop) planes, the pipe was set up, where the slits of $2\times15mm^2$ for incident beam and $2\times20mm^2$ for reflected beam were used. To observe the z(axial) plane, the pipe was reclined, where the slits of $2\times4mm^2$ for incident beam and $2\times6mm^2$ for reflected beam were used. The residual stress was estimated from the observed strain, and was compared with the stress calculated by means of the finite element method.

The experimentally obtained residual stress distribution is shown in Fig.1 and the calculated one in Fig.2. It is found that the coincidence between experimental and calculated stress values for axial direction are good.. However, for radial and hoop direction some difference were observed near the outer and the inner surface. It may be caused by the pre-treatment of the specimen before neutron diffraction.

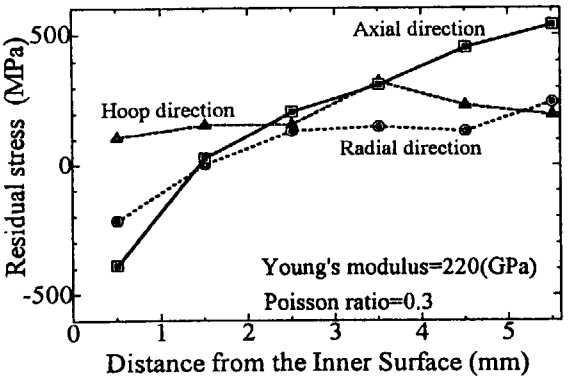

Fig. 1 Residual stress distribution obtained by neutron diffraction.

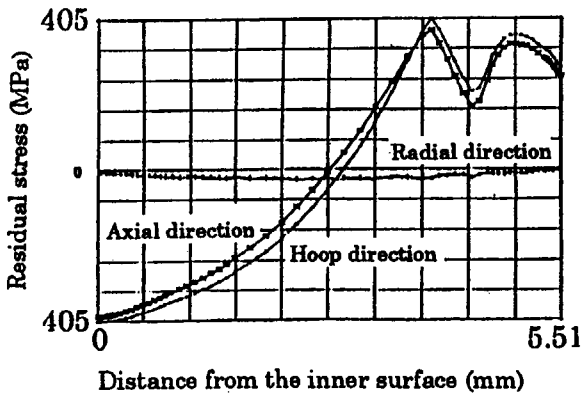

Fig.2 Residual stress distribution calculated by finite element method.

原子炉：JRR-3M　　装置：RESA(T2-1)　　分野：中性子散乱（機械材料）

研究テーマ：実用金属材料の損傷検出に関する研究
表題：直径 40mm の鋼丸棒の残留応力測定

Residual Strain Measurements of a Round Steel Bar with a diameter of 40 mm

K.INOUE, T.HORIKAWA, H.NAKAMURA, N.MINAKAWA,[1] Y.MORII[1] and RUDIONO[2]

Fac. Sci. & Tech. Ryukoku Univ. Seta, Otsu 520-2194, Japan
[1]Japan Atomic Energy Research Institute, Tokai-Mura, Ibaraki 319-1195, Japan
[2]Dep. Materials Sci. Eng. Ibaraki Univ. Hitachi, Ibaraki 316-0033, Japan

A preliminary experiment was done to prove usefulness of neutron diffraction for residual strain measurements of a round steel bar with rather large diameter. The residual stress analyzer RESA of JRR-3M was used. As the first step, the lattice spacing of an annealed steel bar which should be constant at any radial position was measured to confirm the accuracy of the measurements. In case of RESA, the cross section of the neutron beam is at least 2mm in diameter, to obtain a reasonable intensity. The larger sample size is better for good resolution, whereas the long path length of the beam in a large sample reduces the intensity of the scattered beam and the time necessary for measurements increases. In this experiment, the measured sample was S15C round steel bar with an annular circular notch of 40mm diameter. It was annealed at 700℃ for 2 hours and cooled down to room temperature in a furnace to exclude the strain caused by machining.

The wave length of the neutron beam was 2.0996 Å. We tried to measure the three dimensional lattice spacing at a 1mm step of the local position on a radius of the notch root. For the measurements of lattice spacing of (110) planes of radial and hoop direction, the bar was set up, where $2\times15mm^2$ slits were used for incident and reflected beams. For the axial direction, the bar was reclined, where both $2\times8mm^2$ slits were used.

The (110) peak from the axial plane at the center of the notch root is shown in Fig.1. It took 360 sec. to obtain one measuring point. The cross points show the measured raw data. The black circle at each angle shows the averaged value of both three neighboring values. The radial dependence of the obtained lattice spacing for three directions is shown in Fig.2. It is almost constant for all three directions at each position on the radius. This fact is reasonable for the specimen without fatigue test. The effect of the fatigue test on the residual strain of the same type bar will be studied in near future.

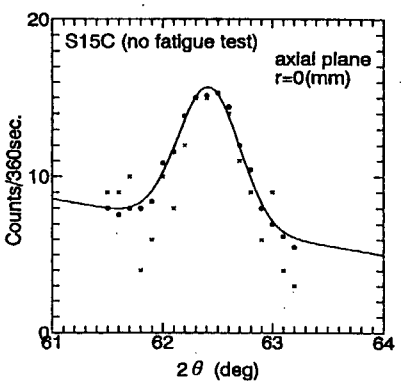

Fig. 1 (110) reflection from the axial plane at the center of the notch root of 40 mm ϕ.

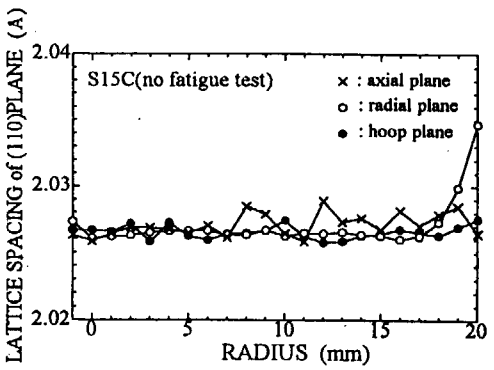

Fig.2 Radial dependence of each lattice spacing.

原子炉：JRR-3M　　装置：RESA(T2-1)　　分野：中性子散乱（機械材料）

研究課題：ジルコニア固溶体の構造相転移のその場観察
表題：高温における$Zr_{0.3}Ce_{0.7}O_2$の正方から立方への相転移のその場観察

In Situ Observation of the Tetragonal-to-Cubic Phase Transition of $Zr_{0.3}Ce_{0.7}O_2$ at High Temperatures

M. Yashima, T. Oketani, O. Yokota, M. Ohashi[1], K. Ohoyama[1], and Y. Yamaguchi[1]

Department of Materials Science and Engineering, Interdisciplinary Graduate School of Science and Engineering, Tokyo Institute of Technology, 4259, Nagatsuta-cho, Midori, Yokohama, 226-8502, Japan.
[1]Institute for Materials Research, Tohoku University, Katahira, Aoba, Sendai, 980-8577, Japan.

The diffusionless cubic-tetragonal phase transition has been suggested to be accompanied by the oxygen displacement along [001] from the ideal fluorite site (4*a* in *Fm*3*m*) as shown in Fig. 1. We have studied the compositional dependence of the displacement at room temperature.[1)] However, temperature dependence of the displacements has not been known as yet. The purpose of the present study is the investigation of the temperature-induced structural change of $Zr_{0.3}Ce_{0.7}O_2$ using neutron powder diffraction.

Compositionally homogeneous $Zr_{0.3}Ce_{0.7}O_2$ solid solutions were prepared by solid-state reactions. The axial ratio c/a_f of the tetragonal $Zr_{0.3}Ce_{0.7}O_2$ was 1.000(1).[1)] Neutron-diffraction experiments at high-temperatures up to 1400°C were performed in air using an electric furnace at KSD (T1-2) in JRR-3M, JAERI. Figure 2 shows temperature dependence of neutron-diffraction profile around 112 peak which is forbidden for the fluorite-type structure. 112 peak intensity decreased with increasing of temperature. The 112 peak seems to disappear around 1200°C, indicating that the long-periodicity of the oxygen displacement disappears in the present experimental resolution. The atomic coordinate of oxygen *z* was estimated from the integrated intensity ratio *I*(112)/*I*(111). The *z* value increased with increasing in temperature (Fig. 3).

Ref. 1) M.Yashima *et al., Appl. Phys. Lett.*, **72** (1998) 182.

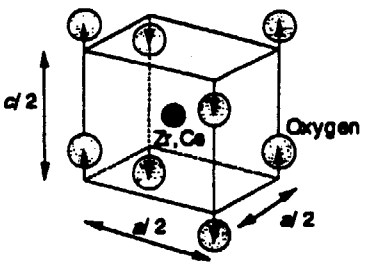

Fig.1 Oxygen displacement in tetragonal zirconia.

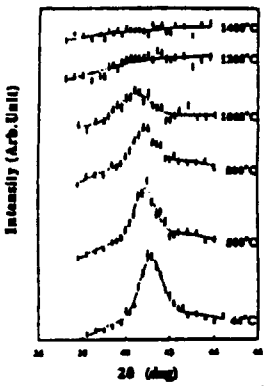

Fig.2 Temperature dependence of neutron diffraction 112 peak profile of ZrO_2-70mol%CeO_2

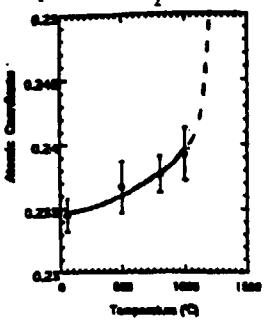

Fig.3 Temperature dependence of atomic coordinate of ZrO_2-70mol%CeO_2.

Reactor: (JRR-3M) Facility: (KSD(T1-2)) Field: (materials)

研究テーマ：イオン交換により合成したリチウム遷移金属酸化物の構造
表題：層状岩塩型リチウム含有鉄酸化物の構造

Crystal Structure of Lithium Iron Oxides with Layered Structure

A. Hirano*, R. Kanno, M. Tabuchi [1], K. Oyama [2], M. Ohashi [2], Y. Yamaguchi [2]

Department of Chemistry, Faculty of Science, Kobe University, Nada, Kobe, Hyogo 657, Japan
[1] *Osaka National Research Institute, AIST, 1-8-31 Midorigaoka, Ikeda, Osaka 563, Japan*
[2] *Institute for Materials Research, Tohoku University, Sendai, Miyagi 980, Japan*

Lithium iron oxide, $LiFeO_2$, with a layered structure was obtained by an ion exchange reaction of α-$NaFeO_2$. It has been studied as a possible candidate for cathode materials for lithium cells. The samples obtained by the ion exchange reaction contained cation disordering at the lithium site which prevents (de)intercalation reactions. Recently we synthesized the layered $LiFeO_2$ directly from Fe^{3+} sources (α-FeOOH) using mixed-alkaline (LiOH - NaOH) hydrothermal method. In this study, the structure of $LiFeO_2$ was determined by neutron diffraction measurements.

The neutron diffraction data were taken on a KPD neutron powder diffractometer at JRR-3M at Tokai Establishment of JAERI. The diffraction data was collected for 30 min at each 0.1 ° step width over a 2θ range from 5 ° to 155 °.

The neutron diffraction pattern was refined by Rietveld method using two structural models, the mono-phasic model of layered $LiFeO_2$ and the two phasic model with layered $LiFeO_2$ and α-$LiFeO_2$. The structural parameters of the layered $LiFeO_2$ were refined with space group R3m using a structural model, Li(1) at 3*a* (0, 0, 0), Fe(1) at 3*b* (0, 0, 0.5), O(1) at 6*c* (0, 0, *z*) with $z \sim 0.24$. Disordering of the lithium and iron at the 3*a* Li site was considered for the mono-phasic model with a constraint that the total occupancy is unity. The refinement using the two phasic model led to slightly lower R values.

Table 1 lists final R factors, lattice parameters, and their estimated standard deviations. Figure 1 illustrates the profile fit and differential patterns for the layered $LiFeO_2$. No significant disorder in the Li site was observed. However, the ratio of the mass fraction layered, $LiFeO_2$ / α-$LiFeO_2$ was 0.84 / 0.16 (wt.%). The results indicated that the synthesis conditions should be optimized to reduce the amount of α-$LiFeO_2$. Further studies on the structure and deintercalation property are necessary.

Table 1 Structural parameters for the layered $LiFeO_2$.

Atom	site	*g*	*x*	*y*	*z*	B*eq*(Å²)
Li(1)	3*a*	1	0	0	0	1.7(8)
Fe(1)	3*b*	1	0	0	0.5	0.5(2)
O(1)	6*c*	1	0	0	0.2424(9)	0.4(2)

$a = 2.95362(14)$Å, $c = 14.5212(6)$Å,
$R_{wp} = 8.85\%$, $R_P = 6.89\%$, $R_e = 4.64\%$, $R_I = 2.44\%$, $R_F = 1.35\%$.
Mass fraction of compounds, layered $LiFeO_2$: α - $LiFeO_2$ = 0.84 : 0.16.
$a = 4.1620(3)$Å for co-existing α - $LiFeO_2$.

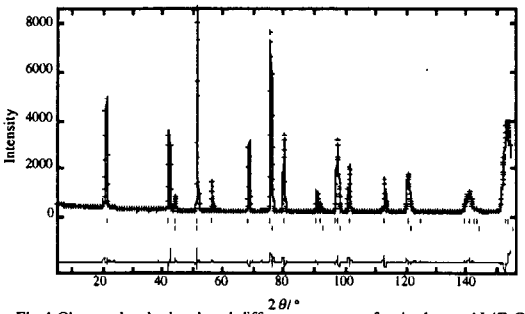

Fig.1 Observed, calculated and difference patterns for the layered $LiFeO_2$.

2. 中性子ラジオグラフィ
(Neutron Radiography)

This is a blank page.

研究テーマ：中性子ラジオグラフィによる矩形流路内沸騰二相流のボイド率計測
表　題　　：片面加熱矩形流路内サブクール沸騰時のボイド率計測と最適解析モデルの検討

片面加熱矩形流路内サブクール沸騰時のボイド率計測と最適解析モデルの検討

呉田 昌俊、 秋本 肇

日本原子力研究所
エネルギーシステム研究部
伝熱流動研究室

大強度陽子加速器のターゲットや大型放射光施設のモノクロメータ等は、片側から強力なビーム入射があり非常に高い熱流束負荷となる。そのため、高熱流束機器の除熱技術に関する研究開発が必要である。そこで、ＪＲＲ－３Ｍ熱中性子ラジオグラフィ施設を利用し、片面加熱矩形流路内を垂直上昇するサブクール沸騰二相流のボイド率計測を目的とする実験を開始した。また、高速度撮像中性子ラジオグラフィ法によりサブクール沸騰流の流動特性を可視化観察し、沸騰特性を明らかにする[1]。得られた高速度撮像画像から時間平均ボイド率の２次元分布を求め、これから沸騰開始条件やバーンアウト位置でのボイド率等熱流体特性上重要な物理量を計測する[2]。そして、得られた沸騰開始条件やボイド率データを用いて、最適ボイド率解析モデルを検討する。最後に、最適ボイド率解析モデルをバーンアウト予測モデルに組み込み、バーンアウト実験で得られたバーンアウトデータと比較・検討する。

実験装置は、水循環ループ、加熱用電源、中性子ラジオグラフィ用テスト部、そして計測・撮像系からなる。流路幅が３０mm、加熱幅が２０mm、加熱部長さが１００mm、流路間隙が3mmで助走区間付きのテスト部を用い、これにイオン交換水を垂直に流した。加熱は、流路の片側に貼り付けたステンレス箔を直流安定化電源を用いて直接加熱した。本実験では、この片面加熱矩形流路内でのサブクール沸騰二相流を中性子ラジオグラフィ法により可視化し、得られた画像を解析しボイド率を計測した。図１は、バーンアウト時の時間平均ボイド率分布を示している。撮像像速度は、1,125 フレーム/秒であり、図１は、バーンアウト直前の 2,250 枚の画像を時間平均化し求めたボイド率分布である。図２は、得られたボイド率データと既存のボイド率モデルによる予測結果の一例を示している。図中太線は、沸騰開始条件やボイド率情報をもとに実験式を作り、これを組み込んだ修正ドリフト・フラックス・モデルによる予測結果を示

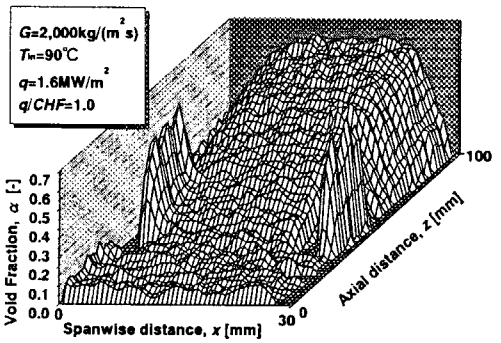

図１　バーンアウト時の時間平均ボイド率の２次元分布

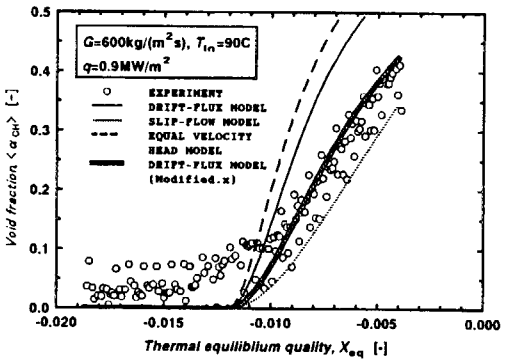

図２　実験値とボイド率モデルの比較

している。本ボイド率モデルにより、本実験条件のボイド率分布が予測可能であることがわかった。また、これを Katto のバーンアウトモデルに組み込むことにより、バーンアウトが物理的モデルにより予測可能であることが分かった。今後は、蒸気泡の長さや移動速度に関して既存のモデルでは問題があることが判明したので、これを中性子ラジオグラフィ法等で測定し、バーンアウトの物理的モデルによる予測手法の高精度化を進める予定である。

参考文献

1）呉田昌俊、秋本肇、日本原子力学会 1998 年春の大会、H11,Ⅱ-333(1998).
2）呉田昌俊、秋本肇、第１１回熱工学シンポジウム講演論文集、B102,(1998)

原子炉：JRR-3 装置：熱中性子ラジオグラフィ施設　分野：中性子ラジオグラフィフィ（流体力学）

研究テーマ：溶融炉心の圧力容器内流動に関する基礎研究
表　　題：下部ヘッド内挙動に関する水／液体金属二相可視化実験

下部ヘッド内挙動に関する水／液体金属二相可視化実験

柴本泰照、　中村秀夫、　安濃田良成
日本原子力研究所　東海研究所　原子炉安全工学部

シビアアクシデント時に、溶融炉心が圧力容器下部ヘッド内へジェット状に落下する場合を想定した液体金属の熱流動可視化実験を行った。

装置は、小型の半円形扁平ステンレス容器(流路幅 10mm, 半径 85mm)の試験部を模擬RPV、溶融金属(Pb-Bi)を模擬デブリとする。初期条件として容器内に飽和水を満たし、液体金属と冷却材との相互作用を観察した[1][2]。液体金属の流速分布を測定するために、熱中性子に不透明なカドミウムを含み、Pb-Bi 合金とほぼ同一の比重を有する金-カドミウム金属間化合物をトレーサとして使用した[3]。撮影は、高利得の image intensifier(I.I.)を用て高速度カメラ（Photoron 製）で行った[2][4]。

実験は、80cc の飽和水中に 523K, 1.82kg の液体金属を落下させた。これまで、高速撮影時には I.I.からのランダムノイズとトレーサとの識別が困難になる場合があり、画像処理上の問題点となっていた。今回この影響を最小にするため、カメラおよび I.I.のゲート機能を off（連続撮影）にすると共に、撮影速度を 125frame/s に低下させ、電気ノイズの抑制を試みた。その結果、ノイズの極めて少ない明瞭な画像が得られ、PIV による流速分布計測に成功した。

メルトは冷却水の激しい沸騰とともに対流・混合していくが、固化を伴うため、ここでは左右対称ではなく片側に偏った堆積挙動となった。デブリジェット落下終了から 4.8s 間（600 images）の積分平均画像を Fig.1 に示す。このとき、容器中央部から右側にかけては対流により撹拌されたため、ほぼ均一な温度を示したが、左側の温度は実験を通じて融点以下だった。画像中で輝度値の明るい部分は、porous 状に凝固した金属で、上方に蒸気の存在が確認できる。元画像からトレーサのみを抽出して積分平均した画像と、その時の流速分布の PIV 解析結果の一例を Fig.2 に示す。この図から、トレーサは一様に分布しておらず、早期に凝固した左上側にはトレーサが移動していないのがわかる。対流しているプールの方は、トレーサ流跡をよく表したベクトル分布を得ることができた。

参考文献

[1] 柴本ら、「混相流シンポジウム 98」B25
[2] Nakamura et al., (on submitting, Nucl. Technol., 1998)
[3] Takenaka et al., Fusion Eng. Des., **27**, 607 (1995)
[4] Hibiki et al., Nucl. Technol., **110**, 422 (1995)

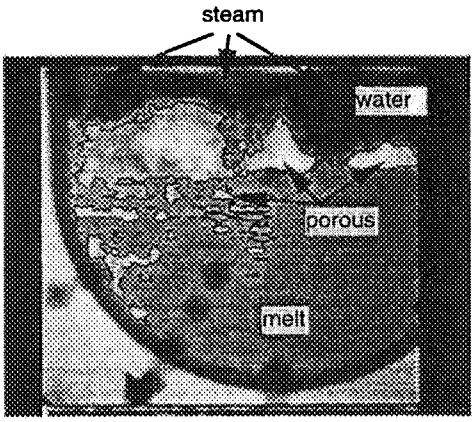

Fig.1 Average taken after the end of melt droping

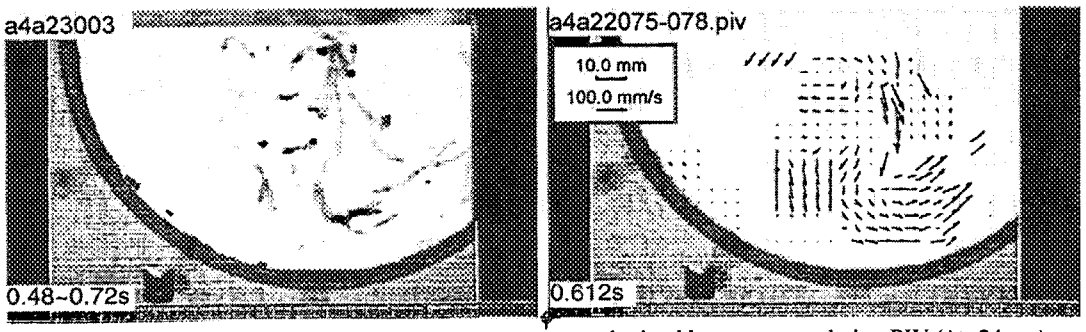

from 30 imeges : 0..48~0.72s　　obtained by cross-correlation PIV (Δt=24 ms)

Fig.2 Tracer path lines and velocity distribution during the multi-phase exp.

原子炉：JRR3-M　　装置：7R(TNRF)　　分野：中性子ラジオグラフィ（流体力学）

研究テーマ: 高温融体と冷却材の混合の可視化に関する研究

表　　題: 水蒸気爆発粗混合過程の中性子ラジオグラフィによる可視化

水蒸気爆発粗混合過程の中性子ラジオグラフィによる可視化

三島　嘉一郎、日引　俊、齊藤　泰司、杉本　純[1]、森山　清史[1]、松林　政仁[2]、市川　博喜[2]

京都大学原子炉実験所

〒590-0494　大阪府泉南郡熊取町野田

[1] 日本原子力研究所　炉心損傷安全研究室

〒319-1195　茨城県那珂郡東海村白方白根

[2] 日本原子力研究所　研究炉技術開発室

〒319-1195　茨城県那珂郡東海村白方白根

原子炉シビアアクシデント時に格納容器の健全性に脅威を及ぼす可能性のある現象の一つとして、溶融炉心と冷却材との相互作用による水蒸気爆発が考えられている。水蒸気爆発では、高温の溶融炉心が安定な蒸気膜に包まれた状態で冷却材中に分散する初期粗混合過程、トリガリングを経て、爆発的な蒸気発生とそれにともなう圧力波の発生が起こることが知られている。このとき、初期粗混合過程における冷却材中での溶融炉心や蒸気の分散状態は、水蒸気爆発の初期条件となり、その結果として生じる水蒸気爆発の発生確率や機械的エネルギーがこれに依存するため、重要な素過程と考えられている。

初期粗混合過程における冷却材中での溶融炉心や蒸気の分散状態を精度良く予測するためには、この素過程を高温溶融金属と水などを用いて模擬した実験を行い、現象を詳細に観察する必要がある。しかし、可視光を用いた方法では蒸気と水の界面における乱反射のため、粗混合領域を詳細に観察することは困難である。そこで、本研究では、界面での乱反射の影響を受けない中性子ラジオグラフィによる高速度撮像法を用いて、水中に落下させた溶融金属の分散、水との混合挙動を可視化し、画像処理により混合領域内の溶融金属、蒸気泡、水の分布に関する物理量の測定を試みている。

平成 9 年度には中性子ラジオグラフィ高速度撮像法を検討し、粗混合過程におけるボイド率変化を詳細に評価するために加熱剛体球を重水中に落下させて実験を行った。中性子源として日本原子力研究所 JRR-3M 熱中性子ラジオグラフィ施設を利用した。シンチレータには残光時間をの短い ^{6}LiF/ZnS を用い、撮像系には高感度の画像増幅器を取り付けた高速度ビデオ（最高撮像速度毎秒 1000 コマ）を用いた。

Fig. 1 に 1000℃に加熱した直径 12mm のステンレススティール製の剛体球を重水中に落下させたときの重水中に形成されるガスドームの様子を、8ms 毎に連続画像で示す。中性子ビームはステンレススティール製金属球を比較的よく透過するため、気相およびガスドーム中における剛体球の位置は静止画像からは明確には分からない。しかし、動画を観察することにより、ある程度の位置を確認することは可能であった。0ms の画像は剛体球が液面に接触した瞬間の画像であり、その後、剛体球の液中への進行に伴い、鉛直方向下向きにガスドームが成長していることがわかる。やがて、剛体球はガスドーム先端を離脱し、水槽下部に沈降していく。20ms を超えると剛体球は画像視野から消失し、水槽下部に沈降していく。その後、ガスドームの先端の鉛直下向の成長速度はやや緩やかになるが、同時に水平方向へガスドームが膨張していくことが分かる。このような膨張は加熱剛体球と接触したガスドーム内の界面近傍の過熱された液膜の急激な蒸発のために生じたと考えられる。

加熱剛体球の落下によって生じたガスドームのボイド率をΣスケーリング法を用いて計算した。

Fig.1 に加熱剛体球の温度および径がそれぞれ 1000℃、12mm の空間平均ボイド率$< \alpha >$の時間変化を加熱剛体球の温度をパラメータとして示す。ここで空間ボイド率 $< \alpha >$ はボイドの中心から左右対称に 36mm、高さ方向に

原子炉：JRR-3M　　装　置：中性子ラジオグラフィ　　分　野：流体力学

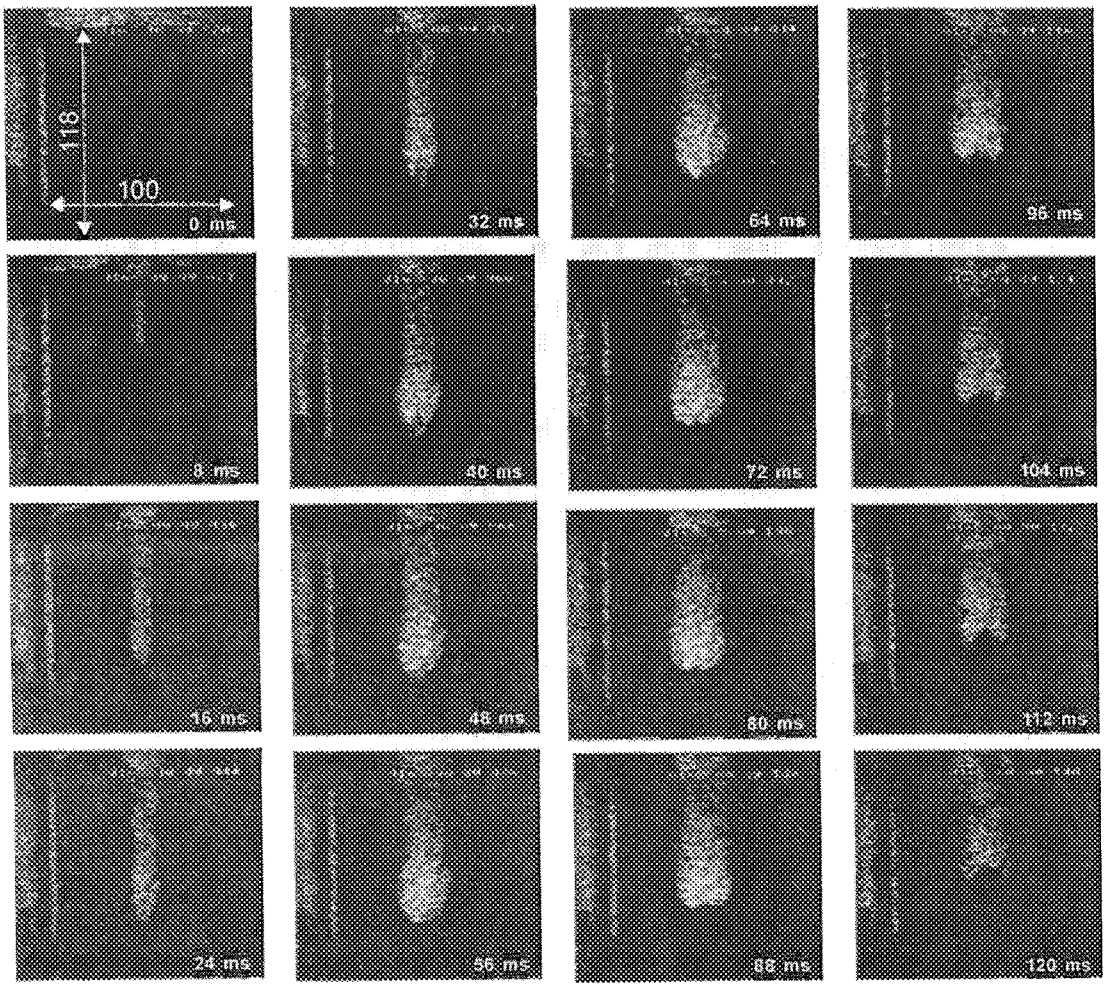

Fig.1 Consecutive images of heated stainless steel particle and heavy water interaction. (Recording speed: 500frames/s, Frame interval: 8ms, Particle temperature: 1000°C, Particle diameter: 12mm)

100mm の区間で平均したボイド率である。ここで、平均化する空間の z 方向の始点は液面の揺動の影響を受けない液面よりもわずかに下方の位置とした。図から、空間平均ボイド率は異なる二つ以上のピークを持つことがわかる。ここで、一つ目のピークは、ガスドームから熱源がなくなることに対応していると考えられる。このことは、いずれの温度の場合においても、ガスドームから剛体球が消失する t =20ms 近傍にピークがあることからも妥当であると考えられる。二つ目のピークは過熱液相の蒸発から凝縮に転じる時間に相当していると考えられる。この第一ピークから第二ピークまでに要する遅れ時間は剛体球の温度によって変化するが、T_p=800℃のデータにおいては複数のピークが存在するようにも考えられ、この点に関して、さらに検討を進める必要がある。

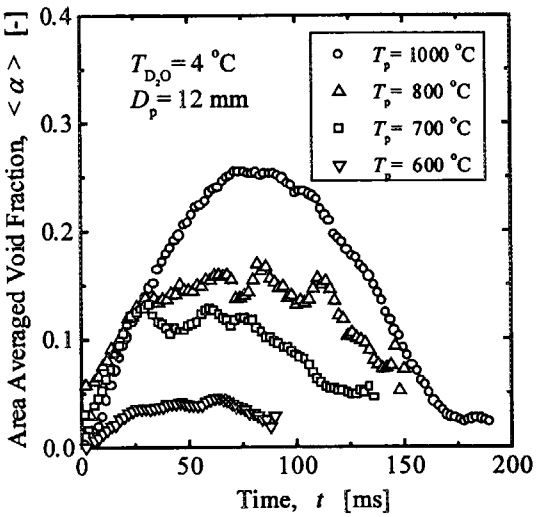

Fig.2 Temporal variation of area averaged void fraction as a parameter of particle temperature.

研究テーマ：研究炉に関する工学的開発研究
表　　題：中性子ラジオグラフィに関する開発研究

中性子ラジオグラフィに関する開発研究

松林　政仁
日本原子力研究所東海研究所

本年度は高解像度撮像システムを用いた中性子CT(Computed Tomography)の植物試料への応用を試みるとともに、平成８年度の黎明研究の成果[1]を別の古文化財に適用した。また、中性子ビーム線質把握の必要性に鑑み、中性子ビーム線質計を製作しJRR-3M中性子ラジオグラフィ装置の線質測定を行った。

1) 中性子CTの植物試料への応用

中性子ラジオグラフィの植物試料への応用のの有効性は東大の中西らによって報告されているが、これまではフィルム法を用いた２次元画像が中心であった。これに対し中性子CTを用いて３次元的に内部情報を捉えることが可能となった。[2] 第１図にユリの蕾への適用例を示す。投影画像のみでは確認が困難であった内部の構造がCT像でははっきりと再現されている。

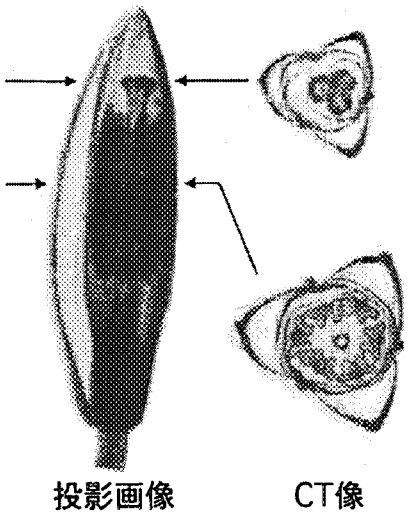

第１図　ユリの蕾の投影画像及びCT像

2) 中性子ビーム線質計の製作及び線質測定[3]

立教大学の小林らが考案した中性子ビーム線質計(BQI)を基本として新たに５個のBQIを製作し、JRR-3M中性子ラジオグラフィ装置の中性子ビーム（冷中性子及び熱中性子）の実効エネルギーを測定した。本線質計はチタンと鉛の実効的全巨視的断面積の中性子エネルギー依存特性が異なることを利用したものである。

測定の結果実効エネルギーとして、熱中性子に対して平均27.5meV、冷中性子に対して平均2.5meVが得られた。さらに熱中性子ビームに単結晶ビスマスをフィルタとして使用した場合、5cm、10cm及び15cmの各厚さに対してそれぞれ24.6meV、15.6meV及び11.5meVが得られ、立教大学炉で鉛フィルタを用いて確認された実効エネルギー低減効果と同様の傾向が観察された。また使用する撮像系に対する依存性は実効エネルギーが低くなる程大きくなることが分かった。

3) 古文化財への応用

平成８年度の黎明研究として実施した検査技術を鉄鉾、鉄製工具、鉄剣等に適用し、有効性の確認を行った。今回はγ線による画像を改善するためにX線によるフィルム撮影で広く用いられている鉛増感紙を新たに使用した。特筆される結果は鉄鉾及び鉄製工具の画像で観察された。鉄鉾では鉾の内部に残されていた柄の部分が中性子による画像で確認され、γ線による画像では確認されなかった。これは内部に残された柄が木質を保っているものと推定される。一方、鉄製工具では、外観から確認できた木部と思われる部分は、γ線による画像でも確認され、木部に鉄等が錆として浸透した結果と考えられた。

参考文献

1) 非破壊検査, 第47巻5号 312-314 (1998)
2) 日本非破壊検査協会放射線分科会, 平成9年7月10日　浜松ホトニクス豊岡製作所
3) International Topical Meeting on Neutron Radiography 3, Lucerne, Mar.16-19, 1998

原子炉：JRR-3M　　装　置：中性子ラジオグラフィ　　分　野：中性子ラジオグラフィ（古文化財、その他）

JRR-3M 高束中性子 NR システムによる熱流動現象の可視化と計測に関する研究 (II)

Studies on Visualization and Measurement of Thermal Hydraulics Phenomena by High Flux Neutron Radiography System at JRR-3M

神戸大学　竹中　信幸、浅野　等、小野　厚夫、後　利彦、瀬川　耕司、和田　哲昌、永江　信也、岩谷　淳二、迫田　健吾、浜田　尚志、隅　信介、水端　稔、西岡　聡、荒川　哲矢、小林　幸司、野口　泰幹、木下　泉、西　義久、古谷　正裕、藤江　政武、西村　聡、柴田　豊、
関西大学　小澤　守、梅川　尚嗣、松田　健、福田　和将、
神戸商船大学　中沢　武、
日本原子力研究所　松林　政仁

1、序

熱中性子線は、多くの金属やセラミックをよく透過する一方、水・有機液体や特定の元素によく減衰する特性を有する。このような熱中性子の透過特性を利用すれば、従来の方法では不可能か極めて困難であった可視化・計測が可能となる。

本研究は、機械、化学、原子力工学の分野で重要な熱流動現象を対象として、現在世界最高性能システムの一つである JRR-3M 高束熱中性子ラジオグラフィシステムを用いて、種々の体系についての可視化法と画像処理による計測法を開発し、従来解明されていない熱流動現象を明らかにすること、またそれによって中性子ラジオグラフィ応用の有用性を示すことを目的とする。

熱流動現象の問題は、流体力学と熱力学の古典力学を基礎とする境界値問題であり、工学的応用に関連した種々の体系での実験が必要である。

熱中性子の特性を有効に利用した可視化・計測の対象として、以下の体系について熱流動現象の解明を行った。

1、液体金属流れの可視化と計測
2、気液二相流のボイド率分布
3、混相流機器の可視化と診断

2、研究方法と結果

2－1、液体金属流れの可視化と計測

液体金属の熱流動現象は、特に原子力工学において重要であるが、液体金属が可視光に不透明であるため流れ場を可視化することは容易ではない。鉛、ビスマス、錫等の重金属合金は、低融点で化学的に不活性であることから熱媒体としての使用が検討されているが、このような液体金属の流れの可視化は中性子線以外では困難であると思われる。

本研究では、すでに開発したトレーサ法・ダイ法を用いて、高速増殖炉（ＦＢＲ）の新型蒸気発生器設計のための基礎実験として液体の鉛・ビスマス・錫合金中の水の蒸発挙動とＭＨＤ流れの解明を目的とした磁場下の噴流の可視化と計測を行った。

JRR3-M7R、中性子ラジオグラフィー装置、熱流動

図1－1に毎秒500コマの高速度ビデオカメラで撮影した溶融金属中の水蒸発挙動の例を連続写真で示す。白く写っているのが蒸気泡であり、このような画像から蒸気泡の成長速度、上昇速度の計測を行い、実験式を作成した。作成した実験式はＦＢＲ新型蒸気発生器の概念設計に使用されている。

図1－2はトレーサ法で鉛・ビスマス合金の速度場を計測した例であり、磁束密度0.25Ｔと磁場無い場合の例を示している。磁場下の液体金属ＭＨＤ流れの可視化は従来報告例が無く、今後ＭＨＤ流れの解明を行ううえで有力な手法であることを実証した。

2－2、気液二相流のボイド率分布

ボイド率は二相流における気相の体積割合であり、二相流研究における重要な計測量であり、中性子線減衰を冷却型ＣＣＤカメラを用いて、高分解能の計測が期待できる。可視化画像を基に、1、2次元、ＣＴ法による3次元の計測を行っている。ラジオグラフィの画像の輝度は中性子や可視光の散乱成分や多くのノイズを含んでいるため定量化を行うには特別な工夫が必要である。中性子、可視光両方の散乱成分を評価できる方法として真影法を改良した手法を開発し、一部については定量的計測も行った。

図2－1は原子炉の安全研究で重要なロッドバンドル内のスペーサ近傍の気液二相流ボイド率分布をＣＴ法によって3次元可視化した例であり、今後定量的計測を行う予定である。図2－2は同様の二相流のボイド率の断面平均値の一次元分布を可視化した例であり、多数の可視化例から従来完全には解明されていないスペーサの影響について多くの定性的知見を得ている。

図2－3は気液二相流における重力と遠心力の効果を解明するために行った渦巻き管内の空気水二相流の可視化例を示す。十字型の暗い部分は散乱成分を測定用のカドミウムテープであり、試験部とビームの間に置き、その輝度から散乱成分を計測する。渦巻き管各部のボイド率を計測することにより二相流に対する遠心力と重力の影響を明らかにした。

2－3、混相流機器の可視化と診断

大抵の機械は金属で製作されている。混相流機器内の流動特性を可視化診断するには中性子ラジオグラフィによる可視化が適しており、実際の機械を可視化することにより運転状態の診断が行える。本研究では、実際の冷凍機と流動層ボイラのコールドモデル機の混相流機械について、可視化と診断を行った。

冷凍機は圧縮機、蒸発器、凝縮器、分離器、分岐器、キャピラリー管の各要素からな成っており、各要素の可視化を行い、起動時、定常運転時、停止時の冷媒挙動の可視化、診断を行った。図3－1は内径2mmのキャピラリー管内のフレオン沸騰二相流のボイド率を計測した例である。管内でフレオンは液単相から沸騰して二相流となるが従来このような細い管内の現象は測定されておらず、現在このような結果をもとに構成式作成を行っている。

冷凍機の高効率化のため、蒸発部、凝縮部の熱交換器を並列に配置することが検討されているが、このためには並列部で二相流を分岐する必要がある。二相流の非線形性のため分岐は、非均一性や不安定性を伴うことが一般的であり、分岐部の設計に工夫が必要である。図3－2は種々の分岐部に対して分岐後のボイド率を測定することによりその性能を検討した結果の例である。まず従来型の分岐器では分岐特性が均等でないことを確認し、流れ場の観察から分岐器を改良し、試験を行った。改良により分岐特性は改善され、分岐部の

最適設計に有用であることが示された。

流動層燃焼はゴミのような雑多な燃料を清浄に燃焼させる方法として注目されている。流動層は砂に燃料を混合し空気を吹き込みことで流動化させ均質な燃焼を起こさせる装置である。砂が中性子線に透明であることから、ガドリニウムやカドミウムで適度に着色することにより、砂と空気の固気二相流を可視化することができる。図3－3は流動層ボイラにおけるチューブバンク部コールドモデル内の固気二相流を可視化して例であり、このような可視化結果をもとに平均体積率測定や熱伝達率と体積率の相関等を測定し、最適なチューブ配置を検討した。また、砂の中に燃料を模擬した異物の挙動を可視化し実験式を作成した。

3、今後の方針

3－1、液体金属流れの可視化と計測

液体金属ＭＨＤ流れの可視化と流れ場の計測を行い、ＭＨＤ効果の解明を行う。特に磁場の印可による加速効果と不安定化の機構を解明することを目的とした実験を行う。

3－2、気液二相流のボイド率分布

真影法を改良したボイド率の定量的測定法を種々の気液二相流に適用し、実験式の提案を行っていく。実験は定量化手法の検証を目的とした円管内二相流の断面平均1次元分布、従来から定性的に行ってきたバンドル内二相流と新たにプレート熱交換機内の沸騰二相流の3次元計測、スペーサ付きの二重管内二相流、ＴおよびＹ分岐管部内二相流について行う予定である。

3－3、混相流機器の可視化と診断

冷凍機内の各要素のうち、特に分離器、分岐器について新たな設計を行ったものを順次試験する予定である。

4、成果の公表

本研究で得られた成果をもとに学術雑誌、国際会議で公表された論文、および研究に参加した学生の卒業・修士論文を示す。

1. Y.Motomura, A.Ono and T.Takenaka,
"Suppression of Isolated Noises in the Dynamic Neutron Radiography Image by Using methematical Morphology",
Nuclear Instrument and Methods in Physics Research A 377, 1996, pp.93-95.

2. N.Takenaka, H.Asano, T.Fujii, T.Wada, M.Matsubayashi and A.Tsuruno,
"Three-Dimensional Void Fraction Measurement of Two-Phase Flow in a Rod Bundle by Neutron Radiography",
Nuclear Instrument and Methods in Physics Research A 377, 1996, pp.115-118.

3. K.Mochiki, Y.Murata, N.Takenaka, H.Kobayashi, M.Matsubayashi and A.Tsuruno,
"Musashi Image Processing System for Dynamic Neutron Radiography",
Nuclear Instrument and Methods in Physics Research A 377, 1996, pp.130-132.

4. M.Ozawa, H.Umekawa, T.Matsuda, N.Takenaka, A.Tsuruno, M.Matsubayashi,
"Void Fraction Profile in Tube-banks of a Simulated Fluidized-bed Heat Exchanger, Nuclear Instrument and Methods in Physics Research, Section A377, 1996, pp.144-147.

5. N.Takenaka, H.Asano, T.Fujii, Y.Murata, K.Mochiki, A.Taguchi, M.Matsubayashi and A.Tsuruno,
"Void Fraction Distribution Measurement in Two-Phase Flow by Real-Time Neutron Radiography and Real-Time Image Processing",
Nuclear Instrument and Methods in Physics Research A 377, 1996, pp.153-155.

6. N.Takenaka, H.Asano, T.Fujii, Y.Motomura, A.Ono, M.Matsubayashi and A.Tsuruno,
"Liquid Metal Flow Measurement of Neutron Radiography",
Nuclear Instrument and Methods in Physics Research A 377, 1996, pp.156-160.

7. H.Asano, N.Takenaka, T.Fujii, Y.Murata, K.Mochiki, A.Taguchi, M.Matsubayashi and A.Tsuruno",

"Application of Neutron Radiography to a Diagnosis of Refrigerator",
Nuclear Instrument and Methods in Physics Research A 377, 1996, pp.170-173.

8. N.Takenaka, H.Asano, T.Fujii, Y.Murata, K.Mochiki, A.Taguchi, M.Matsubayashi and A.Tsuruno,
"Application of Neutron Radiography to Visualization of Cryogenic Fluid Boiling Two-Phase Flows."
Nuclear Instrument and Methods in Physics Research A 377, 1996, pp.174-176.

9. N.Takenaka, T.Fujii, T.Wada, M.Matsubayashi, A.Tsuruno,
"Three-Dimensional Void Fraction Measurement of Steady Air-Water Two-Phase Flow in a Rod-bundle by Neutron Radiography",
Proc. Japan-US Seminar Two-Phase Flow Dynamics, July 1996, Fukuoka, Japan, 1996, pp.331-337.

10. 小澤守、梅川尚嗣、松田健、竹中信幸、松林政仁、鶴野晃、
流動層における粗大粒子の挙動と抗力係数
日本機械学会論文集 (B 編)62巻601号, 1996, pp.3413-3420.

11. N.Takenaka, H.Asano, T.Fujii and M.Matsubayashi
"Three-dimensional Void Fraction Measurement of Steady Two-phase Flow by Neutron Radiography",
Proc. OECD/CSNI Specialist Meeting. on Advanced Instrumentation and Measurement Technique, March, 1997, Santa Barbara, USA, 1997, III-6.

12. N.Takenaka, H.Asano, T.Fujii, T.Wada and M.Matsubayashi
"Three-dimensional Void Fraction Measurement of Two-phase Flow in a Rod Bundle by Neutron Radiography",
in "Fifth World Conference on Neutron Radiography", ed. C.O.Fischer, J.Stade
and W.Bock, Deutsche Gesellschaft Fur Zerstroerungsfreie Pruefung e.V., 1997, pp.118-125.

13. Y.Nishi, I.Kinoshita, M.Furuya, N.Takenaka and M.Matsubayashi, A.Tsuruno
"Application of Neutron Radiography to Visualization of Direct Contact Heat Exchange between Water and Low Melting Point Alloy",
in "Fifth World Conference on Neutron Radiography", ed. C.O.Fischer, J.Stade
and W.Bock, Deutsche Gesellschaft Fur Zerstroerungsfreie Pruefung e.V., 1997, pp.548-555.

14. M.Ozawa, H.Umekawa, T.Matsuda, N.Takenaka, A.Tsuruno and M.Matsubayashi
"Measurement of dynamic behavior of void fraction in tube-banks of a simulated fluidized-bed by neutron radiography",
in "Fifth World Conference on Neutron Radiography", ed. C.O.Fischer, J.Stade
and W.Bock, Deutsche Gesellschaft fuer Zerstoerungsfreie Pruefung e.V., 1996, pp.610-616.

15. H.Asano, N.Takenaka, T.Fujii, Y.Murata, K.Mochiki, A.Taguchi, M.Matsubayashi and A.Tsuruno,
"Application of Neutron Radiography to Diagnosises of a Refrigerator",
in "Fifth World Conference on Neutron Radiography", ed. C.O.Fischer, J.Stade
and W.Bock, Deutsche Gesellschaft Fur Zerstroerungsfreie Pruefung e.V., 1997, pp.623-629.

16. N.Takenaka, H.Asano, T.Fujii, Y.Nishi, M.Furuya, I.Kinoshita and M.Matsubayashi
"Visualization and Image-Processing of Multi-Phase Flow by Neutron Radiography",
Proc. 2nd. Japanese-German Symposium on Multi-Phase Flow, Tokyo, Japan, Sep. 25-27, 1977, pp.383-394.

17. N.Takenaka, H.Asano, T.Fujii, T.Wada, M.Matsubayashi
"Visualization and Three-dimensional Void Fraction Measurement of Steady Air-water Two-phase Flow in a 4x4 Rod Bundle by Neutron Radiography",
Proc. 8th Int. Top. Meet. on Nuclear Reactor Thermal Hydraulics, Kyoto, Japan Sep.30-Oct.4, 1997, Vol.3, pp..1622-1629.

18. N.Takenaka, H.Asano, T.Fujii, K.Yoshii, M.Matsubayashi
"Application of Thermal and Fast Neutron Radiography to Visualization of 3-D Void Fraction Distribution of Gas-liquid Two-phase Flow",
Proc. 1st European-Japanese Two-phase Flow Group Meeting and 36th European Two-phase Flow Group Meeting, Slovenia, June, 1998.

19. N.Takenaka, H.Asano, T.Fujii, T.Mizubata, M.Matsubayashi
"Three-dimensional Void Fraction Distribution of Steady Two-phase Flow in a Rod Bundle by Neutron Radiography""
Proc. 3rd Int, Conf. on Multiphase Flow, ICMF'98, Lyon, June, 1998.

20. M.Ozawa, H.Umekawa, N.Takenaka and M.Matsubayashi
"Flow Pattern and Void Fraction Distribution of Cross-Flow Tube Banks in a Simulated Fluidized-Bed Model",
Proc. 3rd Int, Conf. on Multiphase Flow, ICMF'98, Lyon, June, 1998.

21. Y.Shibata, T.Ebisu, H.Asano, N.Takenaka, T.Fujii, M.Matsubayashi
"Visualization of Refrigerant Gas-liquid Two-phase Flow inside a Distributor by Neutron Radiography",
Proc. 3rd Int, Conf. on Multiphase Flow, ICMF'98, Lyon, June, 1998.

22. M.Ozawa, H.Umekawa, T.Matsuda, N.Takenaka and M.Matsubayashi
"Local Void Fraction Distribution and Heat Transfer in Tube-Banks Immersed in a Fluidized-Bed",
to be published in Proc. Int. 11th. Heat Transfer Conf., Korea, August, 1998.

23. Y.Nishi, I.Kinoshita, M.Furuya, N.Takenaka, M.Matubayashi
"Visualization of Direct Contact Heat Transfer Between Molten Alloy and Water by Neutron Radiography",
to be published in Proc. 11th Int. Heat Transfer Conf., Korea, August, 1998.

24. N.Takenaka, H.Asano, T.Fujii, K.Yoshii, M.Matsubayashi
"Void Fraction Distribution Patterns of Steady Air-water Two-phase Flow in a Rod Bundle with a Spacer",
to be published in ASME paper

25. H.Asano, N.Takenaka, T.Fujii, T.Arakawa, M.Matsubayashi
"Flow Pattern of Gas-liquid Two-phase Annular Flow in a Spiral Tube",
to be published in ASME paper

26. N.Takenaka, H.Asano, T.Fujii and M.Matsubayashi
"Three-dimensional Void Fraction Measurement of Steady Two-phase Flow by Neutron Radiography",
to be pubilished in Nuclear Engineering and Design.

【修士論文】

後利彦、"ねじりテープ付き垂直管内ポストドライアウト熱流動に関する研究"、神戸大学自然科学研究科博士前期課程機械工学専攻 (1996).

和田哲昌、"中性子ラジオグラフィによる気液二相流の可視化と計測"、神戸大学自然科学研究科博士前期課程機械工学専攻 (1997).

永江信也、"蒸気インジェクターノズルの流動特性に関する研究"、神戸大学自然科学研究科博士前期課程機械工学専攻 (1997).

迫田健吾、"T字分岐管による気液二相流の相分離特性に関する研究"、神戸大学自然科学研究科博士前期課程機械工学専攻 (1997).

松田健、"流動層熱交換器におけるフローパターンと伝熱特性"、関西大学大学院工学研究科機械工学専攻 (1997).

【卒業論文】

隅信介、"中性子ラジオグラフィによる液体金属の可視化と計測"、神戸大学工学部機械工学科 (1996).

永森英樹、"ねじりテープ付き垂直管内ポストドライアウト熱流動に関する研究"、神戸大学工学部機械工学科 (1996).

浜田尚志、"中性子ラジオグラフィによる気液二相流の可視化と計測"、神戸大学工学部機械工学科 (1997).

荒川哲矢、"T字分岐管による気液二相流の相分離特性に関する研究"、神戸大学工学部機械工学科 (1997).

水端稔、西岡聡、"中性子ラジオグラフィによる気液二相流の可視化と計測"、神戸大学工学部機械工学科 (1997).

今口信弘、西井真二、"流動層熱交換器におけるフローパターンと伝熱特性"、関西大学工学部機械工学科 (1997).

小倉明雄、"T字分岐管による気液二相流の相分離特性"、神戸大学工学部機械工学科 (1998).

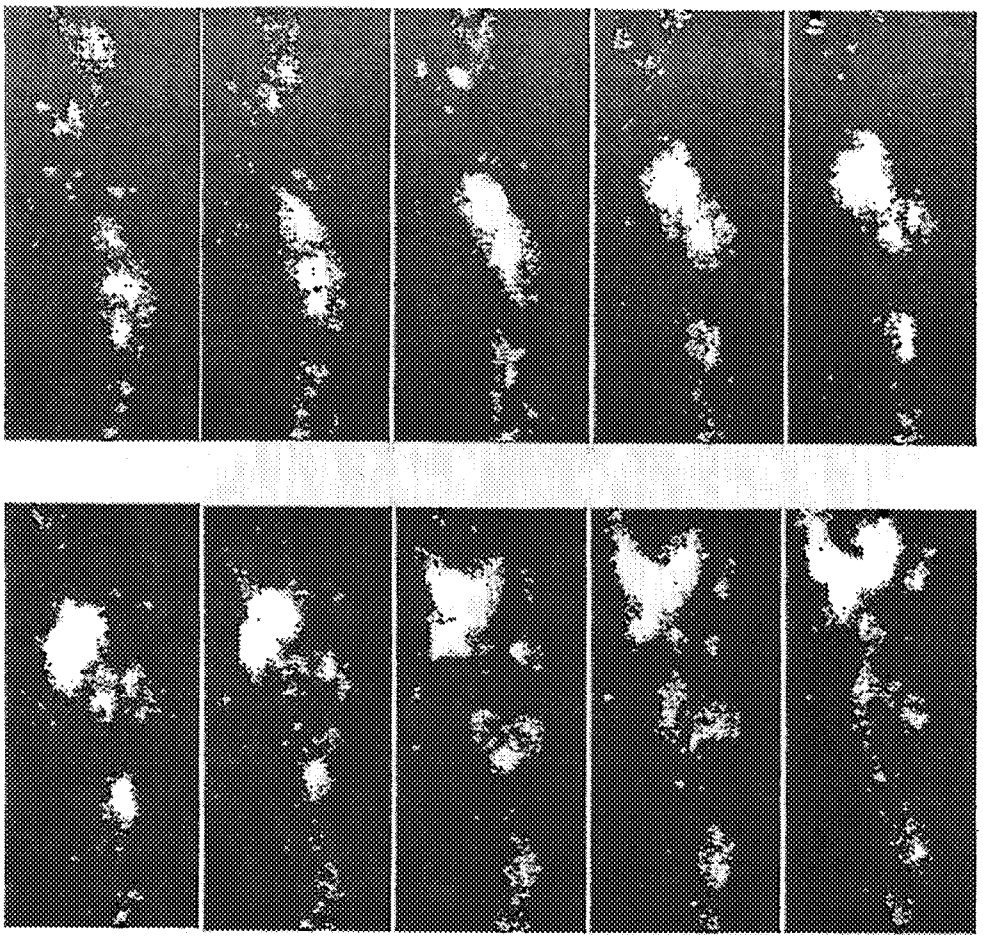

図1－1　溶融鉛ビスマス錫合金中の水の蒸発挙動の連続写真、高速度ビデオカメラ、500コマ／秒

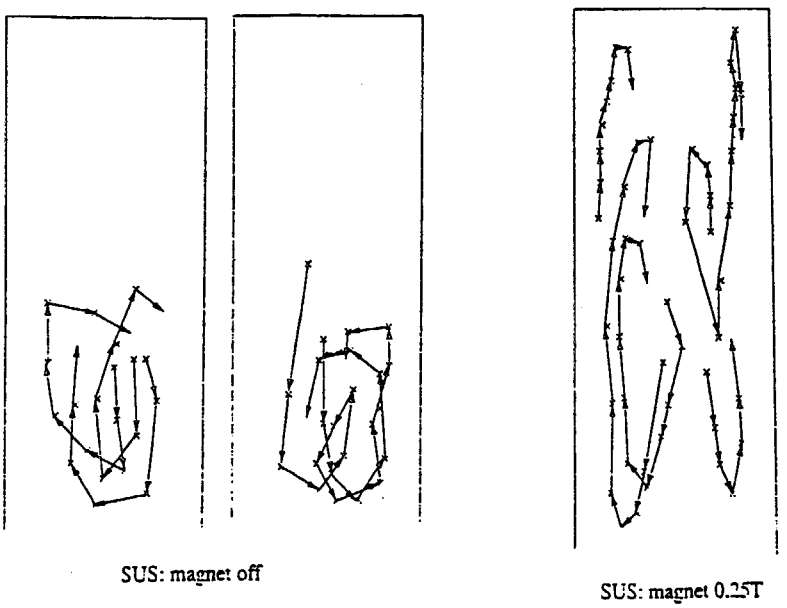

図1－2　鉛ビスマス合金内の噴流に対する磁場の影響、トレーサ法による速度ベクトルの測定

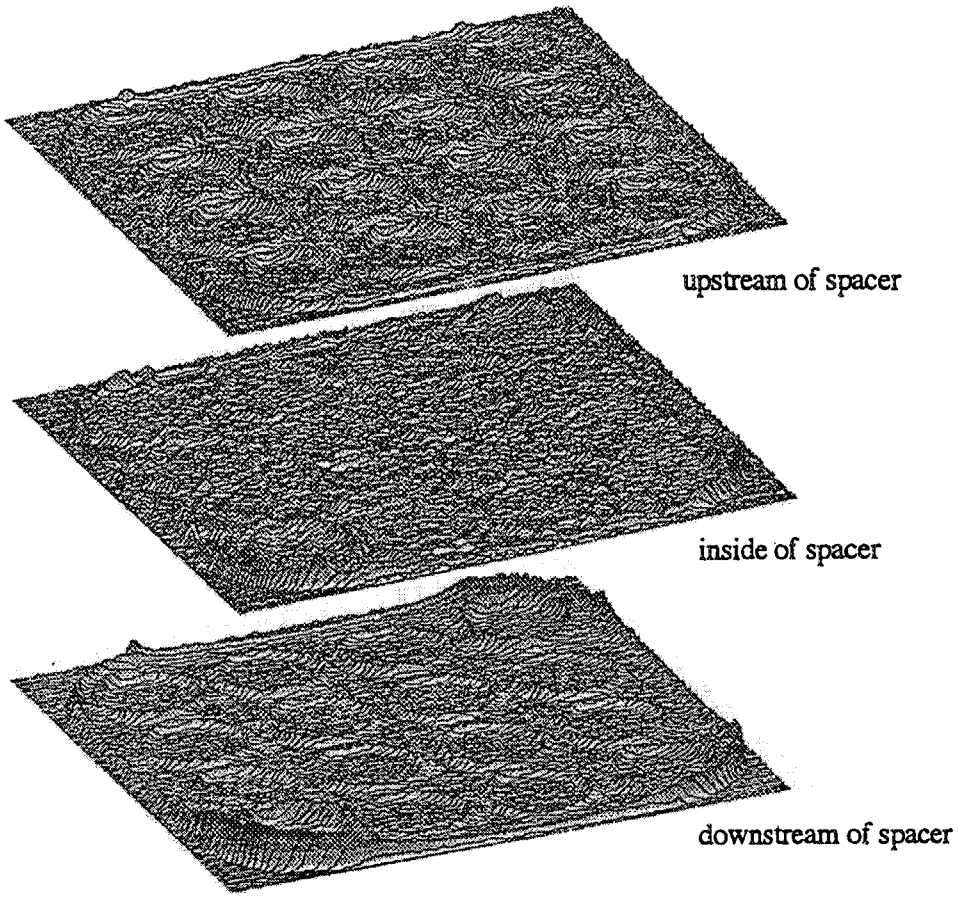

Examples of 3-D void fraction distributions by TNR
jg = 15.8 m/s, jl = 0.028 m/s

図2－1　ロッドバンドル内気液二相流の3次元ボイド率分布の例

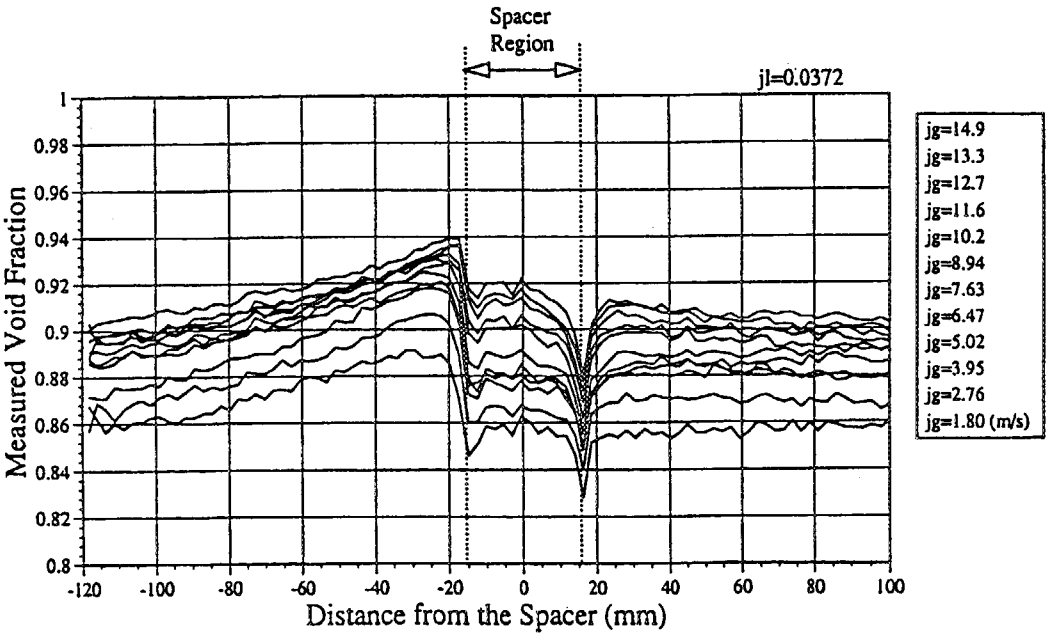

図2－2　ロッドバンドル内気液二相流の管断面平均1次元ボイド率分布の例

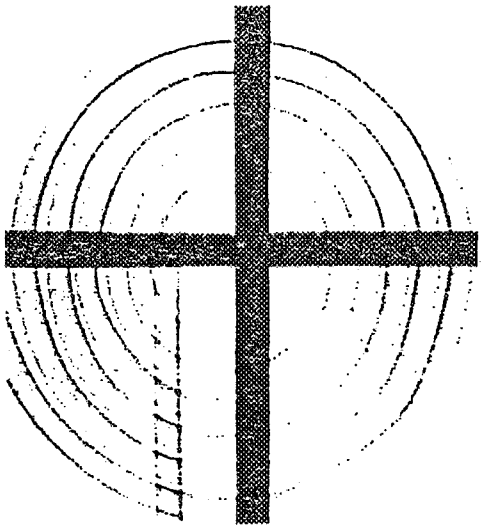

図２－３　渦巻き管内気液二相流の可視化画像、冷却型ＣＣＤカメラ

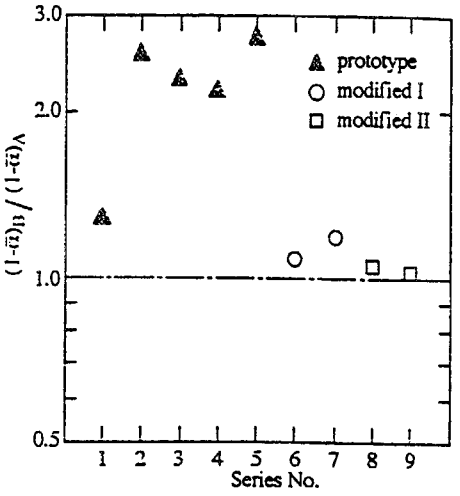

図３－２　各種二相流分岐器の分岐特性

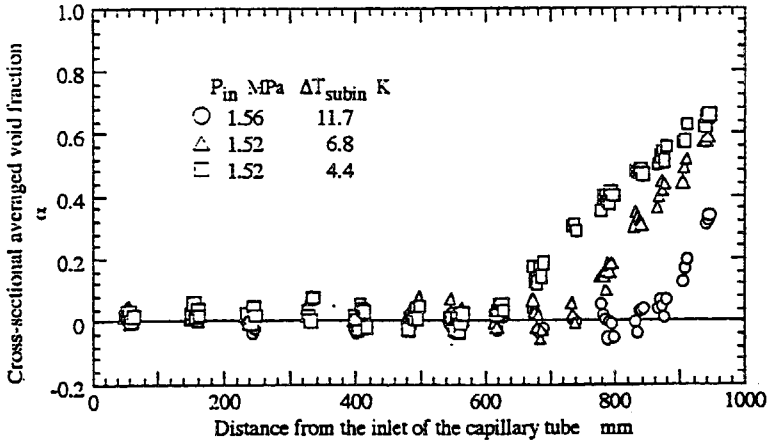

図３－１　キャピラリー管内の冷媒沸騰二相流のボイド率分布、管内径２ｍｍ

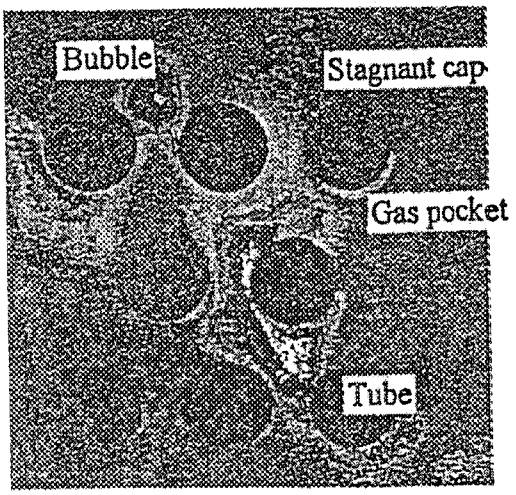

図３－３　流動層ボイラ・コールドモデル内の固液二相流の可視化例、ＳＩＴ管カメラ

ＪＲＲ－３Ｍ　ＴＮＲＦ２を用いたＮＲＧ用電子撮像装置の高解像度化に関する研究

Development of High-Definition Electric Imaging System for Neutron Radiography Using TNRF2 of JRR-3M

持木　幸一[1]、村田　裕[1]、宇野 貴之[1]、三野 勉稔[1]、岩田 秀規[1]、松林　政仁[2]

K. Mochiki , Y. Murata , T. Uno, K. Mitsuno, H. Iwata and M. Matsubayashi

1)武蔵工業大学、 Musashi Institute of Technology

2)日本原子力研究所、 JAERI, Tokai Establishment

１．はじめに

近年、中性子ラジオグラフィの撮像方法としてTV法が広く用いられるようになっている。これはデジタル化が容易であり、各種画像処理が可能である他、動態表示に適しているなどの特徴を持っているからである。被検体の動かない静止画の分野では、広い視野の中でより細かい欠陥を発見できること、つまり、高空間分解能と広視野の両立が求められる場合がある。この要求を満たすためには、高空間分解能は蛍光コンバータの特性で決まるので、１画素をこの限界解像度程度とし、後は画素数を極力多くして撮像すれば良いが、次の制約となるのが撮像系の解像度である。固体撮像素子では１ｋ×１ｋ程度が実用範囲である。

本研究では、静止画に絞り、空間分解能が高く、かつ画素数が多い高解像度システムの開発を目的とし、高解像度撮像管を使用したシステムを製作し、ＪＲＲ－３Ｍで実験を行ったので、その成果について報告する。

２．HARP管によるNRG用高解像電子撮像装置

本報では、NHK放送技術研究所及び日立製作所によって開発された、高感度・高解像度を兼ね備えた撮像管であるHARP管（High-gain Avalanche Rushing amorphous Photoconductor Target）を利用した。

2-1　静止画撮像システム

実験には、当研究室で開発した武蔵工大NRG撮像システムを用いた。実験に使用したNRG撮像システムのブロック図を図１に示す。このシステムはカメラ、アナログ部およびデジタル部とで構成されている。

本システムではＳ／Ｎをよくするために、撮像

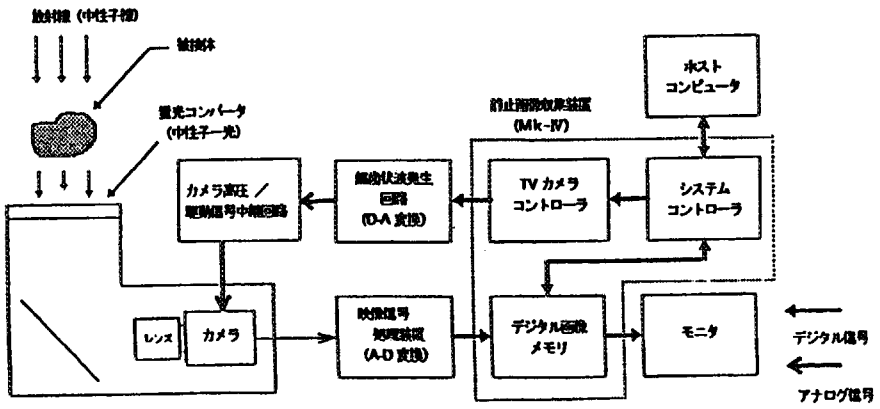

図１　ＮＲＧ静止画撮像システムのブロック図

研究施設：ＪＲＲ－３Ｍ７Ｒ　ＴＮＲＦ２　　研究分野：中性子ラジオグラフィ

本システムではS／Nをよくするために、撮像管での読み出しビームの「緩速走査」、フレームを間引いて読み出す「フレームブランキング走査」、および「フレーム積算」等の撮像手法を用いている。映像信号は 10bit のデジタルデータ信号に変換され、静止画収集装置（MK－Ⅳ）に送られる。本装置には2面のフレームメモリがあり、最大画像サイズ 2048 x 2048 画素、データ長 24bit のフレーム積算処理を行うことが出来る。

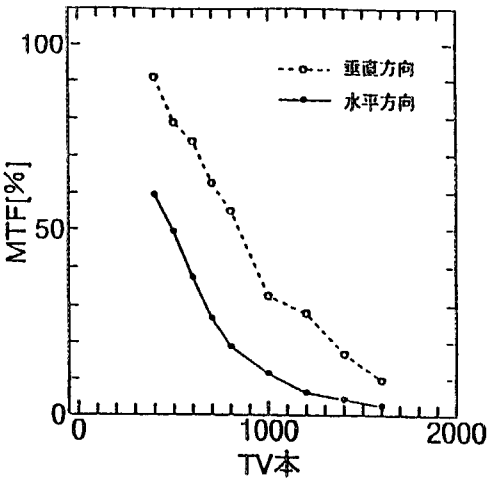

図3　MTF特性（2048 x 2048 画素）

2-2　可視光実験

HARP カメラの限界解像度を実験的に見極めることを目的として、まず可視光で諸特性を取得した。解像度は入射光量とターゲット上の電荷蓄積容量に依存するため、ND フィルタを用いて最適光量に設定した。撮像対象をして EIAJ テストチャート A を使用したが、このチャートの最高解像度が水平・垂直方向に 800TV 本であるため、HARP カメラの解像度を十分評価できないと予想されたため、図2に示すようにテストチャートを規定の 1/4 の大きさで撮像する方法を用いた。

画素サイズを 2048 x 2048 画素として、ピクセルレート 6MHz、積算回数 512 回、フレームブランキング FBR=1 とした。この結果は図3に示されており、水平方向では約 1100TV 本で MTF が約 10%、垂直方向では 1600TV 本で MTF が 10% 以上となっている。通常での視覚的限界解像度は 3～5%といわれており、垂直方向の限界解像度は EIAJ テストチャート A を用いて評価できる限界である 1600TV 本以上であると考えられる。

そこで、次に画素サイズを実質的に 4096 x 4096 画素となるようにして撮像を行った。積算回数 512 回、FBR=1 として、その他の条件は 2048 x 2048 画素と同様にした。

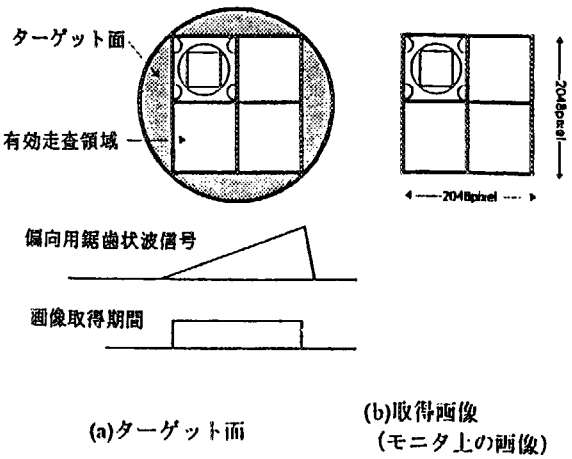

図2　取得画像とターゲット面上の位置関係
（2048 画素 x 2048 画素）

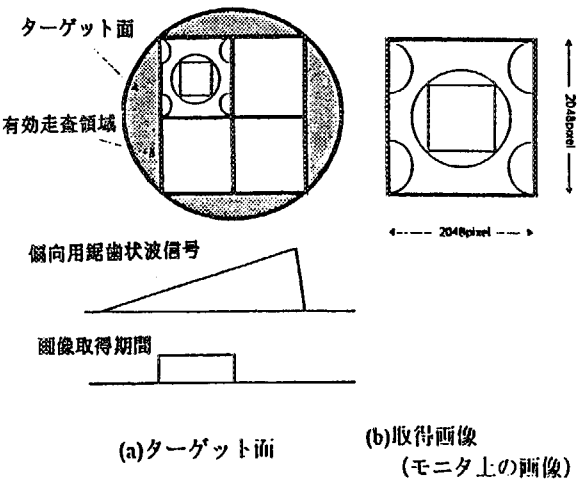

図4　取得画像とターゲット面上の位置関係
（4096 画素 x 4096 画素）

既存のシステムでは、最大 2048 x 2048 画素の画像までしか取得することが出来ない。そこで、実質的に 4096 x 4096 画素とした場合と同様になるように、次の工夫をした（図４参照）。

①取得画像サイズを 2048 x 2048 画素のまま偏向偏向用鋸歯状波信号全体は 4096 x 4096 画素に設定する。

②偏向用鋸歯状波信号の振幅を鋸歯状波発生回路内のアンプによって、実質的に 4096 x 4096 画素の撮像と同様になうよう設定した。即ち、モニタ上には 2048 x 2048 画素で撮像した時の 1/4 の画像が映るようにした。

輝度レベルを従来の蛍光コンバータを使用した場合と同一に設定して撮像すると、“雪積もり現象”が生じた。この雪積もりは走査電子ビームのビームベンディングとビームランディングと呼ばれる現象と密接に関係している。

この為、システムクロック 6MHz（フレーム周期およそ 2.8sec）では遅いと考え、ターゲット面の 1/4 を 2048 x 2048 画素で撮像することとして、実質フレーム周期を４倍にして撮像を行った。（図５）

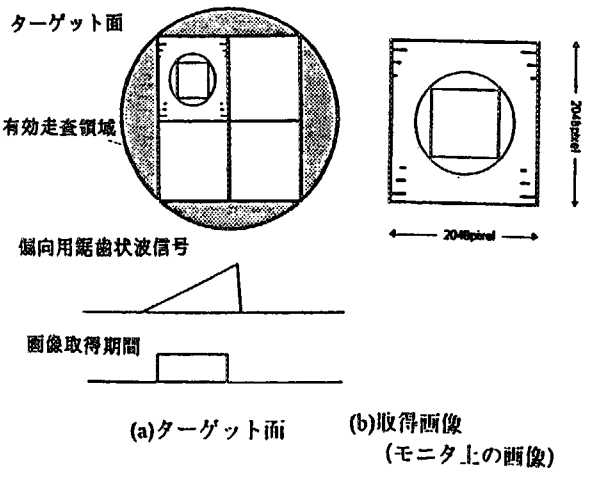

図５　取得画像とターゲット面上の位置関係
（4096 x 4096 画素）　— 改善策 —

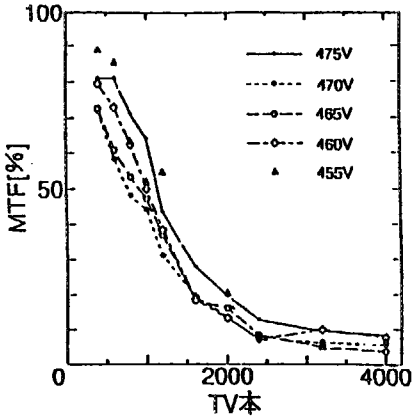

図６　ＭＴＦ特性（4096 x 4096 画素）

図６より、解像度は 2400TV 本相当で MTF は 5%～10%を示しており、この HARP カメラの限界解像度は 2400TV 本相当であると考えられる。

2-3　中性子ラジオグラフィ

フィールド実験は日本原子力研究所東海研究所 JRR-3M TNRF2 を用いて中性子ラジオグラフィによる撮像実験を行った。撮像対象として、植物（大葉の葉）と Cd ステップウェッジを用いた。植物は、細かい葉脈をどこまで確認できるかによって解像度を評価するために用いた。実験によって取得された NRG 画像を図７、図８、図９に示す。また、各画像の取得データを表１に示す。また、視野はいずれの場合も 15.3[cm] x 15.3[cm]であるが、4096 x 4096 画素撮像時には、中心の 2048 x 2048 画素（視野 7.65[cm] x 7.65[cm]）の範囲が取得される。なお、レンズには 2048 x 2048 画素の時は Canon Zoom レンズを、4096 x 4096 画素の時は富士写真光機製 CF50L(F=0.7)を使用した。

表１　NRG 撮像時の設定

Object: 植物（葉） 図７	画素数 積算回数 FBR	2048 x 2048 画素 512 回 FBR=1
Object: 植物（葉） 図８	画素数 積算回数 FBR	4096 x 4096 画素 256 回 FBR=1
Object: Cd ステップウェッジ 図９	画素数 積算回数 FBR	4096 x 4096 画素 64 回 FBR=1

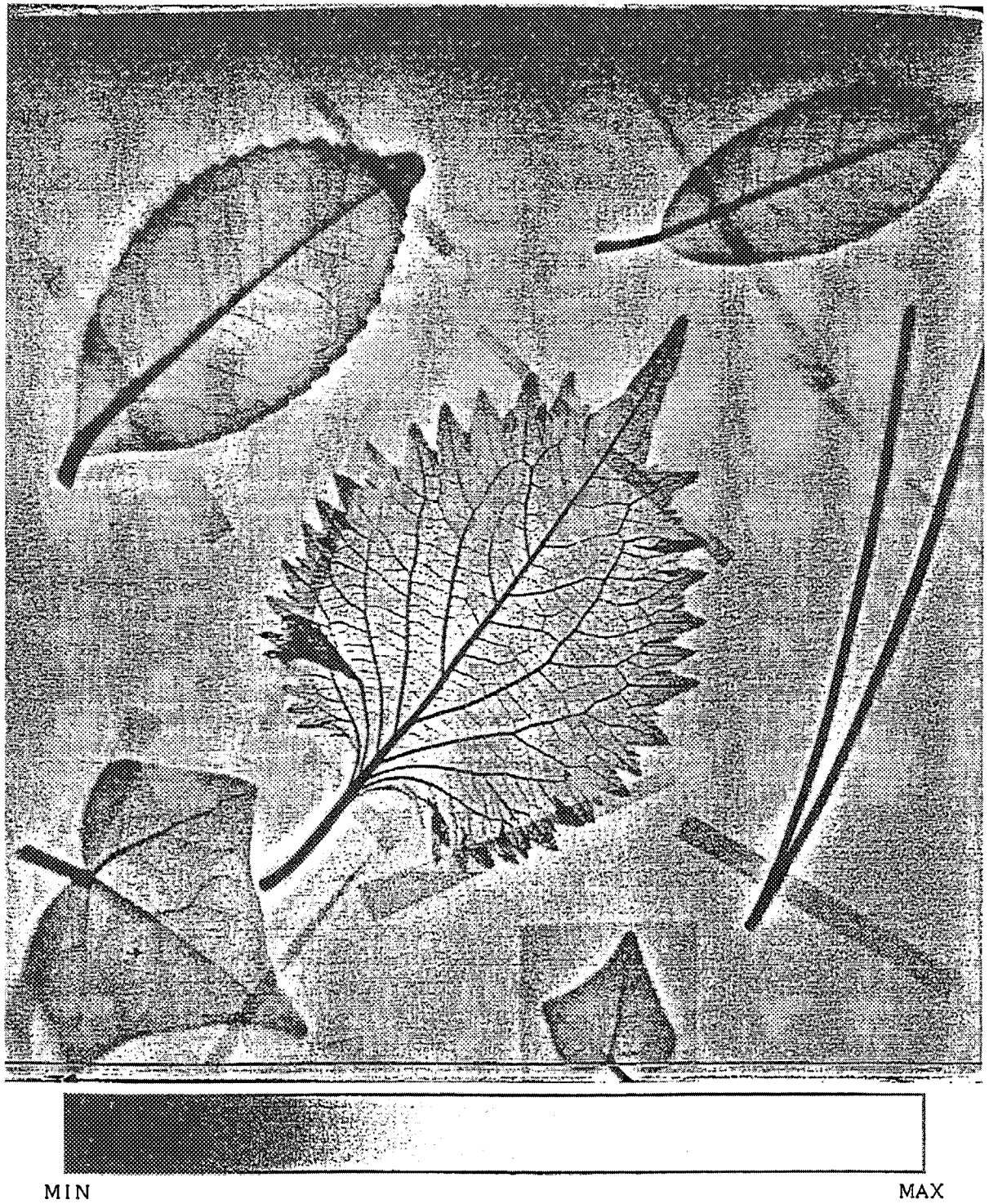

図7　中性子ラジオグラフィ画像
（オブジェクト：葉、2048×2048 画素撮像）

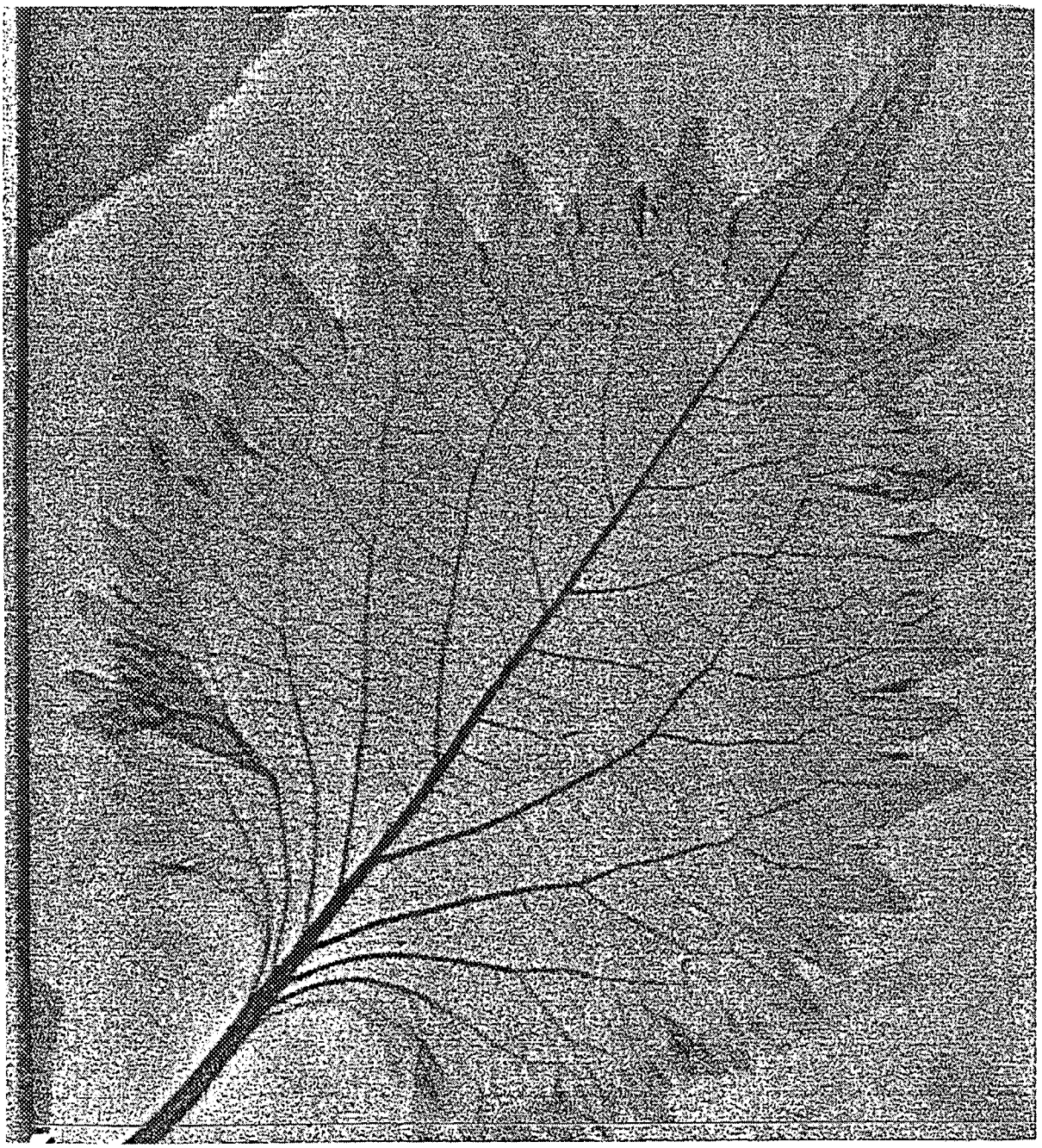

図8　中性子ラジオグラフィ画像
（オブジェクト：葉、4096×4096 画素撮像）

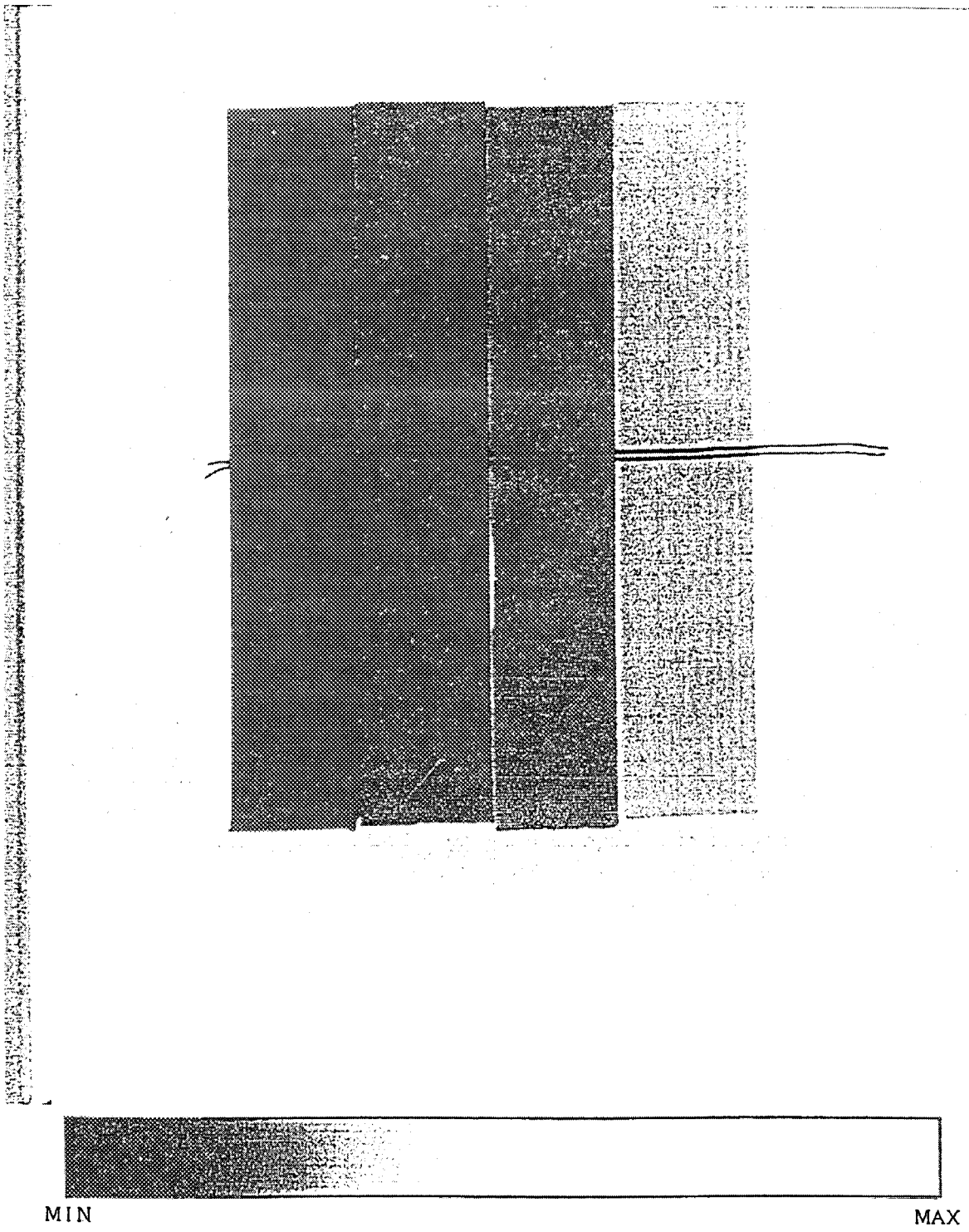

図9　中性子ラジオグラフィ画像
(オブジェクト：Cdステップウェッジ、4096×4096 画素撮像)

非常に薄いもので透過率が良い物であったため、コントラストの出にくい画像となったが、2つの画像を比較すると、2048 x 2048画素で撮像した画像の方が垂直方向の細かい葉脈まで確認することが出来る。これは4096 x 4096画素で撮像した場合には、1画素あたりに蓄積できる電荷量が減り、ノイズによる影響が大きくなってしまうためと考えられる。また、使用した固定焦点レンズは開口径が大きく明るいレンズであるため、各種収差による画像歪みによる劣化も考えられる。

次にCdステップウェッジ（図10）の各ステップの上側にあるエッジ部分のラインプロファイルを図11に示す。更に、それぞれのラインプロファイルを1次微分した時の半値幅を表2に示す。

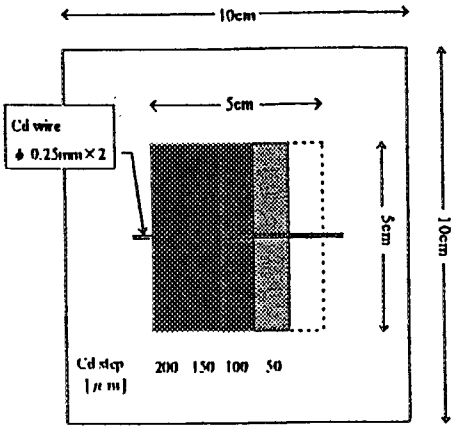

図10　Cdステップウェッジ

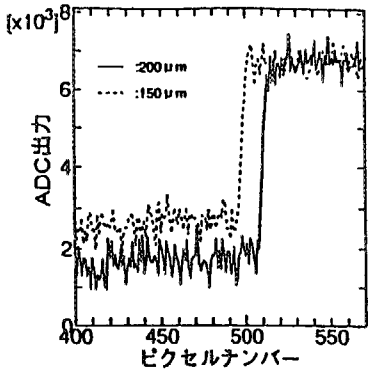

図11　エッジのラインプロファイル

表2　各ステップの半値幅

厚さ[μm]	半値幅[画素]
200	3．3
150	3．3
100	3．6
50	3．3

各ステップの半値幅は約3.3画素分となった。この画像は視野7.65[cm] x 7.65[cm]であるので、解像度は約123μmに相当する。

3．まとめ

HARP撮像管を用い、特殊撮像方法を採用することによって電子撮像システム解像度として2400TV本相当でMTFは5%～10%を達成した。また、このシステムをNRGに適用し、実効解像度123[μm]の高精細画像を得ることができた。

「成果の公表」

・"New electronic imaging camera with high-performance HARPICON tube"
World Conference on Neutron Radiography(1996,Berlin)
K.Mochiki, T.Tanabe, T.Uno, Y.Murata

・"中性子ラジオグラフィ用高解像度電子撮像システムの開発"
日本原子力学会「1997年秋の大会」A66
持木幸一、三野勉稔、村田裕、松林政仁

TNRF2 および C2-3 中性子ラジオグラフィ用照射場の定量化

Quantitative determinations of TNRF2 and C2-3 beam qualities for neutron radiography

立教大原研、小林久夫
日本原子力研究所研究炉技術開発室、松林政仁
神奈川歯大、若尾博美
郵政省、渡辺茂弥
藤田保健衛生大、加藤一夫

1. 目的

JRR-3M に設置された熱および冷中性子ラジオグラフィ(TNRF2 および C2-3)用照射装置は、国内外における基準となる照射場となり得る性能を有している。本研究ではその可能性を探り、基準場とするための基礎研究を行った。

2. 研究の方法

本研究は JRR-3M の熱・冷両中性子ラジオグラフィ装置を利用して行った。この二つの照射装置および立教大学の TRIGA 炉、さらには国内外の他のの中性子場における同様の研究結果を相互比較する。この目的を達成するために、以下を実施した。

(1) 幾何学的因子(L/D)測定治具を用いて L/D および L 値を測定する。
(2) 実効エネルギー測定治具(BQI)の改良およびこれによる様々なビームを用いた測定。
(3) フィルターを用いたビーム線質の変更可能性の確認実験を BQI を用いて実施する。
(4) いくつかの制作し様々な物質の実効的全巨視的断面積を通常のコリメータからのビーム、フィルター挿入ビーム、中性子導管出力ビーム等種々の線質について測定する。

3. 結果

本研究で得られた結果は次の通りである。

3.1. ビームの幾何学的特性の測定：

JRR-3M TNRF1 および TNRF2 の熱中性子ビームおよび C2-3 冷中性子ビームの測定を行った。現在までに得られた結果をまとめると以下の通りである。

(1-1) TNRF1 および TNRF2 の幾何学的因子の設計値と測定値はおのおの以下の通りである。

TNRF1 の幾何学的因子		
因子	設計値(1)	測定値(2)
L/D	$178^{H}\times178^{V}$	$132^{H}\times114^{V}$
L (mm)	$5638^{H}\times5638^{V}$	$5420^{H}\times5500^{V}$
D (mm)	$30^{H}\times30^{V}$	$41^{H}\times48^{V}$

TNRF2 の幾何学的因子		
因子	設計値(1)	測定値(2)
L/D	$238^{H}\times238^{V}$	$176^{H}\times153^{V}$
L (mm)	$7138^{H}\times7138^{V}$	$7280^{H}\times7350^{V}$
D (mm)	$30^{H}\times30^{V}$	$41^{H}\times48^{V}$

(注) 上付きの記号 H および V はおのおの水平方向および垂直方向の値

利用研究施設：JRR-3M 7R (TNRF2) 熱中性子ラジオグラフィ設備および
JRR-3M C2-3 冷中性子ラジオグラフィ設備

(1-2) TNRFのコリメータの実効的開口部寸法は、設計値(正方形)より30 %から50 %大であり、さらに水平方向と垂直方向で異なる。すなわち、実効的には矩形上である。これは、開口部付近が中性子に不透明な材料を用いずAl材で構成されていおり、事実上コリメータ開口部の役割を果たしていないことによる。

(1-3) 開口部の形状が事実上矩形状であるため、幾何学的不鮮明度は水平方向と垂直方向で異なるばかりでなく、方位依存を有する[3]。

(1-4) C2-3 冷中性子ビームは中性子導管の出力を用いている。その幾何学的不鮮明度は、現在までの測定から、L/D～100 の程度であると推定されている。導管の形状から当然この場合も、幾何学的不鮮明度の方向依存が観測されている。しかし、このビームの納得し得る幾何学的特性の評価法はまだ確定しておらず、今後の問題としてなお研究が必要である。

等々が示された。

3.2. 実効エネルギーの測定：

連続スペクトルを有する中性子ビームの実効エネルギーを評価する治具はPbとTiの中性子透過特性のエネルギーによる違いを利用してBQIとして提案されており[4]、本研究でもこの治具を用いた系統的測定が実施された。現在まで、JRR-3MのTNRF2、CNRF、立教炉の中性子場およびそのフィルター付加ビームを中心に、国内外29種の熱・冷中性子ビームの測定を完了した。その結果は、一連の論文にまとめられ報告されている[5-11]。Table 1[11] に最近の結果をまとめて示した。

3.3. 物質の実効的全巨視的断面積の測定：

現在までに14元素、7種の合金、8種の樹脂および水、合計29種の物質に対して、JRR-3Mおよび立教炉のビームを用い、10 meV, 17 meV, 29 meV、さらにInの共鳴 (1.46 eV) エネルギーについての測定を行った。その結果は、逐次報告してきたが最新のデータは文献(11)にまとめている。イメージングプレートを用いた最近の測定結果をTable 2[11] にまとめて示した。なお、従来方式、フイルム法を用いた国内外のビームでの膨大な測定データも、現在協力研究者の若尾、渡辺が中心となって精力的な解析が行われている。今後とも、可能な限り様々な元素、合金、化合物等の、様々なビームを用いての測定と解析を継続追加していく予定である。

本研究は、前節の実効エネルギーとの相関において論じられるべきであり、実際文献(11)において相関をみる試みが開始されている。

3.4. ビーム特性の改良と規格化：

熱中性子線と信じられていたビームが、n/γ 比改善の目的をもって挿入されたフィルターにより、無視し得ないスペクトル変遷を受けていることがわれわれによって指摘されて[5]以降、系統的な研究が実施された[12]。日本原子力研究所においては、TNRFに設置する目的を持ってBe,BiおよびPbフィルターを制作した。それらを用いた実験結果の一部は、最近の国際会議において発表している[13]。その結果、JRR-3M および立教炉共に、上のフィルターをビーム中に挿入することにより、実効エネルギーを 30 meVから10 meV まで容易に変更できるようになっている。

3.5. 応用－中性子断層撮影他：

最近開発、市販されるようになっているイメージングプレートは、いくつかの優れた特徴を有している[14]。この諸特性を考慮した、高信頼度中性子断層像取得法に関連した様々な実験[14]および新しい断層撮影法[15]等が本協力研究に関連して開発されている。また、生体試料の中性子ラジオグラフィの可能性、関連する散乱線評価実験等も協力研究者の加藤が中心となって実施されている。

4. 評価

1994年頃よりビームの諸特性を評価するために、幾つかの提案を世界に発してきたわけであるが、ようやくこの新しい試みが広く理解されるようになっ

Table I Effective Energies for Various Neutron Beams

Facility (country)	Filter (moderator/reflector)	R_{Cd}	$^1E_{mean}$	$^2t_{Pb}/t_{Tl}$	$^3E_{eff}$ (meV)
(Without filter)					
Rikkyo RUR-N2(Japan)	none (graphite)	2	meV	1.67 ± 0.01	28.9 ± 0.2
JAERI JRR3M-TF2(Japan)	none (D_2O)	130	47.2	1.73 ± 0.03	27.5 ± 0.3
PML-FNR-V(USA)	none (D_2O)	200		1.76 ± 0.12	26.7 ± 2.8
Kyoto U. KUR-E2(Japan)	none (D_2O)	400		1.78 ± 0.04	26.6 ± 0.8
Kinki U. UTR(Japan)	none (graphite)	4.3		1.93 ± 0.17	22.8 ± 1.2
(With non-cooled filter)					
JSW-Cyclotron (Japan)	Pb 0.5 cm+Poly 4cm (poly)			1.72 ± 0.01	27.7 ± 0.3
JSW-Cyclotron (Japan)	Pb 0.5 cm+Poly 4cm +C 2cm (poly)			1.77 ± 0.01	26.6 ± 0.3
AECL-NRU(Canada)	quartz/sapphire (graphite)	>1000		1.82 ± 0.04	25.7 ± 0.9
JSW-Cyclotron (Japan)	Pb 0.5 cm+Poly 4cm+Bi 3cm (poly)			1.84 ± 0.02	25.3 ± 0.4
JAERI JRR3M-TF2(Japan)	Bi 5 cm (D_2O)			1.88 ± 0.01	24.6 ± 0.3
McMaster U.MNR(Canada)	Bi 15cm			1.91 ± 0.06	24.2 ± 1.2
PSI-SINQ (Swiss)	Bi 10 cm (D_2O)			1.98 ± 0.02	18.6 ± 0.3
Rikkyo RUR-N2(Japan)	Pb 5 cm (graphite)			2.03 ± 0.01	17.2 ± 0.2
JAERI JRR3M-TF2(Japan)	Bi 10 cm (D_2O)			2.10 ± 0.02	15.6 ± 0.2
PSI-SAPHIR(Swiss)	Bi 10cm+Si 6cm (graphite)			2.24 ± 0.01	13.1 ± 0.1
HFR-HB8-T(Netherlands)	Si 25cm+Bi 25cm (50K) (graphite)			2.25 ± 0.04	13.0 ± 0.4
PML-FNR-E(USA)	Pb 12.7cm (D_2O)		47	2.27 ± 0.10	12.6 ± 0.9
JAERI JRR3M-TF2(Japan)	Bi 15 cm (D_2O)			2.38 ± 0.03	11.5 ± 0.2
AUR (Austria)	Bi 14 cm (graphite)			2.47 ± 0.14	10.6 ± 0.9
Rikkyo RUR-N2(Japan)	Pb 10 cm (graphite)			2.58 ± 0.03	9.8 ± 0.2
Rikkyo RUR-N2(Japan)	Pb 15 cm (graphite)			3.33 ± 0.07	7.1 ± 0.2
Rikkyo RUR-N2(Japan)	Pb 20 cm (graphite)			3.87 ± 0.09	6.2 ± 0.2
U. Virginia MTR(USA)	Pb 6.7cm+Bi 25 cm			7.00 ± 0.40	5.0 ± 0.5
(With cooled filter)					
HFR-HB8-C(Netherlands)	Be30(50K)+Bi25(50K) (graphite)	560		11.60 ± 1.20	3.23 ± 0.53
(Neutron guide tube)					
Kyoto U. KUR-CN3(Jpn)	Characteristic w.l. λ_c=1.8Å (lq.D_2)		12.	11.05 ± 0.31	3.24 ± 0.14
Kyoto U. KUR-CN2(Jpn)	Characteristic w.l. λ_c=2.6Å (liq.D_2)		7.2	12.05 ± 0.77	3.20 ± 0.33
JAERI JRR3M-C2-3(Jpn)	Characteristic w.l. λ_c=4.0Å (lq.H_2)		4.6	17.58 ± 0.50	2.63 ± 0.11

(Revised Feb. 10, 1997)

1 Mean value from TOF measured spectrum.

2 This work: Estimated thickness t_{Pb}/t_{Tl} ratio from the BQI image.

3 This work: Results of analyses from BQI image.

Table II Effective Total Macroscopic Cross Sections of Various Materials for Four Neutron Beams with Different Effective Energies from 9.68 meV to 1.45 eV(unit: 1/cm)

Beam Filter E_{eff}	Sub-thermal Pb = 10 cm 9.68 meV	Sub-thermal Pb = 5 cm 17.0 meV	Thermal none 28.9 meV	In Epi-thermal Cd = 1 mm 1.46 eV	Comment
Al	0.0989 ± 0.0008	0.0986 ± 0.0007	0.1002 ± 0.0006	0.0887 ± 0.0012	
Au	6.976 ± 0.127	6.088 ± 0.089	5.619 ± 0.112	1.925 ± 0.021	Dental
Ag	4.545 ± 0.057	4.066 ± 0.066	3.602 ± 0.048	1.055 ± 0.009	Dental
Cd	114.58 ± 1.38	109.64 ± 1.90	96.74 ± 1.50	0.577 ± 0.008	Dental
Cu	0.921 ± 0.016	0.899 ± 0.009	0.849 ± 0.014	0.586 ± 0.006	Dental
Dy	35.64 ± 0.97	31.35 ± 0.91	28.01 ± 0.55	7.700 ± 0.137	
Graphite	0.380 ± 0.008	0.398 ± 0.009	0.389 ± 0.007	0.3172 ± 0.0042	
Fe	1.022 ± 0.028	1.043 ± 0.021	1.040 ± 0.020	0.5308 ± 0.0161	
In	9.42 ± 0.31	8.23 ± 0.33	7.45 ± 0.22	88.70 ± 47.64	t<0.28 mm
Ni	1.648 ± 0.072	1.592 ± 0.048	1.604 ± 0.040	1.150 ± 0.029	
Pb	0.259 ± 0.006	0.293 ± 0.004	0.312 ± 0.003	0.2620 ± 0.0055	
Rh	11.19 ± 0.34	9.86 ± 0.18	9.11 ± 0.16	36.352 ± 0.149	t=<0.025
Ti	0.637 ± 0.010	0.553 ± 0.010	0.517 ± 0.005	0.239 ± 0.002	
Zn	0.356 ± 0.005	0.346 ± 0.006	0.331 ± 0.004	0.2302 ± 0.0030	
Ag-alloy	4.184 ± 0.064	3.814 ± 0.037	3.416 ± 0.060	5.70 ± 1.12	Dental
Au-Pd	3.808 ± 0.091	3.243 ± 0.062	2.965 ± 0.077	3.26 ± 0.25	Dental
Brass	0.724 ± 0.011	0.670 ± 0.007	0.652 ± 0.008	0.3477 ± 0.0081	
LiF	±	±	±	0.771 ± 0.000	
PBN	30.20 ± 1.58	28.19 ± 1.18	19.83 ± 1.39	5.451 ± 0.041	
Pb(Te)	0.236 ± 0.005	0.274 ± 0.004	0.304 ± 0.004	0.3035 ± 0.0051	Te=0.02%
SUS	1.013 ± 0.022	1.022 ± 0.011	1.006 ± 0.012	0.5208 ± 0.0085	
H_2O	3.557 ± 0.030	3.380 ± 0.047	2.800 ± 0.018	0.489 ± 0.053	
D_2O	0.598 ± 0.005	0.567 ± 0.008	0.497 ± 0.004	0.360 ± 0.009	
Teflon	0.318 ± 0.006	0.321 ± 0.004	0.323 ± 0.003	0.2165 ± 0.0046	
Poly	4.729 ± 0.121	4.398 ± 0.053	3.541 ± 0.085	1.3284 ± 0.0480	t=<0.6cm
Acryl	3.541 ± 0.032	3.254 ± 0.035	2.717 ± 0.040	1.0521 ± 0.0288	t=<0.6cm
Tissue	3.504 ± 0.059	3.183 ± 0.069	2.247 ± 0.125	0.8654 ± 0.0425	t=<1.19cm
Tiss(new)	±	±	±	1.1202 ± 0.0679	t=<1.4cm
Bone	2.729 ± 0.075	2.106 ± 0.143	1.663 ± 0.130	0.6064 ± 0.0574	t=<2.07cm

Neutron beam: Rikkyo TRIGA-II (100kW) – Beam port No.2 with Pb filter (0, 5 and 10 cm).
Measurements of effective energies: BQI with Imaging Plate for neutron detection (BAS NR2025).
Measurements of ETM cross sections: Average slopes of transmission curves after scattered component corrections.
Blank cells: Not measured to date.

てきている。

幾何学的不鮮明度を決定するL/D測定治具は、米国ASTM E803-81[16]などいくつか提案されているが、一定の方位のみのL/Dが決定できるだけであること、画像の拡大率を決定する重要な因子L値の測定が出来ないこと、構造が複雑すぎ高価なものになることなどの欠点があった。

われわれの方式は、単純な構造をしており、L/Dばかりでなくしをも1 %以下の精度で決定できる性能を有している。この治具を用いた幾何学的因子の測定は、JRR-3Mを初めとして国内外のビームにおいて現在もなお継続して実施している。この治具をさらに単純化したL/D治具は、すでにわが国の非破壊検査協会においてNDIS 1402 (1996)[17]として規格化が完了公表されている。

BQIによる連続スペクトルを有したビームの実効エネルギー測定は、日本原子力研究所において新たに設計制作されたBQIを用いて世界各地での測定が行われつつある。今後、米国、カナダの各施設は、Michigan大のDr. J. T. Lindsayが、欧州各国の施設においては、スイスPSIのDr. E. Lehmannが中心となって測定を実施しつつある。

5. 今後の方針

JRR-3Mにおける本研究は、ほぼ完了しているが、なおC2-3を中心にいくつかの測定が必要であり、関連した測定等は次年度以降に実施していく予定である。

なお、BQIの性能は、Pbの断面積のエネルギーに敏感に依存し、BQIに使用した材料そのものを用いたTOFによる測定が欠かせない。この部分の測定の未完の部分は、北大の鬼柳氏との共同で行う予定である。

上述したように、実効エネルギーと実効的全巨視的断面積との相関は、本研究の最終目的に属するが、この点に関しては、既存の核データによる検証が必須である。この点に関する諸計算作業も今後の課題として残っている。

文献

(1) A. Tsuruno et al., WCNR (3), Eds. S. Fujine et al., (Kluwer Acad. Publ., Dordrecht, 1990) p/81-86.
(2) H. Kobayashi, Nucl. Instr. Meth. A377 (1996) 1-10.
(3) H. Kobayashi, Nondestr. Test. Eval. 11, (1994) 77-85.
(4) H. Kobayashi and Y. Kiyanagi, Nucl. Instr. Meth. A 377 (1996) 52-57.
(5) H. Kobayashi, et al., *Proc. 6th ECNDT* (1994) 811-816.
(6) H. Kobayashi, *Proc. International Conference on Neutrons and Their Applications*, SPIE-Vol. 2339, (Western Kentucky Univ., 1995) 175-180.
(7) Hisao Kobayashi, *3rd European Neutron Radiography Working Group Meeting*, (Budapest, Hungary, Sept. 27-29, 1995) 38-41.
(8) H. Kobayashi, M. Nakagawa, and Y. Kiyanagi, *Proc. 5th World Conference on Neutron Radiography*, eds. C. O. Fisher, J. Stade, W. Bock (DGZfp, Berlin, 1997) 313-320.
(9) H. Kobayashi, *Fifth Asian Symposium on Research Reactors*, KAEDO, (Taejon, Korea, 1996), p. 453-460.
(10) H. Kobayashi, *The First US-Japan Symposium on Advances in NDT*, US and Japan NDT (Kahuku, Hawaii, 1996), 139-144.
(11) H. Kobayashi, "A correlated study between effective total macroscopic cross sections and effective energies for neutron beams with continuous spectra", *Third International Topical Meeting on Neutron Radiography*, (Lucerne, 1998); Nucl. Instr. Meth. A (1998) (to be published).
(12) H. Kobayashi et al., Nucl. Instr. Meth. A377 (1998) 37-40.
(13) M. Matsubayashi, J. T. Lindsay and H. Kobayashi, "Preparation of a Beam Quality Indicator for effective energy determinations of continuum beams. – Establishment of traceability." *Third International Topical Meeting on Neutron Radiography*, (Lucerne, 1998); Nucl. Instr. Meth. A (1998) (to be published).
(14) H. Kobayashi, "Basic performance of a neutron sensitive photostimulated luminescence device for neutron radiography", *Third International Topical Meeting on Neutron Radiography*, (Lucerne, 1998); Nucl. Instr. Meth. A (1998) (to be published).
(15) H. Kobayashi, M. Satoh, and M. Matsubayashi, "Study for a novel tomography technique using an imaging plate", *Third International Topical Meeting on Neutron Radiography*, (Lucerne, 1998); Nucl. Instr. Meth. A (1998) (to be published).
(16) *Annual Handbook of ASTM* Standards, Vol.03.03, ASTM E803-91 "Standard method for determining the L/D ratio of neutron radiography beams" (1992) 359-365.
(17) NDIS 1402-1996, "Determining the L/D ratio of neutron radiography beams", (日本非破壊検査協会, 1996) 1-6 (in Japanese and in English).

中性子ラジオグラフィの電池研究への応用

Application of Neutron Radiography to the Research of Batteries.

東京学芸大学教育学部　鎌田正裕
京都大学原子炉実験所　藤根成勲・米田憲司
日本原子力研究所　市川博喜・松林政仁
M.Kamata, Tokyo Gakugei Univ.
S.Fujine and K.Yoneda, Research Reactor Institute Kyoto Univ.
H.Ichikawa and M.Matsubayashi, Japan Atomic Energy Research Institute

（1）研究の背景と目的

リチウム金属を負極に用いた電池は、単位重量あたりのエネルギー密度が大きいため、一次電池として既に多くの製品に利用されている。この電池の二次電池（充電可能な電池）化については、現在広く研究されているものの、十分に高い可逆性を有する電池の開発には至っていない。この種の研究が困難な理由の一つに、放電時に一度溶出したリチウム金属が、充電時にどのような形状で析出するのかを、種々の充放電条件下で繰り返し観察する必要があるにもかかわらず、そのための有効な実験方法が確立されていないことがあげられる。

このような背景をふまえて、著者らは、中性子ラジオグラフィを用いることで、電池内部のリチウムイオンの分布や充電時の金属リチウムの析出形態を非破壊でかつ定量的に求めることができると考え、本年度は特にNRG-CTの有効性を市販のリチウム電池を対象に検証することにした。

（2）実験内容

撮影に用いた市販のリチウム電池は、以下に示す4種類で、いずれの電池についても使用前および放電後の各1個を実験に使用した。また、各電池の構造の概略をFig.1～3に示す。

CR2　円筒型(スパイラル構造)　d=14, h=25

CR1/3･1H　円筒型（スパイラル構造）d=11.5, h=10

CR1220　コイン型　d=12.5, h=2.0

BR435　ピン型　d=4.2, h=35.9

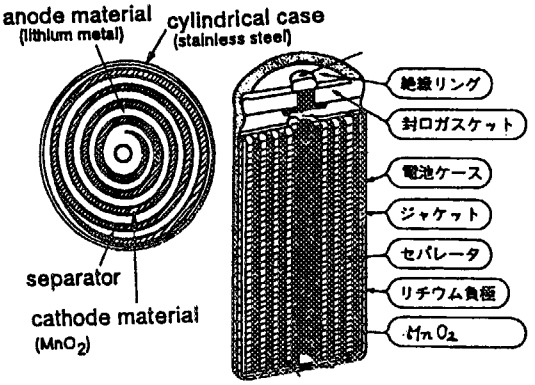

Fig.1　CR2,CR1/3の内部構造

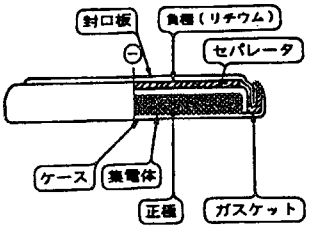

Fig.2　CR1220の内部構造

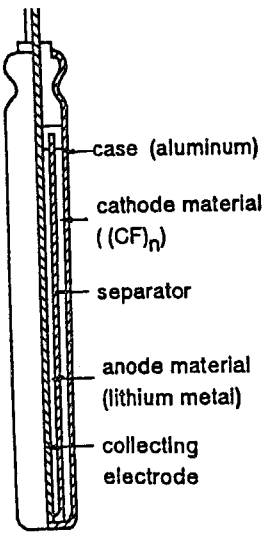

Fig.3　BR435の内部構造

JRR3M7R　中性子ラジオグラフィ装置、電気化学

いずれの電池も、放電が進むにしたがって、負極では、

$$Li \rightarrow Li^{+} + e^{-} \qquad (1)$$

なる反応が進行し、正極では

$$MnO_2 + Li \rightarrow MnO_2 \cdot Li \qquad (2)$$

なる反応等が進行する。この結果、放電前には負極側に偏在していたリチウムが、放電後には、セパレーターを通して正極側に移動することになる。

一方、撮影にはJRR3MのNRG-CTを使用し、撮影の条件はおおむね下記の通りである。

ステップ幅　1°
露出時間　8秒／ステップ
範囲　0～180°

(3)結果と考察

NRによる各電池の透過像およびCT像をphoto1～4に示す。比較的直径の小さなCR1/3については、CT像から電極のスパイラル構造が読みとれ、また放電によってリチウムが電池全体に分布した様子も確認できる。しかしながら、これよりも、直径の大きなCR2、あるいは電解質にボロンの化合物を含むBR435等については、明瞭なイメージは得られていない。

実際の電池研究に利用するためには、少なくとも100ミクロン程度の解像度が望まれ、今回得られたCT像では十分とは言い難い。次年度は被写体（電池）と蛍光板の距離を小さくすることで、解像度の改善を目指す予定である。

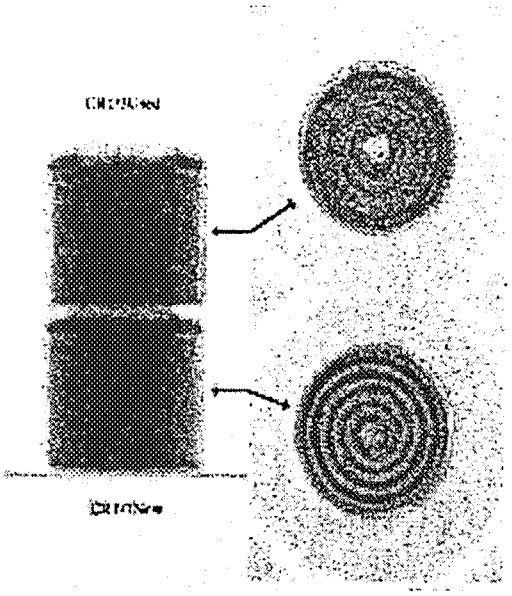

Photo.1　CR1/3の透過像（左）とCT像（右）
（上：使用後　下：使用前）

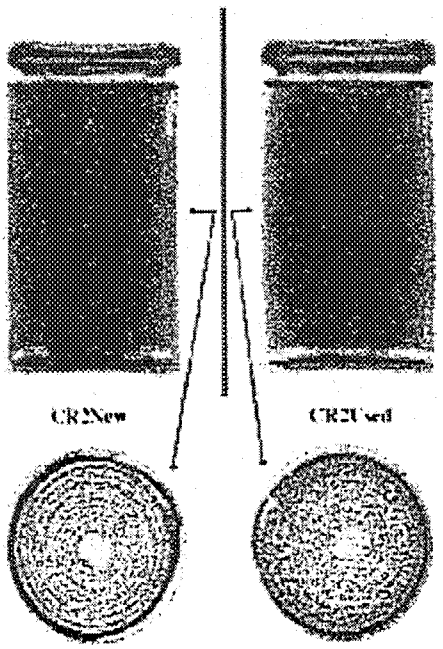

Photo.2　CR2の透過像（上）とCT像（下）
（左：使用前　右：使用後）

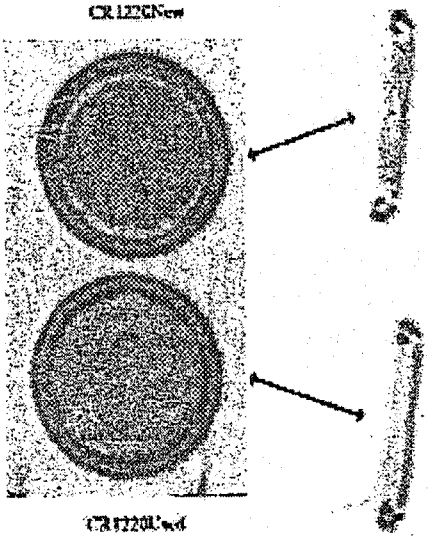

Photo.3 CR1220の透過像（左）とCT像（右）
（上：使用前　下：使用後）

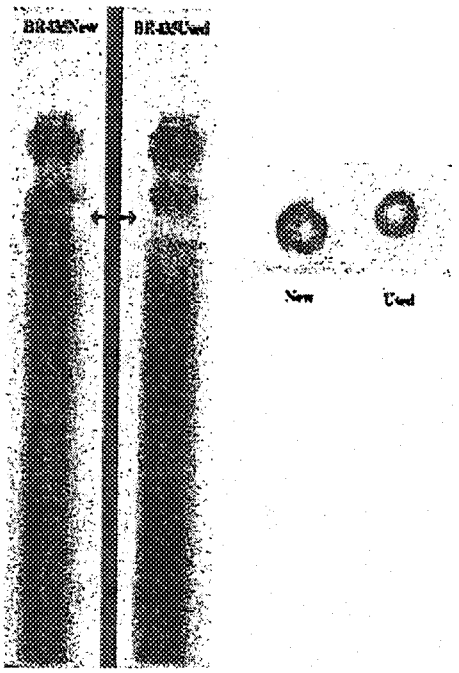

Photo.4 BR435の透過像（左）とCT像（右）
（左：使用前　右：使用後）

3. 即発ガンマ線分析
(Prompt Gamma-ray Analysis)

This is a blank page.

研究テーマ：農林水産研究における原子炉中性子即発ガンマ線分析法の利用
表　　題：中性子即発ガンマ線分析法による農林水産関係試料中のホウ素およびケイ素の定量

中性子即発ガンマ線分析法による農林水産関係試料中のホウ素およびケイ素の定量

宮本進，塩本明弘[1]，山崎慎一[2]，西村宏一，米沢仲四郎[3]，松江秀明[3]，星三千男[3]
農林水産省畜産試験場
[1]*農林水産省遠洋水産研究所*
[2]*農林水産省農業環境技術研究所*
[3]*日本原子力研究所東海研究所*

1．目的

農林水産研究分野においては、近年、分析対象とする環境および生体中の元素、成分が増加し、さらに対象とする試料の形状も多様化しているので、高感度で迅速かつ簡便な分析法の導入が望まれている。そこで、原子炉中性子即発ガンマ線分析法（ＰＧＡ）を導入した研究を農業環境、畜産、水産の各専門分野で実施し、原子炉中性子即発ガンマ線分析法の実用化の確立を図る。

今までに、即発ガンマ線分析法による植物、動物及び海洋性試料中の元素分析法の基礎データを得るため、感度の高いホウ素（Ｂ）を対象元素として、国際標準試料（植物、動物）を用い、測定時における試料形状、試料量、Ｂの測定限界等について検討すると共に、土壌・畜産関連試料中のＢ等の測定をＰＧＡにより行った。また、海洋試料中のケイ素（Ｓｉ）の測定法についても検討した。

また、(1)土壌中の多量元素（Na, Al, SK, Ca, Ti, Mn, Fe等）についてＰＧＡ法による測定　(2)実試料への応用として羊にＢを添加した飲水を給与し、得られた糞、臓器および血漿（一部）中のＢ定量　(3)海洋性プランクトン中のＳｉ等の測定について検討した。平成９年度は(1)(2)(3)について、さらに検討を進めた。

なお、本研究については、平成５年度より農業環境技術研究所、畜産試験場，遠洋水産研究所の３研究機関で研究チームを構成し、日本原子力研究所東海研究所との共同研究の下に実施している。

2．試験研究の概要

土壌中の多量元素のＰＧＡによる定量については、化学分析による含有量既知のものを供試し、試料中の各元素について内部標準元素（Ti等）による補正法を検討した。

また、プランクトンについては、珪藻類を主とする海洋性プランクトン（沿岸域及び外洋域）中のＳｉのＰＧＡによる測定を行った。

畜産関連では、羊３頭にルーサンヘイキューブ（1,100g/日/頭）とＢ添加水（ホウ酸ナトリウム：Ｂとして100ppm）を１８日間給与し、この間に得られた血液（血漿）、尿および実験終了後得られた臓器（肝臓、腎臓、筋肉等）を供試試料とした（試験区：Ｔ）。なお、対照区（Ｃ）の羊２頭（Ｂ非添加水を給与）から得られた試料についても同様に処理した。

各試料は、血漿および尿は1mlをテフロン製容器に入れ、土壌、プランクトン、糞は乾燥後、臓器は凍結乾燥後粉末とし錠剤成形器を用いてペレット状に成形（直径：13mm、重量：土壌は0.5ｇ、他は0.3g程度）FEPフィルム（厚さ25μm）で二重に溶着した。試料はPTFE製保持具の中央にPTFE製糸で固定し、原研ＪＲＲ－３Ｍ熱中性子ガイドビームに設置された即発ガンマ線分析装置を用い、ヘリウムふんい気中でガンマ線スペクトル測定を行った（測定時間1,000から18,000秒/試料）。ホウ素の検量線は、スズ板にHBO_3 標準溶液を滴下乾固した試料、血漿あるいは尿にホウ素を添加した試料を用い478 keVのホウ素のピークの面積を求める方法により作成した。この検量線を用い、試料中のホウ素の定量を行った。珪素の標準としては、純珪素板を用いた。

また、ナトリウム（Na_2CO_3）とホウ素の混合試料を作成し、ナトリウムの 92keV、473keV、ホウ素の 478keVのピーク面積を比較する方法によりＮａ妨害の補正を行った。

血漿および尿（図１）中のＢ濃度はＢ添加水給与開始後急上昇し、３日目頃からほぼ一定レベル

原子炉：ＪＲＲ－３Ｍ　　装置：即発γ線分析装置　　分野：即発γ線分析（農・水産物）

となった18日間B添加水を給与した後、屠殺して得られた臓器中のB濃度は、対照区のそれよりも明らかに高かった（肝臓:22.9ppm(T),2.2ppm(C),腎臓:57.3ppm(T),4.8ppm(C)）。これらの結果、飲水中のBは家畜（羊）に速やかに吸収され血漿および尿中のBレベルは上昇し、臓器に蓄積されることが明らかになった。

ＰＧＡによる土壌中の多量元素の定量について検討した結果、各元素の含有量とガンマ線強度との間には、あまり高い相関が得られなかったが、成分の一つであるチタン（Ti）を内部標準元素として補正を行うと相関関係は大幅に上昇し測定可能であった。図２に一例としてマンガン（Mn）の結果を示したが、他元素についてもほぼ同様の結果が得られた。

珪藻類が多かった海洋性プランクトンのうち、外洋域プランクトンのＰＧＡによるガンマ線スペクトルを図３に示した。沿岸域プランクトンと同様にケイ素のピークが検出された。今後、さらに測定例を増やし検討する予定である。

1)第３４回理工学における同位元素発表会　講演要旨集、（1997）PP.92
2)第３５回理工学における同位元素発表会　講演要旨集、（1998）PP.168
3)日本土壌肥料学雑誌,67(6),(1996),PP.672-676

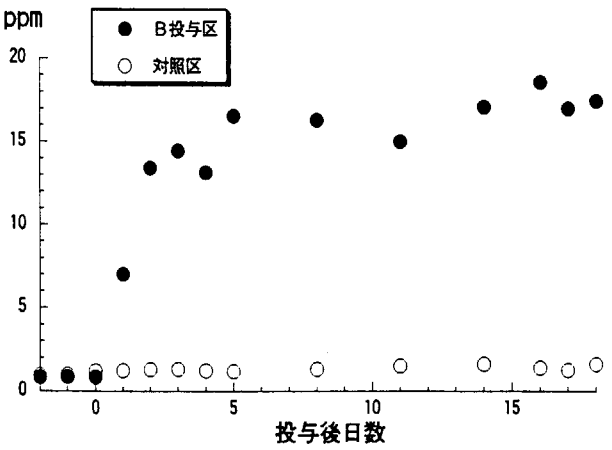

図１．尿中ホウ素濃度の推移（羊）
（平均値）

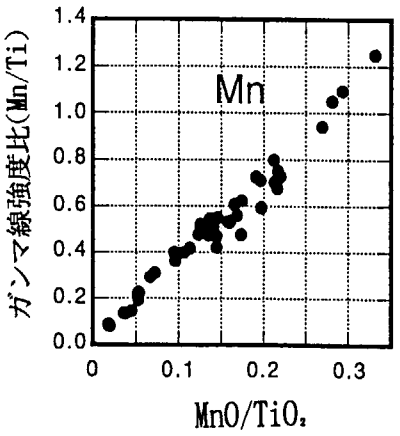

図２．Ｔｉによる補正を行った含量比とガンマ線強度比の関係

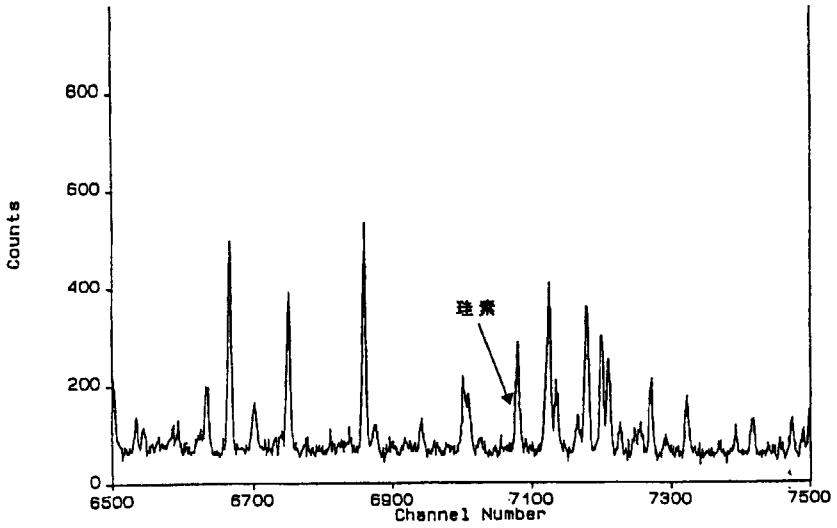

図３．北海道噴火湾における春期珪藻類大増殖時の海洋性プランクトン（主に珪藻類）の即発ガンマ線スペクトル（熱中性子，10000秒）

研究テーマ：火山岩試料の即発γ線分析
表　　題：火山岩中ホウ素の高確度即発γ線分析

火山岩中ホウ素の高確度即発γ線分析

福岡孝昭，佐野貴司[1]，長谷中利昭[2]，米沢仲四郎[3]，松江秀明[3]，澤幡浩之[4]
学習院大学理学部（現立正大学地球環境科学部）
[1]京都大学総合人間学部（現京都大学理学部付属地球熱学研究施設）
[2]東北大学東北アジア研究センター
[3]日本原子力研究所東海研究所燃料研究部分析センター
[4]東京大学原子力研究総合センター

1．はじめに

ホウ素は海底堆積物中あるいは変質した海洋底玄武岩に濃縮している．島弧火山のマグマには，サブダクションで運ばれたこれらの成分が含まれていると考えられるので，火山岩中のホウ素含有量は，島弧マグマの由来を考察するうえで，^{10}Beとともに重要な指標となる．

従来行われてきた，火山岩中ホウ素の湿式分析では，化学操作中の汚染あるいは揮発の問題があった．火山岩中ホウ素の即発γ線分析は非破壊法であるため，これらの問題は生じないうえ，0.1ppm以下の低濃度でも分析可能である．

本研究では，火山岩中ホウ素の即発γ線分析を高確度で，効率よく行う場合の問題点を考察した．

2．実験法

粉末火山岩試料をプレス錠剤化し，フッ素樹脂（FEP）フィルムで作製した袋に封入し，日本原子力研究所のJRR-3M炉の中性子ガイドビームで，He雰囲気中で1,000～10,000秒間照射した．その即発γ線をGe半導体検出器とBGO検出器で測定した．

3．結果および考察

火山岩には一般にナトリウムが含まれるため，472keVのNaピークが478keVのホウ素ピーク（幅広の特徴的なピーク）を妨害する．この妨害の除去法として，ホウ素ピークの高エネルギー側（Naピークのない側）半分を使う方法（図1．method A）が簡便で有効であった．

粉末試料をプレス錠剤化することにより，試料量を増加させ，照射・測定時間を1/3～1/4に短縮した．照射中の中性子束の時間変動および試料の形状，厚さによる試料部位の中性子強度の変化による影響（図2）は，Si（その含有量はXRF等他の分析法で求める）の即発γ線強度で規格化することにより補正できることが明らかになった（図3）．

SiO_2粉末，岩石標準試料（JB-1a, JA-2, JR-2, JG-1a）の錠剤にホウ素標準溶液を添加して作成した検量線は，試料それぞれについて，直線になったが，その勾配は異なった（図4）．Siの即発γ線強度で規格化したホウ素の即発γ線強度をさらに各試料中のH（吸着水に由来すると考えられる）の即発γ線強度で規格化したところ，検量線の勾配は一致した（図5）．この勾配の一致したものを，真の検量線として未知試料の分析を行うことにより，高確度の分析が行えることが明らかになった．

表1に今回の分析結果を示した．JR-1, JR-2が地質調査所（GSJ）の推奨値にくらべやや大きい他は誤差の範囲内で一致している．

参考文献

1) Yonezawa, C. and Wood, A. K. H.: Prompt γ-ray analysis of boron with cold and thermal neutron guided beams, *Anal. Chem.*, **67**, 4466-4470 (1995)
2) Yonezawa, C., Ruska, P. P., Matsue, H., Magara, M. and Adachi, T.: Determination of boron in Japanese geochemical reference samples by neutron-induced prompt gammma-ray analysis, *J. Radioanal. Nucl. Chem.* (in press)
3) Imai, N., Terashima, S., Itoh, S. and Ando, A: 1994 compilation values for GSJ reference samples, "Igneous rock series", *Geochem. J.*, **29**, 91-95 (1995)

原子炉：JRR-3M　　装置：即発γ線分析装置　　分野：即発γ線放射化分析（地球化学・宇宙化学）

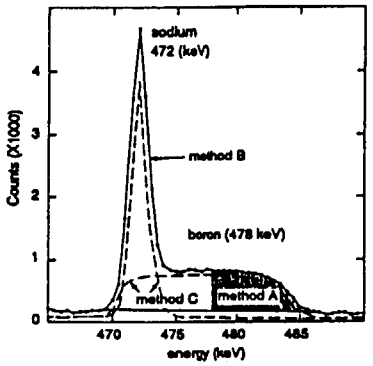

図1．478keVホウ素ピークにおける472keVナトリウムピーク妨害の除去法

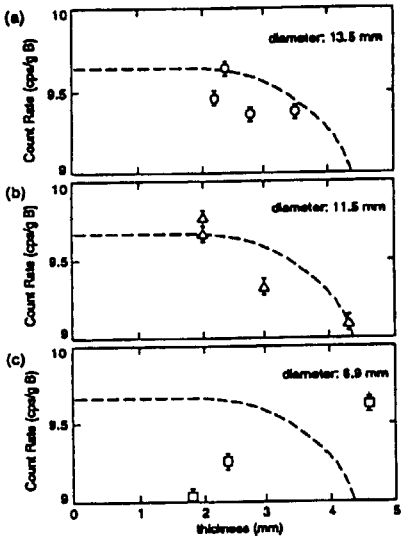

図2．試料の直径・厚さとホウ素の即発γ線強度の関係

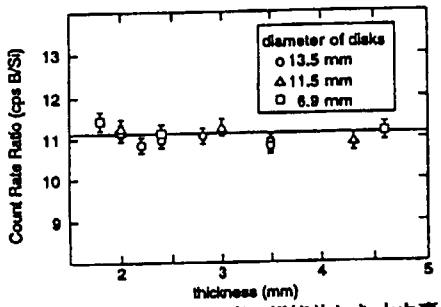

図3．Siの即発γ線強度で規格化したホウ素の即発γ線強度

表1．GSJ火山岩標準試料中ホウ素含有量

Sample	B content, μg/g		
	This study	Previously reported value[1),2)]	Recommended value[3)]
JB-1	8.93±0.28	10.7±0.20	9.35
JB-1a	7.49±0.34	7.31±0.29	7.88
JB-2	31.2±0.40	30.4±0.71	30.2
JB-3	20.4±0.5	20.4±0.35	18.0
JA-1	24.0±0.6	23.1±0.32	21.0
JA-2	21.9±0.47	21.0±0.41	20.7
JA-3	26.5±0.6	25.9±0.42	24.8
JR-1	134±3	131±4.5	117
JR-2	161±4.2	151±7.3	145

Errors of PGA are due to counting statics only.

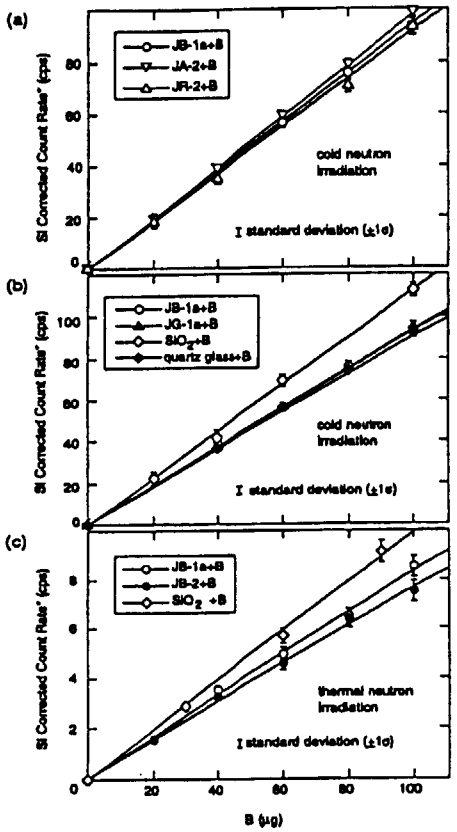

図4．岩石標準試料等のホウ素標準溶液による検量線．岩石試料中に含まれるホウ素からの即発γ線強度は差し引いてある

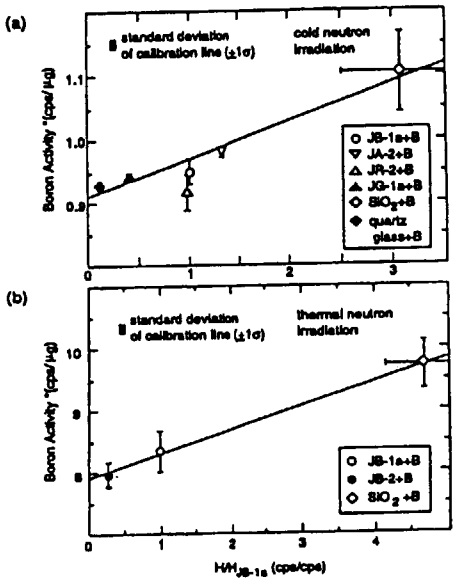

図5．水素の即発γ線強度で規格化した検査量

研究テーマ：隕石試料の即発γ線分析
表題：コンドライト質隕石のケイ素の分析

即発γ線分析によるコンドライト質隕石のケイ素の定量

海老原充、S. K. Latif、大浦泰嗣、G. W. Kallemeyn、中原弘道、
米沢仲四郎[1]、松江秀明[2]、澤幡浩之[3]
[1]東京都立大学大学院理学研究科
[2]日本原子力研究所燃料研究部
[3]東京大学原子力研究総合センター東海分室

本研究では即発γ線分析を利用して、いろいろな種類の隕石試料の元素分析を行っている。本報告では平成９年度に即発γ線分析装置を用いた成果の一部として隕石試料中のケイ素の定量を行った結果について報告する。

ケイ素は多くの隕石にとって主構成元素の一つであり、隕石の成因を議論する上で、その存在度が非常に重要な意味をもつ元素である。本研究では、均一な試料が調整されているAllende隕石（1969年にメキシコに落下した炭素質コンドライト隕石）を用いた。試料約２００mgをFEPフィルムに包み、測定用試料とした。これらの試料に、日本原子力研究所３号炉（JRR-3M）に設置されている即発γ線分析装置を用いて熱中性子、冷中性子ビームを照射し、発生する即発γ線を分析した。

分析法としては、標準試料（高純度金属ケイ素）による比較法（Comparison method）と、内部単一標準法(Internal mono-standard method）を用いて分析した。後者の方法では、内部標準元素とした鉄に対するケイ素の相対組成を求め、鉄の値を機器中性子放射化分析法で求めて、ケイ素含有量の絶対値を求めた。得られた結果を比較すると、比較法でも単一標準法でも系統的な差がなく、ともに文献値と誤差範囲内で等しい値が得られた。また、どちらの方法でも熱中性子と冷中性子を用いたが、この場合も利用する中性子によらず、等しい値が得られた。なお、感度は冷中性子を用いた場合の方が熱中性子を用いた場合に比べて約１５倍高い値が得られた。

この研究を通して、隕石試料のケイ素の含有量が即発γ線分析法によって精度良く求められることがわかった。本研究で用いた試料量は約２００mgであるが、それより大きな試料では熱中性子ビームを用いた内部単一標準元素法を適用することによってケイ素の定量が可能である。また、２００mgよりも小さな試料では照射時間を増やし、冷中性子ビームを用いることによって定量可能である。この方法は非破壊であり、照射後も適当な時間冷却すれば実質上非放射性物質として試料を再利用できるので、隕石試料などのような希少試料の分析には大変有効な方法であるといえる。

参考文献

Asia-Pacific Symposium on Radiochemistry '97, Proceeding (in press).

原子炉：JRR-3M　　装置：即発γ線分析装置　　分野：地球化学・宇宙化学

研究テーマ：即発γ線分析の大型試料への適用
表　　題：銅鏡の即発γ線分析

銅鏡の即発γ線分析

中原弘道，末木啓介，大浦泰嗣，齋藤綾子，富沢威[1]，西川寿勝[2]，米澤仲四郎[3]，松江秀明[3]
東京都立大学大学院理学研究科
[1]慶応大学文学部
[2]大阪府教育委員会
[3]日本原子力研究所分析センター

中性子ビームを用いた即発γ線分析法(PGAA)は，分析試料を原子炉内へ挿入する必要がないため，その大きさの制限がゆるい．そのため，サイズの大きな分析対象物を粉砕・溶解，または，その一部を採集すること無しにそのまま分析可能である．そこで，我々は試料の粉砕や一部採取の困難な大型考古遺物の化学分析にPGAAを適用した．これまでに，江戸時代の陶器の分析を行い，肥前産と瀬戸美濃産の産地推定の可能性があることを示した[1]．今回は，銅鏡の元素組成分析をPGAAで行った．銅鏡は，Cu，Sn，Pbの合金からできており，微量元素としてAs，Sb，Ni，Fe，Znが含まれていると報告されている．

さらに，中性子ビーム放射化分析法(NBAA)を提案する．これは，PGAAとINAAを組み合わせたもので，即発γ線を測定した後，中性子捕獲反応で生成した放射性核種をオフラインでγ線スペクトロメトリーを行う．これにより，PGAAでは困難であった元素が新たな処理を施すことなく定量できることがわかった．

中国で出土した87面の銅鏡を分析に供した．これらは，直径5～21cm，重さ18～1700gで，裏面の文様により製作時代(前漢，後漢，三国六朝，唐，宋，現代の偽物)が鑑定されている．実験は，研究炉JRR-3Mに設置されている即発γ線分析装置を利用して行った．試料をPTFE製糸でつるし，Heガス雰囲気中で熱中性子を照射しながら，即発γ線を約1時間測定した．照射終了5～7時間後，オフラインで照射試料中の中性子捕獲反応による生成放射性核種のγ線スペクトロメトリーを行った(便宜上，INAAと呼ぶ)．PGA，INAAともに先に我々が開発した内標準法[2]により元素比の定量を行った．

即発γ線スペクトルはほとんどがCuからのγ線でその中にSnからのγ線を2本検出することができた．INAAでは，^{66}Cu($T_{1/2}$=12.7h)，^{76}As(26.3h)，^{122}Sb(2.7d)，^{198g}Au(2.7d)を検出することができた．残念ながら主要元素の一つである鉛はPGA，INAAともに最も感度が悪い元素の一つであるため残念ながら検出できなかった．

Cuを内標準元素に選び，PGAAではSn/Cu比を，INAAではAs/Cu，Sb/Cu，Au/Cu比を定量した．図1に定量結果を製作時代の古いものから順に上から並べて示した．Sn/Cu比は前漢から唐まで約1100年にわたりほぼ一定で，平均30%である．しかし，宋の時代になるとその比は小さくなり，平均13%である．この特徴は，これまでにも散発的な分析により報告されていたが，本研究により再確認された．Au/Cu，As/CuならびにSb/Cu比には，製作時代の違いによる明らかな特徴は見いだせなかった．

参考文献

1) K.Sueki et al., *J.Radioaal.Nucl.Chem.* in press.
2) K.Sueki et al. *Anal.Chem.* **68** (1996) 2203.

原子炉：JRR-3M　　装置：即発γ線分析装置　　分野：放射化分析(考古学)

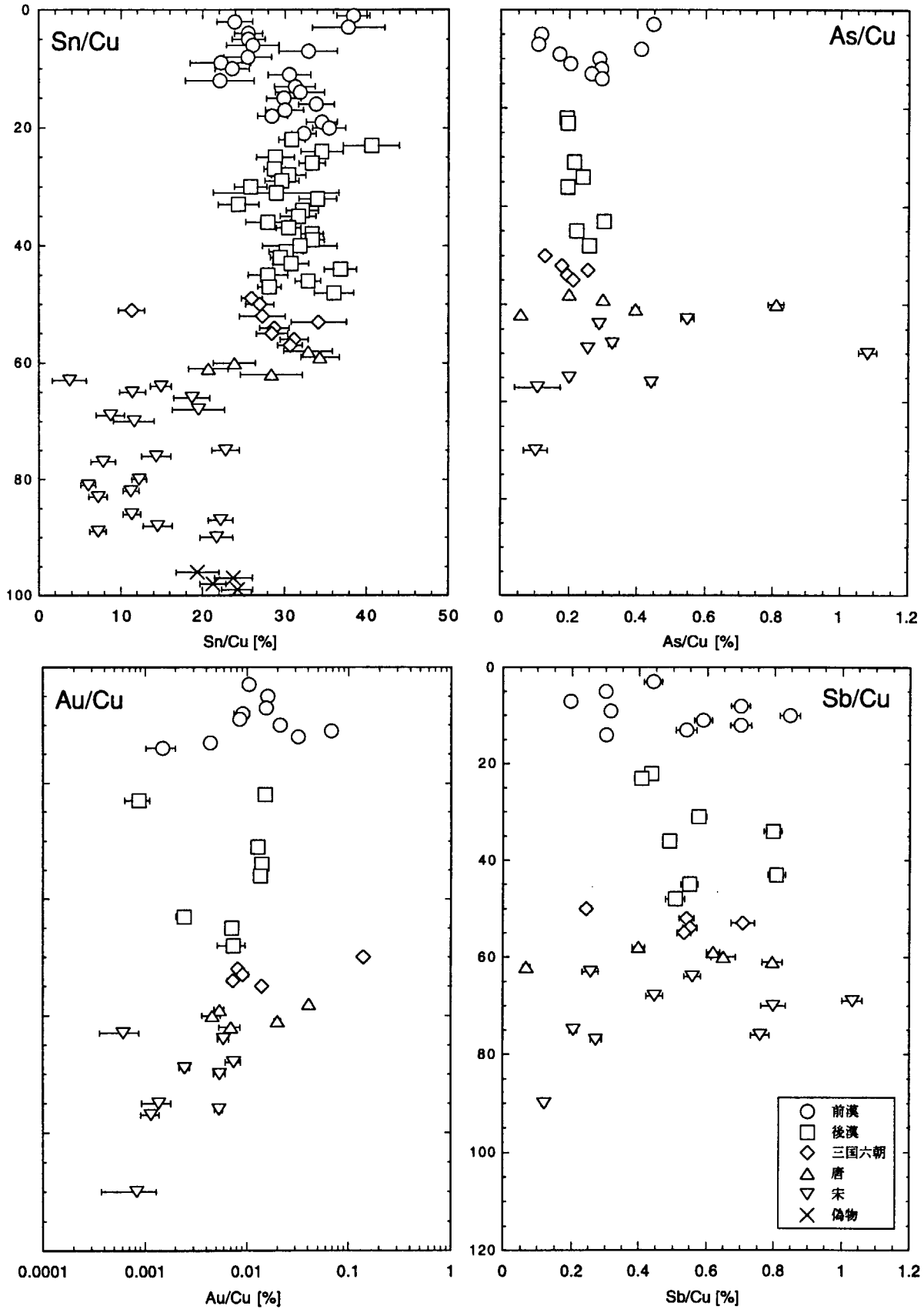

図1　銅鏡の元素濃度比.

研究テーマ：即発ガンマ線分析の化学への応用
標題：　　即発ガンマ線測定による非破壊状態分析の開発

(1)テルミット反応生成物のキャラクタリゼーションへの応用／
(2)即発γ線線形解析法の改良

酒井陽一、久保謙哉[1]、米沢仲四郎[2]、松江秀明[2]、澤幡浩之[3]、伊藤泰男[3]
大同工業大学　工学部
1　東京大学大学院理学系研究科
2　日本原子力研究所物質科学研究部分析センター
3　東京大学原子力研究総合センター

$^{10}B(n,\alpha)^{7*}Li$反応で生成する$^{7*}Li$の478 keV-即発γ線線形は、ドップラー広がりをもって測定される。これは$^{7*}Li$の寿命0.1p秒と物質中での減速の時定数が同程度の値をもつためである。我々はこの現象をホウ素の非破壊状態分析に応用することを目指している。

９年度は上記タイトルに示す２つのテーマに関して研究を行った。

(1) $^{10}B(n,\alpha)^{7*}Li$反応で生成する$^{7*}Li$の478keV-即発γ線線形の測定・解析（PGA法）により、種々の試料中のホウ素の状態を調べてきた。この手法をテルミット反応で生成するホウ素化合物のキャラクタリゼーションに応用した。アルミニウム粉末と鉄などの金属酸化物粉末を混合し空気中で加熱すると爆発的に短時間反応する。これをテルミット反応という。酸素との親和力の強いアルミニウムが酸化物から酸素を奪い、アルミナとなり、そのときの化学反応エネルギーが熱と光として、多量に放出される。金属酸化物は還元され金属状態となるとされている。酸化物として酸化ホウ素と鉄酸化物の混合物を用いテルミット反応を行わせ、ホウ素の状態をPGA法で、鉄の状態をメスバウアー分光法で分析した。テルミット反応後のホウ素の状態はホウ素とアルミニウムの金属間化合物であることがPGA法により示唆された。同一試料における鉄のメスバウアースペクトル（273K, 78K）はシングルピークであり、鉄とアルミニウムの金属間化合物の状態であることがわかった。以上の結果は、国際学会において報告した[1)]。同時に論文誌にも投稿した[2)]。

(2)　これまでの解析法は、ドップラー広がりをもつ線形の計算に２重の数値積分を含むため計算量が多く、多試料、多元素のγ線スペクトル解析に組み込むことには適していなかった。定式化を見直し計算量を減らし、あらたにフィッティングプログラム

新たに開発された解析法（フィッティングプログラム）により、様々な物質中での減速定数Ｄ（減速の時定数の逆数）を迅速に算出できるようになった。このためＤに対する物理学的．化学的な影響を詳細に議論できるようになった。また分析化学的な応用についても展開が期待される。国内の研究発表会において、成果を講演した[3)]。

参考文献

1)　Y.Sakai, K.Ohshita, M.K.Kubo, C.Yonezawa, H.Matsue, H.Sawahata, Y.Ito, S.Iwama,
"Mossbauer characterization and prompt γ-ray analysis of the products of thermit reactions"
Presented in Asia-Pacific Symposium on Radiochemistry (10.1997, at Kumatoto Univ.)
2)　上と同著者、同タイトル
J. Radioanal. Nucl. Chemistry, in press (1999)
3) 久保謙哉、酒井陽一、米沢仲四郎、松江秀明
「ドップラー広がりをもつγ線線形の解析法」
第35回理工学における同位元素研究発表会（国立教育会館、東京、7.1998）

原子炉：JRR-3M　　装置：即発ガンマ線分析装置　　分野：放射化分析

研究テーマ：原子炉冷・熱中性子フルエンスの標準化とその応用に関する研究
表題：球形比例計数管のガス増幅率位置依存性の測定－２－

球形比例計数管のガス増幅率位置依存性の測定－２－

武田直人，工藤勝久，米沢仲四郎[1]，松江秀明[1]，安達武雄[1]，星三千男[1]
電子技術総合研究所 茨城県つくば市梅園1-1-4
日本原子力研究所 茨城県那珂郡東海村白方白根2-4

我々は，中性子計測用ガス計数管のレスポンス関数計算コード(NRESPG)を開発し，中性子フルエンスの絶対測定を行っている．NRESPG では陽極線の両端付近における電界の歪みによるガス増幅率の変化を考慮して検出器のレスポンス関数を計算している．本研究では球形比例計数管におけるガス増幅率の位置依存性を測定し，NRESPG の計算結果と比較した．

ガス増幅率の位置依存性を測定するために，熱中性子ビームを ^{6}Li コリメータ（直径 0.5mm）を通し，直径 5cm の球形 ^{3}He 比例計数管に入射した．測定器を上下（陽極線に対して平行）左右（陽極線に対して垂直）にスイープし，各入射位置における波高分布測定を行った．

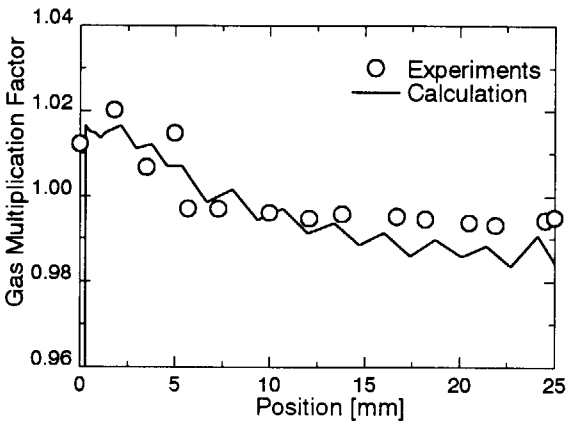

図1．ガス増幅率の変化．

図 1 に陽極線に平行な位置の各測定点におけるガス増幅率の測定結果と NRESPG による計算結果の比較を示す．図中のガス増幅率は計数管全体に中性子を照射した場合を 1 としている．また，計数管の中心は 25mm の位置である．NRESPG で計数管内の電界分布から計算したガス増幅率と測定結果はよく一致している．

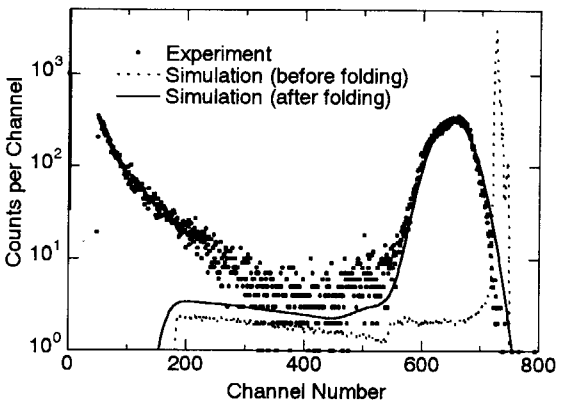

図2．波高分布の比較．

図 2 に NRESPG によるレスポンス関数の計算結果（点線）を熱中性子に対する計数管の波高分布（点）に測定器の分解能を考慮してフィッティングした結果（実線）を示す．実験で観測される全エネルギーピークのこぶは，計算にガス増幅率の場所依存性を取り込むことにより再現できている．しかし，測定器の分解能を考慮してフォールディングしてしまうと 1 つのピークと区別がつかない．また，ガス増幅率を考慮しない場合とした場合では波高分布のフィッティングの具合は，χ^2 判定の結果 20% 程度改善されたことが明らかになった．

原子炉：JRR-3M　装置：冷および熱中性子ビームライン　分野：即発γ線放射化分析（その他）

研究テーマ: 核反応を利用する分析化学
表　　題: 中性子即発γ線分析の研究

中性子即発γ線分析の研究

松江秀明、米沢仲四郎
物質科学研究部 分析センター

1. はじめに

これまでに、JRR-3M 冷中性子及び熱中性子ビームを使用した中性子即発γ線分析法(PGA)の研究を行い、ホウ素及び多元素定量法を確立し、各種試料の分析に応用してきた。今年度は冷中性子ビーム(第 1、2 サイクル)と熱中性子ビーム(第 3～7 サイクル)を使用し、新たに PGA 測定系の正確な検出効率の測定、PGA への k_0 法の適用、昨年度に引き続きマトリックス水素による中性子散乱の影響の評価、大学及び国立研究所との協力研究及び共同研究を実施した。

2. マトリックス水素による中性子散乱の影響の評価

中性子即発γ線分析(PGA)において、生物試料など水素濃度の高い試料の分析の際にマトリックス水素からの中性子散乱の影響が問題となる。水素(^{1}H)は熱中性子散乱断面積が約 80 b と他の核種に比べ非常に大きく、マトリックス水素からの中性子散乱による中性子束の減少、散乱中性子と試料元素との中性子捕獲反応、散乱中性子のエネルギー分布の変化、散乱中性子の散乱角度分布の偏りなどが生じ、これら全てが分析に影響する可能性がある。

昨年度は、マトリックス中の水素濃度の異なる円盤状試料および球状液体試料中の元素(H, B, Cl, Cd)の分析感度を求め、マトリックス水素からの中性子散乱の影響について評価した。その結果、円盤状の固体試料系ではマトリックス水素濃度が増加するにつれ分析感度が若干増加し、一方、球状液体試料系においては水素濃度の増加に伴って分析感度が減少することが認められた。さらにその増加率あるいは減少率は各元素で異なるなどの結果が得られた。

今年度は、新たに重水素置換尿素と尿素との組み合わせで水素濃度の異なるマトリックスを持ち、中性子ビームとの構成角に依存しない球状固体試料を作成し、JRR-3M の即発γ線分析装置によりこれらの試料を測定し、得られた分析感度(H, B, Cl, Cd)から固体球状試料における散乱中性子の影響を評価した。

その結果、冷中性子ビーム時の球状固体試料中における各元素の分析感度は各元素ともにマトリックス水素濃度の増加とともに減少した。さらに、その元素ごとの減少率は水素を除き顕著なものではなかったが H > Cl > B ≈ Cd の順に大きくなった。これらの傾向は熱中性子ビームの際も同様であるが、各元素ともに減少率は明らかに小さなものとなた。この結果は昨年度の本成果集で報告した D_2O/H_2O 球状試料(10, 13 mmφ)のものと大きく矛盾しないものであった。このことから、直径 10 mmφ 前後の球状試料においてはマトリックス水素濃度が増加するにつれ分析感度が減少する傾向を示し、その効果は冷中性子ビームにおいて大きいことが分かった。

3. PGA 測定系の正確な検出効率の測定

米国オークリッジ国立研究所から S. Ramam 博士を招聘し、共同で PGA 測定系における Ge 半導

原子炉: JRR-3M　　装置: 即発γ線分析装置線　　分野:即発γ線分析(分析化学一般)

体検出器の正確な検出効率を求めるための測定を行い、59 ～ 10829 keV におけるγ線エネルギー領域の正確な検出効率を求めることができた。得られた検出効率により、正確なγ線放出確率等の核データの取得及び検証が可能となり、さらに後述する k_0 値の測定の際にもこの検出効率を用いることができた。

4. PGA への k_0 法の適用

現在国外の複数の研究グループにおいて PGA における内標準多元素同時定量法として放射化分析で用いられている k_0 法に基づく方法の適用が検討されている。これまでに IKI(ハンガリー)及び NIST(米国)のグループは、十数元素について塩素に対する $k_{0,Cl}$ 値を報告している。今年度より、本 PGA 装置においても塩化物あるいは塩素含有試料の測定を行い、$k_{0,Cl}$ 値の評価を開始した。今年度は熱中性子ビームポートにおいて $k_{0,Cl}$ 値の測定を行い、十数元素の $k_{0,Cl}$ 値を得ることができた。

5. 協力及び共同研究

JRR-3M の即発γ線分析装置を使用し、大学との協力研究(8 件)及び国立研究所(2 件)を実施した。協力研究としては、即発ガンマ線測定による非破壊状態分析法の開発(大同工業大学工学部)、固体環境試料および地球化学的試料の即発ガンマ線分析(東京大学大学院)、中性子ガイドビームを用いた中性子吸収反応の核・放射化学への応用(熊本大学工学部)、即発γ線分析の大型試料への適用(東京都立大学大学院)、隕石試料の即発γ線分析(東京都立大学大学院)、即発γ線分析を用いた生命起源の鉄の同位体分析(秋田大学教養学部)、X線・低エネルギーγ線検出器による即発γ線分析(武蔵大学人文学部)、中性子即発γ線分析と放射化分析の統合・系統化(東京大学原子力研究総合センター)の研究を行った。また、共同研究としては、農林水産研究における原子炉中性子即発γ線分析の利用に関する研究(農林水産省農業環境技術研究所、畜産試験所、遠洋水産研究所)及び原子炉冷・熱中性子フルエンスの標準化とその応用に関する研究(通産省工業技術院電子技術総合研究所)を行った。

6. 成果の公表

1. C. Yonezawa, H. Matsue, H. Magara, M. Hoshi, H. Sawahata, Y. Ito; "Prompt gamma-ray analysis using cold and thermal guided neutron beams at JAERI", G. L. Molnár, T.Belgy, Zs. Révag eds., "Proceedings of the 9th International Symposium on Capture Gamma-Ray Spectroscopy and Related Topics", p.705, (1997), (Springer, Budapest).
2. M. Magara, C. Yonezawa,; "Decomposition of prompt gamma-ray spectra including the Doppler-broadened peak for born", Nucl Instrum. Methods Phys. Res. A, in press (1998).
3. C. Yonezawa, P. P. Ruska, H. Matsue, M. Magara, T. Adachi; "Determination of born in Japanese geochemical reference samples by neutron-induced prompt gamma-ray analysis", J. Radioanal. Nucl. Chem., in press (1998).
4. 松江秀明、米沢仲四郎: 第 41 回放射化学討論会予稿集、p.240 (1997)
5. 松江秀明、米沢仲四郎: 第 42 回放射化学討論会、発表予定 (1998)

研究テーマ：陽極アルミナ皮膜中の水素含有量と分布
表　　題：アルミニウム陽極酸化皮膜中の水素の濃度と分布

陽極アルミナ皮膜中の水素含有量と分布

森崎重喜
東京都立大学理学研究科

1．研究目的

陽極酸化アルミニウム皮膜中には、電解液中のアニオン成分や水素が皮膜成長時に取り込まれる。本研究では、即発γ線分析（ＰＧＡ）および熱重量測定・示差熱測定（ＴＧ／ＤＴＡ）、液体シンチレーション計測（ＬＳＣ）を用いて、各種の陽極アルミナ皮膜中の水素含有量と深さ方向分布の測定を行い、皮膜の生成機構を検討した。

2．実験方法

高純度アルミニウム（99.99%）を過塩素酸－メタノール溶液中で電解研磨し、リン酸－クロム酸溶液浸せき後陽極酸化を行い、バリヤー型陽極酸化皮膜とポーラス型陽極酸化皮膜を作成した。バリヤー型皮膜の作成には中性電解液（0.5Mホウ酸－0.05M四ホウ酸ナトリウム水溶液）を、ポーラス型皮膜の作成には硫酸浴（10wt%）およびホウ酸・硫酸混合浴（5wt%ホウ酸－5wt%硫酸）を使用した。

バリヤー型皮膜はヨウ素－メタノール法、ポーラス型皮膜は逆電剥離法を用いてＡｌ地金より剥離した後、粉状にしてＰＧＡ分析およびＴＧ／ＤＴＡ測定に供した。

ヨウ素－メタノール法で剥離したままのバリヤー型皮膜は、水分量が極めて少ないため、ＰＧＡ法やＴＧ／ＤＴＡ法ではその定量が難しい。そこで、トリチウム水を用いて調整した0.05M四ホウ酸ナトリウム溶液中でバリヤー型皮膜を化成し、皮膜中に取り込まれたトリチウム量をＬＳＣ法で測定した。また、皮膜を15%硫酸溶液中で溶解し、溶解液中のトリチウム濃度を測定して、皮膜中の水素（トリチウム）の深さ方向分布を求めた。

3．結果と考察

3．1　ＰＧＡ法による分析結果

ＰＧＡおよびＴＧ／ＤＴＡ実験による各皮膜中の水素含有量をTable1に示す。バリヤー型皮膜の場合、水分量は極めて少なく、その組成はほぼAl_2O_3に近いと考えられた。一方、水中に保存後乾燥したバリヤー型皮膜で検出された水分は吸着水と考えられた。

硫酸皮膜、ホウ酸・硫酸皮膜では数%の水分量（各々6.7wt%、7.4wt%）が検出された。内層の組成がバリヤー型皮膜と同様にAl_2O_3に近い組成とすれば外層は一水和物（AlOOH，水分量15wt%）に近い組成となった。

Table 1 Hydrogen content and weight loss of anodic alumina films by PGA and TG/DTA.

Sample of anodic alumina film	PGA (wt%)		Weight loss (wt%) by TG/DTA at each temperature of					Remarks
	Hydrogen content	water content	120℃	150℃	500℃	980℃	1200℃	
Barrier-type 1	0.08	0.72	−0.15	−0.22	−0.10	0.37	0.31	
2	1.79	16.0	5.5	8.3	17.2	18.8	19.3	
3	2.53	23.6	7.9	10.3	22.5	23.7	23.9	
Porous-type 1	0.73	6.7	3.0	3.7	7.7	13.3		Boric/sulfuric acid
Porous-type 2	0.82	7.4	1.7	2.1	4.5	15.4	17.5	Sulfuric acid
3	0.55	5.0						〃 dried at 120℃
4	0.30	2.7						〃 dried at 400℃
5	0.22	1.9						〃 dried at 550℃
6	1.59	14.3						〃 dipped in boiling water

・Barrier-type 1 was separated from Al substrate and dried over silica gel.
・Barrier-type 2 was dipped in water after separation, and dried over silica gel.
・Barrier-type 3 was dipped in water after separation, and air-dried.

研究施設：JRR-3M、装置：ＰＧＡ分析、　研究分野：陽極アルミナ皮膜、水素分析

3．2　TG／DTA法による分析結果

Fig. 1に各皮膜のTG曲線を示す。結晶性アルミナ水和物$Al_2O_3 \cdot H_2O$と$Al_2O_3 \cdot 3H_2O$を加熱すると明確な吸熱ピークを経て550℃までにはAl_2O_3に変化する。水中で保存したバリヤー型皮膜では500℃までにほとんどの水分が離脱している。

硫酸皮膜およびホウ酸・硫酸皮膜の場合、PGA法で検出された水分量の2倍以上の重量減が1000℃までに観測された。特に硫酸皮膜の場合は、950℃付近でアニオン成分に由来する鋭い発熱ピークとそれに引き続く吸熱ピークがみられた。この様に高温領域での重量減は、水素すなわち水分とは直接関係しないものと考えられた。

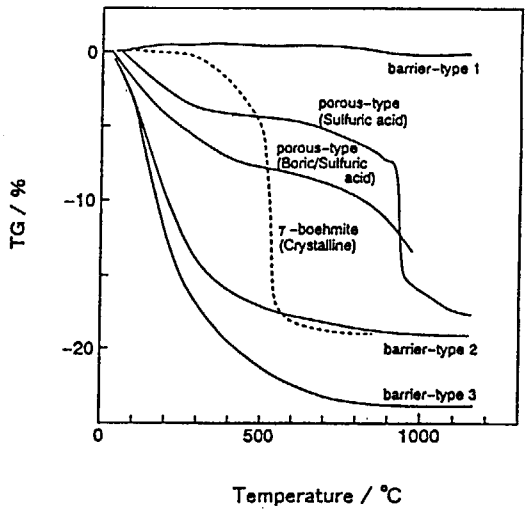

Fig. 1　TG curves of anodic alumina films.

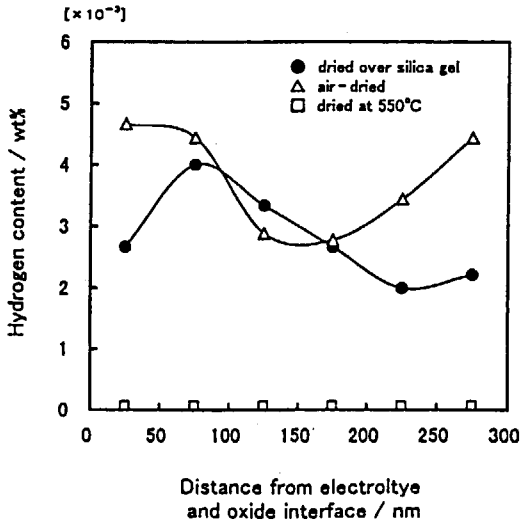

Fig. 2　Depth profiles of hydrogen in barrier-type anodic alumina films.

3．LSC法による分析結果

Fig. 2はバリヤー型皮膜中の水素の深さ方向分布を示している。電解液／酸化皮膜界面から取り込まれる水素は皮膜全体にわたって分布していた。この結果はアニオン成分であるB，P，Sの断面分布とは異なっていた。

B，S，Pは皮膜の電解液／酸化物界面から皮膜中央部の範囲で検出され、中央部から酸化皮膜／アルミ地金の範囲には含まれていなかった。これらの分布は、アニオン成分の吸着取込みとO^{2-}，Al^{3+}の輸率によって合理的に説明できる。一方水素は、純Al_2O_3に近い組成のバリヤー型皮膜の全域でごく微量検出された。これより、皮膜中の水素は負のキャリアーOH^-に由来するものと考えられる。

OH^-が酸化皮膜／Al地金界面に達するとすれば、皮膜深部にも水素が分布していることを合理的に説明できる。また酸化皮膜／Al地金界面での反応として、従来通りの主反応(1)以外に(2)、(3)等をあげることができる。

(1)　$2Al^{3+} + 3O^{2-} \rightarrow Al_2O_3$

(2)　$OH^- \rightarrow O^{2-} + H^+$

$2Al^{3+} + 3O^{2-} \rightarrow Al_2O_3$

(3)　$2Al^{3+} + 3OH^- \rightarrow Al_2O_3 + 3H^+$

ここで生成するH^+の大部分は、電場に従って電解液方向に泳動することになる。

4．まとめ

(1) バリヤー型皮膜中の水素量は極めて少なく一様に皮膜に含まれていることがわかった。

(2) 水素は、OH^-イオンとして酸化皮膜／金属界面へ泳動する事が推察された。従来酸化皮膜中の電荷のキャリアーはO^{2-}，Al^{3+}とされてきたが、キャリアーとしてOH^-イオンを追加し、上記のAl_2O_3生成反応を考慮することによって極微量の水素量とその分布を合理的に説明できる。

(3) ポーラス型硫酸皮膜の場合、水分量は比較的多く、120℃までに放出される吸着水を除く水分量は約15%であり、皮膜組成は$Al_2O_3 \cdot H_2O$（AlOOH：ベーマイト）に相当することが確かめられた。

5．参考文献

1) 森崎重喜他，"アルミニウム陽極酸化皮膜中の水素の濃度と分布"，表面技術，Vol. 49，205-208　(1998)

2) S.Morisaki, et al., "Content of Hydrogen in Anodic Alumina Films", 46th ISE, Amoi (1996)

研究テーマ：中性子ガイドビームを用いた中性子吸収反応の核・放射化学への応用
表　　題：中性子捕獲即発γ線スペクトル中のピーク形状

PHOTOPEAK PROFILE IN NEUTRON CAPTURE PROMPT GAMMA-RAY SPECTRA

T. KISHIKAWA, S. NOGUCHI, C. YONEZAWA*1, H. MATSUE*1, A. NAKAMURA*2, H. SAWAHATA*3

Faculty of Engineering, Kumamoto University, Kumamoto, 860
**1 Department of Chemistry and Fuel Research, Tokai Establishment, Japan Atomic Energy Research Institute, Tokai-mura, Ibaraki, 319-11*
**2 Faculty of Education, Akita University, Akita, 010*
**3 Research Center for Nuclear Science and Technology, The University of Tokyo, c/o JAERI, Tokai-mura, Ibaraki, 319-11*

1 Introduction

Deviation of photon energy values[1] between data obtained by photon spectrometry, i.e. the prompt gamma-ray analysis (PGA) and the decay gamma-ray analysis with Ge or Ge(Li) detectors, and those obtained by crystal diffraction spectrometry, has led that the "conventional" method of energy calibration for the photon spectrometry is not adequate to the precise energy assignment. A "new" method has solved this problem by introducing the concept of an instrument function, which is the transfer function between an input signal-shape function and an output (measured) signal-shape function, as summarized in Refference 1.

General relationship of the input signal-shape function $H(E,x)$, the instrument function $I(x)$ and the output (measured) signal-shape function $M(E, x)$ can be described as follows based on convolution nature of these functions:

$$M(E,x) = I(x) * H(E,x) \qquad (1)$$

where x is the channel number appeared in the spectrometer and the symbol * indicates the convolution integral. Equation (1) implies that if the input signal-shape function is the delta function, then the output (measured) signal-shape indicates the same shape as the instrument functional shape. If the input signal-shape function is, on the other hand, the step function, then the output (measured) signal-shape shows the sigmoid shape. Detailed description of the instrument function can be seen elsewhere[1].

The instrument function is different from the normal distribution (ND) due to distortion caused by the random losses of charge carriers in a Ge detector. The instrument function is a probability density distribution function in which the ND function is convoluted by the random escape probability density distribution (REPDED). The ND folded in the instrument function

原子炉：JRR-3M　装置：即発γ線分析装置　分野：即発γ線分析　エネルギー精密計測

never appears in the spectrum, though it is the key function in the peak shape analysis.

General prospects of the instrument function are as follows: (1) precise measurement of incident photon energy, because of the centroid of ND being the energy reflecting parameter, and (2) precise measurement of photopeak intensity, because of an integration of the instrument function multiplied by the frequency (i.e. the count rate) giving the intensity of photopeak.

For energy chain construction of ultra precise energy calibration, the key signal shapes are those of the single escape (SE) peak and the double escape (DE) peak, besides the full energy (FE) peak shape, for the precise energy measurement by the PGA with photon energy higher than 1.02 MeV, because the energy difference of both the FE and SE and the SE and DE are 0.511 MeV and that of the FE and DE is 1.02 MeV. However, the profiles of the SE and the DE are both completely different from that of the FE, as shown in Fig. 1. While the base profile of the FE indicates a step-down profile, that of the SE seems to show no step-wise profile and that of the DE, a step-up profile.

For these prospects, however, it is indispensable to examine the feasibility of base profile subtraction from overall photopeak profile. Commonly used, pre-base profile subtraction methods for spectral analysis are insufficient for the precise measurement of both the photon energy and intensity[2,3].

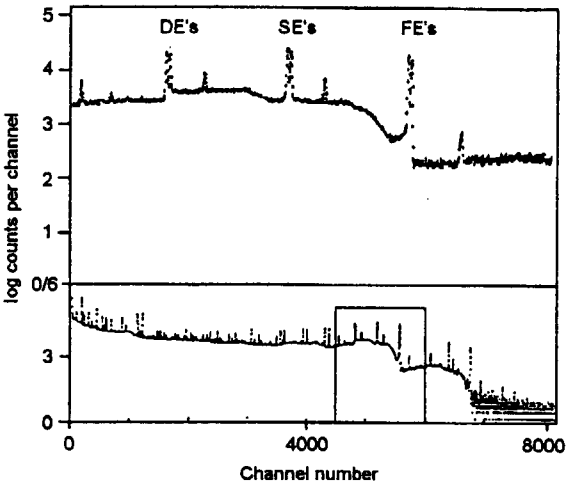

Fig. 1. Typical example of neutron capture gamma-ray spectra obtained by activation on natural iron plate at the single mode operation of BGO/Ge spectrometer installed at the JRR-3M neutron beam guit\de hall. Marked lines are doublet peaks of 7631- and 7645-keV full energy peaks (FE), single escape (SE) and double escape (DE) peaks

2. Modeling of the Base Profile

Modeling has been made after consideration of the following items: (1) gamma-ray interactions in the detector, (2) interaction of positron in a medium, (3) escape events of annihilation photon(s) from the detector, (3-1) relative energy spectrum function of single escape for the TPA process (SE/3A), (3-2) relative energy spectrum function of double escape for the TPA process (DE/3A), (3-3) relative energy spectrum function of triple escape for the TPA process (TE/3A), (4) compton escape events with double photon annihilation in the detector, (4-1) relative energy spectrum function of single Compton escape and single annihilation absorption with the DPA (SCE/SA/2A), (4-2) relative energy spectrum function of single Compton escape and single annihilation escape with the DPA (SCE/SE/2A), (4-3) relative energy

spectrum function of double Compton escape with the DPA (DCE/2A), and (4-4) Compton escape with the TPA photons.

The calculated spectra of the model of double photon annihilation and triple photon annihilation both in a Ge detector as shown, respectively, in Figs. 2 and 3 well reflect experimental prompt gamma-ray spectrum (Fig. 1). Relatively flat base in the vicinity of both sides of the SE/2A peak prifile in the measured doublet peals can be a reflection of counts of the SCE/SA/2A for the high energy side and the DE/3A for the low energy side. Detail of the results has been presented elsewhere.[4]

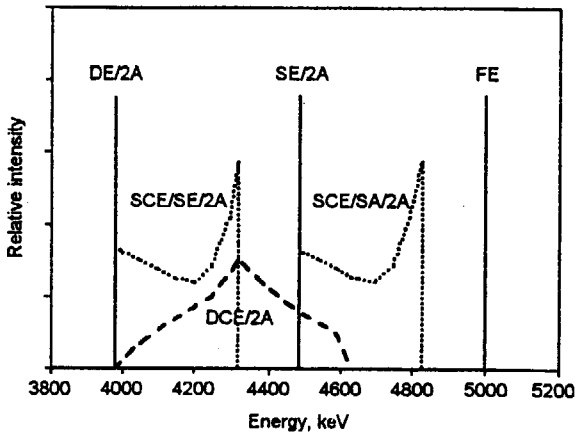

Fig. 2. Theoretical energy spectra of double photin annihilation (DPA) in a Ge detector; DE/2A: double escape of DPA, SE/2A: single escape of DPA, FE: full energy peal of photon energy 5000 keV, SCE/SE/2A: single Compton escape with single escape of DPA, SCE/SA/2A: single Compton escape with single absorption of DPA, DEC/2A: double Compton escape of DPA

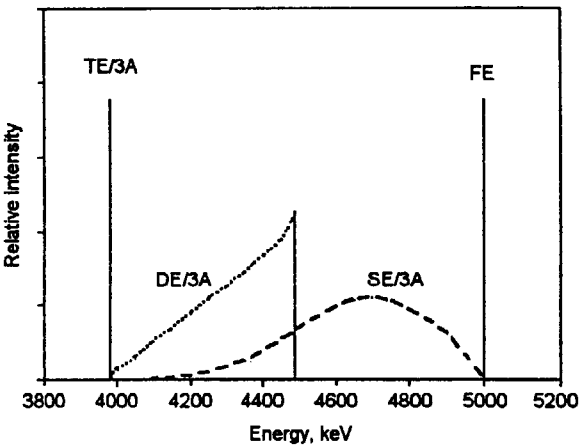

Fig. 3. Theoretical energy spectra of triple photin annihilation (TPA) in a Ge detector; TE/3A: triple escape of TPA, FE: full energy peal of photon energy 5000 keV, DE/3A: double escape of TPA, SE/3A: single escape of TPA

References

1. T. Kishikawa, K. Nishimura, S. Noguchi, Nucl. Instr. and Meth. A 353 (1994) 285.

2. T. Kishikawa, K. Nishimura, S. Noguchi, Y. Nonaka, Appl. Radiat. Isot. 44 (1993) 1389.

3. T. Kishikawa, C. Yonezawa, H. Matsue, Y. Ito and H. Sawahata, Effect of bremsstrahlung and Compton- electron induced summing on Ge-detector photopeak shapes, Proceedings of International Committee for Radionuclide Metrology Symposium on Radionuclide Metrology and its Applications (ICRM'95), Paris, May 15-19, 1995; Nucl. Instr. and Meth. in Phys. Res., A 369 (1996) 689.

4. T. Kishikawa, S. Noguchi, C. Yonezawa, H. Matsue, A. Nakamura, H. Sawahata, J. Radioanal. nucl. Chem., 215 (1997) 211.

固体環境試料および地球化学的試料の即発ガンマ線分析

Neutron-induced prompt gamma-ray analysis of solid environmental samples and geochemical samples

松尾基之, 久野章仁, 大野渉, 久保健一, 米沢仲四郎[1], 松江秀明[1], 澤幡浩之[2]

M. Matsuo, A. Kuno, W. Ono, K. Kubo, C. Yonezawa[1], H. Matsue[1] and H. Sawahata[2]

東京大学大学院総合文化研究科広域科学専攻
[1]日本原子力研究所燃料研究部分析センター
[2]東京大学原子力研究総合センター
Graduate School of Arts and Sciences, The University of Tokyo
[1]Department of Chemistry and Fuel Research, Japan Atomic Energy Research Institute
[2]Research Centre for Nuclear Science and Technology, The University of Tokyo

1．はじめに

固体環境試料や地球化学的試料中に含有される元素を定量し、その分布を明らかにすることは、試料自体の形成過程を知る上でも、試料の置かれた環境を理解する上でも重要な課題と考えられる。中性子誘起即発γ線分析法(PGA)は、通常の機器中性子放射化分析法(INAA)と同様に、多元素同時定量分析が可能なため、多くの元素の分布を総合的に判断するのに適した分析法と言える。さらにＰＧＡは、ＩＮＡＡでは分析が困難なH, B, S, Si等の軽元素やCd等の有害元素の定量が可能である、試料の誘導放射能が低く同分析法で使用した試料を他の分析法で再使用することが可能である、といった特長を持つ優れた分析法である。本研究では、同法を用いることにより、次の３通りの試料について種々の環境化学的、地球化学的な検討を行った。①河口域において深さ３cmごとに採取した河川底質、②関東地方及び伊豆諸島で採取したマイマイ殻、③愛知県犬山地域で採取した遠洋深海性層状チャート。以下に、それぞれの試料ごとに研究内容およびその結果を報告する。

2．河口域底質の即発γ線分析

【序】　河口域は、流域の人間活動や地質環境の特徴を持つ淡水である河川水と、高塩分濃度の海水が混ざり合う場所であり、天然水の化学環境が最も劇的に変わる場所ということができる。そこでは、懸濁物質などが沈降しやすく、有機物を含む堆積物がたまり、嫌気的環境を形成している。そのため、海水起源の硫酸イオンが堆積物中で還元され、悪臭物質に変化することが指摘されている。我々は、メスバウアー分光法を用いた鉄の化学状態の分析により、堆積物中の酸化・還元状態をモニターするとともに、悪臭物質の一つである硫化水素(H_2S)を堆積物中のFeが捕らえてパイライト(FeS_2)として固定することを見いだした。このような堆積環境中での種々の元素の分布は、堆積物の形成過程を知り、環境を理解する上で重要な課題と考えられる。本研究では、中性子誘起即発γ線分析法および機器中性子放射化分析法を用いることにより、多摩川河口域底質中に含まれる元素の垂直分布を調べ、それらの分布を支配する因子について考察を加えた。また、比較のため、多摩川最上流に位置する奥多摩湖の底質およびあまり汚染されていないと考えられる大分県八坂川河口域の底質についても同様の分析に供した。

【実験】　多摩川河口域の底質試料は２km離れた２つの地点（水深約50cm）から深さ45cmのコアをそれぞれ採取した。奥多摩湖の底質試料は湖の中央付近（水深約57m）から 深さ39cmのコ

研究施設と装置名
ＪＲＲ－３Ｍ、即発γ線分析装置

研究分野
環境化学、地球化学、分析化学

アを採取した。採取した底質は深さごとに分け、加圧ろ過により間隙水を除いたものを風乾後、めのう乳鉢で粉砕した。その中から約200 mgを精秤し、錠剤成形器を用いて約100 kgf cm^{-2}の圧力で5分程度置き、直径10mm、厚さ約1mmのペレットに成形した。これを、中性子ビームのサイズである20mm四方以内に収まるように、厚さ12μmのFEPフィルムに封入し、テフロン製の専用ホルダーに固定した上で、日本原子力研究所JRR-3Mの冷中性子ビームガイド（中性子束：1.4×10^{8} n $cm^{-1}s^{-1}$）または熱中性子ビームガイド（中性子束：2.4×10^{7} n $cm^{-1}s^{-1}$）に設置した即発γ線分析装置にセットし、He雰囲気中で3600秒間（冷中性子）または18000秒間（熱中性子）即発γ線を測定した。熱中性子ビームガイドでの分析感度は冷中性子ビームガイドでの分析感度の約1/10程度であるので、マシンタイムの都合も考え測定時間をこのように設定した。測定したγ線スペクトルは通常のγ線スペクトル解析プログラム(SEIKO EG&G DS-P201/MS)でピークサーチとピーク面積の計算を行った。各ピークについて得られた計数率は、中性子束の変動を補正するために、24時間に1, 2回、一定のTiの板(Ti flux monitor) を測定して得られる 342keVと1381keVのピークの計数率の平均値で割り、比較標準試料について報告されている Ti flux monitorの計数率で規格化した分析感度を用いて各元素の含有量を計算した。

【結果および考察】　多摩川河口域、奥多摩湖、および大分県八坂川河口域の底質に対し PGA法を適用した結果、分析感度の報告されている24元素のうち、Al, B, Ca, Cd, Cl, Fe, Gd, H, K, Mn, Na, S, Si, Sm, Tiの15元素が定量でき、INAA法と合わせて40元素の濃度が求まった。しかし、各元素濃度は有機物含量や含水量など他の成分の含量の変動によって相対的に変動するので、こういった影響を除去するため、一般に土壌中で移動しにくいと言われているAlの濃度で規格化して実質的な分布を評価した(Fig. 1)。その結果、やはり移動しにくいと言われている

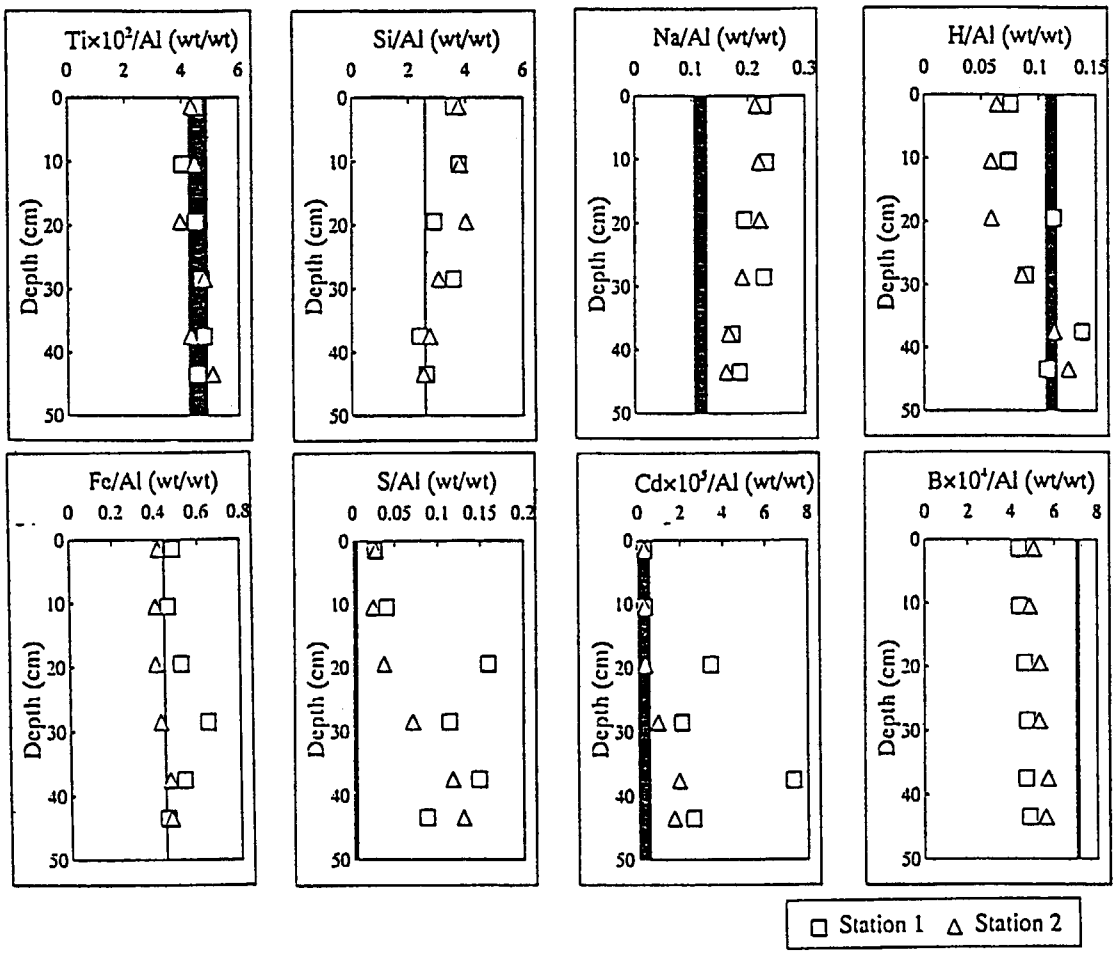

Fig. 1. Al normalized depth profiles of elements in the Tama River estuarine sediments. The shaded area shows the range of the maximum and minimum ratios in the Lake Okutama sediment.

Tiの分布は深さによらずほぼ一定であり、Alで規格化することは妥当と言える。また、奥多摩湖での各元素の垂直分布は深さによる変化があまり見られなかったので、その最大値と最小値の範囲のみを示したが、河口域でのTi／Al比と奥多摩湖でのTi／Al比が一致していることから、両者は同じ母岩に由来しているものと考えられる。

Alの濃度で規格化した各元素の垂直分布に着目すると、Siおよびアルカリ金属、アルカリ土類金属は深層部で減少するのに対し、Hは深層部で増大している。この変化は深層部ほど風化が進行し、一次鉱物が加水分解されケイ酸の溶出を伴い粘土鉱物に変化するためと考えられる。また、Sは深層部で著しく増大するが、これは海水などを起源とする硫酸イオンが、酸素の少ない深層部で硫酸還元菌の活動により還元され硫化物として固定されているためと考えられ、有機物と硫酸イオンに富む河口域堆積物に特徴的な分布と言える。Ag, Cd, ZnはこのようなSの分布と良い相関があり、これらの元素の地球化学的挙動を考え合わせると、硫化物として堆積物中に取り込まれていると考えられる。それでは、河口域堆積物深層部には一般にこのような有害元素が濃集されているのかというと、人為的影響の少ないと考えられる大分県八坂川河口域では、河口域に特徴的な深層部でのSの増大は見られたにも関わらずCdは検出限界以下であった。このことから、多摩川河口域堆積物深層部のCdは人為的影響により供給されたものが硫酸還元過程に伴い硫化物として固定されている可能性がある。一方、もしこのような硫化物としての固定がなかった場合、これらの有害元素が水中に溶存し生物の生命を脅かすことが推察されるという点で、硫酸還元過程の持つ自然浄化能と捉えることができる。またAs, B, Ba, Cs, K, Mn, Rb, Th およびランタノイドについては、奥多摩湖堆積物中の含有量の方が多摩川河口域堆積物中の含有量に比べて有意に高かった。この原因としては、堆積物の由来する母岩の違いなどいくつか考えられるが、これらの元素の多くは粘土鉱物への吸着が知られる元素であるため、堆積環境に基づく吸着量の違いが原因の1つとして考えられる。

3．マイマイ殻の即発γ線分析

【序】　陸棲の貝であるマイマイ(カタツムリ)は、その低い運動能力から生活範囲が限定され、生物指標として利用されている他の貝同様に有害物質等を体内に蓄積すれば、生息域の環境を反映する生物指標として利用できる可能性がある。この特徴に着目し、特に死後も残る殻に含まれる不純物を指標として利用する可能性を検討するため、マイマイ殻の分析を行った。また、生息域の情報を反映するものとして、マイマイ殻採取地点の土壌を採取し分析を行った。

【実験】　調査地域は、人為的影響を強く反映していると思われる地域として、亜鉛精錬工場があることで有名な群馬県安中市を、対照的な地域として伊豆諸島から八丈島、三宅島、新島を、それらの中間的な地域として神奈川県茅ヶ崎市を選び、マイマイおよび土壌試料を採取した。マイマイ殻は有機体部と分離した後、超音波洗浄器を用いて付着した土壌等を除去し、粉砕した。土壌試料は風乾、粉砕し試料とした。また、比較検討のために、マイマイ殻と同じ主成分（$CaCO_3$）を持つ石灰岩の標準試料(地質調査所、JLs-1)を分析した。これらの試料の即発γ線測定条件は、多摩川河口域底質と同様である。

【結果および考察】　Table 1に、PGA法によって得られたマイマイ殻および石灰岩標準試料の分析結果を示す。今回の分析から、マイマイの殻はほぼ純粋な炭酸カルシウムであり、不純物として B, Sr, Cd等を含むことが分かった。石灰岩標準試料と比較すると、石灰岩中にはほとんど含まれていないホウ素がマイマイ殻では比較的多く含まれるのが興味深い。しかしながらホウ素は石灰岩の種類によっては多量に含まれることが報告されており、どのような地球化学的・環境化学的意味を持つのか判断するのは難しいと思われる。また、今回、重金属元素のCdが検出されたが、Cdは特定有害物質に指定されている元素でもあり、環境化学的に重要な意味を持つ。同元素はイオン半径がCaとほとんど同じなので、炭酸カルシウム中に取り込まれることは十分考えられることである。マイマイ殻中のCd含有量が、生息地域の環境（例えば、土壌

Table 1. The composition of snail shells.

Sample	Ca	B	Sr	Cd
	%		ppm	
Annaka1	40.6	1.58	356	2.91
Annaka2	38.9	2.36	395	1.10
Chigasaki	39.1	2.42	301	0.247
Niijima	40.2	2.72	389	0.144
Miyake1	39.2	1.05	326	0.070
Miyake2	35.0	2.18	294	0.226
Hachijo	39.0	2.12	361	0.121
Limestone (JLs-1)	39.5	0.45	285	0.329

のCd汚染）を反映していれば、マイマイ殻中のCd量は、環境指標として使えることになる。そこで、群馬県安中市においては特に、亜鉛精錬工場からの距離の異なる地点でマイマイ及び土壌の採取を行った。この地域では、土壌中のCd含有量は既に調べられており、精錬工場に近づくほどCd濃度が高くなっていることが分かっている。実際にマイマイと同時に採取した土壌試料のPGA分析の結果に基づき、土壌中のCd濃度を横軸にとり、マイマイ殻中のCd濃度を縦軸にとって両者の関係をプロットした結果を Fig. 2に示す。両者の相関係数は 0.898と高く、このことから、マイマイ殻中のCd含有量が環境指標となる可能性が示されたと言えよう。また、土壌中にCdがほとんど含まれない地域のマイマイ殻中には、土壌と比べて低濃度のCdが含まれるのに対し、土壌中に比較的多く含まれる地域のマイマイ殻中では、Cdが濃縮される傾向があるという興味深い結果も得られた。今後さらに、分析データの数を増やし正確な知見を得るために、よりCd濃度の高いと思われる地域で試料の採取を行うとともに、マイマイが食していると考えられる植物を直接採取し分析する予定である。その際、Cdに対して感度が良いという特長を生かして、中性子誘起即発γ線分析法を継続して利用していく予定である。

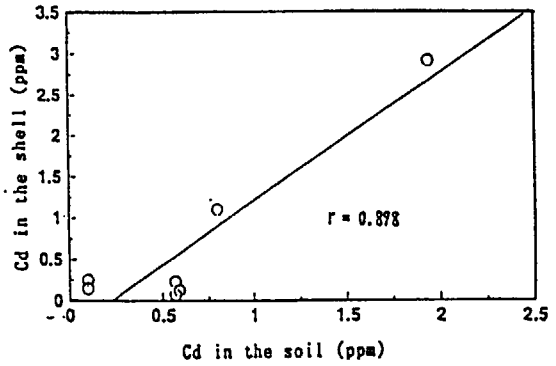

Fig. 2. Correlation between Cd in the shell and Cd in the soil.

4．遠洋深海性チャートの即発γ線分析

【序】　美濃帯・犬山地域に産する層状チャートは、古生代／中生代境界（以下Ｐ／Ｔ境界）直後のトリアス紀の遠洋深海性堆積物である。Ｐ／Ｔ境界においては生物大絶滅が報告されており、その原因となった環境変動を推定する上でこのチャートの分析は重要である。我々はこれまでに、チャート中に含まれる鉄成分の化学状態をメスバウアー分光法を用いて分析し、チャート層の呈する色調と含有される鉄化学種との関連性および遠洋深海の酸化還元環境について考察した。しかしながら、海水という複雑な系の酸化還元状態を正確に推定するためには複数の元素からの情報が必要となる。酸化還元条件の変化は、元素の価数を変化させると同時に、沈殿や溶出を通じて固相中の各元素の量を変化させる。したがって、種々の元素についての層ごとの分布パターンから、堆積時の酸化還元環境が推定できる。本研究では、以上の目的で、ＩＮＡＡおよびＰＧＡ法による多元素同時定量を行い、各元素の層ごとの分布パターンを明らかにした。

【実験】　犬山地域に産する遠洋深海性チャート層から色調ごとに試料を採取した。風化を受けた表面や脈等をダイヤモンドカッターで切り落とした上で、エリス乳鉢およびめのう乳鉢を用いて粉末にし、100メッシュのふるいを通して測定試料とした。即発γ線の測定条件は、多摩川河口域底質と同様である。

【結果および考察】　遠洋深海性層状チャートについて即発γ線分析を行った結果 Al, B, Ca, Cl, Fe, Gd, H, K, Mn, Na, S, Si, Sm, Ti の定量値が得られた。これらの元素のうち K, Al, Tiの３元素は互いに強い正の相関を示した。これらの元素は陸源の砕屑物に由来すると考えられるが、これらの量比が全サンプルを通じて一定であることは、上記チャートの堆積場に流入した砕屑物の母岩は、その堆積時代を通じて変わらなかったことを示している。一方 Fe, Mn, Ｓのように、その挙動が海洋の酸化還元環境に大きく依存すると考えられる元素は、K, Al, Tiとは全く異なる分布を示した。例えばＳは、黒や灰色の試料中に検出されたのに対し、赤や黄色の試料からは検出されなかった。チャートに含まれるＳは、海水中の硫酸イオンが還元されて鉄などの金属と硫化物を作って沈殿した結果、固相中に取り込まれたものと考えられる。従ってＳの分布は、黒や灰色のチャートが還元的な環境で堆積し、赤や黄色のチャートが酸化的な環境で堆積したことを示すものと考えられる。これは、鉄の化学状態をメスバウアー分光法によって測定した結果から導かれる推論と良く一致する。同様にMnやFeの分布が陸源砕屑物の流入量と独立であることは、この時代の海洋の酸化還元環境が大きく変化したことを示唆するものと思われる。実際に、赤褐色の試料にはMnが多く含まれ、酸化的環境でMn^{2+}がMnO_2として堆積したことを示すものと考えられた。

5．成果の公表

学術誌

1. A. Kuno, M. Matsuo, B. Takano, C. Yonezawa, H. Matsue and H. Sawahata, "Neutron induced prompt gamma-ray and instrumental neutron activation analyses of urban estuarine sediments", J. Radioanal. Nucl. Chem., Articles, 218(2), 169-176 (1997)

学位論文

2. 大野　渉 "Land snail shells as an environmental indicator － a basic study －" 東京大学大学院総合文化研究科広域科学専攻　修士論文　(1995年2月)
3. 久野章仁 "河口域堆積物中に含まれる元素の化学状態と垂直分布" 東京大学大学院総合文化研究科広域科学専攻　修士論文　(1997年2月)
4. 久保健一 "堆積物から推定する古海洋の酸化還元環境　－Ｐ／Ｔ境界の遠洋深海チャート層を読む－" 東京大学大学院総合文化研究科広域科学専攻　修士論文　(1997年2月)

学会発表

5. 大野　渉・松尾基之・高野穆一郎・米沢仲四郎・澤幡浩之 "関東地方及び伊豆諸島で採取したマイマイ殻の中性子誘起即発γ線分析" 第38回放射化学討論会 (1994年9月)
6. 久野章仁・松尾基之・米沢仲四郎・松江秀明・澤幡浩之 "多摩川河口域底質の放射化分析および即発ガンマ線分析" 第33回理工学における同位元素研究発表会　(1996年7月)
7. 久野章仁・松尾基之・高野穆一郎・米沢仲四郎・松江秀明・澤幡浩之 "多摩川河口域堆積物中に含まれる元素の分布と移動" 1996年度日本地球化学会年会 (1996年8月)
8. 久野章仁・松尾基之・米沢仲四郎・松江秀明・澤幡浩之 "中性子誘起即発γ線分析法および機器中性子放射化分析法による河口域底質の多元素定量" 第40回放射化学討論会　(1996年10月)
9. 久保健一・松尾基之・磯崎行雄・米沢仲四郎・松江秀明・澤幡浩之 "機器中性子放射化分析法および中性子誘起即発γ線分析法による遠洋深海チャート層の分析" 第40回放射化学討論会　(1996年10月)
10. 久保健一・磯崎行雄・松尾基之・米沢仲四郎・松江秀明・澤幡浩之 "複数の元素から読みとるＰ／Ｔ境界遠洋深海底の酸化還元条件" 地球惑星科学関連学会1997年合同大会　(1997年3月)
11. A. Kuno, K. Sampei, M. Matsuo, C. Yonezawa, H. Matsue and H. Sawahata, "Vertical distribution of elements in non-polluted estuarine sediments determined by neutron induced prompt gamma-ray and instrumental neutron activation analyses", Asia-Pacific Symposium on Radiochemistry '97 (APSORC'97), (Oct. 1997)

This is a blank page.

4. 放射化分析
(Neutron Activition Analysis)

This is a blank page.

研究テーマ：ラジオアイソトープ技術者の養成
表　　題　：実習　放射化分析

貝殻中の銅・ナトリウムの放射化分析

上沖　寛
国際原子力総合技術センター（東京研修センター）

本研究は、ＲＩ技術者の養成を目的とする研修コースの中で実習教科として行うものである。本報告では、平成９年度の研究炉をもちいた成果として、国内原子力技術および放射線利用に関係する人材養成を行った基礎課程、およびアジア・太平洋地域開発途上国の原子力分野人材養成への国際援助としてＪＩＣＡと協力して行った原子力基礎技術コースにおいての実習教科としての放射化分析について報告する。

原子力の基礎として中性子核反応の理論や応用を理解させることは重要である。放射化分析の実際を経験させることはこれらの知識の理解を深めるのに大変重要であり結果としてガンマ線スペクトル解析による放射能測定法および非密封ＲＩの安全取扱法を習得させることになる。

平成９年度は基礎課程とＪＩＣＡ原子力基礎技術コースの中で５回の放射化分析実習を行った。分析試料は海水産の大アサリであり、炭酸カルシウムをマトリックスにして微量元素を含有する。分析目的核種は、放射化生成核種のガンマ線スペクトルで主成分となるナトリウム24、放射化生成物が陽電子壊変を伴い陽電子消滅ピークを主要放射線ピークとする銅64である。照射条件は研究炉の気送管で２～５分間照射とし、ナトリウムと銅の標準試料と共に大アサリ貝殻の照射を５回行った。

銅の分析：

銅64の陽電子消滅放射線は、他の放射化生成核種からの高エネルギーガンマ線や宇宙線が物質にもたらす電子対生成による放射線と同一放射線であるから、銅 64 分析には化学分離を必要とした。簡単な銅の化学分離法として金属亜鉛により銅イオンを還元させて銅の沈殿分離を行った。この化学分離の操作は、30分間の所要時間で 0.1 ppm Cu 濃度に対して５％の精度で分析された。本実習は、生成核種を同定および定量することにより核反応の理解を深め、ＲＩ実験における放射線被曝に対する工夫、除染、サーベイ等の一連の安全取扱いの基礎を習得させるものとして有効であった。

本実験による研修生の被曝線量は、線源が 10^5 Bq位に対し最大１μSv 程度であった。

原子炉：JRR-3M　　装置：気送管　　分野：放射化分析（環境）

研究テーマ：非放射性^{41}Kの長期間追跡のための新たな測定・解析手法の開発
表　　題：^{41}K存在比の高精度測定法と^{41}K追跡法によるカリウムの作物吸収率の算出

放射化分析利用による安定^{41}Kトレーサ法の開発

結田康一
農業環境技術研究所

カリウム（カリ）は三大肥料要素としてリン酸とともに外国から輸入され、主として化成肥料としてチッ素、リン酸とともに大量に施肥されている。さらにカリ高含有家畜糞尿の土壌還元もあり、作物の贅沢吸収、土壌のカリ過剰蓄積や養分アンバランス、水域の富栄養化などが問題にされ、省資源・環境保全型の施肥技術の確立が求められている。これに応えるためには、野外でカリの移動を高精度に追跡できる安定（非放射性）アイソトープトレーサ法を開発する必要がある。本報告では安定^{41}Kの野外・圃場利用を目標に、その前段階として土耕ポット試験を行い、栽培作物等の^{41}K存在比の変動を高精度に分析することで、施肥カリの吸収率等を定量する手法を開発する。

実験方法：表１にカリウムの主な安定アイソトープと放射性アイソトープを示したが、この中の^{41}Kをトレーサとして用いた。

^{41}K（天然存在比6.77%）を放射化分析法、全カリ（^{41}K＋^{40}K＋^{39}K）は炎光光度法で分析。^{41}K存在比4.08～11.82%のKCl水溶液を濾紙、白米、スイトウ茎葉に添加（添加カリウム（^{41}K＋^{40}K＋^{39}K）量はいずれも1,000μg）、繰り返し分析・測定を行い、検量線を作った。

作物中^{41}K、全K分析法の精度・感度を高めるために、乾式灰化濃縮（前処理）法や湿式分解法の検討を行った。長円筒水浸透型ポットに土壌を入れ、^{41}K存在比4.20%の^{41}K標識塩加（KCl）肥料を施肥、スイトウとラジノクローバを収穫期まで栽培、作物中^{41}K存在比などを分析し、^{41}K標識塩加肥料や土壌カリの吸収率を算出した。

結果および考察：1)^{41}K存在比と、^{42}K量（^{41}Kに熱中性子を照射して生成させる）との間の直線性は良かったが、カリ含量が高いスイトウ茎葉ではやや悪くなった。^{41}K存在比で6.54%以下または7.00%以上（^{41}K存在比間差±0.23%以上）あれば追跡可能と推定された。
2)長円筒土耕試験では、^{41}K excess存在比-2.57%（^{41}K存在比4.2%）の^{41}K標識塩加肥料を用いて、収穫期まで栽培、スイトウ、ラジノクローバ（茎葉部の^{41}K excess存在比は-0.87～-1.00%）で追跡が十分可能で、肥料カリや土壌カリの吸収率などを定量的に算出できた（表２）。

参考文献

1）日本土壌肥料学会講演要旨集，第44集，（1998），p.289
2）第35回理工学における同位元素研究発表会要旨集（1998），p.158

原子炉：JRR-3M　　装置：気送管　　分野：放射化分析（環境，農・水産物）

表1　カリウムの安定アイソトープ（SI）と放射性アイソトープ（RI）

アイソトープ		天然存在比（%）	半減期
安定	^{39}K	93.22	安定
	^{41}K	6.77	安定
放射性	^{40}K	0.0114	1.3×10^{9}年
	^{42}K	0	12.4時間
	^{43}K	0	22.4時間

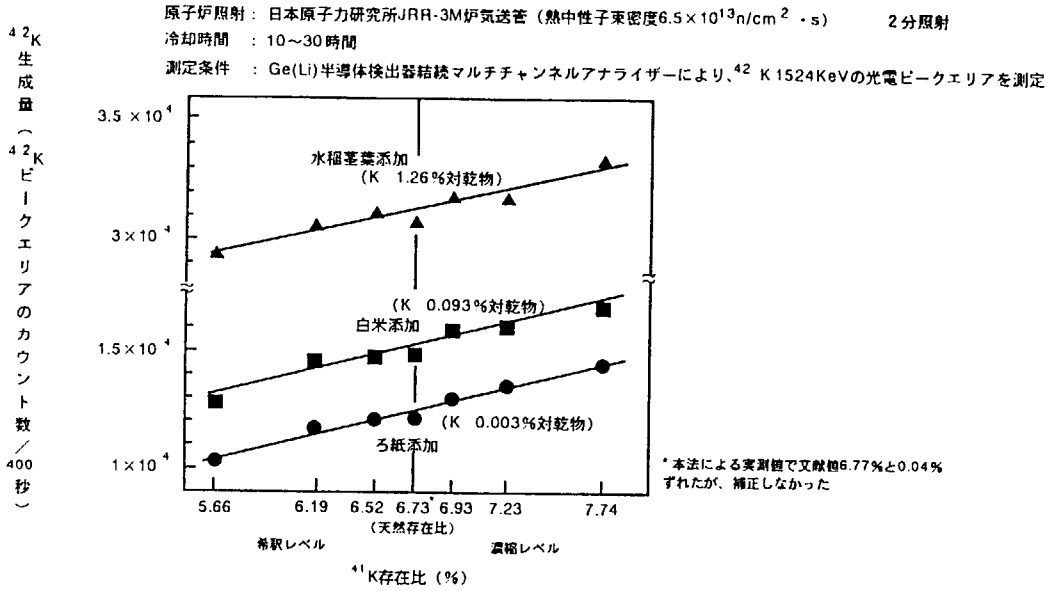

図1　天然存在比レベルでの^{41}K存在比（作物添加物）と^{42}K生成量（ピークエリア）との関係

表2　ポット栽培スイトウによる^{41}K標識Kの吸収率と寄与率

栽培作物・部位	標識塩加肥料中^{41}K excess%[A]（^{41}K存在比%）	作物中K含量（mg/g乾物）	作物中^{41}K含量（mg/g乾物）	作物中^{41}K excess%[B]（^{41}K存在比）	作物中K吸収量 mg/ポット 総吸収量[x+y]	施肥K吸収量[x]1)（施肥K寄与率）	土壌K吸収量[y]2)（土壌K寄与率）	^{41}K標識Kの吸収率3)
茎葉		20.18	1.164	-1.00	494.5	192.4	302.1	38.4
スイトウ	-2.57 (4.20)			(5.77)	(100.0)	(38.9)	(61.1)	
玄米		3.12	0.191	-0.65	72.5	18.3	54.2	3.7
				(6.12)	(100.0)	(25.2)	(74.8)	

施肥K（^{41}K標識）の吸収量[x]の算出式

$x = B/A \times (x+y)$　　x: 施肥Kの吸収量　　y: 土壌Kの吸収量

A: 施肥K中^{41}K excess% = -2.57　B: 作物中Kの^{41}K excess%

1)作物吸収Kの内、^{41}K標識K肥料由来のK吸収量（占める割合%）

2)K肥料以外（土壌Kや以前施肥したK肥料由来K）の吸収量（占める割合%）

3)施用した^{41}K標識K（Kとして500mg）の作物による吸収率（%）

原子炉：JRR-3M　　装置：気送管　　分野：放射化分析（環境，農・水産物）

研究テーマ：農林生態系におけるハロゲン元素の動態
表　　題：世界の土壌・植物系におけるハロゲン元素の含量レベルと動態の解明

タンザニア国キリマンジャロ州と日本国北海道・九州の土壌

結田康一[1)]、井磧昭[2)]
1）農業環境技術研究所
2）元農業技術研究所

ハロゲン元素（ヨウ素、臭素、塩素）の環境での易動性は大きく、動植物での欠乏・過剰・汚染問題が生じやすい。
本研究では、これらの元素の高感度・高精度分析法である化学分離操作を伴う放射化分析法を用いて、世界各地の土壌・植物系における含量・分布と動態を明らかにする。その中で特に気候や地形条件、土壌や植物の種類、土地利用・農業活動等人為的作用との関連を解析する。
前年度はブラジル、タイおよびインドネシア土壌を対象にしたが、本報では、表題の2ヶ国3地域の土壌について、結果を報告する。

対象土壌と分析法：キリマンジャロ州は熱帯サバンナ気候下の高原（平原）土壌の他、キリマンジャロ山等の山麓～中腹にかけての降水量がより大きい土壌を供試。日本国内で最も降水量が少なく寒冷な北海道東部の平野部などの北海道土壌と、降水量が最も多く温暖な屋久島を含む九州土壌を供試。いずれも深度0～100cm程度の層位別土壌で、3元素は放射化分析法で定量。

結果：①キリマンジャロ州の土壌（A層）中ヨウ素、臭素含量（対風乾土）は、平原の土壌が最も低く平均　5.6、6.4mgkg^{-1}で世界の平均的レベル（5、5mgkg^{-1}）であった。
山地では標高が高く、降水量が増えるにつれて両元素も高含量となり、キリマンジャロ山山腹（標高1650m）のHumic Andosolsでは同州で最高の97.4、89.1mgkg^{-1}となった（図1）。これは、これまでの世界一の高含量であった日本の土壌（本州中央部平均43、102mgkg^{-1}）と同レベルか超える含量であった。塩素含量（A層）も平原土壌が最低（平均23.1mgkg^{-1}）で、世界の平均的レベル（100mgkg^{-1}）以下であり、標高が高くなっても最高81mgkg^{-1}にとどまった。ただし、低平地のソロネツ土（Vertisols）の20～50cm層で2237mgkg^{-1}の高濃度を示し、塩類集積土壌であることを示唆していた。

②日本の非水田土壌はヨウ素含量で大きな地域差を示し、少雨寒冷な北海道東部で平均6mgkg^{-1}（A層）に対し、多雨温暖な屋久島では100mgkg^{-1}を越えるものが多く、次表層土で290mgkg^{-1}の世界最高値を示した（表1）。

参考文献

1）日本土壌肥料学会講演要旨集，第44集，（1998），p.219

原子炉：JRR-3M　　装置：気送管　　分野：放射化分析（環境，農・水産物）

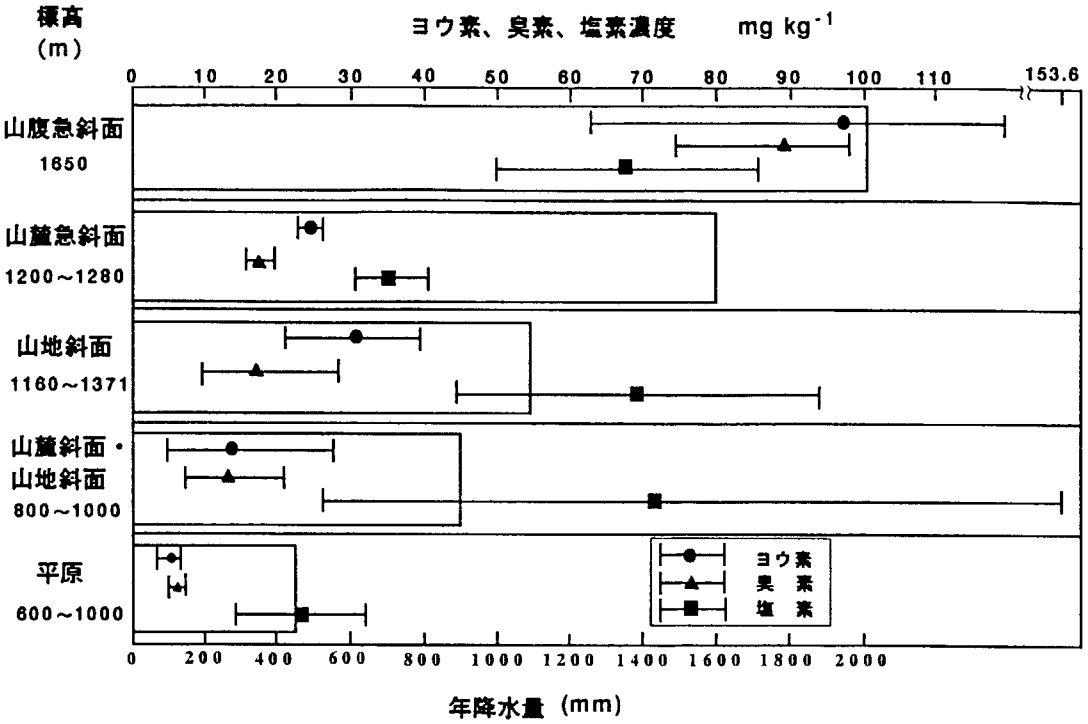

図1　キリマンジャロ州土壌中ヨウ素、臭素および塩素含量と降水量の関係

表1　土壌（AまたはAp層）中ヨウ素、臭素および塩素含量　mgkg^{-1}/乾土

地域	地点数		ヨウ素		臭素		塩素	
キリマンジャロ州 （原野・畑）	18	32	(3.9~112)	26	(5.6~97)	55	(15~154)	
北海道東部 （林地）	6	6.0	(2.7~14)	20	(4.8~36)	80	(62~94)	
屋久島 （林地・樹園地・草地）	6	120	(87~168)	130	(81~207)	98	(62~139)	
屋久島 （水田）	1	0.67		6.6		79		
日本本州中央部 （林地・畑・樹園地）	124	43		102		116		
日本本州中央部 （水田）	31	1.8		5.3		52		
世界の平均レベル[a)] a) Bowen, H. J. M. (1996) 他		5		5		100		

原子炉：JRR-3M　　装置：気送管　　分野：放射化分析（環境，農・水産物）

海洋生物に含まれる微量元素の放射化分析法
Activation Analysis of Trace Elements in Marine Organisms

大西俊之、野矢洋一
北海道大学ｱｲｿﾄｰﾌﾟ総合ｾﾝﾀｰ

１．はじめに

ホタテガイは、体内に高濃度のカドミウムを濃縮することが知られているが、その濃縮機構やカドミウムを含む生体物質等は、未だ解明されていない部分が多い[1]。

ホタテガイは、北海道を代表する海産物の一つであり、各地で養殖、加工が行われているが、加工残さとして廃棄されるウロ（中腸腺）によるカドミウム汚染が環境面から問題になっている。

今回、ホタテガイの部位別の微量元素濃度及びプランクトン、海水のカドミウム濃度を測定し、微量元素の濃縮の程度や機構について検討を行った。合わせて、放射化分析法と原子吸光法によるカドミウム測定について比較検討したので報告する。

２．方法

（１）試料

ホタテガイは、北海道岩内町漁協で購入した３年貝であり、購入後、直ちに貝柱、鰓、外套膜、精巣、卵巣、腎臓、中腸腺及びその他の部位別に分取し、生重量を測定した。その後、３～５日間の凍結乾燥を行い、乾重量を測定した。分析に供した試料数は、貝柱、鰓、外套膜、精巣、卵巣及びその他の部位が６個体、腎臓が２０個体、中腸腺が１０個体である。また、これらとは別にホタテガイの全軟体部４個体の分析も行った。

プランクトン及び海水は、北海道小樽市忍路で採取した。プランクトンは、網目４０μmと３３４μmの２重ネットで採取後、直ちにガラス繊維濾紙を用いてろ別し、生重量を測定した。その後、２日間の凍結乾燥を行い、乾重量を測定した。　海水は、採取後、直ちに0.45μmのメンブランフィルターを用いてろ別し、少量の硝酸を添加した。

（２）放射化分析法

①４５０℃で２４時間灰化し、灰重量を測定した（乾式灰化）。

②ろ紙（短半減期核種分析用）及び石英管（長半減期核種分析用）に５～10mg程度の試料を封入した。

③日本原子力研究所（ＪＲＲ－３）で、ろ紙試料は１０秒間、石英管試料は４時間の中性子照射を行った。

④ろ紙試料は直ちに、石英管試料は３～４週間の冷却後、ピュアゲルマ半導体検出装置により核種分析を行った。

（３）原子吸光法

①ホタテガイとプランクトンは、硝酸－過塩素酸中で加熱分解を行った（湿式灰化）。

②海水は、ジエチルジチオカルバミン酸ナトリウム－メチルイソブチルケトン系で溶媒抽出し、希塩酸で逆抽出を行った。

③ホタテガイはフレーム式、プランクトンと海水はフレームレス式の原子吸光光度計で測定を行った。

３．結果と考察

（１）ホタテガイの微量元素濃度

放射化分析法によるホタテガイの部位別微量

元素濃度を表１に示す。表１より、鰓における亜鉛とセレン、腎臓におけるコバルトとカドミウム、中腸腺における鉄とカドミウム、その他の部位におけるバリウムの濃度が高いことが分かった。特に腎臓と中腸腺におけるカドミウムの特異的な濃縮が明らかである。

（２）放射化分析法と原子吸光法の比較

表２に放射化分析法と原子吸光法によるホタ

表1 放射化分析法によるホタテガイの微量元素濃度

部位 / 元素	貝柱	鰓	外套膜	精巣	卵巣	腎臓	中腸腺	その他
Sc	0.00540	0.0131	0.0445	0.0745	0.0269	0.103	0.223	0.190
Cr	0.217	0.858	0.931	0.595	0.349	0.496	2.48	1.94
Fe	36.3	144	181	359	188	468	1004	865
Co	0.0612	0.992	0.610	0.318	0.222	3.84	0.901	0.654
Zn	96.3	522	491	134	162	450	119	289
Se	N.D	2.36	0.346	N.D	0.548	1.59	1.85	N.D
Rb	11.9	11.5	11.4	18.2	7.19	8.78	4.59	13.0
Zr	6.32	24.9	23.5	19.2	N.D	N.D	N.D	23.1
Ag	0.0536	0.234	0.138	0.269	0.149	0.238	2.65	0.550
Cd	N.D	N.D	N.D	N.D	N.D	1470	97.7	68.6
Sb	0.0493	0.0297	0.0851	0.0483	0.0249	0.0245	0.218	0.104
Cs	0.0256	0.0341	0.0689	0.0621	0.0223	N.D	0.0546	0.0936
Ba	N.D	11.1	13.5	N.D	N.D	N.D	4.69	46.9
Eu	0.00718	0.0254	0.0260	0.0187	0.00317	0.00692	0.0145	0.0312
Tb	0.0427	0.174	0.168	0.0921	N.D	N.D	0.0159	0.157
Yb	0.0450	0.117	0.209	0.0990	N.D	N.D	0.0203	0.132
Hf	0.280	0.849	0.937	0.520	N.D	N.D	N.D	N.D
Ta	N.D	0.0201	N.D	0.0104	0.00857	N.D	0.0194	0.0213
Au	N.D	0.0118	N.D	N.D	N.D	N.D	0.0110	0.00645

1)単位: μ g/g dry wt

2)その他:ホタテガイの軟体部の内、貝柱、鰓、外套膜、精巣、卵巣、腎臓及び中腸腺を除いた部位であり、胃、腸、心臓等が含まれる。

3)N. D:検出限界以下

表2 放射化分析法及び原子吸光法による Cd 濃度と含有量

分析法	項　目	貝柱	鰓	外套膜	精巣	卵巣	腎臓	中腸腺	その他
放射化分析法	濃度(μ g/g dry wt)	N.D	N.D	N.D	N.D	N.D	1470	97.7	68.6
原子吸光法	濃度(μ g/g dry wt)	3.32	4.42	2.30	4.11	10.4	1380	128	53.2
	乾燥重量(g)	4.85	1.15	2.14	1.74	1.85	0.080	1.22	0.602
	含有量(μ g)	16.1	5.10	4.93	7.16	19.2	110	156	32

1)その他:ホタテガイの軟体部の内、貝柱、鰓、外套膜、精巣、卵巣、腎臓及び中腸腺を除いた部位であり、胃、腸、心臓等が含まれる。

2)N. D:検出限界以下

3)含有量:当該部位に含まれる全カドミウム量

表3 海水、プランクトン、ホタテガイのCd濃度と濃縮係数

試料		濃度	濃縮係数
海水		1.94×10^{-5}(μg/ml)	-
プランクトン	40μm～334μm	0.0269(μg/g wet wt)	1.4×10^{3}
	334μm以上	0.0439(μg/g wet wt)	2.3×10^{3}
ホタテガイ	貝柱	0.704(μg/g wet wt)	3.6×10^{4}
	鰓	0.470(μg/g wet wt)	2.4×10^{4}
	外套膜	0.243(μg/g wet wt)	1.3×10^{4}
	精巣	0.772(μg/g wet wt)	4.0×10^{4}
	卵巣	1.85(μg/g wet wt)	9.5×10^{4}
	腎臓	214(μg/g wet wt)	1.1×10^{7}
	中腸腺	23.1(μg/g wet wt)	1.2×10^{6}
	その他	7.43(μg/g wet wt)	3.8×10^{5}

1)濃縮係数:当該試料のカドミウム濃度／海水のカドミウム濃度

2)プランクトンの項の40μm～334μm及び334μm以上は、プランクトンを採取した網目のサイズを示す。

テガイのカドミウム濃度を示す。カドミウムは、核反応断面積が0.3barnと大きくなく、かつ半減期も53.4時間と短いため、貝柱等の低濃度カドミウムを放射化分析で測定することは困難である。また、カドミウムは、高温で飛散しやすいため、高温を用いる乾式灰化には適さないと言われており、一般に、湿式灰化－原子吸光法の組合せで測定されることが多い[2]。しかし、乾式灰化－放射化分析法は、試料の前処理が容易であり、かつ多元素同時分析ができるといったメリットがある。今回の測定においても腎臓や中腸腺等の高濃度部位についての測定は、乾式灰化－放射化分析法で十分可能であり、精度的にも湿式灰化－原子吸光法に劣っていないことが確認できた。

一般に環境面で問題になるのは、カドミウム含有量が大きく、かつ加工残さとして廃棄される中腸腺等の処理である。これらの部分のカドミウム濃度のモニタリングには、手間のかかる湿式灰化－原子吸光法より乾式灰化－放射化分析法を用いることにより、分析に要する労力を大幅に低減することが可能であると考える。

（3）プランクトンとホタテガイのカドミウム濃度

表3に原子吸光法で測定した海水、プランクトン及びホタテガイのカドミウム濃度と濃縮係数を示す。これらの値は、Uthe らによって報告された値[3),4)]とほぼ一致している。しかし、ホタテガイの腎臓のみ、2～4倍程度を示している。これが特異的な値なのかどうか、今後も測定を継続する必要がある。

プランクトンは、334μm以上のもの（主に動物プランクトン）は40μm～334μmのサイズのもの（主に植物プランクトン）に比べて約2倍の濃度を示しており、植物プランクトン－動物プランクトン間で若干の濃縮が行われていることが示唆される。プランクトンは、海水のカドミウム濃度、栄養塩の状況や季節変化によって、含有するカドミウム量が大きく変動するといわれている[5)]。種の同定等も含めて、海水、植物プランクトン、動物プランクトン、ホタテガイのカドミウム濃度の測定は定期的に行う必要があると考えている。

プランクトンによるカドミウムの濃縮係数が$1\sim2\times10^{3}$程度なのに対し、ホタテガイの中腸腺の濃縮係数は10^{6}、腎臓に至っては10^{7}に達しており、極めて高い濃縮率を示している。腎臓と中腸腺を除いても全ての部位で10^{4}を超える濃縮係数を示しており、餌となるプランクトンからさらにカドミウム濃縮が進んでいることが分かる。

別に測定を行ったホタテガイの全軟体部のカ

ドミウム量（３２９μg／個体）との比では、全カドミウム量の内、おおよそ、中腸腺に５０％、腎臓に３０％、その他に１０％、卵巣と貝柱にそれぞれ５％、精巣、鰓、外套膜にそれぞれ１～２％存在している。その他の部位に比較的カドミウムが多いのは、胃や腸等の消化器官が含まれているためであろう。また、精巣と卵巣のカドミウム濃度には有意な差があり、卵巣が精巣の３倍近い濃度を示している。精巣と卵巣のカドミウム濃度は、ホタテガイの成熟度によって異なってくることが予想できる。生殖腺の発育状況による精巣と卵巣のカドミウム濃度の変化、これに関連する生体物質やその生理的意義等は今後の検討課題である。

腎臓や中腸腺の高濃度カドミウムは、メタロチオネイン等のカドミウム含有タンパク質の合成・代謝等との関連が極めて強いと考えられる。中腸腺についてはメタロチオネイン以外のカドミウム含有タンパク質の存在が報告されている[6),7)]。腎臓や中腸腺に含まれるカドミウム結合物質が同一のものであるのか、その特性や生理的意義、さらには化学形の解明を中心に今後の研究を進めていく予定である。

本研究結果を基に現在研究論文を作成中である。

参考文献

1)野矢洋一他,第３１回理工学における同位元素研究発表会要旨集,p131(1994)
2)三島昌夫,環境中の微量金属の測定,東京化学同人,p47(1985)
3)Uthe,J.F.et al.,Can.J.Fish.Aquat.Sci., 44,91(1987)
4)Evtushenko,Z.S.et al.,Mar.Biol.,104,247 (1990)
5)Abe,K.et al.,Mar.Chem.,23,145(1988)
6)Fowler,B.A.et al., Mar.Biol.,97,207 (1988)
7)中山憲司他,北海道立衛生研究所報,第４５集, 13(1995)

植物の葉に含まれるコバルト分布図の作成
Production of Distribution Picture of Cobalt Included in Leaf of Plants

増子捷二、笠原茂
北海道大学アイソトープ総合センター

1．はじめに

イメージングプレート（Imaging Plate、以下「ＩＰ」）を用いて放射線を測定する方法は、従来用いられてきたX線フィルムによるオートラジオグラフィと比較して、幾つかの特徴を持っている。要約すると、

ａ）高感度（従来の約１００倍）である。
ｂ）定量範囲が４桁と広い（従来の方法は約２桁）。
ｃ）放射線量に対する応答が直線的である。

ということになる。

我々は、ＩＰが特に放射線量の積算量だけでなく２次元的な解析に有用であることに加え、ソフトの進展によって３次元的な解析等が可能になったことから、β線とγ線の分離や、葉における特定元素の分布を調べるための測定法の開発を試みた。

2．方法

1）葉の元素濃度

北海道大学植物園に生育しているリョウブ、クマイザサ、ユキザサ、ヤマモミジの葉を採取し、試料とした。これらの試料は以下の方法で測定を行った。

放射化分析法

ａ葉の採取後は、蒸留水で洗浄し、真空凍結乾燥後、葉重量を測定した。
ｂポリエチレン袋に葉を封入した。
ｃ日本原子力研究所（ＪＲＲ－3）で、４０分間の中性子照射を行った。同時に標準試料を作り、同じ条件で中性子を照射を行った。
ｄ試料は６ヶ月間冷却後、ピュアゲルマ半導体検出装置により核種分析を行った。

2）リョウブにおけるコバルトの分布

北海道大学植物園に生育しているリョウブの葉を採取し、試料とした。これらの試料は以下の方法で測定を行った。

ａ葉の採取後は、蒸留水で洗浄し、冷蔵保存後、葉重量を測定した。
ｂポリエチレン袋に葉を封入した。
ｃ日本原子力研究所（ＪＲＲ－3）で、１０分間の中性子照射を行った。
ｄ照射後にポリエチレン袋から取り出し、カバーフィルム（粘着力のあるポリエチレン）に挟んだ。
ｅ５ヶ月経過してから、ＩＰに図１の通り、シールドＢＯＸ内で１２日間露光した（室温）。
ｆ露光後は、バイオ・イメージングアナライザー（富士フィルムＫＫ，ＢＡＳ－５０００）でＩＰを読み取り、ＭＣＩＤイメージングアナライザー（イメージングリサーチ社）によりコバルトの分布図を作成した。

3）結果と考察

葉の元素濃度で測定した放射能濃度から算出した各々の葉に含まれる元素濃度を、表１に示した。これを見ると、リョウブに含まれるＣｏの量がけた違いに多い事が分かる。この結果をもとに、リョウブに着目してβ線の画像分布の作成を試みた。

今回は、放射化したリョウブの葉のコバルトの分布図を作成する方法として、バイオ・イメージングアナライザー（ＢＡＳ－５０００）と画像解析ソフト（ＭＣＩＤ）を用いて行った。

放射化後、葉を長期間放置することで短半減期核種の放射能を減衰できることから、５ヶ月経過後、ＩＰに露光した。また、露光中に葉が変形する可能性があるので、ＩＰ２枚を同時に露光した。

葉から放出するβ線を吸収板（アルミ板、カバーフィルム、ポリエチレン板）に吸収させた画像と吸収板（カバーフィルム）に吸収させた画像の差からβ線の画像（コバルト－６０）を得ようとした。

放射化したリョウブの葉の画像を図２～４に示した。図２、３はバイオ・イメージングアナライザー（ＢＡＳ－５０００）で読み取ったもので、ＩＰの読み取り条件はGradation;65536、

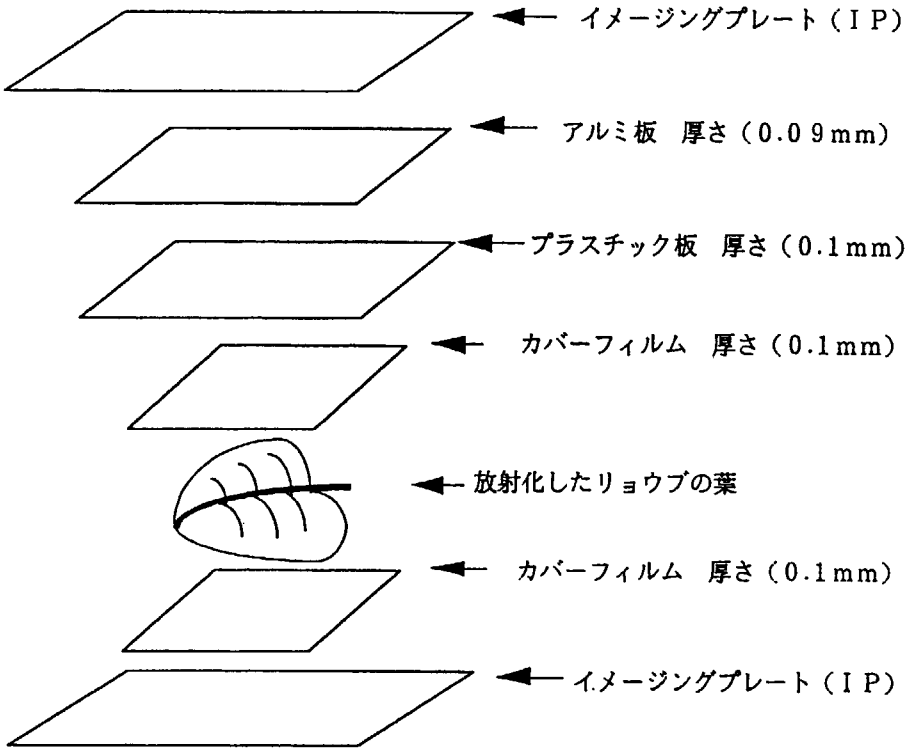

図１．露光詳細図

表１．葉に含まれる元素濃度

元素	濃度（μg/g乾）			
	リョウブ	クマイザサ	ユキザサ	ヤマモミジ
Ｓｃ	0.0058±0.00040	0.0022±0.00016	0.014±0.00039	0.0020±0.00021
Ｆｅ	―――	―――	5.98±1.86	―――
Ｃｏ	8.12±0.031	0.064±0.0033	0.285±0.0086	0.084±0.0046
Ｚｎ	66.5±2.32	24.3±1.05	30.1±1.84	34.4±1.56
Ｃｓ	3.43±0.052	0.388±0.018	1.13±0.039	0.752±0.029
Ｅｕ	0.0080±0.0014	0.0027±0.00052	0.011±0.0011	0.0048±0.0010

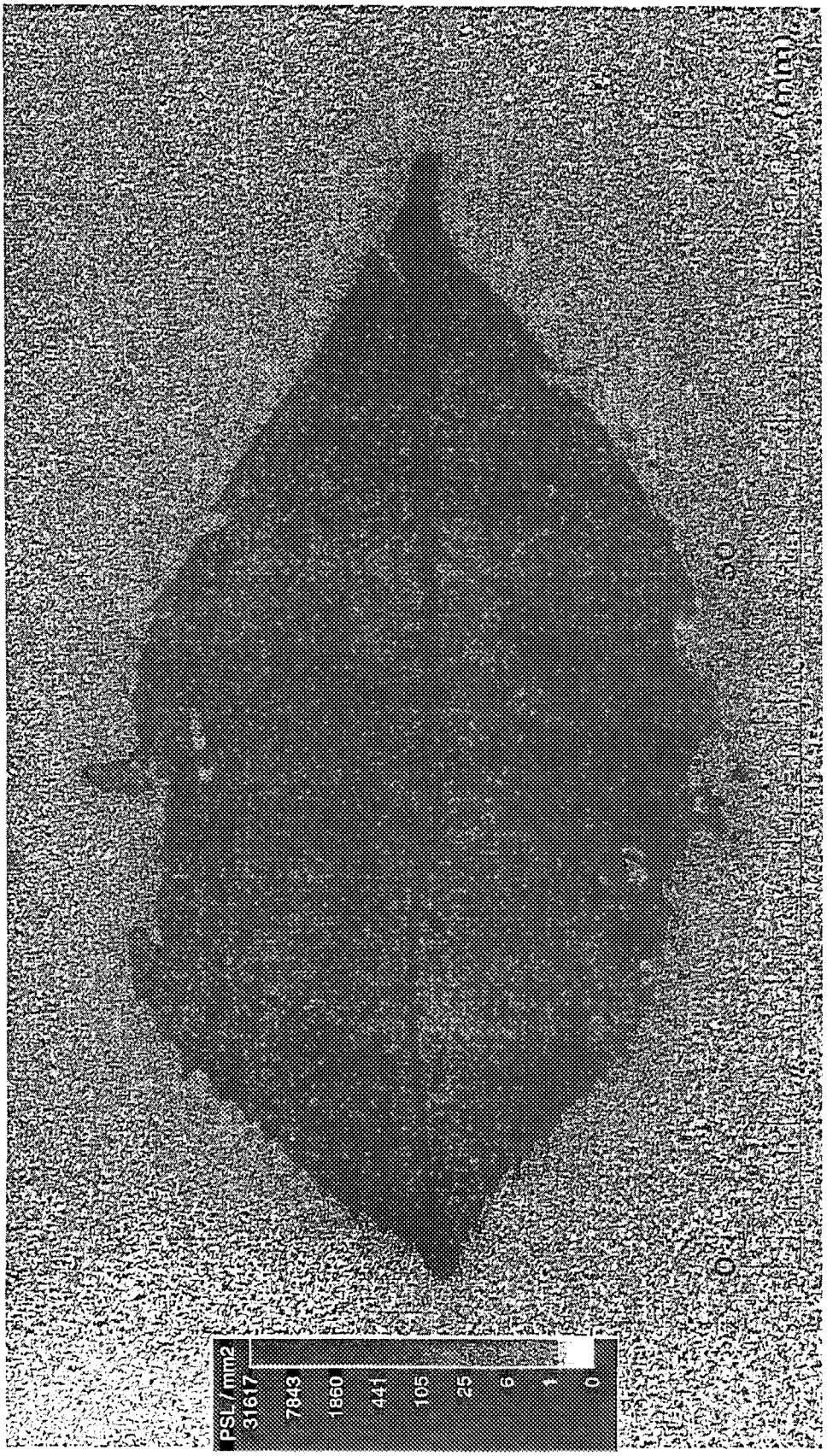

図2. IPによるリョウブの画像

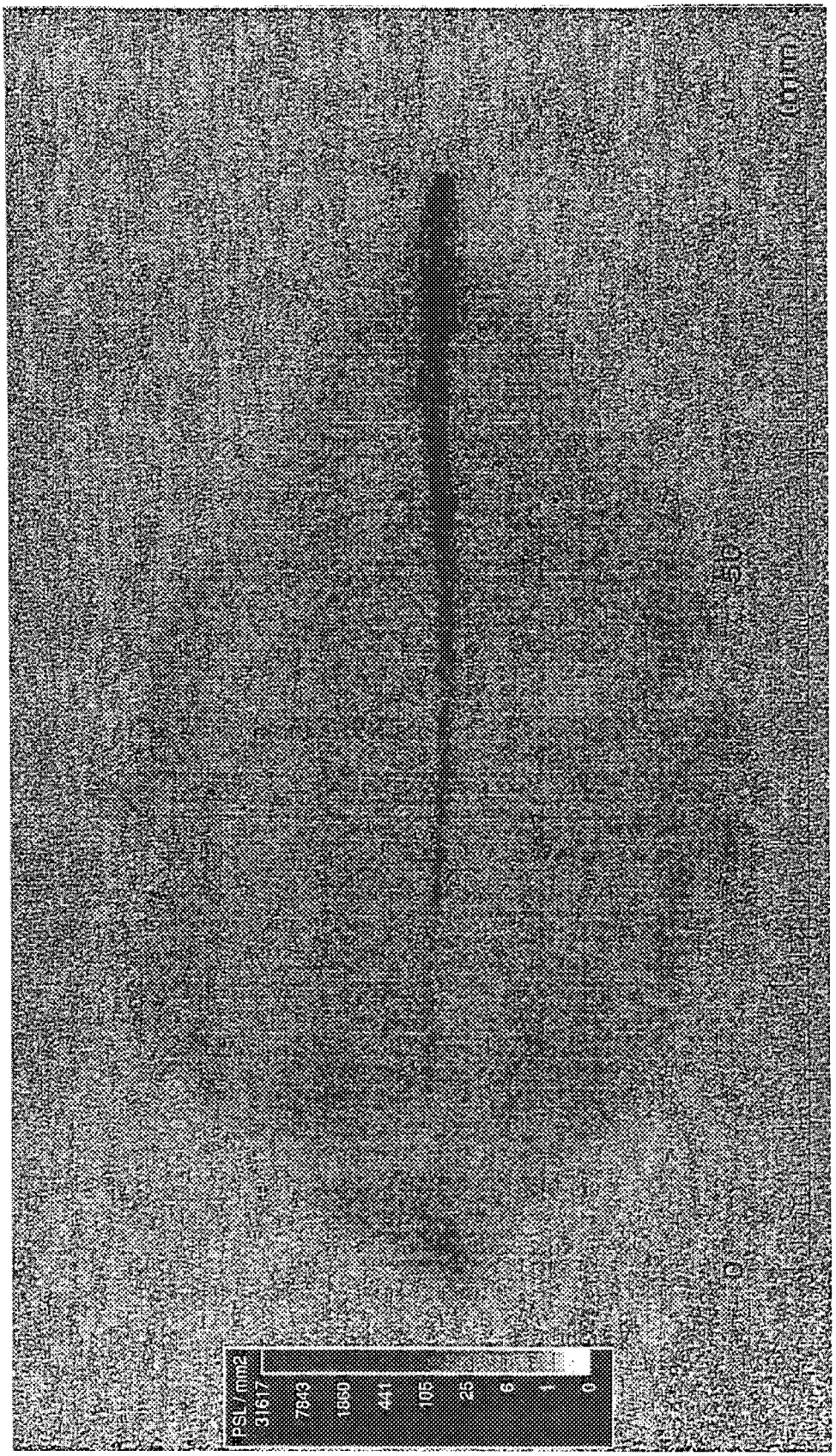

図3．ＩＰによるリョウブの画像

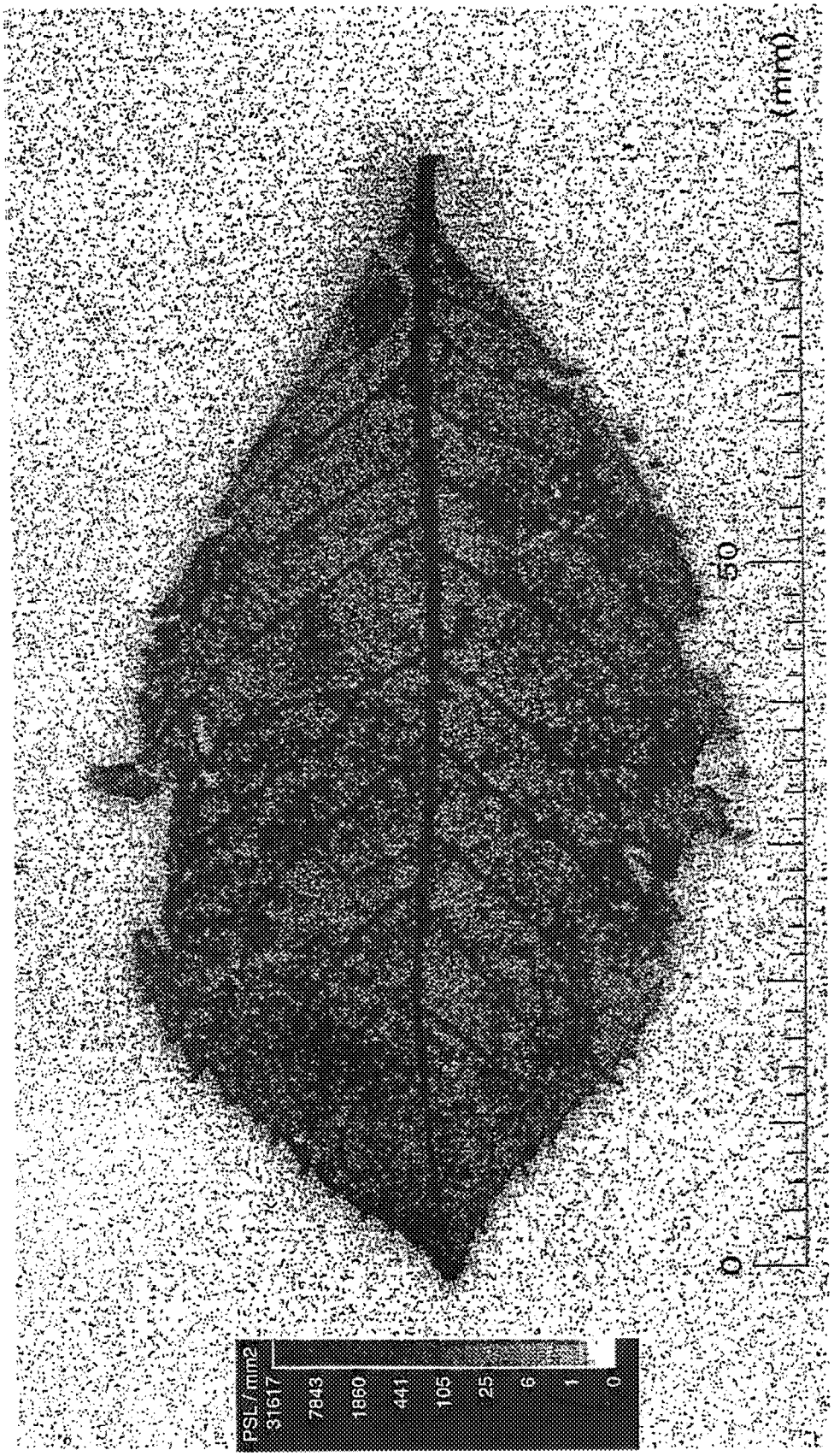

図４．コバルト－６０のβ線の画像

Resolution;25、DynamicRangeSelector;S4000(L5)である。図2は、葉から放出する弱いβ線をカットした残りのγ線とβ線の画像である。図3は、葉から放出する弱いβ線及びコバルトー60のβ線の大半をカットした残りのγ線とβ線（セシウムー134）の画像である。図4は、図2の画像から図3の画像を画像解析ソフト（MCID）を用いて、引いたコバルトー60のβ線の画像である。

この結果、中性子の照射時間や露光の際の吸収板の種類・厚さ等について更に検討する余地があるが、基本的にβ線の画像分布の作成が可能であると思われる。

試料を放射化する時は、Φ25mm×75mmの容器に封入する必要がある。放射化後にリョウブを容器から取り出す際にはクマイザサ、ユキザサに比べて葉が脆くなっていて、粉砕する傾向があることが分かった。葉を丸めないでも照射できる条件が必要である。

放射化した試料は、Coの他にCsが予想以上に多く、これをどう分離測定するかが精度を上げる鍵である。また、吸収板の材質についても検討の余地があると思われるので、継続した課題としたい。この成果をもとに研究論文を作成中である。

謝辞

この実験にあたり、貴重な試料を提供して頂いた、北海道大学農学部附属植物園の関係者に厚くお礼申し上げます。

4.参考文献

1）「微量元素」（山県　登　著）

2）「重金属適応性の作物種間差」田中　明、但野　利明、海老根　愛夫；日本土壌肥料学雑誌第49巻第4号P.314－320（1978）

研究テーマ：惑星物質の元素の移動・分配に関する研究
表題：マグマの希土類元素の組成変化

古富士火山末期から新富士火山にわたるマグマの希土類元素の組成変化

富樫茂子[1]・宮地直道[2]・安井真也[3]・角田明郷[3]・朝倉伸行[3]・遠藤邦彦[3]・鵜川元雄[4]
1地質調査所
2静岡県農業試験場海岸砂地分場
3日本大学文理学部
4防災科学技術研究所

富士山の火山活動を観測するため，防災科学技術研究所により，平成6年度に南麓(富士吉原火山活動観測施設，静岡県富士宮市)に，深度約200mの観測井が掘削された．その際に，富士火山における観測井の層序学的な位置付けを行うためにボーリング試料が得られた．一般に富士山のような成層火山では，岩相の良く似た溶岩が中心噴火口と多数の側噴火口から噴出しており，ボーリング試料は時間順序が明白であるため，マグマの生成・分化・噴出過程の詳細な変化を知る上で極めて貴重である．本論文では，これまでのと比較し，富士山の火山の活動史において，特に古富士火山末期から新富士火山初期にわたるマグマの組成変化を考察した．

分析試料として，識別可能なフローユニット毎に少なくとも1試料，厚いフローユニットでは上部および下部の2試料，あるいは上中下の3試料を採取した．溶岩では発泡の少ない塊状部分を選び，火砕流堆積物では長径が２ｃｍ以上の本質岩片を選んだ．

試料は超音波洗浄後に乾燥し，鉄鉢で粗粉砕後，メノウ乳鉢で微粉砕した．試料は主成分およびV，Cr，Ni，Cu，Zn，Rb，Sr，Y，Zr，Nb，Baについては蛍光X線分析法でSc，Co，Cs，REE，Hf，TaおよびThについては中性子放射化分析法で定量した．分析精度は主成分で2%以下，微量成分については，Cs，TbおよびThは10%以下，Taは30%以下，他の微量成分は5%以下である．分析確度を示すため地質調査所発行のJB-3の分析値を示した．JB-3の公表値(Imai et al.，1995)に比べ，いずれも分析精度程度で一致している．

吉原ボーリング試料では，ステージ1，2，3ー9，10の4種類の親マグマのグループが識別され，ステージ2はインコンパチブル元素に乏しい古富士火山系マグマに，その他はインコンパチブル元素に富む新富士火山系マグマに相当する．希土類元素パターンの違いを示すために，図にLa/SmとYbの関係を示した．この図ではLa/Smが高いほど希土類元素パターンが左あがり，Ybが高いほどパターンの位置が上にあることを意味する．比較のため新富士火山と古富士火山の組成範囲(Togashi et al., in prep)を示した．この図から明らかなように，ステージ2は明らかに古富士火山の領域に，その他は新富士火山の領域に分布する．これらのマグマグループにおけるインコンパチブル元素の濃度の差は，単一の初生マグマの分化と再供給では説明困難で，複数の組成の異なる初生マグマの供給が必要である．多様な初生マグマは，マントルの組成の異なる部分から，部分溶融の程度のほぼ等しい玄武岩マグマとして生成供給された．吉原ボーリング試料は噴出形態，岩石記載および主成分および微量元素組成のいずれの点からも，古富士火山末期から新富士火山初期の活動に対比できる．

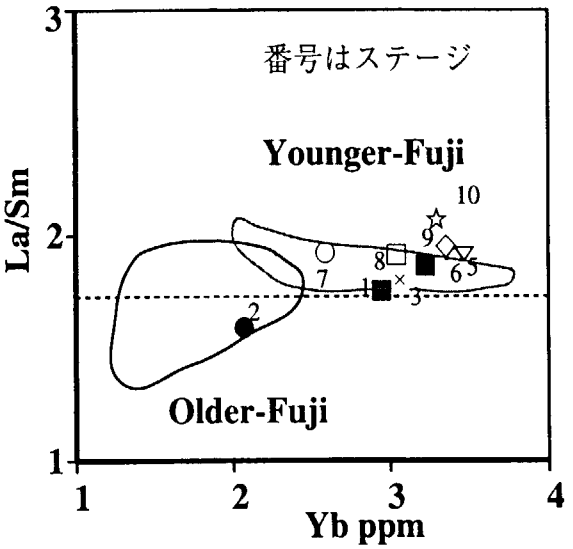

原子炉：JRR-3M　　装置：HR1,HR2　　分野：放射化学　（地球化学・宇宙化学）

研究テーマ：惑星物質における元素の移動・濃集機構の研究
表　　題：堆積岩中の微量元素の挙動

日本で採取された風送塵のSr、Ce、Nd同位体比

○上岡　晃・五十嵐康人[1]・広瀬勝己[1]
地質調査所
[1]*気象研究所*

大陸地殻に由来する風送塵は、海洋への物質供給源の一つとしても重要である。筆者らは、西太平洋で採取されたグアノのCe、Nd同位体比を測定し、CHURに対するイプシロン値としてCeが+1.0～+1.3、Ndが-0.8～-6.4という結果を得た。[1)]一方、太平洋のマンガンノジュールは、Ce、Ndともに負のイプシロン値を持つことが報告されている。5000m前後の深海から採取されたマンガンノジュールに対し、グアノは表層海水を反映しており、その同位体比は、大陸地殻からの風送塵の影響を示している可能性がある。本研究では、アジア大陸に由来する風送塵の同位体的特徴を探ることを目的として、日本で採取された風送塵試料の分析を行った。

用いた試料は、気象研究所で調製された降下物標準試料（日本の14ヶ所で1963年～1979年に採取されたものの混合物）、およびつくば市の気象研究所内で１９９３年～１９９４年にわたって採取されたものの一部である。試料は、面積4m^2(気象研究所内の場合)のプラスチック製大型水盤で１カ月にわたって捕集、蒸発濃縮して採取された。４月前後の試料の乾燥重量は20～30ｇ程度で、他の時期が5～10ｇ前後であるのと比べて量が多く、この時期に見られる黄砂現象と対応している。

中性子放射化分析法で分析した試料の希土類元素存在度パターンの一部を図１に示す。いずれもやや軽希土上がりで、かつEuの弱い負アノーマリーを示し、大陸地殻を代表する物質と考えられる頁岩と類似していることがわかった。

アジア大陸由来の風送塵の起源のひとつと考えられる中国のレスの同位体比は、Srが0.718、CeとNdのイプシロン値がそれぞれ+1.8、-11.2という値が報告されている。本研究で得られた試料の同位体比は、Srが0.707～0.712、Ndのイプシロン値が-2.8～-8.4と地殻物質的な特徴は示すものの、中国のレスとは異なる値であり、ローカルな火山灰等の寄与をある程度受けている可能性があることがわかった。例えば、富士山の玄武岩である岩石標準試料ＪＢ－３と中国のレスを端成分としてSr、Nd同位体比より両者の混合率を求めると、試料中のレス成分の重量フラクションは40％～70％程度となる。また、４月の方が５月よりもSrとCe同位体比は高く、かつNd同位体比は低くなっており、黄砂など大陸起源物質の寄与がより大きいと考えられる。降下物標準試料の同位体比は、他の試料よりも明らかにSrが低く、Ndが高い値を示し、４月前後の試料に比べて大陸起源物質の寄与が薄まっていることがわかる。

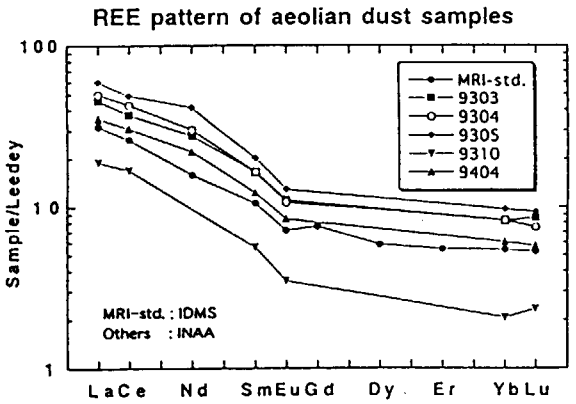

図１　風送塵の希土類元素存在度パターン

参考文献

1)上岡、地球惑星科学関連学会1997年合同大会予稿集、（1997）、pp.454

原子炉：ＪＲＲ－３　　装置：ＨＲ－１　　分野：放射化分析（地球化学・宇宙化学）

研究テーマ：伊豆小笠原弧背弧域における火成活動および熱水活動に関する研究
表題：伊豆小笠原弧背弧海山の斑岩銅型鉱化作用　－関連火成岩の活動時期－

伊豆小笠原弧背弧海山の斑岩銅型鉱化作用　－関連火成岩の活動時期－

石塚　治，湯浅真人，宇都浩三，石井輝秋[1]，A.G. Hochstaedter[2]

地質調査所 つくば市東 1-1-3

[1] *東京大学海洋研究所*

[2] *University of California, Santa Cruz*

伊豆小笠原弧で初めて，背弧域の海山（万治海山，Fig. 1）に斑岩銅鉱床型熱水変質が発見された（石塚ほか，1997資源地質講演要旨）．本講演では，その後の調査において採取された熱水変質岩に伴う深成岩，半深成岩，溶岩等の特徴，化学組成および$^{40}Ar/^{39}Ar$年代を報告し，斑岩銅型鉱化作用の背弧海山の火成活動史の中での位置づけを検討する．

伊豆小笠原弧の第四紀火山フロントの西側には，東から現在活動的な背弧リフト盆地，非活動的な背弧海丘帯が存在し，さらにそこから四国海盆に向かって雁行した海山列が西南西方向に伸びている．これまでの年代測定結果より背弧海山列では，四国海盆拡大終了間際から背弧リフティングの開始までの期間（17.5-2.9Ma）に島弧的火山活動がおきていたことが明らかになった．このうち万治海山において，斑岩銅鉱床における変質帯に相当する変質岩や，石英斑岩が採取され，斑岩銅鉱床を形成するような熱水活動が存在していたと考えられる．この海山において97年に再度調査を行った結果，深成岩（ガブロやトーナライト），石英斑岩，デイサイト溶岩，熱水性マンガン酸化物等が採取された．

今回採取された深成岩類の成因を明らかにするために，深成岩，石英斑岩，溶岩のそれぞれについて40Ar/39Ar年代測定および化学分析を実施した．その結果，ガブロについて6.95 ± 0.24 Ma（角閃石），6.35 ± 0.06 Ma（黒雲母），石英斑岩について7.0 ± 0.4 Ma，デイサイト溶岩について6.86 ± 0.09 Ma，7.85 ± 0.09 Ma，玄武岩質安山岩溶岩について6.53 ± 0.06 Maの年代が得られ（Fig. 2），深成岩の年代は石英斑岩や溶岩の活動時期とほぼ一致することが明らかになった。またガブロ及びトーナライトは鉱物組み合わせや化学組成上の類似性から，有色鉱物の量比が異なるものの一連の火成活動により生成されたと考えられる。以上の結果から，深成岩の年代は，石英斑岩や溶岩の活動時期とほぼ一致し，一連の火成活動の産物である可能性が高い．このことから，カルクアルカリ系列の島弧火山活動がおきていた伊豆小笠原弧の背弧海山列の中で，万治海山では特に酸性火山活動が卓越し，深成岩の活動および斑岩銅鉱床の生成を伴った。深成岩及び斑岩銅鉱床は，海山の，海面上での山体開析により露出したものと考えられる。

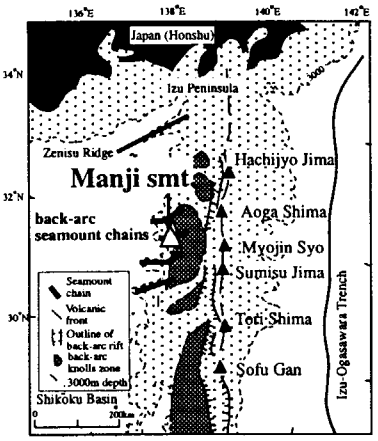

Fig.1 Location of the Manji Seamount

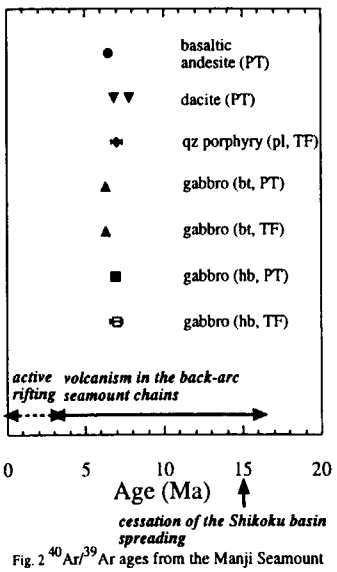

Fig. 2 $^{40}Ar/^{39}Ar$ ages from the Manji Seamount
(TF; total fusion age, PT; plateau age)

原子炉：JRR-3 装置：HR1　分野：放射化分析、$^{40}Ar/^{39}Ar$年代測定（地球化学）

研究テーマ：地球内部物質の放射化分析
表題：海洋島玄武岩類の微量成分元素の挙動と成因

インド洋モーリシャス島火山岩類の地球化学およびK-Ar年代

宇都浩三，徐　勝，兼岡一郎[1]
地質調査所，つくば市東1-1-3
[1]東京大学地震研究所，東京都文京区弥生1-1-1

モーリシャス島は西インド洋に位置する火山島で，インド洋の重要なホットスポットであるレユニオンホット・スポットにより形成されたと考えられている（図2）．その火山活動史を解明しその地球化学的特徴を明らかにするために放射化分析，蛍光X線分析及びK-Ar年代測定を行った．

今回及び即存の年代測定結果 (McDougall and Chamalaun,1969) から，モーリシャスでは，5-7M，2-3Ma，＜0.8Maの3回の火山活動時期が存在したことが判明した．特に，今回の測定で，10万年より新しい玄武岩の噴出が起こったことが分かった．約65Maのデカン高原玄武岩から現在のレユニオン火山までのホット・スポットトラックによれば，モーリシャスの下にホット・スポットが存在したのは7-8Maである．従って，最初期の玄武岩活動は彼らのホット・スポットモデルに良く一致する．2-3Ma＜0.8Maの後侵食期の火山活動は，ハワイホット・スポットに比べ著しく遅い時期に起こっているが，これはプレート運動速度の違いで説明できる可能性がある．即ち，ハワイの場合活動的ホット・スポットから約200km移動したときに後侵食期活動が起こるが，モーリシャスとレユニオンの距離約170kmと一致している．

モリーシャスの火山岩類は，すべてSiO2 45-47.5%の玄武岩であるが，若い時代のものほどK2O量が乏しい傾向が認められ，5.4-6.5Maではインコンパチブル元素に富むアルカリ玄武岩（K2O = 1-1.5%），2-3Maでは漸移的玄武岩（K2O = 1 %），＜0.8Maではインコンパチブル元素に乏しいアルカリ玄武岩（K2O ＜0.5%）が噴出した．これは，主山体形成期にソレアイトが噴出して，後侵食期にアルカリ玄武岩が噴出するというホット・スポット火山の一般則に明らかに一致せず，ハワイに代表される単純なホット・スポットモデルがモーリシャスの火山活動史には適用できないことを示している．モーリシャスの玄武岩類の微量成分元素組成の時間変化を図2に示す．6-7Ma，2-3Maの玄武岩に比べ，0.8Ma>の玄武岩のインコンパチブル元素の濃度が系統的に低いことが分かる．この微量元素組成パターンから，起源マントルはレユニオンホットスポットではなく，それにインド洋の大洋底玄武岩の起源マントルが混合されたものであることが示される．6-7百万年前にレユニオンホットスポットで上昇したプリュームが海洋プレート下面で横に広がり，周囲の大洋底玄武岩起源マントルに熱を供給し，両者の混合物が最近の80万年間に噴出したと推定される．

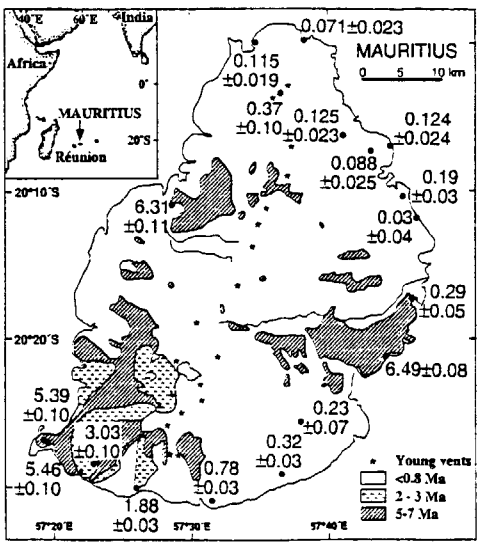

図1　インド洋モーリシャス島火山岩のK-Ar年代

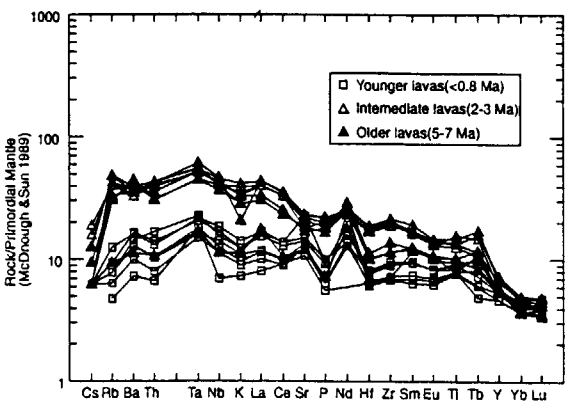

図2　モーリシャス島火山岩微量成分元素パターン

原子炉：JRR-3　装置:：HR2　分野：放射化分析（地球化学）

中性子放射化分析による宇宙・火山起源物質の研究

Geochemical studies on origin of cosmic and volcanic matters
by instrumental neutron activation analysis

学習院大学理学部（現・立正大学地球環境科学部）　福岡孝昭
京都大学理学部　田澤雄二
Takaaki FUKUOKA, Fac. of Sci., Gakushuin Univ. (Present: Fac. Geo-Envi. Sci., Rissho Univ.)
Yuji TAZAWA, Fac. of Sci., Kyoto Univ.

1．はじめに

南極大陸はそのほとんどが氷床で覆われているばかりでなく，他の大陸から離れているため，砂漠の砂などの陸起源の固体粒子による汚染が無いと考えられる．最近はこの氷床上で多数の隕石（いわゆる南極隕石）が発見されるばかりでなく，氷床氷を大量に融解することによる大量の宇宙塵の収集もはじまっている．さらに南極氷床には世界各地の過去の巨大噴火の記録も保存されている可能性が高い．これら南極氷床に過去３０万年にわたって保存されたと考えられる宇宙・火山起源物質の研究から，宇宙塵・隕石の落下頻度の変動が求められるほか，過去の巨大噴火の性質と規模を知ることができる．しかし，氷の年代を正確に入れることが困難なため，落下頻度の算出は一般に困難である．隕石・宇宙塵・火山灰は氷と同一行動をとっていると考えられるので，本研究では氷床中に存在する火山灰（採集量が少ないため，直接噴火年代を測定することは困難）の給源火山を求め，給源火山周辺の試料から噴火年代を求め，氷の年代を算出する方法を提案している．

氷床中から採集される火山灰，宇宙塵試料は微量あるいは微小であるため，これらの微小量の試料の放射化分析法（INAA）の確立（標準試料の開発，気送管照射での操作の迅速化，試料保持物質の純度のチェック）も行う必要がある．

ここでは，これら一連の研究に関連して過去３年間に行われた研究のうち，微小の宇宙塵試料中親鉄元素（Au, Ir, Os等）分析用に作製された標準試料の絶対濃度の決定，均一性のチェックを行った結果，深海底から採集された宇宙塵（球粒）の分析結果，そして南極みずほ氷床コア500m深に存在する目視できるテフラ（火山灰）の給源火山の推定の結果について報告する．

2．試料と分析法

2－1．深海底球粒宇宙塵試料のINAA

球粒試料，JB-1ガラス破片（親石元素分析用標準試料），合金のチップ（親鉄元素分析用標準試料）をそれぞれ約３×３mmの高純度ポリエチレン袋中に融封し，JRR-3M炉のPN-3（～2×10^{13} n/cm^{2}s）で３分間熱中性子照射し，ポリエチレン袋ごとγ線測定を行い，Al, Ti, Mg, Ca, V, Na, Mnの分析を行った．その後同一試料についてポリエチレン袋を除去し，１つ１つ高純度合成石英管に融封し，JRR-3, HR-1または-2の照射孔（1×10^{14} n/cm^{2}s）で10-100時間熱中性子照射を行った．適当に冷却した後，石英管から取り出し２～３回繰り返しγ線測定を行い，Na, Cr, Fe, Sc, REE, Co, Ir, Os, Au等の分析を行った．合金試料は田中貴金属工業（株）により作製された．この合金について，その組成の決定と均一性についてチェックした．

2－2．南極みずほ氷床コア500m深テフラのINAA

JRR-4 Pn, Sパイプ；JRR-3M, HR-1, 2, PN-2, 3　　宇宙地球科学試料の放射化分析

南極みずほ氷床コアの４分の１径について，氷を約10cm間隔に切断し，融解後ニュクレポアフィルター（孔径0.2μm）で濾過した．このフィルター上のテフラ粒子について，実体顕微鏡下でガラス質部分を手選純化し，80μgを高純度合成石英管中に融封，JRR-3M炉HR-2照射孔（1×10^{14}n/cm²s）で８時間熱中性子照射し，適当に冷却後２～３回石英管ごとγ線測定を行い，希土類元素を中心とした微量元素組成を求めた．

３．結果と考察

３－１．合金の組成と均一性

微小宇宙物質中の親鉄元素分析用標準試料としてこれまで適当なものがなく，隕鉄のチップなどが利用されてきたが，不均質なため標準試料として適当か大きな問題であった．本研究で作製された合金の組成は，Table 1に示した通りである．Coは原料中の不純物から供給されたと考えられる．この合金の組成の均一性は10～100μgチップについて，3～4%の標準偏差値内におさまった．これはINAA全体の分析確度の3～5%と同程度であり，INAAの親鉄元素分析用標準試料として均一性の点では大きく進歩した．しかしながらIr, Auの濃度が隕鉄にくらべ高すぎ放射能強度が大きすぎることがわかった．今後100分の1程度の濃度にしたものを再度作製する必要がある．

３－２．深海底堆積物中球粒の化学組成

深海底堆積物中の球粒６個（9～150μg）の分析結果をTable 2に示した．どの試料にもIrあるいはAu，または両者が含まれていることから宇宙起源であることが明かである．この球粒の親鉄元素（Coを除く）の分析の標準試料として合金のチップを用いたが，Ir, Auの放射能強度が強すぎるため，γ線測定では球粒試料と合金チップで検出器から異なる位置で測定し，位置の違いの補正を行った．

３－３．みずほ氷床コア500m深テフラの給源火山

INAAの結果のうち希土類元素（REE）を中心とした微量元素について，C1コンドライト隕石の値で規格化したものをFig. 1にプロットした．このパタン（全体がほぼ平らで，La側が少し下がるREEパタン）は島弧火山マグマに由来する火山噴出物（tholeiite）に典型的なパタンである．

同一テフラについてEPMA分析により主成分元素組成を求めた結果からもこのテフラのマグマはtholeiite質の島弧マグマに由来していることが明かで，南極周辺の島弧火山であるサウスサンドウィッチ諸島の火山の組成と類似していることが明かになった．

さらにこのテフラ粒子のSEM像を用いて粒度分析をした結果，平径粒径は80μmであった．この粒径のテフラが南極地域の７月に15kmの高さまで噴き上げられた時，水平距離で3,800km飛ばされることが推定された．

南極みずほ基地から3,400kmの距離に火山列島であるサウスサンドウィッチ諸島がある（Fig. 2）．この列島の火山群のマグマの性質はtholeiite質の島弧火山マグマである．したがってテフラのサイズ分布，主成分化学組成，微量元素組成の３点から，みずほ氷床コア500m深テフラの給源火山はサウスサンドウィッチ諸島の火山のどれかであると結論される．しかし残念ながら，サウスサンドウィッチ諸島火山のテフラの研究が不十分なため，テフラを特定できなかったので年代を求めることもできなかった．これは本研究手法の問題ではなく今後の研究で解決されるはずである．

４．今後の研究方針

４－１．分析技術の向上

本研究で報告した，宇宙塵試料は球粒試料であった．これは壊れにくく，小粒である以外は比較的取り扱いは容易である．ところが球粒は宇宙塵が地球

大気圏に突入したときに周囲が融解し球になったものと考えられ，化学組成は熱変成の影響を受けている．近年は南極氷中や地球上空で直接採集される非溶融の宇宙塵が注目されている．しかし，この非溶融の宇宙塵は壊れやすく，INAAでの取り扱いはより慎重に行う必要がある．このため，新たな高純度保持体の入手をはじめとして，新たな分析技術の開発が必要である．

今回報告した微小試料中親鉄元素分析用の標準試料として開発された合金についても，Ir, Auの濃度を薄めたものを再度作製し，均一性も検討する必要がある．

南極氷床の氷に年代を入れるのに重要であるテフラ（火山灰）の給源火山の推定についても，南極周辺ばかりでなく，世界の巨大噴火によりもたらされたものはより微小量であると考えられるので，1粒での分析，より少量試料での分析法を開発する必要がある．また氷床中のテフラの分析値がいくら正確に分析できても，候補である給源火山のテフラの化学組成がわからなければ対比できない．候補テフラのINAAを行いテフラの化学組成のカタログ化を行う必要もある．

以上の点から本研究は今後しばらく継続する必要がある．

5．成果の公表

学会発表

1．Y. Tazawa, T. Fukuoka, E. Yamanouchi, Y. Miyano, E. Endo, M. Kohno, and Y. Fujii, "Possible cosmic spherules in the Mizuho ice core, Antarctica.," Twentieth Symp. Antarctic Meteorites (1995年6月)

2．福岡孝昭，田澤雄二 "微小宇宙物質の化学分析（2）" 日本惑星科学会1995年秋季講演会（1995年11月）

3．福岡孝昭，田澤雄二 "微小宇宙・地球化学試料の非破壊中性子放射化分析" 地球惑星科学関連学会1996年合同大会（1996年3月）

4．T. Fukuoka and Y. Tazawa, "Instrumental neutron activation analysis for μg-size of cosmic spherules" Twentyfirst Symp. Antarctic Meteorites. (1996年6月)

5．福岡孝昭，林信幸，河野美香，藤井理行 "みずほ氷床コア500m深火山灰の化学組成" 第19回極域気水圏シンポジウム（1996年7月）

6．福岡孝昭，田澤雄二 "深海底堆積物中の宇宙起源球粒" 日本惑星科学会1996年秋季講演会（1996年10月）

7．福岡孝昭，林信幸，宮野義則，遠藤邦彦，河野美香，藤井理行 "南極みずほ氷床コア500m深テフラの給源火山" 日本火山学会1996年度秋季大会（1996年11月）

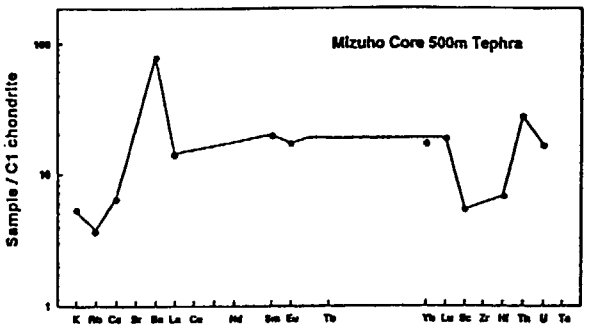

Fig. 1. The C1 chondrites-normalized trace elements compositions

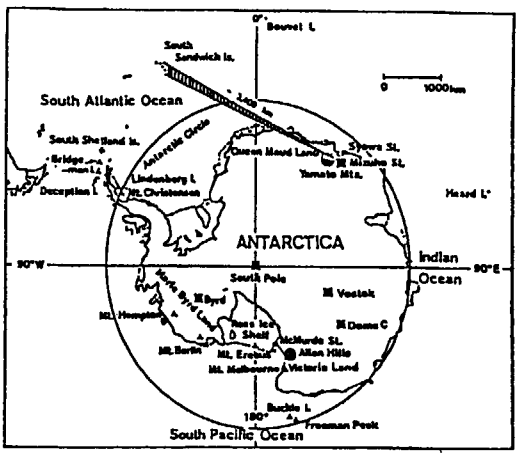

Fig. 2. Possible source volcano for tephra at 500m depth in the Mizuho ice core, Antarctica

8．福岡孝昭，田澤雄二，矢田達，矢野創 "南極産非溶融マイクロメテオライトの宇宙起源の化学的証拠" 日本惑星科学会1997年秋期講演会（1997年9月）

9．中村智樹，今栄直也，橋本麻衣，中井泉，野口孝明，矢野創，寺田健太郎，村上登志男，福岡孝昭，野上謙一，大橋英雄 "南極ドームふじ基地造水槽沈殿物の宇宙塵の一次分析とキュレーション" 地球惑星科学関連学会1998年合同大会（1998年5月）

10. T. Nakamura, N. Imae, I. Nakai, T. Noguchi, H. Yano, K. Terada, T. Murakami, T. Fukuoka, K. Nogami, H. Ohashi, W. Nozaki, M. Hashimoto, N. Kondo, H. Matsuzaki, O. Ichikawa and R. Ohmori "Antarctic micrometeorites collected at the dome Fuji station: initial examination and curation." Twentythird Symp. Antarctic Meteorites (1998年6月)

Table 1. Preliminary results of INAA for the alloy

Element	Row materials			Alloy	
	Purity (%)	Weight (g)	Content (%)	Content (%)	Error* (%)
Ni	99.99	3.9977	82.821	82.6	1
Os	99.99	0.1908	3.953	5.20	1
Ir	99.95	0.0105	0.218	0.192	1
Pt	99.992	0.214	4.433	4.26	5-15
Au	99.992	0.0368	0.762	0.741	1
Al	99.999	0.2091	4.332	4.11	0.5-1
Cu	99.990	0.168	3.480	3.86	1-3
Co	–	–	–	23.8 ppm	10

* Errors for INAA are due to counting statistics.

Table 2. Preliminary results of chemical abundances for spherules in deep-sea sediments by INAA

		Spherules in deep-sea sediments						Canyon	JB-1	Alloy	Error*
		A	B	C	D	E	F	Diablo	glass		(%)
Wt	μg	90.7	152.1	18.9	8.9	12.1	17.1	158.6	31.5	39.8	
Al	%	0.705	0.25	0.034	0.46	0.29	0.64	–	=8.07		1-12
Fe[1]	%	9.84	66.0	67.6		67.0	25.0	90.3	=6.30	–	1-1.5
Mg	%	22.9	–	–	20.1	–	23.5	–	=4.67	–	3-13
Mn	%	0.326	–	0.15	0.10	–	0.18		=0.116		2-10
Cr	%	0.180	0.122	0.202	0.202	0.0052	0.197	–	=0.0414	–	1-9
V	ppm	77	55	96	89	15	96	–	=207	–	3-50
Sc	ppm	6.61	1.98	–	4.91	1.77	6.15	–	=28.9	–	1-5
Co	ppm	27.5	1810	1820	484	2360	257	3990	=39.1	23.8	2-13
Ni	%	0.05	5.16	4.50	1.27	1.59	0.38	11.2	–	=82.6	3-40
Os	ppm	0.30	1.1	–	1.9	–	–	4.7	–	=52,000	10-50
Ir	ppm	0.017	3.97	2.34	0.51	0.41	0.032	3.62	–	=1,920	1-28
Au	ppm	0.010	–	–	0.42	–	–	2.43	–	=7,410	2-20

* Errors for INAA are due to counting statistics.
1) Total iron as Fe.

研究テーマ：農業環境における原子炉利用新技術の開発と拡大に関する研究
表　　題：中性子照射による土壌重金属元素の直接標識化トレーサ利用法の開発

土壌および農業有機資材中元素の直接標識化

櫻井泰弘、結田康一、高橋義明、牧野知之、上村順子
農業環境技術研究所

土壌や土壌に投入された農業資材（汚泥コンポスト、堆肥など）中の無機元素は土壌溶液に溶解後、植物体へ吸収されたり、地下水系へ溶出する。各種の無機元素は生物にとって養分になるものや毒性をもつものなど、元素種と濃度によってそれらの機能は多岐にわたっている。生産性の高い農耕地の維持や人体に安全な作物の生産技術の開発には土壌および農業資材中の無機元素の動態を解明する必要がある。これらの試料中の無機元素は鉱物態、有機物キレート態、水溶態など種々の化学形態で存在し、各元素の動態を解明するためにはこの存在形態を保持したままで、放射化ラベルする手法が有効と考えられる。そこで、本研究では土壌および農業資材への中性子照射による各元素の存在状態の変質を水溶態元素量を測定することで予測し、中性子照射による両試料中の無機元素の標識化手法の有効性を検討した。更に、直接標識化法により農業資材から土壌中への無機元素の溶出量を測定した。

1）中性子照射による土壌の変質の検討（無機元素の水溶出量への影響）

有機物を連用した淡色黒ボク土３種類（対照区土、汚泥コンポスト施用区土：1kg/m^2、堆肥施用区土：2kg/m^2　1977年～1997年）、を供試した。各土壌は100～700mgを原研研究炉(JRR-3)で1～1200分間放射化した。放射化土壌は蒸留水を添加、18時間振とう後、0.2μmのメンブランフィルターでろ過して溶出液を得た。溶出液はろ紙に吸収させ乾燥後Ge-Li半導体検出器でγ線を計測し、各元素の蒸留水による無機元素(Sc, Fe, Co, Eu, Zn)の溶出率を推算した。

2）農業資材の標識化

農業資材として堆肥を供試し、各試料を放射化して水溶出率を測定した。また、非放射化黒ボク土壌（対照区土壌）に放射化した農業資材を土壌重量に対して2, 5, 10%になるように添加した土壌へ蒸留水を加えて12時間振とう後の溶出液中の無機元素濃度をγ線スペクトルから定量した。

土壌中の無機元素の水溶出率を土壌への中性子照射時間を変化させて測定した結果、各元素の水溶出率は中性子照射時間の影響を受け、長時間の中性子照射は土壌中の無機元素の存在形態に影響を及ぼすことが示されたが10分程度の短時間の照射であれば変質は起こらないことが明らかにされた。

土壌に添加した中性子を照射した農業資材（下水汚泥コンポスト）からの無機元素の溶出率は土壌中の資材の濃度が低下するに従って、溶出率も低下し、資材中の水溶態の無機元素は土壌に57～97%が固定されることが明らかにされ(図1)、本法の農業資材への応用の可能性が示された。

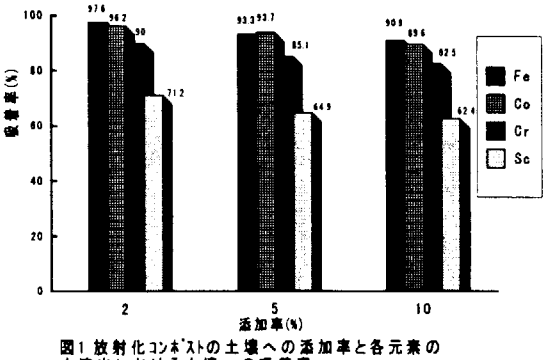

図1 放射化コンポストの土壌への添加率と各元素の水溶出における土壌への吸着率

原子炉：JRR-3　　装置：気送管　　分野：放射化分析（農・水産物）

研究テーマ：新アクチバブルトレーサーをマーカーとした家畜消化管内容物移動の解析手法の開発
表　　題：サマリウム，ランタン等をマーカーとした家畜消化管内容物移動の解析

サマリウム，ランタン等をマーカーとした家畜消化管内容物移動の解析

松本光人，宮本進，山岸規昭
農林水産省畜産試験場

1．目的

家畜の飼養管理の集約化・技術の高度化にともなって、多くの解決すべき問題が研究ニーズとして提起されているが、特に乳牛の糖質代謝が泌乳初期の生産性を高める意味で注目されている。さらに、分娩のストレスにより、泌乳初期では第一胃をはじめとする消化管の機能の回復が十分ではなく、採食性の低下などが生じ、生産性を圧迫している。そのため、摂取された飼料の消化管内での移動を定量的に把握すること、及びその基礎となる標識物質（マーカー）の探索が重要な課題になってくる。本課題では、消化管内の物質移動を知るためのマーカーとして、種々の新しいアクチバブルトレーサーの利用を図り、家畜の第一胃発酵、糖質および微量元素の代謝機構を解明する。

平成９年度は、標識物質（マーカー）としてサマリウム（Sm）、ランタン（La）を用い、山羊（去勢雄，体重45Kg）における飼料の消化管内移動について検討した。

2．試験研究の概要

日本ザーネン種山羊４頭にＳｍで標識した牧乾草、Ｌａで標識した濃厚飼料（各400g/日/頭）を給与し、ソマトスタチン（成長ホルモン放出抑制因子）を連続注入し消化管運動に及ぼす影響をみる試験を行った（ソマトスタチン注入区：ｓｓ、対照区：コントロール）。試験期間中に得られた糞試料を原研東海研究所の原子炉（ＪＲＲ－３Ｍ）を用いて、熱中性子照射を行った。照射時間は３分間とし、ゲルマニウム半導体検出器およびマルチチャンネル波高分析機によりＳｍ、Ｌａの測定を行った。Ｓｍ、Ｌａ標識飼料を給与した山羊から得られた糞中のＳｍ、Ｌａ濃度の放射化分析による結果（一部）を第１図、第２図に示した。ソマトスタチン連続注入による両元素のピーク到達時間、消化管通過速度等の違いについては、試料の大部分が未分析であるためデータが揃った段階で考察する。

新アクチバブルトレーサーのマーカー利用による飼料の消化管通過速度の測定については、引き続き反芻家畜（牛、羊等）の飼料にこれらのマーカー（Sm, Yb, La等）で標識し家畜に給与し研究を進めると共に、ソマトスタチン（成長ホルモン放出抑制因子）が家畜の消化管運動に及ぼす影響について検討する。

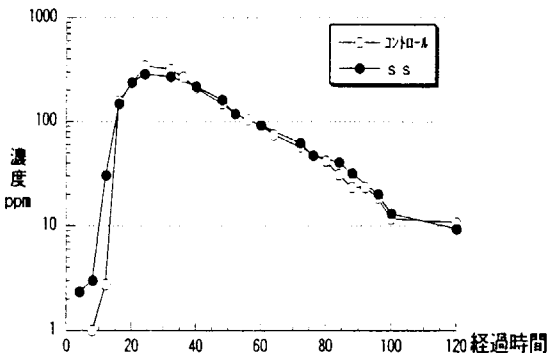

第１図　牧乾草に標識したＳｍの山羊糞中の濃度（山羊No.１）

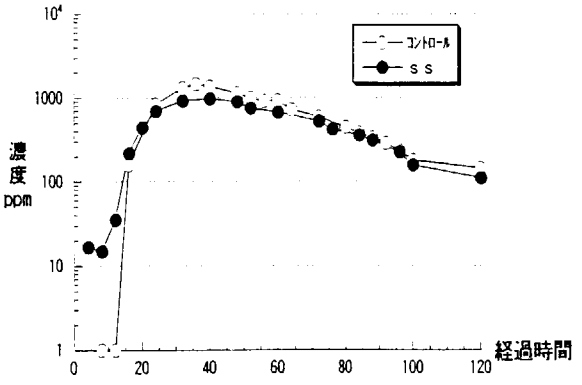

第２図　濃厚飼料に標識したＬａの山羊糞中の濃度（山羊No.１）

原子炉：ＪＲＲ－３Ｍ　　装置：気送管　　分野：放射化分析（農・水産物）

研究テーマ：高温工学に関する先端的基礎研究
表題：高温用低原子番号半導体の中性子転換ドーピングの予備試験

NTDにより生成した単結晶炭化ケイ素中の燐の測定

馬場信一、伊藤久義[1]、荒井長利、梨山勇[1]
日本原子力研究所・核熱利用研究部高温照射研究室
[1]日本原子力研究所・材料開発部技術開発課

本研究では中性子転換ドーピング(Neutron Transmutation Doping, NTD)を利用した単結晶炭化ケイ素(SiC)の半導体製造への適用性に関する検討課題のうち、NTDにより生成した燐の同定／定量を目的に平成９年度に実施した研究炉利用の成果の一部として報告するものである。

供試料としたSiCはCVD法により製造したEpitaxial-SiC、0.04393gである。同試料はJRR-3M/HR-2にて2.5×10^{19} $cm^{-2}s^{-1}$照射し、γ線測定による不純物定量後、包装形状をβ線測定用に変更した後、約２ヶ月間放射能減衰測定を行った。供試料と同時に0～0.25 μgの範囲で５種類の濃度２系列のP基準試料を照射した。測定システムはSSD検出器の信号を分岐して任意の異なる高エネルギー、２領域を２台の計数器で同時測定した。^{32}Pは半減期14.28日、1.711MeVのβ線(100%)を放出する核種で、以下に示す核反応により生成する。

$$^{30}Si(n,\gamma)^{31}Si \xrightarrow[T_{1/2}:2.62h]{\beta} {}^{31}P(n,\gamma)^{32}P \xrightarrow[T_{1/2}:14.3d]{\beta^{(1.711MeV)}} {}^{32}S$$

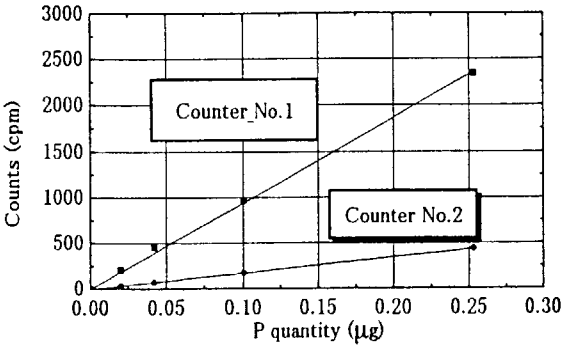

Fig.1 P quantity vs β-ray activity counts

P基準試料の重量－計数率の関係について照射後29日目に測定したﾃﾞｰﾀは、計数器No.1&2ともに良好な直線性を示した(Fig.1)。２系列の両計数器の関係を０点を通過するように直線一次近似式で示した。

p_1 = 9334.0 c_1
p_2 = 1717.1 c_2
p_3 = 8003.1 c_3
p_4 = 1489.6 c_4

p_1 ～ 4:計数率
c_1 ～ 4:重量(μg)

供試料の放射能減衰測定の結果をFig.2に示す。全体の計数率(□)を十分長く経過したﾃﾞｰﾀから外挿した点(○)の直線近似式はy = 2.39 - 0.00675xとなる。係数は^{59}Feの崩壊定数(=-0.4343(0.693/$T_{1/2}$))と一致したので、これを差し引いた点(▲)を^{32}P計数率とした。実際に^{32}Pの係数0.02108で引いた線をプロットした点(▲)に重ね描きするとほぼ一致した。従って、照射後経過日数29日の計数率値を求め、先に求めた計数率－重量の近似式から^{32}Pに相当する重量を算出する。これよりAp及びBp系列の各計数器毎に求めたP重量は次に示す数値となった。

c_1: 0.0081 μg　　c_3: 0.00945 μg
c_2: 0.0113 μg　　c_4: 0.0130 μg

これよりP濃度の平均値としては0.0105 μgを得た。供試料重量0.04393gから重量濃度比は0.239 wppm、原子数濃度比は0.31 appm、原子個数密度は6.56×10^{14} atom/cm^3となる。

今回のEpitaxial-SiC中のP同定／定量の試みは最初のものであり、HTTRへの具体的適用を目標として測定方法、検出精度など今後も精力的に進めていく必要がある。

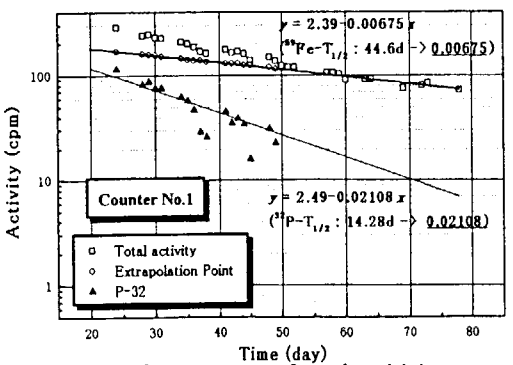

Fig.2 Decay curve of total actitivity for epitaxial-SiC material

原子炉：JRR-3M　　装置：気送管　　分野：放射化分析(工業材料)

研究テーマ：核反応を利用する分析化学
表　　題：中性子放射化分析の研究

中性子放射化分析の研究

米沢仲四郎，松江秀明
物質科学部分析センター

中性子放射化分析法（NAA）は，汚染及び蒸発などの影響が少ないことから，正確さの優れた多元素高感度分析法という特長を持つ。また，近年比較標準試料を使用しないで多元素定量を行う k_0 法（k_0-NAA）の計算プログラムも市販され，非破壊で多元素を簡単に定量することができるようになった。報告者らはこれまでJRR-3Mの放射化分析設備を使用し，短寿命核種を利用したNAAの基礎検討を行うとともに，k_0-NAAを国内でいち早く導入してきた。平成９年度はこれまで検討をしてきたNAAにより，人工ダイヤモンド及び高温工学試験研究炉（HTTR）の炉心に使用された黒鉛中の不純物元素の定量に着手した。

人工ダイヤモンドと黒鉛は共に炭素の同素体であり，核融合炉の中性子の検出器として，また，高温ガス炉の炉心材料として注目されている。人工ダイヤモンドと黒鉛中の極微量不純物が中性子検出及び原子炉の核特性に大きな影響を与えるため，不純物の定量が必要とされる。ダイヤモンドと黒鉛は化学的に分解することは困難であり，高周波誘導プラズマ質量分析法（ICP-MS）等の破壊分析法を適用することができない。しかし，NAAは試料を分解せずにそのまま分析をすることができ，さらにマトリックスの炭素は放射化しないことから不純物分析法として最も適している。さらにまた，原子炉用黒鉛の場合，原子炉の核特性上中性子吸収断面積の大きな元素ほど問題となるが，このような元素はNAAでは高感度であり，NAAは原理的に最適な分析法といえる。

分析は，試料を高純度ポリエチレン袋又は石英管に封入し，JRR-3Mの気送管（PN-1,3）と水力照射設備（HR-2）を使用して行った。測定する核種の半減期により，極短寿命核種（半減期 sec オーダー），短寿命核種（半減期 min オーダー），中寿命核種（半減期 hr オーダー）及び長寿命核種（半減期 day 以上）に分類し，核種の半減期に応じた条件で照射・測定をした。

本分析は着手したばかりで，未だ最終的なデータは得られていない。これまでに得られた予備実験の結果，人工ダイヤモンドからは，Cr, Co, Ni, Sb, Mo, Au が検出され，その含量は高品位ダイヤモンドでは Cr 6.67 ppb, Co 4.86 ppb，また，低品位ダイヤモンドでは Cr 11.9 ppb, Co 25.8 ppb, Ni 537 ppb, Sb 0.066 ppb という結果が得られた。今後さらに分析を積重ね，HTTRに使用された黒鉛（IG-110）と人工ダイヤモンド中の不純物含量を明らかにする予定である。

研究成果の公表

1) 米沢仲四郎，市村茂樹，黒沢達也，松江秀明：”半減期秒オーダーの短寿命核種を利用する中性子放射化分析の基礎検討”，分析化学，印刷中（1998）．
2) 米沢仲四郎，黒沢達也，松江秀明：”機器中性子放射化分析法による窒化ケイ素中こん跡フッ素の迅速定量”，分析化学，投稿中（1998）．

原子炉：JRR-3M　　装　置：PN-1, PN-3, HR-2　　分　野：放射化分析（工業材料）

食餌中セレンと悪性腫瘍に関する研究
On the Effect of Dietary Selenium to Carcinoma

伊藤伸彦　千田伸　甲斐千恵美　田畑ひとみ　夏堀雅宏
北里大学獣医畜産学部獣医学科　獣医放射線学研究室
Nobuhiko ITO, Shin CHIDA, Chiemi KAI, Hitomi TABATA and Masahiro Natsuhori
Kitasato University, School of Veterinary Medicine and Animal Sciences, Lab. of Veterinary Radiology

近年、栄養学的観点から癌との関係が注目されている微量元素に Se がある。Se は免疫機能に影響を与えることも知られており、特に細胞性免疫はガンの抑圧に重要な役割を果たすことから、この経路を通じた Se と抗発ガン作用が推測されている[1,2]。本研究では、細胞性免疫のうち、ウイルス感染細胞や癌細胞を傷害するリンパ球である細胞障害性T細胞（Cytotoxic T cell または Killer T cell 以下 CTL）の活性における Se の効果を調べるため、マウスの脾リンパ球を用いて、リンパ球混合培養(MLC)[3]を行い CTL 細胞障害活性を測定した。活性の測定には一般にクロム遊離法を用い、この測定結果は通常エフェクター数またはエフェクター数／標的細胞比を X 軸に、CTL の細胞障害活性を Y 軸に示したグラフを用いて評価する。しかし、種々の原因によってデータがばらつき、この評価法では実験者により多様な解釈が生じ、客観的な比較ができない[4]。従って、より客観的な比較を可能とするため、今回は CTL 細胞障害活性の評価法に酵素速度論的手法を取り入れることを試みた。

実験材料及び方法

マウス C57BL/6J 雌７週齢を購入し、２週間動物用飼育ケージで育てた。マウスは誘導条件の違いにより５群(各群４匹、陰性対照群のみ３匹、陽性対照群はクローンリンパ球 OE4)に分けた。C57 マウスの抗原刺激として、P815 細胞(DBA/2 マウス由来の肥満細胞腫)を用いた。C57 マウスに in vivo P815 で一回誘導した群(P_1)、２回誘導した群(P_2)、そして *in vivo* で一回誘導し、さらに *in vitro* で一回誘導した群(P_{vitro})の誘導条件を作成した。

活性の測定は、P_1 では C57 マウスに 2×10^7 個の抗原を腹腔内投与後、10 日後に行った。P_2 は、上記の 1 回誘導後 12 日目に 5×10^7 個の抗原を腹腔内投与し、その 6 日後に行った。P_{vitro} は上記の 1 回誘導後 10 日目に C57 マウスの脾臓を摘出し、脾細胞からリンパ球を分離した。リンパ球と抗原が 10 対 1 になるように 24 穴プレートにまき、混合培養を 5 日間行い、その後活性を測定した。

上記の誘導後、*in vivo* の群は摘脾を行い、脾細胞浮遊液を作成し、さらに比重遠心法を利用しリンパ球を分離し、それをエフェクター細胞として利用した。*in vitro* 群は 24 穴プレートから細胞を回収し、リンホライト M にて死細胞を取り除いたものをエフェクター細胞とした。回収した脾リンパ球浮遊液を自動細胞分析器で、CTL(CD8 陽性細胞)および NK 細胞(アシアロ GM_1 陽性細胞)の割合を調べた。リンパ球の細胞障害の測定はクロム遊離試験にておこなった。標的細胞にはクロム標識した P815 を用いた。この標的細胞を 96 穴プレートに撒き、エフェクター細胞はその際標的細胞の 160,80,40,20,10,5 倍になるよう撒き CO2 インキュベーターにて４時間反応させ、その後上清を分取しそれをγカウンターにて放出された ^{51}Cr を計測し、以下の式(*Eq.*0)にて細胞破壊率(specific release)を求めた。

ER(experimental release):エフェクター細胞により破壊された標的細胞の ^{51}Cr の放出(cpm)

MR(maximum release):1N HCl により全破壊した ^{51}Cr の放出(cpm)

$$\text{supecific release}(\%) = \frac{ER-SR}{MR-SR} \times 100$$

SR(spontaneous release):培養中に自然遊離した ^{51}Cr の放出(cpm)

結果

1. 脾リンパ球中の CTL 及び NK 細胞の割合

自動細胞分析器による CTL 及び NK 細胞割合の測定結果を、平均値±標準偏差で比較し Table 1 に示す。

2. リンパ球の細胞傷害活性の測定

^{51}Cr 放出実験により得られたリンパ球の活性

研究施設・装置　JRR-3、気送管　　研究分野　細胞免疫学、放射化分析

測定結果を用い、非線形最小二乗法によって求めた速度パラメータをTable 2に示す。

各群のVmax、Km

P815誘導群における刺激細胞標的群(標的細胞がP815の場合)では、P_{vitro}群のVmax値は、最も値が高かった陽性対照群に対してほぼ同値を示し、*in vivo*誘導群よりもかなり高い値を示した。P_2群はP_1群よりも2倍以上高いVmax値を示した。Km値は1回の誘導よりも2回の誘導で減少した。また、P_{vitro}群で最も低い値が認められた。

3. CTLの細胞傷害活性の測定

非線形最小二乗法によって求めた速度パラメータをTable 2に示す。

各誘導群ともリンパ球におけるVmax値と同様の傾向を示した。即ち、P815誘導群では、刺激細胞標的群、非刺激細胞標的群何れにおいても、1回誘導群に対し2回誘導群でVmax値の増加とKm値の低下が示された。最もKm値の低かったP_{vitro}群のKm値は、P_1群Km値の1/5、P_2群Km値の1/3という結果が得られた。

考察

CTLの細胞傷害活性の測定法は一般に、^{51}Cr遊離法を用い、測定結果の判定には、エフェクター数をx軸に、CTL活性をy軸に示したグラフを用いる[4]。しかし、この評価法には実験者によって多様な解釈法がある事と、測定していないE/T比では細胞傷害活性の予測ができないことが、異なった実験者間でのデータ比較を困難にしている。また、一般的に用いられるE/T比をX軸にとる方法では、直線性が失われた場合の細胞傷害性の予測が出来ない。

今回はCTLの標的細胞に対する細胞傷害活性の解析に酵素反応速度論的手法を取り入れて、種々のCTLの誘導条件下で、従来とは異なるCTL細胞傷害活性の評価法を検討した。

細胞性免疫反応による細胞傷害の主体は、T細胞とNK細胞であるので、今回測定した細胞傷害活性T細胞(CTL)とNK細胞の細胞傷害活性の合計である可能性がある。そこで、NK細胞に対する抗体(アシアロGM_1抗体)と反応させて自動細胞分析器でNK細胞数を測定したところ、NK細胞数は無視できる値であった(Table 1)ので、測定した細胞傷害活性の大半はCTLによるものと判断した。また、全く誘導を行わなかった陰性対照群には、CD8陽性細胞比率が10%あったにもかかわらず、細胞傷害活性は殆ど検出されなかった(Table 2)。従って誘導を行った他群は刺激細胞に反応し、それに特異的に対応するCTLが分化・増殖した結果と見なし得る。

リンパ球活性とCTL活性

一般に、エフェクター細胞と見なして解析に用いるものには、CD8陰性の細胞も含まれている(Table 1)ので、培養後の全細胞数をそのまま解析に用いると、各群内の異なったCD8陽性細胞率のために、実際に標的細胞を破壊するCTL数も異なってしまう。つまり、全細胞数で細胞傷害活性を比較しても、実際には活性率の異なった細胞数で比較していることになり、CTL細胞の反応として正確に解析比較できない。従って今回は自動細胞分析器を用いて、培養後の全細胞中のCD8陽性細胞率を測定し、総リンパ球数にCD8陽性細胞率をかけて換算した値(CTL細胞数)をエフェクター細胞数と見なした。

細胞傷害活性の速度論的解析への応用

Michaelis-Mentenの速度式は通常酵素反応において「量の時間軸への解析」を行う際に用いられる。酵素と基質と生成物の関係を模式的に表すと以下のように示される。

$$E+S \Leftrightarrow ES \qquad (Eq.1)$$

$$ES \Rightarrow E+P \qquad (Eq.2)$$

Eは酵素、Sは基質、ESは基質ー酵素複合体、Pは生成物を示す。*Michaelis*らは*Eq.1*が平衡状態にある、つまり、*Eq.1*で反応が平衡状態に達する速度が*Eq.2*の反応速度に比べて大きいと考えた。この仮定が成り立つならば、反応系に存在するすべての酵素分子がESの形を取る時(酵素が基質で飽和されているとき)、反応速度は最大となる。

今回の研究では、CTLが標的細胞を破壊する免疫反応も上記のような1つの化学反応と見なし、酵素反応速度論を細胞傷害活性解析に応用した。詳説すると、^{51}Cr遊離法により求めたCTL細胞傷害活性を、非線形最小二乗法でシミュレートして、Michaelis-Mentenの速度式(*Eq.*0)におけるVmaxとKmを求めた。Vmaxはエフェクター細胞がある一定時間内(インキュベーション時間：4時間)に標的細胞を破壊し得る最大細

胞数で、シミュレーションカーブ(Fig.1)におけるプラトーの高さがそれを示す。Kmは*Michaelis*定数で、Vmaxが半分になるエフェクター細胞数を示すため、シミュレーションカーブ(Fig.1)の立ち上がりが早いほどKmは小さいということになる。Kmはその値が小さいほど、エフェクター細胞が標的細胞を破壊する特異性が高い、または標的細胞に対して親和性が高いことを意味する。

また、求めたVmaxとKmをScatchard Plot(Fig.2)で示すと、直線のx切片がVmaxである。直線のx切片が大きい程、Vmaxが大きいという事になる。Kmは傾きの逆数の絶対値で、急勾配になるほど小さいKmとなる。

今回の研究では、異なった条件で誘導されたCTLの細胞傷害活性を測定し、速度論的解析の下で、誘導法によるCTL活性パラメータの違いを考察した。

***in vivo*における誘導条件による活性の比較**

生体は1度抗原刺激を受けて、ある期間をおいて2度目の抗原刺激を受けると、初回より激しい免疫応答(ブースター効果)を示す。今回の結果では、P815誘導群に1回誘導群よりも2回誘導群の方が非線形最小二乗法によるシミュレーション(Fig.1)においてプラトーの値が高く、Scatchard Plot(Fig.2)においては、直線のx切片の値がより大きいことから、ブースター効果によってCTL-Vmaxが増加したと考えられる。またシミュレーションカーブの立ち上がりがより早く(Fig.1)、Scatchard Plotの直線の傾きが増加した(Fig.2)ことから、同じくブースター効果によりCTL-Kmが、低下したと考えられる。これは初めて抗原刺激を受けて分化したCTLが、記憶CTLとなり生体内に残存し、再度同一の抗原刺激を受けて速やかに対応し、より激しい免疫応答が起こったためと考えられる。つまり、追加免疫によりCTL活性に量的な変化(Vmaxの上昇)と質的な変化(Kmの低下)が起こったと判断できた。

***in vivo*誘導と*in vivo+in vitro*誘導の比較**

*in vivo+in vitro*誘導は*in vivo*誘導群と比較して顕著に高く、陽性対照であるOE-4(H-2dに特異的細胞傷害活性をもったクローンリンパ球)と殆ど差がなく、ほぼ最大の標的細胞破壊能力を発揮していたことが示された。また標的細胞YAC-1群及びOE-4の特異性(CTL-Km)はほぼ同様であったが、標的細胞P815群における特異性(CTL-Km)は、前2者の約3倍(約1/3)を示した(Table 2, Fig.1)。このことはP_{vitro}群において特に標的細胞P815群にかなり特異性の高い細胞傷害活性を持つCTLが高率に誘導されたことを意味する。

P815誘導群は、P815の表面抗原に対するポリクローンCTLであるから、P815誘導群全体からみると、P815のあらゆる表面抗原に対するCTLが用意されていると考えられる。

解析の結果、*in vivo + in vitro*誘導群におけるVmaxが最も大きく、Kmが最も小さかった。従って、今回行った誘導群のうちでは、*in vivo + in vitro*誘導群における誘導方法が、最も高い標的細胞破壊能力と、最も強い標的細胞特異性を持ったCTLを誘導できると結論づけられた。これは、*in vivo + in vitro*誘導群ではPositive selectionによってP815に特異的なCTLが選択的に誘導、増殖したため、最高のCD8陽性細胞率を示したと考えられる。また、エフェクター中のCTLの割合が大きくなったことから、CTLと標的細胞の接触する機会が*vivo*誘導群よりも確率的に多くなった事も、特異的な細胞傷害活性が高くなった一因と考えられる。

以上のように、数種類のCTL細胞傷害活性について、CTL細胞傷害活性を速度論的に解析しパラメータ化することによって、CTLの傷害活性が標的細胞に対してファクター毎にどの程度優れているかという評価が客観的に可能になった。また本解析手法の最大の利点は、Kmなるパラメータが求められ、実験を実施していないE/T比の範囲でも、シミュレーションにより細胞傷害活性の推定が可能なことである。更にこのアプローチによって、CTL誘導法を改善・最適化できるし、その後の評価もVmax、Kmといったパラメータで行うことにより参照、比較することが容易に出来ると考えられる。

今回の研究では放射化分析により、細胞培養に用いる牛胎児血清のSe濃度を分析し、低Se濃度の血清を選別した。今後は、CTL活性の発現とSeの関連を明らかにすることで、Seの抗発ガン作用の一端を解明する一助としたい。

Table 1 自動細胞分析器によるCD8,アシアロGM1各陽性細胞率

	CD8陽性細胞率(%)±SD	アシアロGM1陽性細胞率(%)±SD
P_1	14.9±1.4	0.09±0.10
P_2	18.9±1.6	0.04±0.03
P_{vitro}	37.5±6.2	0.00±0.01
control	9.2±1.4	0.48±0.54

mean±SD(n=4,contのみn=3)

Table 2 リンパ球およびCTL活性実測値より求めたSimulationにおける速度パラメータ

		Target	P_1	P_2	Y_1	Y_2	P_{vitro}	control	OE4
Vmax	リンパ球	P815	28.9	72.4	1.4	8.5	110.0	2.1	110.5
	CTL	P815	29.7	73.0	2.2	9.4	109.4	2.5	110.5
Km	リンパ球	P815	59.0	34.3	24.1	25.1	5.8	24.1	6.8
	CTL	P815	10.9	6.6	10.8	3.0	2.2	3.7	6.8

Vmax:4hrでEffector細胞がTarget細胞を破壊する最大速度(×10^2個/4r)
Km: ミカエリス定数(Effector細胞数または濃度)
control:陰性対照群
OE4:陽性対照群

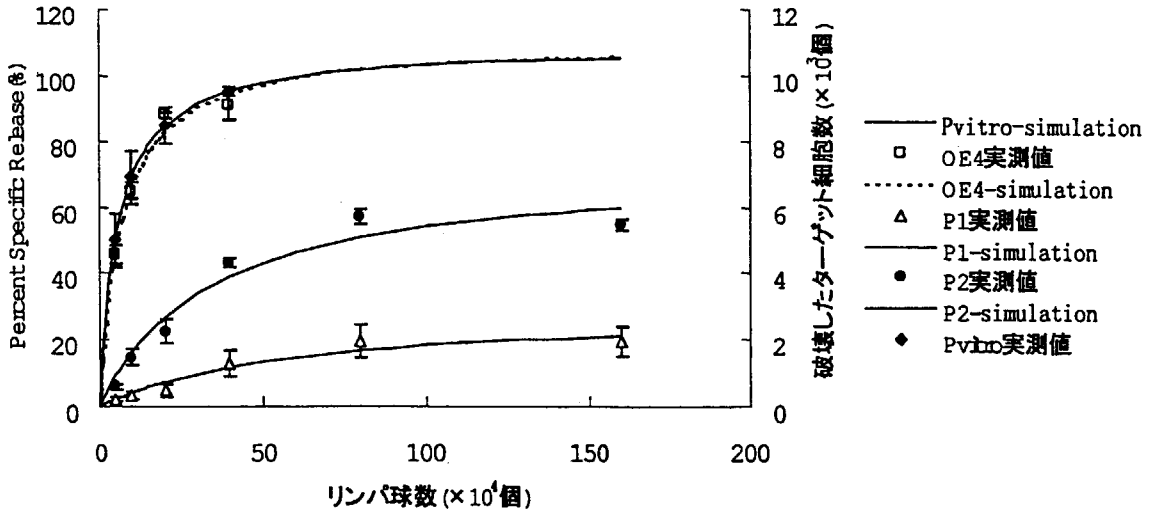

Fig 1、P815誘導による活性およびOE4活性のSimulation

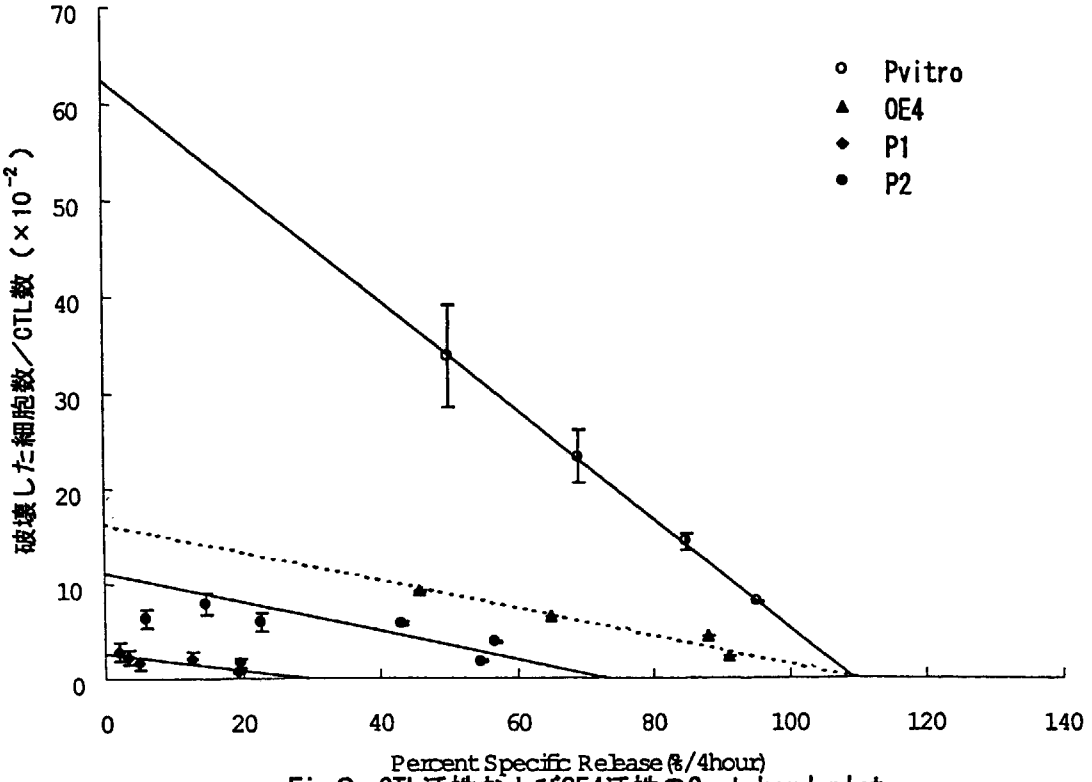

Fig2、CTL活性およびOE4活性のScatchard plot

References

1) Schumacher, L. K., Roy, M., Wishe, H. I., Cohen, M. W. and Stotzky, G.: *The Society for Experimental Biology and Medicine*, **193**, 136-142, 1990
2) Schumacher, L. K., Roy, M., Wishe, H. I., Cohen, M. W. and Stotzky, G.: *Biol. Trace Elem. Res.*, **33**, 23-35, 1992
3) 小林賢: 細胞性免疫機能検査法(Medical Technology 編), 医歯薬出版, 東京, 1993
4) Thorn, R. M. and Henney, C. S.: *J. Immunol.*, **117**, 2213-2219, 1976

成果の公表

［学会発表］夏堀雅宏、甲斐千恵美、田畑ひとみ、伊藤伸彦.　マウスＣＴＬ細胞傷害活性の誘導とその速度論的解析による誘導条件評価の試み、第１２５回日本獣医学会（5-7th,April,1998 栃木)、講演要旨集pp.165、１９９８

バルト海産ネズミイルカ(*Phocoena phocoena*)の有機態ハロゲン(Cl, Br, I)

Extractable Organic Halogen (EOX) in Harbour Porpoise (*Phocoena phocoena*) from the Baltic Sea

研究代表者　脇本忠明(愛媛大・農)
研究協力者　河野公栄(愛媛大・農)
松田宗明(愛媛大・農)

1. はじめに

バルト海は、集水域としてポーランド、旧ソ連、フィンランド、スウェーデン、デンマーク、ドイツなどの国々を擁し、海水が交換し難い閉鎖的な海域で、世界の海の中でも極めて汚染が進んでいることが知られている。汚染が進んだ原因として、製紙工業の廃水による汚濁負荷も考えられる。特に、製紙工業においては、塩素を用いる漂白工程における有機塩素化合物の副次的生成が懸念され、DDTsやPCBsなどの人工有機塩素化合物以外に未検討の有機塩素化合物による汚染も考えられる。人工有機塩素化合物は、先に挙げたDDTsやPCBsに代表されるように、環境中で安定で、しかも生物に対して毒性影響を及ぼすことが知られているが、未検討の有機塩素化合物の中にも、環境残留性を有し、野生生物に対し生態毒性影響を及ぼす化合物の存在が懸念される。さらに、塩素以外の有機ハロゲン化合物による環境汚染も考えられ、それらの生態毒性影響も共通していることが懸念される。

そこで、本研究では沿岸生息性のネズミイルカ(*Phocoena phocoena*)を用い、有機態ハロゲン(Extractable Organic Halogen: EOX)について検討した。

2. 試料と方法

北部ポーランドのバルト海沿岸に漂着した死亡個体(♂4検体、♀5検体)を試料として用いた。これらの試料は1989年から1993年に採取した。分析は、脂肪組織中の有機態ハロゲンを有機溶媒により抽出し、無機ハロゲンを水洗、ゲル浸透クロマトグラフィーにより除去した後、放射化分析によりハロゲン濃度を測定した。放射化分析には日本原子力研究所の研究用原子炉JRR-3を用い、放射化の条件は中性子束3.7×10^{13}n/cm^2・秒、2分間照射後、生成した核種^{38}Cl (1643keV、2168keV)、^{80}Br(617keV、666keV)、^{128}I (443keV)をγ-スペクトロメトリーにより定量した。γ-スペクトロメトリーには、高純度Ge同軸型検出器(EG&G ORTEC MODEL GEN-15180)及び多重波高分析器(CANBERA SERIES 35 PLUS)を用いた。また人工有機塩素化合物としてDDTs, HCHs, クロルデン化合物(CHLs), PCBs及びHCBの分析を行った。これらの化合物の分析は、有機溶媒による抽出後、フロリジルカラムクロマトグラフィーによる分画の後、GC-ECDまたはGC-MSを用い定量した。

3. 結果と考察

有機態塩素(EOCl)、有機態臭素(EOBr)及び有機態ヨウ素(EOI)が、全ての試料から検出された。検出濃度は、EOClが平均濃度36μg/g 濃度範囲22-48μg/g、EOBrでは1.7μg/g 及び0.57-2.2μg/g 、EOIについては0.69μg/g及び0.18-1.4μg/gであり、EOCl>EOBr>EOIの濃度順であった(Table 1)。中でも、EOXに占めるEOClの存在割合が大きい。先に報告している北部北太平洋産のイシイルカ(*Phocoenoides dalli*)など太平洋産の海棲哺乳類に比較して、バルト海産のネズミイルカのEOClの存在割合がより大きい傾向を示した(Fig.1)。このことは、バルト海に棲息するネズミイルカは，相対的に多くの有機塩素化合物に暴露され、それらを体内に取り込んでいることを示唆している。さらにバルト海産のネズミイルカ試料について、DDTs, HCHs, クロルデン化合物(CHLs), PCBs及びHCBなど代表的な人工有機塩素化合物を測定し、EOClに占める割合を明らかにす

研究施設と装置名
JRR-3 気送管(短寿命核種照射用)

研究分野
放射化分析

Table 1 Concentrations (μg/g, wet weight basis) of EOX in Marine Mammals from Baltic Sea and Pacific Ocean.

	n	EOCl	EOBr	EOI	EOX
Baltic Sea					
Harbor Porpoise (*Phocoena phocoena*)	8	36 (22-48)	1.7 (0.57-2.2)	0.69 (0.18-1.4)	38 (23-50)
Pacific Ocean					
Striped Dolphin (*Stenella coeruleoalba*)	15	110 (47-120)	46 (31-54)	5.8 (3.8-7.6)	150 (91-170)
Dall's Porpoise (*Phocoenoides dalli*)	6	25 (33-57)	5.9 (5.5-19)	1.9 (1.6-4.3)	40 (32-80)

Figures in bracket indicate minimum and maximum concentrations on wet weight basis.

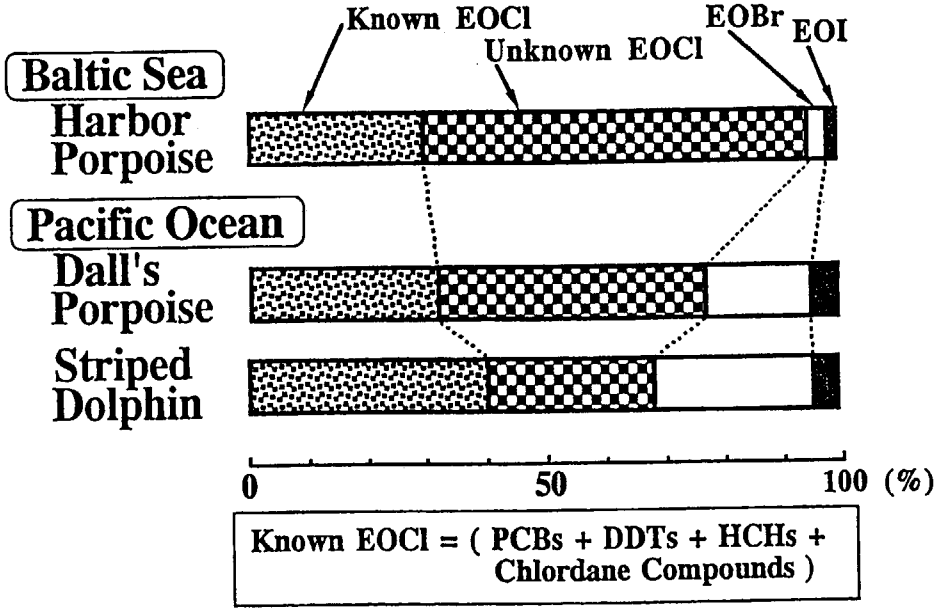

Fig.1 Composition of EOX and EOCl (Known and Unknown Fractions).

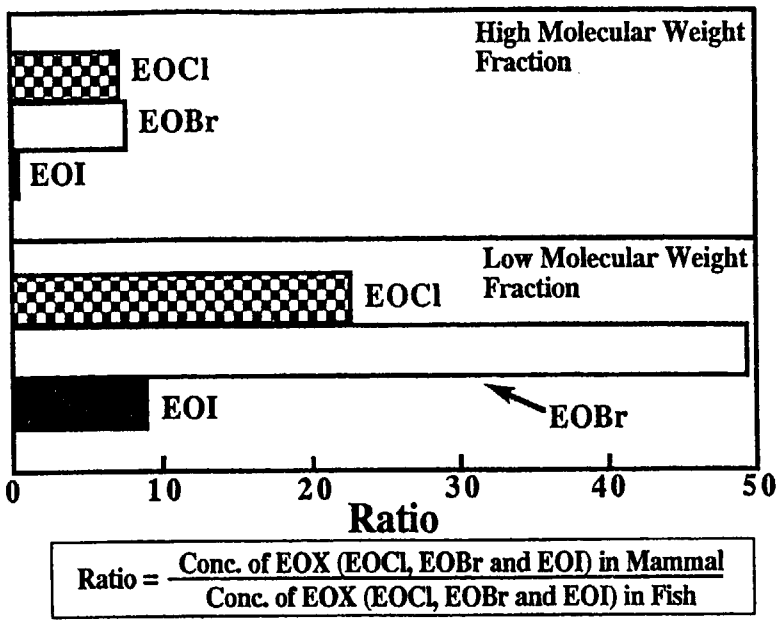

Fig. 2 Concentration Ratios of EOX between Herring and Harbour Porpoise.

ると共に、両者の差し引きにより未知の有機塩素化合物に由来する有機態塩素量を求めた。その結果、未知の有機態塩素のEOClに占める割合は70乃至80%であった。比較のため北部北太平洋の海棲哺乳類について検討したところ、未知の有機態塩素はEOClの30乃至50%であった。次に餌生物としてバルト海の魚(ニシン)試料を用いそのEOXとネズミイルカのEOXについて濃度比を計算した。その結果、低分子量画分のEOBrについて大きい値が得られた(Fig.2)。

以上の検討結果は、バルト海に棲息するネズミイルカが多くの未検討の有機塩素化合物を取り込んでいることを示唆している。その有機塩素化合物の給源として、人為活動による生成と天然生成が考えられる。天然生成に関して、今日、多種類の有機ハロゲン化合物が自然界、特に海洋環境で生成することが知られている。例えば、紅藻類による塩素・臭素原子を有する天然有機ハロゲン化合物の生合成が知られている。もう一つの可能性として、先に述べたように塩素漂白過程で生成した環境残留性を有する有機塩素化合物が、廃水と共にバルト海に流入し、バルト海の海洋生態系の食物連鎖を通して高次の海棲哺乳類に生物濃縮されるなど、人為活動による汚染である。EOClのみならずEOBrについても海洋生態系を通じて生物濃縮されることが推定され、未検討の有機態ハロゲンの構成分として人為活動による生成物を多く含む可能性が強いことが考えられる。

4. 成果の公表

学会等発表

1) Kawano, M., Tanaka, Y., Falandysz, J. and Tatsukawa, R.: Extractable organo-halogens and known organochlorine xenobiotics in harbour porpoise Phocoena phocoena from the southern part of the Baltic Sea, BROMAT. CHEM. TOKSYKOL., XXX, 87-94 (1997)

2) 河野公栄、J. Falandysz, 辻　聡志、北村清司、脇本忠明、北部ポーランドの土壌・底質中の有機態ハロゲン(EOX)と人工有機塩素化合物、環境化学、7, 7-13 (1997)

3) Kawano, M., Falandysz, J., Tanaka, Y. and Wakimoto, T. :Occurrence and behavior of extractable organic halogen (EOX) and man-made organochlorines in harbor- porpoise (*Phocoena phocoena*) from the Polish coast of Baltic Sea, Organohalogen Compounds, 33, 328-332 (1997)

新規な抽出試薬による金属元素の予濃縮－放射化分析

Preconcentration of Trace Metal Elements with New Extraction Systems and Their Use in Activation Analysis

山形大学工学部　阿部重喜、遠藤昌敏、船田俊祐、池田光治
Faculty of Engineering, Yamagata Universiity, ABE, Shigeki; ENDO, Masatoshi; FUNATA, Shunsuke; IKEDA, Kohji

近年、各種のスペクトロメトリー技術が急速に発展し、選択性に優れた機器分析法が数多く開発されている。これらの分析法は非破壊測定法として広く利用されているが、環境試料などを対象とする超微量分析では、マトリックス妨害が測定の正確さ及び精度に大きな問題になる。従って適切な予濃縮技術の確立は重要な研究課題である。特に、中性子放射化分析では照射試料の迅速な作製法と関連した簡便な予濃縮技術の開発が望まれている。平成７年度までの原研共同利用において、チキソトロピー現象を利用する新しい固－液抽出法の可能性を提案し、水銀などの予濃縮分離へ適用した。Ｎ－ラウロイル-Ｌ-グルタミン酸-α,γ-ジブチルアミド(Ｇ-１)をゲル化剤とする金属錯体の固－液抽出分離法は常温での溶媒抽出が可能になり、抽出操作中における器具の破損など不測な事態による放射性物質の飛散及び汚染の拡大を最小化する目的に有用であった。本年度は予濃縮分離のための新規な抽出溶媒及び抽出試薬について基礎的な開発研究を行った。

1. 予濃縮分離のための新規な抽出溶媒の開発

クラウンエーテルあるいはチアクラウンエーテルなどの大環状化合物は、それぞれ硬いルイス酸及び軟らかいルイス酸の金属イオンの抽出に優れた特性を示すことが報告されている。これまでに酸素及び硫黄原子を配位子とする種々の大環状シッフ塩基を合成し、遷移金属イオンに対する抽出試薬としての特性を明らかにした。大環状化合物による陽イオン性の金属錯体の抽出では、かさ高い対陰イオンの存在が不可欠であり、従来まで用いられてきた抽出溶媒に代わる新規な配位性溶媒の開発が望まれた。本研究では、p－ノニルフェノールが水溶液の表面に半球状に浮遊する特性に着目し、陽イオン性金属錯体の抽出分離に対する配位性溶媒としての可能性を検討した。

フェノール類の配位能は古くから広く知られているが、水に対する溶解度が大きいことから抽出溶媒として用いられなかった．長鎖のアルキル基を導入したフェノールは疎水性の増大によって抽出溶媒としての利用が期待された。p-ノニルフェノールの水に対する溶解度は、平衡状態における水相の吸光度測定法によって決定した。長時間の振り混ぜ処理によって溶解平衡状態を達成したのち、水相に分散したp-ノニルフェノール濃度はその極大吸収波長(197 nm)で測定した。その結果、p-ノニルフェノールの溶解度は 5.5×10^{-4} mol/l (イオン強度：0.1)であった。

p-ノニルフェノールによる鉄(Ⅱ)、銅(Ⅱ)及

研究施設と装置名
ＪＲＲ－３

研究分野
分離化学・放射化分析

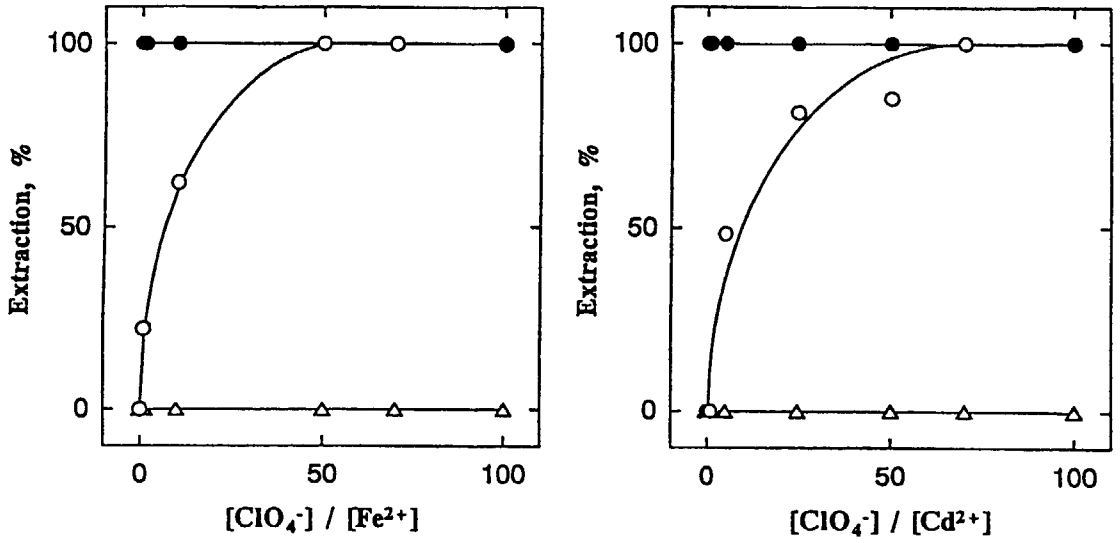

Fig.1 Extraction of iron(II) and cadmium(II)-o-phen complexes

p-nonylphenol:●; nitrobenzene:○; nonylbenzene:△.

びカドミウム(Ⅱ)の抽出挙動を、1,10-フェナントロリン型及びピリジルアゾ色素型の金属陽イオン錯体について検討した。鉄(Ⅱ)及びカドミウム(Ⅱ)の1,10-フェナントロリン錯体は過塩素酸イオンなどのかさ高い陰イオンを添加しない条件下でも酢酸塩あるいはリン酸塩緩衝液から抽出可能であり、それぞれｐＨ２－10及び４－１０の範囲で定量的に抽出された。ニトロベンゼン溶媒による抽出系では陽イオン金属錯体の抽出には過塩素酸イオンなどのかさ高い対陰イオンの存在が不可欠であり、鉄(Ⅱ)錯体の定量的な抽出に50倍量の過塩素酸イオンを必要とした(Fig.1 参照)。一方、ノニルベンゼンを抽出溶媒とする系では、大過剰量の過塩素酸イオンを添加しても鉄（Ⅱ）及びカドミウム(Ⅱ)錯体は全く抽出されないことから、p--ノニルフェノールは放射化分析における予濃縮分離のための抽出溶媒として優れた特性を示した。

鉄(Ⅲ)の還元が比較的容易に進行する鉄(Ⅱ)－鉄(Ⅲ)系では、水相中に存在する鉄(Ⅲ)はＬ－アスコルビン酸などの還元剤が存在しない場合にも迅速に還元され、赤色の鉄(Ⅱ)錯体としてp-ノニルフェノール相に定量的に抽出された。ニトロベンゼン溶媒の抽出系では、鉄(Ⅲ)の抽出は長時間の振り混ぜ処理によっても全く進行しなかった。同様な現象は銅(Ⅰ)－銅(Ⅱ)のネオクプロイン錯体の抽出系で観測された。銅の抽出は特に還元剤を添加しない場合にも、60分の振り混ぜ操作で可能であった。抽出後のp-ノニルフェノール相は黄色を呈し、銅(Ⅰ)－ネオクプロイン錯体の生成はエタノールに溶解した銅錯体の吸収スペクトル（極大吸収波長：454 nm）から確認できた。

錯形成と酸化が同時に進行する系として、コバルト(Ⅱ)と銅(Ⅱ)の5-Br-PADAP錯体の抽出挙動を比較した。正電荷のコバルト(Ⅲ)－5-Br-PADAP錯体は抽出速度が極めて遅く、60分間の振り混ぜ時間によるコバルト(Ⅲ)の抽出率は８％程度であった。コバルト(Ⅲ)－5-Br-PADAP錯体の定量的な抽出には、６時間以上の振り混ぜ処理が必要であった．一方、無電荷の銅(Ⅱ)－5-Br-PADAP錯体は短時間に 100%の抽出率を示した。ニトロベンゼン溶媒によるコバルト(Ⅲ)－5-Br-PADAP錯体の抽出は過塩素酸イオンの存在

下で迅速に進行することから、p-ノニルフェノールの抽出溶媒系では、p-ノニルフェノールがコバルトの錯形成及び酸化に抑制作用を示した。陽イオン性金属錯体とp-ノニルフェノールの相互作用による抽出率の増大は、混合溶媒系における鉄(Ⅱ)－o-phen錯体の抽出データから実証できた。

鉄(Ⅱ)－o-phen錯体は陽イオン化学種の抽出に有効なポリオキシエチレンノニルフェニルエーテル-2 (PONPE-2) 及び長鎖アルキル基構造のオレイルアルコールに抽出されない点で、陽イオン性金属錯体の抽出に対するp-ノニルフェノール溶媒の特異性な役割は注目された。鉄(Ⅱ)及びカドミウム(Ⅱ)－o-phen錯体の抽出は酢酸塩緩衝液が存在しない条件で定量的に進行しないことから、鉛(Ⅱ)－クラウンエーテル錯体の抽出と同様に、酢酸イオンが対陰イオンとして配位している機構を推論した。

本年度の成果を以下のように要約した。抽出溶媒としてのp-ノニルフェノールは 、1,10-フェナントロリン型及びピリジルアゾ型の陽イオン性金属錯体など抽出過程に酸化還元反応が関与する抽出系で特異的な作用を示した。陽イオン性の金属錯体は過塩素酸あるいはテトラフェニルほう酸イオンなどの放射化分析に望ましくない対陰イオンを使用しない条件下で、p-ノニルフェノール相に定量的に抽出された。また、還元操作の必要な抽出系では p－ノニルフェノール自身が還元作用を示し、還元剤の添加を必要としない複合機能溶媒として実用的であった。

2. 硫黄配位子型カリックスアーレンによる遷移金属元素の溶媒抽出

カリックスアーレン及びその誘導体は金属イオンの認識に対する新しい型のホスト化合物として注目されている。これまでに合成されたカリックスアーレンのエステル、ケトン及びアミド誘導体は、希土類元素を含めた金属イオンの抽出に応用された。本研究では、カリックスアーレンの骨格に複数の硫黄原子を導入した酸素及び硫黄配位型の新規な大環状化合物を合成し、二価の遷移金属元素に対する抽出能力を検討した。

新規な10,16,22,23,33,39,45,45-ヘキサキス(1,1-ジメチルエチル)-3,6,26,29-テトラチアヘプタシクロ[41.3.1.^{8,12}.1^{14,18}.1^{20,24}.1^{31,35}.1^{37,41}]ドペンタコンタ-1(47),8,10,12(48),14,16,18(49),20,22,24(50),31,33,35(51),37,39,41(52),43,45-オクタデカエン-47,48,49,50,51,52-ヘキソール(HTDH)は Fig.2の反応によって合成した。金属イオンの分配比は中性子放射化分析法及び原子吸光分析法を併用して測定した。金属イオンを含む試料溶液に対陰イオン(過塩素酸イオンなど) 、緩衝溶液、及び抽出試薬を含む有機溶媒を加えたのち、振り混ぜ操作を行った。遠心分離した両相はその一定量を分取し、シリカろ紙上で乾燥したのち、ポリエチレン袋に二重に封入して原子炉照射 (ＪＲＲ－３, 10あるいは20分間) を行った。各元素の抽出率は(n,γ)反応で生成した放射性核種のガンマ線ピークを利用して算出した。

テトラフェニルほう酸イオンを対陰イオンとするＨＴＤＨ－ニトロベンゼンの溶媒抽出系 (pH 4.7 及び 9.0)では、銅(Ⅱ)のみが定量的に抽出された。マンガン(Ⅱ)、鉄(Ⅱ)、コバルト(Ⅱ)、ニッケル(Ⅱ)及び亜鉛(Ⅱ)はテトラフェニルほう酸イオンの共存下でも弱酸性溶液(pH 4.7)から全く抽出されなかった。銅(Ⅱ)の抽出に対する対陰イオンの効果はテトラフェニルほう酸イオン＞過塩素酸イオン＞ピクリン酸イオンの順序に低下した。

銅(Ⅱ)の抽出に及ぼすpHの影響をテトラフェニルほう酸イオンの存在及び非存在下で検討した。その結果は Fig.3に示した。銅(Ⅱ)はpH 3.5から9.0の範囲で高い抽出率を示した。また、銅(Ⅱ)の抽出はかさ高い対陰イオンを特に添加しない場合にも、pH 6.5から8.0 の範囲で定量的に進行した。銅(Ⅱ)の定量的な抽出に必要な振り混ぜ時間は10分間であった。フェノール性水酸基を含む大環状シッフ塩基による銅(Ⅱ)の

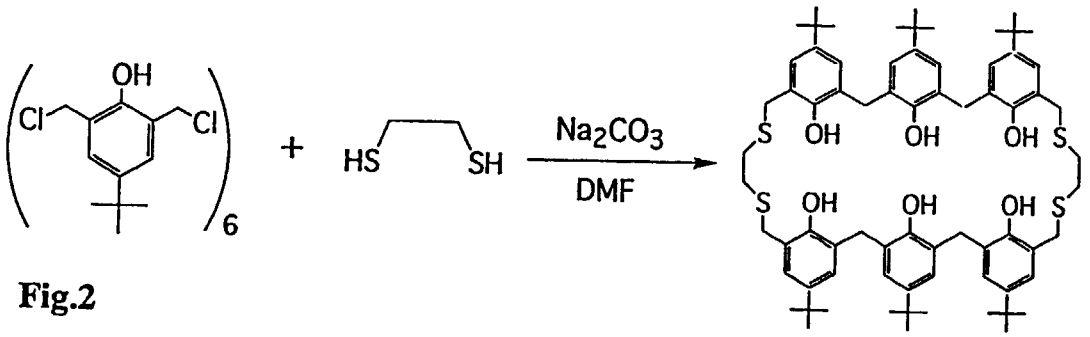

Fig.2

抽出は、イオン対抽出に有利なかさ高い対陰イオンが存在しない抽出系でも定量的に進行することを先に報告した。この現象はフェノール性水酸基のプロトン解離に伴う金属イオンへの酸素原子の配位及び電荷の中和機構によって解釈できた。ＨＴＤＨ系の場合にもフェノール性水酸化基が陽イオン性金属錯体の抽出に関与し、ＴＴＴＨあるいはＰＥＤ系と同様に、特にかさ高い対陰イオンを添加しない条件で銅(Ⅱ)の抽出を促進することは興味ある結果であった。

イオン対抽出系における金属イオンの抽出率は抽出溶媒に大きく左右される。一般に誘電率及び双極子モーメントの大きな溶媒ほど抽出性が増大すること報告されているが、使用する溶媒の選択はほとんど経験に頼っているのが現状である。新規な大環状化合物のＨＴＤＨによる銅(Ⅱ)の抽出率（かさ高い対陰イオンの非存在下）はブロモベンゼン<ニトロベンゼン<1,2-ジクロロエタンの順序に増大した。ＨＴＤＨを用いる銅(Ⅱ)の抽出系では、有機溶媒の抽出能と誘電率の間に明確な相関性が認められなかった。

ニトロベンゼン相に抽出した銅(Ⅱ)化学種の組成について検討した。CuL_mA_n（L=HTDH, A=対陰イオン）の抽出平衡を対陰イオン及び水素イオン濃度の一定条件下で測定し、銅(Ⅱ)錯体の分配比（D）とニトロベンゼン相中の試薬濃度の関係を対数プロットした。その結果、勾配が約２の直線がえられ、抽出化学種は１個の銅イオンに対して２分子のＨＴＤＨが配位していると推論した。なお、抽出化学種の構造に関しては、今後さらに検討を行う予定である。

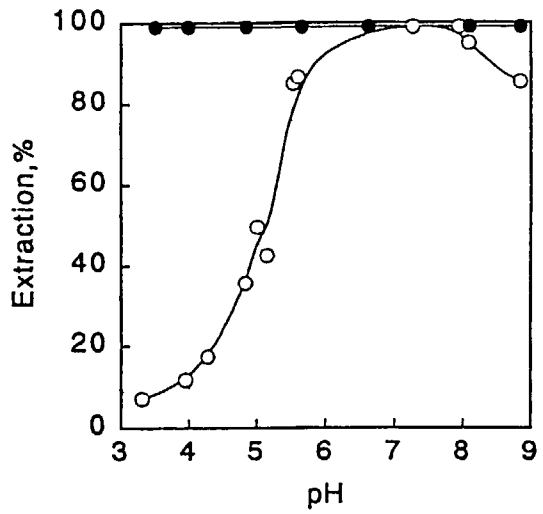

Fig.3

Effect of pH on Cu(II) extraction

—●—: Cu(II)-HTDH-TPB ion-paired complexes

—○—: Cu(II)-HTDH complexes

3.今後の課題

希土類元素の抽出に関して種々の検討を行ったが、現在までに定量的な抽出条件を確立するに至っていない。従来のニトロベンゼン溶媒に代わるp-ノニルフェノールは、クラウンエーテルあるいはチアクラウンエーテルなどの大環状化合物による金属イオンの抽出にかさ高い対イオンを必要としないことから、他の多くの溶媒抽出系への適用性が期待され、詳細な検討が望まれた。新規な抽出剤と特異的な抽出溶媒の組合せに関する方法論的な研究は、微量金属元素の予濃縮分離及びその放射化分析への応用に重要であり、今後の継続した研究が期待された。

「成果の公表」

1. K. Ikeda, M. Endo, S. Abe; "p-Nonylphenol as a versatile solvent for the liquid-liquid extraction of cationic metal complexes", Anal. Communications, 34 (1997) 183.

2. K. Ikeda, S. Abe; "Liquid-liquid extraction of cationic metal complexes with p-nonylphenol solvent: Application to crown and thiacrown ether complexes of lead(II) and copper(II)", Anal. Chim. Acta, 363 (1998) 165.

3. 高橋和浩、伊藤和明、阿部重喜；"硫黄及び酸素原子を含む大環状化合物による銅(II)の抽出分離"、化学系７学協会連合東北地方大会(1997年9月)

4. 阿部重喜、遠藤昌敏、小野寺陵太郎；"大環状シッフ塩基による銀(I)及びパラジウム(II)のに溶媒抽出"、化学系７学協会連合地方大会(1997年9月)

5. 池田光治、遠藤昌敏、阿部重喜；"p-ノニイイルフェノールを抽出溶媒とする金属陽イオン錯体の濃縮分離．鉛(II)及びバリウム(II)－クラウンエーテル系"、第58回分析化学討論会(1997年5月)

6. 池田光治、遠藤昌敏、船田俊祐、阿部重喜；"p-ノニイイルフェノールを抽出溶媒とする銅(I, II)陽イオン錯体の濃縮分離．テトラチアクラウンエーテル系"、第57回分析化学討論会(1996年5月)

隕石試料の放射化分析(II)

永井尚生[1]、本田雅健[1]、堂園克久[1]、今村峯雄[2]
([1]日本大学文理学部、[2]東京大学原子核研究所)

日本原子力研究所JRR3炉を利用して宇宙線生成核種^{53}Mnを測定する方法及びその結果を報告する。従来この測定のためには、旧JRR3, VG7-6 (-1978)のほか、JRR2のアイソトープトレインやVT 5 孔を利用してきたが、最近ではJRR3のDR孔がそれらの代替として使用できるようになった。鉄を主とする各種の隕石資料の測定に関する過去3年間の成果をまとめて報告する。

Activation analysis of meteorites (II)

H.Nagai[1], M.Honda[1], K.Dohzono[1] and M. Imamura[2]
[1] College of Humanities and Sciences, Nihon University, [2] INS, University of Tokyo

A long-lived cosmogenic nuclide, ^{53}Mn in extra-terrestrial materials has been determined using DR-1 hole of the JRR3 reactor, applying well thermalized neutron flux. According to our preliminary experiments, the irradiation conditions were indicated as the function of locations in the capsul. The neutron flux intensities are variable with the depths whereas the fast thermal ratios are not quite variable. Therfore the most convenient position for the samples is to be at the very bottom in the lowest capsul. By this method, ^{53}Mn contents in iron meteorites, metal phases of chondrites, and those of pallasites could be routinely determined in many samples.

1. はじめに

長半減期宇宙線生成物としての^{53}Mn ($T_{1/2}$: 3.7x10^6 y.[1]) は鉄に最も近い核種であるために、地球外物質に多量に含まれておりその測定は重要である。しかしながら直接放射能(X線 Cr Kα) 測定を行うことは, 中性子不足核としてE.C. 壊変のみであるために感度が不十分である。高感度に測るためには現在の所中性子放射化法が賞用されている。その原理は中性子捕獲、80b[1]、によってその一部を半減期の短い^{54}Mn(312d) に変換し、その835keVγにより、測定感度を1000倍以上にするものである。1965年にH. Millard [2] によって考案された方法であるが、1969年以降今村等[3]によって実用化されてきた。通常原子炉中性子は高速中性子を含んでいるために、普通のマンガン, ^{55}Mnが存在すると (n, 2n) 反応によって妨害を受ける。通常Fe/Mnが1000以上であれば、よく熱化した線束が利用出来れば問題は少ないとされている。新3号炉の

研究施設・装置
JRR-3M DR-1

研究分野
宇宙化学

利用に際しては特にDR孔の上部に照射カプセルを設置することによってこの目的の実現化ををかなり高めることが出来た。これは我々ユーザーの要望を容れて対処された原研側の努力によるものである。

現在，隕石の中から金属鉄の部分を取り出して、鉄隕石とまったく同様に扱って、化学処理する方法をとっている。然しながら最も普通の隕石として存在度の高いコンドライト、球粒隕石、に対しては後1桁高速中性子が下げられれば適用できるのであるが、残念ながら旧3号炉のような利用が出来ないのは残念である。

1970年代以降30年近く同じ方法を踏襲してきているのはむしろ驚くべきことと言わなければならないであろう。それほどこの測定が半永久的な要求によって遂行されていることを示しているものといえよう。

2. 実験

1) 測定条件

Table 1a,b に示したような条件で行った。化学収率は50%位であったが同時に同一試料から^{10}Beや^{26}Al等も測定するのでこの程度になるのはやむを得ないであろう。精製したマンガン中のの不純物はGe半導体検出器によるγ線測定に対してほとんど妨害は見られなかった。放射能としては、^{192}Ir, ^{51}Cr, ^{46}Sc, ^{60}Coなどがみられた。^{55}Mn(n, 2n)の妨害は担体として加える100μgMn位の共存ではほとんど問題にならない。

1回の照射に対し20個以上のサンプル処理が実用的におこなわれおり手ごろな方法を提供している。ただし

a) 照射時間として1サイクル、600時間を標準としているので、年に1－2回にまとめなければならない。

b) 照射前のサンプル処理と化学処理及び照射後にそれぞれ化学処理をして精製せねばならない。特にFeから副成する^{54}MnはMnの5倍に相当するので鉄は充分除去して10μg以

Table 1a 照射実験条件－Co monitorによる中性子線束

	^{60}Co (cpm/ μg Co)	Neutron flux (x10^{12}n/cm^{2}sec)
T9611		
low (3.5cm)	16400	4.0
high (4.5cm)	14789	3.6
T9801		
low (3cm)	14481	3.5
high (4cm)	13427	3.3

one cycle, 25 d irrad., DR1, the lowest position. 3.7x10^{12} n_{th}/cm^{2}s, total dose: 8x10^{18} n/cm^2; thermal flux in the unit of 10^{12}n/cm^{2}s can be expressed by 4.01 − 0.0145 × d + 1.36x10^{-5} × d^2 (R=0.999), d: 0-400 in mm from the bottom. Roughly about ±3 %/cm. (n cm): approx. from the lowest end of hydrauric rabbit. used 2.0% for 1333 keV gamma of Co-60, before sum peak correction.

Table 1b JRR3,DR-1を利用する放射化法

Run year,month	dpm^{54}Mn /dpm^{53}Mn	^{53}Mn(n,γ)/^{55}Mn(n,2n) (dpm/dpm)/(dpm/mg)	^{60}Co(n,γ)/^{53}Mn(n,γ)# (dpm/μg)/(dpm/dpm)
1995(T9502)			
3 cm	1116±41	(32)	
10cm	935±38	37 ±2.4	
18cm	618±25	(42)	
1995(T9508)			
3 cm			
18cm	825±58	31.7 ±3	
1996(T9602)			
4cm	2975±45	27.0 ±1.4	
7cm	2375±48	32.2 ±4.2	
1996(T9611)			
3.5 cm	1925±60	[22.6]*	13.3
4.5cm	1925±60		12.0
1998(T9801)			
3 cm	1675±27	33.5 ±0.6	13.5
5cm	?		

count. effic. cpm/dpm = 4.0% for 835keVγ

Mn-53 standard can be replaced with Co monitor.

*: too low, due to too high Mn(n,2n) data.

‡: about 250 in old JRR3 VG7-6, which is 7.5 times better than JRR3, with 2x10^{18} n/cm^2/cycle.

下(equivalent to <50 μgMn) にしなければならないが、其の程度の存在は肉眼でも観察できるので通常はほとんど問題になることはない。

c) 前記のように1000ppmMn/Feをこえる試料には適用できない。

d) 測定感度：1dpm^{53}Mn/kgFe以下の試料に対して試料1グラムではやや不足である。

等々の制約がある。

3. 結果と考察

3. 1 隕石に対する分析例

Table 2 (及びFig.1)に最近3年間の分析例を示した。多くのものは、鉄隕石、石鉄隕石の金属部分、コンドライトの金属部分を試料としている。特に大型の隕石中の表面付近から1000g/cm^{2}位の深さまでの分布を取っていて^{53}Mnの濃度にして3桁くらいの広い幅をカバーしているのが特徴であり、ほかの放射能の^{10}Be, ^{26}Al, ^{36}Cl等のほか、安定な稀ガスのデータと比較している.測定値につけた誤差は試料の計数の統計と標準試料のそれとの複合値を取っている。標準試料で既に2～3%を示しているので総合的に3%を下回るものは少ない。そのほか原子吸光法による回収率の誤差も考慮する必要がある。モニターとしてつねに^{53}Mnの標準を使用することが望ましいがCo等を利用することも出来る。勿論濃度既知の鉄隕石を同時に比較試料として使用してもよいが、測定の手順が増加するのであまりよくない。^{53}Mnの標準試料をいまだに鉄隕石のような天然物から分離した物に頼っていることはおかしなことである。人工的に調製する方法も可能ではあるが、あまり一般的に行われていない。測定値は隕石の場合最高で600dpm^{53}Mn／kgFeまで分布している一

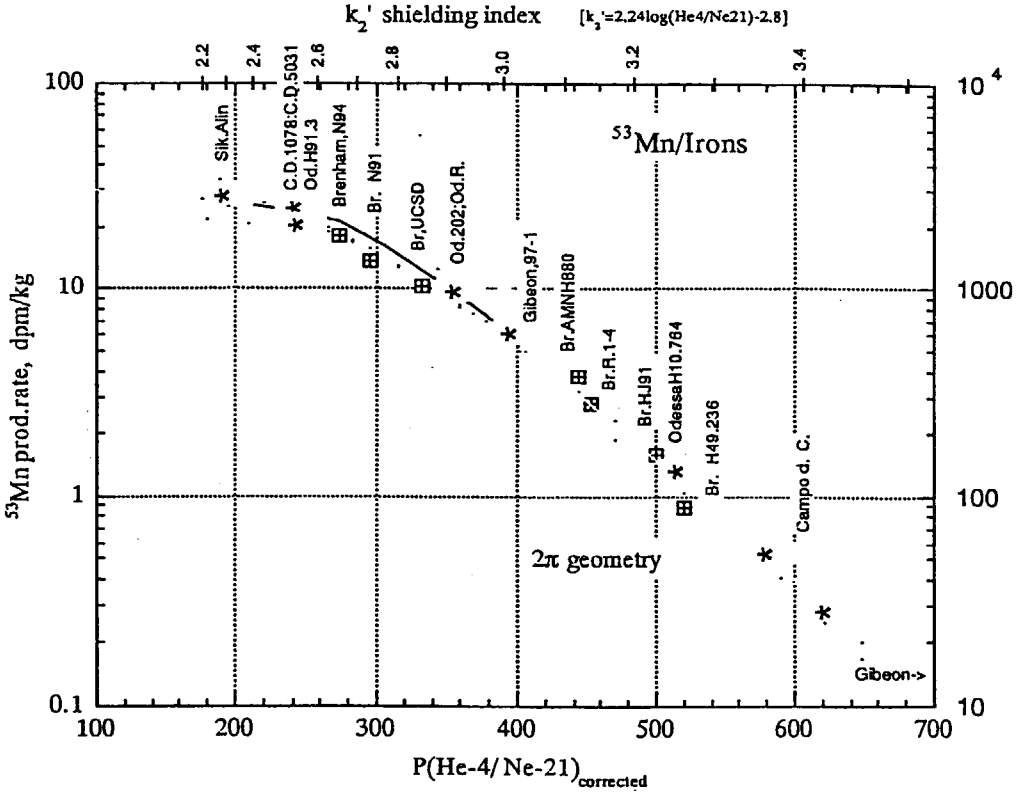

Fig. 1 Examples of ^{53}Mn data found in Meteorites

Production rates found in metallic fraction in large irons and large stony iron meteorites as a function of production ratios of He-4 / Ne-21, a shielding measure in irons. They can equally be classified into a group of 2 π geometry products.

方大型の鉄隕石では上記の様な最低感度，1dpm/kg, を下回ることも珍しくない。

3. 2．本法の実施状況及び将来性

1) ^{53}Mn の重要性については広く認められているが、放射化法の導入実施は容易ではないので広く行われているわけではない。特に適当な原子炉内の照射位置の選択に困難がともなう上化学操作が面倒である為に普及していない。近年，1985-1990 に発表された測定結果でも系統的な誤差や再現性に問題が多い。ドイツで始められているようにAMS法に切り替えられる傾向にあるが精度等まだ問題が残されている。

2) 現在の処理能力を抜本的に改善するためには旧3号炉のように今よりけた違いによい照射位置を見出してコンドライトでもそのまま測定できるようにすることである。今より20年前のほうがはるかに進んでいたといえる。

3) ^{53}Mn 測定値の絶対値は再検定が必要である。標準の^{54}Mn と比較して、X線測定による絶対測定が期待されるが、分析データの集積に追われているのでこのような地味な仕事は、何時の間にか置き忘れられているといえる。少なくとも鉄隕石より担体なしにマンガンを分離精製して、比放射能の高い高純度^{53}Mn 試料を研究者に配布出来るような体制を検討すべきであろう。

4) ^{53}Mn の生成機構のうち標的の違い、Fe / Ni の相対比を正しく見積もることが必要である。原子質量数はそれぞれ56と59に置くことが出来るであろうが、さらにその効果を量的に表現することが求められる。ΔAの違いを遮蔽係数の関数として量的に表現せねばならない。実験的にFe/Niに大きな開きのある試料について比較測定を行う必要がある。

4．おわりに

既に述べて来たように、^{53}Mn の分析方法としては、現在の処放射化法に頼らざるを得ないので、引き続き同一の内容で利用申請を行っている。また、さらに条件の良い照射位置を探すことも引き続き行う予定である。

[文献]

1). M. Imamura, H.Matsuda, K.Horie and M.Honda (1969) EPSL 6, 165-172.

2). M.Honda and M.Imamura (1971) Phys. Rev., C4, 1182-1188.

3) H.T. Millard Jr.(1965) Thermal neutron activation: Measurement of cross section of manganese-53, Science, 147, 503.

[成果の公表]

1) M.Honda and H.Nagai, "Minor components in Antarctic iron meteorites.", 20th NIPR Symposium on Antarctic Meteorites, (1995.6, Tokyo)

2) M. Honda, H. Nagai, K. Nagao and Y. Miura, "Cosmogenic nuclides in the Pallasite.", Todai International Symposium on Cosmochronology and Isotope Geoscience (1996.1, Tokyo)

3) M.Honda, H.Nagai, K.Nagao and Y.N.Miura , "Cosmogenic products in metal phase of the Brenham pallasite.", 21st NIPR Symposium on Antarctic Meteorites, (1996.6, Tokyo)

4) M.Honda, H.Nagai, K.Nagao and Y.N.Miura , "Cosmogenic nuclides in the Brenham pallasite.", 59th Annual Meeting of the Meteoritical Society, (1996.7, Berlin, Germany),Meteoritics, 31, A63-A64(1997)

5) M.Honda, H.Nagai, and T.Kobayashi "Cosmogenic Radionuclides in Large iron Meteorites.",61st Annual Meeting of the Meteoritical Society, (1998.7, Dublin, Ireland)

Table 2 隕石中の ^{53}Mn

Irrad.	Sample	Class	ID		Source	wt. (mg)	^{53}Mn (dpm/kg)	(±)
T9S08	Grant	IIIB	G320		USNMWas.D.C.'76	51.7	523	44
3.1%	Tsarev	H5	#15384	m	Shuk.'92	120	98	7
	Tsarev	H5	#15380	m	Shuk.'92	81.6	86	9
	Tsarev	H5	#15387	m	Shuk.'92	99	49	6
	Brenham	Pal.	HJ91	m	Huss'91	1103	16.4	1.2
	Brenham	Pal.	H49.236	m	Huss'87	1460	9.8	0.8
	Zagora	IA			B.Reed'90	162.6	410	24
	Toluca	IA	H27.36		G.Huss'87	828	62	6
	Toluca	IA	H128.388		Huss'63	1000	54	4
	Warburton Range	IVB			D.New'87	168	404	26
	Tocopilla	Hexh.IIA			D.New'86	141	245	12
	Campod.Cielo	IA			D.New'86	2684	2.0	0.2
	Gibeon	IVA			D.New'86	2865	2.4	0.2
	Canyon Diablo	IA	H34.5031		Huss'66	920	170	7
	Canyon Diablo	IA	H37.1078		Huss'88	1050	206	10
	Odessa	IA	H910.202		Huss'63	1286	94	5
	Odessa	IA	H10.764		Huss'87	709	16	1
T9602	Brenham	Pal.	N91	m	D.New'91	1156	121	5
hi:2%			N94	m	D.New'94	633	175	7
lo:1.5%			R3	m	Reed'91	1378	22	1
			R2	m	Reed'91	983	27	1.4
			AMNH880	m	M.Prinz'95	598	27	1.4
			WardLJS	m	WardShima'63	3084	0.8	0.2
			WardLJS	m	WardShima'63	2049	0.8	0.2
	Dora	Pal.		m	Huss'68	1013	378	14
	Trenton	III A	All-6+Z		Hintenberger'70	493	365	17
			AII-22+2		Hintenberger'70	230	379	16
			AII+14+2		Hintenberger'70	188	373	15
	Merceditas	III A	Chile		D.New'88	353.5	478	23
	ChihuahuaCity	An.			D.New'89	475	250	11
	Y793598				NIPR'95	533	96	5
	DRP78001				NIPR'95	979	87	4
T9611	Brenham	Pal.	N94	m	New'94	562	175	7
3.3%			HJ91	m	Huss'91	662	20	1.2
			AMNH881	m	M.Prinz'96	705	3.2	0.6
	Charcas	IIIA			P.Signer'60	347	506	20
	Sikhote-Alin	IIB			D.New'88	320	317	13
	Chinga	II			D.New'88	748	159	8
	Ocotillo	IA	found'90		D.New'92	691	524	21
	Odessa	IA	H91-3		Huss'63	1051	215	9
			H91-3		Huss'63	636	211	10
	Huckitta			m	Kanazawa#487	139	183	9
T9801	CapeYork	IIIA			Casper'97	997	8.0	0.4
	Canyon Diablo	IA	H37.1078		Huss'88	231	188	7
			H34.5031		Huss'66	1026	198	6
	Odessa	IA	H10.762		Huss'87	385	68.1	3
	Toluca	IAOm	H128.388		Huss'63	655	40.6	2
	Xiquipileo(Toluca)		H128.400		Huss'63	766	112	4
	Giheon	IVA	No.1		Casper'97	698	54	2
			No.2		Casper'97	623	0.8	0.4
			No.3		Casper'97	798	1.9	0.6
			No.5		Casper'97	1322	0.3	0.2
			No.10		Casper'97	292	3.3	0.5

m: metal fraction 60-'97: date received. Shuk.: Y.A.Shukolyukov, Moscow
Huss: G.Huss, Am.Meteor.Lab.,Denver,Col. Ward: received originally from Ward, N.Y. in 1958

This is a blank page.

5. ＲＩの製造
(Production of Radio Isotopes)

This is a blank page.

中性多座配位子を用いるランタニド(Ⅲ)の抽出・選択性

Extractability and Selectivity of Lanthanide(III) Ions with Neutral Multidentate Ligands

井村久則，大橋弘三郎，石倉美保子，亀田直弘，
吉田善行[1]，木村貴海[1]，目黒義弘[1]
茨城大学理学部
[1]原研先端基礎研究センター・アクチノイド溶液化学研究グループ
H.Imura, K.Ohashi, M.Ishikura, N.Kameta, Z.Yoshida[1], T.Kimura[1] and Y.Meguro[1]
Department of Environmental Sciences, Faculty of Science, Ibaraki University
[1]Advanced Science Research Center, Japan Atomic Energy Research Institute

ランタニド(Ⅲ)（Ln）の分離化学は，原子力の分野を初め，材料科学，資源科学，環境科学などの諸分野において重要な研究課題となっている。研究代表者らは，これまでに様々な酸性抽出剤と中性配位子を用いる溶媒抽出系，いわゆる協同効果系におけるLnの抽出化学を研究してきた。その中で，中性配位子としてマクロサイクリックな多座配位子である18-クラウン-6(18C6)を，特定の酸性抽出剤及び有機溶媒と組み合わせた場合に，一般の抽出系とは異なって原子番号の小さなランタニドの方が優先的に抽出され，その選択性も極めて高くなることを見出している。すなわち，強酸性カルボン酸であるペルフルオロオクタン酸－1,2-ジクロロエタン系[1]並びに－ベンゼン系[2]，また，酸性の強いβ-ジケトンであるヘキサフルオロアセチルアセトン(Hhfa)－ニトロベンゼン系[3]において，軽Lnに対する高い選択性が現れることを報告した。

本研究では，上述の特異な選択性を理解するために，強酸性カルボン酸として，より簡単な化合物であるトリクロロ酢酸（Htca）を用い，La及びEuの18C6による抽出並びにそれらの抽出錯体の水和と構造について，レーザー誘起蛍光分光法，^{1}H NMR等により研究した。また，Lnの放射性トレーサーを用いHhfa-18C6-ニトロベンゼン系の抽出平衡を詳細に検討し，抽出種の組成を明らかにするとともにその水和と構造についても上記の分光法により検討した。一方，研究代表者らは極最近，配位飽和で置換不活性なコバルト(Ⅲ)キレートが強いルイス塩基性を有し，中性（多座）配位子として働き得るという注目すべき事実を見いだしており，ここではテノイルトリフルオロアセトン(Htta)とトリス（8-キノリノラト）コバルト(Ⅲ)（$Co(q)_3$）によるLa，Eu，Luの抽出特性を詳細に研究した。

実験

放射性同位体，^{140}La，^{141}Ce，^{142}Pr，^{147}Nd，^{153}Sm，^{152,154}Eu，^{153}Gd，^{160}Tb，^{170}Tm，^{177}Luは対応するLnの硝酸塩をJRR-3内で熱中性子照射して製造した。Hhfa，Htta，18C6はそれぞれ蒸留，真空昇華，再結晶により精製した。$Co(q)_3$は文献を参考に合成し，抽出，シリカゲルクロマトグラフィー，再結晶によって精製した。元素分析，HPLC，^{1}H NMR等により，高純度のmer-$Co(q)_3$であることを確認した。

上記の放射性同位体でラベルしたLnを含む0.10 M(H,Li)ClO_4の水相をHhfa及び18C6を含む同体積のニトロベンゼンと25℃で1時間振とうした。抽出後，NaI(Tl)シンチレーションカウンターにより両相の放射能を測定し分配比（D）を算出した。水相のpHは相分離後直ちにガラス電極により測定した。なおLnの分配比はＩＣＰ発光分析法によっても求めた。

最適化した抽出条件下で，LaあるいはEuを抽出し，その抽出錯体の^{1}H NMR(La及びEu)，レーザー誘起蛍光寿命(Eu)などを測定した。

原子炉：JRR-3　水力照射設備
時間分解レーザー誘起蛍光分光装置

分　野：RI製造(トレーサー)，溶液化学，
放射分析化学

結果と考察

Htca-18C6-1,2-ジクロロエタン系

Fig.1にLaとEuのlogDとpHの関係を示す。HtcaはpK_a=-0.46の強酸であり，このpH領域では完全解離し陰イオンとして水相に存在する。そのためLnの抽出はpHに依存しない。Laに対する高い選択性とともにLiClによる大きな塩析効果がみられる。抽出種の組成を決定するため，常法に従い抽出平衡の解析を行った。LiClの存在の如何に関わらず，logDと$\log[tca^-]$のプロットは，いずれのLnも傾き3の直線となり，また$\log D$と$\log[18C6]_{org}$のプロットは傾き1の直線関係を示した。以上より，主な抽出種は$Ln(tca)_3(18C6)$であることが分かった。

抽出錯体の水和及び構造について検討するために，有機相に抽出した$Eu(tca)_3(18C6)$のレーザー誘起蛍光スペクトル並びに蛍光寿命により，中心金属Eu^{3+}の内配位圏の水和について調べた。pH 3 - 4の1 M Li(tca)(あるいは2 M LiCl共存) 水溶液，並びにその重水溶液から，0.1 M 18C6を含む有機相にEuを抽出し，$^7F_0 \rightarrow {}^5D_0$の励起スペクトルを測定した．発光は616.5nmでモニターした。重水溶液からの抽出種の励起スペクトルには578.4nmと579.1nmに二つの極大がみられ，少なくとも2種類の構造の異なる$Eu(tca)_3(18C6)$錯体が存在することが分かった。水及び重水溶液からの抽出種についてそれぞれの励起極大波長での蛍光の減衰速度定数$k(H_2O)ms^{-1}$と$k(D_2O)ms^{-1}$を求め，$n = 1.05(k(H_2O) - k(D_2O))$より配位水分子数(n)を算出した。25°Cではそれぞれの極大は主として1水和錯体と2水和錯体に対応しており，40°Cではいずれも1水和錯体となることが分かった。またこのような水和は水相のLiClにはほとんど影響されなかった。溶液中でのEuの配位数が一般に8から9であることを考えると，抽出錯体は$[Eu(tca)(18C6)(H_2O)_n]2tca$ (n=1,2)あるいは$[Eu(tca)_2(18C6)(H_2O)]tca$と推察される。一方Laの場合には，カールフィッシャー滴定により抽出錯体が1水和物であることが分かり，$[La(tca)_2(18C6)(H_2O)]tca$の抽出が考えられる。従って，Ln-18C6錯体の水和と電荷の違い（イオン対内での）が抽出の選択性を支配する重要な因子であると言える。

Hhfa-18C6-ニトロベンゼン系

この系では，酸性抽出剤Hhfaのみによっても

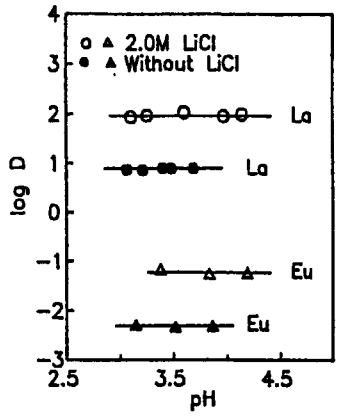

Fig.1. Extraction of Ln with 0.01 M 18C6 in 1,2-dichloroethane and 1 M Litca in the presence or absence of LiCl.

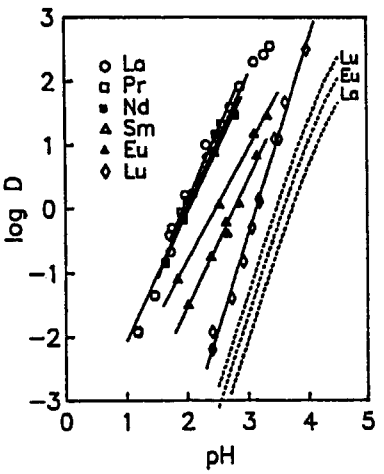

Fig.2. Extraction of Ln with 0.01 M Hhfa and 0.01 M 18C6 in nitrobenzene. Dotted lines: 0.01 M Hhfa alone.

Lnが抽出されるため，まずその抽出平衡を調べた。Lnの抽出種はすべて$Ln(hfa)_3$であり，抽出定数$K_{ex}(=[Ln(hfa)_3]_{org}[H^+]^3/[Ln^{3+}][Hhfa]_{org}^3)$を求めることができた。$K_{ex}$は一般の抽出系で見られるようにLnの原子番号順に増大したが，元素間の差はHttaなどで見られるものよりもはるかに小さかった。これは，18C6を用いて原子番号の小さなLnを選択的に抽出する際に有利に働く重要な性質であると考えられる。

Fig.2に0.010 M Hhfaと0.010 M 18C6によるLnの抽出曲線を示す。図中の点線は，0.01 M Hhfa単独による抽出曲線であり，18C6の共存により原子番号の小さなLnの抽出が著しく増大している。

La-Ndの抽出性は互いに接近し，その後抽出性は原子番号順に減少し，特に中Lnで元素間の差が大きくなっている。プロットの傾きは軽-中Lnで約2，重Ln（この図にはLuしかないがTmも）では約3となり，前者では２分子のhfa⁻が，後者では３分子のhfa⁻の関与が予想される。実際にLaについては，logD-log[hfa⁻]プロットが傾き2.0の直線となり，2分子のhfa⁻の関与が確認できた。

Fig.3にはLaのlogDと有機相中の18C6濃度の対数との関係をプロットする。ここで，ニトロベンゼンのような高誘電率溶媒中ではイオン対の解離が起こるため，テトラブチルアンモニウム（TBA^+）塩を加えて有機相中のイオン強度を$TBA^+ClO_4^-$により一定に保った。TBA^+濃度（イオン強度）によって分配比は変化するが，いずれも傾き１の直線となり，抽出錯体に１分子の18C6が含まれることが確かめられた。従って電気的中性の原理より抽出反応は次のように書くことができる。

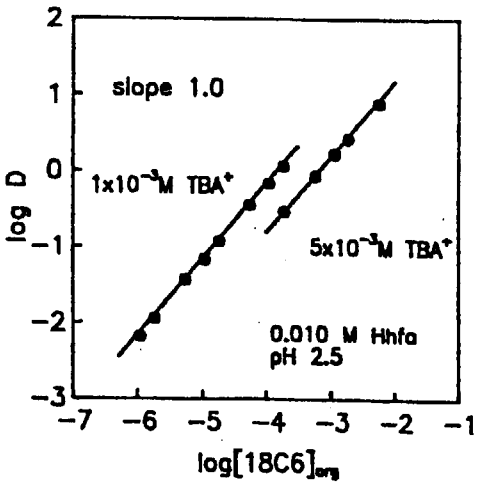

Fig.3. Effect of the 18C6 concentration in the organic phase on the extraction of Ln with 0.01 M Hhfa in the presence of different amounts of TBA^+.

$$La^{3+} + 2\ Hhfa_{org} + 18C6_{org} + ClO_4^- \rightleftharpoons La(hfa)_2(18C6)_{org}^+ + 2\ H^+ + ClO_{4\,org}^- \quad (1)$$

これより，Laの分配比が有機相中の ClO_4^-すなわち，TBA^+濃度の影響を受けることが理解できる。実際，TBA^+の全濃度を変化させて抽出を行い，分配比の対数と有機相中の ClO_4^-活量の対数をプロットすると傾き-1の直線関係が得られ，抽出が(1)式で説明できることを確かめた。La以外でもTBA^+存在下での解析を試みた結果，重LnではlogD-pHプロットの傾きが4に近づくことが分かった。これはTBA^+によって陰イオン錯体$Ln(hfa)_4^-$が抽出されるためと考えられる。ニトロベンゼン中ではイオン性化学種が安定化されるため，hfa^-との結合が弱く18C6の空孔サイズにより適合した軽Ln（特にLa）では$Ln(hfa)_2(18C6)^+$が抽出され，hfaとの結合がより強い重Lnでは$Ln(hfa)_3(18C6)$あるいは$Ln(hfa)_4^-$が抽出されるものと推察される。

抽出錯体の構造に関する知見を得るために，^1H NMR測定を行った。重水素化ニトロベンゼンに抽出された$La(hfa)_2(18C6)^+$中の18C6のCH_2プロトンは4.141ppmに鋭いシングレットのピークを与えることから，NMR時間スケール内では18C6の６個の酸素原子は等価であることが分かった。またこの化学シフトは遊離の18C6に比べて0.477ppm低磁場側へシフトしており，上で述べた$La(tca)_3(18C6)$での化学シフト3.960ppmよりもさらに0.2ppm近くも低磁場にシフトしており，Laと18C6の相互作用がより強いことを示唆している。

ニトロベンゼンに抽出した$Eu(hfa)_3$及び$Eu(hfa)_2(18C6)^+$の蛍光寿命を，励起波長465nm，検出波長612nmで測定したところ，両者の錯体で寿命（減衰速度定数）に大きな差は見られなかった。これは中心金属への水和数が同程度であることを示す結果であるが，さらなる検討を要すると考えている。

Htta-$Co(q)_3$-ベンゼン系

1×10^{-2} M HttaによるLnの抽出において，僅か3×10^{-4} Mの$Co(q)_3$を共存させるとその分配比は，Laで30倍，Euで10倍，Luで4倍高くなり大きな協同効果が観察された。この現象は次のように理解される。

$$Ln^{3+} + 3\ Htta_{org} + m\ Co(q)_{3\,org} \rightleftharpoons Ln(tta)_3(Co(q)_3)_{m\,org} + 3\ H^+ \quad (2)$$

Fig.4には，3×10^{-4} Mの$Co(q)_3$と$(0.5 - 5) \times 10^{-2}$ MのHttaによる抽出曲線を示す。いずれの系でも水相中のtta^-濃度に対し傾き3の直線を与えることから，常に3分子のtta^-が抽出錯体に含まれることが分かる。

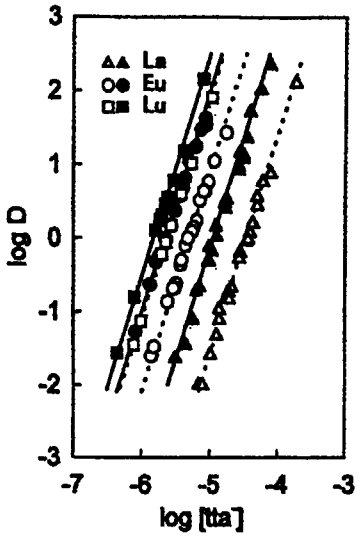

Fig.4. Effect of the tta concentration on the extraction of Ln with (0.5-5) x 10^{-2} M Htta and 3 x 10^{-4} M $Co(q)_3$.

Htta単独でのLnの分配比をD_0, $Co(q)_3$共存下における分配比をDとすると, $\log(D/D_0) = \log(1 + \Sigma\beta_{n,n}[Co(q)_3]_{org}^{n})$が成り立つ。ここで$\beta_{n,n}$は有機相中での$Ln(tta)_3(Co(q)_3)_n$の生成定数である。$\log(D/D_0)$に対して$Co(q)_3$濃度の対数をプロットするとその濃度の高い領域で, いずれのLnも傾き1の直線に近づいた。このことから$Co(q)_3$1分子が関与していることが分かり, n=1として$\beta_{n,1}$を求めた。その値はLaで$10^{4.96}$, Euで$10^{4.56}$, Luで$10^{3.97}$となり, 非常に安定な複核錯体が生成することが明らかになった。

さらに$Co(q)_3$の配位子吸収バンド(400nm付近)が$Ln(tta)_3$の添加によってシフトし, また同時に等吸収点が現れることを見いだした。これは$Co(q)_3$と$Ln(tta)_3$間での単一の化学平衡—複核錯体の生成平衡—があることを支持する。この吸収スペクトル変化の解析から$\beta_{n,1}$を求めたところ, 抽出によって得た値とほぼ一致する結果を得た。一方, $Eu(tta)_3$及び$Eu(tta)_3(Co(q)_3)$の蛍光寿命を測定したところ, 後者ではその寿命は著しく短くなり, 強いクエンチングを受けることが分かった。

参考文献

1)H. Imura, Z. Yoshida, K. Ohashi, M. Ishikura, H. Mito and Y. Meguro, Progress Report of the Inter-University Collaborative Use of JAERI Facilities, Vol. 34, p. 108, 1994.

2)H. Imura and H. Mito, J. Radioanal. Nucl. Chem., 189, 229 (1995).

3)H. Imura, Z. Yoshida, K. Ohashi, H. Mito and Y. Meguro, Progress Report of the Inter-University Collaborative Use of JAERI Facilities, Vol. 33, p. 95, 1993.

成果の公表

1)井村久則, 水戸英樹, 斎藤洋子, 大橋弘三郎, 目黒義弘, 吉田善行, G. R. Choppin ; ハロゲン化カルボン酸—18-クラウン-6協同効果系における希土類(III)の抽出性と抽出種の水和 ; 希土類討論会, 東京, 1995年5月

2)井村久則, 斎藤洋子, 大橋弘三郎, 目黒義弘, 吉田善行, G. R. Choppin ; 18-クラウン-6とトリクロロ酢酸により抽出されたLa及びEu錯体のキャラクタリゼーション ; 希土類討論会, 京都, 1996年5月

3)H. Imura, Y. Saito, K. Ohashi, Y. Meguro, Z. Yoshida and G. R. Choppin; Characterization of the lanthanum(III) and europium(III) trichloroacetate complexes extracted with 18-crown-6; Solv. Extr. Ion Exch., 14, 817-832 (1996).

4)石倉美保子, 目黒義弘, 井村久則, 大橋弘三郎, 吉田善行 ; ヘキサフルオロアセチルアセトンと18-クラウン-6による希土類三元錯体の水和と抽出性に関する研究 ; 希土類討論会, 大阪, 1997年5月

5)井村久則, 亀田直弘, 長田実律, 大橋弘三郎, 木村貴海 ; トリス (8-キノリノラト) コバルト(III)共存下における希土類(III)—2-テノイルトリフルオロアセトンキレートの抽出増大現象 ; 日本分析化学会第46年会, 東京, 1997年10月

6)H. Imura; Role of Acidic Extractants in the Selective Extraction of Light Lanthanides(III) with 18-Crown-6; in "Recent Progress in Actinides Separation Chemistry", ed. by Z. Yoshida et al., World Scientific, Singapore, 1997, pp. 72-80

7)亀田直弘, 井村久則, 大橋弘三郎, 木村貴海 ; トリス (8-キノリノラト) コバルト(III)とトリス (2-テノイルトリフルオロアセトナト) ランタニド(III)間の多核錯体生成反応 ; 日本化学会第74春季年会, 京都, 1998年3月

LIX54と中性二座配位子によるランタノイド(Ⅲ)の協同効果抽出

Synergistic Extraction of Lanthanoids(Ⅲ) with LIX54 and Neutral Bidentate Ligands

東北大学素材工学研究所,八戸工業高等専門学校* 武井 周一,中村 重人*,秋葉 健一

Institute for Advanced Materials Processing Tohoku University,

Hachinohe National College of Technology*

Shuichi TAKEI, Shigeto NAKMURA*, Kenichi AKIBA

1.緒言

ランタノイド元素(Ln)は科学技術のめざましい発達に伴い，その特異な電気、磁気、光学的特性から蛍光体，磁性体やセラミックス超伝導体等、広い分野で用いられていて重要な元素群となっている。ランタノイドは化学的性質が類似しておりその相互分離は非常に難しい。ランタノイドは希土類鉱石中に含まれ、その分離回収には長い時間とコストがかかる。また、原子力の分野においては軽希土を中心に使用済み核燃料中に核分裂生成物として存在しトレーサレベルでの分離回収が重要となっている。

溶媒（液-液）抽出法は，非常に薄い溶液から高濃度の溶液まで金属イオンを抽出分離できる方法である。ランタノイドは水溶液中では通常Ⅲ価の陽イオンとして存在し、β-ジケトンのような酸性抽出剤により有機相に抽出される。ここに、さらに中性配位子を加えることにより、金属イオンの抽出が増大する場合があり、これを協同効果と呼ぶ。協同効果は抽出を増加させるが、一般に金属間の分離係数を低下させる傾向がある。一方、中性二座配位子を用いた協同効果抽出では、特定のβ-ジケトンとの組み合わせにより、分離係数の向上が見い出されている。中性二座配位子は、一般に大きな協同効果を与えるが、その分離係数への影響は未だ十分には検討されていない。

本研究では、水相への溶解度が小さいため工業的に有利と考えられる長鎖β-ジケトンのLIX54(HR)と中性二座配位子(S)である2,2'-ビピリジン(bpy)、1,10-フェナントロリン(phen)、2,9-ジメチル-1,10-フェナントロリン(dmp)を用いてランタノイド(Ⅲ)の協同効果抽出を行い抽出平衡や，分離係数について検討した。

2.実験

2.1 トレーサー溶液

液-液抽出における有機相、水相中のランタノイド濃度は、各金属の放射性同位体をトレーサーとして用いて求めた。La, Tb, Luの各酸化物をJRR-4 S-パイプ、またはJRR-3 HR-2において中性子照射して^{140}La, ^{160}Tb, ^{170}Luを製造し、溶解して硝酸溶液とした。

2.2 中性二座配位子の液-液分配

中性二座配位子単独、またはLIX54を共存させたトルエン溶液10 cm^{3}と、0.1 M硝酸ナトリウムを含む等容の水相を25℃で1時間振とうした。水相を取り出し、水酸化ナトリウム溶液を加えて十分アルカリ性とした後、新しいトルエン10 cm^{3}と振とうして中性二座配位子をトルエン相に抽出し、次に0.1 M塩酸溶液に逆抽出した。有機相中の中性二座配位子についても0.1 M塩酸溶液に逆抽出した。それぞれの水溶液中の中性二座配位子濃度を吸光光度法により求めて，有機相-水相間の分配比を算出した。

2.3 ランタノイド(Ⅲ)の液－液抽出

抽出試薬を含むトルエン溶液4 cm^{3}と、ＲＩでラベルした10^{-5} Mのランタノイド溶液4 cm^{3}を共栓付遠沈管に入れ，25℃の恒温室内で1時間振とうした。遠心分離した後，各相から2 cm^{3}分取しγ-放射能を測定してランタノイドの分配比を求めた。水相のイオン強度は硝酸ナトリウムにより0.1とし、pH緩衝溶液として10^{-3} M酢酸、または5×10^{-3} Mピペラジン-1,4-ビス(2-エタンスルホン酸) (PIPES)の水酸化ナトリウム溶液を用いた。水相の平衡pHは、ガラス電極を用いて測定した。

JRR-4 S-パイプまたはJRR-3 HR-2、　トレーサー製造，分離化学、溶媒抽出

3. 結果と考察

3.1 中性二座配位子の分配

bpy、phen、dmpの分配比D_Sを求め、pHに対して$\log D_S$をプロットした図をFig.1に示す。いずれの系でもpHとともに傾き1の直線に沿って$\log D_S$は増加し、やがて一定値となった。また、0.1 M LIX54を共存させてもほぼ同じ曲線となることから、中性二座配位子とLIX54との相互作用はないと考えられる。中性二座配位子の有機相-水相間の分配比D_Sは次式により表される。

$$D_S = \frac{[S]_{org}}{[S]_{aq}+[HS^+]_{aq}} = \frac{P_S}{1+[H^+]_{aq}/K_{HS}} \qquad (1)$$

ここでP_Sは中性二座配位子の分配係数、K_{HS}はプロトン化した中性二座配位子の酸解離定数、下付のaqは水相、orgは有機相中の化学種であることを示す。この式を用いて実験値から最小自乗法によりP_SとK_{HS}を求め、その値をTable 1に示した。

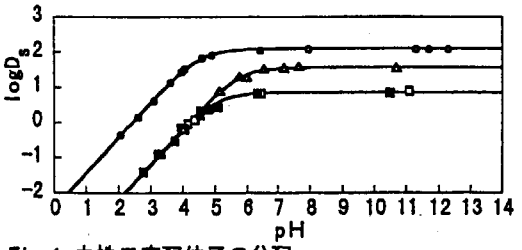

Fig.1 中性二座配位子の分配

有機相: (○) 2×10^{-3} M bpy; (●) 2×10^{-3} M bpy-0.1 M LIX54;
(△) 10^{-3} M dmp; (▲) 10^{-3} M dmp-0.1 M LIX54;
(□) 10^{-3} M phen; (■) 10^{-3} M phen-0.1 M LIX54-トルエン
水相: 0.1 M $NaNO_3$

Table 1 中性二座配位子の酸解離定数と分配係数

中性配位子	$\log K_{HS}$	$\log P_S$
bpy	-4.53	2.09
phen	-5.06	0.85
dmp	-5.76	1.56

3.2 ランタノイド(III)の抽出

ランタノイドのほぼ中間に位置するTb(III)のLIX54による抽出を行い、pHに対する金属の分配比Dの対数(log D)の変化をFig.2に示す。LIX54単独の場合と比べ、中性二座配位子が共存する場合に抽出が増大し協同効果の起こっていることがわかる。また、いずれの場合もプロットの傾きは約3となった。

LIX54濃度の対数に対するlog Dのプロットを Fig.3に示す。LIX54単独の場合でも、中性二座配位子が共存する場合でもプロットの傾きは約3となった。これは抽出化学種中に3分子のLIX54があることを示している。従って、ランタノイドイオン(M^{3+})の抽出平衡はLIX54単独の場合、

$$M^{3+}_{aq} + 3\ HR_{org} \rightleftarrows MR_{3,org} + 3\ H^+_{aq} \qquad (2)$$

となり、協同効果抽出の場合は、

$$M^{3+}_{aq} + 3\ HR_{org} + n\ S_{org} \rightleftarrows MR_3S_{n,org} + 3\ H^+_{aq} \qquad (3)$$

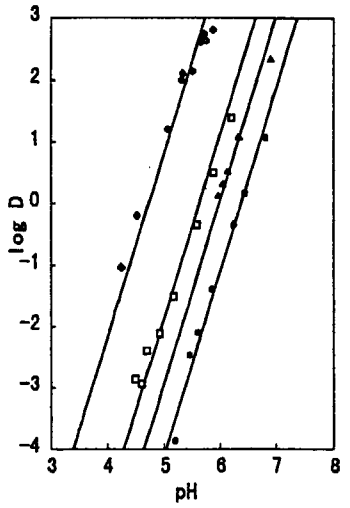

Fig.2 LIX54によるTbの抽出と中性配位子による協同効果

有機相: 10^{-1} M LIX54—(○) LIX54単独, (△) 5×10^{-2} M dmp, (□) 10^{-2} M bpy, (◇) 10^{-2} M phen—トルエン
水相: 0.1 M $NaNO_3$, 5×10^{-3} M PIPES

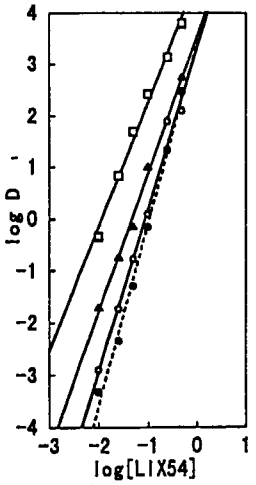

Fig.3 LIX54濃度の影響

有機相: LIX54-S-トルエン
水相: 0.1 M $NaNO_3$, 5×10^{-3} M PIPES
(●) LIX54単独, pH 6.4; (○) 10^{-2} M bpy, pH 6.4;
(△) 5×10^{-2} M dmp, pH 6.4;
(□) 10^{-2} M phen, pH 5.5

となると考えられる。ここで、それぞれの抽出定数をK_{ex}、K_{exs}とする。
LIX54単独の場合の分配比D_0は次式のように表される。

$$D_0 = \frac{[MR_3]_{org}}{[M^{3+}]_{aq}} = K_{ex} \cdot \frac{[HR]_{org}^3}{[H^+]_{aq}^3} \quad (4)$$

協同効果抽出の場合の分配比Dは次式のように表される。

$$D = \frac{[MR_3]_{org} + \sum_{n=1}^{n}[MR_3S_n]_{org}}{[M^{3+}]_{aq}} = K_{ex} \cdot \frac{[HR]_{org}^3(1+\sum_{n=1}^{n}\beta_{s,n}[S]_{org}^n)}{[H^+]_{aq}^3} \quad (5)$$

ここで、$\beta_{s,n}$は付加錯体生成定数であり、次の平衡式の平衡定数である。

$$MR_{3,org} + n\,S_{org} \rightleftarrows MR_3S_{n,org} \quad (6)$$

式(4)、(5)から次式が得られる。

$$D/D_0 = 1+\sum_{n=1}^{n}\beta_{s,n}[S]_{org}^n \quad (7)$$

この式から、有機相中にMR_3S_nの付加錯体が主に存在するとき、D/D_0は中性配位子濃度のn次に比例することが予想される。各中性二座配位子濃度の対数に対して$\log D/D_0$をプロットした図をFig.4に示す。実線はn=1と仮定して(7)式を用いて最小自乗法により求めた計算値を示す。なお、有機相中のS濃度は、P_S、K_{HS}を用いて初期濃度と平衡pHから計算により求めた。bpy、phenではほぼ傾き1の直線となり、また、dmpでは協同効果が小さいため偏差が大きいがほぼ計算値に近いことから、中性配位子が金属キレートに1分子付加していると考えられる。以上から、Tb(Ⅲ)の協同効果抽出における抽出化学種はMR_3Sであることがわかった。

ランタノイドの中で原子番号の最も小さいLa、及び最も大きいLuについて同様に抽出挙動を検討した。La(Ⅲ)の抽出におけるpHに対する$\log D$のプロットをFig.5に、Lu(Ⅲ)の場合をFig.6に示す。どちらも中性二座配位子を添加することにより協同効果の起こることがわかる。LIX54濃度、中性二座配位子濃度の分配比への影響を検討した結果、協同効果抽出における抽出化学種はTb(Ⅲ)の場合と同じくMR_3Sであることがわかった。

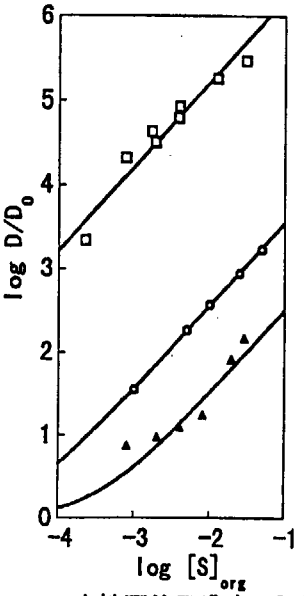

Fig.4 中性配位子濃度の影響
有機相: 10^{-1} M LIX54-S-トルエン
水 相 :0.1 M $NaNO_3$, 5×10^{-3} M PIPES
(○)bpy ; (△)dmp ; (□)phen

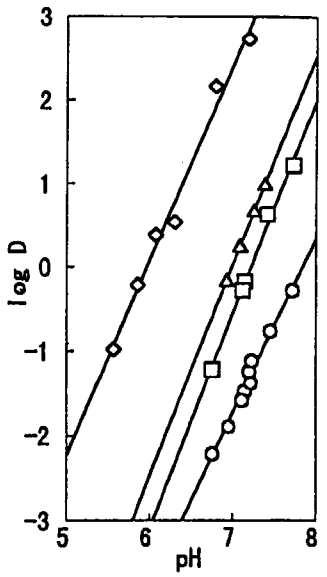

Fig.5 LIX54によるLaの抽出と
中性配位子による協同効果
有機相: 10^{-1} M LIX54−(○)LIX54単独,
(△)5×10^{-2} M dmp, (□)10^{-2} M bpy,
(◇)10^{-2} M phen−トルエン
水 相 : 0.1 M $NaNO_3$, 5×10^{-3} M, PIPES

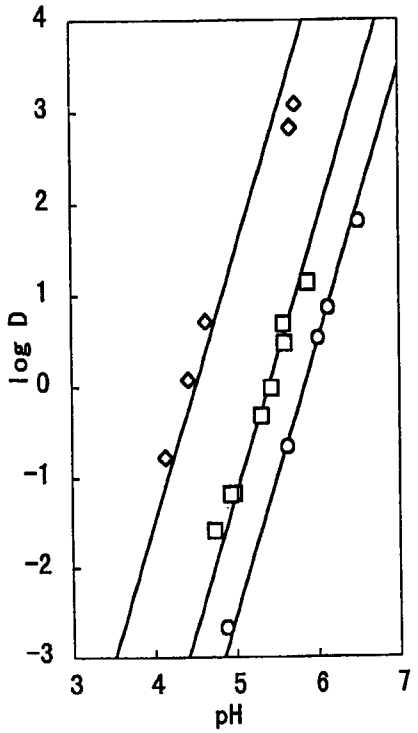

Fig. 6 LIX54によるLuの抽出と
中性配位子による協同効果
有機相: 10^{-1} M LIX54－(○)LIX54単独,
(□)10^{-2} M bpy, (◇)10^{-2} M phen－トルエン
水 相 : 0.1 M $NaNO_3$, 5×10^{-3} M, PIPES

以上から各平衡定数を求め、Table 2に示す。付加錯体生成定数はdmp<bpy<phenの順に大きくなっている。これは、bpyとphenを比べた場合、酸解離定数がphenの方が小さくてより塩基性であるためと考えられる。dmpの値が小さいのは2,9位のメチル基による立体障害と考えられる。金属間では、Tbの付加錯体生成定数が大きく、これと比べてLa、Luで小さくなっている傾向がみられる。抽出定数、協同効果抽出定数ともに原子番号順に大きくなっている。LIX54単独での分離係数と協同効果抽出における分離係数を比べるとLa-Tb間では幾分大きくなり、Tb-Lu間で小さくなる傾向が見られた。

現在、他のランタノイドについても検討を行い、データの比較検討を行っている。

[成果の公表]

「長鎖β-ジケトンと中性二座配位子によるランタノイド(Ⅲ)の協同効果抽出」, 武井 周一, 中村 重人, 秋葉 健一, 日本分析化学会第46年会

Table 2 ランタノイド(Ⅲ)の抽出における各平衡定数と分離係数

Ln(Ⅲ)	LIX54単独		bpy			phen			dmp	
	log K_{ex}	log α	log β_2	log K_{exx}	log α	log β_2	log K_{exx}	log α	log β_2	log K_{exx}
La	-19.95		3.29	-16.66		6.91	-13.04			
		3.84			4.79			3.98		
Tb	-16.11		4.24	-18.87		7.05	-9.06		3.18	-12.93
		1.58			0.60			0.46		
Lu	-14.53		3.26	-11.27		5.93	-8.60			

分離係数 $\alpha = K_{ex}(M_2)/K_{ex}(M_1)$ または $K_{exx}(M_2)/K_{exx}(M_1)$

研究テーマ：非定常放出に対するガスモニタ校正法の開発
表　　題：放射性ガスのパルス注入に対するガスモニタの応答解析

放射性ガスのパルス注入に対するガスモニタの応答解析

大石哲也、吉田　真
保健物理部線量計測課

原子力施設から放出される放射性ガスの管理にはガスモニタが使用されており、その測定精度を向上させるためには、実際の使用状態に即した校正技術が不可欠である。施設内等の空間に拡散した放射性ガスが長時間にわたり徐々に放出される場合（定常放出）に関しては、ガスモニタを含む閉ループ内に放射能濃度が既知な校正用ガスを満たして校正を行う方法（閉ループ校正法）を確立した[1),2)]。一方、放射性ガスが短時間に放出される場合や放射能濃度の急激な変化が生じる場合（非定常放出）には、ガスモニタの過渡的な応答を考慮した校正法が必要である。このため、ガスモニタに放射性ガスを短時間に注入（パルス注入）して応答特性を評価し、非定常放出においても放出放射能を精度良く評価できる校正手法（パルス注入校正法）の研究開発を実施している。

本年度は、1.5L 通気型電離箱を被校正対象モニタとして使用し、放射能既知のガスのパルス注入に対するモニタの応答の解析を行った。放射性ガスとしては、標準線源として供給された^{3}H、^{85}Kr 及び^{40}Ar(n,γ)^{41}Ar 反応に基づいて JRR-3 の気送照射設備において製造された^{41}Ar を使用した。キャリアガスとしては空気を用いた。はじめに、汚染のおそれが少なく、半減期の補正を必要としない^{85}Kr を実験に用いた。電離箱に流入する放射能の時間変化と電離箱の出力の時間変化との関係を Fig.1 に示す。流量率が 5L/min の場合、流入するガスにおける放射能の時間分布の半値幅は 1 s であるが、通常、ガスモニタはより大きな流量率で使用されるため、この半値幅はより小さくなる。流量率、圧力等を一定とし、ガスの時間分布を近似的にデルタ関数として扱うことが可能ならば、電離箱の出力はモニタの応答を決定する重み関数として扱うことができる。そこで、パルス注入によるガスの流入をデルタ関数と仮定した場合と実際の流入の場合とに分け、電離箱内の放射能の変化を決定し、この放射能から電離箱の出力値を計算で求めた。流量率 5L/min における結果を Fig.2 に示す。両者は時間的なずれを除いて良く一致している。また、このずれは、放射能の時間分布の半値幅に起因するため、より大流量率では問題にならない。^{3}H、^{41}Ar に関しても、同様によく一致した。以上により、パルス注入校正法に必要な放射性ガスの注入時間、放射能等のパラメータが決定された。

今後、一般的なガスモニタに対するパルス注入校正法の適用を行っていくとともに、非定常放出時における放出放射能評価法を確立する。

参考文献

1) 吉田　真、他: Radioisotopes, 42, (1993), pp.452-460
2) M. Yoshida, et al.: Nucl. Instr. and Meth. A 383, (1996), pp.441-446

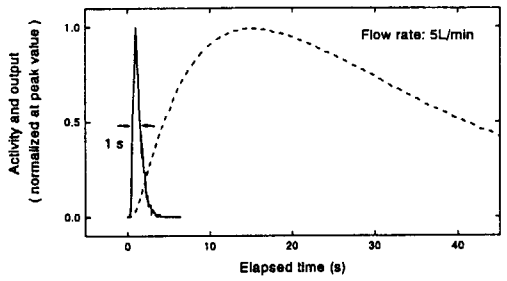

Fig.1 Activity of radioactive gas flowing into 1.5L ionization chamber (solid line) and output of ionization chamber (broken line).

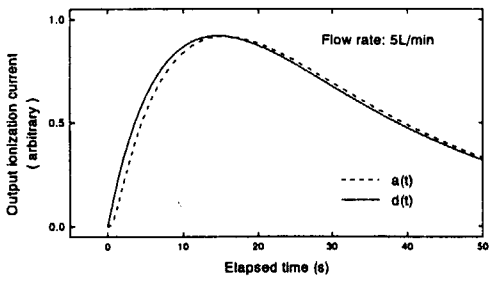

Fig.2 Output ionization current vs elapsed time for the actual injection, a(t), and the postulated injection like delta function, d(t).

原子炉：ＪＲＲ－３　　装置：気送照射設備（ＰＮ－１）　　分野：ＲＩ製造（その他）

This is a blank page.

6. 原子炉材料
(Reactor Materials)

This is a blank page.

研究課題：原子力用機能性材料の研究開発
表題：酸化リチウム焼結体からのヘリウム放出挙動

Helium Release from Neutron-Irradiated Li_2O Sintered Pellets

Takaaki Tanifuji, Daiju Yamaki and Kenji Noda
Japan Atomic Energy Research Institute, Tokai-mura, Ibaraki, Japan.

Figures 1 show the helium release curves from neutron-irradiated Li_2O specimens in the constant heating rate tests. Fig. 1 compares the release curves from various bulk density specimens irradiated up to $2x10^{19}$ n/cm^2 with thermal neutrons, and compares the release curves from 88%T.D. specimens irradiated up to various thermal neutron fluences. The helium release curves seem to consist of four peaks, that is, relatively wide peaks A (peak temperature range : 850-1050 K), and B (peak temperature range : 900-1150 K) , very wide peak C (peak temperature : around 1300 K) and narrow peak D (peak temperature : around 1350 K), as shown in fig. 1. They are divided into two groups by the bulk density dependence of the appearance. The peaks A and B appear for all specimens, while peaks C and D are remarkably observed only for the specimens with bulk density of 85% and 88%T.D, and not observed or negligible small for 71% and 80%T.D. specimens.

Baldwin et al. indicated that the retained helium in Li_2O sintered pellets irradiated with fast neutrons in EBR-Ⅱ are 12-25% of the generated helium at the irradiation temperature of 773 and 973K, while 5-10% at 1173K. In the PIE of BEATRIX-Ⅱ irradiation tests, it was found that, helium bubbles were grown-up in the irradiation temperatures range of 803-913K for Li_2O sintered ring specimens[1]. The results in this study that the main helium release peaks A and B are observed in the temperature range of 900-1150K and that the helium release started at about 800K are consistent with the results of Baldwin et al., and those of PIE in BEATRIX-Ⅱ irradiation tests.

Numerous investigations of tritium release from Li_2O have been performed using Li_2O powder, sintered pellets and single crystals in order to understand the behavior of tritium release from Li_2O. It has been clarified that tritium release process from Li_2O consists of bulk diffusion, grain boundary diffusion, surface desorption and open pore diffusion, etc. On the other hand, the helium release process has not been clarified, since there are few study on helium release behavior from Li_2O. The helium release processes are thought to consist of some diffusion and surface processes by analogy from tritium release processes. However, the surface process may be neglected, since helium atom is inert for Li_2O and sweep gas components. Thus, only some diffusion processes such as bulk diffusion in the grain, grain boundary diffusion, etc. could be taken into account.

The appearance of the peak C and D for the specimens with bulk density of 85% and 88%T.D. seems to suggest the diffusion path which exists only for Li_2O with bulk density higher than 85%T.D. In the ceramography of Li_2O sintered pellets, it was shown that the closed porosity increased with the bulk density for the density higher than 85%T.D., although the porosity was almost constant for the density lower than 85%T.D.. Therefore, there is a possibility that the helium release processes for the peak C and D are the diffusion processes with trapping at closed pores in the grains. On the other hand, the processes for the peak A and B which are appeared for all specimens are considered to be the diffusion processes through the bulk, grain boundaries and open pores, without trapping at closed pores in the grains.

Conclusion

Helium release behavior in post-irradiation heating tests was investigated for sintered Li_2O which had been irradiated with thermal neutrons in JRR-4 and JRR-2. It is clarified that the helium release curves contains of four peaks which are divided into two groups. From the activation energy of the peaks, the dependence of the peak temperatures on the neutron fluence, and the bulk density dependence of the appearance of the peaks, it is considered that the helium generated in the grain is released through the processes of bulk diffusion, grain boundary diffusion and open pore diffusion, with or without trapping at closed pores in the grains. The processes of bulk diffusion and grain boundary diffusion without trapping at closed pore were found to be affected by irradiation defects such as some defect clusters.

References

(1) T.Tanifuji, D.Yamaki and K.Noda Fusion Engineering and design 39-40(1998)723-729

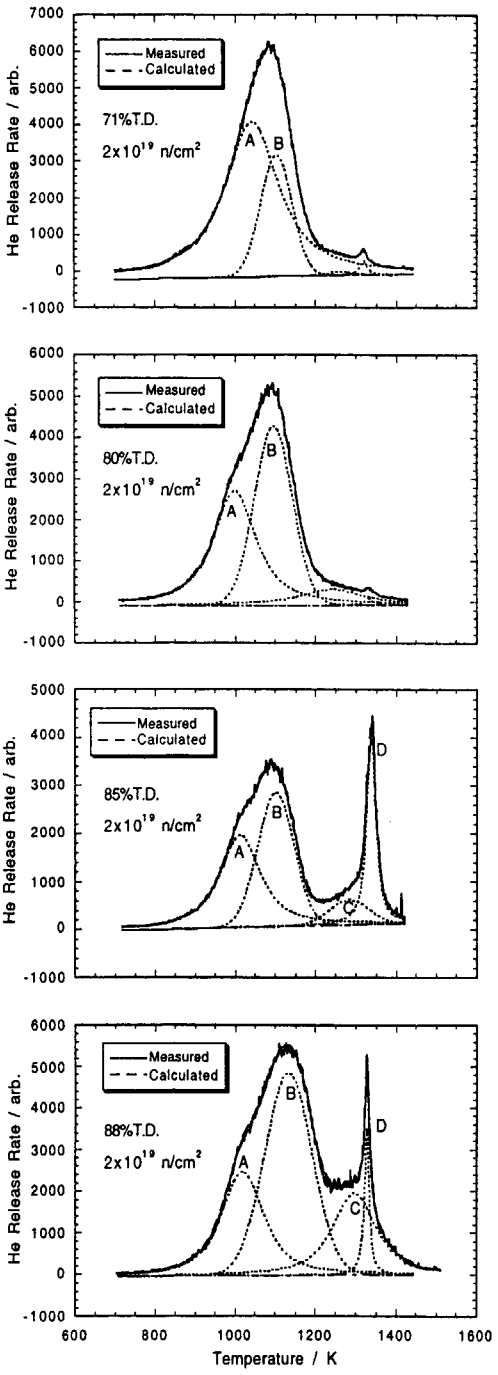

Fig.1 Helium release curve from sintered Li2O of various bulk densities.

研究テーマ：原子力用先進機能性材料の研究開発
課題：照射下セラミック材料の電気絶縁劣化特性試験

Electrical Conductivity Change in Single Crystal Al_2O_3 and MgO under Neutron and Gamma-ray Irradiation

Takaaki Tanifuji, Yoshio Katano, Tetsuya Nakazawa and Kenji Noda
Japan Atomic Energy Research Institute
Tokai-mura, Naka-gun, Ibaraki-ken 319-11 Japan

The apparent electrical conductivity at room temperature was on the order of 10^{-13} S/m for the Al_2O_3 and the MgO specimens before the capsule installation in JRR-3. Installing the capsule in JRR-3 (BR-2 irradiation position), the center, the guard and the HV source currents increased due to the residual gamma-ray ionization level (3 Gy/s or smaller) before the reactor operation start. Fig. 1 shows the center current, the guard and the HV source currents for the Al_2O_3 specimen in the first (#08-02 cycle) and the second (#08-03 cycle) irradiation cycles versus the irradiation time. In the first irradiation cycle, the temperature of the specimens were changed into 623, 673 and 723 K after the irradiation at 573 K by changing He/N_2 ratio of the flowing mixture gas. The center, the guard and the HV source currents changed with the temperature of the specimens only slightly. The HV source current was about 20 times as large as the center and the guard currents. At the reactor shutdown of the first irradiation cycle, substantial decrease of these currents took place rapidly. The current then gradually decreased with time because of decay of the gamma-ray level at the specimen position, and about 10^{-7}, 7×10^{-8} and 10^{-6} A were attained for the center, the guard and the HV source current 140 h after shutdown. Further decrease of the current level took place between the first and the second irradiation cycles and it can be attributed to further decay of the gamma-ray level. The atmosphere of mixture of He and N_2 gas was maintained during the period between the first cycle and the second cycle (102 days) to avoid contamination of specimens and the other materials inside the irradiation capsule due to moisture in the air. Just prior to the reactor start in the second irradiation cycle (gamma-ray dose rate level; 3 Gy/s or smaller) , the center current was about 5×10^{-9} A and this corresponds to an electrical conductivity of 3×10^{-9} S/m. These values are smaller than those before the reactor operation start in the first irradiation cycle.

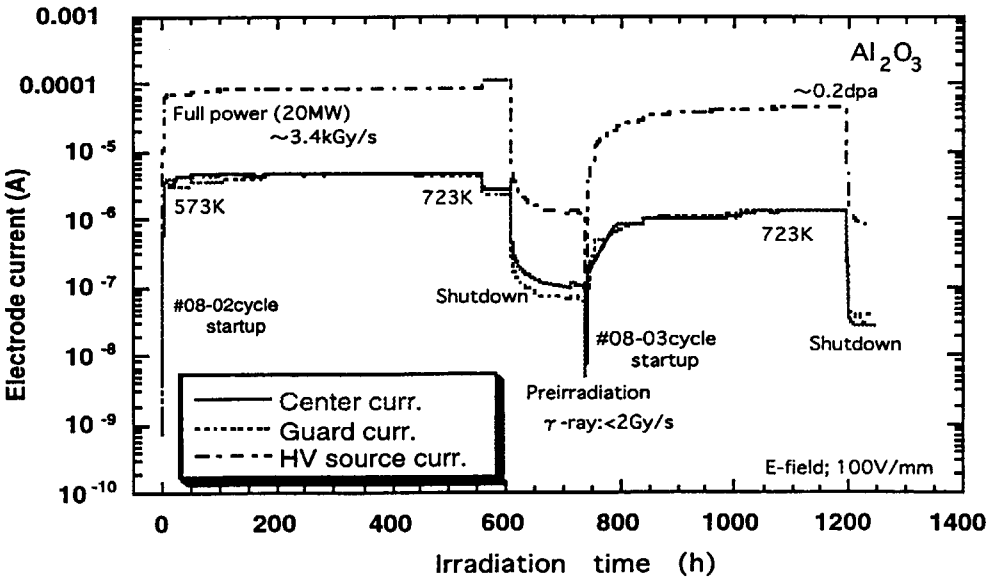

Fig.1 The center current, the guard and the HV source currents for the Al2O3.

Reactor :JRR3-M　　Facility :BR-2　　Field :Fusion Reactor

After the start of the second irradiation cycle, the center, the guard and the HV source currents increased again with the reactor power as well as the temperature of the specimen. At the full reactor power, $9x10^{-7}$, $8x10^{-7}$ and $3x10^{-5}$ A were attained for the center, the guard and the HV source currents at 573 K, respectively (The electrical conductivity of the specimen at 573 K: $5x10^{-7}$ S/m). Then, the temperature of the specimen was raised up to 723 K stepwise (i.e., 573, 673 and 723 K). The measured currents increased slightly with the temperature of the specimen. The current values measured during the second irradiation cycle were smaller than those in the first irradiation cycle. They decreased rapidly at the shutdown of the reactor in the second irradiation cycle too. The current levels measured after the shutdown were also smaller than those in the first irradiation cycle.

The conductivity calculated for the Al_2O_3 specimen is shown as a function of the gamma-ray dose rate evaluated from the rector power in fig. 2. The conductivity increased with the gamma-ray dose rate, and increase of the conductivity with the irradiation fluence was not observed up to 0.2 dpa as mentioned previously. This means that the conductivity increased with the dose rate due to RIC, but no evidence for RIED was observed. The gamma-ray dose rate dependence of the conductivity has the gradient of about 1 in log-log plot and is consistent with (somewhat higher than) the conductivity of the Al_2O_3 specimen which was measured under the ^{60}Co gamma-ray irradiation (5 Gy/s, 573 K) in the present study. Although the temperature of the specimen was raised from room temperature to 540 K due to increase of the reactor power, such conductivity dominantly depends on the gamma dose rate rather than temperature as shown in fig. 2. The increase of conductivity due to RIC arising from an increase of ionizing dose rate has been shown to be much larger than the temperature dependence of the conductivity in this temperature range, according to gamma-ray, electron and 14 MeV neutron irradiation studies on high-purity Al_2O_3.

Fig. 2 also shows a comparison between the ionizing dose rate dependence of the conductivity and the other RIC data on Al_2O_3 including the data for the same kinds of Al_2O_3 (Kyocera SA 100) in the studies of Shikama et al.. The conductivity values estimated in the present study fall within data scatter band of previous studies , although they are larger than the data in some studies such as recent work using HFIR by about one order of magnitude. This seems to suggests that the center current measurements was a reasonably accurate estimator of bulk conductivity of the specimens.

Rerferences

(1) T.Tanifuji, Y.Katano, T.Nakazawa and K.Noda J.Nucl.Mater.253(1988)156-166

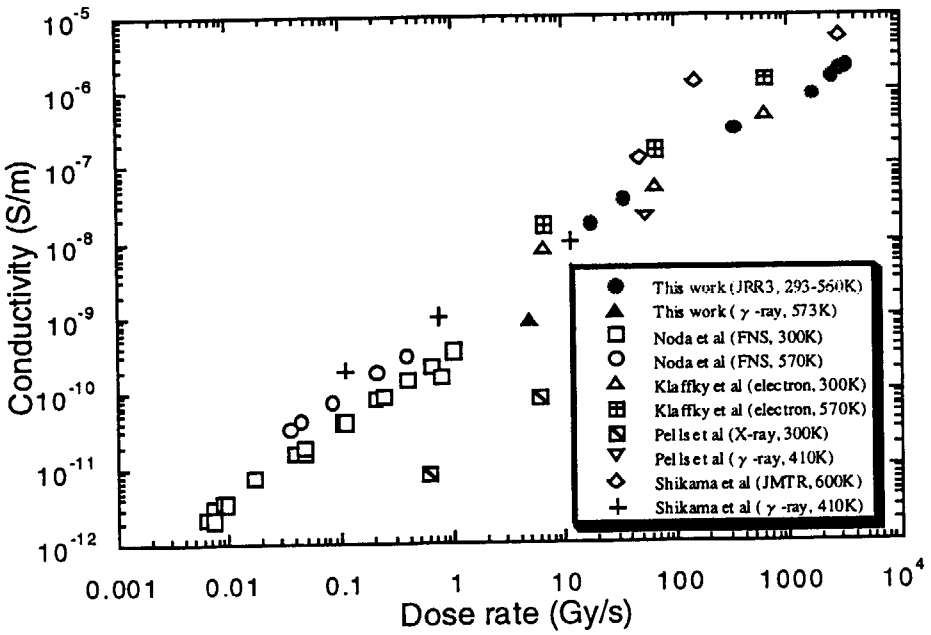

Fig.2 Comparison between the ionizing dose rate dependence of the conductivity and the other RIC data of Al2O3.

7. 核 物 理
(Nucleus Physics)

This is a blank page.

研究テーマ：アイソトープの核化学的研究

表題：マイナーアクチニドの中性子吸収断面積の測定

^{243}Am(n,γ)^{244}Am反応の中性子吸収断面積の測定

初川雄一、篠原伸夫、畑健太郎

日本原子力研究所物質科学研究部核化学研究室

放射化法を用いて^{243}Am(n,γ)^{244}Am反応の中性子反応断面積を測定した。 高純度^{243}Am試料を原研研究炉JRR-3Mにて照射を行ない、^{243}Am(n,γ)^{244g}Am反応の実効中性子断面積として3.92b、^{243}Am(n,γ)^{244m}Am反応にたいしては84.4bを得た。

マイナーアクチニドは原子炉内の連続的な中性子吸収反応により生成され、燃焼率が高まるにつれて燃料中に蓄積されてくる。 このマイナーアクチニド核種の１つである^{243}Amはα放射体であり、しかもその長い半減期（7380年）のため、長期に亘りその放射能が残留するのでこの放射性廃棄物の処理に関しては重大な関心がもたれている。 この様な長寿命核種の放射能を低減するために原子炉や加速器を用いて核反応を起こさせ短寿命の、あるいは安定な核種に変換させる消滅処理法が研究されている。この消滅処理法の基礎データとして正確な核反応断面積が必要である。 そこで本研究では詳細な^{243}Am(n,γ)^{244}Am反応の実効中性子断面積を求めた。

試料は同位体純度99.98 %の^{243}Amを約3 kBqをコルツ管に封入して、日本原子力研究所の研究用原子炉JRR-3M, HR-pipeに於いて10時間の照射を行なった。 中性子束を測定するためにモニター用の合金線（Co/Al）を共に照射カプセルに封入し照射を行った。 この位置での平均の中性子束は9.09×10^{13}n/cm^{2}sであった。照射後、HP Ge検出器を用いて照射試料のγ線測定を行い、154、744、898keV の３本の^{244g}Amからのγ線を検出した。 これら３つのγ線の半減期は報告されている^{244g}Amの半減期10.1hに誤差の範囲で一致しており^{244g}Amに起因する事がわかった。 観測されたγ線強度より^{244g}Amの生成量を見積もった。 一方26分の半減期を有する^{244m}Amは半減期が短いために今回の実験ではそのγ線は観測できなかった。 そこでγ線観測後に、^{244g}Amが十分に崩壊した後にシリコン表面障壁型検出器を用いてα線測定を行い、^{244m}Amの生成量を測定した。 すなわち^{244g}Amと^{244m}Amはβ壊変によって18.11年の半減期を有する^{244}Cmを生じるので、生成した^{244}Cmからの5.80 MeVのα線を検出する事によりその強度から^{244g}Am+^{244m}Amの生成量を得た。 得られた^{244g}Am、^{244m}Amの生成量に基づいて数値解析を行い、^{244g}Am、^{244m}Amの中性子反応断面積を求めた。

本研究により^{243}Am(n,γ)^{244g}Am反応の断面積は3.92b、^{243}Am(n,γ)^{244m}Am反応の断面積は84.4bが得られた。 今回得られた結果を文献値と比較してみると、^{243}Am(n,γ)^{244g}Am反応に対する断面積3.92bは文献値3.8±0.4b[1]と良く一致している。 一方^{243}Am(n,γ)^{244m}Am反応に対する断面積84.4bは文献値75.1±1.8b[1]と比べて10％ほど大きな値になったが、これは1976年にGarrilov[2]らによって得られた、83±6bに一致している。 今後さらにCd比法による^{243}Amの熱外中性子吸収断面積の測定を計画している。

参考文献

1)Lederer, C.M., Shirley, V.S.: Table of Isotopes, (8th ed.), John Wily & Sons, New York(1996).

2)Garrilov, V.D., Grocharov, V.A., Ivanenko, V.V., Kustov, V.N. , and Smirnov, V.P.: Atomnaya Energiya, 41, 185(1976)

原子炉：JRR-3M,　　装置：HR-pipe　　分野：核物理

^{59}Feをプローブとした強磁性体の超微細相互作用の研究

Study of hyperfine interaction in ferromagnetic alloy using 59Fe

大矢 進, 大坪 隆, 趙 徳濟*

S. Ohya, T. Ohtsubo. D.J. Cho*

新潟大学理学部

*新潟大学自然科学研究科

Faculty of Science, Niigata University.

*Graduate School of Science and Technology, Niigata University

1はじめに

この研究の目的は磁性体の鉄基合金の構造と磁性の関係を微視的に調べるものである。硅素鋼であるFeSi はこれまでメッスバウアー、核磁気共鳴などで調べられてきた. 近接の不純物効果はRKKY (Ruderman-Kittel-Kasuya-Yoshida) 理論によって振動減衰するとされているが、SiFeの場合、実際の測定結果はその測定方法及び解析方法で、各近接位置のSiの内部磁場への寄与の値は違っている. 我々はこれまで極低温偏極核の核磁気共鳴 (NMR-ON) の方法で核物性の研究を進めてきて、この方法は感度と分解能が優れている. 硅素鋼FeSi の単結晶に 60Co を表面に熱拡散させNMR-ON の方法で内部磁場の影響を調べた「1」. その共鳴線を図1に示す.

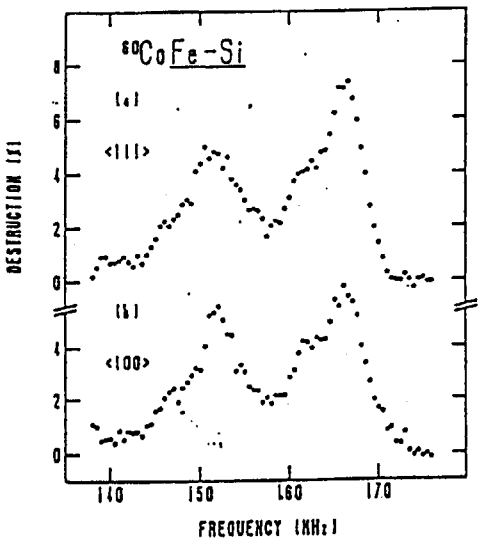

図1 60CoFeSiのNMR-ON from ref.1

60Coの共鳴線は純鉄のみですと1本で, 166 MHz 付近に出る. 結晶の一番近いサイト (第1近傍) にSi があると内部磁場は約8%減少し共鳴周波数もその分小さくなって副共鳴として現われる. 図1の152 MHz 付近の共鳴がそれである. 2近傍, 3近傍のサイトによる影響も出ているが, 分解されていない. 2近傍, 3近傍の位置を確認することでRYKK 相互作用が評価できる. これは結晶の軸を変えて測定して決定することで決定できる. この実験の場合 Fe-Si- 60Coの3核種の相関になる. 鉄のアイソトープは59Fe 以外ベータ, ガンマーの線源としてよいプローブはない. しかし59Feのガンマー線は低温での角度異方性が小さくNMR-ON でのプローブにならない. 最近、此れ迄のγ線を検出する方法では出来なかった^{59}FeFeの NMR-ONの実験にβ線を検出することによって成功した「2」。しかもそれによる共鳴線の幅も狭いため, これにより強磁性体そのものの ^{59}Feをプローブとして、超微細相互作用が観測でき精密研究が可能になった。そこでこの方法でSiFeの問題を解決すると共に強磁性体の超微細相互作用の研究を行うことを目的とした.

2. 試料の製作

NMR-ON の実験は高周波がskin depth しか入らないため試料は薄くしなければならない. SiFe の単結晶は6%のSiを含んでいる. これをエッチングの方法で約8ミクロンの厚さに薄くしたものを用いた. この結晶を4 mmΦに切ったものをJRR3 の原子炉でneutron flux of 1.0 x 1014 neutrons / cm2 sec で約100時間照射した. これにより中性子合金の鉄中の安定元素 ^{58}Fe(0.3%)の熱中性子捕獲の放射化で^{59}Fe (半減期45 d) を製作した. 強度は約2マイクロCi程度である. このあと真空中で800度で1時間の熱処理を行った.

研究施設と装置名

JRR-3M 水力照射孔

研究分野

核物性, 核物理

3．実験

新潟大でNMR-ON の測定は行われた．試料を銅のソースロッドに低温半田で付けて^{3}He/^{4}He希釈冷凍機で約９mKに冷却して外部磁場0.2 T をかけて核スピンを偏極させた．β線検出は０度及び１８０度方向においたSi（８ｍｍΦ，厚さ700ミクロン）検出器で行った．このSi は^{3}He/^{4}He希釈冷凍機内部（温度0.7T ）に設置され窓無しでベータ線を測定するようになっている．プリアンプは冷凍機の外にあるためその間が1.5mほどあり後で述べるノイズを拾う要因になっている．温度は強度の弱い60CoFe を用いてγ線を観測して決定した．

4．測定結果

ベータ線の異方性は０度と１８０度の強度比で約４％であった．鉄の緩和時間はこの温度で16.7(33)m「２」なので各高周波での測定時間（各周波数に対して１５分）の間に前の周波数でのスピンの偏極の崩れの影響を除くため１５分の休みを入れた．そのため実際の測定時間に対して半分の統計しか得られなかった．測定は色々な条件で行われた．高周波の強度を変えて温度が上昇しないレベルのパワーを入れた．試料が厚いのでなるべくパワーを強くしたいが，この熱による温度上昇にさえぎられた．Frquency Modulation Width （ＦＭ幅）を大きく２ＭＨｚして共鳴スペクトルを観測して，そのあとＦＭ幅を狭めて＋－０．４ＭＨｚの測定結果を図２に示す．

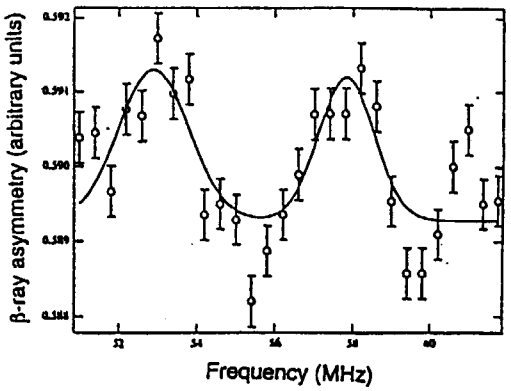

図２　^{59}FeFeSiのNMR-ON

測定は約１週間行なった．前述したようにプリアンプのノイズによる乱れの部分を削除したため実際のデータは４日分になった．実線は２本の共鳴線でフィットしたものである．57.8 MHz 付近にみられる共鳴はFe あるいは第２，第３近傍にSi がある場合で図１のFe-Si- 60Co の１６６MHz付近の共鳴に対応する．53 MHz 付近の共鳴は第１近傍にSiが一個ある場合で図１の１５２ＭＨｚの共鳴に対応する．測定結果をみると統計誤差が大きい．またデータのふらつきがみられる．これ以上ＦＭ幅を狭めた分解能をあげた測定は，共鳴の高さが小さくなるうえ，統計精度を挙げにくいので困難である．

5．検討

測定結果からはマクロな共鳴は得られたが，第２，第３近傍Siの影響の副共鳴線は得られなかった．この原因は次のことが考えられる．

１．高周波が入る厚さ約２ミクロンに比べて試料が厚く（８ミクロン）共鳴のＳ／Ｎ比がよくない．

２．検出器のプリアンプにノイズが入りやすく，連続のベータ線を観測するためこれらの不安定性がでた．

３．試料の^{59}Feの強度があまり強くなく，十分の統計精度が得られなかった．

これらの３つの改善はそんなに簡単なことではないが次のことが考えられる．

◎単結晶FeSiを薄く２ミクロンぐらいにする技術を完成させる．

◎強度を挙げるにはエンリッチアイソトープ^{58}Feを前以てドープしておく．

◎検出器とプリアンプ間を出来るだけ短くしてノイズ対策をする．

6．結び

まだ成果公表出来るデータではないが以上の検討を踏まえて，新たな実験を試みたい．

謝辞

SiFeの試料の提供や有意義な議論をしていただいた，花田黎門氏（東北大金研），箔試料の製作をしてくださった西村克彦氏（富山大工）感謝いたします．

参考文献

1. S. Ohya, *et.al.* Hyp. Int. 59 (1990) 373-376
2. T.Ohtsubo, *et.al.* Phys.Rev.C54(1996)554-558

This is a blank page.

8. そ の 他
(Etc)

This is a blank page.

研究テーマ：研究炉に関する工学的開発研究
表　　題：レプリカスーパーミラーの開発

レプリカスーパーミラーの開発

川端　祐司[1)]　鈴木　正年　田崎誠司[1)]　染宮一政[1)]
日本原子力研究所
[1)]京都大学原子炉実験所

１．はじめに

スーパーミラー等の中性子鏡の基板は良好な表面精度が比較的容易に得られることから、板ガラスを用いているが、耐放射線性、耐ヒートサイクル性などの観点から適切な材料とは言い難い面がある。本研究は、超薄型基板スーパーミラーとして製作されたレプリカスーパーミラーについて、中性子反射率を測定して、性能を確認し、実用化への可能性について検討を行ったものである。

２．レプリカスーパーミラー

超薄型金属基板のスーパーミラー製作の一方法として、ガラス基板に真空蒸着したスーパーミラーの鏡面に銅を電着した上でガラス基板から剥離することにより、超薄型の銅を基板とするスーパーミラーを製作した。この方式で製作したスーパーミラーをレプリカスーパーミラーと呼ぶ。

製作したスーパーミラーは 100 mm X 100 mm X 6 mmのガラス基板に15対層のNi/Tiを真空蒸着したものに銅を0.3mmメッキした後ガラス基板から剥離したものである。

３．中性子反射率

ダイレクトビーム、レプリカスーパーミラー、ガラス基板スーパーミラー及びニッケル単層膜ミラーからの反射ビームのスペクトルを図示する。

反射率の測定は、TOF 型反射率測定装置を用いてＪＲＲ－３Ｍ冷中性子導管（Ｃ２－３）で行った。スペクトルのそれぞれ 4.2 Ａの位置に深いディップが見えるが、これは導管の上流の実験装置で使用しているＰＧの影響である。

レプリカスーパーミラーの反射率はガラス基板スーパーミラーとほぼ一致する反射率を示しており、銅メッキによる基板作成後剥離するという本方式による薄型基板スーパーミラーにおいても十分な中性子反射率を得ることができることが確認された。

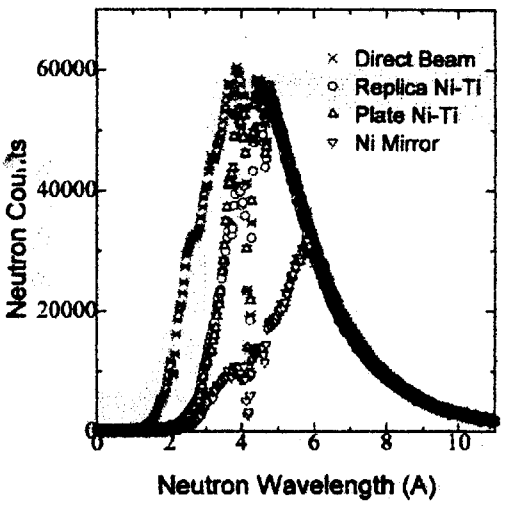

中性子反射率の比較

参考文献：Y.Kawabata,M.Suzuki,S.Tasaki and K.Somemiya, IGORR-6, Taejon,(1998)　in　print.

原子炉：ＪＲＲ－３　装置：TOF 型中性子反射率計　分野：その他（中性子応用）

研究テーマ：フィッション・トラック年代測定における壊変定数を用いた絶対年代較正
表　　題：標準ガラスによる熱中性子線量の絶対測定

新しい標準ガラスIRMM-540を用いた熱中性子線量測定とフィッション・トラック年代較正

岩野英樹・吉岡　哲・檀原　徹
(株)京都フィッション・トラック　京都市北区大宮南田尻町44-4

放射年代測定法の一つであるフィッション・トラック(FT)法において、壊変定数に基づいた絶対年代較正基盤を再構築するには、以下の３つの問題点の解決が不可欠である。それらは、(1)238Uの自発核分裂壊変定数(λ_f)の確定、(2)熱中性子線量値の絶対測定、(3)自発／誘導トラック計数効率の正確な補正である。最近、上述の(2)についての研究・開発が進み、新しい熱中性子線量モニターとして、ウラン濃度既知の標準ガラスIRMM-540が開発された。[1]今回、このガラスを基準とした熱中性子線量値を用いて年代標準試料ジルコンのFT年代値を算出した結果を報告する。

IRMM-540ガラスは、ベルギーのゲント大学のDr. Van den hauteを中心としたグループとＥＣのthe Institute for Reference Materials and Measurements (IRMM)との共同で開発されたものである。このガラスは、(1)分析の障害になるThや中性子を吸収する微量元素(B, Cd, Sm, Eu, Gd, Dy, Ir, Hg)がほとんど含まれていない、(2) 熱中性子線量測定に必要な，既照射ガラスの保証線量値が正確であるという特徴をもつ。従来使われてきたNIST(National Institute of Standards and Technology)-SRM962aは微量元素を多量に含む標準ガラスで、その保証既知線量値は，線量測定モニターの種類(Auと Cu)で約10%異なっていた。

筆者等は、既照射ガラスから熱中性子線量測定係数のＢ値を求め、[2),3)]他の放射年代測定法により正確な年代値が与えられた年代標準試料の一つであるFish Canyon Tuffジルコン(27.8±0.2Ma)の分析に応用した。外部ディテクター法によるFT年代測定を行い、[4)] 熱中性子照射は1997年9月12日に日本原子力研究所(東海)のJRR3の気送管(PN-2)で20秒間行った。熱中性子線量モニターはIRMM-540とSRM962a(Au値)を比較して用いた。 IRMM-540とSRM962aの線量値には約10%の差があるが、両者からのFT年代値は測定誤差範囲内で一致し、かつ標準年代値とも一致する(表1)。この結果は、上述の問題点(1)(3)について、大きなλf値$8.5\times10^{-17}y^{-1}$と、鉱物毎のトラック検出効率補正をしたジオメトリファクター(g)で、絶対年代較正が出来ること[5)]を支持する。 今後、測定精度を高め、さらに両線量モニターの正確度を検討する必要がある。

参考文献

1) De Corte, F., Bellemans, F., Van den haute, P., Ingelbrecht C. and Nicholl, C. Advances in Fission Track Geochronology, (1998), 67-78.
2)岩野英樹・檀原徹 (1996) フィッション・トラックニュースレター, 第9号, 75.
3)岩野英樹・吉岡哲・檀原徹 (1998) フィッション・トラックニュースレター, 第11号, 39-40.
4)岩野英樹・檀原徹 (1997) フィッション・トラックニュースレター, 第10号, 11-20.
5) Iwano, H. and Danhara, T, Advances in Fission Track Geochronology, (1998), 47-66.

表１．FT年代測定結果($\lambda f: 8.5\times10^{-17}y^{-1}$で算出)

試料名	手法	トラック密度(cm^{-2}) ρs	ρi	熱中性子線量 ϕ_{SRM}	ϕ_{IRMM}	g	FT年代値(Ma) T_{SRM}	T_{IRMM}
FC3 900122-1	ED1	6.03×10^{6}	5.18×10^{6}	6.82×10^{14}	7.61×10^{14}	0.68	26.7±0.9	29.8±1.0
87KN900122-1	ED2	3.82×10^{6}	6.72×10^{6}	6.83×10^{14}	7.61×10^{14}	1.34	25.6±1.1	28.5±1.2

原子炉：JRR-3　　装置：気送管　　分野：その他（放射年代学）

高速及び熱中性子照射による石英結晶中の点欠陥生成とESR解析
ESR Analysis of Point Defects Produced in Quartz by Fast and Thermal Neutron Irradiation

福地 龍郎（山口大学理学部地球科学教室）
Tatsuro FUKUCHI
Department of Earth Sciences, Faculty of Science, Yamaguchi University

ESR signals derived from intrinsic lattice defects in quartz, oxygen vacancies and interstitials, were detected by gamma or neutron irradiation. In addition, an unknown ESR signal at g=2.0050 also was detected by neutron irradiation. This unknown signal may be a superoxide (O_2^-) produced in depleted zones in quartz, which are formed by knock-on with fast neutrons. Microwave power characteristics indicates that this unknown signal is quite different from a peroxy center (Si-O-O·) although both signals can be produced by knock-on.

1．はじめに

地殻を構成する主要造岩鉱物である石英から検出されるESR信号は，地球物質の年代測定の他，地殻内地震活動に伴う物質変形の解析に利用することができる[1-2]。ESR信号の原因となる石英結晶中の格子欠陥の同定は，これまで様々な分野の研究者達によって試みられてきたが，不純物を多く含む天然石英から得られるESRスペクトルは多種多様で，現在でも一部のESR信号の同定は確立していない。ESR信号を利用した天然石英の変形解析を行う場合，石英結晶中に特徴的に形成される線欠陥である転位(dislocation)との関連で，酸素空孔，非架橋酸素及び格子間酸素の3種類の点欠陥が特に重要であるが，酸素空孔起源のE'中心を除いては，非架橋酸素及び格子間酸素起源のNBOHC及びperoxy中心には不明な点が多い。

筆者は，平成7年度からJRR-4原子炉を利用して，人工的に石英中に格子欠陥を生成し，ESR装置によって検出される信号の特性を調べる研究を開始した。研究を進めて行く過程でJRR-4原子炉が途中で使用できなくなり，平成8年度からは利用原子炉をJRR-3Mに変更した。このため，照射実験計画が大幅に変更となり，現在もJRR-3Mによる照射実験を続行中である。したがって，本報告書は最終報告ではなく，これまでの実験成果をまとめた中間報告である。

2．石英中のESR信号

石英結晶及びガラスから検出されるESR信号としては，大きく空孔型中心と不純物型中心に大別される。空孔型は石英固有の欠陥中心であり，酸素空孔に電子の捕獲されたE'中心(Si·；g=2.0011 付近)[3-5]，格子間酸素に正孔(Hole)が捕獲されたperoxy中心(Si-O-O·；g_1=2.067，g_2=2.0078，g_3=2.0016)[5-7]及び非架橋酸素に正孔が捕獲されたNBOHC(Si-O·；g_1=2.078，g_2=2.0102，g_3=2.0001)[6]が知られている。E'中心とperoxy中心は，石英中の典型的Frenkel型欠陥ペアと考えられている。NBOHCは，石英ガラスの線引き

研究施設・装置：JRR-3M(PN-1,2,3)，JRR-4(T-パイプ)，コバルト60ガンマ線照射施設，ESR装置
研究分野：地球年代学，ESR応用計測学

工程との関連で詳しく研究されており，Si 原子と O 原子の間の結合が応力で切れることにより生成すると考えられている。当初，peroxy 中心と NBOHC は石英ガラスから低温(77K)でのみ検出されると考えられていた。近年では，石英結晶からも室温(RT)で検出されることが知られるようになったが，これらの信号の特性についての研究例は少なく[2,8]，不明な点が多く存在する。特に，天然の石英結晶の場合，格子中に H^+ イオンや OH^- イオンなどの不純物が存在するため，核スピンを持つこれら不純物による相互作用や酸素空孔や非架橋酸素との化学反応により，得られる ESR スペクトルは複雑な様相を呈している。一方，不純物型には，石英中の Si イオンと置換した Al イオンが正孔を捕獲した Al 中心[9]，Si イオンと Ti イオンや Ge イオンが置換して電子を捕獲した Ti 中心[10]や Ge 中心[11,12]などが存在する。この内，Al 中心と Ti 中心は低温でのみ検出される。これらの不純物型中心も，格子間に存在する不純物イオンとの相互作用により，各々が特徴的な超微細構造(hfs)を示す。

3．実験結果と考察

中性子照射に伴い発生するγ線の ESR 信号に与える効果を調べるために，^{60}Co 線源によるγ線照射を行った。実験に使用した石英試料は，昭和化学株式会社製珪砂（試験番号 SC-3429）である。γ線照射前後に石英から検出される ESR スペクトルを Fig. 1A に示す。γ線照射により，まず Ge 中心の信号が出現・増大するが，照射線量の増加と共に減少する。Ge 中心がほとんど消滅する頃に，E' 中心と peroxy 中心が出現し始める。これらの結果は，γ線照射に伴い励起した電子による O 原子や Ge 原子のたたき出し(knock-on)効果であると考察される。

次に，JRR-4(Tパイプ)による照射を行った結果を Fig. 1B に示す。JRR-4(Tパイプ)における中性子束は，熱中性子が 3.7×10^{13} (n/cm²·s)，速中

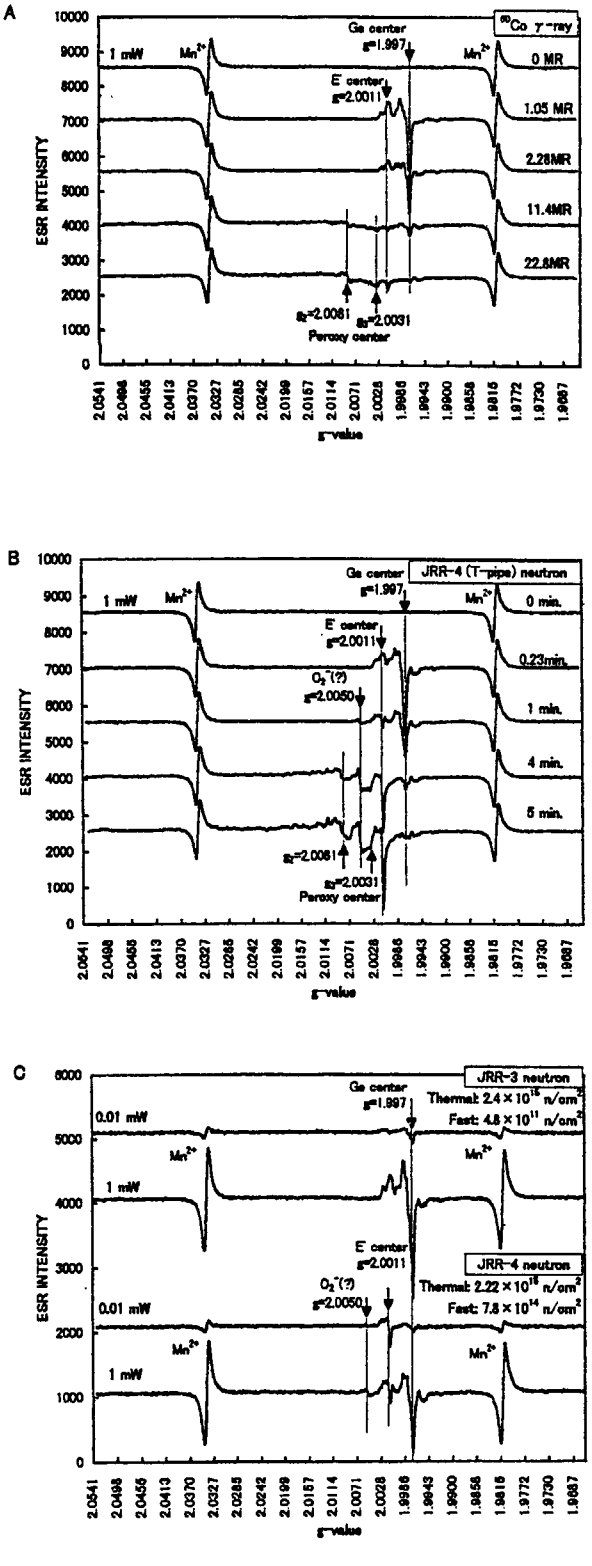

Fig. 1 ESR spectra obtained from quartz by gamma or neutron irradiation. Measurement conditions: Microwave frequency-9.43GHz, Temperature-RT, Microwave power-1 mW (or 0.01mW), Modulation width-100kHz 0.05mT, Response-0.3s, Sweep time-8min. A: gamma irradiation, B: neutron irradiation (JRR-4), C: neutron irradiation (JRR-3M and JRR-4).

性子が 1.3×10^{13} (n/cm^2·s) である。γ線照射の場合と同様に，始めにGe中心の出現・増大が起こり，その後Ge中心は減少し始めるが，γ線照射の場合と異なるのは，Ge中心がまだ大部分残っている内に，E'中心とg=2.0050に別の信号が出現し始めることである。照射量の増加と共に，E'中心とg=2.0050の信号はさらに増大し，peroxy中心の信号も出現し始める。E'中心とperoxy中心の発生・増加は，以前の研究報告通り，高速中性子による顕著なたたき出し効果の結果であると説明されるが，g=2.0050の信号についてはこれまで全く報告されておらず，詳細は不明である。

g=2.0050の未知の信号の生成機構を調べるために，中性子束の異なるJRR-3MとJRR-4による照射比較を行った。熱中性子束をほぼ同一にして，異なった速中性子束で照射した時のESRスペクトルの変化をFig.1Cに示す。JRR-3Mにおける熱中性子束は 2.4×10^{15} (n/cm^2)，速中性子束は 4.8×10^{11} (n/cm^2) であるのに対し，JRR-4における熱中性子束は 2.22×10^{15} (n/cm^2)，速中性子束は 7.8×10^{14} (n/cm^2) である。Fig.1Cに示すように，g=2.0050の信号は熱中性子束がほぼ同じ条件下では，速中性子束が高い場合のみ検出される。したがって，この未知の信号は，熱中性子による放射化に伴うγ線やβ線，あるいはβ反跳によって生成するのではなく，高速中性子によってのみ生成される信号であることが明らかとなった。

高速中性子特有の現象としては，たたき出しとそれに伴う欠乏領域（空格子点が密集した低原子密度領域）の形成が考えられる。g=2.0050の信号が酸素空孔起源のE'中心と共に出現する事を考慮すると，たたき出された格子間酸素原子に起因するESR信号 (O_2^- radical) であることが予想されるが，通常のSiイオンと結合した形ではなく，石英中に形成された欠乏領域で自由な状態で存在するスーパーオキシド

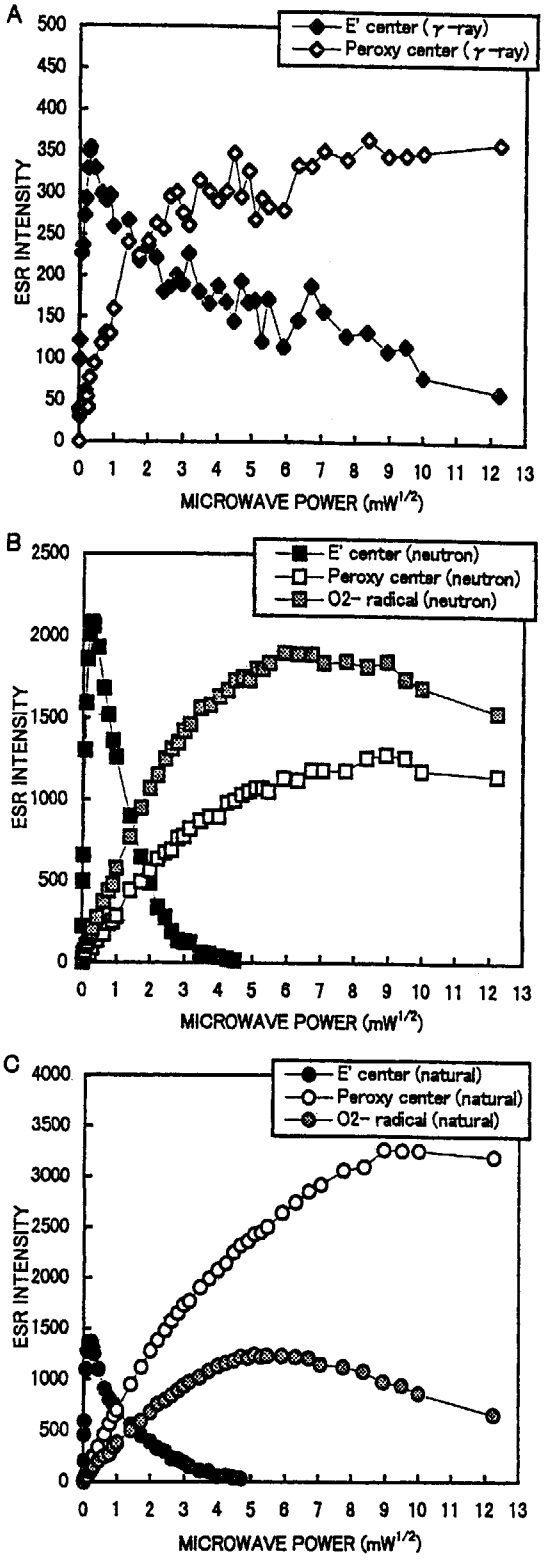

Fig.2 Microwave power charcteristics obtained from each defect center. A: Quartz irradiated with gamma rays, B: Quartz irradiated with neutrons using JRR-4. C: Natural quartz obtained from fault clay of the Nojima Fault.

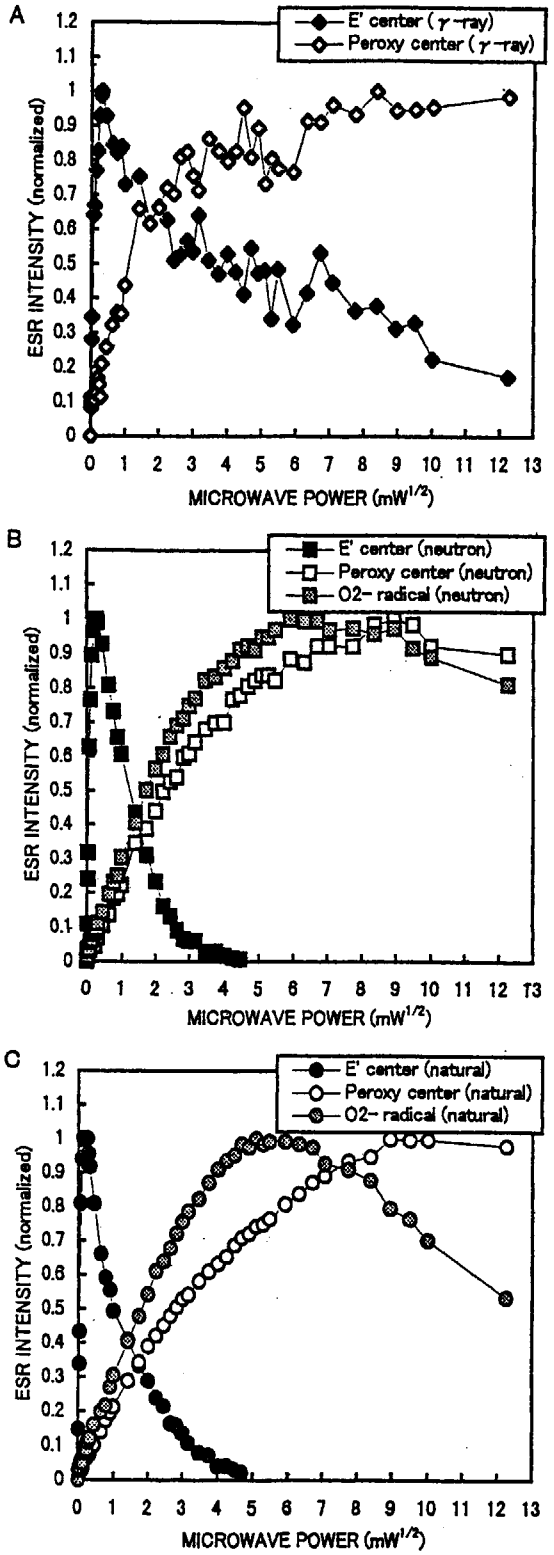

Fig. 3 Microwave power charcteristics obtained from each defect center. ESR intensities were normalized by saturation intensities. A: Quartz irradiated with gamma rays, B: Quartz irradiated with neutrons using JRR-4. C: Natural quartz obtained from fault clay of the Nojima Fault.

（superoxide）である可能性が指摘される。g=2.0050の信号と同様なESR信号は，UやTh濃度の高い粘土中に含まれる石英粒子試料からも検出される[13,14]。こうした高U・Th濃度の天然粘土中において高速中性子の代わりをする高エネルギー粒子線としては，α線が考えられる[2,15]。

γ線及び中性子照射により生成したESR信号の性質を調べるために行った，各ESR信号強度のマイクロ波出力変化をFig. 2に示す。γ線照射によって生成したE'中心とperoxy中心のマイクロ波特性は，生成欠陥濃度が低いこともあり，著しい変動を示している(Fig. 2A)。これに対し，中性子照射により生成した各ESR信号は安定したマイクロ波特性を示す(Fig. 2B)。Fig. 2Cには，天然の断層粘土試料[16]から得られる各ESR信号のマイクロ波特性を比較のために示す。マイクロ波特性はESR信号のスピン濃度に依存するが，飽和信号強度で標準化した時のマイクロ波出力変化曲線（Fig. 3）で比較すると，E'中心とperoxy中心，g=2.0050のO_2^-ラジカル(?)の３つの信号は，中性子照射により生成した場合と天然粘土試料中で生成した場合で非常に良く似た特性を示すことが分かる。またどちらの場合でも，g=2.0050のO_2^-ラジカル(?)の方がperoxy中心よりも早く飽和点に達し，両信号の特性には違いが見られることが明らかとなった。マイクロ波特性の違いは，その信号の物性（スピン－格子緩和時間やスピン－スピン緩和時間）の違いを反映しているので，peroxy中心とg=2.0050のO_2^-ラジカル(?)の信号は別の信号であると考えられる。

３．まとめ

石英結晶のγ線及び中性子照射によって，石英固有の格子欠陥（酸素空孔及び格子間酸素）に起因するESR信号が検出された。また従来の報告には見られない未知のESR信号も検出され，高速中性子によるたたき出しで石英中の欠乏領

域に生成されたスーパーオキシド（O_2^-）の信号である可能性が考えられる。マイクロ波出力特性によると，この信号は同様のたたき出しにより生成するperoxy中心とは異なった特性を示すことが明らかとなった。今後，より詳しい中性子照射実験を行うと共に，様々な分析によってこの信号の同定を行うことを計画している。

謝辞

本研究でご協力頂いた，東京大学原子力研究総合センターの伊藤泰男先生，澤幡浩之氏，小野寺司史氏，開放研究室の皆様，日本原子力研究所東海研究所の長山　尚氏，正木信行氏に深く感謝致します。本研究では，文部省科学研究費基盤研究C(2)（08640574及び10640441：研究代表者 福地龍郎）の一部を使用した。

文　献

1) T. Fukuchi(1993) *Appl. Radiat. Isot.* **44**, 179-184.
2) T. Fukuchi(1996) *Appl. Radiat. Isot.* **47**, 1509-1521.
3) D. W. McMorris(1970) *Nature* **226**, 146-148.
4) K. L. Yip and W. B. Fowler(1975) *Phys. Rev.* B 11, 2327-2338.
5) D. L. Griscom(1979) *Proc. 33rd Freq. Contr. Symp.*, 98-109.
6) M. Stapelbroek, D. L. Griscom, E. J. Friebele and G. H. Sigel Jr.(1979) *J. Non-Cryst. Solids* **32**, 313-325.
7) E. J. Friebele, D. L. Griscom and M. Stapelbroek (1979) *Phys. Rev. Lett.* **42**, 1346-1349.
8) A. L. Odom and W. J. Rink(1989) *Geology* 17, 55-58.
9) R. Schnadt and A. Rauber(1971) *Solid State Com.* **9**, 159-161.
10) P. M. Wright, J. A. Weil, T. Buch and J. H. Anderson(1963) *Nature* **197**, 246-248.
11) F. J. Feigl and J. H. Anderson(1970) *J. Phys. Chem. Solids* **31**, 575-596.
12) E. J. Friebele, D. L. Griscom and G. H. Sigel Jr.(1974) *J. Appl. Phys.* **45**, 3424-3428.
13) T. Fukuchi(1996) *Jpn. J. Appl. Phys.* **35**, 1977-1982.
14) T. Fukuchi and N. Imai(1998) *Geol. Soc. London, Special Publ.* **144**, 261-277 (in press)
15) T. Fukuchi and N. Imai(1998) *Quat. Sci. Rev.* **17**(in press)
16) 福地龍郎・今井　登(1998) 月刊地球号外 **21**, 180-185.

成果の公表

1) T. Fukuchi and N. Imai(1998) ESR isochron dating of the Nojima Fault gouge, south-west Japan, using ICP-MS; an approach to fluid flow events in the fault zone. *In*: Parnell, J.(ed.) *Dating and Duration of Fluid Flow and Fluid-Rock Interaction.* Geol. Soc. London, Special Publ. **144**, 261-277 (in press)
2) T. Fukuchi and N. Imai(1998) Resetting experiment of E' centers by natural faulting - The case of the Nojima Earthquake Fault in Japan. *Quat. Sci. Rev.* **17** (in press)
3) T. Fukuchi and N. Imai(1996) Assessment of fault activity by direct ESR dating of fault clay gouge - the cases of major active faults in Japan. The 8th International Conference on Luminescence and Electron Spin Resonance Dating. At Australian National University, Canberra, Australia, p. 85.

4πNaI(Tl) γ線検出器による ^{166m}Ho の放射能精密測定法の開発

Study of Precise Activity Measurement of ^{166m}Ho Using 4πNaI(Tl) γ-ray Detector

名古屋大学工学研究科*1　宮原 洋*1、上田 直由*1、森 千鶴夫*1、竹内 紀男*2、大久保 昌武*2
日本原子力研究所*2　(MIYAHARA, Hiroshi; UEDA, Naoyoshi; MORI, Chizuo; TAKEUCHI, Norio; OHKUBO, Masatake)

1. はじめに

HPGe 検出器でγ線の測定を行う場合、検出効率の校正は重要である。検出効率の校正方法としては、崩壊率既知の複数の標準線源を測定し、得られた各γ線エネルギーでの検出効率から検出効率曲線を決定するのが一般的である。この検出効率を校正する際に用いる標準線源に対しては次のような条件が要求される。半減期が長く、強度の強いγ線を放出することである。また現実的な点としては、崩壊率が精度よく決定された線源の入手の容易なこともあげられる。

一般に使用されるシングルγ線放出核種としては、^{51}Cr(320.1 keV)、^{54}Mn(834.8 keV)、^{57}Co(122.1, 136.5 keV)、^{60}Co(1173.2, 1332.5 keV)、^{65}Zn(1115.5 keV) などがあり、マルチγ線放出核種としては、^{133}Ba(53.2, 79.6, 81.0, 276.4, 302.9, 356.0, 383.9 keV)、^{152}Eu(121.8, 244.7, 344.3, 778.9, 964.1, 1085.9, 1112.1, 1408.0 keV) などがある。しかし、検出効率の変化が大きく、検出効率の校正の重要性がより高い、130 から 250 keV のエネルギー領域では上の条件を満たす適当な標準線源は少ない。即ち^{75}Se(136.0, 198.6 keV)、^{182}Ta(152.4, 222.1 keV)、^{139}Ce(165.9 keV)、^{141}Ce(145.4 keV)等が考えられるが、半減期が短く、また崩壊率が精度良く決定された線源の入手が困難である。

^{166m}Ho は 184 keV のγ線を 73%の強度で放出し、半減期 1200 年と長いため、標準線源化が有望視されており、日本原子力研究所でも試験製造している。しかし、半減期が長いために比放射能は低く、崩壊率精密測定は困難である。

4πNaI(Tl) γ線検出器は NaI(Tl)結晶が井戸型の形状をしており、井戸内部に試料を入れて測定を行うため幾何学的効率が高く、さらに大きな体積の検出器を使用すれば、一層絶対的な検出効率が高くなる。そこで 4πNaI(Tl) γ線検出器を用いて ^{166m}Ho 線源の測定を行えば、^{166m}Ho が 1 崩壊で多数のγ線を放出するため、1 崩壊当たりの検出効率が極めて高くなり、高精度での崩壊率測定が可能になると考えられ検討した。本研究では崩壊率測定で実際に使用する、井戸の直径の異なる2つの 4πNaI(Tl) γ線検出器の全検出効率をモンテカルロ計算コード EGS4 を用いて計算し、数種の標準線源を用いて測定した値と比較したのち、実際にこれを用いて ^{166m}Ho の崩壊率測定を行い、4πβ-γ同時計測法により求めた値と比較した。

2. 研究方法

モンテカルロ法により電磁カスケードを計算するコードである EGS4 を用い、4πNaI(Tl) γ線検出器と線源を入れたポリエチレン製容器を、円筒平板形状で模擬した幾何条件を用いて、外径 127 mm、高さ 127 mm、井戸の直径が 12 mm 及び 27 mm、深さ 65 mm の 2 つの検出器について計算を行った。線源は単色γ線を発生する点等方線源を仮定し、単色γ線の計算エネルギー範囲は 40 keV から 1300 keV とした。

計算結果と実測値の比較を行うため、4πβ-γ同時計測法によりあらかじめ崩壊率を求めた ^{46}Sc(889.3, 1120.5 keV)、^{51}Cr(320.1 keV)、^{54}Mn(834.8 keV)、^{57}Co(122.1, 136.5 keV)、^{60}Co(1173.2, 1332.5 keV)、

研究施設・設備：　JRR-3M　4πNaI(Tl)γ線検出器
HR, PN　　研究分野：　放射能絶対測定

^{65}Zn(1115.5 keV)、^{241}Am(26.3, 59.5 keV)線源を用いて4πNaI(Tl) γ線検出器の全検出効率の測定を行った。

そののち、^{166m}Ho について、崩壊核データとシミュレーションより得られた全検出効率曲線から、4πNaI(Tl) γ線検出器における1崩壊当たりの検出効率を計算し、これを用いて (2000 Bq 程度)の崩壊率を測定した。この際、^{166m}Ho 線源の強度に対する崩壊率測定結果の依存性を調べるため、1400 Bq から10000 Bq の線源について同様の測定を行った。さらにほかの方法として HPGe 検出器を用いて ^{166m}Ho の比較的強度の弱い線源との相対γ線強度測定を行うことにより、比較的強度の強い線源(25000 Bq 程度)の崩壊率を求め、この結果を 4πβ-γ同時計測法により得られた結果と比較した。

3. 結果

計算により求めた全検出効率曲線と実験により求めた全検出効率を井戸の直径 12 mm のものを図1(a)に、井戸の直径 27 mm のものを図1(b)にそれぞれ示す。

井戸の直径の違いを反映して、EGS4 を用いた計算による全検出効率曲線はグラフ(b)ではグラフ(a)に比べ、高いエネルギーのほぼ直線の部分で、4%弱低い値をとっている。井戸の直径 12 mm の検出器では実験点と計算点の差は最大の ^{46}Sc の場合でも、1%強とよく一致している。井戸の直径 27 mm の検出器では ^{51}Cr で約 2.2%の差がみられた。

次に、この検出効率曲線と崩壊核データより求めた ^{166m}Ho における 1 崩壊当たりの検出効率及びこれを用いて測定した比較的強度の弱い線源の崩壊率の結果を表 1 に示す。

^{166m}Ho が 1 崩壊で多数のγ線を放出するため、1 崩壊当たりの検出効率が極めて高くなっていることが判る。また、井戸の直径の異なる両検出器から得られた結果はよく一致している。

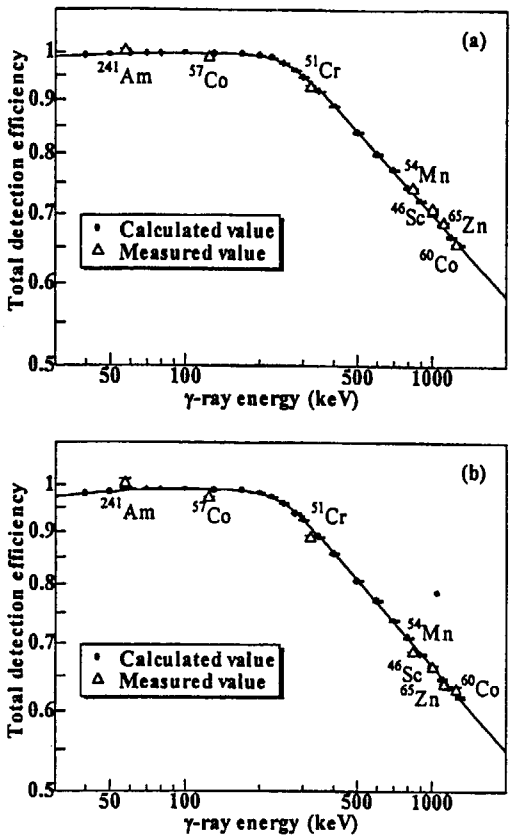

図1 外径 127 mm、高さ 127 mm の 4πNaI(Tl) γ 線検出器の全検出効率曲線
(a) : 井戸の直径 12 mm 深さ 65 mm
(b) : 井戸の直径 27 mm 深さ 65 mm

表 1 ^{166m}Ho に対する 1 崩壊あたりの検出効率と崩壊率測定結果

検出器	1崩壊当たりの検出効率	崩壊率
802-6W1 (12 mmϕ)	1.0000(0)	2184.6(16)
802-6W2 (27mmϕ)	0.9999(1)	2179.4(16)
	平均	2181.9(11)

図2に様々な強度の ^{166m}Ho 線源に対する 4πNaI(Tl) γ線検出器による崩壊率測定結果と 4πβ-γ同時計測法により得られた結果との比較を示す。

図2から両方法により測定した崩壊率はよく一致し、また線源の崩壊率に対する依存性は認められないことが判る。

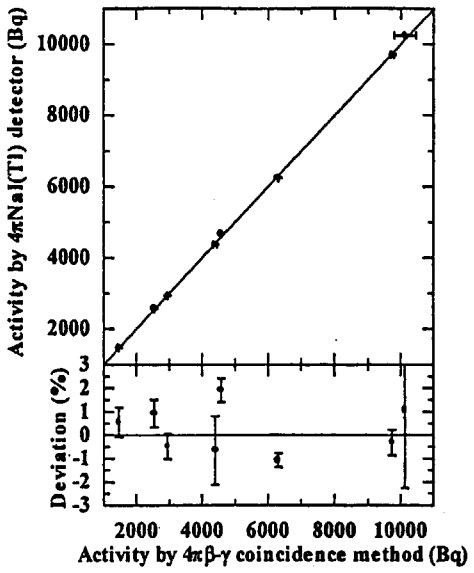

図 2　4πNaI(Tl) γ線検出器と 4πβ-γ同時計測法により得られた崩壊率測定結果結果の比較

表 1 に示した線源を標準線源として、HPGe 検出器を用いて相対γ線強度測定を行うことにより比較的強度の強い線源の崩壊率を求めた結果は 24223(66) Bq であった。一方、4πβ-γ同時計測法により得られた結果は 24420(122) Bq で、両者は約 0.8%でよく一致した。

次に、他の核種に対する本崩壊率測定法の応用の可能性を検証するため、同様の方法により、マルチγ線放出核種である ^{133}Ba, ^{152}Eu 線源の崩壊率を求めた。まず、これらの核種について 4πNaI(Tl) γ線検出器における 1 崩壊当たりの検出効率及びこれを用いて測定した比較的強度が弱い線源の崩壊率測定結果を表 2 に示す。1 崩壊当たりの検出効率は ^{133}Ba については 98%以上の高い値であった。しかし ^{152}Eu では EC 崩壊において高いエネルギー準位から直接基底準位へ遷移するγ線が放出されるため、検出効率は比較的低い値となった。崩壊率については両核種とも、2 つの検出器から得られた結果はよく一致している。この 3 核種の測定結果から判るように検出効率が 1 に近い程その不確かさは小さく、これら以外の核種への応用もこの点が重要である。

表 2　^{133}Ba(a), ^{152}Eu(b)に対する 1 崩壊あたりの検出効率と崩壊率測定結果

(a)　^{133}Ba

検出器	1崩壊当たりの検出効率	崩壊率
802-6W1 (12 mmϕ)	0.9861(13)	2144.8(32)
802-6W2 (27mmϕ)	0.9808(15)	2147.6(36)
	平均	2146.0(24)

(b)　^{152}Eu

検出器	1崩壊当たりの検出効率	崩壊率
802-6W1 (12 mmϕ)	0.9525(35)	1585.6(59)
802-6W2 (27mmϕ)	0.9395(38)	1587.4(65)
	平均	1586.4(44)

次に、^{133}Ba, ^{152}Eu について HPGe 検出器を用いて上の線源との相対γ線強度測定を行うことにより強度の強い線源の崩壊率を求めた結果と 4πβ-γ同時計測法により得られた値の比較を表 3 に示す。両核種とも、2 つの方法から求めた崩壊率は互いによく一致している。

表 3　^{133}Ba, ^{152}Eu の強度の強い線源の崩壊率測定結果

線源	崩壊率 (Bq)		差 (%)
	NaI	4πβ-γ	
^{133}Ba	25062(91)	25376(126)	-1.2
^{152}Eu	23298(99)	23168(209)	0.6

以上に述べた ^{133}Ba, ^{152}Eu 及び ^{166m}Ho の強い線源及び 4πβ-γ同時計測法により崩壊率を求めた ^{57}Co, ^{60}Co の線源を用いて HPGe 検出器のγ線ピーク検出効率の校正を試みた。その結果を図 3 に示す。

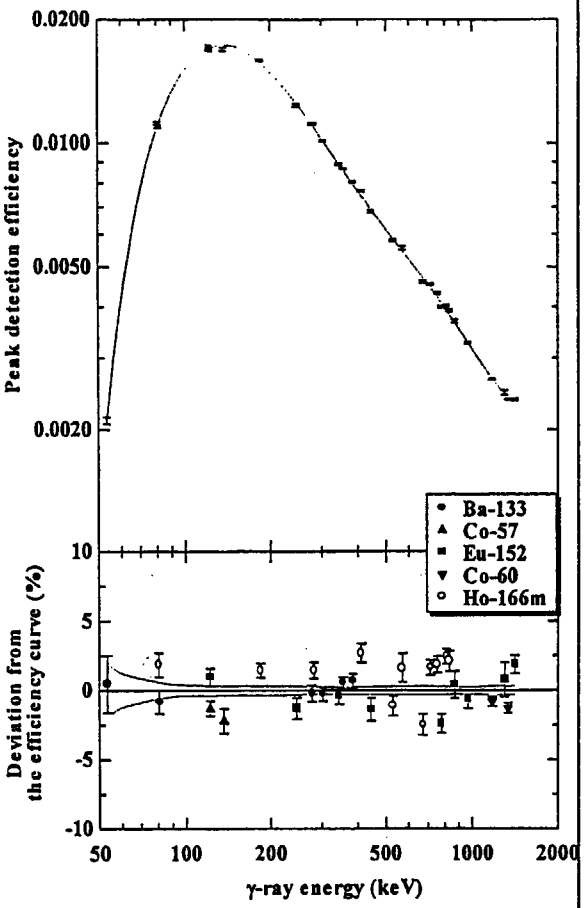

図3　HPGe検出器のピーク検出効率曲線

図3において検出効率曲線は共分散法により7次式で当てはめた結果である。下の図は測定点の曲線からの差を示していて、異なる線源から得られたデータ点も比較的よく一致した検出効率を与えている。このように、比較的簡便な装置でマルチγ線放出核種の崩壊率を比較的高精度で絶対的に決定できることが判った。

4. 成果の公表

学会発表

・上田直由，宮原 洋，森千鶴夫，源河次雄，竹内紀男，“4πNaI(Tl)γ線検出器の全検出効率の計算”，日本原子力学会中部支部第 29 回研究発表会，名古屋，1997年12月

・上田直由，宮原 洋，森千鶴夫，竹内紀男，大久保昌武，“EGS4による4πNaIγ線検出器の全検出効率計算とその応用”，第 35 回理工学における同位元素研究発表会，東京，1998年6月

Developement of the Precise Measurement Method for Gamma-Ray Energy of Neutron Induced Radioactive Nuclides

中性子放射化核種のガンマ線エネルギー精密測定法の開発

KISHIKAWA, Toshiaki, UEMURA, Jitsuya;
Kumamoto Univ. Faclty. Engring.

熊本大学工学部　岸川俊明、上村実也

Goal of the research is to develope a new energy calibration method to perform precise measurement of photon energy by gamma-ray spectrometry. Here, we regard reference standard energies to be those of photon of radioactive isotopes measured basing on a laser wavelength of ^{86}Kr (606 nm) together with energy-wavelength conversion factor $E\lambda$ = 1.239 842 44 x 10^{-6} eV m ± 0.03 ppm (CODATA 1986). As such the reference standard we use ^{192}Ir isotope.

Deviation of photon energy values[1] between data obtained by photon spectrometry, i.e., the decay gamma-ray analysis and the prompt gamma-ray analysis with Ge or Ge(Li) detectors, and those obtained by crystal diffraction spectrometry, has led that the "conventional" method of energy calibration for the photon spectrometry is not adequate to the precise energy assignment. A "new" method has solved this problem by introducing the concept of an instrument function, which is the transfer function between an input signal-shape function and an output (measured) signal-shape function, as summarized in reference 1. Present status of photon energy values has been examined for the nuclear-decay gamma-rays, the nuclear excitation gamma-rays and the mesonic-atom X-rays.

At the previous stage of research[2,3] we evaluated that a commonly-used internal stasndard method, mainly used for activation analysis study, was inadequate for the precise measurement of photon energy, so fa as we use base subtraction method.

In the present study, we examined the cause of the inadequacy of a base-subtraction method for obtaining the photopeak line shape for the precise energy measurement.

RESEARCH OUTLINE

The key model for the new energy calibration is the instrument function. Several types of instrument functions have been proposed. The concept of instrument function is as follows: the function generated by photoelectric effect in a detector, is a transmission function of an input photon signal function to an output signal shape function on a display of a pulse height analyzer. Fluctuation of the charge-carriers (electron-hole pair) creation generates the normal distribution (ND). The centroid (x_c) of the ND folded in the instrument function is the position correspond to the incident photon energy, instead of an apparent maximum position of the photopeak shape. The random escape probability density distribution caused by an escape of charge carriers by trapping (which is the main origin of distortion of the photopeak shape from the normal distribution) was formulated.

Based on the instrument function we develop new energy calibration method. To estimate the key parameter, x_c, it is indispensable to elucidate noise width of the detection system, because both the ND and the REPDED are the function of x_c so far as we perform parameter estimation by the maximum likelihood estimation method.

Facilities and Instruments:
JRR-3,4 Pneumatic Tube

Research Field:
Nuclear Spectrometry, Activation

RESULTS

Commonly used, pre-base profile subtraction methods for spectral analysis are insufficient for the precise measurement of both the photon energy and intensity[15]. For these prospects it is indispensable to examine the feasibility of base profile subtraction from overall photopeak profile.

The general profile of a measured, full energy (FE) photopeak is an overall function of the individual input-signal shape functions convoluted with the instrument function:

(FE peak profile)
= (FE peak shape) + (base profile)
= (FE peak shape) + (SAS + LE + RS + CO shapes)

where SAS is the small angle scattering, LE is the edge loss, RS is the random summing and CO is the continuum (which is the shape due to photons coming from sources and Compton events produced by higher photons). Schematic diagram of the full energy peak profile is shown in figure 1.[4] The ND shape in fig. 1 is the normal distribution function folded in the instrument function and never appears in the spectrum, although it is the key function in the peak shape analysis.

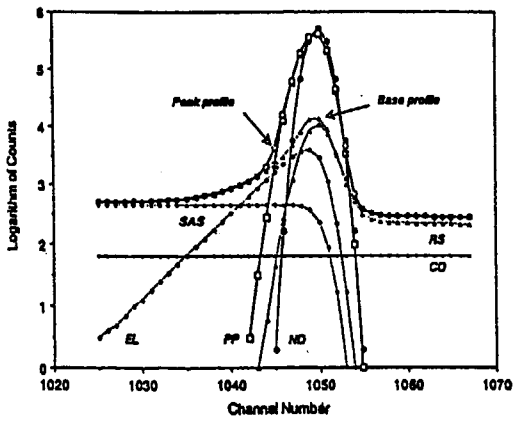

Fig. 1. Typical peak profile observed with a HPGe detector. (PP) the photopeak shape proportional to the instrument function; (ND) the normal distribution folded in the Peak; for the other symbols see text.

By the method of pre-base subtraction, definite quantity of the base components is remained in the subtracted photopeak shape which cause one of origins of the deviation of the precise energy, as well as the uncertainty of precise photopeak counts. Therefore, non-base subtraction method for the spectral analysis is the promising way of parameter estimation to obtain the centroid of ND.

A well known coincidence summing effect is the cascade-sum event, when two or more gamma-rays of different energy levels in cross-over relation are emitted in cascade. RS is defined as the coincidence summing between the monoenergetic photon of interest and other randomly incident photon(s) within the resolution time of a detection system. The RS includes the event of coincident summing with the bremsstrahlung photon generated by a beta-emitting source (Case 1) and with those produced by Compton effect in the detector (Case 2).

Detailed discussion for the Case 1 has been given in ref. 5. There, the evidence of the Case 1 has been demonstrated with a pulser and a beta-ray emitting source (^{90}Sr) which generates the bremsstrahlung continuum. Because of the paralleled input of the pulser and photon signals into the preamplifier (PA), the RS is generated in the circuit of the PA. As a result, a decrease in total counts of pulser peak and an increase in the sum of RS counts appears as a function of effective bremsstrahlung-source intensity. However, the bremsstrahlung photons with an energy of several eV are well attenuated by the window material (aluminium) of HPGe coaxial detector. Therefore, the contribution of RS counts in the vicinity of the pulser peak must be attributable to the Compton electron caused by bremsstrahlung photon of higher energy in the detector.

Evidence of RS for Case 2 has been demonstrated by the EC source (^{54}Mn) or the b$^-$-IT source (^{137}Cs-^{137m}Ba) together with the pulser signals. Figs. 2a and 2b show the spectra obtained, respectively, with PHA-4 (single

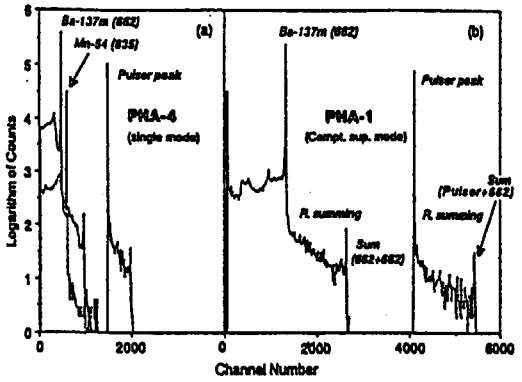

Fig. 2. (a) Gamma-ray spectra of ^{54}Mn and ^{137}Cs–^{137m}Ba measured with a HPGe detector with PHA-4 (single mode); pulser signals (250 Hz) of an appropriate amplitude, higher than twice the photopeak-energy equivalence, were introduced during accumulation; partial spectrum of the pulser peak and the higher region for the ^{54}Mn are omitted in the figure. (b) Gamma-ray spectrum of ^{137}Cs–^{137m}Ba measured with PHA-1 (Compton suppression mode); pulser signals, identical to those of the PHA-4 mode, were introduced during accumulation; *R. summing* is the random summing shape and *Sum* is the sum position of the peaks in parentheses.

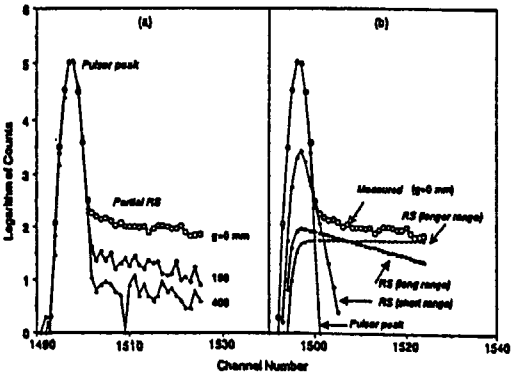

Fig. 3. Partial spectra around the pulser peaks for PHA-4 (single mode). (a) The ^{137}Cs–^{137m}Ba source was placed at the nearest (g = 0 mm), intermediate (190 mm) and far apart (400 mm) position from the HPGe detector in the sample box [1]; the distance between the detector head and the nearest position was 200 mm. (b) Analysis of the partial spectra (g = 0 mm); the source-originated random summing (*RS*) input signal function was approximated as the sum of short, long and longer range exponential functions; the output functions are the *RS* component functions folded with the instrument function.

mode) and PHA-1 (Compton suppression mode). The ^{137m}Ba has a single excited level and emits 662-keV photon. The slight difference of spectral patterns of the region below the 662 keV photopeak between fig. 2a (single mode) and fig. 2b (Compton suppression mode) is due to contribution of the Case 1 by accompanying bremsstrahlung radiation of ^{137}Cs (E_b = 514 keV (94.6 %) and 1176 keV (5.4 %)).

Figure 3a shows partial spectra for the pulser peaks with the partial RS continua obtained by the ^{137}Cs-^{137m}Ba for several geometries in the PHA-4 (single) mode. The RS shape increases when the source-to-HPGe detector distance decreases.

The RS signal shape appears as a result of complicated process of the Cases 1 and 2 depending on the nature of the source characteristics and detection conditions. Therefore, the RS (input) signal shape is to be expressed better by suitable fitting function(s) than by the probability density distribution functions. For this purpose, we consider exponential function expressions with the short, long and longer range decay channels.

In a previous report wereported peak position variation with and wsithout the use of Ir-192 as an internal standard[5,7]. There, we introduced the base subtraqction method. After subtaction of the base component on each portion of the photopeak profile of the gamma-ray peak, the peak position was obtained by the method of first-order zero crossing. The peak index was calculated by equation

$$x_p(E)\, c_w / E = 1 + \delta_{peak}(E)$$

with the channel width of cw,t = 0.5 keV/channel. The peak position variation comes from inadequate method of the base-subtrasction.

CONCLUSIONS

The goal of the photopeak shape analysis is, essentially, to estimate parameters of the instrument function. So far, as we perform the base subtraction with an appropriate *fitting* function(s), some of the base components may, unavoidably, remain in the peak component (Fig. 1). Thus the photopeak shape function[5,6] is different from the shape of instrument function.

The estimation of parameters of the functions composing peak profile by the maximum likelihood estimation should be performed without subtracting the

base components by estimation algorithms, such as the simplex, the Davidon-Fletcher-Powell, the Marquardt and the stabilized Gauss-Newton.

Publications

1. T. Kishikawa et al., Gamma-ray spectrometry with a Ge detector: an importance of instrument function on a new energy calibration method, Nucl. Instrum. and Meth. in Phys. Res., A353 (1994) 285-290.
2. T. Kishikawa et al., Energy calibration: Peak position variation by the use of ^{192}Ir as a reference standard source with HPGe detectors, Appl. Radiat. Isot. 44 (1993)1389-1398.
3. T. Kishikawa, Effect of distortion of electronic noise shape on ultra precise measurement of photon energy with a Ge spectrometer, Proc. 1996 SERNIA Symposium on Radioactive Impact in Asia (1996) pp. 389-392.
4. T. Kishikawa, C. Yonezawa, H. Matsue Y. Ito and H. Sawahata, Effect of bremsstrahlung and Compton-electron induced summing on Ge-detector photopeak shapes, Nucl. Instr. and Meth. in Phys. Res. A 369 (1996) 689-692.
5. T. Kishikawa et al., Energy calibration: Peak position variation by the use of 192Ir as a reference standard source with HPGe detectors, Appl. Radiat. Isot. 44 (1993)1389-1398.
6. -T. Kishikawa, Methodological errors in precise measurement of gamma-ray energies with Ge detectors, J. Nucl. Sci. Tech., 28 (1991) 487-499.
7. T. Kishikawa et al., Re-evaluation of gamma-ray energy by the use of 192Ir as an internal-reference standard, UTRCN-G-25 (1995) 14-18.

LiAlの電気的性質の中性子照射効果の研究

Neutron Irradiation Effects of Electrical Properties on LiAl

矢萩正人（青森大学工学部）
Masahito YAHAGI (Faculty of Engineering, Aomori University)

栗山一男、浜中廣見（法政大学工学部）
Kazuo KURIYAMA, Hiromi HAMANAKA
(College of Engineering, Hosei University)

須貝宏行、棚瀬正和（日本原子力研究所　東海研究所）
Hiroyuki SUGAI, Masakazu TANASE
(Tokai Establishment, JAERI)

1. はじめに

金属間化合物 β-LiAl は、NaTl 型結晶構造（空間群 Fd3m）を有し、格子欠陥に起因すると考えられている電子物性に、通常の化合物に見られない大きな特徴をもっている。その特徴は、3種類の格子欠陥（Li原子空孔 V_{Li}、Al格子点に置換したLi原子 Li_{Al}、複合欠陥 V_{Li} - Li_{Al} ）を多数含有しながら、Li濃度が48～56 at.%にわたり均一なβ相を保持していることである。特に、Li濃度が少ない領域では、その多量に含む格子欠陥（～10^{21} cm^{-3} ）がもとで、低温（90 K付近）において V_{Li} の規則-不規則変態に起因する電気抵抗率の異常が観測される。[1] 一方、Li 濃度が増加し、50 at.% 付近になると低温における電気抵抗の異常がなくなってくる。これは、V_{Li} - Li_{Al} の欠陥濃度が増加するためと考えられる。この組成を有する試料（β-^{6}LiAl）に中性子を照射すると、電気抵抗率の値がLi不足の相境界の値に近くなることから、キャリア（ホール）の主要な散乱中心と考えられる複合欠陥（V_{Li} - Li_{Al} ）が分解し、その散乱中心が消滅したことによるものと報告してきた。[2]

本研究では、中性子をβ-^{6}LiAl に照射し、^{6}Li (n, α) ^{3}H反応によるトリチウム（T）とヘリウム（He）の中性子核変換注入による伝導機構への影響、照射損傷の電気的性質及び結晶構造への影響を

(1) Li 不足の相境界付近の組成を有する試料に中性子を照射したとき、低温における V_{Li} の規則-不規則変態に起因する電気抵抗率の異常が観測されるかどうか。
(2) 複合欠陥を含むLi濃度が 50 at.% 付近の試料への中性子照射において、低温における電気抵抗の異常が現れるかどうか。

等から解明することを目的とした。

2. 実験

照射試料は、99.5%濃縮^{6}LiとAl（純度99.999%）をタンタルルツボに入れ、アルゴンガス中、約750℃で溶融し作成した。[3] 作成した試料の組

研究施設と装置名
JRR-3、JRR-4、ラジオアイソトープ製造棟

研究分野
材料科学、放射線損傷

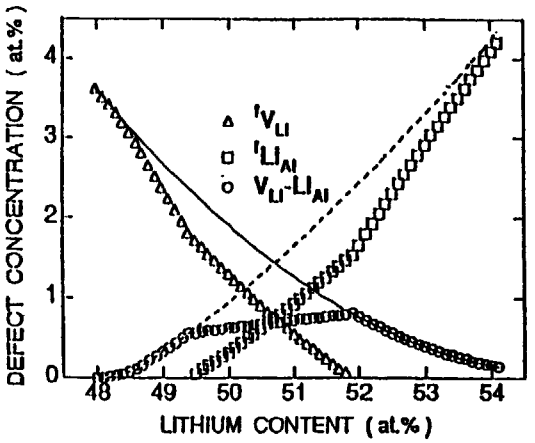

図 1. β相内における格子欠陥濃度とLi濃度の関係 $^{f}V_{Li}$：複合欠陥を形成しないLi原子空孔、$^{f}Li_{Al}$：複合欠陥を形成しないAl格子点上の置換Li原子.[2)]

成は、図 1 に示したように、Li 濃度が 各々 48.0 at.% （V_{Li} のみのを含む）、50.2 at.%（欠陥濃度：$V_{Li} > V_{Li}$ - $Li_{Al} > Li_{Al}$）、51.6 at.% （欠陥濃度：$Li_{Al} > V_{Li}$ - Li_{Al}）である。これらの試料（5 x 5 x 1 mm³）は、Al 箔でカバーした後、石英ガラス管に真空封入した。中性子照射実験は、JRR－4 とJRR-3で行った（表1）。このとき、^{6}Li (n, α) ^{3}H 反応で生成される T と He は各々10^{19} cm^{-3} のオーダーである。電気抵抗率の測定は、ヘリウムガスを満たした密閉容器内で、10 ～ 300 Kの温度範囲で、Van der Pauw 法[4)] によって行った。

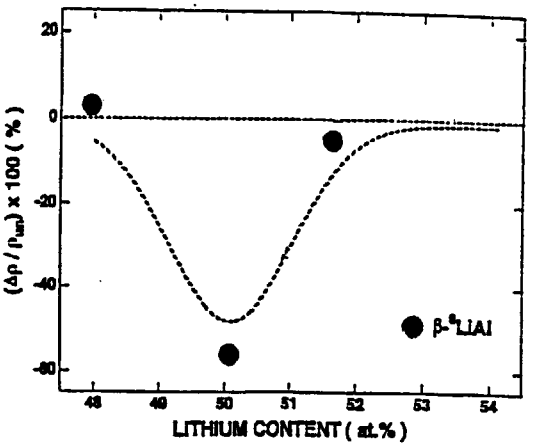

図 2. 中性子照射したβ-^{6}LiAlの室温における電気抵抗率の変化率（$\Delta\rho/\rho_{un}$）とLi濃度. $\Delta\rho = \rho_{irr} - \rho_{un}$ 、点線は以前筆者らが報告したものである。[2)]

3. 結果と考察

図 2 は、中性子照射前後の室温における電気抵抗率の変化率をLi 濃度に対してプロットしたものである。今回の結果では、Li 濃度が 48.0 at.% と 51.6 at.% の組成を有する試料では、大きな変化は見られないが、50.2 at.% の試料の電気抵抗率は 約 55 %の大きな減少率を示した。これは、以前報告したもの[2)] と同じ結果を示している。

一方、β相境界付近の組成である48.0 at.%Liの試料の照射前後の電気抵抗率の温度依存性を図3に示した。この図から、V_{Li} の 規則-不規則変態に起因する電気抵抗率の異常が、双方の試料におい

表1. β-^{6}LiAlへの中性子照射条件

Sample	^{6}LiAl (48.0 at.% Li, 51.6 at.%Li)	^{6}LiAl (50.2 at.%Li)
Neutron Sourse	JRR-4 (T-pipe)	JRR-3 (HR-pipe)
Neutron Flux	ψ_{th} = 8.0 x 10^{13} n/cm²sec ψ_{f} = 1.2 x 10^{12} n/cm²sec	1.0 x 10^{14} n/cm²sec 6.0 x 10^{11} n/cm²sec
Irradiation Time	120 min.	67 min.

て90 K付近に現れることがわかる。この結果は、Li不足相境界のV_{Li}のみのを含む試料では^{6}Li (n, α) ^{3}H 反応により生成されるTとHeの注入効果、さらにその核反応における放射線損傷の影響がなかったことを示している。このことは、この組成の試料に含まれるV_{Li}の数（～10^{21} cm^{-3}）と注入されるTとHeの数（～10^{19} cm^{-3}）を比較すると、後者のほうが2桁程少なく、注入されたTとHeは多数存在するV_{Li}にトラップされ、キャリアの散乱として大きな効果をもたらさなく、また、低温におけるV_{Li}の再配列であるV_{Li}の規則-不規則変態にもに影響を及ぼさなかったものと考えられる。

次に、格子欠陥濃度中で Li_{Al} が主流になり、$^{f}V_{Li}$の量が少ない組成領域に相当する51.6 at.%Liの試料の場合は、図4に示したように電気抵抗率の値が若干減少しているが、その温度依存性に変化は見られない。この現象は、核反応及びそれに伴う放射線損傷を受けてもキャリアの散乱中心となるものが変化しないことを示しており、新たな格子欠陥の導入が少ないものと考えられる。この理由として、この組成領域では、放射線損傷時にLiイオンの移動パスとしての役割をする$^{f}V_{Li}$の量が非常に少ないためと思われる。

図5は、Li濃度が50.2 at.%の試料の電気抵抗率の温度依存性を示したものである。この図では、中性子照射前に電気抵抗率の温度依存性に現れなかった90K付近の異常抵抗が、照射後に観測されたこと、そして、急激に抵抗値が減少したことがわかる。初めに、照射後の抵抗値の減少を次のようなキャリアの散乱モデルから考察する。

β相内の室温の電気抵抗率は、リンデの法則（荷電不純物による残留電気抵抗率は、不純物原子と母体原子間の原子価の差の2乗に比例する）に基づくキャリア散乱モデルにより、

$$\rho\ (C_{Li}, T) = Rv\ [^{f}V_{Li}] + 4\,Ra\ [^{f}Li_{Al}] + 9Rc\ [V_{Li} - Li_{Al}] + \rho_0\ (RT)$$

で表すことができる。[2] ここで、Rv、Ra、Rcは定数、[ ]は各々の欠陥の濃度、ρ_0 (RT) はLi不足境界の組成（48.0 at.%Li）における室温の電気抵抗率である。この式は、キャリアの散乱中心として最も効果的に働くものは、複合欠陥（V_{Li} - Li_{Al}）であることを示している。従って、電気抵抗率の急激な減少は、中性子照射によって、この複合欠陥が破壊されたことに起因するものと予想される。この破壊過程を、Li濃度が50.2 at.%の試料に多数存在する $^{f}V_{Li}$ をLiイオンの移動パスとして、V_{Li} - Li_{Al} が $^{f}V_{Li}$と$^{f}Li_{Al}$に分離したものと推定した。この推定をもとに、上式から照射後の電気抵抗率を算出した。その結果、電気抵抗率の変化

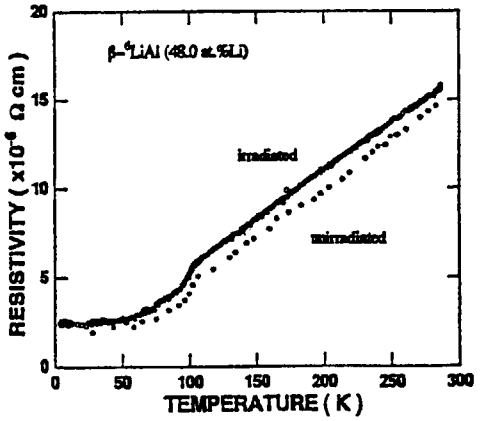

図3. 中性子照射前後のβ-^{6}LiAl(48.0 at.%Li)の電気抵抗率の温度依存性.

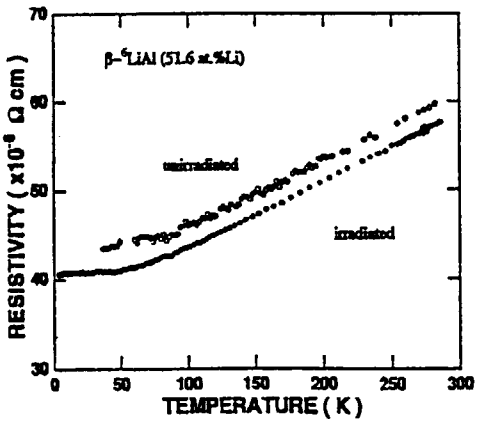

図4. 中性子照射前後のβ-^{6}LiAl(51.6 at.%Li)の電気抵抗率の温度依存性.

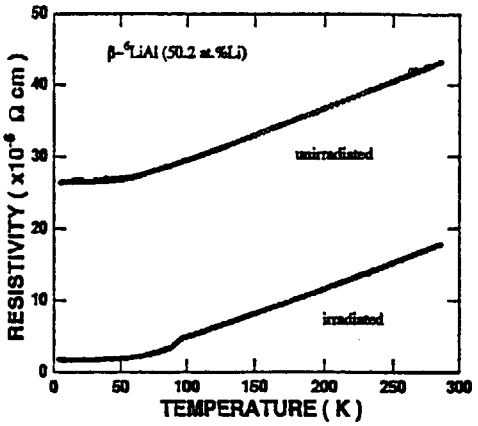

図5. 中性子照射前後のβ-⁶LiAl(50.62at.%Li)の電気抵抗率の温度依存性.

率（$\Delta\rho/\rho_{un}$）は、-20％となり、測定された値-55％と一致しなかった。この理由は、複合欠陥の破壊のみが電気抵抗率の減少を引き起こしているのではなく、別の要因もあることを示唆している。特に、照射後の電気抵抗率の値が、Li不足境界（48.0 at.%Li）の値に近くなっており、組成変化の考慮も必要である。

以上のことから、中性子照射 β-⁶LiAl（50.2 at.%Li）の電気抵抗率の減少は、核反応に伴う放射線損傷とそのときの反応熱により、複合欠陥が破壊され、同時に $^{f}V_{Li}$ をLiイオンの移動パスとして、Li原子が移動し局部的にLiが析出し、組成がβ相境界の48.0 at.%Liになったためと考えられる。また、照射後に低温で観測されたV_{Li} の規則－不規則変態は、Li の析出に伴い組成が 48.0 at.%Li 付近になったことを裏付けるものである。

4. まとめ

(1) Li不足相境界のV_{Li} のみのを含む試料への中性子照射では、^{6}Li (n,α) ^{3}H 反応により生成されるTとHeの注入効果、さらにその核反応における放射線損傷の影響がなかった。従って、中性子照射後も低温における V_{Li} の規則-不規則変態に起因する電気抵抗率の異常が観測された。

(2) Li濃度が50.2 at.% の組成を持つ試料への中性子照射では、電気抵抗率の急激な減少と低温における異常抵抗が観測された。これは、核反応に伴う放射線損傷とそのときの反応熱により、複合欠陥が破壊されると同時にLi原子が移動し、局部的にLiが析出し、組成がβ相境界の48.0 at.%Liになったためと考えられる。

今後の課題として、中性子照射による電気抵抗率減少のメカニズムの詳細を解明するために、更に、照射試料の電気的性質の測定、X線回折、金属顕微鏡による表面観察、比熱測定等が必要であると考えられる。

参考文献

[1] K.Kuriyama, T.Kamijoh and T.Nozaki, Phys. Rev. B22, 470 (1980).

[2] H.Sugai, M.Tanase, M.yahagi, T.Ashida, H.Hamanaka, K.Kuriyama and K.Iwamura, Phys. Rev. B52, 4050 (1995).

[3] M.Yahagi, J. Cryst. Growth 49, 396 (1980).

[4] L.J.Van der Pauw, Philips Tech. Rev. 20, 220 (1958).

成果の公表

学会発表

矢萩正人、須貝宏行、棚瀬正和、浜中廣見、栗山一男：「中性子を照射したβ-LiAl中のLi原子空孔の規則-不規則変態」、日本物理学会講演概要集秋の分科会2 3a-N-7 (1997).

隕石中の微小構成粒子の同位体・化学組成とその形成環境の研究

Isotopic and chemical compositions of small constituents of meteorites and their formation environment

田中　剛、岩森　光、平原靖大、矢来博司、米澤千夏、
ドラグシャヌ・クリスチャン、林　正人、戸上　薫
T.Tanaka, H.Iwamori, Y.Hirahara, H.Yarai, C.Yonezawa,
C.Dragusann, M.Hayashi, K.Togami

名古屋大学大学院　理学研究科
Graduate School of Science, Nagoya University

1．研究目的及び意義

1969年にメキシコに落下したアレンデ隕石には、1㎜以下から10㎜を越える様々な大きさのカルシウム・アルミニウムに富む包有物（ＣＡＩ）が含まれる。ＣＡＩは難揮発性元素に富むため、太陽系形成初期の情報を保持していると思われ、数多くの研究がなされてきた。包有物はその形状により主にCoarse grained inclusionとFine grained inclusionの2種類に分けられ、形状のみならずその微量元素組成も異なる。とくにTanaka and Masuda（1973）によって発見されたPink inclusionの全岩希土類元素存在度（のちにグループ2に分類された）が、その後Boynton（1975）の物理化学的計算との対比によりその生成環境が考察されたように、包有物全体についての微量元素の分析は太陽系形成初期の環境を研究していくうえで非常に重要なものである。そのため、Grossman and Ganapathy（1976）、Mason and Taylor（1982）など多くの研究者によって包有物の全岩組成の分析が盛んに行なわれてきた。

しかしながら、これらの研究の大部分では包有物としては異常に大きな直径5㎜以上のものしか分析されておらず、それ以下の大きさの包有物については数としては圧倒的に多いにも関わらずほとんど検討対象となっていない。さらに、分析機器やその手法は個々の研究ごとに異なったものである。このため、これらのデータを単純にまとめても分析方法に由来する不均一性が残存する。このことを考慮し、本研究では同じ実験条件、同じ標準試料で49個の包有物を分析した。特に直径2㎜程度の従来あまり分析されていない中程度以下の大きさを持つ包有物についても分析を行った。

同じ1969年、オーストラリアに落下したマーチソン隕石には、コンドリュールCAIs（Ca-Al rich Inclusions）、Olivineなどの他に、球形や不規則な形をした、直径30～200 μm程度の不透明鉱物粒子が含まれている。この粒子は主にPyrrhotite〔$Fe_{1-x}S$〕、Pentlandite〔$(Fe,Ni)_9S_8$〕、あるいはそれらの組み合わせからなり、MagnetiteやFe-Ni metalを含むこともある。アレンデ隕石など他の非平衡コンドライトにもコンドリュールやマトリックス中に同様の粒子が含まれており、その組成や起源についていくつかの研究がある（例えばS.E.Haggerty and B.M.McMahon,1979など）。しかし、マーチソン隕石についてはこのような研究が少なく、またこれらの粒子を直接取り出しての研究はほとんどない。そのでこれらの非珪酸塩粒子をマーチソン隕石から直接取り出し、その形状と化学組成について調べた。

研究施設　ＪＲＲ－３Ｍ（ＨＲ－２）　研究分野　Cosmochemistry, Geochemistry

2．研究内容

まず、アレンデ隕石のスラブの表面から様々な包有物を任意に選び出し、その形状構成鉱物により6種類に分類した。包有物は顕微鏡下において、高純度のチタン製のピンセットを使用して300 μg程度を取り出した。このとき、マトリックスが混入しないよう細心の注意を払った。このようにして取り出した試料は、ブランクを低減するために高純度の石英管（スプラシル）を用いて作成した小型試料カプセルに封じた。小型試料カプセルの重さは7−40 mgである。試料の重さはウルトラミクロ天秤で10回測定し、その平均値を試料の重さとした。また同じ方法で、包有物を含まないマトリックス成分のみを採取した。

マーチソン隕石から目的の粒子をできるだけ破壊せずに取り出すために、Freeze-thaw法を用いて隕石を分解した。約2.5 gのマーチソン隕石から約300個の粒子を顕微鏡下で取り出すことができた。取り出した粒子の表面構造をSEMで観察した後、研磨し、粒子の断面をEPMAで観察、分析した。分析はFe, Ni, Co, Ti, Cr, S について行った。その後、一部の粒子について上記と同様の高純度石英管に封入し、中性子放射化分析法（INAA）で元素分析を行った。

3．実験課程

まず試料を日本原子力研究所の原子炉ＪＲＲ−3（熱中性子フラックス9.0×10^{13} n/cm・sec）で6−31時間照射を行った。その5−7日後に試料からのγ線強度を計測することにより、カルシウム、ランタン、サマリウム、イッテルビウム、ルテチウム、レニウム、オスミウム、ナトリウム、金などの短半減期核種を生成する元素の存在度を求めた。さらに約1カ月後に、もう一度計測して、スカンジウム、セリウム、ユーロピウム、イリジウム、亜鉛、クロム、鉄、コバルトなどの長半減期核種を生成する元素の存在度を求めた。

レニウム、オスミウム、イリジウム、金については試薬溶液から作成した試料を、その他の元素については、地質調査所発行の岩石標準試料ＪＢ−1を標準試料とした。γ線の計測は地質調査所放射化分析室、および名古屋大学アイソトープ総合センターにおいて行い、測定に用いたγ線エネルギー等、解析の詳細は、田中ほか（1988）によった。

4．結果

アレンデ隕石包有物49個中の微量元素存在度を分析の結果、coarse grained inclusion 中の難揮発性元素は、過去の研究ではＣ1コンドライト中の濃度に比べほぼ均一に約20倍濃集しているのに対し、本研究で分析した試料では5倍程度しか濃集していなかった。これは、本研究において分析されたcoarse grained inclusionが二次的な変成を受け、様々な程度に揮発性元素が混入し、鉱物（ソーダライト、エンスタタイト等）が生成したため相対的に揮発性元素の濃度が薄まったためと思われる。本研究で扱った試料の方が揮発性元素の存在度が高いことが、このことを裏付ける。さらに、この薄まり方の度合いは包有物の大きさと関係があり、小さな包有物ほど難揮発性元素の存在度は低い値を示した。（図1）

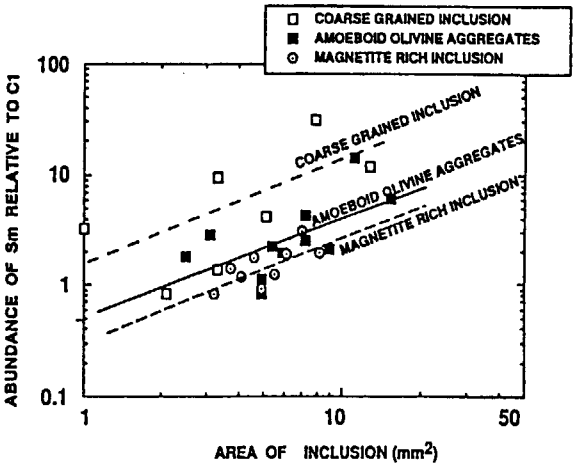

図1　coarse grained inclusions における inclusions の大きさとSm濃度の関係。大きいinclusionほどSm濃度も高い。

また、包有物の断面積を難揮発性元素の存在度の対数をとったものとが、断面積の大きいところにまで比例すると仮定するならば、Ｃ1コンドライトに対

して20倍濃集するためには、包有物の直径は5㎜以上でなくてはならないという結果を得た。過去の報告は大部分が直径5㎜以上なので、この結果は妥当といえる。一方これに対しfine grained inclusionは大きさに関係なくほぼ過去の報告と同じ値すなわち軽希土ではC1コンドライト中の濃度に比べ20倍、重希土では3倍以下を示した。(図2)

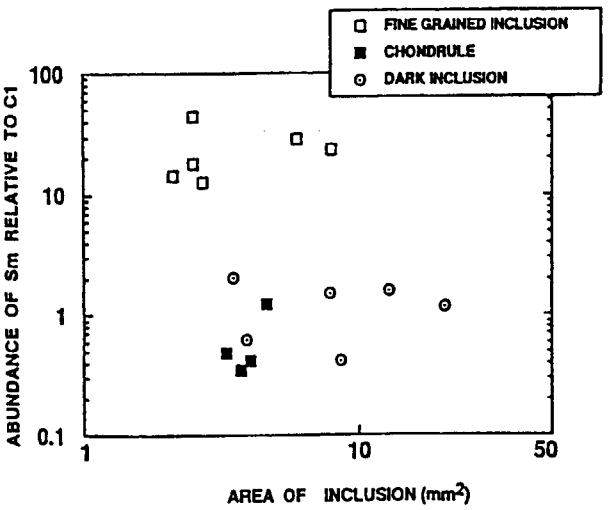

図2 fine grained inclusionsの大きさとSm濃度の関係。両者の明瞭な関係は見られない。

これはfine grained inclusionが二次的な変成をうけていないことを意味する。これらのことから、包有物の生成順序としては、coarse grained inclusionが部分溶融によりガスと反応して二次的な変成を受けた後、fine grained inclusionがガスから生成した、またはcoarse grained inclusionとfine grained inclusionは生成した場所が異なり、coarse grained inclusionができた場所のみが温度が上昇し部分溶融が起こったと考えられる。

マーチソン隕石中の不透明鉱物粒子は、鉱物学的に(1) pyrrhotite (Po) only、(2) pentlandite (Pn) only、(3) Po+Pn (+magnetite)、(4) Po+Pn+Fe-Ni metal (+madnetite)に分類することができた。またこれらの鉱物の他に、珪酸塩鉱物、schreibersite〔(Fe,Ni)$_3$P〕や、GeとNiに富むphaseが含まれることがわかった。含まれる珪酸塩鉱物はforsterite〔Mg_2SiO_4〕、enstatite〔$MgSiO_3$〕、Ca-pyroxeneなどである。

Poには、Niに富むものとNiをほとんど含まないものが存在する。Niに富むPoについては一部のものにラメラが観察された。ラメラが見られないものについては1μm以下のbeadがみられた。また、ラメラは粒子の中心部に限り存在し、粒子の周辺部にはbeadが分布していることがわかった。このラメラとbeadは粒子内でNi-Coについてよい相関を示し、同一起源であると考えられる。しかし、ラメラ、beadとPnは異なる傾向を示す。ラメラ、beadがC1コンドライトよりも高いCo/Ni比を示すのに対し、PnはC1と同じか、それよりも低い値を示す。

INAAでは、0.2~10μgの試料から、Fe、Co、Ni、Cr、Se、Zn、Ru、Re、Os、Ir、Auが検出された。(図3)

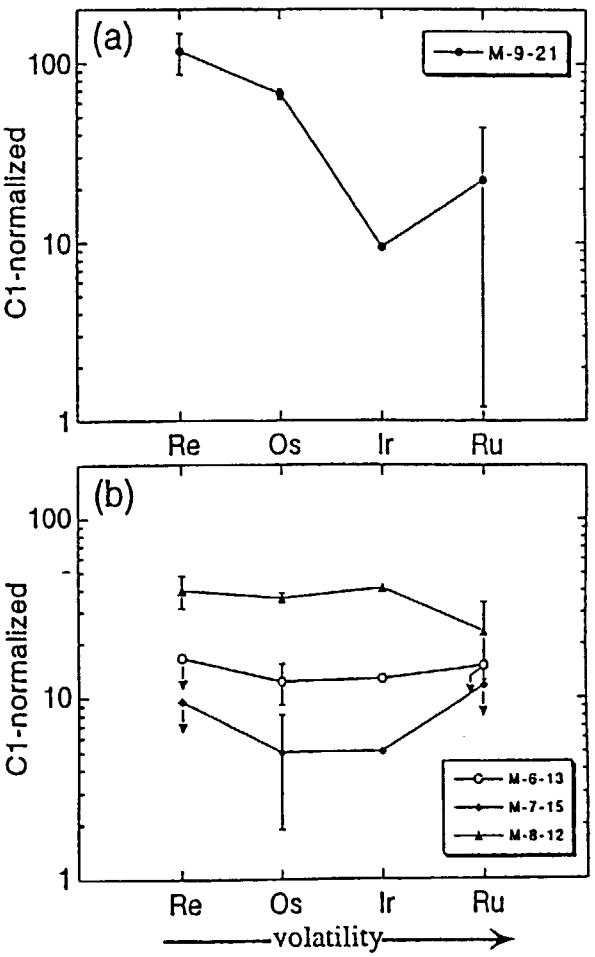

図3 C1コンドライト中の値で規格化した硫化物包有物中の白金族元素存在度パターン。

Crについては全ての粒子でClコンドライトの0.01～0.5倍と低い濃度を示した。Osが検出された粒子についてはRe、Ir、Ruも検出され、Clコンドライトの5～100倍と高い濃度を示した。Re、Os、Ir、Ruといった元素は、難揮発性の元素であり、高温での凝縮物に高い濃度で含まれていると考えられる。したがって、これらの粒子は高温での凝集物を含んでいる可能性がある。この中の一つについては、非常に低いRu/Re比、Ir/Os比を示し、特に高い温度での凝縮物を含む可能性がある。また、難揮発性元素に富むこれらの粒子には構成要素としてPnが必ず含まれている。

不透明鉱物粒子の形成過程については、

(1) silicate melt中に形成された、硫黄に富む不混和液

(2) 星雲中で凝縮したFe-Ni metalがH_2Sと反応

(3) Fe-Ni sulfideが直接星雲から凝縮

(4) その他

が考えられる。しかし、PoのCo/Ni比がClコンドライトよりも大きいこと、不透明鉱物粒子がCrに乏しいことなどは(1)や(2)のモデルでは説明できず、それ以外の形成過程を考える必要がある。

5. 結果とその評価

Allende隕石中のインクルージョンについての分析はおおむね満足できるものであった。しかしマーチソン隕石の硫化物粒子についてはとくにその大きさが数μg～数十μgと小さかったこともあり、ブランク値を差し引いて、十分信頼するに足るデータが得られた試料は少なかった。今後よりバックグラウンドの少ない封入方法を考える必要がある。Allende隕石の結果については印刷公表1)を行ったが、マーチソン隕石については今少しの検討を行ってから印刷公表を行いたい。

本研究題目そのものではないが、惑星表面の風化変質を考える基礎としてγ線照射下での水ー岩石反応生成物の分析を中性子放射化法により行った。γ線の照射は著しく水ー岩石反応を促進することがわかり、予備的な結果ではあるが印刷公表した2)。今後より詳細な実験を行いたい。

6. 本研究にともなう成果のうち公表されたもの

1) 林　正人、田中　剛、上岡　晃(1995)　アレンデ隕石中のCAIの大きさと化学組成からみたCAIの生成場について. 地球化学, 29 (1) ,37-50

2) C.Yonezawa, T.Tanaka, and H.Kamioka (1996) Water-rock reactions during gamma-ray irradiation. Applied Geochemistry,11,461-469

3) 戸上　薫、田中　剛、岩森　光(1997)　愛知県北東部津具地域の元素濃度分布とその規定要因. 資源地質, 47 (6) , 305-318

低速陽電子ビーム発生の基礎実験

研究代表者　東京大学・原子力研究総合センター　伊藤泰男
協力者　理化学研究所　伊東芳子

Basic Experiments on Slow Positron Beam Generation

Yasuo ITO (RCNST,, Univ. of Tokyo), Yoshiko ITOH (RIKEN)

要旨

JRR-4 水力ラビットを用いて生成した^{64}Cu～30mCiを用いて低速陽電子ビームを発生させる実験を行い、W減速体の熱処理等を実用的な条件を検討した。その結果、Wは2000℃程度まで熱処理すれば良いこと、処理後空気に曝しても低速陽電子発生の効率が著しく低減されることはないこと、などが明らかになった。これらの知見は我々のそれ以降の低速陽電子ビーム発生実験の基礎となった。本報告では、その後加速器を用いて行った低速陽電子ビーム発生の新しい試みについても記す。

ABSTRACT

^{64}Cu of about 30mCi was produced using hydraulic tube of JRR-4 and was used as the positron source for the basic studies of slow positron beam production, where the conditions of thermal annealing of the W moderator and the effect of exposure to air were examined. The results formed the practical basis for our works of slow positron beam development thereafter. Described also are the new trials of slow positron beam production using accelerators.

1. はじめに

低速陽電子ビームとは、高速の陽電子を減速させて eV～数十keV 程度の低エネルギーにしてビームとして取り出したものを云う。低速陽電子ビームを作ることが出来ることが知られる以前は、^{22}Naのようなラジオアイソトープから放出された、平均エネルギー数百keVでゼロから最大エネルギーEmaxまで連続分布したスペクトルで，ラジオアイソトープから4πの立体角に放出される陽電子をそのまま使う方法が採られていた。1985年あたりからこのような陽電子をビームとして取り出す技術が開発され、現在、低速陽電子ビームを軸に新しい陽電子の利用が発展している。

低速陽電子ビームを発生させるためには、高速の陽電子を減速体に入射させてエネルギーを失わせて再放出させて、これをビームとして取り出す。陽電子が再放出される機構は大きく分けて２つある。

1) 減速途中で飛び出す。
2) 熱化した陽電子が負の仕事関数で押し出される。

1)の機構で得られる低速陽電子ビームはエネルギー単色性とエミッタンスが悪いが、強度は入射高速陽電子の数%と比較的大きい。2)の方法で得られる低速陽電子ビームは、エネルギー単色性（ΔE～2eVの程度）とエミッタンスに優れるが、強度は入射高速陽電子の10^{-4}以下である。このため、元になる高速陽電子源の強度の大きいものが必要となる。本研究は、低速陽電子ビームを発生させる研究の一環として、原子炉照射によって得られる陽電子源として^{63}Cu(n, γ)^{64}Cu 反応を用いることを想定して申請したのもである。本研究期間の初期にこのような照射を行って成果を報告しているが[1]、本報告ではこれも含めて，我々の陽電子ビーム発生実験のこれまでの概要を報告する。

2. 陽電子源

陽電子源としては、

1) β^+崩壊するラジオアイソトープ
2) 制動放射X線による対生成

が用いられる。(2)の方法で行った我々の(電子

JRR-4 水力ラビット / 第３研究棟ホット実験室　　陽電子消滅・低速陽電子ビーム発生

線リニアックを用いた）研究[2-3]は、本報告の範囲内でないので割愛する。β^+崩壊するラジオアイソトープは原子炉や加速器による照射で極めて多くの種類のものが得られる。これらの内、長寿命のものは照射後にゆっくりと取り扱うことが出来るが、短寿命のものは原子炉・加速器による照射とオンラインで低速陽電子ビームを取り出すことが必要になる。これら無数の可能性の中から、我々が試みたものを以下に報告する。

3) ^{64}Cuによる低速陽電子ビームの発生

^{64}Cuの半減期は12.8時間であり、1gのCu金属を原研の原子炉（熱中性子束:～4x10^{13}/cm^{2}s）で一半減期相当時間照射すると、ほぼ 1Ciの線源が得られる。しかし陽電子が線源中で自己吸収されては意味が無いので、事実上は数十ミクロン程度の厚さの銅箔を用いることになり、事実上数十mCi程度の強度の線源を得て利用することになる。この程度の強度では、半減期が短いこともあって実用にならない（かつてBrookhaven National Lab. で行われていたように、もっと中性子束の大きな原子炉を用いるならば実用になる可能性がある）。しかし、低速陽電子ビームの開発段階では半減期が短いことが逆に有利となる。開発実験中に仮に汚染が起こっても減衰を待っていれば良いので、多少の冒険が可能となるからである。

実験で用いた装置の概略を図１に示す。source chamberに原子炉照射で得た^{64}Cuを線源として置く。実際に用いた線源の強度は30mCiであった。annealing chamberは減速体であるW多結晶箔を200℃以上に加熱して表面処理し、直線導入端子で線源の位置まで移動させる。^{64}Cuから放出された高速陽電子はW中で減速し、その一部が表面に近づいて負の仕事関数(～-2eV)によって真空側に押し出される。この低速陽電子を数十eVに加速してソレノイドコイル(Sol1/Sol2 と書かれた90° 曲がった及び直線の飛行管）の磁束に巻き付いて輸送され、detector chamber内のターゲットで対消滅する。この時の低速陽電子ビームのプロファイルはMCPA(Micro channel Plate Assembly)でモニターされ、低速陽電子の数は１対のシンチレーション検出器 BGOA/BGOB による消滅ガンマ線の同時計数から測定される。

この装置を用いて、種々の処理を行ったW減速体の効率を決定し、比較することがこの実験の目的であった。

図２に高速陽電子→低速陽電子の変換効率εがW多結晶（厚さ10μm）の熱処理温度によってどのように依存するかを実験した結果を示す。εは900℃から2000℃の処理温度までほぼ１桁増加するが、ε～2x10^{-4}で頭打ちになる。このことから2000℃以上の熱処理はあまり意味が無いことがわかる。更に、一度熱処理したWを空気に曝したら効率がどのように影響を受けるかを調べたが（図２下）、約２時間程度で効

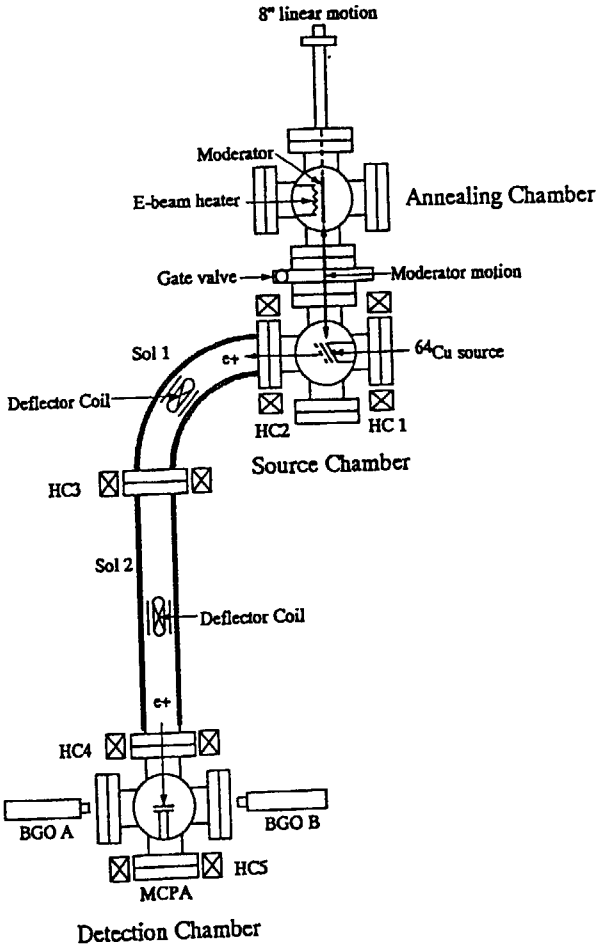

図１装置図
システムは annealing chamber, source chamber, transport tube, detection chamber の４部分からなる。W減速体は, annenaling chamber で熱処理された後、source chamber 内の線源（^{64}Cu）の手前に移動させられる。低速陽電子はソレノイド飛行管を通して detection chamber に入り、対消滅して計測される。計測は１対のシンチレーション検出器(BGO A&B) による消滅ガンマ線の同時計数による。

率が～3/4程度に低下するが、その後10数時間後も効率はそれ以上低下しないことが分かった。このことから、W熱処理後一度空気に曝しても効率に大きな影響を与えることがないこと、従って、実用的には、図1のようにannealing chamberとsource chamberとを設けてWが両者間を直線導入端子で移動するようにすることはしなくても良いと結論される。これによって以後の我々の低速陽電子ビーム発生装置ではこの部分を省略して簡略かつ経済的になった。

高速→低速陽電子への変換効率 $\varepsilon = 2\times10^{-4}$ は経験的にはそれほど悪い値ではない(多くの場合この程度かそれ以下)が、より良い変換効率が得られればそれに越したことは無い。そこで、種々のガスを導入して表面処理をして変換効率の向上を狙う実験も行った。図3にその結果を示す。ここで変換効率 ε は2100℃でアニールしたW多結晶の値を規準に示してある。酸素ガス雰囲気中で加熱したのは、Cなどの元素がW表面に偏析していたとして、それを除去することを狙っている。水素ガス雰囲気中で加熱したのは、Sなどの元素を還元除去することを狙っている。しかしいずれの場合も効率が相対効率が向上することは無かった。W減速体の処理について、還元雰囲気中で加熱すると効率が向上するとの報告[4]もあるが、我々の結果はこれと一致しない。

図2
(上:熱処理温度の効果)W減速体の熱処理温度と高速陽電子から低速陽電子への変換効率εの関係。効率は2000℃までは処理温度と共に増大するが、それ以上の温度で処理しても効率は向上しない。
(下:空気の効果)一度2000℃で処理したW減速体を空気に曝しても効率は著しくは減少しない。

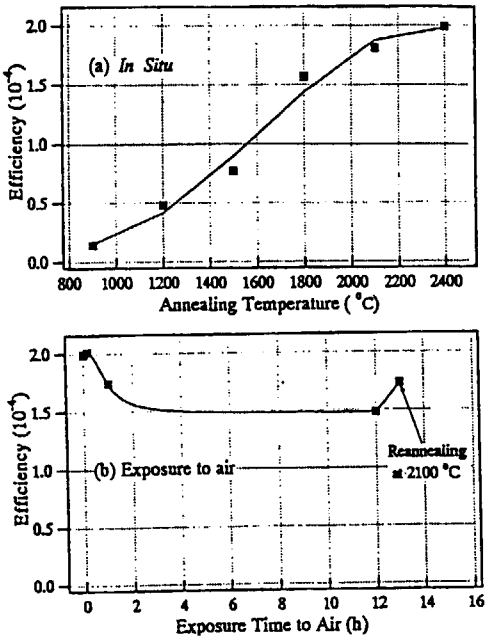

図3　W減速体を種々のガス雰囲気中で熱処理した時の変換効率。実験は2100℃で熱処理したW多結晶を初期材料として、同じ材料について実験番号(横軸)の順に行われた。

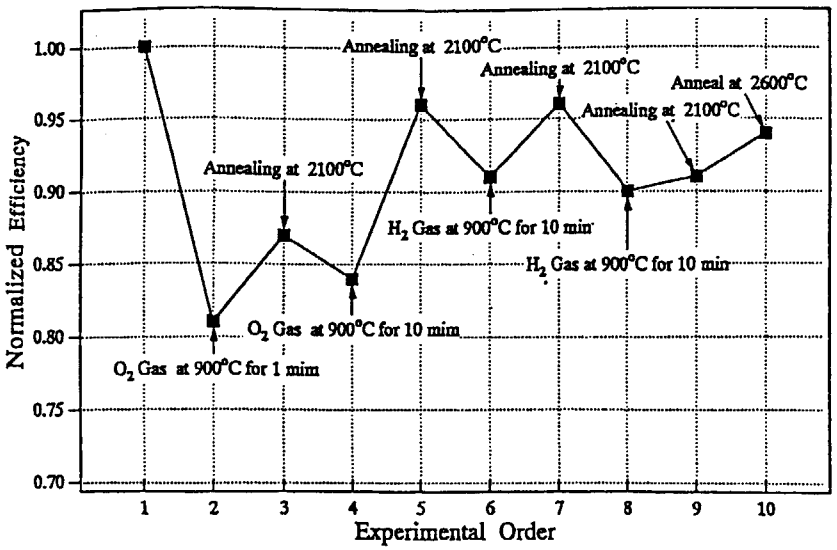

4. イオンビーム照射による陽電子源作成

原子炉を用いた中性子照射では(n, γ), (n,p), (n,n)反応などが主となるので中性子過剰の、即ち、β^-崩壊性のラジオアイソトープが出来やすい。一方、加速器を用いてイオンビームで核反応を起こさせると、(p,n), (d,n)反応などで中性子不足の，即ち、β^+崩壊性のラジオアイソトープが出来やすい。このため陽電子実験のためには本来加速器を用いた方が多くのラジオアイソトープの選択の可能性があることは、PET (Positron Emission Tomography)で種々のβ^+エミッターが用いられている例を見るまでもない。p,dビーム照射で作ることの出来る代表的なβ^+エミッターの例をその半減期の値とともに下に示す。

$^{12}C(d,n)^{13}N$ 10m
$^{12}C(p,n)^{12}N$ 0.125s
$^{14}N(p,n)^{14}O$ 72s
$^{14}N(p,\alpha)^{11}C$ 20m
$^{14}N(d,n)^{15}O$ 2m
$^{18}O(p,n)^{18}F$ 2m
$^{27}Al(p,n)^{27}Si$ 4s
$^{28}Si(p,n)^{28}P$ 0.3s
$^{48}Ti(p,n)^{48}V$ 16d
$^{58}Fe(p,n)^{58}Co$ 71d

これから分かるように、多くのものが半減期が分のオーダー以下であるので、線源を作製してから図1のようなチェンバーに据え付けるということが出来ない。このため、イオンビーム照射とオンラインで低速陽電子ビームを発生させることが必要になる。住友重機では$^{27}Al(p,n)^{27}Si$反応を用いたオンライン低速陽電子ビーム発生装置を開発している[5]が、我々はそれ以外のβ^+エミッターを利用する方法を試みた。

ここで低速陽電子ビーム発生の基本的な方法は図1と同じであるが、図1の^{64}Cuの位置に^{13}N, ^{11}Cのようなβ^+エミッターを配置できなくてはならない。半減期の極めて短いSiやAlをターゲットとする場合は、線源をいじっている暇はないのでオンラインとせざるを得ない。そこで、図4のようにターゲットチェンバーの中でイオン照射しかつ低速陽電子を取り出すことを試みた。図4の中程の挿入図のように、サイクロトロンからのイオンビームに対してターゲットを60° 斜めに置き、ターゲットの面に平行にW減速体を出来るだけ近づけて置き、更にこれに平行に低速陽電子引き出しのための電極 (mesh) を置く。この時ビームがW減速体を照射して損傷を与えないように、幾何学的な配置に工夫が必要である。図5に示すような幾つ

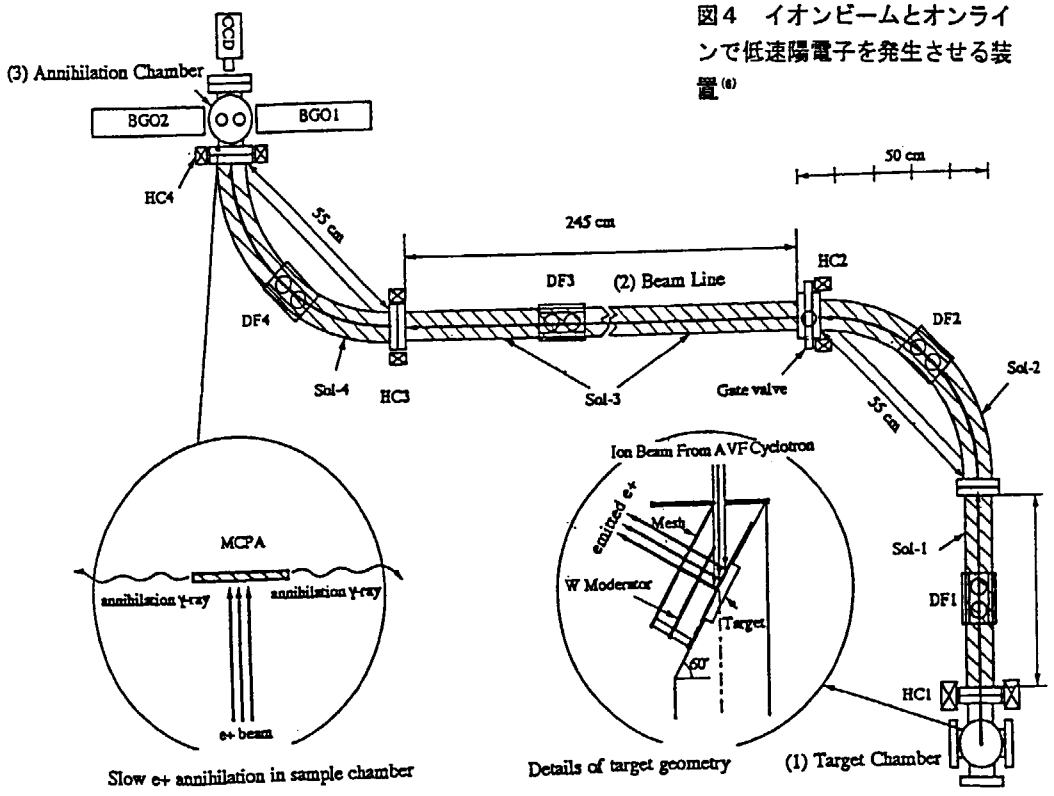

図4 イオンビームとオンラインで低速陽電子を発生させる装置[6]

かの幾何学的な配置を実際に試みた。

ターゲットしてはBN, NaF, AlN, Al, C, SiN, SiC, SiO_2 などを用いた。表一にこれらの材料の核的なデータをまとめてある。得られた結果を表二に示す。用いたターゲット全てについて結果が得られた訳ではなく、多くのものはチャージアップが原因と思われる不安定性に影響された。

この段階ではプロトンビーム4μAの照射で $5.6x10^4$ slow e^+/s が最も良い成績であった。これは実用的には不十分であり、強度の改善が必要である。そのためには、ターゲット内での陽電子の自己吸収を少なくすること、幾何学的な配置を改善することがポイントである。

表一　用いたターゲット材料とその核的なデータ。最大断面積は ALICE プログラムによる計算結果

Various target materials for β^+-decay radioisotopes. Maximum cross sections are calculated from the ALICE program [9]

Target	Nuclear reaction	Isotope (max. of β^+)	Half life	Max. cross section (mb/MeV) ALICE [9]
BN	$^{11}B(p, n)^{11}C$	^{11}C (0.97 MeV)	20.4 min	72 mb at 12 MeV
	$^{14}N(p, \alpha)^{11}C$	^{11}C (0.97 MeV)	20.4 min	75 mb at 12 MeV
NaF	$^{23}Na(p, n)^{23}Mg$	^{23}Mg (3.03 MeV)	12 s	119 mb at 14 MeV
	$^{19}F(p, n)^{19}Ne$	^{19}Ne (2.22 MeV)	18 s	28 mb at 9 MeV
AlN	$^{27}Al(p, n)^{27}Si$	^{27}Si (3.85 MeV)	4.2 s	113 mb at 14 MeV
	$^{14}N(p, \alpha)^{11}C$	^{11}C (0.97 MeV)	20.4 min	75 mb at 12 MeV
Al	$^{27}Al(p, n)^{27}Si$	^{27}Si (3.85 MeV)	4.2 s	113 mb at 14 MeV
C	$^{12}C(d, n)^{13}N$	^{13}N (1.2 MeV)	10 min	205 mb at 4 MeV
SiN	$^{28}Si(d, n)^{29}P$	^{29}P (3.95 MeV)	4.5 s	89 mb at 5 MeV
	$^{14}N(d, n)^{15}O$	^{15}O (1.74 MeV)	123 s	153 mb at 4 MeV
SiC	$^{28}Si(d, n)^{29}P$	^{29}P (3.95 MeV)	4.5 s	89 mb at 5 MeV
	$^{12}C(d, n)^{13}N$	^{13}N (1.2 MeV)	10 min	205 mb at 4 MeV

図5　イオンビーム入射、ターゲット、W減速体、引き出し電極の幾何学的配置の色々。1, 2ではビームがWを直撃しないようになっているが、3ではWがビームに高かれることを恐れずにターゲットに近づけて幾何学的な効率を向上させている。

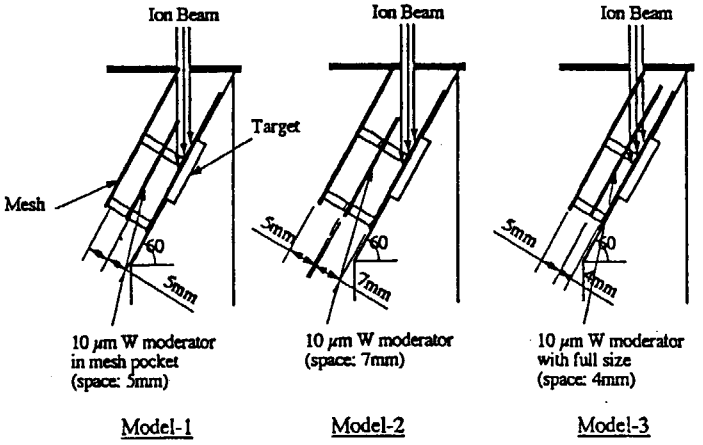

表二　実験結果

Measured slow positron counts from each target irradiated with different ion beam energies and different types of moderator and conditions (three different types of moderators are shown in the bottom section)

Energy of beam (MeV)	Target	Current of beam (μA)	Measured e^+ counts at operated μA (e^+/s)	Type of moderator (condition)	Maximum e^+ counts at max. current (20 μA) (e^+/s)
proton beam					
7	BN	4	1.3×10^4	Model-1	6.5×10^4
	BN	5	8.5×10^2	Model-2 (used)	3.4×10^3
	BN	4.4	4.5×10^3	Model-3 (new)	2.0×10^4
	Al	4.4	0	Model-3 (used)	0
10	BN	3.6	1.02×10^4	Model-3 (used)	5.7×10^4
	Al	3.6	5.5×10^2	Model-3 (used)	3.1×10^3
14	BN	4.0	7.8×10^3	Model-3 (used)	3.9×10^4
	BN	4.0	5.6×10^4	Model-3 (new)	2.8×10^5
deuteron beam					
8	carbon	1.3	4.2×10^3	Model-2 (new)	3.2×10^4
	Si_3N_4	1.3	3.4×10^3	Model-2	2.6×10^4

5. 流体ターゲット

4節冒頭に記した^{11}C, ^{13}N, ^{14}O, ^{15}O, ^{18}F などは、窒素ガス、炭酸ガス、水などをターゲットにして得られる。PETではこのような放射化した流体ターゲットを輸送して標識化合物などに合成してから用いる。低速陽電子ビーム発生では、ラジオアイソトープをマトリクスから分離して、出来るだけ高密度に集めてW減速体の後ろに配置すれば良い。半減期は分のオーダーであるから、それは迅速に行われなければならない。我々は、2つのケースについてこのような流体ターゲットを低速陽電子源とする試みを行った[7]。

5-1 $^{11}CO_2$

高純度・高圧 (7 atm) の窒素ガスに 16 MeV のプロトンビームを照射すると^{11}Cが生成し、不純物としてわずかに存在する酸素と結合して$^{11}CO_2$になる。炭酸ガスは液体窒素温度のトラップによってマトリクス窒素ガスから分離される。このトラップを昇温してHeガスをキャリアとしてWモデレータの背後に導き、ここに再度$^{11}CO_2$を集めて蓄積させる。(以上図6参照)

$^{11}CO_2$を集める方法として、

1) ゼオライトのような吸着剤を用いる

2) 局所的なコールドヘッドにトラップさせる

方法を試みたが、1)ではゼオライトの厚みのために陽電子がW減速体に入射する割合が減少して効率が得られない。2)では、小さい(10mmφ)面積のコールドヘッドを形成すること、そこに$^{11}CO_2$を効率よくトラップさせること、が難しい。

本装置を用いて低速陽電子ビームを発生させられることは実証できたが、現在までのところ、低速陽電子強度において十分な結果を得ていない。

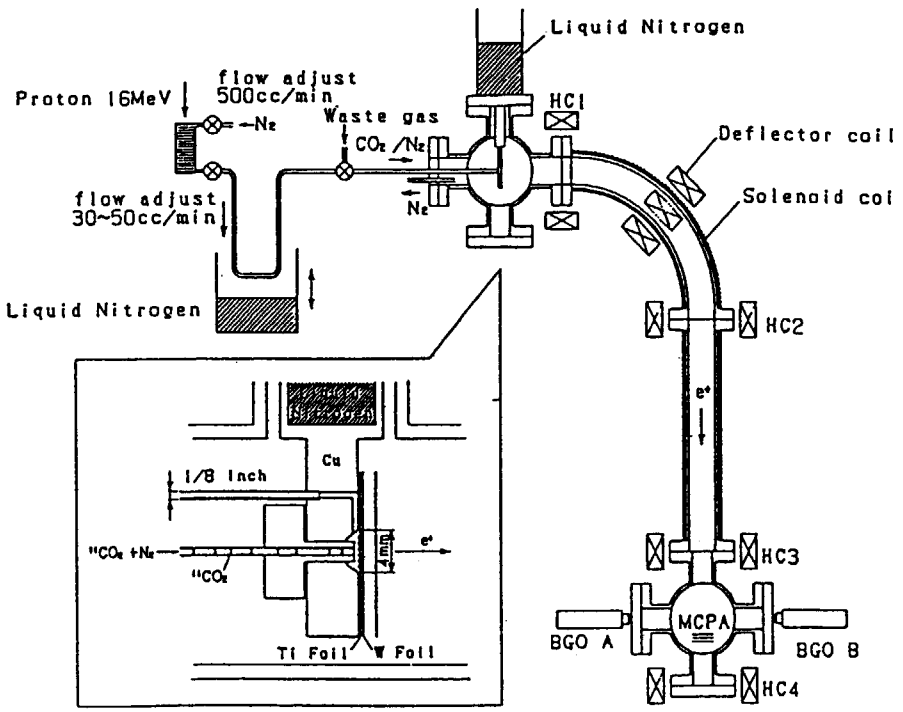

図6　窒素ガスをターゲットとして$^{11}CO_2$を生成し、低速陽電子源とする方法
挿入は低速陽電子発生部の詳細図、W減速体の背後の小さな面積に効率よく$^{11}CO_2$を集めることが必要。

5-2 $H^{18}F$

$^{18}O(p,n)^{18}F$ 反応によって生成した ^{18}Fをそのまま水をキャリヤーとして輸送し、薄い吸着膜に ^{18}F をトラップさせて水は回収する。半減期が２分なので、このプロセスを半連続的に行う必要があり、図７のように２つのヘッドを持った線源部を作り、一方がW減速体の背後にある(図の左部分) 時には、他方は^{18}F生成のループ (図の右半分) にあり、一定時間ごとにスイッチされる。

^{18}Fをトラップさせるヘッド部で吸着材を用いると、その厚みで陽電子が吸収されるという問題がやはり起きる。吸着材を用いる代わりに、このヘッド部で水を蒸発させて$H^{18}F$を沈着させる方法が原理的に可能であるが、これはまだ試みていない。

図７　$H^{18}F$線源作製のための自動装置
水へのプロトン照射、輸送、$H^{18}F$分離、水の回収を行うループ (右側) と、分離された$H^{18}F$をW減速体の背後にセットして低速陽電子ビームを発生させる部分 (左側) とからなる。$H^{18}F$ヘッドは２つあり、一定時間ごとに入れ替えられる。

6. おわりに

本研究は短寿命のラジオアイソトープを用いて低速陽電子ビームを発生させる開発研究として行われた。JRRを用いて^{64}Cuを生成する方法はプロセス自体としては本命に成り得ず、開発過程の一段階で必要となっただけのものである。加速器を用いて試みた実験は理研のAVFサイクロトロンで行われたものであり、多くの貴重な経験を積むことが出来た。この研究は理研の研究者を中心に継続されると思われるが、研究代表者(伊藤)は他の研究に専念するために、本研究は休息する。とはいえ、ラジオアイソトープを用いる低速陽電子ビームは高いスピン偏極度を持っているので、電子線リニアックなどを用いて発生される低速陽電子ビームでは行えないような利用が可能である。チャンスがあれば、再び取り組んでみたい課題である。

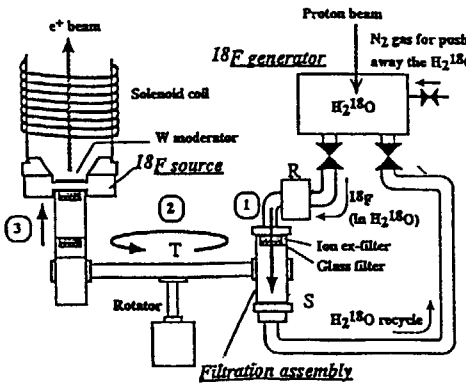

-文献 (1,6,7 が本研究に関連して発表した論文、他は参考文献)
(1) K.H.Lee, Y.Itoh, I.Kanazawa, N.Oshima, T.nakajou and Y.Ito; "Practical Usage of a W Moderator for Slow Positron Beam Production", phys. stat. sol., 157, 93 (1996)
(2) Y.Ito, M. Hirose, S.Takamura, O.sueoka, I.Kanazawa, K.Mashiko, A.Ichimiya; "Brightness Enhanced Slow Positron Beam Produced using an Electron Linac", Nucl. Instr. Methods in Phys. Res.A305, 269-274 (1991)
(3) I.Kanazawa, Y.Ito, M.Hirose, H.Abe, O.sueoka, S.Takamura, A.Ichimiya, Y.Murata; "Production of an Intense slow Positron Beam bu Using an electron Linac and its Applications", applied Surface Sciences, 85, 124-131 (1995)
4)N.Zafar, J. Chevallier, F.M. Jacobsen, M. charlton, G. Laricchia; Appl. Phys. A47, 409 (1988)
(5) M.Hirose, M.Washio, Appl. Surface Science, 85, 111 (1995)
(6) Y.Itoh, K.H.Lee, T.nakajou, A.Goto, N.Nakanishi, N.Oshima, Y.Ito; "Slow Positron Production Using the RIKEN AVF Cyclotron", applied. surface science, 85, 165-171 (1995)
(7) T.Nozaki, Y.Itoh, Z.L.Peng, Y.Ito, N.Nakanishi, H.Yoshida, A.Goto; "Preparation of Positron source for Slow Positron Beam by Ion Bombardment on Liquid and Gas Targets", Materials science Forum, 255-257, 799-801 (1997)

ランタノイド(III)錯体の安定度の順序
Order of Stability of Lanthanide(III) Complexes

薬袋佳孝[1]、広瀬彰一[2]、高橋嘉夫[3]、小橋浅哉[3]、長谷川佑子[2]、富永 健[3]
[1]武蔵大学基礎教育センター、[2]東京理科大学理学部、[3]東京大学大学院理学系研究科
Yoshitaka MINAI[1], Syoichi HIROSE[2], Yoshio TAKAHASHI[3], Asaya KOBASHI[3],
Yuko HASEGAWA[2], and Takeshi TOMINAGA[3]
[1]Center for Arts and Sciences, Musashi University
[2]Faculty of Science, Science University of Tokyo
[3]School of Science, University of Tokyo

ランタノイド(III)の相互分離には溶媒抽出法がしばしば用いられる。特に、リン酸エステルの抽出剤としての利用については、研究が活発に進められている。しかし、溶媒の種類なども抽出効率や分離選択性に関与することが知られており、研究の一層の推進が望まれている。特に、分離機構についての詳細を知ることは、分離効率の一層の向上を図る上で特に重要と考えられている。分離機構の解明には、溶液中のランタノイド(III)の存在形態についての情報が必須であり、これは同時にランタノイドの溶液化学にも重要な知見をもたらすと考えられる。また、ランタノイドの地球化学的挙動には、原子番号に対応した系統的な変化がしばしば観察される。これは、ランタノイド(III)のイオン半径などが原子番号に対して系統的に変化することにより、ランタノイド相互の微妙な化学的性質の相違が地球化学的プロセスに反映されるためと考えられる。特に、地球表層でのランタノイド(III)の化学的挙動には、ランタノイド(III)相互の溶液化学的性質の相違が強く反映されている。本研究課題では、ランタノイド(III)の分離化学並びに地球化学に関する基礎として、ランタノイド(III)相互の化学的性質の系統的な変化を明らかにすることを目的に据え、トレーサーを用いたランタノイド溶液化学に関する研究を行う。

このような溶液中の金属イオンの溶存状態に関する研究では、放射性トレーサーの利用は極めて有効である。これは、放射性トレーサーの利用には、検出におけるマトリックス効果の影響がない、高感度、検出・データ処理に特別なモデルを要しない、実験操作・データ処理の簡便化による実験精度の向上などの特徴があるためである。ランタノイド(III)を対象とした場合には、軽ランタノイド、中ランタノイド、重ランタノイドを代表するトレーサー(ランタン、サマリウム、イッテルビウム)が利用可能な点も重要である。これらの特徴を有効に利用するためには、原子炉中性子照射による高比放射能の放射性トレーサーの製造が是非とも必要である。

本研究課題(平成6年度-平成8年度)では、主に、I. ランタノイド(III)-チオシアナート錯体の溶媒抽出挙動、II. ランタノイド(III)-フミン酸錯体の安定度について、研究成果を得た。以下に、その概要を記す。

I. ランタノイド(III)-チオシアナート錯体の溶媒抽出挙動

ランタノイド(III)の相互分離には、リン酸トリブチルなどの中性抽出剤などによる溶媒抽出がよく用いられる。しかし、隣接するランタノイド(III)の分離係数を支配する因子についてはさらに研究が必要とされている。分離係数を支配する要因を解明することは、分離プロセスの効率化と共に、ランタノイドの溶液化学にも重要な知見をもたらすと考えられる。平成6-8年度は、主に、チオシアン酸イオンを含む水溶液からのトリオクチルホスフィンオキシド(TOPO)によるランタノイド(III)の抽出について研究を進めたので、これについて以下に述べる。

研究施設と装置名
JRR-3M　気送管

研究分野
放射化学・分析化学

[実験] Analytical Gradeまたは特級の試薬を実験に用いた。ランタノイド(III)とチオシアン酸ナトリウムを含む水溶液とTOPOを含む有機溶媒を混合し、ランタノイド(III)を水相および有機相に分配させた。遠心分離後、有機相の一部を採り、抽出されたランタノイド(III)を硝酸溶液に逆抽出した。ICP発光分光法によってランタノイド(III)を定量し、有機相に抽出されたランタノイド(III)の濃度を求めた。^{140}La, ^{153}Sm, ^{175}Ybの放射性トレーサーを原子炉で製造し、同様の実験を行なった。市販の^{152,154}Euも実験に使用した。分配比は両相間のランタノイド(III)の濃度比あるいはγ線測定により求めた両相間の放射能比として得た。

[研究の結果] ヘキサンおよびクロロホルム溶媒について、チオシアン酸イオンとTOPOによるランタノイド(III)の抽出における分離係数を求めた。ヘキサンへ抽出した場合とクロロホルムへ抽出した場合で、隣接したランタノイド(III)の分離係数が大きく異なることが見い出された。例えば、ヘキサン系では、ランタン(III)とルテチウム(III)の分配比は1桁程度しか違わないのに対して、クロロホルム系ではこの分配比に5桁の相違がみられた。このようなランタノイドの溶媒抽出における溶媒効果とその原因について、無極性溶媒である四塩化炭素と極性溶媒である1,2-ジクロロエタンを対象にさらに検討を加えた。

まず、ランタン(III), サマリウム(III), イッテルビウム(III)の分配比のTOPO濃度に対する依存性を求めた。金属イオンの初期濃度は放射性トレーサーを用いた場合10^{-5}M以下、ICP発光分析法を用いた場合には約10^{-3}Mであった。放射性トレーサーを用いた場合には、ランタノイド(III)の濃度が低い状態で実験が可能であることから、横軸のTOPO濃度は平衡時のTOPO濃度とみなすことができる。ランタン(III)では傾きが4に近い直線が得られるのに対して、イッテルビウム(III)では傾き3に近い直線が得られた。これは、ランタン(III)では主として4分子のTOPOを伴って抽出されるのに対して、イッテルビウム(III)では抽出化学種は3分子のTOPOを伴った形で抽出されることを意味する。

ICP発光分光法ではランタノイド(III)の濃度を高くする必要がある。このため、抽出率が低いランタン(III)では放射性トレーサーでの実験結果と一致するが、イッテルビウム(III)などではランタノイド(III)に配位していないTOPOの減少のために放射性トレーサーでの実験結果と大きな相違がみられた。このため、ICP発光分光法では得られた傾きから直接に抽出定数を決定することは出来ない。そこで、放射性トレーサーを用いた実験結果に基づいて抽出化学種を推定した上で、ICP発光分析法の実験結果を逐次近似法によって解析して抽出定数を求めた。

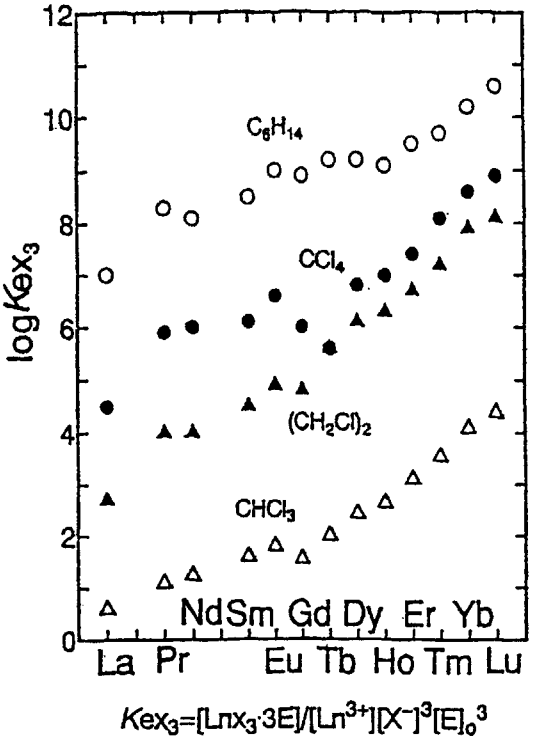

図 1: 1Mチオシアン酸ナトリウム水溶液からTOPOを含む種々の溶媒へのランタノイドの抽出における抽出定数の原子番号依存性(TOPOは3分子が配位)

ジクロロエタンを溶媒に用いた場合も、放射性トレーサー実験からはランタン(III)で傾き4、イッテルビウム(III)で傾き3の直線が得られた。ICP発光分光法により同様の実験を行ったが、それぞれ放射性トレーサーで得た結果に比べて、小さい傾きをとった。これは、ICP発光分光法では金属イオン濃度を高くする必要があったためである。このため、放射性トレーサー実験で抽出化学種を推定し、これに基づいてICP発光分光法での実験結果を解析して抽出定数を得ることとした。

1Mチオシアン酸ナトリウム水溶液からTOPOを含む種々の溶媒へのランタノイドの抽出について、抽出定数の原子番号依存性を示す(図1,2)。3分子のTOPOが配位した抽出化学種に対する抽出定数(K_{ex_3})を図1に、4分子のTOPOが配位した抽出化学種に対する抽出定数(K_{ex_4})を図2に示す。溶媒の違いにかかわらず、K_{ex_3}は軽ランタノイドから重ランタノイドに向かうに連れて増加する傾向が認められる。これに対して、K_{ex_4}では溶媒による違いも認められるが、全体としてランタノイド間の相違が小さくなる傾向がある。

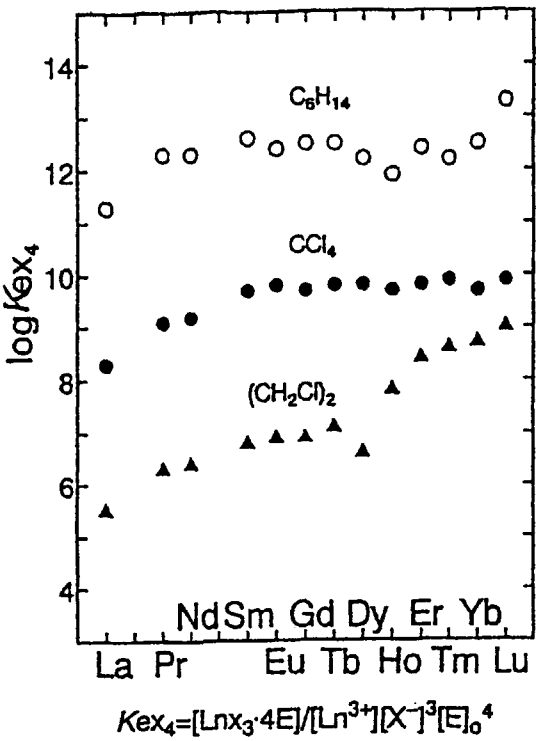

図2: 1Mチオシアン酸ナトリウム水溶液からTOPOを含む種々の溶媒へのランタノイドの抽出における抽出定数の原子番号依存性(TOPOは4分子が配位)

このような抽出挙動の相違は、ランタノイド(III)とTOPOとの静電的相互作用の強さと4番目のTOPO分子の配位に要するランタノイド(III)周辺の空間の広がりが、ランタノイド(III)相互で異なっていることを反映しているとみられる。

K_{ex_3}における溶媒効果についてみると、ヘキサン、四塩化炭素、1,2-ジクロロエタン、クロロホルムの順番に小さくなることがわかった。また、K_{ex_4}についてもヘキサンで一番大きい値をとり、以下、四塩化炭素、1,2-ジクロロエタンの順番で小さくなる傾向がみとめられた。クロロホルムについてはK_{ex_4}を得ることが出来なかったが、1,2-ジクロロエタンの場合に比べてはるかに小さい値をとるとみられる。溶媒の種類による抽出挙動の相違はTOPOと溶媒分子との相互作用の強さの相違に起因する可能性が指摘される。

以上のように、ランタノイド(III)相互の溶媒抽出挙動を比較することによって、ランタノイド(III)錯体の溶液内挙動について新たな知見を得ることができた。トレーサー実験は極微量のランタノイド(III)の化学的挙動を追跡する上で必須であり、溶媒抽出機構の解明に有効に利用することが出来た。

II. ランタノイド(III)–フミン酸錯体の安定度

地球上の岩石や堆積物中のランタノイドの含有量を隕石中の含有量で規格化すると、原子番号またはイオン半径に対応した連続的な変化が見られる。これは、イオン半径などのランタノイドの化学的性質に関与するパラメーターがランタノイド相互で連続的に変化するためと解釈される。堆積物や海水中のランタノイドの含有量を決定する要因について考えてみると、固液間のランタノイドの分配や固液界面での吸着平衡などが重要と考えられる。これらの溶液が関与するプロセスの詳細を理解するためには、海水などの溶液中でのランタノイドの存在状態を明らかにする必要がある。

海水や生物起源の堆積物についてみると、隕石や大陸地殻を代表するshale中の含有量で規格化されたランタノイドの含有量には、テトラド効果と呼ばれる微細構造がみとめられる場合がある。これには、有機錯体の生成が関与していることも可能性として指摘されている。有機錯体としては、環境中に普遍的に存在するフミン酸との錯体が候補の一つとして考えられる。本研究では、ランタノイド全体を通して、フミン酸との錯体の安定度を測定することを意図した。安定度のランタノイド相互間での相違は僅かであると考えられることから、複数のトレーサーを実験系に同時に適用して、相対的な安定度の違いを求めることとした。

平成6–8年度では当初の目的を達成するに至らなかったが、以下に経過を略述し、今後の研究の方針について述べる。

[実験] ランタノイドトレーサーの原子炉での製造に先立ち、市販の^{152}Euを用いて、フミン酸錯体の安定度を測定した。ジ(2-エチルヘキシル)リン酸による溶媒抽出における分配係数を求め、フミン酸濃度に対する依存性から、フミン酸錯体の安定度を求めた。pH、電解質濃度を変えて、安定度を求めた。また、複数トレーサーの同時適用の有効性を検証するために、理化学研究所で製造されたマルチトレーサーを用いて、ランタノイド相互並びに他の元素との安定度の相違について調べた。この部分の実験については、理化学研究所との共同研究であることから、本報告書の範囲を超えるものと思われる。このため、原研施設利用共同研究の実施のための予備実験と位置づけられるものに限り、その経過を述べるのに止める。

[研究の結果] 図3にユウロピウム(III)フミン酸錯体のみかけの安定度定数を示す。pH滴定で求めた遊離カルボキシル基濃度をフミン酸濃度として、安定度定数を得た。同じ方法で得たプロピオン酸錯体の安定度定数はいずれの測定条件でもほぼ一致した値を示した。これに対して、フミン酸錯体ではpHの増加に対して

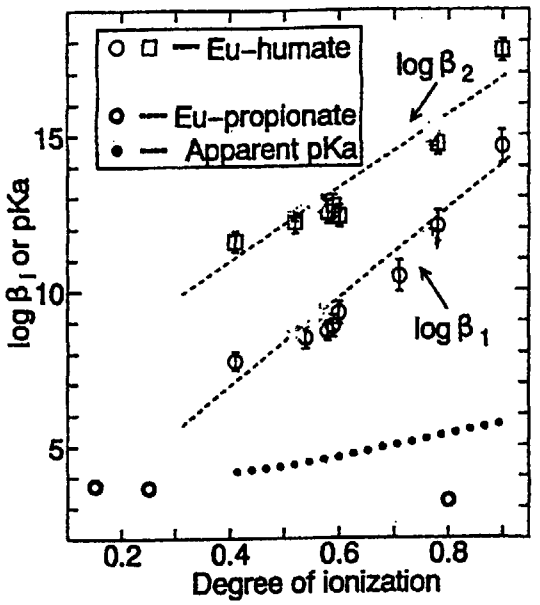

図3: フミン酸の解離度に対するユウロピウム(III)フミン酸錯体のみかけの安定度定数の依存性

みかけの安定度が増加する傾向がみとめられた。これは、pHの増加によるフミン酸の解離度の増加のために、フミン酸分子表面の負電荷密度が増加することによって、金属イオンとフミン酸分子との間の静電相互作用が強くなるためと考えられる。

得られた安定度定数のpHまたは電解質濃度に対する依存性から、地下水や海水環境でのフミン酸錯体の安定度を求めた。炭酸錯体の安定度や加水分解定数との関係並びにこれらの地球表層環境でのフミン酸濃度から、溶存ユウロピウム(III)中に占めるフミン酸錯体の割合を求めた所、フミン酸錯体の割合が大部分を占める場合があることが示された。この見積もりでは、フミン酸錯体の生成についてのユウロピウム(III)と他の金属イオンとの競合などを考えていないため、溶存化学種中に占めるフミン酸錯体の割合は過大に評価されている。その点を差し引いても、水圏に溶存するユウロピウム(III)の内、相当の部分がフミン酸錯体として存在している可能性は依然として高い。他のランタノイド(III)についても同様の可能性が指摘されることから、天然物でみられるテトラド効果の原因として、フミン酸錯体の生成を想定することは妥当とみられる。

金をターゲットとした重イオン核破砕反応により製造したマルチトレーサー中には、数種のランタノイド(III)のトレーサーが含まれていた。マルチトレーサー実験の結果は、ランタノイド(III)フミン酸錯体と他の金属イオンとの錯体との安定度の相違については多くの成果を得ることが出来た。しかし、ランタノイド(III)相互間では有為の差は認められなかった。透析膜を用いて錯体の安定度を相対的に評価することも試みたが、テトラド効果の存在を議論するに足る証左は得られなかった。このため、これらの実験で得られた成果は、本報告の予備的研究と位置づけるのは適当とは考えられず、本報告書における成果の公開とはみなさないこととした。また、テトラド効果に関する研究は実験精度の面で現状では問題があることから中断し、実試料の分析と室内実験データを組み合わせた形で、ランタノイド(III)と他の金属イオンとの地球表層での挙動の比較に研究の方向を転換することとした。

III. 成果の公表

1. Y. Hasegawa, F. Watanabe, and M. Takahashi, "Separation Factors in the Extraction of Thiocyanatolanthanoids(III) with Trioctylphosphine Oxide in Hexane and in Chloroform", Anal. Sci., 10, 167 (1994)
2. 山田、長田、広瀬、長谷川、「ナフタレン環を持つカルボン酸によるランタノイド(III)キレートの付加錯体生成」、第55回分析化学討論会1B04 (1994年6月11日)
3. 渡辺、関口、宮内、長谷川、「チオシアナトランタノイド(III)の抽出の大きさと分離係数に与える溶媒効果」、日本分析化学会第43年会1I16 (1994年10月13日)
4. Y. Minai, "Study on Environmental Behavior of Actinide and Lanthanide Elements", 8th Joint Russian-Japan Symposium on Analytical Chemistry, Moscow and Saratov, (1996年8月28日)
5. 薬袋、「アクチノイドの地中移行挙動へのフミン酸の影響」、武蔵大学人文学会雑誌、28(4), 134 (1997)

付　録 (1)
[Appendix (1)]

This is a blank page.

付 録(1)

事情により、研究炉利用の成果・連絡票のみの提出となった利用者について、その内容をここに示す。

(1/2)

研究テーマ「表題」	所属 担当者	利用原子炉及び装置名	報告書等	利用分野
原子力技術者の養成「イオン交換分離法によるFPの相互分離実験」	原研 燃料研究部 分析センター 佐々木祐二	JRR-3M HR-1	原子力総合研修センター、RI研修部門からの依頼により、基礎過程でイオン交換分離法によるFPの相互分離の実験を担当している。この実験に用いるFPを研究炉を利用し製造した。	トレーサー用RIの製造
環境試料中の重金属・有害元素の放射化分析	原研 環境安全研究部 環境化学研究室 上野 隆	JRR-3M PN-1,3	平成9年度は、十分なデータが揃っていないため、成果本文の提出はできない。	放射化分析
MPR-30(インドネシア)におけるエアゾル(^{131}Cs,^{11}Rb)の同定分析	原研 研究炉部 技術管理室 吉島 哲夫	JRR-3M PN-3	インドネシア研修生による研修のためで、独自で報告書をまとめたため。	放射化分析
高燃焼度用PWR燃料の照射特性に関する研究(三菱重工共同研究)	原研 核熱利用研究部 高温照射研究室 林 君夫	JRR-3M BR-3	平成9年度から照射開始で、18サイクル照射を継続する予定のため、まだ成果を得ていない。	原子炉燃料
再処理施設セル換気系安全性実証試験	原研 燃料サイクル安全工学部 エアロゾル安全工学研究室 高田 準一	JRR-3M PN	本テーマ(特会事業)の一環として、平成9年度第四半期にセシウムを含む模擬アスファルト固化体の燃焼時に気相へ放出されるセシウムエアロゾルの生成・挙動を調べる試験を実施したが、公開論文等が未発表のため成果本文を提出できない。	放射化分析
環境中^{129}Iの濃度調査	動燃 東海事業所 中野 政尚	JRR-3M HR-1	本研究テーマの成果は、原子力安全委員会月報により公開される。	放射化分析
陸上系環境放射能安全性実証試験	(財)環境科学技術研究所 塚田 祥文	JRR-3M PN-2	本研究テーマでは、大気中化学形態別ハロゲン濃度変化、土壌および農作物中元素濃度を放射化分析で測定しています。なお本研究は科学技術庁からの依頼により行われており、成果については報告できません。	放射化分析

(2/2)

依頼試料の分析	（財）放射線利用振興協会 吾勝　常勲	JRR-3M HR-1,2 PN-1,2,3	当協会では、諸機関から依頼された試料の放射化分析を行っています。結果については機密保持が契約条件であるため、成果報告の提出ができません。	放射化分析
炭素試験片の放射化分析	（株）豊田中央研究所 日比　章五	JRR-3M HR-1	予備検討段階であり、本文に報告するほどの内容になっていない。	放射化分析
中性子照射によるシリコン半導体の製造	（財）放射線利用振興協会 佐藤　久男	JRR-3M SI-1	シリコン・インゴットに中性子を照射してシリコン半導体（電子材料）を、定常的な業務として製造 している。	その他
低放射化ﾌｪﾗｲﾄ鋼の照射後疲労特性	原研　材料研究部 照射解析研究室 三輪　幸夫	JRR-3M BR-2	本件は材料照射研究で、照射後試験が必要。現在照射を開始したばかりであるため、成果報告の提出はできない。	原子炉材料
高純度Fe-Cr合金の照射効果研究	原研　材料研究部 照射解析研究室 三輪　幸夫	JRR-3M BR-2	本件は材料照射研究で、照射後試験が必要。現在照射中のため成果報告の提出はできない。	原子炉材料

付　録　(2)
[Appendix (2)]

This is a blank page.

付 録(2)

原研研究炉の利用設備一覧

1．ＪＲＲ－３Ｍ

1）実験設備

実　験　孔	実　　験　　装　　置
１Ｇ	高分解能粉末中性子回折装置（ＨＲＰＤ）
１Ｇ－Ａ	生体高分子結晶構造解析用中性子回折計（ＢＩＸ－Ｉ）
２Ｇ	三軸型中性子分光器（偏極機能付、ＴＡＳ－１）
３Ｇ	中性子トポグラフィ及び精密光学実験装置（ＰＮＯ）
４Ｇ	汎用三軸型中性子分光器（ＧＰＴＡＳ）
５Ｇ	偏極中性子散乱装置（ＰＯＮＴＡ）
６Ｇ	東北大学中性子散乱分光器（ＴＯＰＡＮ）
７Ｒ	中性子ラジオグラフィ装置（ＴＮＲＦ）
Ｔ１－１	中性子偏極回折装置（ＨＱＲ）
Ｔ１－２	単結晶中性子回折装置（ＫＳＤ）
Ｔ１－３	粉末中性子回折装置（ＫＰＤ） （ＨＥＲＭＥＳ）
Ｔ１－４－１	即発ガンマ線分析装置（ＰＧＡ）
Ｔ１－４－３	ＴＯＦ型中性子反射率計
Ｔ２－１	残留応力測定用中性子回折装置（ＲＥＳＡ）
Ｔ２－２	中性子単結晶４軸回折装置：未設置
Ｔ２－３	中性子ｲﾒｰｼﾞﾝｸﾞﾌﾟﾚｰﾄ付生体物質中性子回折計（ＢＩＸ－II）
Ｔ２－４	高分解能三軸型中性子分光器（ＴＡＳ－２）
Ｃ１－１	高エネルギー分解能三軸型中性子分光器（ＨＥＲ）
Ｃ１－２	二次元位置測定小角散乱装置（ＳＡＮＳ－Ｕ）
Ｃ１－３	超高分解能後方散乱装置（ＵＬＳ）
Ｃ２－１	冷中性子散乱実験デバイス開発装置（ＬＴＡＳ）
Ｃ２－２	中性子スペクトル変調・時間分析装置（ＮＳＭ） 中性子スピンエコー分光器（ＮＳＥ）
Ｃ２－３－１	冷中性子ラジオグラフィ装置（ＣＮＲＦ）
Ｃ２－３－２	即発ガンマ線分析装置（ＰＧＡ）
Ｃ２－３－４	ＴＯＦ型中性子反射率計
Ｃ３－１－１	高分解能パルス冷中性子分光器（ＡＧＮＥＳ）
Ｃ３－１－２	多層膜中性子干渉計（ＭＩＮＥ）
Ｃ３－２	中性子小角散乱装置（ＳＡＮＳ－Ｊ）

2）照射設備

水力照射設備	HR－1，2
気送照射設備	PN－1，2
放射化分析用照射設備	PN－3
均一照射設備	SI－1
回転照射設備	DR－1
垂直照射設備	VT－1，RG－1～4 BR－1～4，SH－1

2．JRR－4

1）実験設備

プール
中性子ビーム設備
散乱実験設備
冷却水循環ループ
医療照射設備（BNCT）
即発ガンマ線分析装置

2）照射設備

簡易照射筒	Tパイプ（水力）
	Sパイプ
	Dパイプ
	Nパイプ
気送管照射設備	PN

Appendix(2)

Utilization Facilities of Research Reactor

1.JRR-3M

1) Experimental Equipments

Beam Port	Experimental Equipments
1G	High Resolution Powder Diffractometer (HRPD)
1G-A	Diffractometer for Biological Crystallography- I (BIX- I)
2G	Triple-Axis Spectometer-1(TAS-1)
3G	Apparatus for Precise Neutron Optics and Neutron Diffraction Topography (PNO)
4G	Triple-Axis Spectometer (GPTAS)
5G	Polarized Neutron Triple-Axis Spectometer (PONTA)
6G	Tohoku-University Polarization Analysis Neutron Spectometer (TOPAN)
7R	Thermal Neutron Radiography (TNRF)
T1-1	High Q-Resolution Triple-Axis Spectometer (HQR)
T1-2	KINKEN Single-Crystal Diffractometer (KSD)
T1-3	KINKEN Powder Diffractometer (KPD) (HERMES)
T1-4-1	Prompt Gamma-ray Analysis (PGA)
T1-4-3	TOF Neutron Reflectometer (TOF)
T2-1	Diffractometer for Residual Stress Analysis (RESA)
T2-2	Four-Circle Diffractometer:Under Construction
T2-3	Diffractometer for Biological Crystallography- II (BIX- II)
T2-4	Triple-Axis Spectometer-2(TAS-2)
C1-1	High E-Resolution Triple-Axis Spectometer (HER)
C1-2	Small Angle Neutron Scattering Instrument University of Tokyo (SANS-U)
C1-3	Ultra Small Angle Neutron Scattering Instrument (ULS)
C2-1	Low Energy Triple-Axis Spectometer (LTAS)
C2-2	Neutron Spectral Modulation Spectrometer (NSM) Neutron Spin Echo Spectrometer (NSE)
C2-3-1	Cold Neutron Radiography (CNRF)
C2-3-2	Prompt Gamma-Ray Analysis (PGA)
C2-3-4	TOF Neutron Reflectometer (TOF)
C3-1-1	Angle Focusing Cold Neutron Spectrometer (AGNES)
C3-1-2	Multilayer Interferometer for Neutrons (MINE)
C3-2	Small Angle Neutron Scattering Instrument (SANS-J)

2) Irradiation Facilities

Hydraulic Rabbit Irradiation Facility	HR-1,2
Pneumatic Rabbit Irradiation Facility	PN-1,2
Activation analysis Irradiation Facility	PN-3
Uniform Irradiation Facility	SI-1
Rotating Irradiation Facility	DR-1
Capsule Irradiation Facility	VT-1,RG-1～4 BR-1～4,SH-1

2.JRR-4

1) Experimental Equipments

Pool
Scattering Experimental Faculity
Neutron Beam Facility
Coolingwater Circulation Loop
Medical Neutron Irradiation (BNCT)
Prompt Gamma-ray Analysis

2) Irradiation Facilities

Irradiation Tubes	T-Pipe
	S-Pipe
	D-Pipe
	N-Pipe
Pneumatic Rabbit Irradiation Facility	PN

国際単位系 (SI) と換算表

表 1　SI 基本単位および補助単位

量	名称	記号
長さ	メートル	m
質量	キログラム	kg
時間	秒	s
電流	アンペア	A
熱力学温度	ケルビン	K
物質量	モル	mol
光度	カンデラ	cd
平面角	ラジアン	rad
立体角	ステラジアン	sr

表 2　SI と併用される単位

名称	記号
分，時，日	min，h，d
度，分，秒	°，′，″
リットル	l，L
トン	t
電子ボルト	eV
原子質量単位	u

1 eV = 1.60218 × 10^{-19} J

1 u = 1.66054 × 10^{-27} kg

表 5　SI 接頭語

倍数	接頭語	記号
10^{18}	エクサ	E
10^{15}	ペタ	P
10^{12}	テラ	T
10^{9}	ギガ	G
10^{6}	メガ	M
10^{3}	キロ	k
10^{2}	ヘクト	h
10^{1}	デカ	da
10^{-1}	デシ	d
10^{-2}	センチ	c
10^{-3}	ミリ	m
10^{-6}	マイクロ	μ
10^{-9}	ナノ	n
10^{-12}	ピコ	p
10^{-15}	フェムト	f
10^{-18}	アト	a

表 3　固有の名称をもつ SI 組立単位

量	名称	記号	他の SI 単位による表現
周波数	ヘルツ	Hz	s^{-1}
力	ニュートン	N	m·kg/s^2
圧力，応力	パスカル	Pa	N/m^2
エネルギー，仕事，熱量	ジュール	J	N·m
工率，放射束	ワット	W	J/s
電気量，電荷	クーロン	C	A·s
電位，電圧，起電力	ボルト	V	W/A
静電容量	ファラド	F	C/V
電気抵抗	オーム	Ω	V/A
コンダクタンス	ジーメンス	S	A/V
磁束	ウェーバ	Wb	V·s
磁束密度	テスラ	T	Wb/m^2
インダクタンス	ヘンリー	H	Wb/A
セルシウス温度	セルシウス度	℃	
光束	ルーメン	lm	cd·sr
照度	ルクス	lx	lm/m^2
放射能	ベクレル	Bq	s^{-1}
吸収線量	グレイ	Gy	J/kg
線量当量	シーベルト	Sv	J/kg

表 4　SI と共に暫定的に維持される単位

名称	記号
オングストローム	Å
バーン	b
バール	bar
ガル	Gal
キュリー	Ci
レントゲン	R
ラド	rad
レム	rem

1 Å = 0.1 nm = 10^{-10} m

1 b = 100 fm^2 = 10^{-28} m^2

1 bar = 0.1 MPa = 10^5 Pa

1 Gal = 1 cm/s^2 = 10^{-2} m/s^2

1 Ci = 3.7 × 10^{10} Bq

1 R = 2.58 × 10^{-4} C/kg

1 rad = 1 cGy = 10^{-2} Gy

1 rem = 1 cSv = 10^{-2} Sv

（注）

1. 表 1 − 5 は「国際単位系」第 5 版，国際度量衡局 1985 年刊行による。ただし，1 eV および 1 u の値は CODATA の 1986 年推奨値によった。
2. 表 4 には海里，ノット，アール，ヘクタールも含まれているが日常の単位なのでここでは省略した。
3. bar は，JIS では流体の圧力を表わす場合に限り表 2 のカテゴリーに分類されている。
4. EC 閣僚理事会指令では bar，barn および「血圧の単位」mmHg を表 2 のカテゴリーに入れている。

換　算　表

力

N(=10^5 dyn)	kgf	lbf
1	0.101972	0.224809
9.80665	1	2.20462
4.44822	0.453592	1

粘度　1 Pa·s(N·s/m^2) = 10 P(ポアズ)(g/(cm·s))

動粘度　1 m^2/s = 10^4 St(ストークス)(cm^2/s)

圧力

MPa(=10 bar)	kgf/cm^2	atm	mmHg(Torr)	lbf/in^2(psi)
1	10.1972	9.86923	7.50062 × 10^3	145.038
0.0980665	1	0.967841	735.559	14.2233
0.101325	1.03323	1	760	14.6959
1.33322 × 10^{-4}	1.35951 × 10^{-3}	1.31579 × 10^{-3}	1	1.93368 × 10^{-2}
6.89476 × 10^{-3}	7.03070 × 10^{-2}	6.80460 × 10^{-2}	51.7149	1

エネルギー・仕事・熱量

J(=10^7 erg)	kgf·m	kW·h	cal(計量法)	Btu	ft·lbf	eV
1	0.101972	2.77778 × 10^{-7}	0.238889	9.47813 × 10^{-4}	0.737562	6.24150 × 10^{18}
9.80665	1	2.72407 × 10^{-6}	2.34270	9.29487 × 10^{-3}	7.23301	6.12082 × 10^{19}
3.6 × 10^6	3.67098 × 10^5	1	8.59999 × 10^5	3412.13	2.65522 × 10^6	2.24694 × 10^{25}
4.18605	0.426858	1.16279 × 10^{-6}	1	3.96759 × 10^{-3}	3.08747	2.61272 × 10^{19}
1055.06	107.586	2.93072 × 10^{-4}	252.042	1	778.172	6.58515 × 10^{21}
1.35582	0.138255	3.76616 × 10^{-7}	0.323890	1.28506 × 10^{-3}	1	8.46233 × 10^{18}
1.60218 × 10^{-19}	1.63377 × 10^{-20}	4.45050 × 10^{-26}	3.82743 × 10^{-20}	1.51857 × 10^{-22}	1.18171 × 10^{-19}	1

1 cal = 4.18605 J (計量法)
= 4.184 J (熱化学)
= 4.1855 J (15 °C)
= 4.1868 J (国際蒸気表)

仕事率　1 PS (仏馬力)
= 75 kgf·m/s
= 735.499 W

放射能

Bq	Ci
1	2.70270 × 10^{-11}
3.7 × 10^{10}	1

吸収線量

Gy	rad
1	100
0.01	1

照射線量

C/kg	R
1	3876
2.58 × 10^{-4}	1

線量当量

Sv	rem
1	100
0.01	1

（86 年 12 月 26 日現在）

研究炉利用における研究成果集（平成9年度）